

AR0 27596.3-BS-CF

AD-A226 300



VOLUME 166

Neutron Scattering For Materials Science

EDITORS

S. M. Shapiro

S. C. Moss

J. D. Jorgensen

DTIC FILE COPY

90 08 27 328

DTIC
SELECTE
AUG 29 1990
S D

DISTRIBUTION STATEMENT A

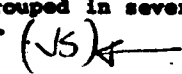
Approved for public release
Distribution Unlimited



REPORT DOCUMENTATION PAGE

Form Approved
OMB No. 0704-0188

Public reporting burden for this collection of information is estimated to average 1 hour per response, including the time for reviewing instructions, searching existing data sources, gathering and maintaining the data needed, and completing and reviewing the collection of information. Send comments regarding this burden estimate or any other aspect of this collection of information, including suggestions for reducing this burden to Washington Headquarters Services, Directorate for Information Operations and Reports, 1215 Jefferson Davis Highway, Suite 1204 Arlington, VA 22202-4302, and to the Office of Management and Budget, Paperwork Reduction Project (0704-0188), Washington, DC 20503.

1. AGENCY USE ONLY (Leave blank)		2. REPORT DATE 1990	3. REPORT TYPE AND DATES COVERED Book	
4. TITLE AND SUBTITLE Materials Research Society Symposium Proceedings: Neutron Scattering for Materials Science			5. FUNDING NUMBERS DAAL03-90-G-0014	
6. AUTHOR(S) John B. Ballance (Principal Investigator)				
7. PERFORMING ORGANIZATION NAME(S) AND ADDRESS(ES) Materials Research Society Pittsburgh, PA 15237			8. PERFORMING ORGANIZATION REPORT NUMBER	
9. SPONSORING/MONITORING AGENCY NAME(S) AND ADDRESS(ES) U. S. Army Research Office P. O. Box 12211 Research Triangle Park, NC 27709-2211			10. SPONSORING/MONITORING AGENCY REPORT NUMBER ARO 27596.3-MS-CF	
11. SUPPLEMENTARY NOTES The view, opinions and/or findings contained in this report are those of the author(s) and should not be construed as an official Department of the Army position, policy, or decision, unless so designated by other documentation.				
12a. DISTRIBUTION/AVAILABILITY STATEMENT Approved for public release; distribution unlimited.			12b. DISTRIBUTION CODE	
13. ABSTRACT (Maximum 200 words) Neutron Scattering is by now a well-established technique which has been used by condensed matter scientists to probe both the structure and the dynamical interactions in solids and liquids. The use of neutron scattering methods in materials science research has in turn increased dramatically in recent years. The symposium was assembled to bring together scientists with a wide range of interest, including high-T _c superconducting materials, phase transformations, neutron depth profiling, structure and dynamics of glasses and liquids, surfaces and interfaces, porous media, intercalation compounds and lower dimensional systems, structure and dynamics of polymers, residual stress analysis, ordering and phase separation in alloys, and magnetism in alloys and multilayers. The symposium included invited talks covering the latest advances in broad areas of interest such as Rietveld structure refinement, triple axis spectrometry, quasielastic scattering and diffusion, small angle scattering and surface scattering. Contributed papers reporting recent research results were often grouped in several subfields covered by invited, tutorial lectures. (JS) 				
14. SUBJECT TERMS Neutron Scattering, Materials, Condensed Matter, Symposium			15. NUMBER OF PAGES	
			16. PRICE CODE	
17. SECURITY CLASSIFICATION OF REPORT UNCLASSIFIED	18. SECURITY CLASSIFICATION OF THIS PAGE UNCLASSIFIED	19. SECURITY CLASSIFICATION OF ABSTRACT UNCLASSIFIED	20. LIMITATION OF ABSTRACT UL	

Neutron Scattering For Materials Science

Neutron Scattering For Materials Science

**Symposium held November 27-30, 1989, Boston,
Massachusetts, U.S.A.**

EDITORS:

S.M. Shapiro

Brookhaven National Laboratory, Upton, New York, U.S.A.

S.C. Moss

University of Houston, Houston, Texas, U.S.A.

J.D. Jorgensen

Argonne National Laboratory, Argonne, Illinois, U.S.A.

Sponsors

Argonne National Laboratory

Army Research Office

Brookhaven National Laboratory

Los Alamos National Laboratory

National Institute for Standards and Technology

Oak Ridge National Laboratory



MATERIALS RESEARCH SOCIETY

Pittsburgh, Pennsylvania

This work was supported in part by the U.S. Army Research Office under Grant Number DAAL03-90-G-0014. The views, opinions, and/or findings contained in this report are those of the authors and should not be construed as an official Department of the Army position, policy, or decision unless so designated by other documentation.

Single article reprints from this publication are available through University Microfilms Inc., 300 North Zeeb Road, Ann Arbor, Michigan 48106

CODEN: MRSPDH

Copyright 1990 by Materials Research Society.
All rights reserved.

This book has been registered with Copyright Clearance Center, Inc. For further information, please contact the Copyright Clearance Center, Salem, Massachusetts.

Published by:

Materials Research Society
9800 McKnight Road
Pittsburgh, Pennsylvania 15237
Telephone (412) 367-3003
Fax (412) 367-4373

Library of Congress Cataloging in Publication Data

Printed in the United States of America



Accession For	
NTIS CRA&I	<input checked="" type="checkbox"/>
DTIC TAB	<input type="checkbox"/>
Unannounced	<input type="checkbox"/>
Justification	
By <u>47⁰⁰</u> per call	
Distribution	
Availability Codes	
Dist	Avail and/or Special
A-1	21

AVAILABLE FOR \$47.00 from Materials
Research Society, 9800 McKnight Road
Suite 327, Pittsburgh, PA 15237
TELECON 8/28/90 VG

Contents

PREFACE	xi
MATERIALS RESEARCH SOCIETY SYMPOSIUM PROCEEDINGS	xiii
PART I: INTRODUCTION TO NEUTRON SCATTERING	
*NEUTRONS: THE KINDER, GENTLER PROBE OF CONDENSED MATTER John D. Axe	3
*NEUTRON SCATTERING METHODS FOR MATERIAL SCIENCE Roger Pynn	15
*THE ADVANCED NEUTRON SOURCE John B. Hayter	27
PART II: EXPERIMENTAL TECHNIQUES	
*NEUTRON POWDER DIFFRACTION: A POWERFUL MATERIALS RESEARCH TECHNIQUE W.I.F. David	41
THE APPLICATION OF NEUTRON TOPOGRAPHY TO THE STUDY OF X-RAY SENSITIVE ORGANIC CRYSTALS - A POSSIBLE ALTERNATIVE TO X-RAY TOPOGRAPHY M. Dudley	55
MULTIPLE SMALL ANGLE NEUTRON SCATTERING CHARACTERIZA- TION OF THE DENSIFICATION OF ALUMINA S. Krueger, G.G. Long, and R.A. Page	61
THERMAL DIFFUSE SCATTERING IN NEUTRON TIME-OF-FLIGHT POWDER PATTERNS Michael J. Radler	67
REAL SPACE METHOD OF POWDER DIFFRACTION FOR NON-PERIODIC AND NEARLY PERIODIC MATERIALS T. Egami, B.H. Toby, W. Dmowski, Chr. Janot, and J.D. Jorgensen	75
NEUTRON RIETVELD ANALYSIS OF ANION AND CATION DISORDER IN THE FAST-ION CONDUCTING PYROCHLORE SYSTEM $Y_2(Zr_xTi_{1-x})_2O_7$ Sossina M. Haile, B.J. Wuensch, and E. Prince	81
A SMALL ANGLE NEUTRON SCATTERING INVESTIGATION OF COMPACTED NANOPHASE TiO_2 AND Pd J.E. Epperson, R.W. Siegel, J.W. White, J.A. Eastman, Y.X. Liao, and A. Narayanasamy	87

*Invited Paper

PART III: SURFACES, FILMS AND INTERFACES

*SURFACE INVESTIGATION BY NEUTRON REFLECTION B. Farnoux	95
INTERDIFFUSION OF CADMIUM ARACHIDATE IN LANGMUIR- BLODGETT FILMS Pieter Stroeve, John F. Rabolt, Russ O. Hilleke, Gian P. Felcher, and Sow-Hsin Chen	103
A NEUTRON REFLECTIVITY STUDY OF THE INTERFACIAL MAGNETISM OF AN Y/Gd FILM J.F. Ankner, H. Zabel, D.A. Neumann, C.F. Majkrzak, A. Matheny, J.A. Dura, and C.P. Flynn	109
NEUTRON DIFFRACTION STUDIES OF Cd _{1-x} Mn _x Se EPILAYERS AND ZnSe/MnSe MULTILAYERS T.M. Gebultowicz, P. Klosowski, J.J. Rhyne, N. Samarth, H. Luo, and J.K. Furdyna	115
LOCAL ENVIRONMENTAL EFFECTS IN MAGNETIC ALLOYS AND MULTILAYERS: CALCULATIONS OF THE STATIC RESPONSE FUNCTIONS D.D. Johnson, J.B. Staunton, B.L. Györfy, F.J. Pinski, and G.M. Stocks	121
DETERMINATION OF HYDROGEN (DEUTERIUM) DENSITY PROFILES IN THIN METAL FILMS AND MULTILAYERS BY NEUTRON REFLECTION C.F. Majkrzak, S. Satija, D.A. Neumann, J.J. Rush, D. Lashmore, C. Bradshaw, L. Passell, and R. DiNardo	127
MAGNETOELASTICITY IN RARE-EARTH MULTILAYERS AND FILMS R.W. Erwin, J.J. Rhyne, J. Borchers, M.B. Salamon, R. Du, and C.P. Flynn	133
THE MORPHOLOGY OF SYMMETRIC DIBLOCK COPOLYMERS AS REVEALED BY NEUTRON REFLECTIVITY S.K. Satija, C.F. Majkrzak, S.H. Anastasiadis, and T.P. Russell	139
TEMPERATURE DEPENDENCE OF THE MORPHOLOGY OF THIN DIBLOCK COPOLYMER FILMS AS REVEALED BY NEUTRON REFLECTIVITY T.P. Russell, S.H. Anastasiadis, S.K. Satija, and C.F. Majkrzak	145
THE STUDY OF SURFACES AND INTERFACES ON THE REFLECTOMETER CRISP AT THE ISIS PULSED NEUTRON SOURCE J. Penfold	151

PART IV: PHASE TRANSFORMATIONS AND HIGH T_c

*PHONONS AT MARTENSITIC PHASE TRANSITIONS OF bcc-Ti, bcc-Zr, AND bcc-Hf W. Petry, A. Heiming, and J. Trampenau	161
--	-----

*Invited Paper

POLARIZATION RELAXATION IN KDP-ISOMORPH FERROELECTRICS Vicki Homer and Ronald Edge	175
STRUCTURE OF $\text{ErBa}_2\text{Cu}_3\text{O}_x$ IN THE COMPOSITION RANGE $6.1 \leq x < 7.0$ E. Pörschke, P. Meuffels, and B. Rupp	181
NEUTRON POWDER DIFFRACTION STUDY OF THE STRUCTURES OF $\text{La}_{1.9}\text{Ca}_{1.1}\text{Cu}_2\text{O}_6$ AND $\text{La}_{1.9}\text{Sr}_{1.1}\text{Cu}_2\text{O}_{6+\delta}$ A. Santoro, F. Beech, and R.J. Cava	187
NEUTRON DEPOLARIZATION BY FLUX LATTICES IN HIGH- T_c MATERIALS S.J. Pickart, A.C. Nunes, M.L. Crow, Bo Fu, T.R. McGuire, S. Shinde, and S.A. Shivashankar	193
USE OF NEUTRON DIFFRACTION IN DETERMINING STRAINS IN HIGH-TEMPERATURE SUPERCONDUCTING COMPOSITES D.S. Kuperman, J.P. Singh, S. Majumdar, R.L. Hitterman, and J. Faber Jr.	195
HIGH RESOLUTION NEUTRON POWDER DIFFRACTION STUDIES OF THE FERROELASTIC PHASE TRANSITION IN LaNbO_4 W.I.F. David	203

PART V: ALLOYS

*NEUTRON SCATTERING FROM LATTICE DEFECTS Johann Peisl, Helmut Dosch, and Stefan Kirchner	211
SHORT-RANGE ORDER IN α -BRASS L. Reinhard, B. Schoenfeld, G. Kostorz, and W. Buehrer	219
A FIRST-PRINCIPLES STUDY OF SHORT RANGE ORDER IN Cu-Zn M. Sluiter, P.E.A. Turchi, D.D. Johnson, F.J. Pinski, D.M. Nicholson, and G.M. Stocks	225
ORDERING MECHANISM IN Ni-Cr ALLOYS: THEORY AND EXPERI- MENT P.E.A. Turchi, F.J. Pinski, R.H. Howell, A.L. Wachs, M.J. Fluss, D.D. Johnson, G.M. Stocks, D.M. Nicholson, and W. Schweika	231
PHONON DISPERSION AND KOHN ANOMALIES IN THE ALLOY $\text{Cu}_{0.84}\text{Al}_{0.16}$ Henry Chou, S.M. Shapiro, S.C. Moss, and Mark Mostoller	237
PHASE DIAGRAMS AND DIFFUSE NEUTRON SCATTERING Rene Caudron, Maurice Sarfati, Alphonse Finel, and Francine Solal	243
DIFFUSE NEUTRON SCATTERING STUDY OF SHORT-RANGE ORDER IN $\text{Fe}_{0.8}\text{Al}_{0.2}$ ALLOY Werner Schweika	249

*Invited Paper

LATTICE MISFIT AND DECOMPOSITION IN Ni-Al-Mo ALLOYS Hector Calderon and Gernot Kostorz	255
INFLUENCE OF INTERSTITIAL OXYGEN ON THE LATTICE PARAMETERS OF SOLUTION-TREATED AND AGED Ti-8.6 wt% Al ALLOYS G.T. Gray III and A.C. Lawson	261
IN-BEAM SMALL-ANGLE SCATTERING STUDIES OF PHASE SEPARATION IN Ni-Ti SINGLE CRYSTALS Alberto Cerri, Bernd Schoenfeld, Gernot Kostorz, and Albert F. Wright	267
SANS MEASUREMENT OF DEUTERIUM-DISLOCATION CORRELATION IN PALLADIUM Brent J. Heuser, G.C. Summerfield, J.S. King, and J.E. Epperson	273
PART VI: RESIDUAL STRESS AND ANALYTICAL TECHNIQUES	
*RESIDUAL STRESS ANALYSIS WITH NEUTRONS Aaron D. Krawitz	281
RESIDUAL STRESS MEASUREMENTS BY MEANS OF NEUTRON DIFFRACTION H.J. Prask and C.S. Choi	293
RESIDUAL STRESS ANALYSIS BY NEUTRON TIME-OF-FLIGHT AT A REACTOR SOURCE H.G. Priesmeyer and J. Schröder	299
NON-DESTRUCTIVE MEASUREMENT OF RESIDUAL STRESSES IN U-0.8 wt% Ti BY NEUTRON DIFFRACTION A. Salinas-Rodriguez, J.H. Root, T.M. Holden, S.R. MacEwen, and G.M. Ludtka	305
NEUTRON MEASUREMENT OF RESIDUAL STRESSES IN A USED RAILWAY RAIL P.J. Webster, K.S. Low, G. Mills, and G.A. Webster	311
NEUTRON DIFFRACTION MEASUREMENT OF THE STRESS FIELD DURING FATIGUE CYCLING OF A CRACKED TEST SPECIMEN M.T. Hutchings, C.A. Hipsley, and V. Rainey	317
*THE MEASUREMENT OF BORON AT SILICON WAFER SURFACES BY NEUTRON DEPTH PROFILING R.G. Downing, J.P. Lavine, T.Z. Hossain, J.B. Russell, and G.P. Zenner	323
NEUTRON DEPTH PROFILES OF BORON IMPLANTED SEMICONDUCTORS Robert C. Bowman, Jr., John F. Knudsen, and R. Gregory Downing	331
TOF MEASUREMENTS OF PULSED NEUTRONS FOR TEXTURE ANALYSIS OF LOW SYMMETRY MATERIALS Allen C. Larson, Phillip J. Vergamini, and Hans-Rudolf Wenk	337

*Invited Paper

PART VII: DISORDERED SYSTEMS

*STRUCTURE AND DYNAMICS OF GLASSES AND LIQUIDS David L. Price	345
DYNAMICS OF WEAKLY CONNECTED SOLIDS: SINTERING OF POLY- MERIC AEROGELS D.W. Schaefer, D. Richter, B. Farago, C.J. Brinker, C.S. Ashley, B.J. Olivier, and P. Seeger	355
VIBRATIONAL SPECTRA FOR HYDROGENATED AMORPHOUS SEMI- CONDUCTORS W.A. Kamitakahara, R. Biswas, A.M. Bouchard, F. Gompf, and J.B. Suck	361
INELASTIC NEUTRON SCATTERING STUDIES OF NONLINEAR OPTICAL MATERIALS: p-NITRONANILINE ADSORBED IN ALPO-5 Jacqueline M. Nicol, Terrence J. Udovic, J.J. Rush, Sherman D. Cox, and Galen D. Stucky	367
DIFFUSE NEUTRON SCATTERING FROM EXCESS OXYGEN IN UO _{2.13} J.P. Goff, M.T. Hutchings, K. Brown, W. Hayes, and H. Godfrin	373
COMPARISON OF NEUTRON ELASTIC AND INELASTIC SCATTERING FROM FUSED QUARTZ, CAB-O-SIL AND AEROGEL John H. Root, William J.L. Buyers, John H. Page, Dale W. Schaefer, and C.J. Brinker	379
THERMAL EXPANSION OF GRAPHITE AND HNO ₃ -GRAPHITE INTER- CALATION COMPOUNDS, A NEUTRON DIFFRACTION STUDY Haim Pinto, Mordechai Melamud, and Hagai Shaked	385
CHARACTERIZATION OF SOL-CLAY COMPOSITES BY SMALL-ANGLE NEUTRON SCATTERING Ahmad Moini, Thomas J. Pinnavaia, and P. Thiyagarajan	391
NEUTRON SCATTERING STUDY OF LAYERED SILICATES PILLARED WITH ALKYLAMMONIUM IONS D.A. Neumann, J.M. Nicol, J.J. Rush, N. Wada, Y.B. Fan, H. Kim, S.A. Solin, T.J. Pinnavaia, and S.F. Trevino	397
OBSERVATION OF MICELLAR FORMATION IN THE CAVITY OF POROUS SILICA GLASS K.F. Bradley, S-H. Chen, and P. Thiyagarajan	403
ANALYSIS OF SANS FROM CONTROLLED PORE GLASSES N.F. Berk, C.J. Glinka, W. Haller, and L.C. Sander	409
CHARACTERIZATION OF CHEMICALLY MODIFIED PORE SURFACES BY SMALL ANGLE NEUTRON SCATTERING C.J. Glinka, L.C. Sander, S.A. Wise, and N.F. Berk	415
SMALL ANGLE NEUTRON SCATTERING AND SMALL ANGLE X-RAY SCATTERING FROM BULK MICROPOROUS SILICA G.G. Long, S. Krueger, D.R. Black, J.P. Cline, P.R. Jemian, and R.A. Gerhardt	421

*Invited Paper

SMALL ANGLE NEUTRON SCATTERING STUDY OF CRITICAL BINARY FLUIDS IN POROUS GLASSES S.B. Dierker and P. Wiltzius	427
SMALL ANGLE NEUTRON SCATTERING STUDY OF SOL-GEL GLASSES P. Wiltzius and S.B. Dierker	433
NEUTRON IRRADIATED URANIUM SILICIDES STUDIED BY NEUTRON DIFFRACTION AND RIETVELD ANALYSIS R.C. Birtcher, M.H. Mueller, J.W. Richardson, Jr., and J. Faber, Jr.	437
GAS DENSITY IN HELIUM BUBBLES IN NICKEL AND IRON DETER- MINED BY SMALL ANGLE NEUTRON SCATTERING D. Schwahn	443
A SANS STUDY OF CAPILLARY CONDENSATION IN POROUS MEDIA M.Y. Lin, S.K. Sinha, J.S. Huang, B. Abeles, J.W. Johnson, J.M. Drake, and C.J. Glinka	449
PART VIII: POLYMERS	
*DYNAMICS OF STAR-BRANCHED POLYMERS IN SOLUTION J.S. Huang, L.J. Fetters, D. Richter, B. Farago, and B. Ewen	457
MICROSTRUCTURE AND ISOTOPIC LABELING EFFECTS ON THE MISCIBILITY OF POLYBUTADIENE BLENDS STUDIED BY THE SMALL- ANGLE NEUTRON SCATTERING TECHNIQUE Charles C. Han, Hirokazu Hasegawa, Takeji Hashimoto, I. Glen Hargis, and S.L. Aggarwal	469
CHARACTERIZATION OF MOLECULAR NETWORK OF THERMOSETS USING NEUTRON SCATTERING Wen-Li Wu	475
SHEAR INDUCED PHASE BEHAVIOR OF POLYMER BLENDS BY SMALL ANGLE NEUTRON SCATTERING Alan I. Nakatani, Hongdoo Kim, and Charles C. Han	479
SURFACE ENRICHMENT AND EVAPORATION IN A POLYMER MIXTURE OF LONG AND SHORT CHAINS Russell J. Composto, Richard S. Stein, Gian P. Felcher, Abdelkader Mansour, and Alamgir Karim	485
AUTHOR INDEX	491
SUBJECT INDEX	495
FORMULA AND COMPOUND INDEX	499
MATERIALS RESEARCH SOCIETY SYMPOSIUM PROCEEDINGS	501

*Invited Paper

Preface

This proceedings volume contains the refereed invited and contributed papers from the symposium "Neutron Scattering for Materials Science" held November 27-30, 1989 at the MRS Fall Meeting in Boston.

Neutron Scattering is by now a well-established technique which has been used by condensed matter scientists to probe both the structure and the dynamical interactions in solids and liquids. The use of neutron scattering methods in materials science research has in turn increased dramatically in recent years. The symposium was assembled to bring together scientists with a wide range of interest, including high- T_c superconducting materials, phase transformations, neutron depth profiling, structure and dynamics of glasses and liquids, surfaces and interfaces, porous media, intercalation compounds and lower dimensional systems, structure and dynamics of polymers, residual stress analysis, ordering and phase separation in alloys, and magnetism in alloys and multilayers. The symposium included invited talks covering the latest advances in broad areas of interest such as Rietveld structure refinement, triple axis spectrometry, quasielastic scattering and diffusion, small angle scattering and surface scattering. Contributed papers reporting recent research results were often grouped in several subfields covered by invited, tutorial lectures.

We were extremely pleased by the response to this symposium. Approximately 80 papers were presented, and the attendance was excellent leading us to believe that the application of neutron methods to materials research may well be at a watershed stage.

We wish to thank the Materials Research Society for supporting our proposal to sponsor such a symposium and to the MRS staff for their extraordinary help in the organization of this symposium. We thank the many scientists who contributed by discussing the basic concepts of neutron scattering and presenting their latest research results. We also give thanks to Argonne National Laboratory, Army Research Office, Brookhaven National Laboratory, Los Alamos National Laboratory, National Institute for Standards and Technology, and the Oak Ridge National Laboratory without whose generous support this symposium could not have been held. Finally, we wish to thank Ms. Eileen Morello whose help was indispensable in preparing this book.

January 1990

Stephen M. Shapiro
Simon C. Moss
James D. Jorgensen

MATERIALS RESEARCH SOCIETY SYMPOSIUM PROCEEDINGS

Recent Materials Research Society Symposium Proceedings

- Volume 145—III-V Heterostructures for Electronic/Photonic Devices, C.W. Tu, V.D. Matterna, A.C. Gossard, 1989, ISBN: 1-55899-018-6
- Volume 146—Rapid Thermal Annealing/Chemical Vapor Deposition and Integrated Processing, D. Hodul, J. Gelpey, M.L. Green, T.E. Seidel, 1989, ISBN: 1-55899-019-4
- Volume 147—Ion Beam Processing of Advanced Electronic Materials, N.W. Cheung, A.D. Marwick, J.B. Roberto, 1989, ISBN: 1-55899-020-8
- Volume 148—Chemistry and Defects in Semiconductor Heterostructures, M. Kawabe, T.D. Sands, E.R. Weber, R.S. Williams, 1989, ISBN: 1-55899-021-6
- Volume 149—Amorphous Silicon Technology-1989, A. Madan, M.J. Thompson, P.C. Taylor, Y. Hamakawa, P.G. LeComber, 1989, ISBN: 1-55899-022-4
- Volume 150—Materials for Magneto-Optic Data Storage, C.J. Robinson, T. Suzuki, C.M. Falco, 1989, ISBN: 1-55899-023-2
- Volume 151—Growth, Characterization and Properties of Ultrathin Magnetic Films and Multilayers, B.T. Jonker, J.P. Heremans, E.E. Marinero, 1989, ISBN: 1-55899-024-0
- Volume 152—Optical Materials: Processing and Science, D.B. Poker, C. Ortiz, 1989, ISBN: 1-55899-025-9
- Volume 153—Interfaces Between Polymers, Metals, and Ceramics, B.M. DeKoven, A.J. Gellman, R. Rosenberg, 1989, ISBN: 1-55899-026-7
- Volume 154—Electronic Packaging Materials Science IV, R. Jaccodine, K.A. Jackson, E.D. Lillie, R.C. Sundahl, 1989, ISBN: 1-55899-027-5
- Volume 155—Processing Science of Advanced Ceramics, I.A. Aksay, G.L. McVay, D.R. Ulrich, 1989, ISBN: 1-55899-028-3
- Volume 156—High Temperature Superconductors: Relationships Between Properties, Structure, and Solid-State Chemistry, J.R. Jorgensen, K. Kitazawa, J.M. Tarascon, M.S. Thompson, J.B. Torrance, 1989, ISBN: 1-55899-029
- Volume 157—Beam-Solid Interactions: Physical Phenomena, J.A. Knapp, P. Borgesen, R.A. Zuhr, 1989, ISBN 1-55899-045-3
- Volume 158—In-Situ Patterning: Selective Area Deposition and Etching, R. Rosenberg, A.F. Bernhardt, J.G. Black, 1989, ISBN 1-55899-046-1
- Volume 159—Atomic Scale Structure of Interfaces, R.D. Bringans, R.M. Feenstra, J.M. Gibson, 1989, ISBN 1-55899-047-X
- Volume 160—Layered Structures: Heteroepitaxy, Superlattices, Strain, and Metastability, B.W. Dodson, L.J. Schowalter, J.E. Cunningham, F.H. Pollak, 1989, ISBN 1-55899-048-8
- Volume 161—Properties of II-VI Semiconductors: Bulk Crystals, Epitaxial Films, Quantum Well Structures and Dilute Magnetic Systems, J.F. Schetzina, F.J. Bartoli, Jr., H.F. Schaake, 1989, ISBN 1-55899-049-6
- Volume 162—Diamond, Boron Nitride, Silicon Carbide and Related Wide Bandgap Semiconductors, J.T. Glass, R.F. Messier, N. Fujimori, 1989, ISBN 1-55899-050-X
- Volume 163—Impurities, Defects and Diffusion in Semiconductors: Bulk and Layered Structures, J. Bernholc, E.E. Haller, D.J. Wolford, 1989, ISBN 1-55899-051-8
- Volume 164—Materials Issues in Microcrystalline Semiconductors, P.M. Fauchet, C.C. Tsai, K. Tanaka, 1989, ISBN 1-55899-052-6
- Volume 165—Characterization of Plasma-Enhanced CVD Processes, G. Lucovsky, D.E. Ibbotson, D.W. Hess, 1989, ISBN 1-55899-053-4
- Volume 166—Neutron Scattering for Materials Science, S.M. Shapiro, S.C. Moss, J.D. Jorgensen, 1989, ISBN 1-55899-054-2

MATERIALS RESEARCH SOCIETY SYMPOSIUM PROCEEDINGS

- Volume 167—Advanced Electronic Packaging Materials, A. Barfknecht, J. Partridge, C.-Y. Li, C.J. Chen, 1989, ISBN 1-55899-055-0
- Volume 168—Chemical Vapor Deposition of Refractory Metals and Ceramics, T.M. Besmann, B.M. Gallois, 1989, ISBN 1-55899-056-9
- Volume 169—High Temperature Superconductors: Fundamental Properties and Novel Materials Processing, J. Narayan, C.W. Chu, L.F. Schneemeyer, D.K. Christen, 1989, ISBN 1-55899-057-7
- Volume 170—Tailored Interfaces in Composite Materials, C.G. Pantano, E.J.H. Chen, 1989, ISBN 1-55899-058-5
- Volume 171—Polymer Based Molecular Composites, D.W. Schaefer, J.E. Mark, 1989, ISBN 1-55899-059-3
- Volume 172—Optical Fiber Materials and Processing, J.W. Fleming, G.H. Sigel, S. Takahashi, P.W. France, 1989, ISBN 1-55899-060-7
- Volume 173—Electrical, Optical and Magnetic Properties of Organic Solid-State Materials, L.Y. Chiang, D.O. Cowan, P. Chaikin, 1989, ISBN 1-55899-061-5
- Volume 174—Materials Synthesis Utilizing Biological Processes, M. Alper, P.D. Calvert, P.C. Rieke, 1989, ISBN 1-55899-062-3
- Volume 175—Multi-Functional Materials, D.R. Ulrich, F.E. Karasz, A.J. Buckley, G. Gallagher-Daggitt, 1989, ISBN 1-55899-063-1
- Volume 176—Scientific Basis for Nuclear Waste Management XIII, V.M. Oversby, P.W. Brown, 1989, ISBN 1-55899-064-X
- Volume 177—Macromolecular Liquids, C.R. Safinya, S.A. Safran, P.A. Pincus, 1989, ISBN 1-55899-065-8
- Volume 178—Fly Ash and Coal Conversion By-Products: Characterization, Utilization and Disposal VI, F.P. Glasser, R.L. Day, 1989, ISBN 1-55899-066-6
- Volume 179—Specialty Cements with Advanced Properties, H. Jennings, A.G. Landers, B.E. Scheetz, I. Odler, 1989, ISBN 1-55899-067-4

MATERIALS RESEARCH SOCIETY MONOGRAPH

Atom Probe Microanalysis: Principles and Applications to Materials Problems,
M.K. Miller, G.D.W. Smith, 1989; ISBN 0-931837-99-5

Earlier Materials Research Society Symposium Proceedings listed in the back.

PART I

Introduction to Neutron Scattering

NEUTRONS: THE KINDER, GENTLER PROBE OF CONDENSED MATTER

JOHN D. AXE
Brookhaven National Laboratory, Upton NY 11973

ABSTRACT

Neutrons play an increasingly important role in the characterization of advanced modern materials. They provide information that complements rather than competes with that provided by other scattering probes. Although neutrons require heroic efforts to produce, the techniques for using them are not particularly difficult, and with the advent of sufficient user friendly facilities, are becoming a routine tool in the arsenal of expanding numbers of materials scientists.

INTRODUCTION

Perhaps our growing understanding of elementary particles will someday allow us to design probes of condensed matter in much the same way as we manipulate the properties of molecules or genes today. But even with such unlimited possibilities it is hard to imagine improving much upon the particle that James Chadwick discovered in 1932.

Unlike beams of electromagnetic radiation, electrons or other charged particles which are used as probes and which interact primarily through the long-range Coulomb fields, neutrons interact primarily by way of nuclear forces. Although these forces are strong they are sufficiently short-ranged to allow neutrons to penetrate deeply (several centimeters) into most materials, whereas electrons or x-rays of comparable wavelength are confined to the surface. As a consequence neutrons easily probe materials in the bulk, even perhaps in a complex high pressure or low temperature environment. (Neutron scattering measurements have studied the spontaneous nuclear magnetization in silver at temperatures as low as $2 \times 10^{-9} \text{K}$ [1].) The nuclear forces vary from isotope to isotope (even for the same element) in an erratic way, a fact that has been used to advantage in structural investigations of materials containing light atoms, and has been rendered more powerful by ingenious isotopic labeling schemes in the study of polymers, molecular assemblies such as micelles, and biological systems.

Thermal neutrons, which are readily produced in the core of a reactor or through moderation of spallation neutrons in a pulsed proton accelerator have a wavelength distribution peaked around 1.6Å, and are well suited for studying variations in atomic structure on a microscopic scale. Yet, thermal neutrons, which by definition have no more energy than a room temperature air molecule, cannot disrupt even the most delicate of materials under study. This is a direct consequence of the relatively heavy mass of the neutron. (By contrast, x-rays or electrons with wavelengths around 1Å have energies around 12 keV and 3.3 eV, respectively.) An even more fundamental consequence of neutron mass is that thermal neutrons have energies comparable to the thermally induced fluctuations in solids (about 1/40 eV), making them uniquely well suited to the study of the thermally important dynamics of materials by inelastic scattering. In addition, the magnetic moment of the neutron provides it with a unique

4

capability of examining the magnetic properties of materials, crystal field levels, and particularly the dynamics of such systems.

INSTRUMENTATION AND SOURCES

Perhaps less well known than these special properties of neutrons is the quiet progress that has been made in the energy range available for neutron studies, which has expanded greatly due to new developments in sources and instrumentation in the last one and a half decades. Figure 1 shows the energy-momentum region available to the modern practitioner of neutron scattering. With current techniques one can study excitation energies varying over some seven orders of magnitude, and excitation wavelengths varying over six orders of magnitude.

Studies that involve large energy or momentum transfer naturally require epithermal neutrons. Pulsed spallation neutron sources have greatly expanded our capabilities in this area. To see why this is so, note that the very short pulses (sub-microsecond duration) of 500-1000 Mev protons supplied by the accelerator produce equally short bursts of fast neutrons. The energy of these neutrons must be slowed by collisions in a surrounding moderator. These moderators must achieve a compromise between slowing power and burst width of the slowed neutrons, which varies between 1 to 50 microsecond duration. As a result, the spectral characteristics of neutrons from pulsed sources differ from those of reactor neutrons, in that there is a much larger component of higher-energy neutrons (energies above 100 meV). The exploitation of this new energy regime is one of the great opportunities presented by spallation sources.

A more fundamental difference between reactor and pulsed neutron sources is that all experiments at pulsed sources involve time-of-flight techniques to analyze the scattering events. Since the neutron bursts are spaced 20 to 100 milliseconds apart, the duty cycle is low. Furthermore, the peak intensity of the neutron bursts from existing spallation sources do not greatly exceed the steady state value from the highest flux research reactors. Fortunately, for many types of experiments the time structure of the bursts can be used in a very efficient way to more than overcome the disparity. A comparison of a typical diffraction experiment with steady state and pulsed neutron sources is outlined in Figure 2. On the left, a monochromator crystal selects a narrow band of neutron energies from the thermal distribution of a reactor. This monochromatic beam falls on a sample, which scatters the beam from one diffracting plane into the detector. The detector signal is constant in time. On the right, the pulsed source allows a wide spectrum of neutron energies to fall on the sample in sharp pulses. Neutrons of many energies are then simultaneously scattered by different diffracting planes and their times of arrival are analyzed to determine the nature of the scattering. Thus the time-of-flight method uses a much larger interval of the energy spectrum than does the steady state method (center panel of Figure 2).

Table I shows a comparison of the major U.S. research reactor facilities in the U.S. Also shown is the major European neutron scattering center at Institute Laue-Langevin in Grenoble, France. Note that the characteristics of the ILL source are very similar to those of the HFBR and HFIR, but that there are many more instruments. This is the result of the extensive use of neutron guides, which totally reflect long wavelength neutrons, leading them to guide halls physically removed from the crowded central reactor floor. In such a low background environment there is ample room for additional instruments. Table II shows a similar comparison of the U.S. pulsed neutron

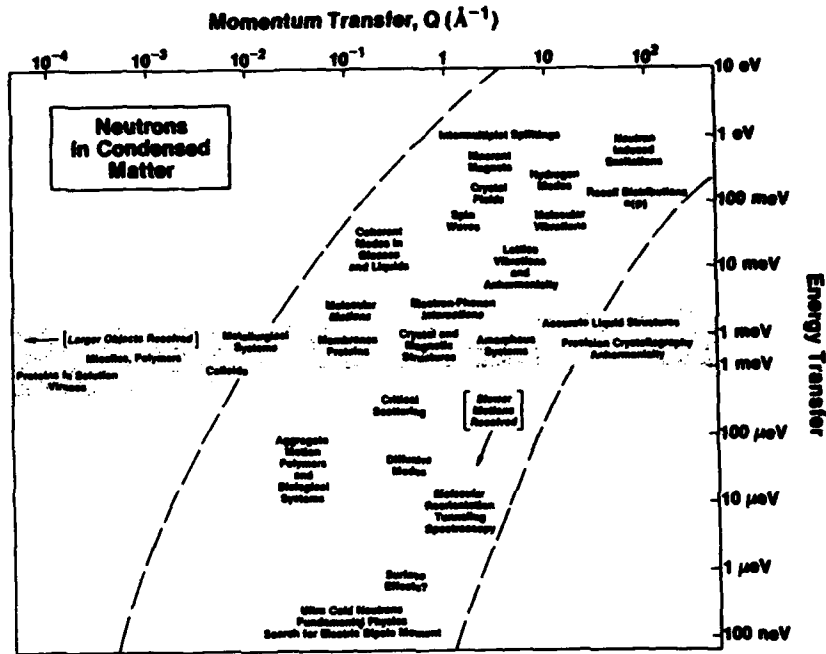


Figure 1. Schematic representation of some of the fields of science covered by neutron scattering. The fields are roughly represented by the area in which the words appear. The center-shaded-area represents elastic scattering with no energy discrimination.

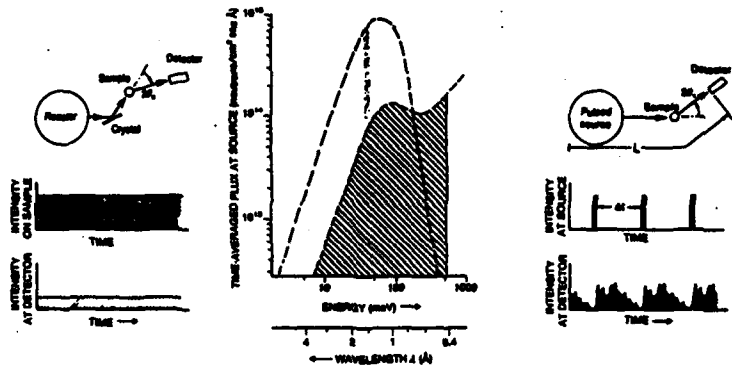


Figure 2. Comparison of diffraction experiments with steady state and pulsed neutron sources. In steady state experiment (left) steady beam of monochromatic neutrons diffract into detector. In pulsed experiment (right) pulses of white neutrons are diffracted and their energies are deduced by their arrival time at detector. Thus pulsed source makes efficient use of a smaller average neutron flux.

scattering facilities with the major new U.K. facility, SNS, at Rutherford-Appleton Laboratory. The peak thermal flux depends upon neutron energy and details of the moderator design, but the stated numbers for a "standard" room temperature moderator are included for comparison with reactor sources. Average spallation neutron fluxes are down from the peak fluxes by a duty factor of about 10^3 . Roger Pynn surveys neutron instrumentation at reactor and pulsed sources in the following contribution to this Symposium.

The European experience has proven beyond doubt the desirability and cost effectiveness of neutron guide halls. A new guide hall is in advanced construction at the NIST reactor, and plans exist for a similar extension of the capabilities of the HFBR. But the most ambitious and exciting U.S. plans are for an Advanced Neutron Source, which is presently in conceptual design. If funded, this facility will surpass the flux performance of existing reactors, make extensive use of hot and cold sources, and be the major focus of U.S. neutron scattering activities for the next century. A description of plans for ANS is given by John Hayter in this Symposium.

Table I. Research Reactors for Thermal Neutron Scattering.

	Thermal Power MW	Av. Thermal Flux (10^{14} n/cm ² sec)	No. of Instruments	Comments
High Flux Isotope Reactor Oak Ridge, TN	100	15	9	Transplutonium Production
High Flux Beam Reactor Brookhaven, NY	60	12	14	Cold Source
NIST Research Reactor Gaithersburg, MD	20	2	11	Cold Source, Guide Hall
Missouri Univ. Reactor Columbia, MO	10	1	7	Irradiation Facilities
Institute Laue-Langevin Grenoble, France	60	12	-40	Cold & Hot Sources, Guide Hall
Advanced Neutron Source Oak Ridge, TN	350	80-90	-40	Cold & Hot Sources Guide Hall

Table II. Spallation Sources for Thermal Neutron Scattering.

	Av. Fast Neutron Production (10^{15} n/s)	Pulse Frequency (HZ)	Peak Flux (10^{14} n/cm ² sec)	No. of Instruments	Comments
LANSCE, Los Alamos, NM	6	12	14	9	Cold Source Guide Hall
IPNS Argonne, IL	4	30	9	9	Enriched U-target Cold Source
SNS, Rutherford U.K.	16	50	14	14	Depleted U-target Cold Source

POWDER DIFFRACTION

The use of neutron powder diffraction for both basic and applied research has increased dramatically in recent years. At facilities which provide dedicated powder

diffraction capabilities to users, the requests for instrument time consistently exceed availability. This increased interest in powder diffraction is largely the result of improved data analyses that collectively are known as profile refinement methods [2]. These techniques attempt to redress the main inherent difficulty of powder methods, namely that in even moderately simple crystal structures different Bragg reflections become increasingly crowded together as the scattering angle, 2θ , increases. It is impractical to circumvent this by arbitrarily increasing the resolution of the instrument in order to cleanly separate the peaks. However, having characterized the resolution of the instrument, it is possible with modern computers to calculate the intensity profiles of partially overlapping patterns by least-square refinements of the individual peak positions and intensities. At the current high flux sources, a resolution of $\Delta d/d=3 \times 10^{-4}$ can be achieved [3].

The method offers the natural advantages of constant scattering factor (no form factor), high penetration power and freedom from texture and preferred orientation which are often associated with small x-ray samples. The additional beauty of the technique is that it can be more or less routinely and reliably applied to the refinement of crystal structures with of the order of 50 positional parameters. This includes many materials in such technologically important areas as superconductivity, catalysis, magnetism, and fast-ion conductivity. Zeolites, for example, have considerable commercial importance as ion-exchangers, molecular sieves and heterogeneous catalysts for hydrocarbons reactions. Figure 3 shows the result of a recent determination of the localization of benzene in sodium Y zeolite, in which a powder refinement was first obtained for the base zeolite, and the position of the absorbed benzene deduced by difference Fourier techniques [4].

NEUTRONS, MAGNETISM AND SUPERCONDUCTIVITY

Neutron diffraction has played an important role in the structural characterization of the new copper oxide high temperature superconductors. The discovery of $\text{YBa}_2\text{Cu}_3\text{O}_7$, for example, was quickly followed by several x-ray determinations of the cation positions. However, because of twinning problems and the relatively weak oxygen scattering, x-rays were unable to establish the oxygen stoichiometry and location with much certainty. This knowledge, which is vital to a proper understanding of these materials because oxygen vacancies provide the necessary electronic doping, came only as a result of neutron powder diffraction studies [5].

An atom with a magnetic moment has, in addition to a nuclear scattering amplitude, a magnetic scattering amplitude,

$$p = \gamma r_0 S f = 0.54 S f \times 10^{-12} \text{cm}$$

where γ is the nuclear gyromagnetic ratio, r_0 the classical radius of the electron, S the spin quantum number of the atom and f the form factor of the magnetic electrons. In general, the magnitude of p is comparable with nuclear scattering lengths. The phase of the magnetic amplitude depends upon the relative orientations of the moments of the electrons and neutrons, and causes polarization of the scattered neutron beam, an effect which can be additionally employed to distinguish nuclear and magnetic scattering.

Consequently, magnetic neutron scattering provides a unique tool for the study of the spatial magnetic order (ferro- and anti-ferromagnetic, spin glass, etc.). Once again, high temperature superconductors provide important, topical examples. Antiferromagnetism has been detected by powder neutron diffraction in the insulating prototypes of most CuO-based superconductors, in spite of the small (0.5 Bohr magneton) moment [6]. Figure 4 shows an example of the magnetic phase diagram of $\text{YBa}_2\text{Cu}_3\text{O}_{6+x}$ deduced by neutron scattering studies [7]. As examples of quasi-two dimensional spin 1/2 antiferromagnets, these systems have considerable intrinsic interest. However, even more interesting from the standpoint of superconductivity is the observation that although the magnetic long-range order disappears quickly with metallic doping, careful magnetic diffuse scattering measurements show that substantial magnetic short-range order persists even into the superconducting phase. Such behavior is contradictory to that of conventional superconductors, and is thought by many to provide an essential clue to the mechanism of high temperature superconductivity, which is still not understood. Neutron scattering techniques have also made important contributions to the study of magnetic penetration effects, including magnetic flux lattices.

METALLURGY AND CERAMICS

The traditional, but no less essential, uses for neutrons in these fields are concerned with structure, stoichiometry and order on the atomic scale, and the changes in these properties that occur at phase transformations. Many of these questions are answered by standard elastic diffraction techniques, although the understanding of disorder and the mechanism of phase changes often center on elastic or inelastic diffuse scattering measurements. Increasingly, however, materials scientists are finding that the great penetration depth and non-destructive nature of neutrons are also making them indispensable in characterizing real materials on a more macroscopic scale using small-angle scattering techniques.

Grain boundary cavitation, whereby small voids develop and accumulate at grain boundaries of materials subjected to deformation at elevated temperature, is an important and poorly understood damage mechanism in real high temperature materials. The type of information needed to understand this phenomenon includes the number densities of the voids and their size distributions as functions of time, temperature and deformation parameters. A large number of voids should be sampled, even though the void volume fraction is low. Void volume fractions of less than 10^{-6} can be measured. A wide range of void sizes (a few nanometers to nearly a micrometer) can be detected and analyzed, making possible comparisons with various theories of cavitation nucleation and growth. Of course, similar techniques are also routinely used to study a variety of other precipitation phenomena.

Another use of neutron scattering in the study of real materials is the measurement of bulk residual stress. Other methods commonly employed (e.g., strain gauge measurements of trepanned samples, ultrasonics) are either destructive or are strongly affected by texture in the sample. Yet the ability to reliably measure the distribution of internal stress fields in fabrications and weldments, as well as in composite materials such as cermets, is vital to the safe and effective design of parts using such materials. The principle of the neutron scattering technique is identical to that using x-rays, in which the local internal lattice stress in a material is determined from the measured elastic lattice strain it produces. The magnitude of the strain is

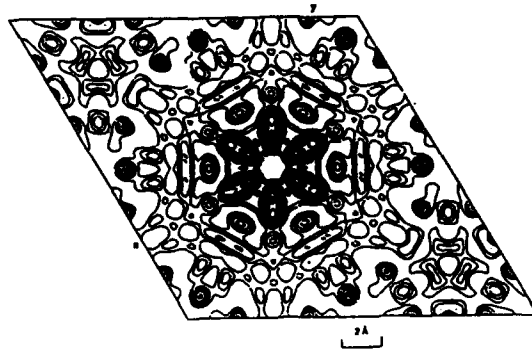


Figure 3. Fourier difference map showing the location of absorbed benzene molecule in sodium Y zeolite derived from powder profile refinement. (After Fitch, et al., Ref. 4.)

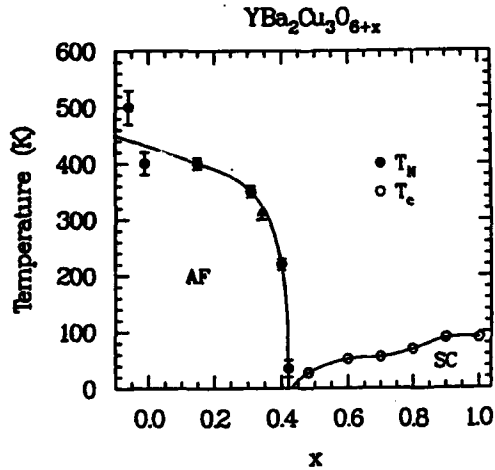


Figure 4. Phase diagram for $\text{YBa}_2\text{Cu}_3\text{O}_{6+x}$ showing the antiferromagnetic phase boundary as determined by neutron diffraction on powder samples. Superconductivity onsets abruptly after the disappearance of antiferromagnetic long range order.

deduced from the lattice plane spacing using Bragg law, and the direction of the strain is that of the scattering vector. The strains are small, typically $\Delta d/d=10^{-3}$ to 10^{-4} , so that extremely good instrumental resolution is required. The volume of the sampled material is defined by the overlap of the paths of the incident and diffracted beams, which are in turn determined by neutron absorbing apertures. The best spatial resolution occurs when the beam is diffracted at right angles. Figure 5 shows some sample data, taken after the release of the applied stress, on a mild steel bar subjected to plastic strain [8]. The bending causes strains which exceed the elastic limit in the outer (tensile) and inner (compressive) regions of the bar. But on release of the applied bending moment, the elastic strains in the previously plastically deformed extreme outer and inner regions of the bar reverse and, at equilibrium, oppose the strains in the central regions of the bar.

POLYMERS, MACROMOLECULES AND BIOLOGY

This is the realm of large, noncrystalline molecular assemblies, and it is often impractical to attempt detailed structure determination at the atomic level. Fortunately, lower resolution small angle scattering studies are both useful and feasible. (It is customary to describe the measured scattering in terms of a function $S(Q)$, which is the Fourier transform of the real-space correlation function, $G(r)$. Thus small momentum-transfer, Q , implies large, coarse-grained real-space resolution. In terms of the scattering kinematics $Q=(4\pi/\lambda)/\sin(\theta/2)$, where θ is the scattering angle. Consequently, small Q is achieved by some appropriate combination of small scattering angle and long de Broglie wavelength, λ , for the probe.) The choice of neutrons rather than x-rays for this purpose has largely to do with the unique neutron scattering properties of the isotopes of hydrogen.

Table III compares the scattering lengths of most of the atoms of any significance in macromolecular assemblies. The scattering lengths for x-rays are proportional to atomic number, making the heavy elements far more conspicuous than hydrogen. In the case of neutrons, not only are all scattering lengths of the same magnitude, but the H scattering length is negative. This signifies that in a certain sense H acts like a negative hole with respect to other atoms, including D. Since most of the atoms of a typical macromolecule are hydrogen, very large changes in the scattering properties can be effected by selective deuteration techniques.

The ramifications of selective deuteration are so numerous that only a few examples suggesting the power of the coupling of this technique with SANS will be mentioned [10]. It can be used to study the configuration of a single polymer molecule both in dilute solutions or bulk. Such studies show how the "size" (radius of gyration) and thus the conformation of a polymer molecule varies with changes in molecular weight and intermolecular interactions. Many macromolecules (e.g. block copolymers, micelles, most biological objects) are composites of different chemical species with different average neutron scattering power. Low resolution information on the spatial disposition of the components can be easily obtained by the "contrast variation" method, in which mixtures of hydrogenated and deuterated solvent are used to match the scattering density of the solvent to one of the components. The neutrons only "see" the unmatched components of the original object. Of course, in favorable cases the experiment can be repeated by matching the solvent to each of the components separately. The method is particularly powerful in differentiating, for example, the protein coat of a virus from its DNA interior.

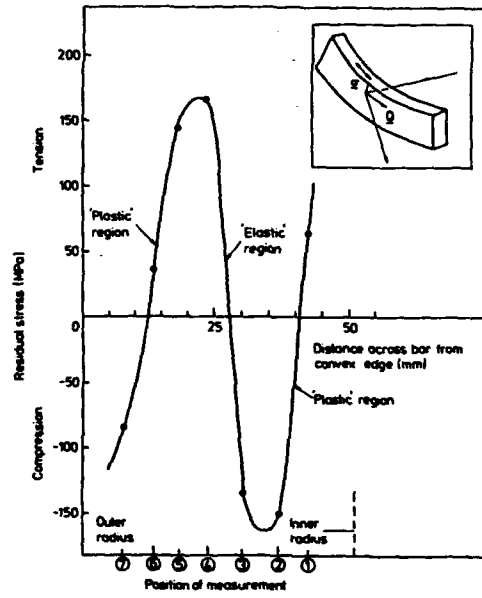


Figure 5. Variation of residual stress with position across plastically deformed steel bar after relaxation of the applied bending stress. (After Allen, et al., Ref. 9.)

Table III. Scattering Lengths for Neutrons and x-rays of Elements of Importance for Macromolecules.

	Neutrons ($b \times 10^{12}$ cm)	x-rays ($b \times 10^{12}$ -cm)*
H	-0.374	0.28
D	+0.667	0.28
C	+0.665	1.69
N	+0.94	1.97
O	+0.58	2.25
P	+0.51	4.23
S	+0.28	4.50

*x-ray scattering lengths are given for a scattering angle of zero

NEUTRON REFLECTOMETRY

As with any other wave-like disturbance, a neutron beam on traversing an interface between two transparent materials with differing index of refraction (which is in turn determined by the scattering density) is partially reflected. The way that the reflected intensity falls off with angle of incidence is determined by the apparent sharpness of the interface. The interface may become unsharp either through true diffusion of material across the boundary or through local roughness which produces a similar average blurring of the interface. Scattering from multiple nearby interfaces interfere, and the contrast of the resulting interference pattern once again provides information on the sharpness of the interface. Since neutron scattering cross sections are typically very weak (in comparison, for example, to visible light) appreciable reflected intensity is restricted to glancing angles (5 degrees or less). Over the last few years, several specialized instruments have been constructed for studying neutron reflectometry.

Once again, neutrons offer special advantages over x-rays in the study of polymer interfaces because of the possibilities of deuteration as discussed above. Interdiffusion of entangled polymer molecules across a boundary have been studied by this method with resolution of about 10A, better by an order of magnitude than is possible with competing techniques (IR and forward recoil spectroscopy and secondary ion mass spectrometry). These studies have helped both to confirm and refine current models of polymer diffusion. The neutron index of refraction is also sensitive to magnetic fields, and this has been used to measure the magnetic penetration depth in superconductors.

NUCLEAR TRANSMUTATION AND ACTIVATION

Although they do so with a lower probability, neutrons are absorbed as well as scattered by matter. No discussion of the role of neutrons as a probe in the material sciences would be complete without mention of processes which depend upon

absorption rather than scattering [10]. Silicon doping by transmutation furnishes one example. Every year more than 50 metric tons of silicon for the electronics industry are processed in research reactors around the world. In the processing some of the Si^{30} , which is 3% naturally abundant, is transmuted to stable P^{31} . The uniformity of distribution of the phosphorus, which vastly exceeds anything achievable by other means, translates into superior performance characteristics for devices as diverse as high power rectifiers and infrared detectors. Also, because the doping level can be very precisely controlled by adjusting the neutron flux, neutron transmutation doping is now widely used to compensate for inevitable trace boron to produce what is in effect ultrapure silicon starting material.

As the name implies, in neutron activation analysis samples placed in a neutron flux are temporarily rendered slightly radioactive by neutron capture. The nature of the radioactive decay can provide a unique signature of the elemental composition of the sample. The sensitivity varies from element to element, but exceeds one part in 10^{12} in favorable cases. As an example of the scope of this technique, a geochemical survey of a number of western states was carried out in which the sedimentary distributions of over 30 strategically important elements were logged in this manner. Only the broad applicability and specificity of neutron activation analysis made such a large scale program feasible.

Such exquisite sensitivity has found other unique applications in many fields where the non-destructive nature of the testing is often of paramount importance. In archeology, trace element neutron activation analysis has helped to sort ancient pottery by the composition of its clay. It has been used to detect art forgeries, is routinely used in forensics to establish the identity of hair and fiber samples, and is the basis of a luggage scanning system with sufficient sensitivity to detect small but lethal quantities of plastic explosives.

ACKNOWLEDGMENTS

This work was supported by the U.S. Department of Energy, Division of Materials Sciences under Contract No. DE-AC02-76-CH00016.

REFERENCES

1. O.V. Lounasmaa, *Physics Today* **42**, 26 (1989).
2. H.M. Rietveld, *J. Appl. Crystl.* **2**, 65 (1969).
3. A.W. Hewat, *Mater. Sci. Forum* **9**, 69 (1986).
4. A.N. Fitch, H. Jobic and A. Renouprez, *J. Phys. Chem.* **90**, 1311 (1986).
5. There are many individual references. For a review see J.D. Jorgensen, *Jpn. J. Appl. Phys.*, **26**, Suppl. 2018 (1987).
6. For a review of magnetic properties of HTSC see R.J. Birgeneau and G. Shirane in "Physical Properties of High Temperature Superconductors," D.M. Ginsberg, ed., (World Scientific Publishing, Feb. 1989).
7. J.M. Tranquada, *et al.*, *Phys. Rev.* **B38**, 2477 (1988).
8. A.J. Allen, M.T. Hutchings and C.G. Windsor, *Adv. Phys.* **34**, 445 (1985).
9. For reviews of neutron scattering in biology and polymer science, see P.B. Moore, *Physics Today* **38**, 62 (1985), and R.S. Stein and C.C. Han, *ibid.*, **38**, 74 (1985).
10. See, for example, A.D. Bromley, *Physics Today* **36**, 30 (1983), for a description of other uses of neutrons in science and technology.

NEUTRON SCATTERING METHODS FOR MATERIALS SCIENCE

ROGER PYNN, Manuel Lujan, Jr. Neutron Scattering Center, Los Alamos National Laboratory, Los Alamos, NM 87545

ABSTRACT

This article describes some of the neutron scattering techniques which can be used to probe structures of materials on length scales which range from less than 1 Å to 1 μm. The intent is to remove the veils of secrecy and mystery which have apparently prevented the wide application of these techniques to problems in materials science.

Introduction

As a probe of materials, neutron scattering suffers from a number of important limitations: it is expensive, non-portable, and signal-limited. Quite clearly, the method should not be used unless it provides information which cannot be obtained by other means. Fortunately the technique offers some unique advantages. It is non-destructive, able to give structural information about bulk samples which cannot be penetrated by x-rays or electrons, and well-matched to the length scales which are important in the study of materials.

Although all neutron scattering experiments are conceptually similar, the inherently low flux available from neutron sources means that neutron spectrometers have to be carefully optimised for particular purposes. The same instrument cannot be used to measure residual strain, polymer conformations and surface roughness, for example. For this reason, a veritable zoo of distinctly different neutron spectrometers has been developed since the technique was first used forty years ago. Rather than try to describe each species in the zoo, I shall restrict this article to a consideration of those spectrometers which are most useful for materials science, defined in its narrowest sense. For this reason, I shall not describe spectrometers which measure neutron inelastic scattering, even though this is an area in which neutrons have made seminal contributions to solid-state physics. Readers interested in a perspective which is broader than that provided here should consult earlier review papers [1,2] and books [3,4].

The Principles of Neutron Scattering

Conceptually, neutron elastic scattering is a simple technique: a well-collimated beam of neutrons of a known wavelength, λ , is allowed to impinge on a specimen and the scattered neutrons are detected as a function of the angle, 2θ , through which their trajectory has been deviated. With this arrangement, structure on a length scale of about $\lambda/\sin\theta$ is probed. This is demonstrated in Figure 1 [5]. In practice, λ may vary between a fraction of an Ångström

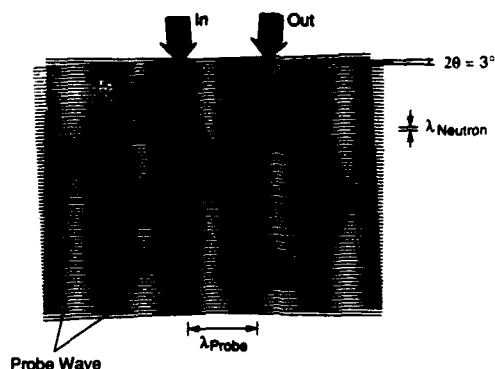


Figure 1. The probe-wave view of neutron scattering. The ingoing and outgoing neutron waves, each of wavelength λ_{neutron} , set up a probe wave of wavelength λ_{probe} . The probe wavelength decreases with increasing scattering angle, 2θ , and decreasing λ_{neutron} . The neutron wavelength and the scattering angle are chosen so that λ_{probe} is roughly equal to the length scale to be probed.

and about 20 \AA , while θ is between 0.5° and 90° . Structures of materials may thus be examined routinely by neutron scattering on length scales which vary between 0.1 \AA and 1000 \AA . This range extends all the way from interatomic to microstructural distances.

The neutrons used in scattering experiments are obtained either from nuclear reactors or from so-called spallation sources where neutrons are produced by bombarding a heavy metal target with energetic protons [3]. The techniques used for neutron scattering experiments at these two sources differ because the neutron spectra differ radically (Figure 2). At a reactor, neutrons are produced continuously with a Maxwellian wavelength spectrum. At a spallation source, on the other hand, neutrons are produced in short ($< 100 \mu\text{sec}$) bursts, twenty to fifty times per second, with a spectrum which extends to shorter wavelengths than the reactor Maxwellian. At a reactor it is necessary to select a small band of wavelengths from the neutron spectrum in order to define the wavelength of the neutrons which impinge upon the sample. Such monochromatization may be avoided at spallation sources by measuring the time at which each scattered neutron is detected. Since the time at which every neutron pulse starts from its source is known, the velocity of a detected neutron may be calculated from a knowledge of its time-of-flight and the distance between source and detector. The neutron velocity is directly related to its wavelength by the relation $\lambda = h/mv$, where h is Planck's constant, v the neutron velocity and m its mass.

Neutrons are used more efficiently at spallation sources than at reactors. However, the two types of source are either equivalent or complementary from the experimenter's point of view. Usually, similar data may be obtained at either source, although there are a few cases in which one or the other is superior.

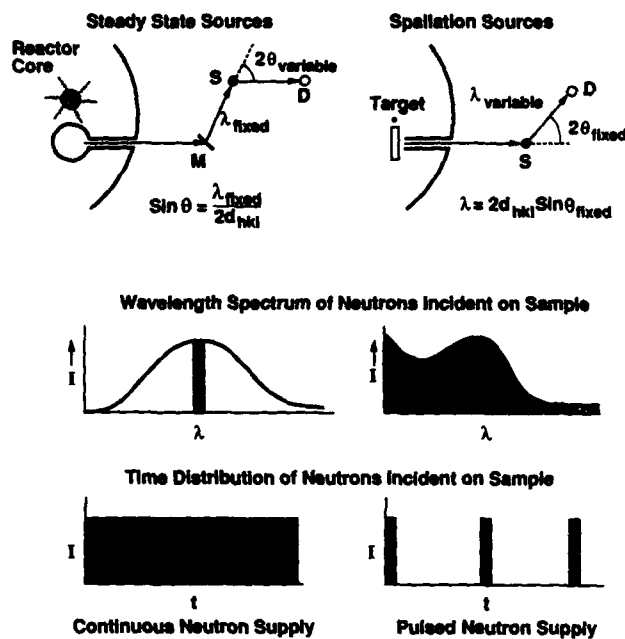


Figure 2. Reactor and spallation neutron sources are used differently for neutron scattering. The neutron spectrum from a *reactor* is continuous so beams must be monochromated (M) before impinging on the scattering sample (S) in a diffraction experiment. The scattering angle, 2θ , is scanned to obtain a diffraction pattern. The pulse structure of neutron beams from *spallation sources* allows the time-of-flight of detected neutrons (D) to be measured and used to determine neutron wavelength, the scanned variable in this case.

Small Angle Scattering

Small angle neutron scattering (or SANS) is by far the most popular neutron scattering technique in the materials community. With this method, structures on length scales between 10 \AA and 1000 \AA in materials as diverse as polymers, ceramics, metals and composites have been studied [4,6] with a distance resolution of about 10%. For such experiments, a position-sensitive neutron detector covering an area of about 1 m^2 is placed directly behind the sample at a distance between 4 m and 40 m (Figure 3). The spatial resolution of the detector is usually between 3 mm and 10 mm.

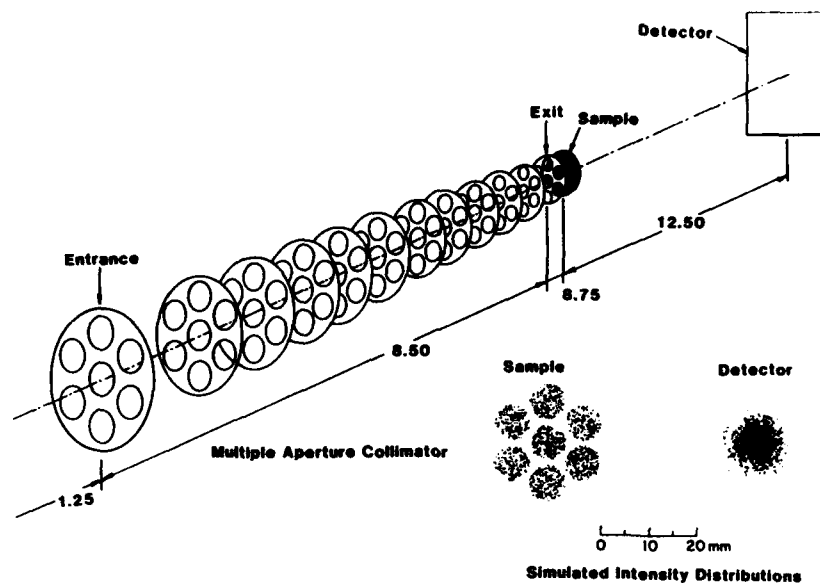


Figure 3. A schematic diagram of a SANS spectrometer. The multiple aperture "pepper-pot" collimator produces seven spots over a large area of the sample but gives only a single spot at the detector (bottom right of figure). The numbers on the sketch of the collimator are distances from the neutron source in metres.

The first SANS spectrometers were built 20 years ago in Germany and France. They proved so popular, however, that they were cloned at most neutron scattering centers, including those in the United States. In contrast to reactors, where experiments at several sample-detector separations are required to access a wide range of length scales, spallation sources provide SANS spectrometers which can probe structures between 10 \AA and 1000 \AA simultaneously. On the other hand, the better reactor spectrometers are able to measure structures larger than 1000 \AA : at the Institute Laue-Langevin in Grenoble, France, length scales of $10,000 \text{ \AA}$ or $1 \mu\text{m}$ can be accessed, for example. Thus the choice of instrument depends on the problem. For studies of composite materials, for example, where one is interested in both the surface structure (length scale $\sim 10 \text{ \AA}$) and the conformation (length scale $\sim 1000 \text{ \AA}$) of a filler [7], a SANS instrument at a spallation source is probably most suitable. For studies of large objects, such as heavy polymers, reactor instruments may be preferable.

Most samples of interest to materials scientists scatter neutrons strongly at small angles. For typical experiments with such materials only about 100 mm^3 of sample is

needed, generally in the form of a sheet approximately 1 mm thick. Liquid samples, such as colloids, microemulsions or polymers in solution can be contained in standard quartz cells which scatter weakly and add very little background. Measurements of strong scatterers take an hour or less at most national user facilities. To simplify studies of multiple samples, many SANS instruments are equipped with automatic sample changers which can be loaded with a dozen or more samples and whose operation is controlled by the same computer that handles data acquisition. Sample changers generally operate at room temperature and pressure, but facilities are often available which allow variable temperature and the application of modest magnetic fields for single samples. Pressure cells suitable for SANS and capable of a few tenths of a GPa and shear cells which achieve 15000 sec^{-1} are available at some facilities but are not yet common.

Although not necessary for many materials science applications, spectrometers which can accommodate weak scatterers have been constructed at the National Institute for Standards and Technology (NIST) at Gaithersburg and, more recently, at the Manuel Lujan Jr. Neutron Scattering Center (LANSCE) at Los Alamos. These instruments use converging collimators composed of successively smaller "pepper-pot lids" (Figure 3). Each aligned series of holes in the collimator plates transmits neutrons which illuminate a small area (usually about 100 mm^2) of the sample. The overall effect is to place several SANS instruments with pin-hole collimators beside one another, with each "instrument" looking at a different small area of a large (1000 mm^2) sample. With this arrangement, weak scatterers can usually be measured.

The computers which control the acquisition and reduction of SANS data are becoming increasingly sophisticated. Most simple analyses, such as radial averaging of the data to obtain the structure factor, $S(Q)$, as a function of wavevector transfer, Q , can be performed during the experiment, almost as soon as the data have been collected. Guinier plots, absolute normalisation, measurement of fractal dimension and even fitting to simple models such as scattering from monodisperse spherical particles can usually be accomplished during a typical one- or two-day experiment. More sophisticated analyses, such as the use of Maximum Entropy methods to determine particle-size distributions [8], are available at some Centers.

Powder Diffraction

Neutron powder diffraction provides a method for determining the atomic structures of polycrystalline materials. The essential difference between powder diffractometers and SANS spectrometers is that the neutron detectors on the powder machines are placed closer to the sample and cover a larger range of scattering angles. The range of scattering angles allows typical interatomic distances between 0.3 \AA and 10 \AA to be probed. Although powder diffractometers at reactors and spallation sources differ in appearance, there is very little difference in the potential performance of spectrometers at the two sources. Powder patterns

from either type of instrument may be analysed by the Rietveld technique [9], in which all of the Bragg reflections in the pattern are fit simultaneously to determine the atomic coordinates of the sample.

A very successful recent addition to techniques for the determination of atomic structures has been the use of simultaneous refinement of x-ray and neutron diffraction data [10]. Since the scattering powers of atoms for x-rays and neutrons do not vary in the same manner across the periodic table, two independent diffraction patterns are obtained when measurements are made with both types of radiation. Simultaneous refinement tends to avoid the false minima sometimes encountered when neutron or x-ray data alone are fitted and the results are usually more accurate than can be obtained with either technique on its own. Sophisticated software is required to accomplish refinement of multiple data sets, but is now available [11]. The joint-refinement technique may be extended by making measurements close to x-ray adsorption edges at synchrotron radiation facilities. Since x-ray scattering cross sections change considerably close to such edges, additional linearly independent data sets can be obtained for Rietveld refinement. Furthermore, site-specific valence of the atoms in a material can be deduced because the x-ray scattering depends on valence close to atomic adsorption edges. Measurements of this sort have been made successfully with 1-2-3 superconductors both above and below their transition temperatures [10]. Neutron diffraction measurements are an essential component for joint refinements because they define the thermal vibration parameters, which are strongly coupled to site occupancies in the refinement.

For most neutron powder diffraction experiments, about 5 cm³ of sample is adequate, although specialised spectrometers are available, albeit with lower resolution, for the investigation of milligram specimens [12]. Most neutron scattering facilities provide variable temperature capabilities on their powder diffractometers. High pressure (up to 0.3 GPa), uniaxial stress and magnetic fields are also frequently available.

Residual Strain

Powder diffractometers can be used to measure residual strain in engineering components made from metals, ceramics and composites [13]. Homogeneous strain gives rise to a shift in diffraction peaks corresponding to changes in the crystal lattice parameters. Fine slits are placed before and after the sample to define the volume within which neutron diffraction occurs and the lattice parameter is measured. This gauge volume is usually a few mm on a side but may be as small as 1 mm³. By moving the sample on an x-y translation stage between measurements, the gauge volume may be moved through the specimen and the residual strain mapped out. Measurement of residual strain places stringent requirements on the ability of a powder diffractometer to determine accurate values for the interatomic spacing corresponding to a particular Bragg peak. Most diffractometers can measure interatomic spacings with an accuracy of 0.01% ($\Delta d/d$), but a value two or three times smaller

than this is probably required for measurements of small strains, for example in ceramics. Such high resolution is achieved only by a few instruments.

Even though they are not generally able to accommodate specimens as large as their reactor counterparts, powder diffractometers at spallation sources offer a number of advantages for measurements of residual strain. The natural scanning variable is neutron wavelength rather than scattering angle, so the gauge volume remains constant during each measurement. Furthermore strains can be measured simultaneously in two mutually perpendicular directions when detectors at $+90^\circ$ and -90° scattering angles are used. Finally, diffraction from several lattice planes is recorded during each measurement, providing information on strain anisotropy and texture. For measurements of strain close to surfaces, for example in shot-peened samples or bearings, the ability to measure several sets of parallel lattice planes simultaneously is probably crucial [14] because it allows the zero of the scattering angle to be defined even when the gauge volume is not entirely within the specimen.

Texture

Measurement of texture in bulk samples have been made using powder diffractometers at many different facilities in Europe and the U.S. [15]. Diffraction patterns are recorded for several orientations of the sample and the intensities of a particular Bragg peak are used to produce a pole figure for that peak. The pole figure for a set of lattice planes is a stereographic representation of the orientation density of the normals to these planes. From a measurement of several pole figures, the full orientation distribution function of the specimen may be deduced by using the Maximum Entropy method [8] or one of its derivatives [16]. While powder diffractometers are generally suitable for measurement of texture in large (several tens of cm^3) samples, texture of small samples (typically 10 mm^3) may be obtained using single crystal diffractometers [17].

Strain Radiography

A technique for measuring the spatial distribution of strains perpendicular to a thin, plate-like sample has been proposed recently by Priesmeyer [18]. The method makes use of a white, pulsed beam of neutrons and is therefore ideally suited to spallation sources. The wavelength (or time of flight) spectrum of neutrons transmitted by a polycrystalline specimen has a sawtooth structure in which each sharp break corresponds to a Bragg edge, that is to neutrons Bragg diffracted out of the transmitted beam (Figure 4). These edges are well defined [19] and their positions can be used to calculate the lattice spacing of atomic planes which are perpendicular to the neutron beam. If a position-sensitive neutron detector is used to record the transmitted spectrum, a map of the lattice parameters, and hence of the strain, may be obtained over an area of several hundred square millimeters with a resolution of a

millimeter or so. The measured strain is an average value along the trajectory of the neutron beam so the most useful results are obtained when the strain does not vary significantly in this direction.

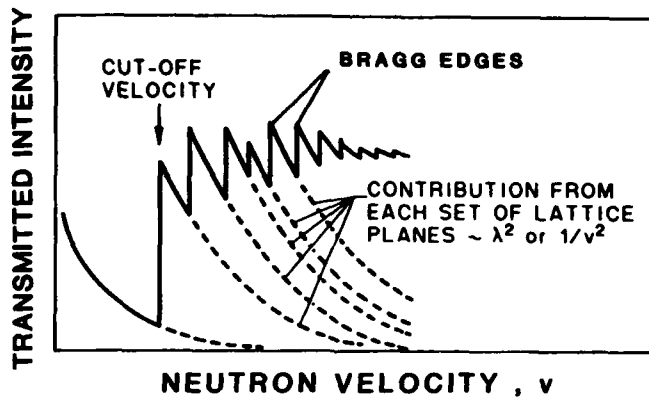


Figure 4. Neutron intensity transmitted through a polycrystalline material.

Very recently, Priesmeyer et al. [20] have shown that the transmission spectrum described above may be measured with acceptable statistical accuracy during a single pulse of neutrons from a high intensity pulsed spallation source. This development opens up the possibility of making time-dependent measurements of the distribution of lattice parameters within a sample because a snapshot of the strain can be taken every tenth second or so. Ultimately, it may be possible to probe high strain-rate processes with this method.

Investigation of Surfaces and Interfaces

One of the advantages of neutrons in the study of materials is that they penetrate bulk samples easily because they are only weakly scattered by matter. For this reason, neutron scattering is a signal-limited technique which one would not expect to be applicable to studies of interfaces. After all, there are many fewer atoms close to the interface than in the bulk of a sample and if the bulk scatters weakly, interfacial scattering ought to be negligible. This is true in most cases. However, at sufficiently small angles of incidence, neutrons are strongly reflected from almost all materials provided the interface from which they are scattered is flat and smooth. This fact allows neutrons to be used to probe the structures of materials within a $1 \mu\text{m}$ or so of their interfaces with a spatial resolution of a few Angstroms.

To do this, the specular reflectivity, $R(Q_z)$, of the surface is measured as a function of the neutron wavevector transfer, Q_z , perpendicular to the surface ($Q_z = 4\pi \sin\theta/\lambda$ where θ is angle between the neutron beam and the interface). In the simplest approximation, $R(Q_z)$ is related directly to the density gradient of a material evaluated perpendicular to its interface [21].

Reflectometers are a relatively new addition to neutron scattering facilities. The first such apparatus was built at the Intense Pulsed Neutron Source at Argonne National Laboratory less than a decade ago to study vertical surfaces [22]. Subsequently, several similar spectrometers have been constructed at other spallation sources and at reactors to examine horizontal surfaces. Such a geometry allows liquid surfaces, Langmuir films and surfactant layers at liquid-air or liquid-liquid interfaces to be examined. Neutron reflectometers are to be preferred to their x-ray counterparts for studies of hydrogenous materials, such as polymer films or surfactants, and for investigations of magnetic materials. Just as in the case of powder diffraction, it is an advantage to have both x-ray and neutron reflection data for the same surface, because this tends to prevent artifacts in the density profile deduced from the measurement.

To obtain accurate data, the incident neutron beam of a reflectometer must be well collimated. At pulsed sources, the angle between the incident beam and the surface to be studied is fixed at a value between 1° and 2° and the scan of Q_z is accomplished by recording the time-of-flight of specularly reflected neutrons. Angular collimation, which is the principal contribution to resolution, may be adjusted and is generally chosen to be less than 10% (FWHM) of the angle of incidence. At a reactor, the incident beam is monochromated as well as collimated and the scan of Q_z involves changing the angle at which neutrons impinge on the surface under investigation. For this reason, the illuminated surface (generally several tens of cm^2) changes during a scan and the data must be corrected appropriately. At a pulsed source, data for all Q_z are accumulated simultaneously, whereas, at a reactor, the Q_z scan is accomplished point by point. On the other hand, it is probably possible to make measurements close to the critical angle more accurately at a reactor source. In either implementation the factor which limits the performance of reflectometers is background. This determines the lowest value of reflectivity which can be measured (Figure 5) and, hence, the quality of the information which can be derived from the data. The best reflectometers at reactors or spallation sources are currently able to measure reliably reflectivities down to about 10^{-6} . Measurement of a complete reflection profile for a 50 cm^2 sample usually takes less than a day.

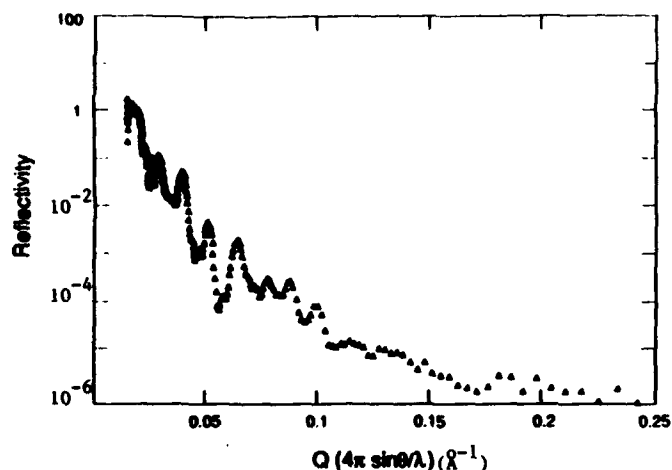


Figure 5. Typical reflectivity profile obtained on an annealed, 1500 Å thick film of block copolymer deposited on a silicon substrate provided by Tom Russell of IBM.

In addition to specular scattering, surfaces which are not perfectly smooth reflect neutrons at angles which differ from the angle of incidence. Such diffuse scattering may be used to measure the height-height correlation function of an interface. Although such measurements are not yet routine, they offer promise for the study of surface roughness on length scales between 1 Å and 50 Å [26].

If the neutron beam of a reflectometer can be spin polarised and if suitable spin flippers are available, contributions to the reflectivity caused by variations of magnetisation close to a surface may be separated from those due to variations in atomic density [22]. Polarised neutron reflectometry has been successfully used to probe magnetic recording materials and to determine the magnetic penetration depth of superconductors [23].

Radiography

Cold neutron radiography has been used widely to examine items as diverse as ancient Egyptian urns, operating helicopter engines, and the wings of fighter aircraft. Neutrons are able to penetrate substantial thicknesses of material and, if the absorption contrast is good, provide accurate images. The examples quoted above all take advantage of the fact that neutrons are strongly scattered by hydrogen and that materials containing this element can be radiographed through metallic or ceramic containers. Since the quality of thermal neutron radiography depends only on the total number of neutrons incident on the

sample, and since monochromatisation is not required, reactor neutron sources are the most appropriate for this technique.

A lesser known type of radiography makes use of the fact that most elements with atomic numbers above 25 have resonances at well defined energies in their neutron scattering cross sections [24]. At these resonances, neutrons are strongly adsorbed, so that when a radiograph is recorded as a function of neutron energy, components of the sample which contain different elements may be imaged. Resonances usually occur at energies of between 1 eV and 100 eV and have widths which are on the order of 100 meV. The high energy of most resonances coupled with the fact that time-of-flight analysis provides a natural method for obtaining energy-dependent neutron radiographs, implies that resonance radiography can only be carried out easily at spallation neutron sources. The method has applications in a variety of areas within the nuclear industry. If required, tomography could probably be developed with a spatial resolution less than 1 mm. Since the resonances in neutron cross sections broaden with temperature, it is possible to use resonance radiography for non-invasive measurements of temperature [25]. It is quite conceivable, for example, that the temperature of turbine blades in an operating jet engine could be measured by this means.

Neutron Adsorption Techniques

Two neutron adsorption techniques have been used at reactors, in particular at the National Institute for Standards and Technology (NIST), for materials testing. Neutron depth profiling allows the concentration profiles of elements such as helium, lithium and boron to be determined in the first few microns below the surface of a sample. The method relies on the detection of prompt energetic charged particles which are produced when neutrons are adsorbed by these atoms [27]. In neutron activation analysis, the energy and intensity of prompt gamma rays which result from neutron-capture are used to determine the abundance of particular elements [28]. Both of these techniques will be enhanced by the cold neutron facilities which are currently being installed at NIST.

Conclusion

Neutron scattering is a technique with a wide variety of applications in materials research. With the growth of national user facilities for neutron scattering in the United States the method has become widely available. The only limit on its application is the imagination of materials scientists.

Acknowledgement

This work was supported by the U.S. Department of Energy, Office of Basic Energy Sciences.

References

- [1] R. Pynn, *Rev. Sci. Instrum.*, **55**, 837 (1984)
- [2] J. M. Carpenter, G. H. Lander and C. G. Windsor, *Rev. Sci. Instrum.*, **55**, 1019 (1984)
- [3] C. G. Windsor, *Pulsed Neutron Scattering*, (Taylor and Francis, London, 1981)
- [4] *Treatise on Materials Science and Technology*, Vol 15, *Neutron Scattering*, G. Kostorz ed: (Academic Press, New York, 1979)
- [5] This figure was inspired by an article written by Colin Windsor
- [6] G. D. Wignall, in *Encyclopedia of Polymer Science and Engineering* (2nd edition), J. I. Kroschwitz ed: (Wiley Interscience, 1985)
- [7] D. W. Schaefer, *Rev. Phys. Appl.*, **C4**, 121 (1989); and *Science*, **243**, 1023 (1989)
- [8] D. S. Sivia, *Proc. ninth annual workshop on maximum entropy and Bayesian methods*, P. Fougere ed: (Kluwer Academic Publishers, 1990)
- [9] H. M. Rietveld, *J. Appl. Cryst.*, **2**, 65 (1969)
- [10] G. H. Kwei, R. B. Von Dreele, A. Williams, J. A. Goldstone, A. C. Lawson II, and W. K. Warburton, (accepted for publication in *J. Mol. Structure*)
- [11] A. C. Larsson and R. B. Von Dreele, *The Generalised Structure Analysis System*, LA-UR-86-748 (Los Alamos National Laboratory Report)
- [12] *Condensed Matter Research at LANSCE*, LALP 88-4 (Los Alamos National Laboratory Report)
- [13] A. J. Allen, M. T. Hutchings, and C. G. Windsor, *Advances in Physics*, **34**, 445 (1985)
- [14] This was pointed out to me by Tom Holden of Chalk River Nuclear Laboratory.
- [15] H-R. Wenk, H. Kern, J. Pannetier, S. Hofer, W. Schafer, G. Will and H. G. Brokmeier, *Proc. Int. Conf. Textures of Materials*, **8**, 229. TMS, Warrendale (1987)
- [16] J. S. Kallend, U. F. Kocks, H-R. Wenk and A. D. Rollett, (submitted to ICOTOM IX, Avignon, France, Sept 1990)
- [17] A. C. Larsson, P. J. Vergamini and H-R. Wenk, (this conference)
- [18] H-G. Priesmeyer (preprint, 1989: *Neutron Strain Radiography*)
- [19] R. G. Johnson and C. D. Bowman, *AIP Conf. Proc. No. 89, Neutron Scattering*, J. Faber ed: (AIP 1982)
- [20] H-G. Priesmeyer, C. D. Bowman, V. W. Yuan, S. J. Seestrom, S. A. Wender, R. Richardson, O. A. Wasson, J. Xzu and P. A. Egelstaff (to be published)
- [21] A. Braslau, M. Deutsch, P. S. Pershan, A. H. Weiss, J. Als-Nielsen, and J. Bohr, *Phys. Rev. Lett.*, **54**, 114 (1985)
- [22] G. P. Felcher, R. O. Hilleke, R. K. Crawford, J. Haumann, R. Kleb, and G. Ostrowski, *Rev. Sci. Instrum.*, **58**, 609 (1987)
- [23] R. Felici, J. Penfold, R. C. Ward, E. Olsi and C. Mattacotta, *Nature*, **329**, 523 (1987)
- [24] *Neutron Resonance Radiography*, J. E. Lynn and D. K. Hyer eds: LA-11393-C (Los Alamos National Laboratory Conference Report)
- [25] P. H. Fowler and A. D. Taylor in [24]
- [26] S. K. Sinha, E. B. Sirota, S. Garoff, and H. B. Stanley, *Phys. Rev. B*, **38**, 2297 (1988)
- [27] R. G. Downing, J. T. Maki, and R. F. Fleming, *J. Radioanal. and Nucl. Chem., Articles*, **112** (2), 321-330 (1987)
- [28] R. M. Lindstrom, R. Zeisler, and M. Rossbach, *J. Radioanal. and Nucl. Chem., Articles*, **112** (2), 321-330 (1987)

THE ADVANCED NEUTRON SOURCE

JOHN B. HAYTER

Solid State Division, Oak Ridge National Laboratory, P.O. Box 2008, Oak Ridge, Tennessee 37831-6393.

ABSTRACT

The Advanced Neutron Source (ANS) is a new user experimental facility planned to be operational at Oak Ridge in the late 1990's. The centerpiece of the ANS will be a steady-state research reactor of unprecedented thermal neutron flux ($\phi_{th} \approx 9 \cdot 10^{19} \text{ m}^{-2} \cdot \text{s}^{-1}$) accompanied by extensive and comprehensive equipment and facilities for neutron-based research.

INTRODUCTION

Neutron scattering was pioneered by C. G. Shull and E. O. Wollan at the X-10 (natural uranium) graphite reactor at Oak Ridge National Laboratory about half a century ago. The flux available, although low ($1 \cdot 10^{16} \text{ m}^{-2} \cdot \text{s}^{-1}$), was sufficient to show the importance of neutron scattering as a fundamental technique in materials science, and the many papers offered at this Symposium indicate the continued health of the field. Many reactors of increasingly higher flux were designed and built in the 1950's and 1960's, culminating with the high flux reactors at Brookhaven National Laboratory (HFBR) and at Oak Ridge National Laboratory (HFIR) in the United States, and at the Institut Laue-Langevin in France; all of these reactors offer fluxes of order $1.5 \cdot 10^{19} \text{ m}^{-2} \cdot \text{s}^{-1}$. However, while new research reactors have either come on-line (or are about to come on-line) since that time in Western Europe, Japan and Russia, it is now about 25 years since the last research reactor was constructed in the United States. In the late 1970's, it was clear that the lead in the field of neutron scattering had passed decisively to Western Europe, and the Department of Energy set up panels under the chairmanship of W. F. Brinkman to review the situation in 1980 and 1982. The National Research Council also became concerned, and after reviewing the needs of neutron scattering *per se* [1], undertook a thorough review of neutron scattering facilities in the context of all major national facilities for materials research [2].

The major facilities review concluded that a new, steady-state high-flux neutron facility was a high priority requirement for the United States, and recommended that design begin immediately. Among the factors contributing to this recommendation was the age of existing reactors, the evident European leadership in a field in which the U.S. had been predominant, and the important (and often unique) future applications of neutron scattering in many important areas of condensed matter physics, polymer and colloid science, metals, alloys and ceramics, chemistry, biology and medicine, and the earth sciences. Detailed needs of the community, and the means to realize them, were defined in several major workshops [3-5], and the project has been guided since 1987 by the National Steering Committee for the Advanced Neutron Source. The fundamental project objective is to design and construct the world's highest flux research reactor for neutron scattering. The reactor should also provide isotope production and materials irradiation facilities which are as good as, or better than, the High Flux Isotope Reactor, since it is likely that the latter will be shut down once the Advanced Neutron Source (ANS) is operational.

THE NEUTRON SOURCE

The *sine qua non* of the new facility is a reactor which can provide a flux at least five times higher than any existing neutron beam reactor, while meeting extremely stringent safety requirements. To this end, it was decided to base the design on existing technology (although advantage will be taken of any gains from new research and development), and to carry out probabilistic risk assessment simultaneously with design; the latter is a first for such a project, and reflects the fact that safety considerations are of primordial concern. A major achievement of the project to date has been the completion of preconceptual nuclear and thermal hydraulic design work on the reactor, showing that the objectives can be met with a safe design. The key feature has been to choose a coaxial, split-core in which the two halves are axially separated and separately cooled (see Figs. 1 and 2). The reactor volume of 67.4 L contains 18 kg of ^{235}U (93% enriched) in the form of involute plates of U_3Si_2 in an Al matrix. The unperturbed peak thermal flux generated in the reflector is of order $9 \cdot 10^{19} \text{ m}^{-2} \cdot \text{s}^{-1}$ at a power of 350 MW. The reactor core is cooled by a heavy water primary coolant loop, with coolant *upflow*. The choice of upflow provides a very desirable added safety feature, since it ensures an immediate transition to natural convection cooling (without any time delay for flow reversal) in the unlikely event of rupture of the primary circuit at a point which forestalls compensation by the independent backup circuit. (It should be noted that the normally low probability of major pipe rupture is being further reduced by designing for leak-before-break, with continuous leak monitoring.) The maximum coolant outlet temperature is 98°C , so that boiling will not occur on loss of pressure.

The reactor is controlled by four hafnium control rods in the central core channel. Each rod is provided with an independent scram mechanism, and any three of the four are able to shut down the reactor. A second, independent, shutdown mechanism is provided by eight shutdown rods placed outside the core. Each rod is again provided with an independent scram mechanism, and any seven of the rods are sufficient for total shutdown. Thus, the reactor may be shut down, even if there is total failure of one complete set of independent scram mechanisms, and partial failure of the other.

There are six major types of experimental facilities in the reactor assembly (Fig. 2). Materials irradiation (for example, for fusion research) takes place in either instrumented or uninstrumented capsules placed inside the upper fuel element, while transuranium elements are produced in targets just outside the lower fuel element. One of the achievements of the core design is that these facilities, which provide appropriate fast and epithermal neutron spectra, have minimal effect (<2%) on the fluxes of the neutron beams which will be the main concern of this Symposium. The large volume of high thermal flux available in the reflector tank is well suited to isotope production and analytical chemistry operations. To accommodate these activities, various experiment holes and "rabbit" tubes penetrate the top of the reflector tank. Seven vertical and two slant holes will provide a range of thermal fluxes for isotope production; these holes will be complemented by four hydraulic rabbit tubes, and three pneumatic rabbit tubes for materials analysis.

Neutron beams are extracted from the reflector by beam tubes which penetrate either into the peak thermal flux region (about 400 mm from the core centerline), or terminate at the graphite hot source at the reflector tank wall. The hot source is one of two types of spectral convertor which are placed in the reflector to tailor beam energies for specific applications; conversion to sub-thermal energies is accomplished by two liquid- D_2 cold sources. Cold neutrons are transported by horizontal neutron guides into a neutron guide hall adjacent to the containment building, or by slant guides to the second-floor beam room.

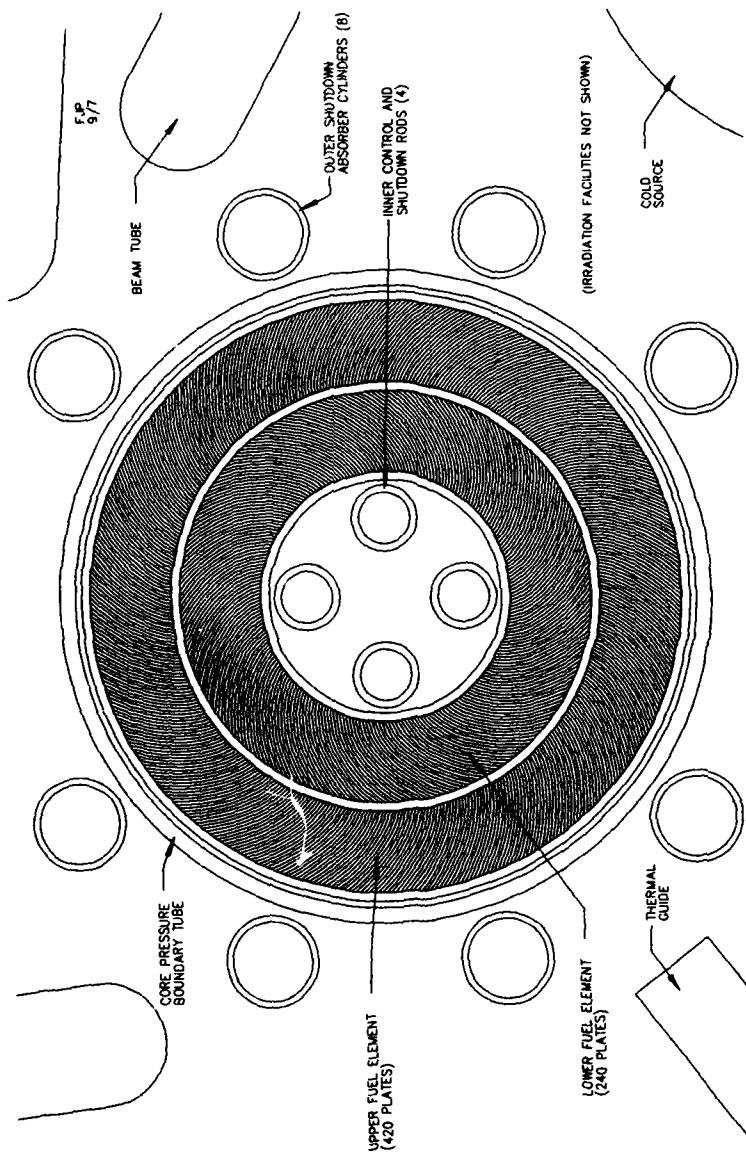


Figure 1. The ANS 2-element reactor core

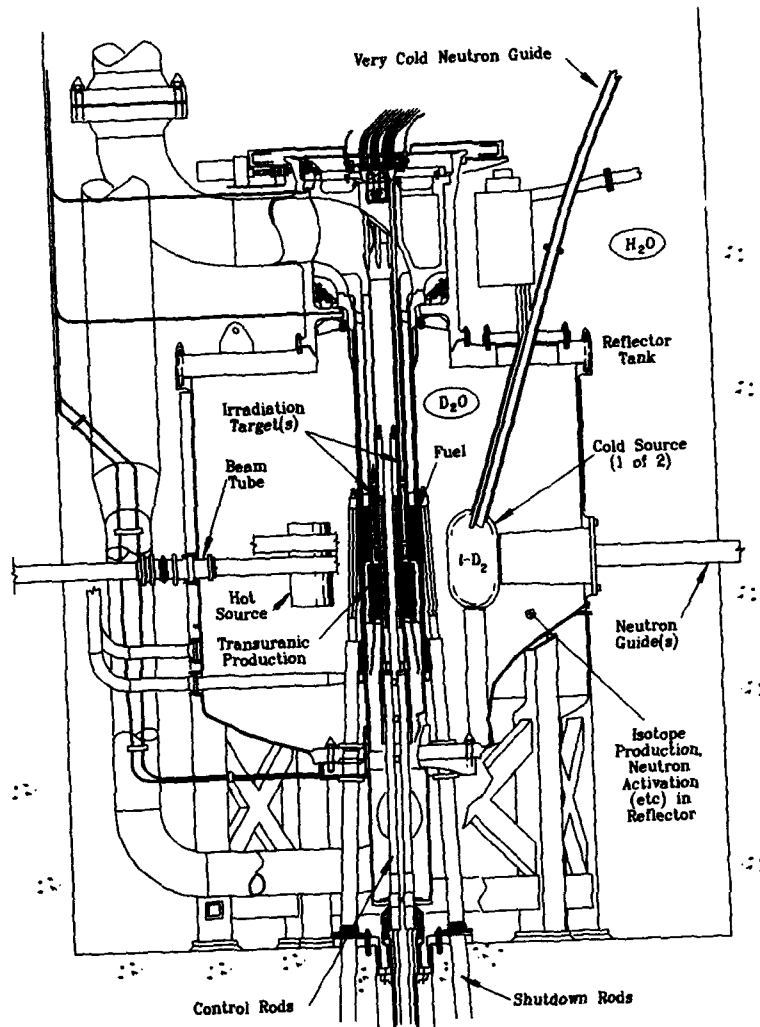


Figure 2. The ANS reactor assembly

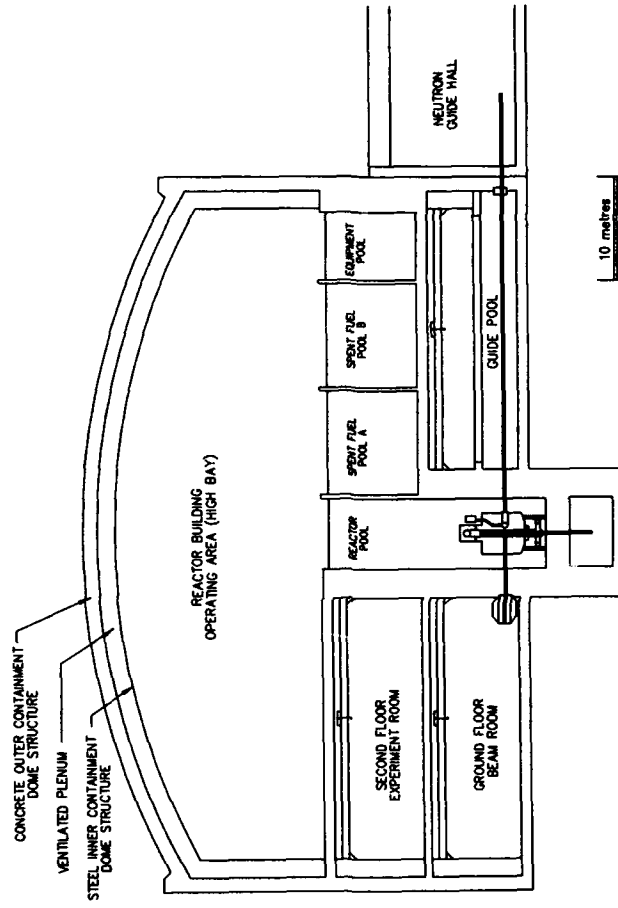


Figure 3. Section through reactor containment building

NEUTRON SCATTERING FACILITIES

There will be three user halls provided for experimental work at the ANS (Fig. 3). The *Ground Floor Beam Room* will provide "conventional" access to thermal and hot neutrons from the reactor via horizontal beam tubes terminating at the outside of the biological shielding. Inclined beams and certain other services, such as rabbit tubes, will terminate on a higher level in the *Second Floor Experiment Room*. Very cold and ultracold neutron research will take place on this level, as well as such activities as neutron depth profiling and some of the fundamental and nuclear physics work. The third main experimental area is the *Neutron Guide Hall*, which will provide the primary instrumentation for cool and cold neutron research. The layouts which will be presented below are designed to accommodate today's needs and priorities [3,4]. These are regularly updated via input from the National Steering Committee, as better estimates become available for the best probable instrument mix at the turn of the century, but they are considered sufficiently representative to act as a basis for major layouts.

Ground Floor Beam Room

The ground floor beam room layout is shown in Fig. 4. This layout currently assumes that, apart from a single through tube for nuclear physics, all beams will lie in the same plane; as neutronics calculations evolve, it may become necessary to stagger the beam heights alternatively above and below this reference plane, to minimize flux perturbations due to the beam tubes themselves.

Thermal beam scattering instruments for diffraction include 4-circle diffractometers on a thermal tube (T1) or guide (T2). A polarized beam is earmarked for single crystal diffraction (T3), but, in general, it is expected that polarized neutrons (and polarization analysis) will be routinely available whenever warranted on any instrument on the ANS. High resolution (T4) and high intensity (T5) powder diffractometers and two diffuse scattering spectrometers (T6/7) complement the single crystal instruments. Inelastic spectrometers are time-of-flight (T8) or 3-axis (T11/12).

The hot source provides beams to a high energy transfer 3-axis spectrometer (H3), a high momentum transfer single crystal diffractometer (H1), and a general purpose high incident energy diffractometer (H2) for studies of liquids and amorphous materials.

Neutron Guide Hall

The guide hall building (Fig. 5) is a wedge-shaped, single floor structure contiguous with the reactor containment building and office/laboratory complex. Two polar segment cranes will serve the guides and instruments. The guide shield structure reaches out to a distance of about 50 m from the reactor axis, and the experiment area extends a further 60 m. Apart from the two extreme guides, which serve special positions for nuclear physics (L12) or materials analysis (D16), the guides will generally be straight, so that cool as well as cold energies will be available. It will be noted that about one third of the experimental stations are for nuclear or fundamental physics; only the scattering instruments will be described here.

The most prevalent elastic scattering instruments are the small-angle neutron scattering cameras ((D3-6,L1,L2,L11), which offer varying degrees of resolution, and at least one of which will have reflectometer capabilities for surface studies. Diffuse scattering and high resolution powder diffraction will be available (L5,L6),

together with a general purpose area detector for efficiently scanning large regions of reciprocal space, for example, to study incommensurable lattice structures. A specially isolated mounting (to screen thermal and acoustic noise) will be provided for a neutron interferometer station (L7).

Conventional, variable k_{\parallel} focussing monochromator cool and cold 3-axis spectrometers will form the workhorses for inelastic scattering studies in the guide hall (D11,D12,L8,L9,L10), together with multichopper (D1) and time focussing (D9) time-of-flight spectrometers. Higher resolution inelastic studies will use backscattering (L4,D10) or neutron spin-echo (D2) as appropriate.

Second Floor Experiment Room

The main purpose of the second floor of the containment building is to provide experimental areas for users of the inclined beams and guides (Figs. 6 and 7). The prototypical layout shown in Fig. 7 demonstrates several key features, of which the most notable is the division of the area into two zones, one *secure*, the other *general access*. This is a particular example of the general site philosophy adopted for the ANS plant: separation of reactor operations from experimental areas, so that users may have straightforward access to their experiments and related areas (such as chemical laboratories), without requiring access to high security zones. One important role played by the second floor beam room will thus be to accommodate those experiments which have more commonly been situated in the reactor operations areas of other reactors (such as the ultracold neutron facility at ILL, Grenoble).

Current plans call for each cold source to be fitted with an inclined, curved guide (Fig. 6) for very cold neutrons (VCN). It is likely that one of these will be used directly while the other will be used as a feed for an ultracold (UCN) source (Fig. 7). A cold slant guide will provide a station for neutron depth profiling (NDP), which is a sensitive means of measuring concentration vs depth profiles by using reactions such as $^{10}\text{B}(n,\alpha)^7\text{Li}$ and detecting the resulting charged particles, whose range is a strong function of the distance they must travel in the surface being probed. NDP, which is quantitative and non-destructive, is applicable to a variety of technologies, such as microelectronics, optical signal processing, ultra-light alloys, and surface-modified materials.

A novel possibility for the ANS is to provide isotope separation on-line (ISOL). In this technique, a fission-fragment mass separator is used as the front end of an ion-implantation accelerator, providing a number of unique ions for studies of electron emission, channelling, and hyperfine interactions associated with ion-implanted radioactive atoms. Since charged beams are involved, they may be transported to ancillary equipment situated at some distance from the reactor.

PROJECT SCHEDULE AND COST

Preconceptual design of the ANS started in 1987, and the project is currently about halfway through the conceptual design phase, which will be finished at the end of 1990. Conceptual design embraces, apart from the key engineering elements, the choice of a site which meets all environmental criteria, and the considerable plant and equipment associated with the research activities planned at the ANS, for example, offices, shops and laboratories, library and conference rooms, etc. Once this has been completed and reviewed, the next stage is preliminary engineering design. (Specific aspects of the project are reviewed at about monthly intervals, with a major Department of Energy review at least annually.) To date, the project

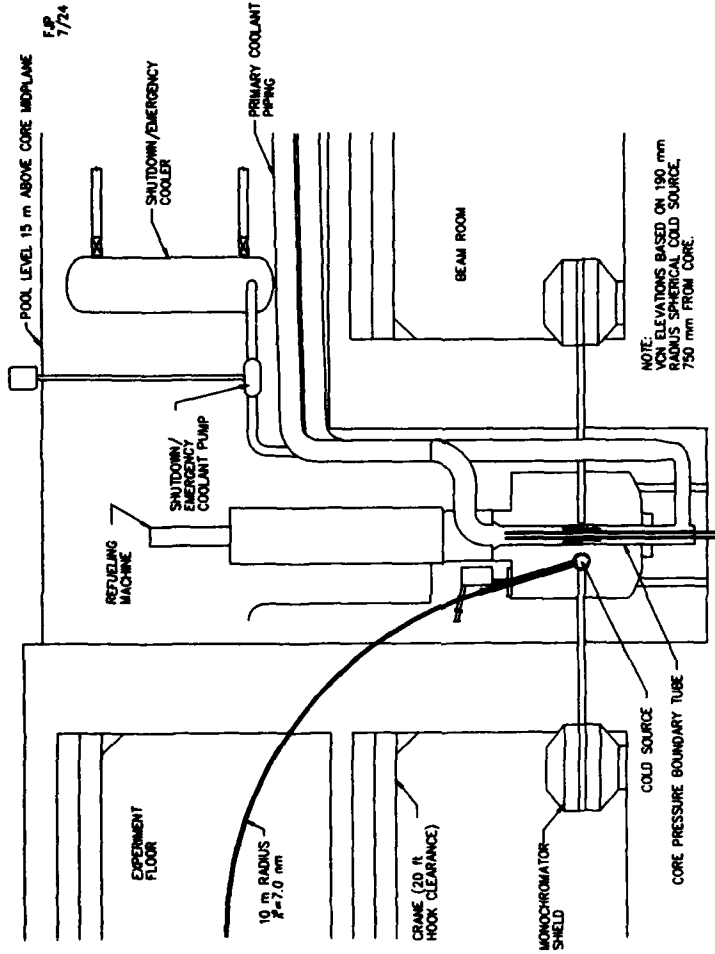


Figure 6. Curved very cold neutron guide to second floor

F.P.
6/9

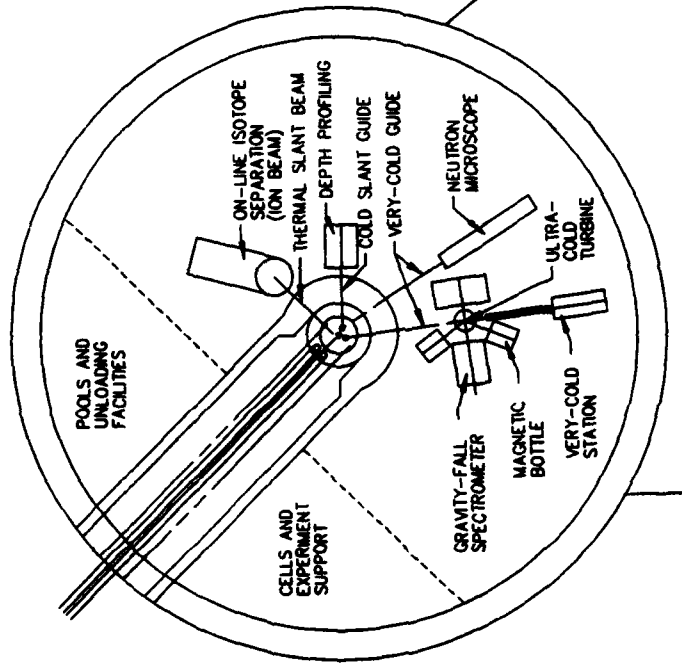


Figure 7. A possible second floor beam room layout

has been funded by operating funds, but detailed design for a project of this magnitude is sufficiently expensive that a 3-year line item request will be made to Congress for *design-only* funding, starting in 1991. The line item design cost is currently estimated at \$82.2M (1989 values).

Assuming the design is validated, the next step is to request construction funding, which is currently scheduled for 1994. The construction line item cost is presently estimated at about \$400M, so that the project cost is about \$500M (at 1989 prices), spread over 9 years. If the schedule is maintained, this will lead to reactor operation in late 1998, and will take the U.S. materials science community into the next millenium with the world's best facility of this type.

Oak Ridge National Laboratory is operated by Martin Marietta Energy Systems, Inc., for the U.S. Department of Energy, under Contract No. DE-AC05-84OR21400.

REFERENCES

1. Panel on Neutron Scattering, National Research Council, *Current Status of Neutron Scattering Research and Facilities in the United States* (National Academy Press, Washington D.C., 1984)
2. Major Materials Facilities Committee, National Research Council, *Major Facilities for Materials Research and Related Disciplines* (National Academy Press, Washington, D.C., 1984)
3. R. M. Moon, ed., *Proceedings of the Workshop on Instrumentation for the Advanced High-Flux Reactor*, Oak Ridge National Laboratory Report CONF-8405192 (1984)
4. G. H. Lander and V. J. Emery, eds., *Proceedings of the Workshop on Scientific Opportunities with Advanced Facilities for Neutron Scattering*, Argonne National Laboratory Report CONF-8410256 (1984); Nucl. Instr. and Meth., B12, 525 (1985)
5. R. M. Brugger, ed., *Proceedings of the Workshop on an Advanced Steady-State Neutron Facility*, Nucl. Instr. and Meth., A249 (1986)

PART II

Experimental Techniques

NEUTRON POWDER DIFFRACTION: A POWERFUL MATERIALS RESEARCH TECHNIQUE

W I F DAVID, Rutherford Appleton Laboratory, Chilton, Didcot, Oxon, OX11 0QX, UK

ABSTRACT

Neutron powder diffraction is a powerful technique that provides a detailed description of moderately complex crystal structures. This is nowhere more apparent than in the area of high temperature superconductors where neutron powder diffraction has provided precise structural and magnetic information, not only under ambient conditions but also at high and low temperatures and high pressures. Outside superconductor research, the variety of materials studied by neutron powder diffraction is equally impressive including zeolites, fast ionic conductors, permanent magnets and materials undergoing phase transitions. Recent advances that include high resolution studies and real-time crystallography will be presented. Future possibilities of neutron powder diffraction will be discussed.

INTRODUCTION

Neutron powder diffraction has come to the forefront of materials research over the past three years as a result of the successful application of the technique to the area of high temperature superconductivity. The accurate structure determination of the 90K superconductor, $\text{YBa}_2\text{Cu}_3\text{O}_7$, using neutron powder diffraction by several laboratories almost simultaneously [1-5] highlighted to the scientific community the power and the usefulness of the technique. Of course, practitioners of neutron powder diffraction have always been aware of the power of the technique since the important advance in data analysis by Rietveld [6-7]. Rietveld realised that the point-by-point fitting of a powder diffraction profile yields the maximum information content; crystallographic information may still be usefully extracted from weak and overlapping reflections. The advent in the past decade of high resolution and high intensity neutron powder diffractometers has permitted moderately complex materials such as zeolites not only to be refined to high precision but also to be determined from first principles with no prior knowledge. Indeed, structures obtained from high resolution neutron powder diffraction can now rival single crystal data in terms of precision and accuracy. This article does not intend to review comprehensively the area of neutron powder diffraction. For a recent review see [8]. Instead, selected highlights are given with the intention of indicating the scope and possibilities of a powerful materials science technique.

INSTRUMENTATION

The modern generation of neutron powder diffraction instrumentation falls into two distinct groups with distinctly different attributes. These are constant wavelength machines at nuclear reactors and time-of-flight diffractometers at pulsed spallation neutron sources.

Neutron diffraction experiments, whether at a reactor or on a spallation neutron source, are governed by Bragg's law,

$$\lambda = 2 d \sin \theta$$

Reactor-based instruments resemble traditional diffractometers with a monochromator crystal to select a particular wavelength. Different d-spacings are measured by scanning as a function of scattering angle, i.e.

$$\lambda_0 = 2 d_{hkl} \sin \theta_{hkl} \quad (\text{monochromatic})$$

At spallation neutron sources, because the neutron beam is produced in a pulsed manner, neutrons with different wavelengths may be discriminated by their time of arrival at the detector and thus different d-spacings may be measured at a fixed scattering angle, i.e.

$$\lambda_{hkl} = 2 d_{hkl} \sin \theta_0 \quad (\text{polychromatic})$$

The linear relationship between the wavelength of a neutron and its time-of-flight may be obtained from de Broglie's hypothesis relating to momentum, $p = m_n v$, to wavelength :

$$p = m_n v = m_n (L/t) = h/\lambda$$

where L is the total combined flight path from moderator to sample (primary flight path, L_1) and sample to detector (secondary flight path, L_2). t is the time-of-flight of the neutron over this distance. Thus

$$t_{hkl} = (m_n/h) L \lambda_{hkl} = 2(m_n/h) L d_{hkl} \sin \theta_0$$

In convenient units these equations become

$$t_{hkl}(\mu\text{s}) = 252.77843(20) L(\text{m.}) \lambda_{hkl}(\text{\AA}) = 505.55685(40) L(\text{m.}) d_{hkl}(\text{\AA}) \sin\theta_0$$

Given that there is a finite time width to the initial neutron pulse at a spallation neutron source, neutrons of a particular wavelength will propagate non-dispersively (because wavelength and hence velocity are constant) with a pulse structure that is independent of flight path. The principal consequence of this flight-path independent pulse structure is that resolution improves with increased flight path. For a given flight path, the $\Delta d/d$ resolution of a time-of-flight diffractometer is almost constant. This is particularly useful in the study of phase transitions where peak splittings occur with equal magnitude in all orders of reflection. By contrast, on constant wavelength machines high resolution may only be obtained around the monochromator take-off angle. However, this apparent disadvantage is offset in the area of structure refinement by the fact that the resolution characteristics of constant-wavelength diffractometers are well matched to the density of Bragg peaks.

THE HIGH TEMPERATURE SUPERCONDUCTOR $\text{YBa}_2\text{Cu}_3\text{O}_{7-x}$

Neutron powder diffraction has enjoyed an increased interest since the discovery of high temperature superconductivity and it is therefore appropriate in choosing an example to discuss structural studies of the system, $\text{YBa}_2\text{Cu}_3\text{O}_{7-x}$ ($0 < x < 1$), by neutron powder diffraction.

The general features of the system, $\text{YBa}_2\text{Cu}_3\text{O}_{7-x}$ ($0 < x < 1$), are well-known. One end member, $\text{YBa}_2\text{Cu}_3\text{O}_{7-x}$ ($x < 0.1$), is an orthorhombic 92K superconductor while the other, $\text{YBa}_2\text{Cu}_3\text{O}_6$, is a tetragonal antiferromagnetic insulator. A continuous range of compositions is possible between these two limits. The superconducting transition temperature falls rapidly as x approaches 0.5; the antiferromagnetic Néel temperature mirrors this effect. Somewhere near $x = 0.5$ the orthorhombic superconducting structure transforms continuously into the tetragonal insulating structure. The effect of oxygen partial pressure in the sintering of $\text{YBa}_2\text{Cu}_3\text{O}_{7-x}$ at high temperatures is crucial. A high oxygen pressure results in a high temperature superconductor; work in vacuo leads to the antiferromagnetic insulator, $\text{YBa}_2\text{Cu}_3\text{O}_6$.

Although many groups have qualitatively confirmed the above properties using structural techniques, only one group has succeeded in establishing the thermodynamically stable phase diagram as a function of temperature and oxygen partial pressure [9]. Their work, part of which is summarised below, is testimony to the precision and accuracy of careful neutron powder diffraction measurements.

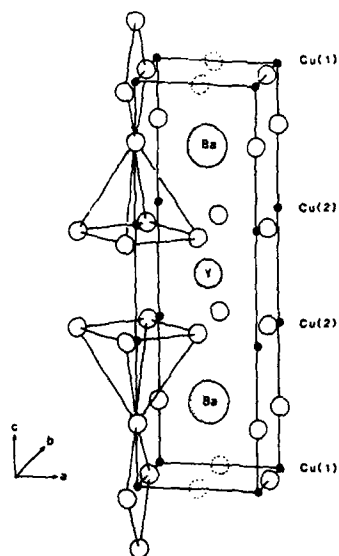


Figure 1. The crystal structure of $\text{YBa}_2\text{Cu}_3\text{O}_{7-x}$. The hollow circles are oxygen atoms; the dotted circle represents the oxygen vacancy site at $(\frac{1}{2} 0 0)$.

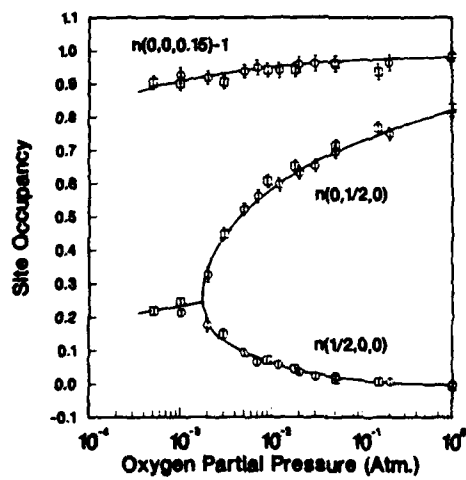


Figure 2. Site occupancies of oxygen atoms in $\text{YBa}_2\text{Cu}_3\text{O}_{7-x}$ versus oxygen partial pressure at 490°C [10]

Samples of $\text{YBa}_2\text{Cu}_3\text{O}_{7-x}$ were studied in-situ by neutron powder diffraction at 490°C and 440°C as a function of oxygen partial pressure on the Special Environment Powder Diffractometer, SEPD, at IPNS, Argonne National Laboratory. These were compared with samples that were quenched from a constant temperature (500°C) at various oxygen partial pressures [10]. These quenched samples exhibited the 'two-plateau' behaviour in superconducting transition temperature. The disappearance of superconductivity correlated with the transformation from orthorhombic to tetragonal structures at $x \sim 0.6$. Neutron diffraction measurements indicated vacancies on the $(0,0,z)$ oxygen site (see Figure 1) bridging the copper plane and chain sites. This has been corroborated independently by accurate single crystal X-ray measurements [11] and provides an explanation of why the orthorhombic to tetragonal transformation occurs at $x \approx 0.6$ and not $x \approx 0.5$. The occurrence of these vacancies is explained by Goodenough [12]. The corresponding in-situ experiments at constant temperatures of 490°C and 440°C showed that the quenched samples broadly preserve the structural properties corresponding to the temperature and oxygen partial pressure from which they are quenched. In particular the bridging oxygen site shows up to a maximum of 0.1 vacancies. This is displayed in Figure 2 along with the site occupancies of the two oxygen sites at $(0 \frac{1}{2} 0)$ and $(\frac{1}{2} 0 0)$. The precision with which these sites are determined allow the authors to perform statistical mechanical calculations [13] and to conclude that at the structural phase transition the combined occupancies of $(0 \frac{1}{2} 0)$ and $(\frac{1}{2} 0 0)$ sites is $\frac{1}{2}$ to within experimental error. Further subtle differences between quenched and in-situ samples are expounded in reference [10]. The confidence with which these statements are made arises directly from the precision with which structural parameters may be determined by the Rietveld method and from painstaking care to ensure thermodynamic equilibrium in the in-situ measurements.

PRECISE AND ACCURATE STRUCTURE REFINEMENT

Benzene, C_6H_6 , is one of the most important organic molecules, forming the basic building unit of all aromatic compounds. Because of its central role in organic chemistry, benzene has been extensively studied by numerous experimental and theoretical techniques. The simplicity of the chemical formula, C_6H_6 , belies, however, the complexity of its crystal structure. As a result of a complex packing configuration, benzene adopts an orthorhombic structure, space group Pbca ($Z=2$), with a moderately-sized unit cell ($a=7.3550 \text{ \AA}$, $b=9.3709 \text{ \AA}$, $c=6.6992 \text{ \AA}$, $V=461.7 \text{ \AA}^3$) (see figure 3). The successful structure determination by Cox in 1928 [14] located only the carbon atoms. However, the observed molecular planarity resolved a debate about whether the molecule was flat or puckered, as favoured by a number of eminent

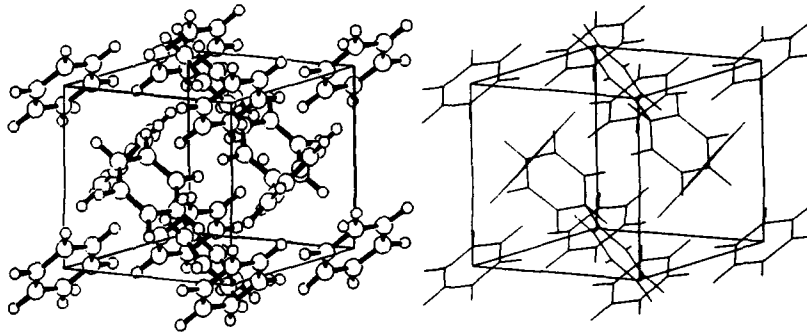


Figure 3. A plot of the crystal structure of benzene

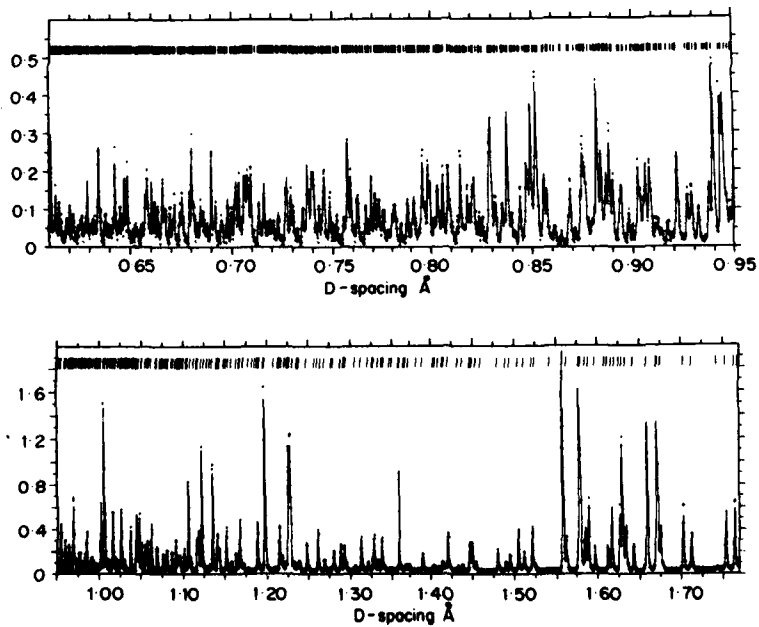


Figure 4. The final profile fit to the benzene data obtained on HRPD at ISIS. The d-spacing ranges shown are 0.61–0.95Å and 0.95–1.78Å. The tags at the top of each plot indicate the positions of the Bragg reflections.

scientists including Bragg. Not surprisingly this result had a significant impact on the basic understanding of chemical bonding.

Successive X-ray single crystal investigations improved the precision and accuracy of structure determination. The use of neutrons as a structural probe confirmed the planarity not only of the carbon but also the hydrogen atoms. A recent single crystal neutron diffraction investigation on deuterated benzene, C_6D_6 [15] sought to investigate any deviations from planarity. The molecular symmetry, $\bar{1}$, permits a "chair" but forbids a "boat" configuration. Although this study was concerned with subtle structural details and small departures from planarity, the principal criterion for investigation was the same as the first crystallographic study in 1928 - namely an improved understanding of the chemical bond. Indeed, these experimental results have been compared with the latest theoretical calculations to assess the current status both of experimental technique and theoretical calculation. One further justification was given by the authors for performing another single crystal neutron diffraction experiment: benzene "should be repeatedly investigated by each scientific method whenever there is a significant advance with respect to the detail or accuracy that the method can offer". HRPD is the most powerful powder diffractometer for elucidating the detailed description of crystal structure and is the only neutron diffractometer that routinely operates with a $\Delta d/d$ resolution of 5×10^{-4} . It was thus decided that a detailed structural investigation of benzene should be performed on HRPD. Such an investigation addresses several important questions, the two most significant being (i) how well do the best powder diffraction experiments compare with equivalent single crystal studies for moderately complex structures with unit cells of the order of 500 \AA^3 and (ii) can reliable temperature factors be obtained from time-of-flight powder diffraction experiments? The existence of both high precision single crystal data and detailed theoretical calculations provide a very rigorous test for the benzene data collected on HRPD.

Benzene melts at 6°C . A powder sample was thus prepared by grinding 5 cm^3 of deuterated benzene in a glove box under a cold nitrogen atmosphere. The sample was then loaded into a cylindrical vanadium can and rapidly cooled to liquid helium temperatures (4 K) to avoid problems with preferred orientation. Data were collected at the high resolution 2 m position ($\Delta d/d \sim 5 \times 10^{-4}$) on HRPD over a period of approximately nine hours ($174 \mu\text{A-hr}$). The raw data were corrected for incident flux (using a vanadium calibration), and cryostat and sample attenuation. The last correction was derived from consideration of the transmitted neutron flux and showed significant structure from multiple-scattering self-attenuation effects. Rietveld refinement was performed using the powder diffraction package developed at RAL [16] and based upon the Cambridge Crystallography Subroutine Library. The data ranged in d -spacing from 0.606 \AA to 1.778 \AA , consisted of 5382 points and included 1040 reflections. Small impurity peaks were obtained in the diffraction pattern, caused somewhat remarkably

by vanadium from the sample can and cryostat tails. At present these have not been considered in the data analysis. Using a peak shape consisting of a double exponential decay convoluted with a Voigt function (itself the convolution of Gaussian and a Lorentzian function) an excellent least-squares fit to the powder diffraction data was obtained (figure 4). The refined structural parameters, including 18 atomic coordinates and 36 anisotropic temperature factors, are listed in Table I. Table lists bond lengths, uncorrected for libration, obtained in the present study and from the work of Jeffrey et al [15]. The agreement is good, with few statistically significant differences, these probably resulting from systematic errors in the powder diffraction data. Experimental and theoretically calculated anisotropic temperature factors are presented in Table II. With the exception of the B_{22} temperature factors for three carbon atoms, there is a remarkable agreement between the temperature factors obtained from HRPD and from the single crystal data. More importantly, the anisotropic temperature factors for the deuterium atoms calculated using harmonic lattice dynamical calculations [17] significantly different from those obtained by powder and single crystal diffraction techniques.

At the present stage of analysis it is clear that the end results obtained from refinement of HRPD data are only marginally inferior to the best single crystal data. Both experimental techniques agree closely with each other, and differ from the theoretical calculations, particularly in the values obtained for the anisotropic temperature factors for the deuterium atoms. The powder diffraction experiment thus strongly supports the single crystal study and indicates that further improved theoretical calculations are required. The quality of powder diffraction results represents present state of the art at ISIS. Further improvements in normalisation procedure and multiphase analysis are currently under development and should lead to a precision and accuracy in moderately complex structure determination that compare very favourably with the best single crystal results.

TABLE I - Refined Structural Parameters for Benzene from HRPD
space group $Pbca$

$Z=2$ molecular symmetry = $\bar{1}$

$a = 7.3551(3) \text{ \AA}$, $b = 9.3712(4) \text{ \AA}$, $c = 6.6994(3) \text{ \AA}$, $V = 461.76 \text{ \AA}^3$

x/a	y/b	z/c	$B_{iso} (x 10^{-4} \text{ \AA}^2)$	
C1	-0.06120(15)	0.14123(10)	-0.00519(20)	68(6)
C2	-0.14023(15)	0.04469(10)	0.12722(15)	68(6)
C3	-0.07770(15)	-0.09689(12)	0.13264(20)	77(6)
D1	-0.10853(15)	0.25050(15)	-0.01187(25)	202(9)
D2	-0.24908(20)	0.07682(15)	0.22600(20)	202(9)
D3	-0.13821(20)	-0.17136(15)	0.23703(20)	203(9)
$R_p = 13.2\%$ $R_{wp} = 15.7\%$ $R_E = 10.8\%$ $\chi^2 = 2.1$				

Benzene: Bond-lengths (uncorrected for libration)
HRPD data (4 K) (present work)

C1-C2 = 1.3940(20) Å	C1-D1 = 1.0825(30) Å
C2-C3 = 1.4047(30) Å	C2-D2 = 1.0815(30) Å
C1-C3 = 1.3948(20) Å	C3-D3 = 1.0836(25) Å
mean = 1.3978(15) Å	mean = 1.0825(20) Å

Single crystal neutron diffraction (15 K) (after Jeffrey et al 1987)

C1-C2 = 1.3969(7) Å	C1-D1 = 1.0879(9) Å
C2-C3 = 1.3970(8) Å	C2-D2 = 1.0869(9) Å
C1-C3 = 1.3976(7) Å	C3-D3 = 1.0843(8) Å
mean = 1.3972(5) Å	mean = 1.0864(7) Å

TABLE II - Benzene at Low Temperatures: Anisotropic Temperature Factors ($\times 10^4 \text{ \AA}^2$)

Atom	B ₁₁	B ₂₂	B ₃₃	B ₂₃	B ₁₃	B ₁₂
C1	90	66	89	3	7	0
	77	58	77	3	0	7
	79(2)	67(2)	88(2)	4(1)	7(2)	6(2)
	77(7)	42(6)	87(7)	1(5)	5(5)	-3(4)
C2	84	87	82	-2	17	6
	71	79	70	-2	17	9
	74(2)	81(2)	79(2)	0(2)	17(2)	9(2)
	71(7)	58(7)	68(6)	9(4)	26(5)	12(4)
C3	86	79	82	10	11	6
	73	72	70	10	11	-5
	81(2)	75(2)	82(2)	10(1)	14(2)	-3(2)
	83(7)	57(7)	92(7)	0(5)	18(5)	-1(4)
D1	216	173	212	11	39	38
	222	165	199	11	39	38
	224(3)	114(2)	239(3)	12(2)	25(2)	46(2)
	218(8)	121(7)	267(9)	19(5)	22(6)	31(5)
D2	184	226	215	5	56	56
	170	217	202	5	55	56
	183(2)	204(3)	208(3)	-8(2)	88(2)	35(2)
	170(8)	212(8)	225(9)	-2(6)	120(6)	33(5)
D3	228	208	171	60	37	-2
	215	199	158	59	36	-1
	214(3)	171(2)	199(3)	58(2)	61(2)	-18(4)
	241(9)	155(8)	214(8)	75(6)	66(7)	-20(5)

Key to parameters in above table :

- Line 1 Harmonic lattice-dynamical calculation (15 K)
(Filippini et al Acta Cryst A45 261-263 (1989))
- Line 2 Harmonic lattice-dynamical calculation (0 K)
- Line 3 Neutron single crystal diffraction data (15 K) (Jeffrey et al 1987)
- Line 4 Neutron powder diffraction data (4.2 K) (present work)

FULL AND PARTIAL STRUCTURE DETERMINATION

The single most important contribution to high resolution powder diffraction over the past decade is widely recognised to be the Rietveld method which has, with current machines, enabled complex structures with up to 100 parameters to be refined. Structure determination, however, has proved for the most part to be intractable as a routine procedure because of limited resolution and the resultant inability to resolve a sufficient number of independent intensities to allow analysis by direct methods or Patterson techniques. The new generation of instruments that possess ($\Delta d/d$) resolutions of better than 0.001, have, in principle, the resolving power to separate a sufficiently large set of reflections to permit structure determination. The successful determination of the structure of ferric arsenate, FeAsO_4 [18] indicates that the most significant contribution of the new high resolution machines may be the routine structure determination of moderately-complex materials that are unavailable or costly to produce as single crystals. Maximum entropy [19] and simulated annealing [20] techniques also facilitate structure determination from powders.

The ab initio determination of a structure, whether from single crystal or powder data, can best be understood in terms of five discrete steps :

1. Automatic indexing of the powder diffraction pattern
 - determination of the crystal system and cell constants.
2. Identification of possible (perhaps several) space groups from systematic absences.
3. Evaluation of individual integrated intensities
 - where N peaks overlap apportion intensities as $1/N$
 - assign a small intensity I_s for unobserved systematically present intensities where I_s is \sim one-tenth of the smallest observed intensity of similar d-spacing.
- 4a. Extraction of structural information, from the Patterson function, consisting of orientation and/or positioning of fragments and polyhedra, followed by either 4b or 5.
- 4b. Solution of the phase problem and determination of an approximate structure by direct methods for possible space groups.
5. Refinement, either from integrated intensities or by profile analysis, of the approximate structure to obtain the final answer.

In many crystallographic problems, although a substantial fraction of the structure is known, the position of a crucial fragment may be undetermined. A good example of this, that is particularly applicable to neutron powder diffraction, is the location of hydrogens in organic materials where only the non-hydrogen atoms (e.g. carbon, nitrogen and oxygen) have been accurately determined from X-ray structure studies. Two techniques have proved useful: (i) difference Fourier, and (ii) bond length and

bond angle slack constraints in conjunction with profile refinement. An elegant example of the former method is the location of benzene in sodium zeolite-Y [21].

REAL TIME NEUTRON POWDER DIFFRACTION

High intensity neutron powder diffraction at medium resolution has become an increasingly powerful tool over the past five years [22]. Applications have included reaction kinetics and thermal diffractometry (the study of the evolution of a diffraction pattern as a function of temperature). High temporal resolution is required; counting times must realistically be less than ten minutes. Such measurements provide direct information on the progress of a reaction but also may indicate structural transformations and changes in morphology. Great care must be taken in thermal diffractometry measurements that thermodynamic equilibrium has been achieved for meaningful results to be obtained. A notable example of this work, the study of $\text{YBa}_2\text{Cu}_3\text{O}_{7-x}$ as a function of temperature and composition, is described in an earlier section of this paper. Equilibrium was monitored by repeated measurements of lattice parameters; at low partial pressures of oxygen equilibrium took as long as 24 hours (c.f. run times were ca. 30 minutes).

Real time neutron powder diffraction has been pioneered on the D1b diffractometer, ILL, Grenoble. The following example performed on this machine serves to illustrate the power of the technique. For a comprehensive survey see references [22].

Dehydration of $\text{WO}_3 \cdot 1/3\text{H}_2\text{O}$

$\text{WO}_3 \cdot 1/3\text{H}_2\text{O}$ is a relatively recently discovered hydrate of tungsten trioxide and has an orthorhombic structure that is closely related to a hexagonal tungsten bronze. On heating, this structure transforms into a new form of tungsten trioxide that at higher temperatures changes into perovskite-related WO_3 . A neutron thermodiffractometric measurement of this sequence of dehydration and reconstructive phase transformation shows that the initial dehydration transformation reaction occurs in two steps (see figure 5). Firstly, the dehydration reaction occurs (note in figure 5 the decrease in the incoherent hydrogen background confirming this) that does not change the initial WO_3 framework. This is then followed by a reconstructive transformation to the hexagonal tungsten bronze structure. Of note in the latter transition is the anomalously large widths of the $0k0$ reflections associated with the dehydrated original framework. In the tungsten bronze phase these peaks can be represented by the sum of two gaussian functions at the same Bragg angle, but with an intensity ratio of 1:2. The stronger component has

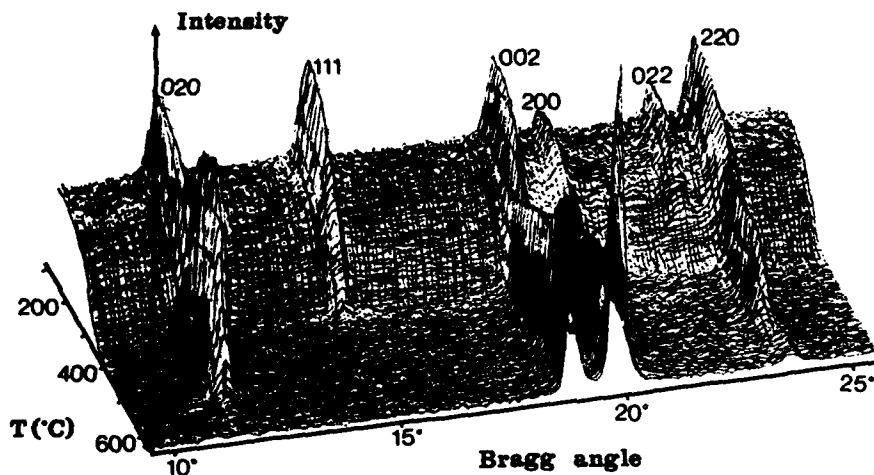


Figure 5. Temperature variation of the neutron powder diffraction pattern of $\text{WO}_3 \cdot 1/3\text{H}_2\text{O}$ [23].

a relatively narrow width consistent with the instrumental resolution of D1b; the weaker contribution is rather broad and corresponds to an average crystal dimension of around 200Å along the *b*-axis of the original structure. This observation provides information about the reconstructive phase transition mechanism suggesting that it proceeds via a shear of the initial structure perpendicular to the *b* axis. Thus, it is possible not only to detect intermediate stages in the course of a reaction, but also to obtain information about the structural mechanism of transformations.

NEUTRON POWDER DIFFRACTION: FUTURE PROSPECTS

The preceding paragraphs give an indication of the diversity of problems that may be tackled using neutron powder diffraction and the precision and accuracy with which structural and related parameters may be determined. What does the future hold? Will time-of-flight powder diffractometers supersede constant wavelength machines? Will X-ray powder diffraction at synchrotron sources replace neutron diffraction?

Although high resolution neutron powder diffractometers have greatly increased the scope and possibilities of the technique, the need for yet higher resolution ($\Delta d/d < 3 \times 10^{-4}$) is debatable. At present, the majority of diffraction patterns that are collected on machines such as the high resolution powder diffractometer, HRPD, at ISIS are dominated by sample-dependent effects. However, there is a clear need for high resolution diffractometers to have higher intensities. High resolution machines are capable of tackling more complex crystal structures. Since the total scattering power from a sample depends on the number of atoms then the average peak intensity is inversely proportional to the size of the unit cell. Very precise studies of moderately complex materials such as benzene (this paper) with unit cell volumes of around 500 \AA^3 take around 12 hours. Extrapolating this precision to unit cells of $\sim 3000 \text{ \AA}^3$, a reasonable limit for the present generation of high resolution neutron powder diffractometers, necessitates an order of magnitude increase in count rate for reasonable counting times. Additionally, advances in powder diffraction software will allow, for example, complex line-shape analysis and the study of incommensurate structures.

The spectacular success of high intensity, medium resolution powder diffractometers in the materials science highlights another area of development in neutron powder diffraction. The ability to collect diffraction data with a $\Delta d/d$ resolution better than 3×10^{-3} in typically one minute will make an important impact in materials science. Multiphase mixtures may be analysed in a quantitative manner. Reaction kinetics measured in-situ in, for example, a zeolite catalytic rig will significantly increase our understanding of such processes. Simultaneous structure refinement and line-broadening studies will permit not only structural transformations to be studied but also transformation mechanisms to be understood. The ability to perform a complete structural study of small samples in, for example, a high pressure cell at 150 kbar is currently under study at ISIS. Finally high intensity will be invaluable in the volume pixel-by-pixel scanning of heterogeneous materials (e.g. a commercial battery under discharge) or components under residual stress.

The three final examples mentioned in the previous paragraph benefit from measurement at fixed angle on a time-of-flight diffractometer. This feature, along with the ability to probe d -spacings of ca. 0.3 \AA , gives time-of-flight diffractometers the edge over their constant wavelength counterparts. However, both types of machine are valuable instruments for materials science. The accuracy and precision with which structures can be refined using neutron diffraction is impressive and unlikely to be supplanted by synchrotron X-ray powder diffraction.

REFERENCES

1. M. A. Beno, L. Soderholm, D. W. Capone II, D. G. Hinks, J. D. Jorgensen, J. D. Grace, Ivan K. Schuller, C. U. Segre and K. Zhang, *Appl. Phys. Lett.* **51** 57 (1987)
2. J. J. Capponi, C. Chailout, A. W. Hewat, P. Lejay, M. Marezio, N. Nguyen, B. Raveau, J. L. Soubeyroux, J. L. Tholence and R. Tomler, *Europhys. Lett.* **3** 1301 (1987)
3. W. I. F. David, W. T. A. Harrison, J. M. F. Gunn, O. Moze, A. K. Soper, P. Day, J. D. Jorgensen, M. A. Beno, D. W. Capone II, D. G. Hinks, Ivan K. Schuller, L. Soderholm, C. U. Segre, K. Zhang and J. D. Grace, *Nature* **32** 310 (1987)
4. F. Beech, S. Miraglia, A. Santoro and R. S. Roth, *Phys. Rev. B* **35** (1987)
5. J. E. Greedan, A O'Reilly and C. V. Stager, *Phys., Rev. B* **35** 8770 (1987)
6. H. M. Rietveld, *Acta. Cryst.* **22** 151 (1967)
7. H. M. Rietveld, *J. Appl. Crystallogr.* **2** 65 (1969)
8. J. C. Taylor, *Aust. J. Phys.* **38** 519 (1985)
9. J. D. Jorgensen, M. A. Beno, D. G. Hinks, L. Soderholm, K. J. Volin, R. L. Hitterman, J. D. Grace, I. K. Schuller, C. U. Segre, K. Zhang and M. S. Kleefisch, *Phys. Rev. B.* **36** 3608 (1987)
10. J. D. Jorgensen, H. Shaked, D. G. Hinks, B. Dabrowski, B. W. Veal, A. P. Panlikas, L. J. Nourichi, G. W. Crabtree, W. K. Kwok and L. H. Nunez, *Physica C* **153-155** 578 (1988)
11. W. W. Schmahl, E. Salje and Y. W. Liang, *Phil. Mag. A* **56** 173 (1988)
12. J. B. Goodenough, *Mater. Res. Bull.* **23** 401 (1988)
13. H. Shaked, J. D. Jorgensen, J. Faber Jr., D. G. Hinks, B. Dabrowski, *Phys. Rev. B* **29** 7363 (1989)
14. E. G. Cox, *Nature* **112** 401 (1928)
15. G. A. Jeffrey, J. R. Ruble, R. K. McMullan and J. A. Pople, *Proc. R. Soc. Lond* **A414** 47 (1987)
16. W. I. F. David, D. E. Akporiaye, R. M. Ibberson and C. C. Wilson, Rutherford Appleton Laboratory Report No. RAL-88-103, 1988
17. P. Filippini and E. Gramaccioli, *Acta Cryst* **A45** 261 (1989)
18. A. K. Cheetham, W. I. F. David, M. M. Eddy, R. B. Jakeman, M. W. Johnson and C. C. Torardi, *Nature* **320** 46 (1986)
19. W. I. F. David, *J. Appl. Crystallogr.* **20** 316 (1987)
20. M. W. Deem and J. M. Newsam, *Nature* **342** 260 (1989)
21. A. N. Fitch, H. Jovic and A. Renonprez, *J. Chem. Soc. Chem. Comm.* 1311 (1985)
22. J. Pannetier in *Chemical Crystallography with Pulsed Neutrons and Synchrotron X-rays* edited by M. A. Carrondo and G. A. Jeffrey (D. Reidel Publishing Company, 1988) pp313-355
23. J. Pannetier, *Chemica Scripta* **26A** 131 (1986)

**THE APPLICATION OF NEUTRON TOPOGRAPHY TO THE STUDY
OF X-RAY SENSITIVE ORGANIC CRYSTALS - A POSSIBLE
ALTERNATIVE TO X-RAY TOPOGRAPHY.**

M. DUDLEY

Department of Materials Science and Engineering,
State University of New York at Stony Brook,
Stony Brook, New York 11794, U.S.A.

ABSTRACT.

Neutron topography has been carried out on organic single crystals of varying X-ray sensitivity, in order to test the feasibility of the technique as an alternative to X-ray topography for the study of the influence of defects on the solid state reactivity of X-ray sensitive single crystals. Specimens studied include the diacetylene PTS, and Pyrene. A comparison of the strain sensitivity and spatial resolution of the neutron and X-ray based techniques is made. Preliminary results of dynamic neutron topographic studies of the UV induced polymerization in PTS are presented. These results are compared to those obtained from similar X-ray topographic studies.

Results indicate that the neutron technique can be a useful ally technique to the analogous X-ray techniques in studies of the influence of defects on reactivity in specimens of moderate X-ray sensitivity. In cases of extreme sensitivity, the neutron technique is the only one available for studies of this nature.

INTRODUCTION.

Over a period of many years, considerable effort has been directed towards the understanding of the role of crystalline defects in the reactivity of bulk single crystals. A prerequisite for the capability to gather this understanding is the availability of a non-destructive technique which combines high strain sensitivity with the capability of imaging defects and strain in bulk single crystals. Generally, electron microscopic techniques are not applicable in such studies due to induced beam heating, the fact that the field of view of the technique is so small, and insufficient strain sensitivity. On the other hand, X-ray diffraction topography [1],[2] (e.g. the conventional monochromatic Lang technique) is a technique which allows both characterization of the bulk defect and general strain distribution in large (cm^3) single crystals prior to reaction and subsequent monitoring of this distribution during reaction, in a dynamic fashion. As such it has found application in this kind of study [3]. In many instances reaction induced bending and strain make it necessary to utilize White Beam Synchrotron Radiation Topography which by nature has a greater inherent tolerance of lattice distortion than conventional monochromatic techniques. Unfortunately, many of the reactive systems of interest are also X-ray sensitive, which in some cases precludes extensive use of X-ray imaging techniques. In some systems, it has been shown that suitable filtering of a Synchrotron Beam to remove the generally more highly absorbed longer wavelength X-rays can reduce X-ray induced reaction (or damage) to tolerable levels [4]. However, such methodology would not be applicable in cases of extreme X-ray sensitivity. In these latter systems, there is a need for a truly non-destructive imaging technique analogous to the X-ray topographic technique. Neutron Topography is such a technique.

In the past, Neutron Topography has been applied to, for example, the characterization of crystals which have prohibitively high X-ray absorption [5]. Without a doubt

the major thrust in Neutron Topographic research has been in the area of imaging of magnetic structures in materials [6], [7] which exploits the magnetic scattering effect due to the interaction of the neutron magnetic moment with the magnetic configuration in the crystal. To date, no application of neutron topography to the study of X-ray sensitive, reactive organic crystals has been reported. Here we report the first systematic investigation of the feasibility of such applications of the technique.

Two systems were primarily studied. Pyrene ($C_{16}H_{10}$) single crystals, which are relatively X-ray insensitive, and 2,4 Hexadiyne-1,6-Diol-Bis-(*p*-Toluene Sulphonate) (PTS) monomer single crystals which can be polymerized readily in an X-ray beam. These latter crystals are consequently classed as relatively highly X-ray sensitive. Details on the preparation of these crystals can be found in other papers [4],[8],[9].

EXPERIMENTAL TECHNIQUES.

For all systems studied here, neutron absorption is very low, and neutron induced reaction is not expected to occur. Consequently, restrictions on exposure times are not necessary.

Neutron topographic experiments, performed on both the S20 and D13 instruments at the Institut Laue-Langevin (ILL), were designed so as to make maximum use of the available neutron flux with minimum resolution loss from geometric effects [9],[10]. The neutron flux is so low compared with typical X-ray fluxes, that a high resolution, collimated beam experiment similar to the Lang technique is not feasible due to what could be prohibitively long exposure times. Thus, a "Barth-Hosemann" [11] type geometry is utilized, monochromatization of the incident "white" beam being provided by a copper single crystal. However, this type of geometry inevitably implies some resolution loss compared with conventional Lang type X-ray topographic geometries (or geometries used with synchrotron sources), since specimen-film distances must be made large enough to avoid impingement of the direct beam on the detector.

In considering diffraction geometries, only transmission geometries were sought as the overall bulk defect structure of the crystals was of interest rather than near surface structures. Criteria used in selecting diffraction geometries for the neutron topographs included: (a) Accessibility; obviously not all reflections are accessible in the transmission Laue geometry, (b) Minimization of geometric resolution losses [9],[10], (c) Maximization of diffracted intensity, achieved through choice of high Structure Factor reflections, and (d) Correspondence with X-ray reflections; if possible, so that neutron and X-ray images might be directly compared.

RESULTS.

(a) Pyrene

Figure 1 shows a Lang topograph ($g = \bar{2}20$, Mo $K_{\alpha 1}$ radiation) taken from a (100) cut protonated pyrene crystal platelet which contained the seed. This topograph is recorded in the optimum X-ray diffraction geometry for this material, i.e. this reflection gives the best dislocation images. Note the growth dislocations propagating towards the $\{110\}$ growth faces. Analysis of these dislocations on different reflections shows that they are mixed in character. Unfortunately, neutron topographs recorded with the same reflection vector had very poor resolution due in part to the relatively small Bragg angle for the reflection which meant that specimen film distances had to be increased to avoid impingement of the transmitted beam on the detector. Therefore no comparison was

attempted between neutron and X-ray topographs recorded with $\{220\}$ type reflection vectors.



Figure 1. Lang topograph ($g = \bar{2}20$, Mo $K_{\alpha 1}$ radiation) recorded from a pyrene crystal.

Figure 2 (a) shows a white beam synchrotron X-ray topograph ($g=44\bar{1}$, $\lambda=0.5\text{\AA}$) recorded from the same crystal. The image is a composite made from several separate images, each recorded with the relatively small area white beam, available at the topography station, X-19C, the NSLS Brookhaven, USA. The dislocation structure is seen to be the same as in figure 1, although the images are a little broader and more diffuse, due to the narrower inherent perfect-crystal reflection curve width. For comparison, figure 2 (b) shows the corresponding neutron topograph ($g=44\bar{1}$, $\lambda=1.7\text{\AA}$) recorded from part of the same crystal. The dislocation structure observed on figure 2 (b) is recognizable as being the same as that on figure 2 (a), although clearly the definition and resolution of the dislocation images on the neutron image is much inferior.

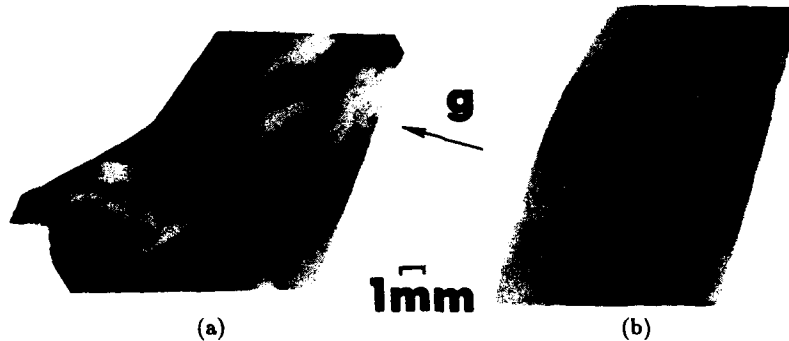


Figure 2. (a) White beam synchrotron X-ray topograph ($g=44\bar{1}$, $\lambda=0.5\text{\AA}$) from pyrene, and (b) corresponding neutron topograph ($g=44\bar{1}$, $\lambda=1.7\text{\AA}$).

(b) PTS.

Figure 3 (a) shows a filtered white beam synchrotron X-ray topograph ($g=\bar{1}04$, $\lambda=1.0\text{\AA}$) recorded on fast X-ray film (to minimize exposure [4], [12]) from a PTS monomer crystal. Note the "end-on" images of dislocations in the central growth sector. Figure 3 (b) shows a neutron topograph ($g=\bar{1}0\bar{2}$, $\lambda=1.7\text{\AA}$) recorded from a similar crystal. It is obviously very difficult to discern any clear evidence for the "end-on" dislocations on the neutron topograph, and only by comparison with the X-ray image can the presence of very weak contrast in the dislocated volume of crystal be discerned. The resolution

of dislocation images on the neutron topograph (which is recorded in near optimum geometry) is therefore grossly inferior to that on the X-ray topograph (also recorded in near optimum geometry).

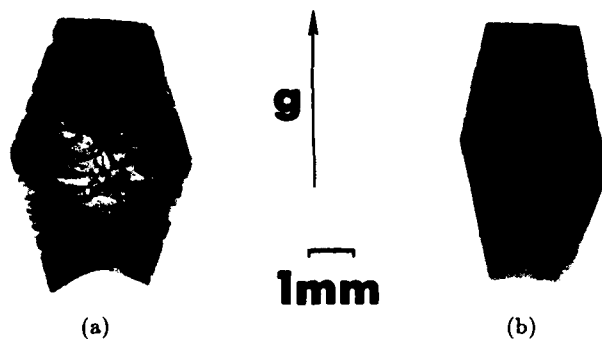


Figure 3. (a) Filtered white beam synchrotron X-ray topograph ($g=\bar{1}04$, $\lambda=1.0\text{\AA}$) recorded from a PTS monomer crystal, (b) neutron topograph ($g=\bar{1}0\bar{2}$, $\lambda=1.7\text{\AA}$) recorded from a similar crystal.

Neutron topographs recorded in situ during UV induced polymerization, from the PTS crystal imaged in figure 3 (b), show little or no change in microstructural detail. However, reaction was accompanied by changes in both experimental rocking curve width (from which the sample mosaicity can be calculated [9]) and integrated intensity. Figures 4 (a) and 4 (b) show plots of measured integrated intensity, and calculated sample mosaicity, respectively ((102) reflection), as a function of time in the UV beam.

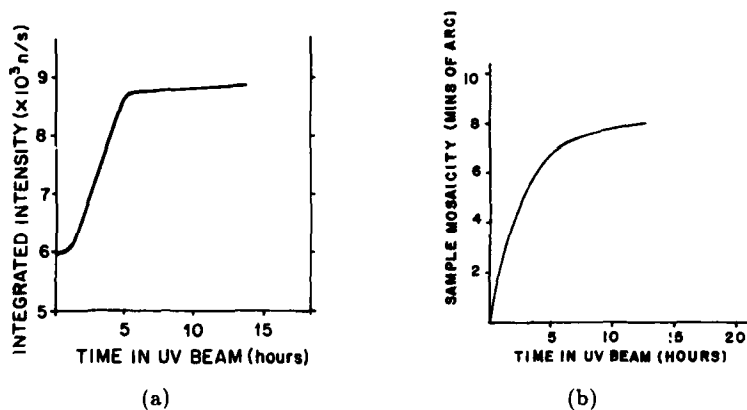


Figure 4. Plots of (a) integrated intensity, and (b) calculated mosaic spread, respectively, versus UV exposure, for PTS.

DISCUSSION.

One of the most important factors determining the resolution of dislocation images in neutron topography is the width of the image itself. Generally the width of a dislocation image on topographs recorded under low absorption conditions, such as are encountered

in neutron topography, is determined by the projection (in the diffracted beam direction) of the limiting width of the zone surrounding the dislocation line for which the effective misorientation $\delta(\Delta\theta)$ is greater than the inherent perfect-crystal reflection curve width [13]. For a very narrow (wide) inherent perfect crystal reflection curve width the limiting distance from the dislocation line for which this is true will be quite large (small) and so, wide (narrow) dislocation images would be predicted.

Such considerations have enabled the poor resolution of dislocation images on neutron topographs versus X-ray topographs, of crystals such as silicon, to be attributed to the extremely narrow inherent perfect-crystal neutron reflection curve widths [14]. However, inherent perfect-crystal neutron reflection curve widths for the crystals studied here generally wider than their X-ray counterparts, so that based on strain sensitivity considerations neutron dislocation image widths can sometimes be expected to be narrower than the corresponding X-ray image widths. This is mainly due to the fact that the neutron scattering length for carbon can be comparable to, or even greater than, the product of X-ray scattering factor and classical electron radius (depending, of course, on the relevant value of $\sin\theta_B/\lambda$), whereas in the case of materials such as Silicon, the neutron scattering length can be up to an order of magnitude smaller [15]. This means that neutron Structure factors can be comparable or greater than the product of X-ray Structure Factor and classical electron radius.

For example, calculation shows [9] that the inherent perfect-crystal neutron reflection curve width for the $(44\bar{1})$ reflection (4.48×10^{-6} radians) is broader than the corresponding X-ray width (0.97×10^{-6} radians), so that based on strain sensitivity considerations alone, dislocation image widths on the neutron topograph should be narrower than those obtained on the X-ray topograph. However, observations indicate that, in the case of protonated pyrene, dislocation images obtained on the $(44\bar{1})$ neutron topograph (Figure 2 (b)) are clearly broader, and thus inferior, in both resolution and definition, to those obtained on the $(44\bar{1})$ X-ray topograph presented (Figure 2 (a)). It is concluded that the ill-defined, broad dislocation images are mainly due to the poor geometrical resolution attained in the neutron topographic set-up even under optimum conditions. In addition, the general noise due to the incoherent scattering from the hydrogen in the system is expected to contribute to the lack of resolution.

In the case of PTS crystals it is not possible here to compare neutron and X-ray images recorded with the same reflection vector [9]. It is, however, possible to compare neutron and X-ray images recorded under the respective optimum conditions. From examination of Figures 3 (a) and 3 (b) it can be concluded that dislocation images obtained on neutron topographs recorded from PTS crystals are grossly inferior to their X-ray counterparts. Neutron topographs recorded during in situ UV induced polymerization showed little evidence of image modification, not showing the kind of contrast changes routinely observed on synchrotron topographs. However, analysis of neutron experimental rocking curves, recorded during reaction, provides a unique insight into reaction induced strains. The observed increase in experimental rocking curve width is attributable to a calculable increase in the mosaicity of the specimen crystal, which is probably due to the fact that the UV induced reaction in PTS is restricted to the top few microns of crystal, so that the lattice parameter changes accompanying reaction, in conjunction with the heterogeneous reaction profile, lead to the formation of inhomogeneous distortion fields. The decrease in extinction resulting from this increase in mosaicity would then account for the increase in integrated intensity with UV dose. Such analysis of experimental rocking curves as a function of UV dose affords invaluable information on reaction induced strains, under conditions where the investigative probe (the neutron beam) cannot itself induce reaction.

CONCLUSIONS.

Diffraction geometries, desirable for high resolution imaging, in neutron topography of organic materials can be very restricted, due in part to the inherent nature of the Barth-Hosemann geometry employed, with the constraints of minimization of geometric resolution losses [9], and to the difficulty in locating strong reflections suitable for transmission imaging (dependent, of course, on the specific material). In some structures geometries can be optimized, in others optimization can be difficult or impossible. However, even in optimum geometries, the relatively large diffracted beam divergences lead to significant resolution loss. On the other hand, in situ neutron rocking curve analysis can provide important, non-destructive, information on reaction induced strains. In conclusion, provided suitable geometries can be found for the material of interest, neutron topography can provide information analogous to that provided by X-ray topography but with poorer spatial resolution. For the case of crystals which have extreme X-ray sensitivity it is envisaged that neutron topography may be the only non-destructive bulk imaging technique available, for large single crystals, which is capable of detailed defect structure and strain analysis, and of analysis of strain evolution during reaction.

Acknowledgements.

Research supported in part by the SERC through Rutherford Appleton Laboratory. Synchrotron topography performed in part on beamline X-19C at the NSLS, which is supported by the U.S. DOE under Grant No. DE-FG02-84ER45098. The author is grateful to Jose Baruchel without whose help these experiments would not have been possible, and to J.N. Sherwood for helpful discussions.

REFERENCES.

1. B.K. Tanner, "X-ray Diffraction Topography", Pergamon, (1976).
2. B.K. Tanner and D.K. Bowen (eds.), "Characterization of Crystal Growth Defects by X-ray Methods", Proceedings of NATO ASI, Series B. Physics, Volume B63, Plenum, (1980).
3. I.D. Begg, P.J. Halfpenny, R.M. Hooper, R.S. Narang, K.J. Roberts, and J.N. Sherwood, Proc. Roy. Soc., A386, 431, (1983).
4. M. Dudley, J.N. Sherwood and D. Bloor, Polym. Mater. Sci. & Engin., 54, 426, (1986).
5. J. Baruchel, M. Schlenker, A. Zarka, and J.F. Petroff, J. Cryst. Growth, 44, 356, (1978).
6. M. Schlenker and J. Baruchel, Physica 137B, 309, (1986).
7. J. Baruchel, Phase Transitions 14, 21, (1989).
8. R.M. Hooper and J.N. Sherwood, J.C.S. Faraday I, 72, 2872, (1976).
9. M. Dudley, J. Baruchel and J.N. Sherwood, submitted to J. Appl. Cryst., (1989).
10. J. Baruchel, C. Malgrange and M. Schlenker, in "Position Sensitive Detection of Thermal Neutrons", Edited by P. Convert and J.B. Forsyth, Academic Press, London, pp. 400, (1983).
11. H. Barth and R. Hosemann, Z. Naturf., 13a, 792, (1958).
12. M. Dudley, Mat. Res. Symp. Proc., 143, 253, (1989).
13. J.E. Miltat and D.K. Bowen, J. Appl. Cryst., 8, 657-669, (1975).
14. C. Malgrange, J.F. Petroff, M. Sauvage, A. Zarka and M. Englander, Phil. Mag., 33, 743, (1976).
15. G.E. Bacon, "Neutron Diffraction", 3rd edition, Clarendon Press, Oxford, (1975).

MULTIPLE SMALL ANGLE NEUTRON SCATTERING CHARACTERIZATION
OF THE DENSIFICATION OF ALUMINA

S. KRUEGER*, G.G. LONG* and R.A. PAGE†

*Materials Science and Engineering Laboratory, National Institute of Standards and Technology (formerly NBS), Gaithersburg, MD 20899

†Department of Materials and Mechanics, Southwest Research Institute, 6220 Culebra Road, San Antonio, TX 78228

ABSTRACT

Multiple small angle neutron scattering (MSANS) was used to follow the evolution of the pore size distribution in α -Al₂O₃ through the intermediate and final stages of sintering. This technique makes it possible to determine microstructure morphology in the 0.08 to 10 μ m size regime under conditions where the total scattering cross-section is dominated by elastic incoherent multiple scattering, as is often the case for ceramics. The MSANS results indicate an initial decrease in the effective pore radius from 0.19 μ m at 57% of theoretical density (TD) to 0.17 μ m at 79% TD. As the sample density further increased, there was a transition region after which the effective pore radius grew rapidly to ≥ 0.5 μ m at 98% TD. Standard Porod analysis on scattering by the same samples also indicates a transition between the intermediate and final stages of processing. Both sets of results support a topological model of sintering in which the interconnected pore network in the intermediate stage of sintering decays in a stable manner. The pores become fewer, while retaining the same diameter, as densification proceeds. In the final stage, isolated pores remain.

INTRODUCTION

Knowledge of the microstructure evolution as a function of thermal processing is important for the development of process models in ceramics. For dilute concentrations of scatterers between 1 nm and 100 nm, small angle neutron scattering (SANS) is invaluable for the determination of bulk microstructural parameters. The complementary MSANS technique, first described by Berk and Hardman-Rhyme [1,2], is applicable when the scatterers are in the 0.08 μ m to 10 μ m size range. In such cases, the total scattering cross-section is dominated by elastic incoherent multiple scattering. Effective (volume-weighted average) radii of the scatterers are extracted by measuring the wavelength dependence of the scattering curves at low scattering vector. Thus, it becomes possible to investigate thicker and denser materials than is possible with SANS. Of the many methods available for the determination of microstructure morphology, MSANS and SANS have the advantage of being able to measure both open and closed pores.

In this work, an investigation of the microstructure evolution of α -Al₂O₃ as a function of thermal processing was conducted. This is a system for which the process models [3] are comparatively well-understood, and thus it can serve as a model system for the new scattering techniques. An earlier study of microstructure evolution as a function of thermal processing in porous silica [4] has demonstrated that MSANS and SANS effectively cover the full range of relevant microstructure sizes. For the alumina system, MSANS was used throughout the intermediate and final stages because the pore sizes were large. Standard Porod [5] analysis, performed on the high angle portion of the scattering curves, was used to determine

total scattering surface areas, from which effective (surface area-weighted average) pore radii were calculated.

MSANS THEORY

The interaction of neutrons with matter is determined by the phase shift, ν , that a plane wave undergoes in traversing a particle of radius, R . This phase shift depends on the index of refraction of the particle or void, Δn , relative to the scattering matrix such that $\nu = (4\pi/\lambda)\Delta nR$, where λ is the neutron wavelength. $\Delta n = \Delta b\lambda^2/2\pi$, where Δb is the relative scattering length density, or contrast, of the particle or void:

$$\Delta b = \sum_{\text{cell}} b_i / V_{\text{cell}} - b_{\text{matrix}} \quad (1)$$

Thus, the phase shift ν is given by

$$\nu = 2\Delta bRA, \quad (2)$$

meaning that it is directly dependent on the material contrast, the dimensions of the scatterer and the neutron wavelength.

If $\nu \ll 1$, the measurement is in the conventional SANS diffraction regime. The form of the scattering curve as a function of the scattering wavevector Q (where $|Q| = 2\pi\epsilon/\lambda$, and ϵ is the scattering angle) is independent of neutron wavelength and depends only on the particle dimensions. On the other hand, if $\nu \gg 1$, the experiment involves multiple refraction, where every particle scatters and geometrical optics applies.

The scattering curve depends on neutron wavelength as λ^2 . When $\nu \leq 1$, the MSANS diffraction formalism applies [1,2] and the scattering curve broadens as a function of neutron wavelength. The predicted neutron intensity is approximately gaussian at $Q = 0$ and has a width nearly proportional to λ^2 . Even though the wavelength dependence is the same as that for multiple refraction, the fact that $\nu \leq 1$ allows an effective particle radius, $R_{\text{eff}}(0)$, to be determined from the wavelength dependence of the radius of curvature, r_c , at $Q = 0$ of the scattering spectrum.

A measure of the amount of multiple scattering is given by the parameter \bar{z} which is the sample thickness, z , divided by the statistical mean free path length, l .

$$\bar{z} = z/l = 1.5 \phi z (\Delta b\lambda)^2 R_{\text{eff}}(0), \quad (3)$$

where ϕ is the volume fraction of scatterers and the dimensions of the parameters are expressed in centimeters. \bar{z} is related to the scattering radius of curvature via an empirical relation [2]

$$r_c[\text{QR}] = 0.926(\bar{z} \ln^{0.85} \bar{z})^{0.5} \text{ for } \bar{z} > 5. \quad (4)$$

For $\bar{z} > 10$, the agreement with the theory is better than 0.1%. The analysis requires only the sample thickness, the wavelength dependence of the radius of curvature, the scattering volume fraction (which is a refinable parameter) and the scattering length density to derive $R_{\text{eff}}(0)$. For large Q , the scattering is determined by the single scattering Porod law [5], which applies even when the region near $Q = 0$ is dominated by multiple scattering [1].

ALUMINA SAMPLES

The samples were Baikowski alumina powder (CR6), slipcast to an average green density of 53% TD. The slip consisted of 43.5 vol.% alumina powder mixed into water, along with 0.5 wt.% of a polyelectrolyte dispersant (Darvan C). The suspension was ultrasonicated for 15 min and allowed to set overnight before being poured into moulds with teflon rings on top of plaster-of-paris blocks. After 55 minutes, the moulds were removed from the blocks and sealed in a container overnight. The partially-dried samples were then removed from the moulds and sealed in containers for 2 days. The containers were then opened to the air for an additional 5-7 days before a series of oven-drying steps were performed as follows: 2 days at 64°C, 1 day at 81°C, 1 day at 102°C and 1 day at 116°C, after which a dry, solid green body is obtained. In this fashion, a family of eight nearly-identical samples were prepared.

During sintering, samples were removed one by one from the furnace to yield examples of material between 56.5 and 98% TD. Figure 1 is a time-temperature curve for the sintering. Each circle represents a sample removed from the furnace and the number alongside is the measured %TD.

NEUTRON SCATTERING MEASUREMENTS

Measurements were made at the 20 MW research reactor at the National Institute of Standards and Technology (NIST, formerly the National Bureau of Standards). The NIST SANS facility [6] includes a velocity selector for choosing the mean incident wavelength, λ , of the neutrons with a spread, $\Delta\lambda/\lambda = 0.25$. Copious neutron fluxes can be obtained in the wavelength region between 0.5 and 2.0 nm due to a cryogenic moderator installed in the reactor core. The neutron beam is collimated with a 12 mm aperture which follows the velocity selector and a 8 mm aperture which precedes the sample

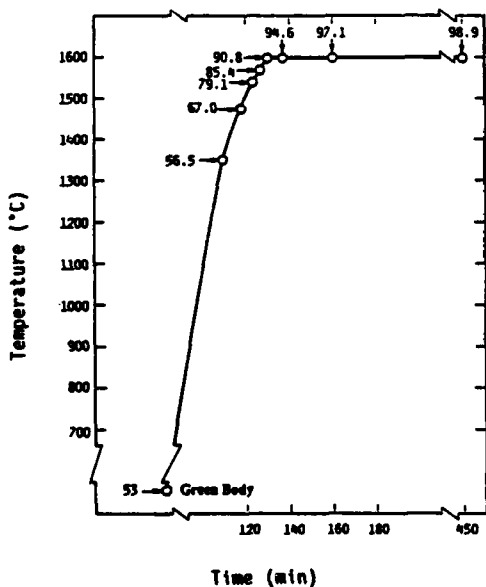


Figure 1. Sintering time-temperature curve for the alumina samples sintered to densities ranging from 56.5 to 98% TD.

position. Scattered neutrons are detected by a $64 \times 64 \text{ cm}^2$ position-sensitive detector divided into 128×128 pixels. The data are circularly averaged to produce one-dimensional intensity, $I(Q)$, versus Q curves. For Porod analysis, scattering cross-sections are placed on an absolute scale by normalizing to that of a standard silica gel sample measured under the same conditions.

RESULTS AND DISCUSSION

MSANS measurements were performed on each sample at a minimum of 5 different neutron wavelengths. The scattering curves exhibited the expected broadening with increasing neutron wavelength. Gaussian fits were made to each curve in the range extending from 90% of $I(0)$, the intensity at $Q=0$, to 45% of $I(0)$. The scattering curves no longer fit well to a gaussian in the higher Q region, where the scattering intensity falls below 40% of $I(0)$. For each fit, a radius of curvature was extracted from the standard deviation, $r_c = \sqrt{1/2\sigma}$. Blank spectra (with no scatterer in place), measured at each wavelength, were also fitted in order to make a correction for the instrument function. The measured values of r_c (symbols) along with the theoretical values determined using the MSANS formalism (solid lines) are plotted versus neutron wavelength in Figure 2 for each sample. The densities measured volumetrically and those determined by the neutron scattering are shown in the inset to the figure. The derived values of $R_{\text{off}}(0)$ fit the theory well for all samples measured.

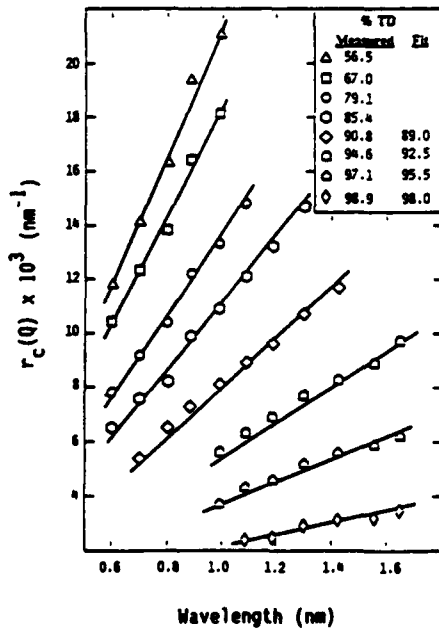


Figure 2. Measured radii of curvature (symbols) and the corresponding theoretical radii (solid lines) as a function of neutron wavelength for all samples measured. The sample densities measured volumetrically are shown in the inset, along with those determined by the neutron scattering measurements, if different.

$R_{\text{eff}}(0)$ was derived from Figure 2 for each alumina sample. A plot of $R_{\text{eff}}(0)$ as a function of %TD is illustrated in Figure 3, along with the average pore radius, $R_{\text{eff}}(\infty)$, derived from single particle Porod measurements assuming spherical scatterers. The MSANS determinations, which are strongly weighted to the larger volume particles [4], indicate that the average pore radius for the distribution within the alumina decreases slightly from 0.19 μm to 0.17 μm in the intermediate sintering stage and increases sharply to $>0.5 \mu\text{m}$ in the final stage. The Porod determinations, which are weighted to the smaller volume particles, indicate an average pore radius that is slowly increasing during the intermediate stage of sintering and more rapidly increasing during the final stage. Both results indicate a transition in the microstructure morphology between 85 and 95% TD. The quantitative differences arise in part because $R_{\text{eff}}(0)$ is derived from a measure of the volume fraction of voids in the system and $R_{\text{eff}}(\infty)$ from a measure of the total surface area in the spaces (or necks) between tetrahedrally positioned particles. Mercury porosimetry measurements (R.A. Page, unpublished results) performed on the samples below 85% TD, where open porosity is expected, agree qualitatively with both sets of SANS results and the average pore radii are quantitatively closer to the $R_{\text{eff}}(\infty)$ values.

The important result of both the SANS and porosimetry measurements is that the effective pore radius remains relatively constant through the intermediate stage of sintering. This is consistent with intermediate stage sintering models in which topological decay of an interconnected pore network is taking place [7]. Throughout the intermediate stage of sintering, the ratio ϕ/S_v , or volume fraction to surface area per unit volume, is constant [8]. Consequently, the pore channels retain a constant diameter as densification proceeds.

The effective pore radii measured with MSANS correspond to the cross-section of the pore channels. The average length of the pore channels is $>10 \mu\text{m}$, which is beyond the range of the MSANS technique. Thus, $R_{\text{eff}}(0)$

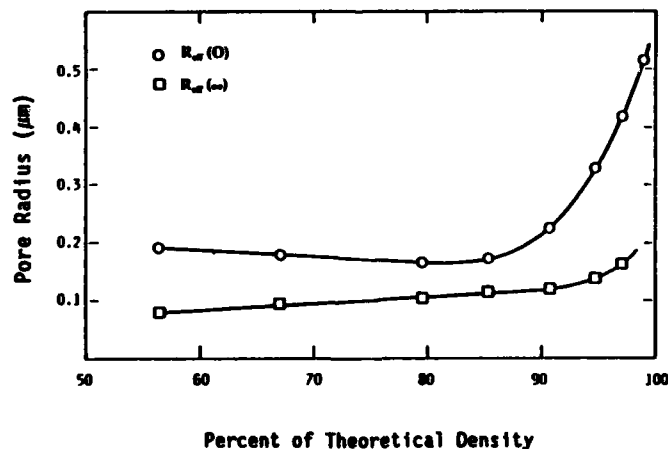


Figure 3. Effective pore radii for the alumina samples as a function of percent theoretical density determined from the MSANS formalism ($R_{\text{eff}}(0)$) and from the single particle Porod measurements ($R_{\text{eff}}(\infty)$).

remains relatively constant as densification proceeds and the pore channel network decays.

Before the channels have disappeared altogether, a transition into the final sintering stage occurs in which the porosity becomes isolated. Pore isolation possibly occurs due to a rupture or "pinching off" of the channels as they can no longer maintain their length while at the same time remaining stable against the increasing sintering force [7]. The isolated pores are more spherical, having diameters which are greater than the cross-sectional diameters of the original channels, yet small enough to be within the NSANS range. As the number of isolated pores increases, the larger dimension makes an increasing contribution to the total scattering, until it finally dominates the NSANS cross-section. Thus, $R_{eff}(\theta)$ increases gradually as the transition from intermediate to final sintering stage begins. Late in the final stage, a more rapid increase is seen as the microstructure becomes dominated by the isolated pores.

CONCLUSIONS

The transition from one sintering stage to another in sintered alumina was detected by small angle neutron scattering. The effective radius of the pore size distribution, as measured by both multiple small angle neutron scattering and single particle Porod scattering, remained fairly constant throughout the intermediate stage of sintering, with a rapid increase as densification proceeds beyond 85% of theoretical density. The results are consistent with sintering models which equate the intermediate stage with the decay of the topological network of channels and junction pores in the system. Before complete decay can occur, a transition into the final sintering stage occurs in which the porosity becomes isolated spherical voids.

ACKNOWLEDGEMENTS

This work was supported in part by the U.S. Army Research Office under contract no. ARO-MS26123 and in part by the Department of Energy under grant no. DE-FG05-84ER45063.

REFERENCES

1. N.F. Berk and K.A. Hardman-Rhyme, *J. Appl. Crystallogr.* **18**, 467-472 (1985).
2. N.F. Berk and K.A. Hardman-Rhyme, *J. Appl. Crystallogr.* **21**, 645-651 (1988).
3. R.L. Coble, *J. Appl. Phys.* **32**, 787-792 (1961) and *J. Appl. Phys.* **32**, 793-799 (1961).
4. G.G. Long and S. Krueger, *J. Appl. Crystallogr.* **22**, xxx-xxx (1989).
5. G. Kostorz, *Treatise on Materials Science and Technology*, Vol. 15 (Academic Press, New York, 1979).
6. C.J. Glinka, J.M. Rowe and J.G. LaRock, *J. Appl. Crystallogr.* **19**, 427-439 (1986).
7. F.N. Rhines and R.T. DeHoff, in *Sintering and Heterogeneous Catalysis, Materials Science Research*, Vol. 16, edited by G.C. Kuczynski, A.E. Miller and C.A. Sargent (Plenum Press, New York, 1984) pp. 49-61.
8. R.T. DeHoff, R.A. Rummel, H.P. LaBuff and F.N. Rhines, in *Modern Developments in Powder Metallurgy*, Vol. 1, edited by H.H. Hausner (Plenum Press, New York 1966) pp. 310-331.

THERMAL DIFFUSE SCATTERING IN NEUTRON TIME-OF-FLIGHT POWDER PATTERNS

Michael J. Radler

Department of Materials Science & Engineering, The Robert R. McCormick School of Engineering and Applied Science, Northwestern University, Evanston, IL 60208

ABSTRACT

Inelastic scattering from lattice phonons contributes a significant fraction of the observed Bragg intensity in time of flight neutron powder patterns of transition metal monoxides at elevated temperatures. Ignoring this thermal diffuse scattering (TDS) leads to errors in the site occupations of defects present in these materials. The intensity from one phonon TDS has been calculated as a function of time-of-flight and used to correct the measured intensities. The effect of this correction on the results of Rietveld profile refinement is discussed.

INTRODUCTION

As the use of profile refinement techniques coupled with time-of-flight (TOF) neutron powder diffraction are extended to refine not only atomic positions but also site occupations, data corrections such as extinction, absorption and thermal diffuse scattering (TDS) become more important. While these corrections have been formulated for constant wavelength experiments, for wavelength dispersive measurements only simple empirical corrections are commonly employed in the profile refinement, and corrections for TDS are usually ignored. In particular when samples are maintained at elevated temperatures, where neutron-phonon interactions are most significant, the TDS correction can be quite large.

A correction for the one-phonon scattering in a TOF powder pattern for monatomic cubic materials has been derived [1]. However few calculations of this contribution to TOF powder patterns have been made. Higher order (two phonon, three phonon etc.) scattering processes also occur, but in general these give a featureless background that is taken care of with background subtraction [2]. In this paper we report TDS calculations for the rocksalt structure monoxide, Fe_{1-x}O , at elevated temperatures.

EXPERIMENT

In a TOF powder diffraction experiment it is the total time of flight that is measured; there is no way to discriminate inelastic scattering events. The detected TOF is related to the magnitudes of the incident and scattered wavevectors, k_i and k_f respectively, by:

$$t(k_i, k_f) = \frac{m_n}{h} \left(\frac{L_1}{k_i} + \frac{L_2}{k_f} \right) \quad (1)$$

where L_1 and L_2 are the path lengths for incident and scattered neutrons, m_n is the mass of the neutron, and h is Planck's constant. For any time t there will be inelastic scattering contributions due to many different combinations of $k_i, k_f, (k_i \neq k_f)$, each combination weighted by the incident neutron flux on the sample, $i(k_i)$. The cross-section for first-order thermal diffuse scattering will then really be a function of k_i and k_f and not simply the TOF. An effective cross-section as a function of TOF can be calculated by

integrating over all combinations k_i, k_f giving scattering vectors in the Brillouin zone, and for each pair determining if both energy and momentum are conserved. If one-phonon scattering can occur, the intensity is calculated, divided by the incident flux on sample for the appropriate TOF channel to yield the effective cross-section, and added to the sum in a histogram. (In an experiment, neutron events occurring over a time increment Δt , of order a few microseconds, are summed together in one time channel. The entire spectrum is then represented by several thousand time channels.)

Several simplifying assumptions are used in deriving the one-phonon cross-section and these are worth noting : 1) Only cubic crystals are considered, 2) the Brillouin zone is replaced by a sphere of equal volume, with radius q_m , thereby preserving the total number of phonon modes, 3) the mean number of phonons, $n_i(q)$, of frequency $\omega_i(q)$ at temperature T , is evaluated in the high temperature limit, 4) all phonon modes are either pure longitudinal or pure transverse, and 5) linear chain dispersion approximates the true phonon dispersion. The last two assumptions are reasonable in that the calculation is for a powder, where the exact orientation of each grain is unknown. Averaging over all possible orientations will average out the distinct phonon polarizations. In the case of the one-phonon contribution to x-ray powder patterns of cubic metals, a model neglecting dispersion and using only one velocity for all phonons [3] differed in TDS contributions to the Bragg peaks by only 5% from a model that accounted for dispersion and phonon polarization [4]. The phonon frequencies are given by:

$$\omega_i(q) = \frac{2V_i q_m}{\pi} \sin\left(\frac{\pi q}{2q_m}\right) \quad (2)$$

where $\omega_i(q)$ is the phonon frequency associated with phonon wavevector q , and V_i is the sound velocity for phonon branch (polarization) i . The velocities V_i are calculated from the elastic constants and macroscopic densities.

The probability that an incident neutron, of wavevector k_i , scatters inelastically from a phonon in the powder sample into solid angle Ω , subtended by the detector at the sample, with final wavevector k_f is given by :

$$\frac{d^2\sigma_{TDS}}{d\Omega dk_f} = \frac{N\sigma_c \hbar^3 k_f^2}{16\pi M m_n k_i} \sum_{i,\epsilon} \frac{|\mathbf{H} \cdot \mathbf{e}_i(q)|^2 (n_i(q) + 1/2 + \epsilon/2) q}{\omega_i(q) \hbar r V_i \cos\left(\frac{\pi q}{2q_m}\right)} \quad (3)$$

where \mathbf{H} is the scattering vector, $\boldsymbol{\tau}$ is a reciprocal lattice vector, q is the phonon wavevector, and $\mathbf{e}_i(q)$ is the phonon polarization. The sum over i includes the three acoustic branches, and ϵ is +1 for phonon absorption, and -1 for phonon creation. The bar above the L.H.S. denotes an average over all grain orientations. The derivation of Equation 3 can be found in Ref. 1. In calculating the first-order phonon scattering in polyatomic cubic materials like FeO, some additional changes in the cross-section derived in Ref.1 were necessary. There are two atoms per primitive cell, and this introduces optic modes in the phonon spectra. To be rigorous the sum over the polarization states, i in Equation 3, should now extend to six to include the optic modes. Since the cross-section goes as $1/\omega^2$, and the optic mode frequencies are much higher than the acoustic frequencies, they contribute much less to the phonon

scattering. Furthermore, the optic mode frequencies don't go to zero as q goes to zero, so the contribution under the Bragg peaks, which is the primary concern, does not peak as it does for the acoustic modes. For the calculations that follow the contributions to the inelastic scattering from the optic modes have been ignored. Acoustic modes represent in-phase motions of the atoms in the unit cell, so the atomic mass is replaced by the average atomic mass M of the different atoms in the unit cell. Furthermore with two atoms per unit cell the temperature factor is no longer easily represented as one factor; instead isotropic temperature factors for each atom are applied within the coherent cross-section σ_c , defined as :

$$\sigma_c = \left| \sum_n b_n e^{-i\mathbf{h}\cdot\mathbf{r}_n} \exp[-2\pi i(hx_n + ky_n + lz_n)] \right|^2 \quad (4)$$

The one-phonon intensity for one point k_i, k_f will be approximated as :

$$I_{TDS}(k_i, k_f) = i(k_i) \frac{d^2 \sigma_{TDS}}{d\Omega dk_f} P(k_f) \Delta k_i \Delta k_f \Delta \Omega \quad (5)$$

where $P(k_f)$ is the calculated efficiency of a cylindrical ^3He detector for scattered neutrons of wavevector k_f , and Δk_i and Δk_f are the spread in wavevectors k_i and k_f equivalent to the time channel width Δt , which can be obtained by differentiating Equation 1 with respect to t . The number of neutrons incident on the sample over the time channel that encompasses time t is :

$$i(k_0) P(k_0) \Delta \Omega \Delta k_0 \quad (6)$$

where k_0 is the wavevector of elastically scattered neutrons ($k_i = k_f = k_0$) giving time-of-flight t , and Δk_0 is evaluated by differentiating Equation 1. Dividing Equation 5 by Equation 6 gives the contribution to the cross-section from the point k_i, k_f as :

$$\frac{d\sigma_{TDS}}{d\Omega}(t, k_i, k_f) = \frac{i(k_i) P(k_f) N \sigma_c h^3 k_f^2 \Delta k^2 t^2}{i(k_0) P(k_0) 16\pi M^2 \omega_n^2 L k_i \Delta t} \sum_{1, \epsilon} \frac{|H \cdot e_i(q)|^2 (n_i(q) + 1/2 - \epsilon/2) q}{\omega_i(q) H^2 V_i \cos(\frac{\pi q}{2q_n})} \quad (7)$$

The cross-section has two singular points. As q goes to zero the cross-section diverges as $1/q$. This divergence is handled by always excluding the $q=0$ point from the calculation. Once all the other points on the grid have been sampled, the central element containing $q=0$, is subdivided into smaller elements. The central element is subdivided into more and more elements until the calculated cross-section over the whole central element, excluding the small element containing the $q=0$ point, changes by less than five percent.

Similarly as q approaches its maximum value, q_n , at the zone boundary, the argument of the cosine in the denominator of Equation 5 goes to $\pi/2$, the cosine goes to zero, and again the cross-section diverges. The divergence at $q=q_n$ is eliminated by limiting q to 0.90 of q_n or less. This will have an

effect only on the TDS profile near the zone boundary, far away from the Bragg peak.

To calculate all possible combinations k_i, k_f in the Brillouin zone, a discrete summation over the magnitudes of k_i and k_f is performed. This two dimensional grid of points is centered at the wavevectors giving the Bragg peak, point $k_i=k_f=k_p$, determined by equating Bragg's Law with the neutron wavelength :

$$\lambda = \frac{2\pi}{k_p} = \frac{ht}{m_n L} = 2d_{hk1} \sin\theta \quad (8)$$

where $L=L_1+L_2$, and is bounded by a circle of radius q_n . The grid spacings Δk in k_i and k_f are set equal to one another and evaluated for $t=t_{\text{peak}}$ and a time channel width Δt of a few microseconds. For a material of lattice constant 4\AA the radius of the grid, q_n , is of order 1.5\AA^{-1} while the grid spacing Δk is in the range $5 \cdot 10^{-5}$ to $5 \cdot 10^{-3} \text{\AA}^{-1}$, depending on the TOF of the Bragg peak. Calculation of the TDS for one Bragg peak involves $\pi q_n^2 / \Delta k^2$ iterations ($2 \cdot 10^6$ to $2 \cdot 10^9$ iterations). Note that the grid spacing Δk increases in size as $1/t^2$, while the grid area, πq_n^2 , remains constant. The number of iterations goes as $1/\Delta k^2$ or as t^4 . The bulk of the calculation time is therefore spent on peaks at large TOF (with large d-spacings). A typical calculation time for 30 peaks for FeO takes about 12 hours of CPU time on a DEC VAX 11/730 computer.

Neutron powder diffraction patterns of Fe_{1-x}O held in-situ at elevated temperatures in an appropriate gaseous environment were obtained at the Intense Pulsed Neutron Source at Argonne National Laboratory. The details of these measurements have been reported elsewhere [5]. Powder patterns were collected at 90° two-theta with a time channel increment of $8\mu\text{s}$ over a TOF range of 3000 to 30,000 μs . TDS calculations were performed over the same TOF range for temperatures in the range 1123 to 1373 K. Elastic constants were taken from Ref. 6 and densities from Ref. 7.

The units in the TDS spectrum calculated with Equation 7 are barns/unit cell and have magnitudes in the range 0 to 10. Before the calculated TDS can be subtracted from the raw data, two conversions must be performed. First the TDS cross-section, Equation 7, must be converted to neutron counts for the given number of monitor counts. The conversion to units of counts is performed by first calculating the incident beam power in units of counts/barn/monitor count from the incoherent scattering of a vanadium standard sample measured in the same scattering configuration (this eliminates evaluating $\Delta\Omega$). After multiplying the calculated TDS spectrum by this beam power and the sample volume in units of unit cells, the resultant spectrum is then scaled to the data of interest based on the total number of counts in an incident beam monitor. With the TDS on the same scale as the raw data, the TDS profile must be convoluted with the Bragg peak shape. This serves two purposes : the Bragg peak shape is a first order approximation to the instrumental resolution function which has not been included so far, and second, this conditions the shape of the calculated data so that when it is subtracted from the raw data it does not introduce an error in the shape of the remaining Bragg peak. Since the peak shape function utilized in Rietveld analysis of TOF powder patterns is computationally simple [8], the convolution with the calculated profile is straightforward and the TDS is then subtracted on a point by point basis.

RESULTS

The calculated profile of first-order TDS for Fe_{1-x}O at 1123 K is shown

in Figure 1 on the same scale as the measured powder profile. The TDS intensity for the less intense odd hkl reflections at large TOF are nearly indistinguishable from the background. The intensity of the TDS peaks increases smoothly with increasing $\sin\theta/\lambda$ until the temperature factor decrease becomes predominant. Unlike single crystal samples [9] no large increase in TDS is observed at the point where the neutron velocity exceeds the velocity of sound in the crystals. This is probably due to the many combinations of k_1, k_2 that contribute to any one point. However, the small size of the TDS peaks at low TOF is deceiving. Integrating the Bragg peaks before and after the TDS correction, one finds that at low TOF the correction is of order 20 percent. (Calculations for isostructural MnO at 1673°K show this percentage can easily be 30 percent or more.) The magnitude of the correction to the integrated intensities are in good agreement with corrections calculated for constant wavelength x-ray powder diffraction on FeO at similar temperatures [10].

The effects of the TDS correction are easily found by refining the powder profile both before and after the correction. Wüstite has the rocksalt structure (Fm $\bar{3}m$) with cations that incompletely fill the 4a sites, anions at the 4b sites, and a small percentage of interstitial cations on the 8c sites. The temperature factor for the interstitial cations was constrained to always equal that of the octahedral cations, and the sum of the site occupations for the octahedral and tetrahedral cations was constrained to equal the known sample composition. The results of these refinements for the tetrahedral site occupation, t_{Fe} , in Fe_{0.913}O at 1323°K are given in Table I. To eliminate uncertainties due to other data corrections the values for the extinction and absorption were fixed at the values determined from the uncorrected data refinement. As expected the isotropic temperature factors B_{Fe} and B_O for the corrected data were slightly higher than for the uncorrected data [2]. The increase in the temperature factors are in good agreement with the increase observed when a TDS correction was made to Bragg intensities from Fe_{1-x}O collected with constant wavelength neutrons [11]. The occupation of the interstitial cation site appears to increase by 10%, a significant amount considering the small site occupation, but when confidence limits are placed on these values the data overlap. Most important the fitting statistics changed only slightly, indicating peak shape changes were not the cause of the observed parameter changes. Copies of the program are available on request from the author or from IPNS.

CONCLUSIONS

1) First-order thermal diffuse scattering profiles have been calculated for Fe_{1-x}O at elevated temperatures. The magnitude of the corrections to the integrated Bragg intensities are in good agreement with calculations performed by others for constant wavelength x-ray and neutron powder diffraction on the same material.

2) As expected the temperature factors increased slightly, but the interstitial site occupation remained the same.

3) Thermal diffuse scattering profiles for cubic materials can be generated in several hours, and incorporated directly into the profile refinement process.

ACKNOWLEDGEMENT

The author would gratefully like to acknowledge discussions of the present work with Prof. Jerome B. Cohen at Northwestern University, and Dr. John Faber, Jr. at Amoco Corporate Research, Naperville, IL. This research has been supported by the Department of Energy under contract DOE-FG02-84ER45097 at Northwestern University and contract BES-Materials Sciences W-31-109-ENC-38 at Argonne National Laboratory.

Table I. Results of Rietveld Refinements Before and After Correction for First-Order TDS in $\text{Fe}_{0.913}\text{O}$ at 1323K

	Before	After
$t_{\text{Fe}}(\%)$	3.33(12)	3.65(18)
$B_{\text{Fe}}(\text{\AA}^2)$	2.79(2)	2.90(4)
$B_{\text{O}}(\text{\AA}^2)$	3.16(2)	3.30(4)
Scale	0.1629(7)	0.165(5)
OBS.	453	453
VAR.	15	13
R(P; %)	2.3298	2.4574
R(WP; %)	3.2998	3.5410
R(F ² ; %)	4.3524	3.5419
R(EXP; %)	1.9698	2.0467
χ^2	2.81	2.99

$$R(F^2; \%) = 100 * \sum |I_{\text{OBS}} - I_{\text{CALC}}| / \sum I_{\text{OBS}}$$

$$R(P; \%) = 100 * \sum |Y_{\text{OBS}} - Y_{\text{CALC}}| / \sum Y_{\text{OBS}}$$

$$R(WP; \%) = 100 * (\sum (W * (Y_{\text{OBS}} - Y_{\text{CALC}})^2) / \sum (W * (Y_{\text{OBS}})^2))^{1/2}$$

$$R(EXP; \%) = 100 * (\# \text{ DEGREES OF FREEDOM} / \sum (W * (Y_{\text{OBS}})^2))^{1/2}$$

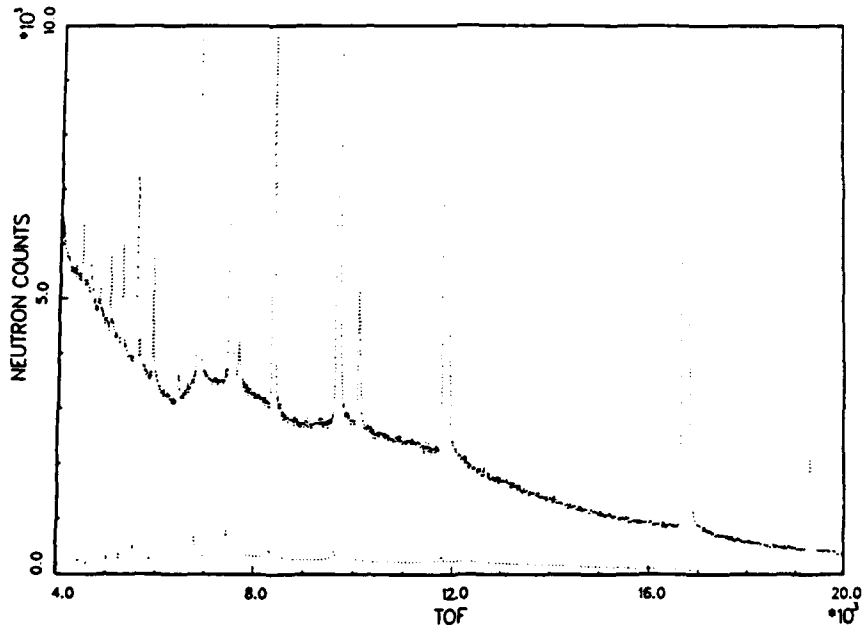


Figure 1. Calculated one-phonon TDS (lower curve) for $\text{Fe}_{0.93}\text{O}$ at 1123K on same scale as measured powder diffraction profile.

REFERENCES

- 1) I. Cole and C.G. Windsor, Acta Cryst. A36, 697 (1980).
- 2) B.T.M. Willis, Acta Cryst. A25 277 (1969).
- 3) B.E. Warren, X-Ray Diffraction, p.164,200 ,Addison Wesley (1969).
- 4) C.B. Walker and D.R. Paskin, Acta Cryst. A28, 572 (1972).
- 5) M.J. Radler, J. Faber,Jr., and J.B. Cohen, accepted for publication in J.Phys.Chem.Solids
- 6) G. Kugel, C. Carabatos, B. Hennion, B. Prevot, A. Revcolevschi, and D. Tocchetti, Phys. Rev. B16, 378 (1977).
- 7) CRC Handbook of Chemistry and Physics, 66th ed., (CRC Press, 1985), p. B107,B113.
- 8) R.B. Von Dreele, J.D. Jorgensen, and C.G. Windsor, J.Appl.Cryst. 15, 581 (1982).
- 9) B.T.M. Willis, C.J. Carlile, and R.C. Ward, Acta Cryst. A42, 188 (1986).
- 10) E. Cartstein, Ph.D. Thesis, Northwestern University, (1984).
- 11) A.K. Cheetham, B.E.F. Fender, and R.I. Taylor, J.Phys.C:Solid St. Phys. 4, 2160 (1971).

REAL SPACE METHOD OF POWDER DIFFRACTION
FOR NON-PERIODIC AND NEARLY PERIODIC MATERIALS

T. EGAMI¹, B. H. TOBY¹, W. DMOWSKI¹, Chr. JANOT² AND J. D. JORGENSEN³

¹Department of Materials Science and Engineering, University of Pennsylvania, Philadelphia, PA 19104-6272

²Institut-Laue-Langevin, 156X-38042 Grenoble Cedex, France

³Materials Science Division, Argonne National Laboratory, Argonne, IL 60439

ABSTRACT

The use of high-energy neutrons from pulsed or hot sources allows the method of atomic pair distribution analysis to be applied to the structural determination of crystalline as well as amorphous solids. This method complements the standard crystallographic methods in studying non-periodic aspects of solids with or without long range order.

INTRODUCTION

The method of atomic pair distribution function (PDF) analysis has traditionally been used almost exclusively in studying the structure of liquid and amorphous materials for which the standard crystallographic methods are powerless [1,2]. In principle, however, this method is applicable to any powdered materials including crystalline solids. If the solid is perfectly crystalline, there is no advantage in using this approach, while if the solid contains a high density of defects or a high degree of disorder, the PDF method is an attractive alternative to the standard methods. What prevented the wide use of this technique for ordered materials so far was the termination errors which were often introduced in the course of Fourier-transformation and reduced the accuracy of the PDF [2]. This situation was greatly improved by the advent of pulsed and hot neutron sources and synchrotron radiation, which provide neutrons and x-rays with higher energies than have been normally available. In this paper we briefly describe the method, review recent results obtained by this method, and discuss future promises held by this method which we propose to call the "real space method for powder diffraction".

THE PDF ANALYSIS

The instantaneous isotropic atomic pair distribution function, $\rho(r)$, is determined by the Fourier transformation of the total structure factor $S(Q)$,

$$\rho(r) = \rho_0 + \frac{1}{2\pi^2 r} \int [S(Q) - 1] \sin(Qr) Q dQ \quad (1)$$

where ρ_0 is the average atomic number density, Q is the scattering vector [1,2], and

$$S(Q) = \int S(Q, \omega) d\omega \quad (2)$$

where $S(Q, \omega)$ is the dynamic structure factor, ω is the energy transfer by scattering, and the integration covers only the energy range for phonons [3]. For x-ray scattering Q is almost independent of ω for phonons, so that the measured scattering intensity corrected for absorption, Compton scattering, multiple scattering and the atomic scattering factor $\langle f(Q) \rangle^2$, directly gives $S(Q)$. For neutron scattering without an energy analyzer the measured intensity is not exactly equal to $S(Q)$ because of the ω dependence of Q , but after the Placzek correction [4] $S(Q)$ is obtained in approximation.

The range of integration in equation (1) is from 0 to ∞ , however, in practice $S(Q)$ can be determined only up to a limiting Q value, Q_{\max} , which

depends upon the energy of the incident photons or neutrons, and the integration is terminated there. With a room temperature thermal neutron source Q_{\max} cannot exceed 12 1/Å, which is hardly sufficient in evaluating the integration accurately. On the other hand a large portion of neutrons emitted from a pulsed source are epithermal, and have higher energies. Accordingly $S(Q)$ can be determined up to 30 - 40 1/Å, and $S(Q)$ and $\rho(r)$ can be obtained with a high accuracy as shown in Figs. 1 and 2 for f.c.c. aluminium. The data shown in Figs. 1 and 2 [5] were obtained at the SEPD station of the Intense Pulsed Neutron Source (IPNS) of Argonne National Laboratory. Since $\rho(r)$ describes an instantaneous nuclear correlation, the peaks have a non-zero width even at $T = 0$ K due to the zero-point oscillation. The peak width which fits the best to the data, 0.086 Å, is very close to the one expected from the Debye model, $\sqrt{2\langle u^2 \rangle} = 0.083$ Å [6].

In general, if the PDF peaks are Gaussian with the standard deviation of σ_r , then the structure factor is given by the Debye-Waller form

$$S(Q) = [S_0(Q) - 1] \exp(-2BQ^2) + 1, \quad (3)$$

where $B = \sigma_r^2/2$ and $S_0(Q)$ is the structure factor for a system with a PDF composed of δ -function-like peaks. Thus a rule of thumb for the range of Q is

$$Q_{\max} \sigma_r \geq 3. \quad (4)$$

This ensures that the integrand of (1) is of the order of the 3σ value of the Gaussian distribution (~ 0.01). For metallic glasses, for instance, σ_r is about 0.15 Å or so, thus Q_{\max} should be at least 20 - 25 1/Å, while for crystalline solids it has to be larger, typically 30 - 40 1/Å. For complex solids such as quasicrystals, $Q[S(Q) - 1]$ decreases rapidly with Q , and Q_{\max} does not have to be greater than 20 1/Å.

On the other hand experimental limitations in the resolution in Q do not present a significant problem in the PDF analysis. If the resolution function is Gaussian with the standard deviation of σ_Q , it results in a slow decay of the PDF with a Gaussian envelope,

$$\rho(r) = \rho_0 + [\rho_g(r) - \rho_0] \exp(-r^2/2\lambda^2), \quad (5)$$

where $\rho_g(r)$ is the PDF determined with a perfect resolution, and $\lambda (= 1/\sigma_Q)$ is the resolution distance. For a medium range resolution such as 0.01 1/Å (HWHM), the resolution distance is over 100 Å, so that unless the PDF is calculated up to very large distances the Q resolution is unimportant.

In fact for carrying out a successful PDF analysis it is better to reduce the experimental Q resolution and increase the neutron or photon count in order to reduce the statistical noise, which is the most important source of inaccuracy since the range of Q accessible with pulsed neutrons is sufficiently large and renders the termination error less significant. From equation (1) it can be shown that the statistical noise is given by

$$\begin{aligned} \Delta\rho(r) &= \frac{1}{2\pi^2 r} \left[\int \frac{\sin(Qr)}{I_c(Q)} Q \, dQ \right]^{1/2} \\ &= \frac{1}{2\sqrt{2}\pi^2 r} \left[\int \frac{Q^2 dQ}{I_c(Q)} \right]^{1/2}, \end{aligned} \quad (5)$$

where $I_c(Q) = N(Q)/\Delta Q$ is the scattered neutron intensity, with $N(Q)$ being the actual neutron count and ΔQ the spacing of the Q values at which the data were taken [7]. Thus $\Delta\rho(r)$ decreases inversely with r , as seen in Fig.

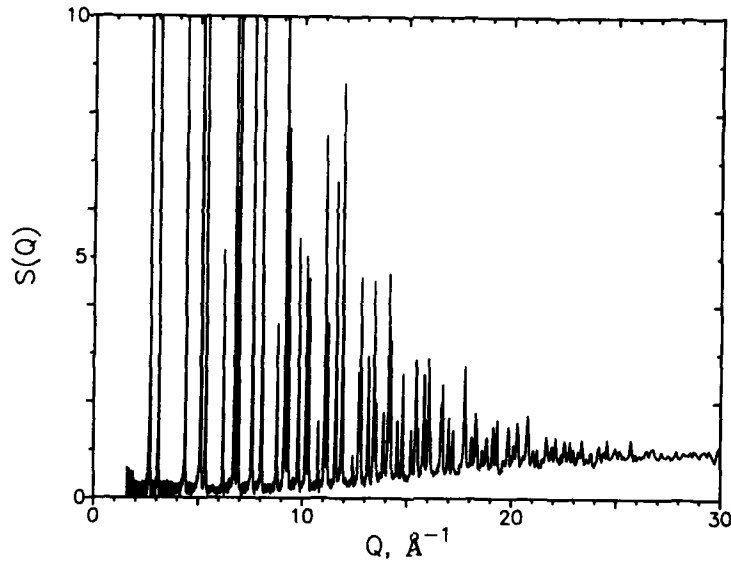


Fig. 1. Total structure factor of f.c.c. aluminium at $T = 10$ K determined by the pulsed neutron scattering at the IPNS. The value of $S(Q)$ at the peaks below $Q = 10$ \AA^{-1} is out of scale. It exceeds 100 in this resolution ($\Delta Q = 0.01$ \AA^{-1} below 10 \AA^{-1}) at some peaks.

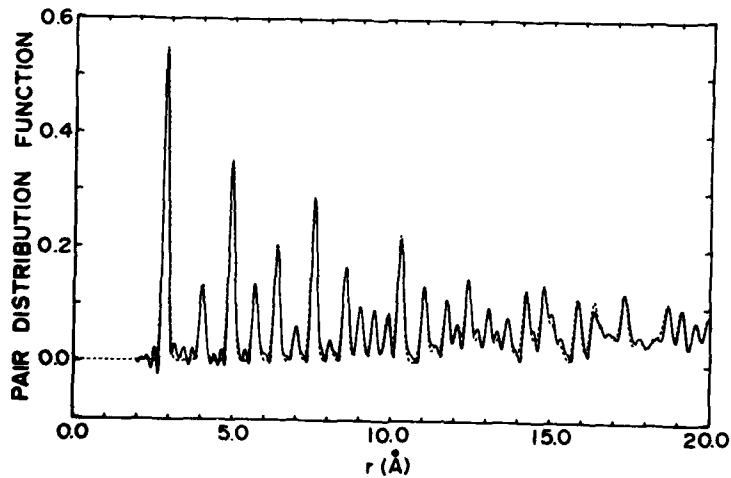


Fig. 2. The atomic pair distribution function of f.c.c. aluminium obtained by the Fourier transformation of $S(Q)$ shown in Fig. 1 [5]. The dashed line is the calculated PDF with Gaussian broadening to represent the zero-point lattice vibration.

2. In collecting the diffraction data, consideration should be given to minimize equation (5), by spending more time at high Q ranges than low Q ranges.

If we use a triple-axis spectrometer we can determine the elastic scattering intensity, $S(Q,0)$, within the energy resolution of the analyzer. The Fourier transform of $S(Q,0)$ is the average density-density correlation function which is slightly different from the instantaneous PDF in that the dynamic correlations are missing. This method was first applied to the study of SiO_2 glass [8], and was recently used for the study of superconducting $\text{Tl}_2\text{Ba}_2\text{CaCu}_2\text{O}_8$ using the hot neutron source of ILL. The data from this experiment are being analyzed.

RECENT EXAMPLES: SUPERCONDUCTING $\text{Tl}_2\text{Ba}_2\text{CaCu}_2\text{O}_8$

The structure of superconducting oxides has been extensively studied by various methods, and their average crystallographic structure is now well known. However, these structures often contain anomalously large temperature factors which describe the amplitude of thermal lattice vibration [9,10]. Such large temperature factors usually imply displacive disorder on a local level which is not adequately modeled in the standard crystallographic analysis. We applied the PDF analysis on the pulsed neutron powder diffraction data of superconducting oxides obtained at the IPNS, and were able to determine the local atomic correlations undetected by crystallographic methods. Here we briefly describe some of the recent results obtained for $\text{Tl}_2\text{Ba}_2\text{CaCu}_2\text{O}_8$ ($T_c = 110$ K).

Displacive Order of Tl and O

The amplitude of thermal vibration of oxygen in the Tl-O plane determined by single crystal x-ray scattering as well as powder neutron scattering [9,10] is as large as 0.4 Å, while it is expected to be of the order of 0.1 Å. By analyzing the pulsed neutron PDF we found that both Tl and O atoms in the Tl-O plane are deviated from the crystallographic high-symmetry sites, forming displacive short range order [11]. The distance between the Tl and O sites in the crystallographic (tetragonal) structure is 2.73 Å, while the sum of the ionic radii of Tl and O is 2.28 Å [12]. The displacements cause half of the Tl-O pairs move closer to a distance of about 2.3 Å while the rest of them move further apart, thus as a whole minimizing energy.

Anomalous Temperature Dependence

A careful study of the temperature dependence of the pulsed neutron PDF produced evidence of structural anomaly in the vicinity of the superconducting transition temperature. It was found that the PDF shows a qualitative change across the transition, and as shown in Fig. 3 [13] the PDF amplitude, $\Delta\rho$, defined as the average height of the PDF peaks at 3.4 and 3.85 Å measured from the valley at 3.6 Å, deviates from the normal temperature dependence shown by a solid curve. This curve was calculated based upon the phonon density of state of this compound determined by an inelastic neutron scattering measurement carried out at the ILL using a triple-axis-spectrometer IN-1. The result shown in Fig. 3 was produced using primarily the data from the detector bank placed at the scattering angle (2θ) 150° , while a more recent result using also the 90° detector bank shows an even more pronounced anomaly, suggesting that the nature of this anomaly may be dynamic, since the Placzek correction is more reliable at lower angles. The origin of this anomaly is still being investigated, but a strong possibility is that this is due to the displacement of oxygen atoms in the Cu-O plane. Note that no anomaly has been observed in crystallographic parameters such

as the lattice constants and the atomic position parameters determined by the Rietveld method [10,14]. This example illustrates the unique capability of the PDF method to detect local atomic displacements which can go unnoticed by standard crystallographic methods. Further investigation of this anomaly might shed some light on the origin of the superconducting phenomena in cuprates.

ADVANTAGES OF PDF METHOD IN STUDYING NEARLY PERIODIC MATERIALS

Since the PDF is nothing but a direct Fourier-transform of the structure factor, $\rho(r)$ and $S(Q)$ contain the same information. Thus superficially there appears little to be gained by using the PDF method. However, in practice this difference in the representation can have important consequences in the strategy of structural analysis of crystalline or nearly crystalline materials. For instance, lattice symmetry and lattice constants are directly determined by the Bragg peak position of $S(Q)$, while atomic positions are only indirectly determined by examining the diffraction peak intensities. On the other hand $\rho(r)$ is all but useless in determining the lattice symmetry while it provides direct information regarding the atomic separations. Therefore in determining the atomic positions within the unit cell the PDF method offers significant advantages. In fact it is equivalent to the Patterson analysis for single crystals, except that it is averaged over all orientations and all the non-Bragg, diffuse intensities are included. Thus these two approaches are complementary, and should be used in tandem in the structural study of complex systems.

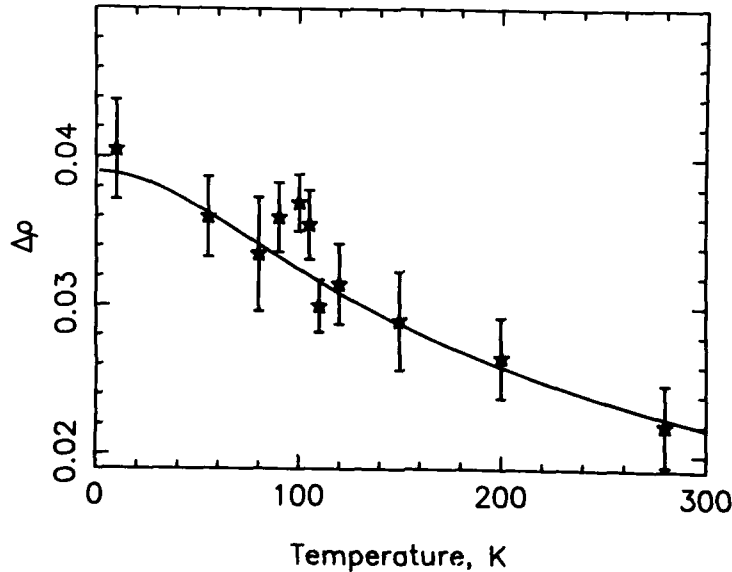


Fig. 3. Temperature dependence of the PDF amplitude defined as the average of the PDF peak heights at 3.4 Å and at 3.85 Å, measured from the valley in-between at 3.6 Å. The vertical bars indicate the statistical error evaluated by eq. (5), and the solid line is the normal temperature dependence calculated from the phonon density of states determined by inelastic neutron scattering [13].

When analyzing the powder pattern of a complex crystalline solid with a large unit cell, one might start off with the Rietveld analysis and then use the PDF method to refine the atomic positions. Comparison of the experimental PDF with the calculated PDF based upon the Rietveld parameters will clearly demonstrate discrepancies, if there are some, between the atomic distances in the model and those in the actual structure. While such discrepancies are usually noted by chemical intuition, this method offers a more direct and reliable means of confirming and improving the structural model. The model can be refined, for instance, by the Monte-Carlo process to minimize the difference between the measured and calculated PDF's [11].

If the sample contains a high density of defects or intrinsic disorder, the PDF method shows its unique strength, as demonstrated in the examples shown above. In particular if displacive disorder is present it results in shifting or splitting of the PDF peaks which is often easily observable, while in Q-space it only produces diffuse scattering at high values of Q which is difficult to isolate. In general the ability to model the short range order by terminating $\rho(r)$ at some distance makes this method exceptionally useful, since from the diffuse scattering in $S(Q)$ alone it is not easy to speculate the nature of the disorder. After the local displacement is determined one may then go back to $S(Q)$ to determine the spatial extent of the correlation.

We thus identified two areas where the PDF method is particularly useful in determining the atomic structure of crystalline or nearly crystalline solids. We suggest that this "real space" approach may be included in some crystallographic analysis package such as the Rietveld software, so that the user can move to the real space method when the structure is either very complex or the temperature factor is too large and some displacive disorder is suspected.

ACKNOWLEDGMENTS

This work was supported by the National Science Foundation through the Grant DMR-8617950 and by the Department of Energy, division of Materials Sciences, through the Contract No. W-31-109-Eng-38.

REFERENCES

1. B.E. Warren, X-Ray Diffraction, (Addison-Wesley, Reading, 1969).
2. G.S. Cargill, III, Solid St. Phys., **25**, 227 (1975).
3. S.W. Lovesey, Theory of Neutron Scattering from Condensed Matter, (Clarendon Press, Oxford, 1984).
4. G. Placzek, Phys. Rev., **86**, 377 (1952).
5. S. Nanao, W. Dmowski, T. Egami, J. W. Richardson, Jr. and J. D. Jorgensen, Phys. Rev., **B35**, 435 (1987).
6. International Tables for X-Ray Crystallography, edited by J.A. Ibers and W.C. Hamilton (The Kynoch Press, Birmingham, 1962), Vol. 3, p. 237.
7. B.H. Toby and T. Egami, unpublished.
8. A.C. Wright and R.N. Sinclair, J. Non-Cryst. Solids, **76**, 351 (1985).
9. M.A. Subramanian, J.C. Clabrese, C.C. Torardi, J. Gopalakrishnan, T.R. Askew, R.B. Flippen, K.J. Morrissey, U. Chowdhry and A.W. Sleight, Nature, **332**, 420 (1988).
10. D.E. Cox, C.C. Torardi, M.A. Subramanian, J. Gopalakrishnan and A.W. Sleight, Phys. Rev., **B38**, 6624 (1988).
11. W. Dmowski, B.H. Toby, T. Egami, M.A. Subramanian, J. Gopalakrishnan and A.W. Sleight, Phys. Rev. Lett., **61**, 2608 (1988).
12. R.D. Shannon, Acta Cryst., **A32**, 751 (1976).
13. T. Egami, B.H. Toby, W. Dmowski, S. Billinge, P.K. Davies, J.D. Jorgensen, M.A. Subramanian and A.W. Sleight, Physica C, in press.
14. B.H. Toby, W. Dmowski, T. Egami, J.D. Jorgensen, M.A. Subramanian, J. Gopalakrishnan and A.W. Sleight, Physica C, in press.

NEUTRON RIETVELD ANALYSIS OF ANION AND CATION DISORDER IN
THE FAST-ION CONDUCTING PYROCHLORE SYSTEM $Y_2(Zr_xTi_{1-x})_2O_7$

SOSSINA M. HAILE*, B. J. WUENSCH*, AND E. PRINCE**

*Department of Materials Science and Engineering, Massachusetts Institute of
Technology, Cambridge, MA 02139

**Reactor Radiation Division, National Institute of Standards and Technology,
Gaithersburg, MD 20899

ABSTRACT

All information on the site occupancies and atomic displacements which relate a pyrochlore superstructure to the parent fluorite-type subcell is contained in the normally-weak superstructure diffraction intensities. As Ti has a negative scattering length, the supercell maxima in the present phases are up to three times as intense as the fluorite-like reflections, and neutron diffraction provides an especially sensitive probe of the state of disorder. $Y_2Ti_2O_7$ is found to have a fully-ordered anion array and slight disorder, $Y_{0.984}Ti_{0.015}$, among the cations. In $Y_2(Zr_{0.6}Ti_{0.4})_2O_7$ the oxygen site normally vacant in pyrochlore is half filled and on the order of 15% exchange between cation sites has occurred.

INTRODUCTION

Pyrochlore, $A_2B_2O_7$, is a superstructure with cell edge double that of a fluorite-type subcell. A large cation, A^{3+} , and smaller cation, B^{4+} , order in space group $Fd\bar{3}m$ at the sites of an undistorted fcc array. Two crystallographically-independent oxygen ions occupy positions $48f \times 1/8 \ 1/8$ and $8a \ 1/8 \ 1/8 \ 1/8$, Fig. 1, to fill seven-eighths of the available tetrahedral interstices. A vacant site remains at $8b \ 3/8 \ 3/8 \ 3/8$. The O(1) ions relax in the direction of the vacant anion site and the smaller B^{4+} ions. Thus $x > 3/8$, the ideal O(1) positional parameter. The coordinations of O(1) and O(2) consist of $2A + 2B$ and $4A$, respectively; A^{3+} and B^{4+} have eight and six oxygen neighbors, respectively.

The anions and cations in the pyrochlore structure will both disorder at elevated temperature to produce a non-stoichiometric, defect fluorite structure. Disorder occurs at progressively lower temperatures in phases in which the size of B increases relative to A. Such disorder may exist on an atomic scale. Alternatively, domains of pyrochlore existing in a matrix of disordered fluorite have been reported [1-3].

Moon and Tuller [4] examined the ionic conductivities of solid solutions in the systems $Gd_2(Zr_xTi_{1-x})_2O_7$ and $Y_2(Zr_xTi_{1-x})_2O_7$. An increase in oxygen ion conductivity by three orders of magnitude (to significant levels of, for example, $10^{-2} \text{ ohm}^{-1}\text{cm}^{-1}$ at 1000°C) accompanied a transition from an ordered pyrochlore state ($x = 0$) to the disordered fluorite structure ($x = 0.7$). The questions of whether and how disorder in the anion and cation arrays is coupled, and whether Zr^{4+} and Ti^{4+} , which have dissimilar ionic radii, disorder with Y^{3+} with equal probability, are relevant to full interpretation of the conduction mechanism. All information on the ionic ordering and anion displacements that give rise to the pyrochlore supercell is contained in the normally-weak set of superstructure intensities. In

addition to the magnitude of the anion displacement, the structure factors for these reflections depend on the difference between the individual scattering powers of the cations and the average cation scattering power. The numbers of electrons on Y^{3+} , Ti^{4+} , Zr^{4+} , and O^{2-} are 36, 18, 36, and 10. The corresponding nuclear scattering lengths for neutrons are 0.775, -0.3438, 0.716, and $0.581 \cdot 10^{-12}$ cm, respectively. Thus, Y^{3+} and Zr^{4+} , being isoelectronic, are virtually indistinguishable in x-ray diffraction. The small differences of cation scattering power from the mean, together with the relatively feeble scattering power of oxygen, cause the set of superstructure intensities to be exceedingly weak in x-ray diffraction. In contrast, the negative scattering length of Ti^{4+} for neutron scattering results in the difference between cation scattering lengths and their mean being *greater* than the average scattering length. The superstructure intensities in neutron diffraction patterns, Fig. 2, thus exceed the magnitudes of the set of fluorite-like subcell maxima. Neutron diffraction accordingly provides an unusually sensitive probe of the structural state of the present materials, especially in those solid solutions that are highly disordered. We present here the results of a neutron Rietveld powder-profile analysis of $Y_2Ti_2O_7$ as well as preliminary results for $Y_2(Ti_{0.4}Zr_{0.6})_2O_7$.

SPECIFICATION OF SITE OCCUPANCIES

In our model for cation disorder in $Y_2(Zr_xTi_{1-x})_2O_7$ we allow partial occupancy of both the A and B sites by all three cations and assume only that each site is fully occupied by a combination of species. The combined occupancy of both sites must conform to the known stoichiometry. Let N_i^A and N_i^B be the atomic fraction of species i which occupies each site. Then

$$N_Y^A + N_Y^B = 1 \quad (1)$$

$$N_{Zr}^A + N_{Zr}^B = x \quad (2)$$

$$N_{Ti}^A + N_{Ti}^B = 1-x \quad (3)$$

$$N_Y^A + N_{Zr}^A + N_{Ti}^A = 1 \quad (4)$$

-  A^{3+} in $16c \bar{3}m 000$
-  B^{4+} in $16d \bar{3}m 1/2 1/2 1/2$
-  $O(1)$ in $48f mm x 1/8 1/8$
-  $O(2)$ in $8a \bar{4}3m 1/8 1/8 1/8$
-  VO in $8b \bar{4}3m 3/8 3/8 3/8$

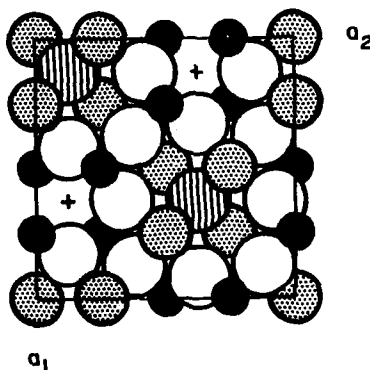


Figure 1. Projection of the contents of the pyrochlore supercell for $0 < z < 1/4$. The displacement of the oxygen ions (0.46\AA) from their ideal tetrahedral locations in the fluorite structure corresponds to that found for $Y_2Ti_2O_7$ in the present work.

A relation analogous to (4), which summed the occupancies of site B to unity would not be linearly independent, given Eqs. (1) through (3). By analysis of neutron diffraction data one may obtain an experimental value for the effective scattering length of the A site, b_A , which is related to the site occupancies by:

$$b_A = N_Y^A b_Y + N_{Zr}^A b_{Zr} + N_{Ti}^A b_{Ti} \quad (5)$$

A similar expression holds for b_B , but the relation is not independent as the total scattering power of the cation sites is constrained by stoichiometry:

$$b_A + b_B = b_Y + x b_{Zr} + (1-x) b_{Ti} \quad (6)$$

Equations (1-5) provide five equations in six unknown site occupancies. Thus, although it is not intuitively obvious, refinement of site occupancies subject to chemical constraints does *not* provide enough information to permit specification of the distribution of three species over two independent crystallographic sites. The problem may be resolved by combined analysis of neutron and x-ray data. The latter measurements provide an independent equation analogous to (5) but in terms of the x-ray scattering power, f , for each cation.

A model for anion disorder which allows partial occupancy of the O(1), O(2) positions and the normally-vacant site at 8b requires that the partial occupancies of each site conform to

$$6N^1 + N^2 + N^V = 7 \quad (7)$$

where the superscripts denote the three types of possible anion sites. As only one scattering length is involved, these site occupancies may be established as two independent and one dependent parameter in a constrained refinement based upon only one powder diffraction profile.

EXPERIMENTAL

Powder samples were kindly prepared for us by P. K. Moon using the Pechini process. Soluble compounds of the cations (Y hydroxide, Ti alkoxide and Zr alkoxide) were dissolved in appropriate ratios in a citric acid-ethylene glycol mixture which was subsequently polymerized by heating. Water produced as a by-product of the reaction was eliminated by further heating. The resinous product was charred in a third heating, ground, calcined at 700°C, and annealed at 1350°C for 60 hr to establish an equilibrium state of order. The resulting powders were well-ordered and extremely homogeneous as the process provided no opportunity for segregation of the components from the uniformity of their initial state in solution.

Neutron diffraction data were collected with the five-detector powder diffractometer at the Research Reactor at the National Institute for Standards and Technology. The diffraction profile was recorded in steps of 0.05 2 θ for the range 12° < 2 θ < 120° using 1.5525(3) Å thermal neutrons monochromated by reflection from (220) of a Cu crystal. The analyses were performed using the procedure and computer program of Rietveld [5] as modified for the multidetector diffractometer by Prince. A total of 32 adjustable parameters were required for the model. A scale

Table 1. Atomic Coordinates and Anisotropic Temperature-Factor Coefficients for $Y_2Ti_2O_7$ and $Y_2(Ti_{0.4}Zr_{0.6})_2O_7$
(Estimated standard deviation in last digit is in parentheses.)

	$Y_2Ti_2O_7$	$Y_2(Ti_{0.4}Zr_{0.6})_2O_7$
Lattice constant (Å)	10.0947(1)	10.2910(4)
Y in $16c \bar{3}m 000$ $B_{11} = B_{22} = B_{33}$ $B_{12} = B_{13} = B_{23}$	0.00160(8) -0.00048(11)	0.0035(2) 0.0007(4)
Ti in $16d \bar{3}m 1/2 1/2 1/2$ $B_{11} = B_{22} = B_{33}$ $B_{12} = B_{13} = B_{23}$	0.00067(17) -0.00023(21)	0.0046(5) -0.0001(8)
O(1) in $48f mmx 1/8 1/8$ x B_{11} $B_{22} = B_{33}$ B_{23} ($B_{12} = B_{13} = 0$)	0.42082(9) 0.00157(10) 0.00114(9) -0.00051(12)	0.4012(4) 0.0102(6) 0.0065(3) -0.0006(4)
O(2) in $8a \bar{3}m 1/8 1/8 1/8$ $B_{11} = B_{22} = B_{33}$ ($B_{12} = B_{13} = B_{23} = 0$)	0.00103(12)	0.0060(5)
O(3) in $8b \bar{3}m 3/8 3/8 3/8$ $B_{11} = B_{22} = B_{33}$ ($B_{12} = B_{13} = B_{23} = 0$)	—	0.0101(15)
Bragg Residual, R_B	2.17%	11.85%
Profile Residual, R_P	7.03%	10.17%
Weighted Profile Residual, R_{WP}	9.96%	13.26%
Expected Residual, R_E	7.36%	8.45%

factor, a lattice constant, one atomic coordinate, eight or nine thermal parameters and three site occupancies were required to describe the structure. The necessary instrumental variables consisted of fourteen parameters to describe the variation in background recorded by the five detectors, a zero-point for the 2 θ readings, and three parameters to describe a Gaussian peak shape. The quality of the refinement was assessed by three residuals: the weighted profile residual, R_{WP} , is defined as $(w_i [y_i(\text{obs}) - C^{-1}y_i(\text{cal})]^2 / \sum w_i [y_i(\text{obs})]^2)^{1/2}$, where $y_i(\text{obs})$ and $y_i(\text{cal})$ are individual intensities in the step-scanned profile which are observed and calculated, respectively; C is the scale factor and w_i is a weight applied to each observation which is equal to the reciprocal of the square of standard deviation of the measured intensity. R_{WP} may be compared with the expected residual, R_E , which is equal to $[(n-p) / \sum w_i [y_i(\text{obs})]^2]^{1/2}$, where n is the number of intensity measurements and p is the number of parameters employed in the model. Also of interest is the Bragg residual R_B , analogous to the conventional figure of merit evaluated in structure refinements performed with single crystal data:

$\frac{\sum |I_B(\text{obs}) - C^{-1} I_B(\text{cal})|}{\sum I_B(\text{obs})}$, where I_B is the integrated intensity of the individual Bragg peaks evaluated, in regions where maxima overlap in the powder pattern, by assigning observed intensity in proportion to the values calculated for the individual maxima.

RESULTS AND DISCUSSION

The neutron powder diffraction profile obtained for $\text{Y}_2\text{Ti}_2\text{O}_7$ was of high quality. The maxima had Gaussian shape, were for the most part individually resolved, and easily detected above background over the entire range of 2θ . Figure 2 illustrates the quality of the fit to the profile measured by the last detector of the spectrometer. The weighted profile residual of 9.96% and R_B of 2.17% are quite satisfactory. Refinement of the oxygen site occupancies, subject to the constraint that the total occupancy conform to a cell content of 56 ions, provided 1.003(2) for O(1) and 0.990(9) for O(2). The occupancy of the vacant 6b site, treated as the dependent parameter, was -0.013(7). With all departures from the ideal site occupancies less than two standard deviations and, in any case, with shifts in a direction which suggest no need for partial occupancy of the vacant site, the oxygen array is shown to be fully ordered. The O(1) and O(2) positions were thus assigned full occupancy in the final cycles of refinement. The effective scattering length of the A site refined to 0.984(4) by. This corresponds to a very small (but statistically significant) degree of disorder, Y having been replaced by 0.0115 Ti.

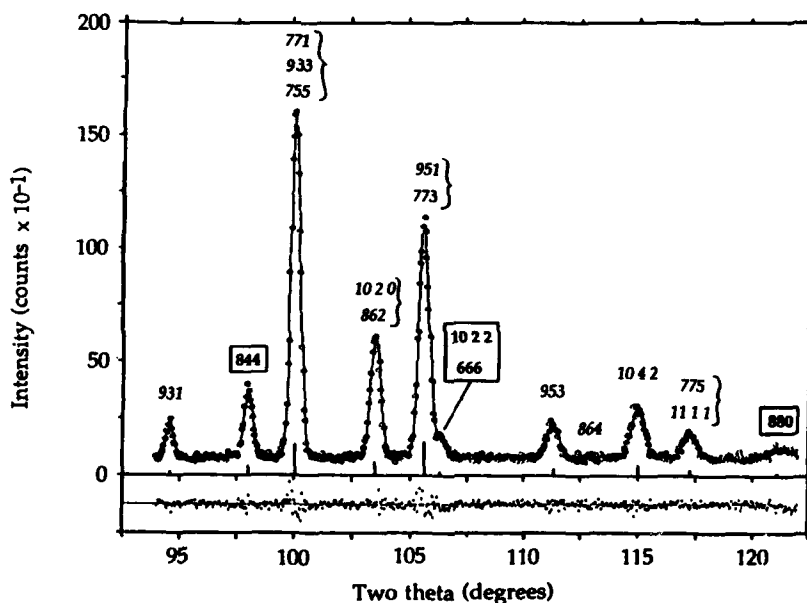


Figure 2. Neutron powder diffraction pattern recorded for $\text{Y}_2\text{Ti}_2\text{O}_7$ with 1.5525(3) Å thermal neutrons at high angles. Data points are experimental intensities; lines represent the fitted profile. The difference between observed and fitted intensity is shown at the same scale directly below the profile. Maxima arising from the fluorite subcell are indicated with boxed, bold-faced indices.

The values of other parameters obtained in the refinement are summarized in Table I. The O(1) coordinate corresponds to a significant displacement of 0.462 Å from the center of the tetrahedron, a consequence of the small size of the Ti⁴⁺ ion. The thermal parameters indicate lack of pronounced anisotropy in the thermal vibration of the ions.

Greatly diminished intensity of the superstructure intensities in the neutron diffraction pattern obtained for Y₂(Zr_{0.6}Ti_{0.4})₂O₇ indicated substantial disorder within both the cation and the anion arrays. Tentative values for the structural parameters are listed in Table I. The occupancies found for the oxygen sites are 0.917(7) for O(1), 1.00(2) for O(2) and 0.50(3) for the normally-vacant site at 8b. The oxygen vacancy is thus half occupied with the majority of the ions seemingly coming from O(1) rather than O(2) positions. The refined effective scattering lengths for the cation sites A and B are 0.700(16) and 0.367(16) × 10⁻¹² cm, respectively, compared with the values of b_Y = 0.775 and (0.6 b_{Zr} + 0.4 b_{Ti}) = 0.292 × 10⁻¹² which would obtain if Zr⁴⁺ and Ti⁴⁺ remain confined to the B site. If one assumes that both species on B disorder with A with equal probability, the contents of the 16c Y site represent A_{0.846(16)}B_{0.154} or Y_{0.846}Zr_{0.093}Ti_{0.062}. Table I further shows the lattice constant to have increased as a result of substitution of the larger Zr⁴⁺ ion for Ti⁴⁺ and, similarly, that the position of O(1) is less displaced from the ideal tetrahedral site as a consequence of the larger effective radius of the cation which constitutes B. As the occupancy of no site in this phase may be specified *a priori*, there is strong correlation between scale factor and site occupancies and, in addition, between occupancies and temperature-factor coefficients. For this reason, the results reported in Table I for Y₂(Zr_{0.6}Ti_{0.4})₂O₇ must be regarded as preliminary. Further refinement is necessary (as the residuals suggest) as well as a concurrent refinement of x-ray data to permit specification of the site occupancies for all three cations.

ACKNOWLEDGEMENTS

The powder specimens employed in this study were prepared by Dr. P. K. Moon. His assistance, and that of Professor H. L. Tuller, is gratefully acknowledged. This work was performed under contract DE-FG02-86ER45261 with the Division of Materials Sciences, Office of Basic Energy Research, U.S. Department of Energy. We are further pleased to acknowledge the support provided by a Bell Laboratories Fellowship (S.M.H.) and the TDK Chair in Materials Science and Engineering (B.J.W.).

REFERENCES

1. T. van Dijk, R. B. Helmholtz and A. J. Burggraaf, *Phys. Stat. Sol. (b)* **101**, 765 (1980).
2. M. P. van Dijk, A. J. Burggraaf, A. N. Cormack, and C. R. A. Catlow, *Solid State Ionics* **17**, 159 (1985).
3. T. Moriga, A. Yoshiasa, F. Kanamaru, K. Koto, M. Yoshimura and S. Somiya, *Solid State Ionics* **31**, 319 (1989).
4. P. K. Moon and H. L. Tuller, *Solid State Ionics* **28-30**, 470 (1988); *Mater. Res. Soc. Proc.* **135**, Pittsburgh, PA 1989, pp. 149-163.
5. H. M. Rietveld, *J. Appl. Cryst.* **2**, 65 (1969).

A SMALL ANGLE NEUTRON SCATTERING INVESTIGATION OF COMPACTED NANOPHASE TiO₂ and Pd

J. E. EPPERSON,^{*} R. W. SIEGEL[†], J. W. WHITE[†], J. A. EASTMAN[†], Y. X. LIAO^{†,*},
AND A. NARAYANASAMY^{†,Δ}

^{*}Materials Science Division, Argonne National Laboratory, Argonne, IL 60439

[†]Research School of Chemistry, Australian National University, Canberra, Australia and
Argonne Fellow, Argonne National Laboratory

ABSTRACT

Nanocrystalline compacts of TiO₂ and Pd were prepared by first condensing the Ti or Pd vapors in an inert gas atmosphere. The Ti was oxidized *in situ* to TiO₂. Samples were prepared by scraping off and compacting the nanophase materials into thin disks. The small angle neutron scattering was measured in the as-prepared condition and after isothermal anneals of up to 23 hrs at 550°C for the TiO₂ and up to 3.3 hrs at 300°C for the Pd. Scattering data were obtained in absolute cross sections. Integrated small angle scattering and maximum entropy methods were used in estimating the structural parameters. The results are interpreted in terms of a model which consists of nanometer sized grains of the materials separated by boundary regions which are, on average, much less dense than the respective bulk materials; 21% for the TiO₂ and about 56% for Pd. However, the boundary regions contain voids or pores, which contribute to these density decrements. Possible sources of error are discussed.

INTRODUCTION

Nanophase materials are polycrystals with typical grain sizes ranging from 2 to 20 nm. Such materials are usually produced by evaporation of metallic vapors into an inert gas atmosphere and controlled nucleation of nanometer sized clusters under ultraclean conditions, followed by *in situ* consolidation in vacuum. Because of the small crystallite sizes, such materials have a high interface-to-volume ratio; it is even possible for a majority of the atoms to be associated with the boundary regions. Consequently, the chemical and physical properties of nanophase materials may differ markedly from those of conventionally prepared materials; e.g., sintering may take place hundreds of degrees lower in temperature. The work done to date on nanophase materials and their potential for further applications has been reviewed [1-3]. Small angle neutron scattering investigations are capable of yielding information about the fine scale microstructure of such materials and, hence, may be used in helping to understand their properties and behavior.

Sample Preparation and Experimental Procedure

The nanophase compacts used in the present study were produced by the gas-condensation method, as described by [4]. High-purity Ti or Pd (99.7% for Ti and 99.99% for Pd) was evaporated from a resistance heated W boat into a 0.3 to 0.7 kPa He atmosphere. The nanophase

^{*} Permanent address: Measure and Testing Center, Sichuan University, Chengdu, People's Republic of China

^Δ Permanent address: Department of Nuclear Physics, University of Madras, Madras 600 025, India

particles condensed in the purified He atmosphere were collected on a liquid-nitrogen cooled cold-finger. In the case of Ti, the chamber was evacuated and then rapidly filled with about 2 kPa of O₂ and the material oxidized *in situ* to TiO₂. After evacuation, the nanophase TiO₂ or Pd was scraped off the cold-finger, collected and consolidated into disks about 9 mm in diameter and about 0.5 mm thick.

The small angle neutron scattering (SANS) measurements were carried out at the Argonne, Intense Pulsed Neutron Source (IPNS). In this facility, neutrons are produced when 450 MeV protons impact on a heavy metal target. The resulting spallation neutrons were made more suitable for SANS studies by use of a solid methane moderator operated at about 22K. A liquid-nitrogen cooled, single crystal MgO filter in the incident beam removed most of the unwanted fast neutrons. Collimation and focusing were achieved by use of a crossed pair of Soller collimators. Scattering data were collected in a constant $\Delta\lambda/\lambda = 0.05$ binning mode, using an area-sensitive, gas-filled proportional counter of the Kopp-Borkowski type [5]. All scattering spectra were normalized to a common monitor value and corrected for the presence of a high-purity quartz-cell sample holder. During data reduction, corrections were also made for sample thickness, sample transmission and for the contribution from delayed neutrons [6]. Using neutron wavelengths between 2.16 and 14Å, these SANS data were binned into an S(q) array from 0.009 to 0.25Å⁻¹ and were converted to absolute cross sections by comparison with the scattering from a secondary intensity standard [7]. A maximum entropy program, a generic version of which was obtained from Potton [8] and which was modified for SANS analysis, was used in obtaining particle size distributions.

Results and Discussion

The coherent scattering cross section at small values of momentum transfer (\vec{q}) results from correlations in the scattering length density ($\rho(\vec{r})$) ranging upwards from atomic dimensions and can be expressed as

$$S(\vec{q}) = \left| \int_{-\infty}^{\infty} \rho(\vec{r}) e^{i\vec{q} \cdot \vec{r}} d^3r \right|^2, \quad (1)$$

where \vec{r} is a position vector in real space. In a preliminary investigation of the nanophase TiO₂, it was proposed [9] that the microstructure of compacted, nanophase TiO₂ could be understood on the basis of a model which consists of nanometer sized grains of theoretically dense material separated by boundary regions that are, on average, much less dense, but which may contain voids. Mainly, they attempted to use the maximum entropy method [10] to extract the particle size distribution $N(r)$ from the observed, scattering cross sections. The scattering was represented by

$$S(q) = \int_0^{\infty} [V_p(r) \Delta\rho \Phi(qr)]^2 N(r) dr, \quad (2)$$

where $\Delta\rho$ is the difference in scattering length density and $V_p(r)$ the volume of a particle of radius r . For homogeneous, spherical particles,

$$\Phi(qr) = \frac{3}{(qr)^3} [\sin(qr) - (qr) \cos(qr)]. \quad (3)$$

As is clear from the discussion concerning the microstructural model, the contrast required in Eq. 2 is not known *a priori*. Consequently, only upper limits for the material parameters could be established [9]. An additional piece of experimental information is required, and Jorra et al. [11] have reminded us that this is conveniently provided by a measurement of the bulk density of the sample. The so-called invariant [12] for SANS can be written as

$$Q_0 = \int_0^{\infty} q^2 S(q) dq. \quad (4)$$

Consider a two-phase model consisting of homogeneous grains of one phase embedded in an otherwise homogeneous second phase. For this two-phase model, the invariant can be expressed as [11]

$$Q_0 = 2\pi^2 (\Delta\rho)^2 f_g (1-f_g), \quad (5)$$

where f_g is the volume fraction of grains. Our experimental observations extend only over a finite range in q -space, so in order to evaluate the invariant (Eq. 4) the Guinier approximation [13] is invoked for the low- q region and the Porod approximation [14] for the high- q end of the scattering profile. Based on the assumptions just stated, the density of the sample is

$$d_s = f_g d_g + (1-f_g) d_b, \quad (6)$$

where d_b is the density of the boundary region. If one further assumes that the boundary region has the same stoichiometry as the grains, but with lower density, the contrast can be written as

$$\Delta\rho = \left(1 - \frac{d_b}{d_g}\right) \bar{\rho}_g. \quad (7)$$

This allows for straightforward solution in terms of f_g , f_b and d_b , given input values for Q_0 , $\bar{\rho}_g$, d_g and d_s . The values for these parameters for as-compacted TiO_2 and Pd are given in Table I. Note that the TiO_2 sample was about 68% of theoretical density and the Pd compact was about 80% dense.

TABLE I

Two-phase integrated SANS analysis of as-compacted, nanophase TiO ₂ and Pd		
parameter	TiO ₂	Pd
Q ₀ (cm ⁻⁴)	0.206x10 ²²	0.165x10 ²²
$\bar{\rho}_g$ (cm/cm ³)	2.64x10 ¹⁰	4.14x10 ¹⁰
d _g (gm/cm ³) [†]	4.26 (nat. rutile)	12.02 (20°C)
d _b (gm/cm ³)	2.9	9.16
f _g	0.602	0.463
f _b	0.398	0.537
d _b (gm/cm ³)	0.895	6.70

[†]From 69th (1988-1989) Edition of CRC Handbook of Chemistry and Physics

The smallness of the mean density of the boundary regions as estimated from the two-phase model is striking; in the case of TiO₂, it amounts to some 21% that of theoretically dense rutile and 56% in the case of Pd. On the basis of positron annihilation experiments [4] on similar TiO₂ samples, it was concluded [9] that the first peak in the maximum entropy size distribution could be ascribed to voids or pores. The first peak tends to disappear upon annealing in air at 550°C as is shown in Fig. 1. Even so, the first peak in the size distribution could account only for about 8% of the sample volume. If the boundary region between adjacent grains is to have a reasonable thickness, it must be concluded that a significant volume fraction of still larger voids is probably present. This conclusion is consistent with results recently reported by Hahn et al. [15].

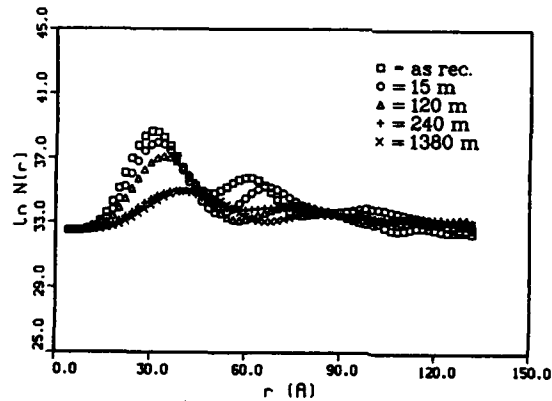


Figure 1. Semi-logarithmic plot of the maximum entropy size distribution obtained from nanophase TiO₂ compacts sintered at 550°C in air.

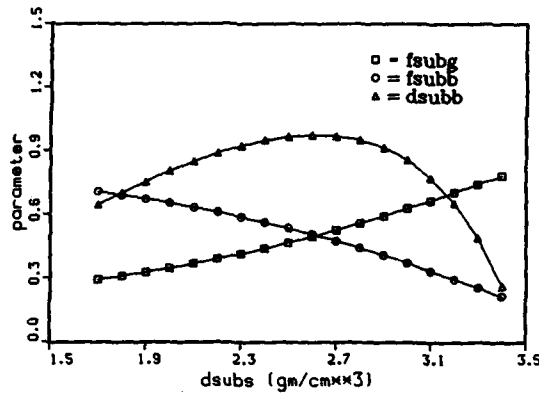


Figure 2. The effect of varying the value of the sample density (d_s) on f_g , f_b and d_b . Here $Q_0 = 0.206 \times 10^{22} \text{ cm}^{-4}$, $\bar{\rho}_g = 2.64 \times 10^{10} \text{ cm/cm}^3$ and $d_g = 4.26 \text{ gm/cm}^3$.

The present value for d_b for Pd shown in Table I is well within the range of 42 to 66% that for bulk Pd reported recently by Jorra et al. [11] for nanophase Pd. Although it is presumed that voids are present in Pd as well, we are unable to estimate this contribution inasmuch as the peaks in the maximum entropy size distribution are not resolved. Thus, d_b values are lower limits to actual grain boundary values when porosity is fully taken into account.

Aside from the simplifying assumptions in the two-phase model, there are significant uncertainties with regards to each of the four input parameters listed in Table I. For example, obvious possible sources of error in determining Q_0 are: (1) the absolute intensity conversion factor, (2) transmission coefficient determination, (3) delayed neutron correction, (4) extrapolation to $q=0$ by use of the Guinier approximation, and (5) use of Porod's law to integrate Eq. 4 to infinity. In the case of TiO_2 , there is concern about the stoichiometry of the grains, which would factor into $\bar{\rho}_g$, d_g and Q_0 . From an experimental point of view, the most uncertain parameter at present is surely the effective sample density, d_s , for TiO_2 ; i.e., the mean density of the material exclusive of the larger voids which do not contribute to SANS in the range of our measurements. The dependence of the derived values of f_g , f_b and d_b on d_s is illustrated in Fig. 2. Given the effect that, for example, an error of 10% in the value of d_s could have on d_b , it is clear that if sintering behavior in nanophase compacts is to be understood, careful density measurements in conjunction with the SANS measurements are required. The effect of uncertainties in the input parameters and the possibility of an additional source of scattering will be explored more fully in a forthcoming paper.

ACKNOWLEDGMENT

This work was supported by the U.S. Department of Energy, BES, Department of Materials Sciences, under Contract W-31-109-ENG-38.

REFERENCES

- 1). R. Birringer, U. Herr and H. Gleiter, *Suppl. Trans. Jpn. Inst. Met.* **27**, 43 (1986).
- 2). R. W. Siegel and H. Hahn, in Current Trends in the Physics of Materials, M. Yussouff, ed. (World Scientific Publ. Co., Singapore, 1987), p. 403.
- 3). R. W. Siegel and J. A. Eastman, *Mat. Res. Soc. Symp. Proc.* Vol. **132**, 3 (1989).
- 4). R. W. Siegel, S. Ramasamy, H. Hahn, Z. Li, T. Lu and R. Gronsky, *J. Mater. Res.* **3**, 1367 (1988).
- 5). C. J. Borkowski and M. K. Kopp, *Rev. Sci. Inst.* **46**, 951 (1975).
- 6). J. E. Epperson, J. M. Carpenter, P. Thiyagarajan and B. Heuser, *Nucl. Instr. Methods*, in press (1990).
- 7). F. S. Bates and G. D. Wignall, *Macromolecules* **19**, 934 (1986).
- 8). J. A. Potton, private communication, January 1988.
- 9). J. E. Epperson, R. W. Siegel, J. W. White, T. E. Klippert, A. Narayanasamy, J. A. Eastman and F. Trouw, *Mat. Res. Soc. Symp. Proc.* Vol. **132**, 15 (1989).
- 10). J. A. Potton, G. J. Daniell and B. D. Rainford, *J. Appl. Cryst.* **21**, 663 (1988).
- 11). E. Jorra, H. Franz, J. Peisl, G. Wallner, W. Petry, R. Birringer, H. Gleiter and T. Haubold, *Phil. Mag.* **B60**, 159 (1989).
- 12). G. Porod, in Small Angle X-ray Scattering, eds. O. Glatter and O. Kratky, Academic Press, London and New York, p.17 (1982).
- 13). A. Guinier and G. Fournet, Small Angle Scattering of X-rays, John Wiley and Sons, New York (1955).
- 14). G. Porod, *Z. Kolloid* **124**, 83 (1951); *Z. Kolloid* **125**, 51 and 108 (1952).
- 15). H. Hahn, J. Lucas and R. S. Averback, submitted to *J. Mater. Res.* (1990).

PART III

Surfaces, Films and Interfaces

SURFACE INVESTIGATION BY NEUTRON REFLECTION

B. FARROUX

Laboratoire Léon Brillouin (CEA-CNRS), CEN-Saclay
91191 Gif-sur-Yvette Cedex, France

ABSTRACT

Several phenomena analogous to those observed in classical optics, such as reflection, refraction and interference, are also observed with slow neutrons. Information on surface properties, described by a refractive index profile, can be extracted from reflection experiments. This information is similar to that obtained by X-ray reflection. However, there are some instances where the new neutron method provides a distinct advantage. The refractive index is related to the scattering length density, a parameter which describes the neutron-matter interaction. Owing to the magnetic interaction, magnetic materials have a neutron spin dependent refractive index, and a critical reflection of polarized neutrons is a particularly sensitive probe of surface magnetism. On the other hand, in contrast to X-rays, neutron scattering length values vary randomly from element to element. Isotopic substitution can then produce a contrast in the scattering length density. Of particular importance is the large difference between hydrogen and deuterium. This is a distinct advantage for studying many problems in surface chemistry, particularly in the polymer field.

INTRODUCTION

Many techniques are used to investigate the structure of materials near the surface. Some are concerned with atomic structure on the scale of a few angstroms, but it is important to understand the structure on the macroscopic scale of a few hundred nanometers. Reflection of X-rays has been successfully applied to the study the density profile close to the surface [1][2]. Reflection of slow neutron beams is now used for surface investigation in various system such as multilayers, polymer layers, and magnetic layers. The information given by this technique is formally the same as for X-rays, but owing to the specific neutron-matter interaction [3], this information is complementary and sometimes unique.

NEUTRON REFLECTION

Many optical phenomena observed with electromagnetic radiation such as reflection (total or partial), refraction, and interference are also observed with slow neutron beams [4]. All these effects are described by using the same optical law corresponding to the electric vector perpendicular to the plane of incidence (s-waves). In this frame, a neutron refractive index of a medium in vacuum is defined as :

$$n = \left(1 - \frac{V}{E} \right)^{1/2} \quad (1)$$

where $E = \frac{h^2}{2m} \lambda^2$ is the kinetic energy of the neutron (h Planck's constant, mass m and de Broglie wavelength λ) in vacuum and V the potential experienced in the medium. The reflection process is forward scattering. Then, for a pure nuclear interaction, the potential is derived from the Fermi pseudo-potential

$$V_n = \frac{h^2 Nb}{2\pi m} \quad (2)$$

with b the bound coherent scattering amplitude and N the number of scattering nuclei per unit volume. The quantity Nb , the coherent scattering length density, is a characteristic of the medium. When polarized neutrons are used, with a magnetized sample, the magnetic part of the potential is given by [5]

$$V_m = \pm \mu_n B \quad (3)$$

where the \pm signs refer to the neutron spin direction parallel or antiparallel to the magnetic induction B and μ_n is the neutron dipole moment. The index of refraction is then spin direction dependent.

Taking into account the absorption cross section σ_a of the medium and considering pure nuclear interaction, the neutron refractive index is expressed as [6]

$$n = 1 - \delta + i\beta \quad (4)$$

$$\text{with } \delta = \left(\frac{Nb}{2\pi}\right) \lambda^2 \text{ and } \beta = \left(\frac{N\sigma_a}{4\pi}\right) \lambda.$$

For most materials β is negligible and δ is positive and small. Two facts must be noted : 1) Total external reflection can occur at the interface between vacuum and medium if the value of the angle θ of the neutron beam and the surface is less than a critical value θ_c which is given by $\cos\theta = n$,

$$\theta_c = \lambda \left(\frac{Nb}{\pi}\right)^{1/2} \quad (5)$$

Alternatively, for a fixed angle θ , total reflection occurs for neutron wavelengths larger than a critical value λ_c .

By isotopic substitution, values of Nb and then the index of refraction can be changed to some extent. This is a distinctive feature of the neutron technique. Values of Nb , critical angle and refractive index for some selected materials are given in Table I.

One of the variables used to describe the specular reflection process (elastic scattering) is the wave vector transfer perpendicular to the surface

$$q = \left(\frac{4\pi}{\lambda}\right) \sin\theta \quad (6)$$

TABLE I
 Values of scattering length density (Nb), critical angle (θ_c/λ or θ/λ_c), deviation of the refractive index from unity (1-n), for some selected solid and liquid materials. (PDMS Polydimethyl-Siloxane)

Materials	Nb (10^{-10})(cm/cm ³)	θ/λ (10^{-3})(radians/Å)	1-n (10^{-6})
SiO ₂	3.959	1.1226	0.630
Si	2.073	0.812	0.330
Ge	3.637	1.076	0.579
Ni	9.406	1.730	1.497
Ni ⁵⁸	13.151	2.046	2.092
C (diamond)	11.712	1.931	1.864
Ti	-1.945	-	-0.302
Mn	-2.944	-	-0.445
H ₂ O	-0.561	-	-0.089
D ₂ O	6.398	1.427	1.017
Toluene H	0.943	0.548	0.150
Toluene D	5.718	1.349	0.910
PDMS H	0.064	0.143	0.010
PDMS D	5.008	1.263	0.797

For q values smaller than the critical value

$$q_c = 4(\pi Nb)^{1/2} \quad (7)$$

total reflection occurs. For $q > q_c$ the neutron beam is partially reflected and partially transmitted in the medium. For a perfect homogeneous surface corresponding to a step function in the potential V, the reflectivity profile, defined as the ratio of the reflected and the incoming intensity, is given by the Fresnel's law [7]

$$R_f = \frac{2X^2 - 1 - 2X\sqrt{X^2 - 1}}{2X^2 - 1 + 2X\sqrt{X^2 - 1}} \quad (8)$$

with $X = q/q_c$ or θ/θ_c or λ_c/λ . The reflectivity curve is composed of two parts: the total reflection plateau ($R=1$) for $X \leq 1$, and the reflectivity profile for $X > 1$ where the intensity decays rapidly. For large values of X ($X > 5$), R behaves as

$$R_f \approx \frac{1}{16} X^{-4}$$

If the surface is not perfect, the reflection profile deviates from the Fresnel value R_f . This deviation contains information about the surface structure in a direction perpendicular to the surface.

EXPERIMENTAL METHODS

Considering the expression (8) the reflectivity profile is a function of two variables, θ and λ . Then two experimental methods can be used in neutron reflectometry. i) In the classical method a monochromatic beam impinges upon the surface with an angle θ . A θ -2 θ scan is performed. The reflectivity profile is then recorded as a function of the angle for angles greater than θ_c (eq.(5)). This method is currently used with X-rays and for some neutron reflectometers (see Table II). ii) The second method uses a fixed geometry; the angle of incidence is kept at the same value and the incident wavelength varies. The beam intensity is sorted by a Time-Of-Flight (TOF) method. The reflectivity profile is recorded as a function of the wavelength for wavelengths shorter than the critical value λ_c (eq.(5)). This TOF method is naturally used at pulsed neutron sources, but also at some steady state reactors [8] (Table II). It offers some advantages with respect to the conventional monochromatic beam method. First, a constant geometry is used, which means that the illuminated sample surface is the same for the whole wavelength range covered. Second, a large wavelength range is measured simultaneously. Third, the rapid decrease of the reflected intensity can be compensated by the shape of the spectral neutron distribution.

In a neutron reflection experiment the sample size is of the order of few cm^2 . Owing to the rather low source intensity compared to X-rays, the beam is defined by slits of a few tenths of a millimeter. The resolution function of the experimental set-up is determined by measuring the reflectivity of a bulk material with known coherent scattering length density. The procedure to extract physical information from a reflectivity measurement is rather indirect. In many cases, one starts with a given model of the surface structure, calculates the theoretical reflectivity curve, and then checks the fit with the experimental data. In the case of a bulk sample, the calculation is done by using the Fresnel formula (8). For more complicated systems (multilayers or a density profile near the surface) the calculation can be done by using the optical matrix method [9] in which the near surface is divided into a number of layers whose thickness and scattering length densities are chosen from a given model. Roughness effects [10] can be introduced in-between each layer as a gaussian distribution [11][12]. An alternative method is to start from the interaction potential (eq.(2)) and to use the formalism of the Schrödinger wave equation in one dimension [13]. This formalism has been used for example to predict the reflectivity curve for a concentration profile of a polymer solution [14].

EXPERIMENTS

Since the first observation of the neutron total reflection in the early days of the fifties [15][16], this technique was only used for many years for technical applications. It was an important method for the determination of the coherent scattering length values. Twenty years after, these measurements were done with great accuracy by using the effect of gravity in the determination of the neutron wavelength [17]. In the seventies, the neutron reflection process has been extensively used at nuclear research reactors which have cold neutron sources and long neutron guides [18][19] (about 100 meters). In this way it was possible to accommodate many experimental spectrometers in large halls away from the reactor building. Other optical devices has been developed such a multilayer monochromators [20] for long wavelength neutrons or polarising mirrors to produce polarized neutron beams [21][22].

It is only recently that the measurement of the reflection curve has been used to determine surface structure at the scale of a few hundred nanometers with a resolution of about one nanometer. As can be seen by

looking at Table II, a large number of dedicated instruments have been designed or commissioned during the last decade.

TABLE II NEUTRON REFLECTOMETERS
() = variable parameter : W wavelength, A angle,
Detector : ld = linear, XY = area

Laboratory	Source	Reflectometer	Type	Date	Detector
JULICH (G)	Steady	TOREMA	W, (A)	1988	ld
HMI (G)	Steady		W, (A)	?	ld
ISIS (GB)	Pulsed	CRISP	(W), A	1986	ld (XY)
ILL (F)	Steady	D17	W, (A)	1983	XY
		UCN	(W), A	1989	single
		EVA	W(A)	1990	ld
LLB (F)	Steady	SESI	(W), A	1984	XY
		EROS	(W), A	1990	XY
DELFT (NL)	Steady		(W), A	1990	single
RISO (DK)	Steady		W, (A)	1990	single
ANL (USA)	Pulsed	POSY-1	(W), A	1984	XY
		POSY-2	(W), A	1988	XY
BNL (USA)	Steady		W, (A)	1988	single
NIST (USA)	Steady		W, (A)	1989	single
LANSCE (USA)	Pulsed	SPEAR	(W), A	1989	ld (XY)

The technique has been applied to investigate interfacial phenomena in physical chemistry including structures of fatty acid multilayers [23], structural properties of adsorbed polymer layers at the air-water interface [24], and a polymer solution interface [25]. An example is given in figure 1 : the sample is a polymer (Polydimethyl-Siloxane) in dilute solution in Toluene. This case is known as a strong adsorption of the polymer at the free interface [26]. Isotopic substitution (deuterated polymer in hydrogenated solvent) enhances the contrast. The concentration profile created is revealed by checking the reflectivity curve with a calculation obtained from scaling law predictions [27] of a self-similar concentration profile. Experimental data are in good agreement with the proposed model of a thin (1.3 nanometers) layer of adsorbed polymer followed by a concentration profile decreasing with a power law up to a distance of the order of the radius of gyration (5 nanometers) [28].

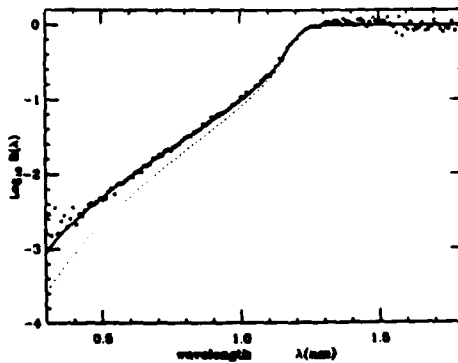


Figure 1. Decimal logarithm of the reflectivity versus wavelength, for a dilute solution of Deuterated PolyDimethyl-Siloxane (molecular weight 19000 ; polydispersity 2.3 ; radius of gyration 5 nanometers ; volume fraction $3 \cdot 10^{-2}$) in toluene. Crosses: experimental points, solid line : theoretical prediction, dotted line : theoretical curve for a bulk sample. Angle of reflection 0.4° .

Interfacial phenomena, such as the enrichment of the surface in one specie [29][30] or the process of interdiffusion of two polymer layers [31], can also be investigated by neutron reflection. In many cases these layers are deposited on bulk substrate [32]. The knowledge of the surface structure is then also important. In figure 2, the neutron reflectivity curve of a Sodocalcite glass used as a support for metallic multilayers is shown together with the X-ray measurement [33]. Clearly the neutron experiment shows the existence of a depletion layer which is important for the efficiency of the multilayer.

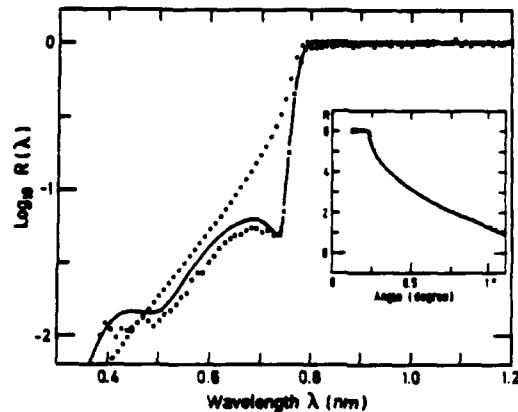


Figure 2. Decimal logarithm of the reflectivity versus wavelength for a polished surface of Sodocalcite glass. Angle of reflection 0.5° . Crosses : experimental points, points : theoretical calculation for a bulk homogeneous sample, solid lines : Best fit taking into account a depletion layer of 56 nanometers at the surface with a density lower than the bulk. In the insert : X-ray measurement (Reflectivity versus angle) for the same sample. The best fit is obtained by using the density of the depletion layer as the bulk density.

The study of surface magnetism is another instance where neutron reflection is of prime importance as seen by the increasing number of experiments [13]. For example, the magnetic field profile perpendicular to the surface can be probed [34]. It has been measured in superconducting films for example [35]. As predicted [36] and proven [37], this technique is sensitive enough to detect a magnetic layer of a thickness of one atomic plane.

CONCLUSION

Neutron reflection is a new non-destructive method to test the near interface structure at the scale of a few hundreds of nanometers with a resolution approaching one nanometer or less. This young technique (developed at the beginning of the eighties) is complementary to the well known X-ray method, but offers some distinct advantages when contrast can be enhanced by isotopic labelling or when magnetic phenomena are involved.

REFERENCES

1. A. Braslau, M. Deutsch, P.S. Pershan, A.H. Weiss, J. Als-Nielsen and J. Bohr, *Phys. Rev. Lett.* **54**, 114 (1985)
2. B.C. Lu, and S.A. Rice, *J. Chem. Phys.* **68**, 5558 (1978)
3. G.E. Bacon, *Neutron Diffraction*, (Clarendon Press, Oxford 1975)
4. V.F. Sears, *Neutron Optics*, (Oxford University Press, 1989)
5. W. Gavin Williams, *Polarized Neutron*, (Clarendon Press, Oxford 1988)
6. A.G. Klein and G.A. Werner, *Rep. Prog. Phys.* **46** (1983)
7. M. Born and E. Wolf, *Principles of Optics*, Pergamon Press, Oxford 1970)
8. B. Farnoux in *Neutron Scattering in the Nineties*, (IAEA Vienna 1985)
9. F. Abeles, *Ann. Phys. (Paris)* **3**, 504 (1948)
10. S.K. Sinha, E.B. Sirota, G. Garoff and H.B. Stanley, *Phys. Rev.* **B38**, 2297 (1988)
11. L. Nevot and P. Croce, *Rev. Phys. Appl.* **15**, 761 (1980)
12. J. Meunier, *C.R. Acad. Sci. Paris Ser.B*, **292**, 1469 (1981)
13. G.P. Felcher, *SPIE vol. 983, Thin-Film Neutron Optical Devices* (1988)
14. O. Guisselin, to appear in *J. Phys. Paris* (1989)
15. E. Fermi and W.H. Zinn, *Phys. Rev.* **70**, 103 (1946)
16. D.J. Hughes, *Neutron Optics*, (Interscience Pub., New-York, 1954)
17. L. Koester, *Neutron Physics*, (Springer Verlag, Berlin 1977)
18. H. Maier-Leibnitz and T. Springer, *J. Nucl. Energy A/B17*, 217 (1963)
19. B. Farnoux, B. Hennion and J. Fagot in *neutron Inelastic Scattering*, vol.2 (AIEA Vienna, 1968)
20. A.M. Saxena and B.P. Schoenborn, *Acta Cryst.* **A33**, 805 (1977)
21. O. Schaerpf in *Neutron Scattering in the Nineties*, (IAEA Vienna 1985)
22. C.F. Majkrzak, *Physica* **136B**, 69 (1986)
23. J.B. Hayter, R.R. Highfield, B.J. Pulmann, R.K. Thomas, A.I. McMullen, J. Penfold, *J. Chem. Soc. Faraday Trans. 1*, 1437 (1981)
24. A.R. Rennie, R.J. Crawford, E.M. Lee, R.K. Thomas, T.L. Crowley, S. Roberts, M.S. Qureshi and R.W. Richards, *Macromolecules* **22**, 3466 (1989)
25. X. Sun, E. Bouchaud, A. Lapp, B. Farnoux, M. Daoud and G. Jannink, *Europhys. Lett.* **6**, 207 (1988)
26. R. Ober, L. Paz, C. Taupin and P. Pincus, *Macromolecules* **16**, 50 (1983)
27. P.G. de Gennes and P. Pincus, *J. Phys. Lett. (Paris)* **44**, L241 (1983)
28. O. Guiselin, Private Communication
29. R.J. Composto, R.S. Stein, E.J. Kramer, R.A.L. Jones, A. Mansour, A. Karim and J.P. Felcher, *Physica* **B156/157**, 434 (1989)
30. S.H. Anastasiadis, T.P. Russel, S.K. Satija and C.F. Majkrzak, *Phys. Rev. Lett.* **62**, 1852 (1989)
31. M.L. Fernandez, J.S. Higgins, J. Penfold, R.C. Ward, C. Shackelton and D.J. Walsh, *Polymer* **22**, 1023 (1988)
32. T.P. Russel, A. Karim, A. Mansour and G.P. Felcher, *macromolecules* **21**, 1890 (1988)
33. M. Maaza, Private Communication
34. G.P. Felcher, R.O. Hilleke, R.K. Crawford, J. Haumann, R. Kleb and G. Ostrowski, *Rev. sci. Instrum.* **58**, 609 (1987)
35. G.P. Felcher, R.T. Kampwirth, K.E. Gray and R. Felici, *Phys. Rev. Lett.* **52**, 1539 (1984)
36. G.P. Felcher, K.E. Gray, R.T. Kampwirth and M.B. Brodsky, *Physica* **B136**, 59 (1986)
37. J.A.C. Bland, D. Pescia and R.F. Willis, *Phys. Rev. Lett.* **58**, 1244 (1987)

INTERDIFFUSION OF CADMIUM ARACHIDATE IN LANGMUIR-BLODGETT FILMS

PIETER STROEVE*, JOHN F. RABOLT**, RUSS O. HILLEKE, GIAN P. FELCHER***, AND SOW-HSIN CHEN****.

*Department of Chemical Engineering, University of California, Davis, CA 95616

**IBM Almaden Research Center, 650 Harry Road, San Jose, CA 95120

***Argonne National Laboratory, Intense Pulsed Neutron Source, Argonne, IL 60439

****Department of Nuclear Engineering, Massachusetts Institute of Technology, Cambridge, MA 02139

ABSTRACT

The interdiffusion of Cadmium Arachidate (CdA) in Langmuir-Blodgett films has been studied by neutron reflection at the Intense Pulsed Neutron Source of Argonne National Laboratory. One of the samples consisted of a few layers of perhydro H-CdA deposited on a silicon support, overlayers with a few layers of deuterated D-CdA, for a total thickness of ~300 Angstroms. In a second sample the layers of perhydro- and deuterated- CdA were separated by two monolayers of H-n-octadecene/co-maleic acid copolymer. When heated for 15 minutes at 70° C, well below the disorder temperature [1], approximately 25% of the D-CdA molecules were replaced by H-CdA molecules, although the overall Langmuir-Blodgett film structure is known to remain unchanged [1]. The presence of copolymer layers limited the interdiffusion process to about 5%.

INTRODUCTION

Neutron reflectivity principals are well-known and have been extensively treated in the literature [2]. The reflectivity of neutrons provides a useful method to investigate surface and interfacial phenomena on a nanometer size scale. With neutron reflectivity the density profile of a thin film can be quantitatively assessed by isotopic substitution of hydrogen by (for example) deuterium for selective species present in the film. For example, Anastasiadis et al.[3] used neutron reflectivity to study behavior of thin films of symmetric poly(styrene-b-methylmethacrylate) diblock copolymers. Selective deuterium labeling of one block provided ample contrast and highlighted specific blocks of the copolymer chain. Neutron reflectivity has also been used to evaluate the concentration profile of polymer segments near the air-solution interface [4]. Russell et al.[5] have applied

neutron reflectivity to investigate the interdiffusion of two layers, composed of polymer molecules where one type of the molecules is deuterated and the other is protonated.

Limited studies have been conducted on Langmuir-Blodgett (LB) films, but the use of neutrons to probe biological and LB films is of great current interest [6]. For example, neutron reflection of LB films have been reported by Nicklow et al. [7] and Highfield et al. [8]. To our knowledge neutron reflection has not yet been used to study interlayer diffusion in multilayer LB films. LB films can be considerably thinner than the polymer films discussed earlier. In this work we report the first results on interlayer diffusion of Cadmium Arachidate in LB films.

One of the most important problems in the use of LB films in integrated optics devices is to know the equilibrium structures of LB films at ambient temperatures and to determine any change in the structures at elevated temperatures. The determination of the interlayer diffusion coefficients is very important, leading to methods for predicting aging for such characteristics as SHG. It has been shown that LB films of optically active chromophores interleaved with neutral spacer layers of fatty acids or salts show promise in attaining the theoretically predicted quadratic enhancement of the SHG signal with the number of optically active layers [9,10]. It has also been shown that interleaved layers of the chromophore hemicyanine and cadmium arachidate give more stable films than pure LB films of hemicyanine at moderate temperatures as determined by FTIR spectroscopy [11]. Interleaved structures are necessary because SHG requires noncentrosymmetric structures. Interdiffusion may destroy or alter the noncentrosymmetric nature of interleaved films.

EXPERIMENTAL

Langmuir-Blodgett films were prepared in a Joyce-Loebl Langmuir trough. The trough was enclosed by a class 100 laminar flow modular clean room. For the subphase deionized and filtered water with a resistance of 18.3 M Ω -cm was used. Cadmium chloride was added to the subphase to a concentration of 10^{-3} M. Deuterated Arachidic Acid was obtained from Cambridge Isotope Laboratories and used without further purification. The arachidic acid was more than 97% deuterated, with the composition verified by Raman spectroscopy. Concentrations about 1 mg ml $^{-1}$ in chloroform were used as spreading solutions. Starting with an upstroke, Langmuir-Blodgett layers were deposited on 187 mills thick, 2 inch diameter silicon wafers with one side polished (Semiconductor Processing Company). One of the samples

consisted of 6 layers of perhydro Cadmium Arachidate (H-CdA) deposited on the silicon support and then overlayered with 5 layers of deuterated Cadmium Arachidate (D-CdA). In a second sample, 4 layers of H-CdA were first overlayered with 2 monolayers of perhydro n-Octadecene/co-maleic acid copolymer. The copolymer layers deposited only on the upstroke so that these were of Z-type. After the copolymer layers, the LB film was overlayered with 4 layers of D-CdA. All CdA layers deposited as Y-type. The copolymer layers constituted a diffusion barrier between the deuterated and perhydro CdA. The surface pressures for deposition were 30 mN m⁻¹.

Neutron reflection on the LB films was performed at the Intense Pulsed Neutron Source at the Argonne National Laboratory. The POSY II neutron reflectometer was used for this purpose. Angles of 0.4°, 0.8° and 1.2° were used for the experiments. The time of each experiment was at least 12 hours. After specular reflection profiles were obtained, each sample was heated for 15 minutes at 70°, and a second neutron reflectivity measurement was conducted.

RESULTS AND DISCUSSION

To measure interlayer diffusion in the two LB films with the neutron reflectometer, reference samples were prepared and analyzed. Two reference samples had either an LB film of H-CdA or a LB film of D-CdA. The specular reflection profiles of these two samples were not expected to change from the profiles obtained at room temperature if the samples were heated for 15 minutes at 70° C. From the experiments we found no change, suggesting that no ablation of the LB films occurred and that the thickness of the films was not changed.

The neutron reflectivity results for the sample consisting of 6 layers of H-CdA covered by 5 layers of D-CdA is shown in Fig. 1. The room temperature reflectivity is plotted versus the neutron momentum perpendicular to the sample surface $k_z = 2\pi \sin\theta/\lambda$, where θ is the angle of incidence with the surface, and λ is the neutron wavelength. The open circles represent the data taken before heat-treating the sample and the full circles are the data taken after heating the sample to 70° C for 15 minutes. The oscillations represent the interference pattern of neutrons reflected from layers of different refractive index. The most relevant feature of Fig. 1 is the decrease in the reflectivity after the heat treatment. Since the refractive index of D-CdA is much stronger than that of H-CdA, the lowering of the reflectivity indicates that the two layers are mixing, and in particular the D-CdA molecules of the upper layer are

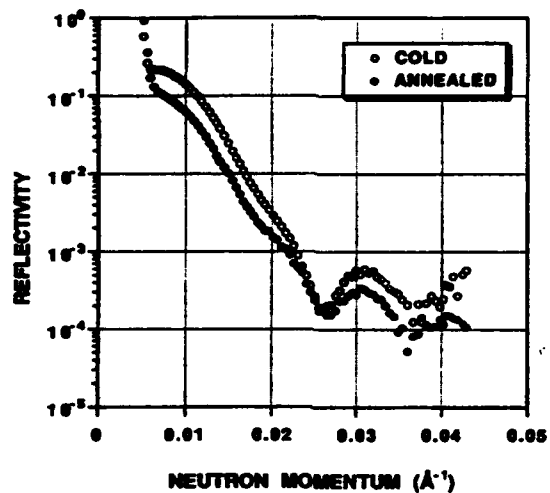


Fig. 1. Reflectivity profile of a Langmuir-Blodgett film consisting of 6 layers of H-CdA on silicon, covered by 5 layers of D-CdA. The measurements were taken at room temperature, before (open circles) and after (full circles) annealing the sample for 15 minutes at 70°C.

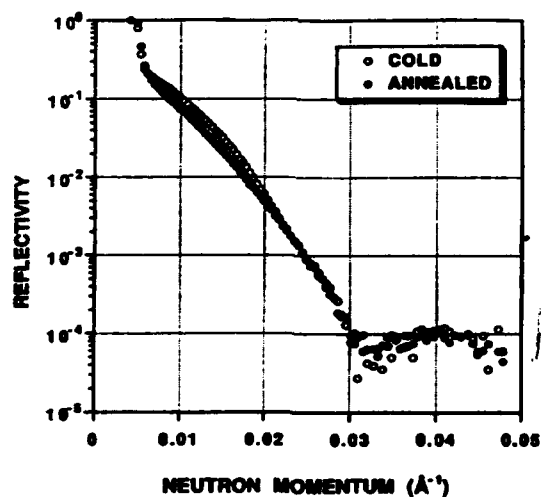


Fig. 2. Reflectivity profile of a Langmuir-Blodgett film if 4 layers of H-CdA on silicon, covered by 2 layers of a copolymer and 4 layers of D-CdA. The measurements were taken at room temperature, before (open circles) and after (full circles) annealing the sample for 15 minutes at 70°C.

replaced with those containing light hydrogen by approximately 25%.

The placement of two polymer layers between the H-CdA and the D-CdA layers retards dramatically the diffusion between the layers. This is shown in Fig. 2, where is presented the reflectivity of a 4 layers H-CdA/2 layers copolymer/4 layers D-CdA sample before (open circles) and after (full circles) annealing at 70°C for 15 minutes. In this case, less than 5% of the molecules have interdiffused.

The results are surprising for the sample of H-CdA and D-CdA only. It is known from FTIR studies that heating to 70° C and cooling causes no significant change in the orientation of CdA molecules in LB layers of CdA [1]. Thus our results suggest that interdiffusion takes place without causing a change of orientation of the fatty salts in the LB layers. The presence of a polymer layer can present a barrier to the interdiffusion process.

ACKNOWLEDGEMENTS

This work has benefited from the use of the Intense Pulsed Neutron Source at Argonne National Laboratory. This facility is funded by the U.S. Department of Energy, BES-Materials Science, under contract W-31-109-Eng-38.

REFERENCES

1. C. Naselli, J.F. Rabolt and J.D. Swalen, *J. Chem. Phys.* **82**, 2136 (1985).
2. S.A. Werner and A.G. Klein, in *Neutron Scattering*, D.L. Price and K. Skold, eds. (Academic Press, New York, Chapter IV, 1984).
3. S.H. Anastasiadis, T.P. Russell, S.K. Satija, and C.F. Majkrzak, *Phys. Rev. Lett.*, **62**, 1852 (1989).
4. E. Bouchard, B. Farnoux, X. Sun, M. David and G. Jannink, *Europhys. Lett.*, **2**, 315 (1986).
5. T.P. Russell, A. Karim, A. Mansour and G.P. Felcher, *Macromolecules*, **21**, 1890 (1988).

6. M. Pomerantz, in *Molecular Engineering of Ultrathin Polymeric Films*, P. Stroeve and E. Franses, eds. (Elsevier Applied Science Publishers, Barking, Essex, England, 1987).
7. R.M. Nicklow, M. Pomerantz and A. Segmüller, *Phys. Rev. B*, **23**, 1081 (1981).
8. R.R. Highfield, R.K. Thomas, P.G. Cummins, D.P. Gregory, J. Mingins, J.B. Hayter and O. Scharpf, *Thin Solid Films*, **92**, 165 (1983).
9. L.M. Hayden, B.L. Anderson, J.Y.S. Lam, B.G. Higgins, P. Stroeve and S.T. Kowel, *Thin Solid Films*, **160**, 379 (1988).
10. B.L. Anderson, J.M. Hoover, G.A. Lindsay, B.G. Higgins, P. Stroeve, and S.T. Kowel, *Thin Solid Films*, **172**, in press (1989).
11. P. Stroeve, D.D. Saperstein, and J.F. Rabolt, *J. Chem. Phys.*, submitted (1989)

A NEUTRON REFLECTIVITY STUDY OF THE INTERFACIAL MAGNETISM OF AN Y/Gd FILM

J.F. ANKNER*, H. ZABEL*, D.A. NEUMANN**, C.F. MAJKRZAK**, A. MATHENY*, J.A. DURA*, AND C.P. FLYNN*

*Department of Physics and Materials Research Laboratory, University of Illinois, 1110 W. Green St., Urbana, IL 61801

**Institute of Materials Science and Engineering, National Institute of Standards and Technology, Building 235 A106, Gaithersburg, MD 20899

ABSTRACT

Using the technique of polarized-neutron reflectometry, we have studied the magnetic moment distribution in the interfacial region of an epitaxial film consisting of 97 Å Y(0001) atop 1000 Å Gd(0001). At $T = 151$ K, with an 80 gauss field applied parallel to the surface (basal plane), we observe two distinct ferromagnetic regions: the Gd bulk and a layer with reduced magnetic moment at the Y/Gd interface. Above the bulk Curie temperature, at $T = 295$ K ($T_C^{\text{Gd}} = 293$ K), we observe no net magnetization in either the bulk or the interface.

INTRODUCTION

The interfacial magnetism of Gd has been a subject of intensive study over the past several years. These experiments fall into two main categories: work on Gd surfaces (Gd/vacuum interfaces)^{1,2} and studies of synthetic Y/Gd superlattices.^{3,4} In this paper, we describe work that represents something of a hybrid of these two fields. Using polarized-neutron reflectometry, we probe beneath the surface to study the layer-averaged magnetic moment as a function of depth of a single Y/Gd interface. Our particular aim is to study the magnetic moment of the Gd layers at the Y/Gd interface as a function of temperature and compare this behavior with that of the free Gd surface. This paper describes our initial efforts toward that goal.

X-RAY CHARACTERIZATION OF SAMPLE

Our sample was grown by molecular-beam epitaxy (MBE) at the University of Illinois by A. Matheny, J.A. Dura, and C.P. Flynn. The substrate is $\text{Al}_2\text{O}_3(11\bar{2}0)$ on which is grown a 1000 Å Nb(110) buffer layer, followed by a 300 Å Y(0001) seed for 1000 Å of Gd(0001), which is covered by a 97 Å Y(0001) cap. X-ray diffraction measurements show the rare-earth layers to be good three-dimensional single crystals with mosaic spreads of 0.4° fwhm.

We measured the x-ray reflectivity of the sample in order to obtain its chemical depth profile. Figure 1 shows the logarithm of the x-ray reflectivity as a function of momentum transfer Q normal to the surface. The oscillations are caused by the 97Å-thick Y cap layer and are very sensitive to the topmost Y/Gd interface; the absence of

higher-frequency oscillations indicates that, as a result of the roughness of the lower-lying interfaces and the resolution of the instrument ($\delta\theta = 0.48$ mradian), we are not sensitive to those interfaces below the vacuum/Y and Y/Gd. We have developed a multi-layer fit routine based on the recursion formula of Parratt.⁵ The solid line in Figure 1 shows the best fit to the data with the Gaussian-distributed roughnesses of the Gd/Y, Y/Nb, and Nb/Al₂O₃ interfaces fixed at 20 Å. The overall intensity, thickness of the Y cap layer, and the roughnesses of the vacuum/Y and Y/Gd layers were optimized by non-linear least-squares to yield $d_Y = 97$ Å, $\sigma_{0Y} = 13$ Å, and $\sigma_{YGd} = 11$ Å. These parameters are used in the fits to the neutron data.

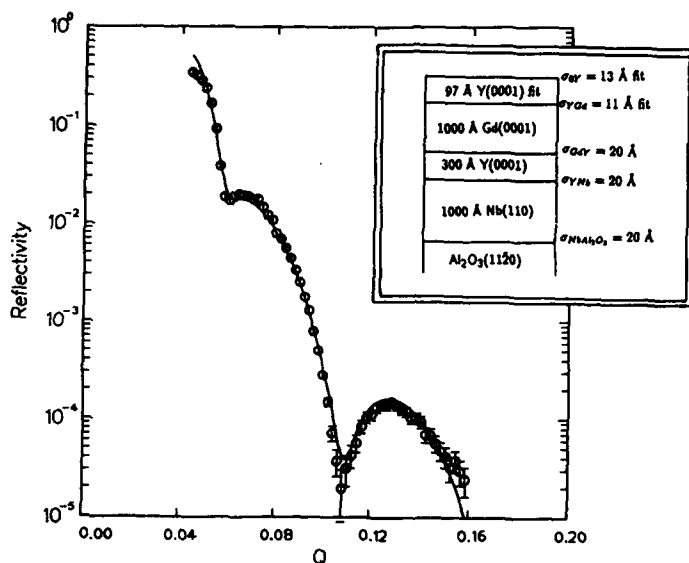


Figure 1. The x-ray reflectivity of the sample is fit to the model shown in the inset. The solid line is the fitted curve.

NEUTRON REFLECTIVITY

We used the BT-4 instrument at the National Institute of Standards and Technology (NIST) Neutron Beam Split-Core Reactor (NBSR) to carry out our measurements. A graphite monochromator produces a beam with $\Delta\lambda/\lambda = 0.01$, which passes through Cd collimating masks with single slits that reduce its angular divergence to 1' (0.3 mradian). An Fe-Si supermirror array (93% polarization efficiency) and an rf spin flipper polarize the beam before the sample, which sits between Helmholtz coils that apply an 80 gauss magnetic field in the plane of the sample surface parallel or anti-parallel to the incident neutron polarization. The specularly reflected intensity is collected in a ³He detector as a function of incident angle and neutron polarization.

The reflectivity of a spin-polarized neutron beam depends very sensitively on the

magnetic moment profile of the sample. The neutron refractive index is:⁶

$$n_{\pm} = 1 - \frac{\lambda^2}{2\pi} N[b \pm C\mu(z)], \quad (1)$$

where λ is the neutron wavelength, N the density of scatterers, b the neutron-nuclear scattering length, $\mu(z)$ the layer-averaged magnetic moment, and $C = 0.2695 \times 10^{-12}$ cm/ μ_B . By measuring the reflectivity of neutrons polarized parallel and anti-parallel to the sample moment one can, in principle, determine $\mu(z)$. Figure 2 (top) plots the parallel (I_{\parallel}) and anti-parallel (I_{\perp}) reflected intensities (corrected for incident polarization efficiency and background) of our sample at $T = 151$ K. A convenient measure of the sample magnetization is the spin asymmetry,

$$A = \frac{I_{\parallel} - I_{\perp}}{I_{\parallel} + I_{\perp}}. \quad (2)$$

Figure 2 (bottom) shows the spin asymmetry of the data along with the best-fit curves for the two models of magnetic profile shown in the inset. The dashed line is the best fit when one considers the Gd layer to have uniform magnetization and fits that magnetization and the Y/Gd interfacial roughness. We obtain a better fit by allowing the interfacial region to have a different moment from the bulk and varying that moment, the bulk moment, and the thickness of the interface. The 66 Å interfacial thickness should be taken only as an upper limit, since we have not scanned far enough out in Q to determine the true thickness. Clearly, one must consider the interfacial region as having a different magnetic moment from that of the bulk. Vettier, et al⁴ have observed a similar behavior in Y/Gd synthetic superlattices. We have also measured the reflectivity at $T = 295$ K (above $T_C^{\text{Gd}} = 293$ K) and detect no magnetic moment ($\pm 0.2 \mu_B$), in contrast to the free Gd surface, which exhibits an interface moment above the bulk Curie temperature.^{1,2}

COMING ATTRACTIONS

We have described here the first measurements in our survey of the Y/Gd interface. We have observed that this interface exhibits a different moment from the bulk at $T = 151$ K and that both moments go to zero above $T_C^{\text{bulk}} = 293$ K, in contrast to the behavior of the free Gd surface. Recently, in collaboration with Y.Y. Huang and G.P. Felcher at the IPNS at Argonne National Laboratory, we have investigated more thoroughly the reflectivity for temperatures near T_C and will study the field dependence of the in-plane moment in an upcoming experiment. We plan to measure the temperature dependence of the easy axis of magnetization⁷ using exit-beam polarization analysis⁸ and grazing-angle diffraction⁹ since these methods are sensitive to out-of-plane magnetization, while simple specular reflectivity is not. We hope, by these experiments, to perform a complete analysis of Gd interfacial magnetism in this system.

ACKNOWLEDGMENT

The work by J.F. Ankner and H. Zabel at the University of Illinois has been supported by the U.S. DOE under contract DE-AC02-ER01198.

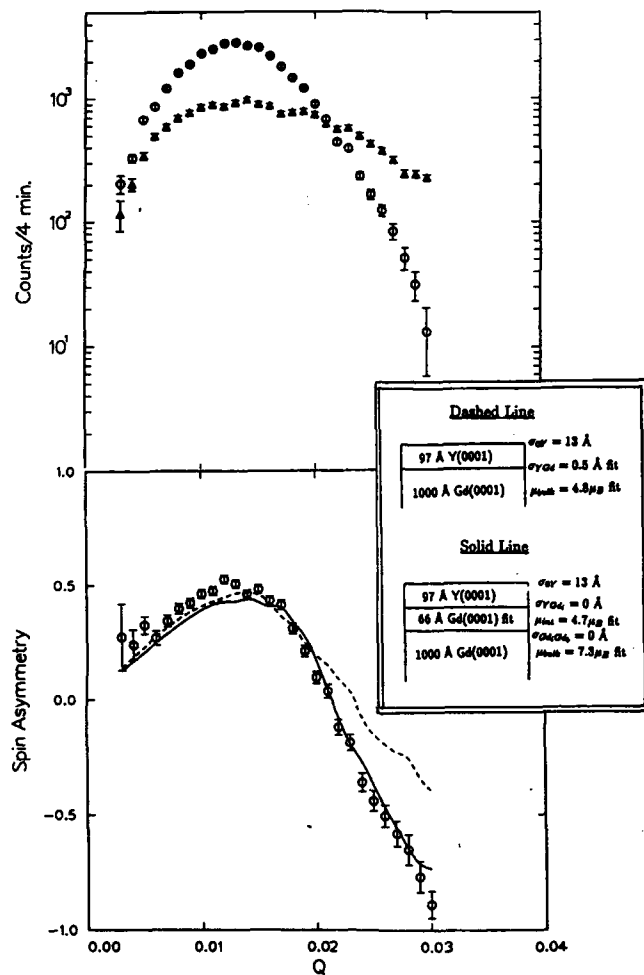


Figure 2. (top) The neutron reflected intensity for incident spin up (I_{\uparrow}) and spin down (I_{\downarrow}) neutrons. (bottom) Spin asymmetry $A = (I_{\uparrow} - I_{\downarrow}) / (I_{\uparrow} + I_{\downarrow})$ with the best fit curves of the models in the inset.

REFERENCES

1. D. Weller, S.F. Alvarado, W. Gudat, K. Schröder, and M. Campagna, Phys. Rev. Lett. **54**, 1555 (1985).
2. C. Rau and M. Robert, Phys. Rev. Lett. **58**, 2714 (1987).

3. C.F. Majkrzak, J.W. Cable, J. Kwo, M. Hong, D.B. McWhan, Y. Yafet, J.V. Waszczak, and C. Vettier, *Phys. Rev. Lett.* **56**, 2700 (1986).
4. C. Vettier, D.B. McWhan, E.M. Gyorgy, J. Kwo, B.M. Buntschuh, and B.W. Batterman, *Phys. Rev. Lett.* **56**, 757 (1986).
5. L.G. Parratt, *Phys. Rev.* **95**, 359 (1954).
6. G.P. Felcher, *Phys. Rev. B* **24**, 1595 (1981).
7. H.E. Nigh, S. Legvold, and F.H. Spedding, *Phys. Rev.* **132**, 1092 (1963).
8. G.P. Felcher, R.O. Hilleke, R.K. Crawford, J. Haumann, R. Kleb, and G. Ostrowski, *Rev. Sci. Instrum.* **58**, 609 (1987).
9. J.F. Ankner, H. Zabel, D.A. Neumann, and C.F. Majkrzak, *Phys. Rev. B* **40**, 792 (1989).

NEUTRON DIFFRACTION STUDIES OF $\text{Cd}_{1-x}\text{Mn}_x\text{Se}$ EPILAYERS
AND ZnSe/MnSe MULTILAYERS

T. M. Giebultowicz⁺, P. Klosowski⁺, J. J. Rhyne^{*}, N. Samarth⁺, H. Luo⁺,
and J.K. Furdyna⁺

⁺ Department of Physics, University of Notre Dame, Notre Dame, IN 46556

^{*} National Institute of Standards and Technology, Gaithersburg, MD 20899

ABSTRACT

Neutron diffraction patterns of MBE-grown single crystal zinc-blende epilayers of $\text{Cd}_{1-x}\text{Mn}_x\text{Se}$ with $x=0.70$ and 0.75 reveal the onset of *long-range* Type-III AF ordering at low T , in sharp contrast with earlier studies of bulk II-VI diluted magnetic semiconductors, where only short-range Type III correlations are observed. Results of first neutron diffraction studies of magnetic ordering in MBE-grown ZnSe/MnSe superlattices are also reported.

INTRODUCTION

We report the first neutron diffraction studies of new $\text{A}_{1-x}^{\text{II}}\text{Mn}_x\text{B}^{\text{VI}}$ diluted magnetic semiconductor (DMS) systems prepared in the form of thin films and multilayer structures using molecular beam epitaxy (MBE). The $\text{A}_{1-x}^{\text{II}}\text{Mn}_x\text{B}^{\text{VI}}$ DMS materials have been extensively investigated during the last decade due to their many unique properties (for reviews, see, e.g., Refs. [1,2]). Zinc-blende (ZB) structure $\text{A}_{1-x}^{\text{II}}\text{Mn}_x\text{B}^{\text{VI}}$ systems (such as $\text{Zn}_{1-x}\text{Mn}_x\text{Te}$ or $\text{Cd}_{1-x}\text{Mn}_x\text{Te}$) are of considerable importance to contemporary studies in magnetism because they offer practical examples of strongly frustrated, randomly diluted 3D Heisenberg antiferromagnets with well-characterized and predominantly short-range Mn-Mn exchange interactions [2,3]. Both the frustration due to the fcc spin lattice and the random dilution presumably play a key role in driving the transition to a spin-glass-like phase observed in these alloys at low temperatures [4]. The exact nature of this phase is still a matter of debate, especially for higher Mn concentrations ($x \geq 0.4$), with conflicting arguments that favor either a spin-glass transition [5] or a dynamically inhibited AF transition [6].

The only direct microscopic picture of the low- T magnetic phase in DMS alloys has been provided by neutron diffraction experiments on bulk materials [7]. These studies have indicated the formation of Type III AF order

(AFM-III), in agreement with Anderson's theory of fcc antiferromagnets [8]. However, even for the highest magnetic concentrations studied so far ($\text{Zn}_{0.32}\text{Mn}_{0.68}\text{Te}$ and $\text{Cd}_{0.30}\text{Mn}_{0.70}\text{Te}$ [7]), the AFM-III order is only short-range, with a maximum observed correlation range of $\sim 70\text{\AA}$. The SRO-LRO transition is expected to occur at fairly high Mn concentrations that are inaccessible by usual bulk-growth techniques [1].

The limitations on alloy composition can be overcome by using the non-equilibrium MBE growth technique. For instance, it has been recently demonstrated that using this method one can prepare ZnSe/MnSe superlattices with ZB-type MnSe layers [9], which offers the first opportunity of investigating a DMS system in the $x=1.0$ limit (it should be noted that MnSe does exist in a bulk form, but those crystals are of the NaCl-type and belong to a different magnetic class than the DMS alloys). Another recent development in MBE growth of entirely new DMS systems has been the preparation of ZB-type $\text{Cd}_{1-x}\text{Mn}_x\text{Se}$ epilayers [10]. In bulk, $\text{Cd}_{1-x}\text{Mn}_x\text{Se}$ exists only in the wurtzite form with $x \leq 0.50$. However, the epilayers can be obtained in the ZB form up to Mn concentrations as high as $x=0.75$, and with thicknesses up to $2\mu\text{m}$.

In this paper, we present results of neutron diffraction studies of magnetic ordering phenomena in the new MBE-grown DMS systems. The magnetic properties of ZnSe/MnSe superlattices have been studied using SQUID magnetometry [11] which indicated that MnSe layers with larger thicknesses ($d \geq 30\text{\AA}$) exhibit a clear tendency toward AF ordering. The results of our experiments provide the first detailed microscopic picture of the AF structure which forms in such layers. This order is of the AFM-III type, and has a very long range in the layer plane. More surprisingly, the formation of long-range AFM-III order has also been observed in $\text{Cd}_{1-x}\text{Mn}_x\text{Se}$ epilayers with $x=0.70$ and 0.75 . This latter observation sharply contrast with all previous studies of magnetically diluted II-VI DMS alloys in which, as noted, only short-range AFM-III correlations have been seen.

EXPERIMENTAL RESULTS

The measurements were carried out at the NBS 20 MW reactor at National Institute of Standards and Tehnology using a triple axis spectrometer operated in the elastic diffraction mode. The energy of the incident neutrons was 14.8 meV , and the beam collimation was $40'$ throughout the spectrometer for most of the data. The samples were placed in a variable-T cryostat, and were oriented with the scattering plane coincident with the (001) or (010) plane, and hence perpendicular to the (100) epilayer (or multilayer) surface.

Cd_{1-x}Mn_xSe Epilayers

The growth of Cd_{1-x}Mn_xSe epilayers on (100) GaAs has been fully described elsewhere [10]. The samples examined in the present neutron diffraction study had compositions $x=0.40, 0.54, 0.70$ and 0.75 , as deduced from lattice parameter measurements, and thicknesses up to $2\mu\text{m}$. Measurements of the in-plane and out-of-the plane lattice parameters show no detectable tetragonal distortion, which indicates that the strain resulting from the lattice mismatch between the substrate and the epilayers is relieved in a relatively thin area adjacent to the substrate by the formation of dislocations. Apart from such dislocations, transmission electron microscopy studies indicate the formation of stacking faults, typically spaced at intervals of $300\text{-}500\text{\AA}$.

Neutron diffraction measurements on epilayers with $x=0.70$ and 0.75 revealed that, below a well-defined critical temperature T_N , additional diffraction maxima are observed corresponding to magnetic AFM-III superstructure points. The AFM-III structure has a tetragonal unit cell, corresponding to doubling of the crystallographic unit cell along one of the cubic axes. The allowed $(hk\ell)$ reflections for this structure have an odd half integer index $n/2$ which corresponds to the doubling direction, and of the remaining indices one is even and one is odd [e.g. $(3/2, 5, 0)$]. Normally, one observes three families of reflections at $(n/2, k, \ell)$, $(h, n/2, \ell)$, and $(h, k, n/2)$, arising from domains with the tetragonal axes oriented, respectively, along the $[100]$, $[010]$, and $[001]$ directions.

A striking feature of the AFM-III correlations observed in the present data is the LRO shown by domains with the tetragonal axes within the epilayer plane. In experiments on bulk DMS crystals [7], the magnetic peaks are much broader than the nuclear peaks, and Lorentzian in shape, indicating short-range AFM-III correlations. In contrast, the magnetic peaks arising from the in-plane AFM-III domains in the epilayers are clearly Gaussian in shape (see Fig. 1), and, as has been checked by performing a series of high-resolution measurements, their widths are comparable to the intrinsic nuclear reflection widths. In other words, the AFM-III correlations are long-range in character, with a length ($\sim 400\text{\AA}$) comparable to the crystallographic coherence of the Cd_{1-x}Mn_xSe lattice itself. It should be noted, however, that the LRO *does not* develop in the AFM-III domains with the tetragonal axis *normal* to the epilayer plane: as illustrated in Fig. 1, the peaks arising from such domains are decidedly weaker and broader than the peaks from the in-plane domains, clearly indicating SRO with a correlation length well below 100\AA .

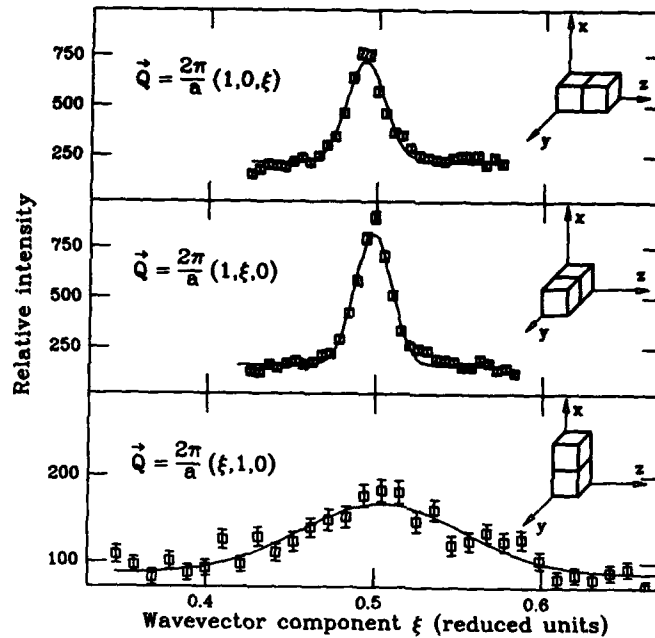


Fig. 1. The magnetic peaks observed at $(10\frac{1}{2})$, $(1\frac{1}{2}0)$, and $(\frac{1}{2}01)$ reflection points in a $\text{Cd}_{0.30}\text{Mn}_{0.70}\text{Se}$ epilayer at 4.2 K. The insets show the orientation of the AFM-III unit cell with respect to the epilayer plane (YZ) corresponding to each reflecting point. Note the striking difference between the reflections for the in-plane and normal-to-the plane orientations.

Epilayers with $x=0.40$ and 0.54 do not show detectable magnetic peaks. This is attributed to the fact that at these concentrations only SRO with a relatively small correlation length is possible, which results in insufficient neutron scattering intensity.

ZnSe/MnSe multilayers

The ZnSe/MnSe multilayer samples were grown by MBE on (100) GaAs substrates. The samples consisted of 100-200 ZnSe/MnSe bilayers, with the MnSe layer thicknesses between 22 and 55Å.

As in experiments on $\text{Cd}_{1-x}\text{Mn}_x\text{Se}$ epilayers, the low-T diffraction patterns of the ZnSe/MnSe superlattices have revealed distinct magnetic maxima at AFM-III points. However, in contrast to those results, the data from the multilayers clearly show the formation of AFM-III domains with the tetrago-

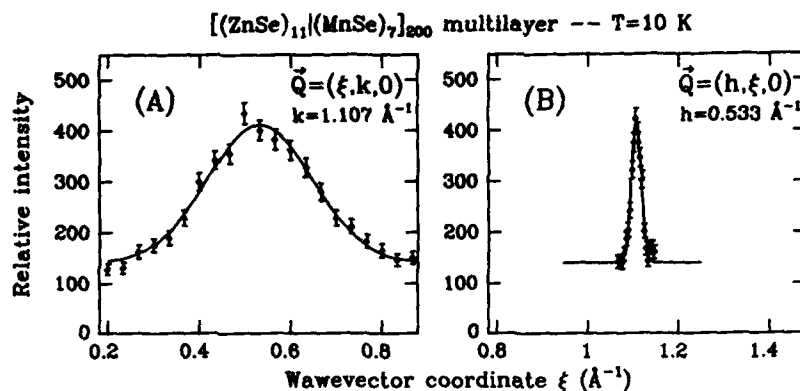


Fig. 2. Diffraction maxima observed in a ZnSe/MnSe superlattice at the $(\frac{1}{2}10)$ AFM-III reflection point for (A): [100] scanning direction (normal to the MnSe layers), and (B): [010] scanning direction (parallel to these layers).

nal axis *normal* to the growth plane, while there are no detectable peaks at the superstructure points corresponding to the in-plane axis orientation. Examples of the data obtained from scans through the $(\frac{1}{2}10)$ reflection point in a superlattice consisting of 200 periods with 22 \AA MnSe layers (corresponding to 7 monomolecular planes) are shown in Fig. 2. The peak observed for the [100] scanning direction (Fig. 2 A) is extremely broad, and its width ($\Delta Q = 0.25 \pm 0.01 \text{ \AA}^{-1}$) indicates that the magnetic correlation range in this direction ($\xi = 0.94 \frac{2\pi}{\Delta Q} = 23 \pm 1 \text{ \AA}$) is essentially the same as the MnSe layer thickness. The maximum exhibits no detectable interference features indicating propagation of the AFM-III order through the non-magnetic ZnSe layers, which is consistent with the short-range nature of the exchange interactions in magnetic semiconductors. In contrast, the peaks observed in scans along the [010] direction are strikingly narrow (Fig. 2 B). The width of these peaks is only slightly broader than the instrumental linewidth, indicating a very long range ($>500 \text{ \AA}$) of the AFM-III correlations in the layer plane.

DISCUSSION AND CONCLUSIONS

In summary, neutron diffraction experiments on ZnSe/MnSe superlattices provide the first clear picture of the AF structure that forms in individual MnSe layers in these systems. The observed preference of the AFM-III domain orientation can be attributed to tetragonal distortion effects. Because of the relatively large mismatch between the ZnSe and MnSe lattices (-4.1%),

one can expect that the MnSe lattice contracts in the layer plane, and expands in the direction normal to this plane. In fact, the observed positions of the magnetic reflections are slightly shifted from the $(\frac{1}{2}10)$ position for a perfectly cubic MnSe lattice, suggesting such a distortion. The existence of this distortion is also confirmed by the results of analysis of nuclear peak intensities. This effect may lead to an anisotropy in the Mn-Mn exchange -- namely, one can expect that the exchange parameter for the "in-plane" bonds (J_{\parallel}) is larger than that for the "out-of-the-plane" bonds (J_{\perp}). As can be readily checked, in the case of $J_{\parallel} > J_{\perp}$ the AFM-III configuration with the tetragonal axis normal to the layer plane leads to a lower system energy than the configuration with an in-plane axis orientation.

However, our present understanding of the results of experiments on $\text{Cd}_{1-x}\text{Mn}_x\text{Se}$ epilayers is not entirely clear. As suggested by the results of experiments on equivalent bulk magnetic systems, $\text{Cd}_{1-x}\text{Mn}_x\text{Te}$ and $\text{Zn}_{1-x}\text{Mn}_x\text{Te}$, which do not exhibit noticeable tendencies of forming LRO even for Mn concentrations approaching $x=0.70$, the LRO observed in the epilayers cannot be attributed solely to the high Mn concentrations. Considering the observed strong preference in domain orientation, it is likely that the onset of LRO in the epilayers is a combined effect of both the high Mn concentration and residual strain that is not detected by lattice parameter measurements. On the other hand, one would expect in this case the same preferred domain orientation in the epilayers that is seen in the ZnSe/MnSe multilayers. In fact, quite the opposite tendency is observed. It points out that further experimental and modelling studies are needed to clarify the magnetic behavior of these new layered structures.

REFERENCES

1. *Diluted Magnetic Semiconductors*, vol. 25 of *Semiconductors and semimetals*, ed. by J.K. Furdyna and J. Kossut (Academic Press, Boston, 1988).
2. J.K. Furdyna, *J. Appl. Phys.* **64**, R29 (1988).
3. B.E. Larson, K.C. Hass, H. Ehrenreich, and A.E. Carlsson, *Phys. Rev. B* **37**, 4137 (1988).
4. See, e.g., S. Oseroff and P.H. Keesom, in Ref. 1, p. 73.
5. M. Ayadi, J. Ferre, A. Mauger, and R. Triboulet, *Phys. Rev. Lett.* **57**, 1165 (1986).
6. S. Geshwind, A.T. Ogielski, G. Devlin, J. Hegarty, and P. Bridenbaugh, *J. Appl. Phys.* **63**, 3738 (1988).
7. T.M. Giebultowicz and T.M. Holden, in Ref. 1, p. 125.
8. P.W. Anderson, *Phys. Rev.* **79**, 705 (1953); see also J.S. Smart, *Effective Field theories in Magnetism* (Saunders, Philadelphia, 1966).
9. L.A. Kolodziejski, R.L. Gunshor, N. Otsuka, B.P. Gu, Y. Hefetz, and A.V. Nurmikko, *Appl. Phys. Lett.* **48**, 1482 (1986).
10. N. Samarth, H. Luo, J.K. Furdyna, Y.R. Lee, R.G. Alonso, E.K. Suh, A.K. Ramdas, S. Quadri, and N. Otsuka, *Surface Science* (to be published).
11. S.-K. Chang, D. Lee, H. Nakata, A.V. Nurmikko, L.A. Kolodziejski, and R.L. Gunshor, *J. Appl. Phys.* **62**, 4835 (1987).

LOCAL ENVIRONMENTAL EFFECTS IN MAGNETIC ALLOYS AND MULTILAYERS: CALCULATIONS OF THE STATIC RESPONSE FUNCTIONS.

D. D. Johnson¹, J. B. Staunton², B. L. Györfy², F. J. Pinski⁴, and G. M. Stocks⁵

¹Theoretical Division, Sandia National Laboratories, Livermore, CA

²Department of Physics, University of Warwick, Coventry, U.K.

³H.H. Wills Physics Laboratory, University of Bristol, Bristol, U.K.

⁴Department of Physics, University of Cincinnati, Cincinnati, OH

⁵Metals and Ceramics Division, Oak Ridge National Laboratory, Oak Ridge, TN.

ABSTRACT

We have developed an ab-initio method for calculating the static response functions in substitutional alloys. For magnetic alloys, in addition to the nuclear diffuse scattering, a contribution to the alloy diffuse scattering intensities results from the response of the local moments to changes in the 'local' chemical environment (i.e. $\partial\mu_i/\partial c_j$). We present results of first-principles calculations of these 'local' response functions in magnetic alloys. These response functions, which may be directly compared to neutron-scattering and Mößbauer experiments, are derived via a mean-field statistical mechanical description of compositional fluctuations in alloys. The statistical averages are performed via the Korringa-Kohn-Rostoker coherent potential approximation, which incorporates the electronic structure of the high-temperature, chemically disordered state. As a first application of the theory, we have investigated the environmental dependence of the moments in NiFe alloys and FeV alloys and multilayers. We compare our results with experiments on bulk alloys and multilayers. Also, a comparison is made to a set of first-principle 'supercell' calculations. Although preliminary, the results demonstrate the utility of these response functions for investigating the effects of changes in the chemical environment on the alloy moments and for aiding experimental interpretation in other multilayer systems that are less experimentally amenable than FeV.

INTRODUCTION

In general, atoms in substitutional alloys are not randomly distributed on lattice sites, but are spatially correlated. These correlations govern the properties of the alloy, and, as such, it is desirable both to determine them by experimental techniques (e.g., neutrons or X-rays) and to calculate them from a reliable alloy theory. This comparison offers a fundamental understanding of the underlying "driving forces" giving rise to particular properties. For magnetic alloys in particular, neutron scattering is a particularly powerful technique for determining the correlation because the total scattering cross section has contributions from nuclear disorder, magnetic, and nuclear-magnetic scattering, along with the incoherent and multiple scattering processes. In recent years we have developed the first-principles KKR-CPA method [1,2] which allows the calculation of the electronic structure and total energy for disordered alloys, and is currently the "state-of-the-art" method for studying these systems from a microscopic approach. The CPA (coherent potential approximation) is a mean-field approximation with which to perform configurational ensemble averaging, or statistical averaging at finite temperatures. Within the theory of concentration fluctuations, this approach may be extended to investigate the finite-temperature, static, pair correlation functions [3,4]. The only inputs to these calculations are the atomic numbers.

RESPONSE FUNCTIONS: THEORY AND EXPERIMENT

In terms of the site occupation variables the atomic pair correlation functions, also known as the Warren-Cowley atomic short-range order (ASRO) parameter, may be expressed as $\alpha_{ij} = \langle \zeta_i \zeta_j \rangle - \langle \zeta_i \rangle \langle \zeta_j \rangle$, where $c_i = \langle \zeta_i \rangle$. The set of site occupation variables $\{\zeta_i\}$ describe a given configuration, e.g. for an $A_c B_{1-c}$ alloy $\zeta_i = 1(0)$ if the site i is occupied by an A(B) atom. In the completely disordered state all sites are equivalent and uncorrelated so $c_i = c$ for all sites i and $\alpha_{ij} =$

0. At lower temperatures α_{ij} takes on a non-zero value depending on whether the alloy phase-separates or orders.

In this concentration fluctuation approach to calculating the alloy correlation functions for any A_cB_{1-c} alloy, a local density approximate (LDA), finite-temperature, electronic grand potential $\Omega(\{\zeta_i\})$ may be formally obtained [3,4]. The (mean-field) CPA allows one to perform the required thermal averaging (denoted by $\langle \dots \rangle$) with the central result that the thermal averaged electronic grand potential $\langle \Omega(\{c_i\}) \rangle$ depends directly on the local concentrations $\{c_i\}$, and indirectly on the local moments $\{\mu_i\}$. Formally, variations of $\langle \Omega(\{c_i\}) \rangle$ with respect to c_i and μ_i may be performed to obtain the various response functions [3,4]. Within the disordered state, where $c_i=c$, these expressions are numerically tractable since there is translational symmetry. Note, all the underlying electronic structure via the KKR is included in the calculation of the response functions. Details may be found elsewhere, see ref. 3-4. For sake of the present discussion, the most important results are summarized below.

We find that the lattice Fourier transform of the atomic pair correlation function is given by

$$\alpha(\mathbf{k}) = c(1-c) [1 - \beta c(1-c)S^{(2)}(\mathbf{k})]^{-1} \quad (1)$$

where $\beta = (k_B T)^{-1}$. Because of the single site nature of the CPA averaging, only an ideal entropy contribution is included and eq.(1) has the Bragg-Williams' form. $S^{(2)}(\mathbf{k})$ is the lattice transform of the direct correlation function which involves all second-order variations of $\langle \Omega(\{c_i\}) \rangle$ with respect to concentration and moments. Note, $S^{(2)}(\mathbf{k})$ is determined from the electronic structure of the disordered alloy via the KKR-CPA equations and contains interactions to all orders, and not only of the pair-wise form. $S^{(2)}(\mathbf{k})$ is the first-principle generalization to the $V(\mathbf{k})$ used by Krivoglaz and by Clapp and Moss in their pair potential approach to ASRO and is the energy associated with long-wavelength concentration fluctuations in the system. Only in this sense, S_{ij} , the real-space representation of $S^{(2)}(\mathbf{k})$, may be regarded as the effective pairwise interchange energies for the system.

For magnetic systems, $S^{(2)}(\mathbf{k})$ depends on the Fourier transform of

$$\gamma_{ij}^{\alpha} = \frac{\delta \mu_i^{\alpha}}{\delta c_j} \quad (2)$$

Evidently, γ_{ij}^{α} describes the response of the α moment at the site i to a change in the chemical environment, and, hence, a non-rigid moment effect [4]. This 'local' response function can, for example, be used to investigate how moments vary in response to an order-disorder transformation or a concentration gradient within an alloy. We discuss these quantities in more detail in the next section.

Experimentally, both $\alpha(\mathbf{k})$ and $\gamma(\mathbf{k})$ (the lattice transform of γ_{ij}^{α}) may be measured directly via spin-polarized neutron scattering [5,6]. That is, for neutrons polarized (anti-) parallel to the magnetization, $\epsilon = \pm 1$, the cross-section per atom may be written as

$$\left. \frac{d\sigma}{d\Omega} \right|_{\epsilon} \sim \chi(\mathbf{k}) + \epsilon \alpha(\mathbf{k}) \gamma(\mathbf{k}) + \alpha(\mathbf{k}) \quad (3)$$

where the three terms are the magnetic, nuclear-magnetic, and nuclear correlations, respectively. It is interesting that the form of eq.(3) which results from our theoretical derivation using the KKR-CPA is the same form as the Marshall model [7] which is used by neutron scatterers in their interpretation of the scattering data. The contributions to the cross-section from cross-correlations may be extracted by measuring scattering from both polarizations. Note, $\gamma(\mathbf{k})$ is the magnetic response of the entire system (at a given concentration) to changes in the chemical environment. For an AB alloy, the total moment response is given by $\gamma(\mathbf{k}) = (\mu^A - \mu^B) + c_A \gamma^A(\mathbf{k}) + c_B \gamma^B(\mathbf{k})$. If the A and B moments are almost environmental independent, then the first term will dominate and the subtle environmental effects may be difficult to measure. On the other hand, if the moments are parallel and about equal in magnitude, then the entire cross-correlation contribution will be coming

from the (possibly small) environmental changes. It is also possible that the ASRO can be dramatically altered through the environmental dependence of the moments. Clearly, this will then be evident through the experimental diffuse scattering data.

This first-principles theory of concentration fluctuations has been applied recently to NiFe alloys to study the mechanism responsible for the chemical ordering in the Ni-rich alloys [8]. The Cu₃Au ordering was found to be stable at low temperatures, as observed experimentally. It was also found that the magnetism is solely responsible for the chemical ordering in this system. High-temperature thermochemical data supports this conclusion [9]; however, we hope for further experimental study on this alloy to confirm our results conclusively. More recently, we have investigated $\alpha(k)$ for Fe-13.5%V since Cable and coworkers have performed the relevant measurements on the single crystals [10] with which we are able to compare directly in k-space. In this case, we obtain very good agreement for the cross-sections, moments, and ordering tendency, etc. [11], which allows for the first time a direct comparison of experiment and an unbiased, first-principles theory. Cable is currently performing spin-polarized neutron experiments on these samples in order to obtain the $\gamma(k)$ directly. We feel this opens up a very fruitful avenue of comparison between experiment and theory, in particular in understanding the underlying interactions in these alloys.

CHEMICAL ENVIRONMENT EFFECTS ON MAGNETIC PROPERTIES

The Fourier transform of $\gamma(k)$, γ_{ij}^A , has a particularly revealing physical interpretation. These quantities describe the change in the size of the moment on a site i in the lattice if it is occupied by an A(B) atom and if the probability of occupation is altered on another site j . Thus,

$$\gamma_{ij}^{A(B)} \Delta c_j = \gamma_{ij}^{A(B)} (1-c) \quad (4)$$

describe the change in the moment on the site i , occupied by an A(B) atom, if the site j in the alloy is definitely occupied by an A atom. Similarly,

$$\gamma_{ij}^{A(B)} \Delta c_j = \gamma_{ij}^{A(B)} (0-c) \quad (5)$$

described the change if the site j is now definitely occupied by a B atom. The change in probability, Δc_j , equals $1-c$ ($-c$) since the probability that the A(B) atom is definitely at site j is $1(0)$ and the probability for the random alloy is c . Now a study of the moments as a function of actual chemical environments can be made using the relation

$$\mu_{\alpha,j} = \mu_{\alpha}^{cpa} + \sum_j \gamma_{ij}^{A(B)} \Delta c_j = \mu_{\alpha}^{cpa} + \sum_j \gamma_{ij}^{A(B)} ((1-c)a_j + (-c)b_j) \quad (6)$$

where $a_j(b_j)$ is the number of A(B) atoms in the shell j . [We denote a given environment by the notation (a_1, b_1 ; a_2, b_2 ; etc.).] For example, with an environment consistent with the ordered Ni₃Fe alloy, i.e. (8,4; 6,0) for the Ni atoms and (12,0; 0,6) for the Fe atoms, we calculate that the average moment increases by 7% compared with that in the disordered alloy upon ordering, in good agreement with experiment [12].

For our preliminary study of multilayers we chose FeV alloys for two reasons. First, experimentally the FeV multilayers are ideal for Mößbauer studies, since little alloying occurs outside the interfacial layer, and these data are available. Second, since band-structure ('supercell') calculations and simple model calculations on FeV multilayers have been performed, we can use these for a comparison.

Obviously, the calculations of the quantities involved in determining the $\alpha(k)$ and $\gamma(k)$ are very involved, but, more importantly, are based on a complicated derivation. The $\gamma(k)$'s are proportional to a k -independent denominator of $(1-N_{\alpha})$, where N_{α} should be of order zero. At

this time we neglect this effect by setting $N_\alpha=0$; we will include this term in the future. As such, must make a caveat for the absolute numbers for the γ_{ij} 's reported here. Note, the overall trends will be unchanged when a correct value of this normalization is obtained.

In this system recall that the vanadium moments are antiparallel to the iron moments and, more importantly, are induced by the large exchange-splitting on the iron sites. So, as a vanadium atom is surrounded by more iron atoms, its moment should increase in magnitude; similarly, as an iron atom is surrounded by more vanadium atoms, its moment should decrease. This tendency is reflected in the $\gamma(k)$'s calculated for BCC Fe-50%V, see fig.(1). Note, the sign of $\gamma(k=0)$ dictates the sign of the first-shell γ_1^α . Thus, the environmental dependence of the moments, eq.(6), reveals that with more Fe (V) atoms in the first-shell of neighbors the moment on an Fe site will increase (decrease) in magnitude, since $\gamma^{\text{Fe}}(k=0)$ is positive. Similarly, with more Fe (V) atoms in the first-shell of neighbors, the V site will increase (decrease) in magnitude, since $\gamma^{\text{V}}(k=0)$ is negative.

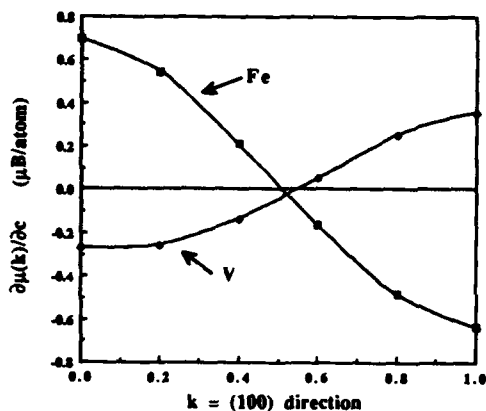


Figure 1. The Fourier transform of γ_{ij}^α , the environmental dependence of the moments for each species $\alpha = \text{Fe or V}$, is shown for BCC Fe-50%V along the $k=[100]$ direction. As discussed in the text, many qualitative trends of the moments in varying environments may be understood from this quantity.

For BCC Fe-50%V, the calculated values of γ^{Fe} for the first and second nearest neighbors are +0.076 and +0.010, respectively. The third nearest neighbor contribution are zero to 3 significant figures. Similarly, the calculated values of γ^{V} are -0.038 and -0.002 for the first two nearest neighbor shells. [Recall, $\gamma(k)$'s do not contain the effect of the N_α . From calculations of the bulk magnetizations versus concentration, we have estimated that γ^{Fe} would increase in magnitude and improve our results.] From the SCF-KKR-CPA calculations, the CPA moments for $\text{Fe}_{0.50}\text{V}_{0.50}$ are $\mu^{\text{Fe}} = +1.57 \mu_B$ and $\mu^{\text{V}} = -0.21 \mu_B$.

We may now calculate the moments in various multilayers from eq.(6). For example, layers of iron and vanadium atoms with a [110] texture will only have three possible environments when two nearest neighbor shells are considered. The possible stacking sequences of iron and vanadium layers, the associated number of A and B atoms in the first and second neighbor shells (the environment), and the moments for these stackings, calculated via eq. (6), are given in Table I. As a more stringent test, we compare calculated moments via this approach and actual LAPW multilayer calculations by Hamada et al. [13] for three different multilayers. For [110] textures, there were two different stacking sequences, 3V/3Fe (V-V-Fe-Fe-Fe-V-V) and 5V/Fe (V-V-V-Fe-V-V-V), where the unit cells are denoted in parentheses. The associated moments are given in Table 2. For case 1, there are two inequivalent iron and vanadium sites; whereas, for case 2, there are three inequivalent vanadium sites and only one iron site. We see that the moments from the response theory compare very favorably with the values from a first-principles multilayer calculation, except for iron (because, as noted above, N_α was set to zero). In addition, the trends are given very well. For case 2, the single layer of iron has a large discrepancy, perhaps due to the breakdown of our response theory for ultra-thin layers. Overall, for thicker multilayers, if the magnetic moments are of interest, we may generate any number of stacking sequences without further calculation, in contrast to the standard band structure approaches.

Table I. Considering only two near-neighbor shells, the stacking sequence, environment, and moments for sites in the central plane are presented for FeV multilayers with a [110] texture. The stacking sequence and environment of the central V plane is obtained by interchanging Fe and V.

		central Fe plane	central V plane
local stacking	environments	Fe moments	V moments
-Fe-Fe-Fe-	(8,0 ; 6,0)	1.90	-0.05
-Fe-Fe-V-	(6,2 ; 4,2)	1.73	-0.13
-V-Fe-V-	(4,4 ; 2,4)	1.56	-0.21

Table II. A comparison of moments calculated via the response functions (left-hand columns) and supercell electronic structure calculations (right-hand columns) of Hamada et al. [13]. The stacking sequence of each texture is described in the text.

site / plane	[110] textures				[100] texture	
	case 1	case 2	case 3	case 1	case 2	case 3
V (III)			-0.05	+0.01		
V (II)	-0.05	-0.06	-0.05	-0.01	-0.06	-0.07
V (I)	-0.13	-0.18	-0.13	-0.12	-0.21	-0.24
Fe (I)	1.73	1.90	1.56	1.33	1.59	1.62
Fe (II)	1.90	2.20			1.89	2.39
Fe (III)					1.90	2.21

For the [100] texture with 3V/5Fe repeated (case 3), there are two (three) inequivalent vanadium (iron) sites. The same comparison as above is made for this multilayer and is given in Table II. Note the trends of the moments are given well by the response theory; however, we do not find the moment oscillation that is found by Hamada et al. It would be possible to achieve this oscillation only if the second shell γ_2 were negative. From the form of $\gamma^{\text{Fe}}(\mathbf{k})$, this can never be the case in FeV alloys; also, this would require an oscillation of the Fe moment in all multilayers. Experimentally, Jaggi et al. [14] rule out the possibility of an oscillatory behavior of the iron moments, in agreement with our results.

Notably, Hamada et al. [13] went on to interpret their results in terms of a 'magnetic-interaction' distance, arbitrarily chosen as the second nearest neighbor distance, and a 'local' concentration variable defined by the percentage of next-nearest neighbor vanadiums. The number of vanadium atoms in the first-nearest-neighbor shell was used to determine the immediate environment. From the present work, it is now clear why their prescription worked well for FeV heterostructures. Firstly, the γ_1 and γ_2 give the dominant contribution to the environmental effects, which justifies the assumption of a magnetic interaction length confined to two nearest-neighbor shells. Secondly, they explicitly try to account for the effect on the moment due to various first shell occupancies. In the present case, this is done implicitly by γ_1 . Thirdly, their 'local' concentration variable gives information similar to the γ_2 contribution in eq. (6), i.e. the second shell environment and enhancement. It should be clear now that the Hamada et al. [13] prescription will not work for systems where the number of contributing shells is larger than two.

Finally, it is important to address the problem of interfacial alloying in multilayers. Applying standard band structure approaches to this problem is rather difficult and computationally taxing. However, it should now be obvious that with the present theory we may estimate the effects of interfacial alloying without any added computational effort. A complete essay on this subject is beyond the scope of this paper and shall be presented elsewhere when N_{α} may be properly calculated [15]. However, it is important to point out that all interfacial alloying trends in

FeV multilayers that have been observed experimentally are given by the above theory. This may be verified by the reader from the information given above.

It is noteworthy that our entire theory was established from the KKR-CPA, single-particle Green's function so that we could investigate chemical short-range ordering effects in magnetic alloys and associated changes in the magnetic properties with chemical environment changes. However, other quantities are related to the Green's function, such as, the local density of states, hyperfine fields, and Knight shifts. All these quantities may similarly be investigated [15] through equations that are similar in form to eq. (6).

SUMMARY

Within this theory of concentration-fluctuations, the KKR-CPA electronic structure method may be used to investigate the underlying correlations, or interactions, responsible for the instability of the high-temperature, chemically disordered state to short-range order. Moreover, the effects of chemical environment changes to the alloy magnetism is an offshoot of the theory, allowing study of changes of the moments upon a chemical ordering transition, and, more generally, the multilayer problems mentioned above. The theory is first-principles in the sense that no input parameters, other than the atomic numbers, are required, and at no stage may our prejudices regarding the nature of the interaction influence the results. One important goal is then comparison, especially to single crystal neutron results, or aid to experiment, since many quantities obtained from the theory are directly measurable by experiment.

Research at Sandia is supported by the U.S. Department of Energy, Office of Basic Energy Sciences, Division of Materials Sciences; and at the Universities of Warwick and Bristol through the Science and Engineering Council of the U.K.; and at Oak Ridge by the Division of Materials Sciences, U.S. Department of Energy under contract #DE-AC05-84OR21400. FJP and JBS acknowledge partial support from a NATO research grant.

REFERENCES

1. B. L. Györfy, D. D. Johnson, F. J. Pinski, D.M. Nicholson, and G. M. Stocks, Alloy Phase Stability, eds. G. M. Stocks and A. Gonis, NATO-ASI Series E: Physics, (KLUWER, The Netherlands, 1989).
2. D. D. Johnson, D. M. Nicholson, F. J. Pinski, B. L. Györfy, and G. M. Stocks, *Phys. Rev. Lett.* **56**, 2088 (1986), ppg 421-468.
3. B. L. Györfy and G. M. Stocks, *Phys. Rev. Lett.* **50**, 374 (1984).
4. J. B. Staunton, B. L. Györfy, D. D. Johnson, F. J. Pinski and G. M. Stocks, Alloy Phase Stability, eds. G. M. Stocks and A. Gonis, NATO-ASI Series E: Physics, (KLUWER, The Netherlands, 1989), pp. 469-507.
5. V. Pierron-Bohnes, M. C. Cadeville, and F. Gautier, *J. Phys.* **F113**, 1689 (9183).
6. J. W. Cable and W. E. Brundage, *J. Appl. Phys.* **53** (1982).
7. W. Marshall, *J. Phys.* **C1**, 88 (1968).
8. D.D. Johnson, F.J. Pinski, J.B. Staunton, B.L. Györfy, and G.M. Stocks, to be published in Physical Metallurgy of Controlled Expansion (INVAR-type) Alloys, eds. K. C. Russell and D. Smith, (Materials Research Society, 1989).
9. Ying-Yu Chung, Ken-Change Ksieh, and Y. Austin Chang, *Metall. Trans.* **A17**, 1373 (1986).
10. J. W. Cable, H. R. Child, and Y. Nakai, preprint, International Conf. on Neutron Scattering, Grenoble, France, 12-15 July 1988.
11. J. B. Staunton, D. D. Johnson, B. L. Györfy, F. J. Pinski, and G. M. Stocks, to be submitted to *Phys. Rev. Lett.*
12. M. F. Collins, *Proc. Roy. Soc.* **86**, 973 (1965).
13. N. Hamada, K. Terakura, and A. Yanase, *J. Phys.* **F14**, 2372 (1984), and *J. Magn. Magn. Mat.* **35**, 7 (1983).
14. N. K. Jaggi, L. H. Schwartz, H. K. Wang, and J. B. Ketterson, *J. Magn. Magn. Mat.* **42**, 1 (1985).
15. D. D. Johnson, J. B. Staunton, and B. L. Györfy, to be published.

DETERMINATION OF HYDROGEN(DEUTERIUM) DENSITY PROFILES IN THIN METAL
FILMS AND MULTILAYERS BY NEUTRON REFLECTION

C. F. MAJKRZAK*, S. SATIJA*, D. A. NEUMANN*, J. J. RUSH*, D. LASHMORE*,
C. JOHNSON*, J. BRADSHAW**, L. PASSELL** AND R. DINARDO***

*National Institute of Standards and Technology, Gaithersburg, MD 20899

**Optoline Associates, Andover, MA 01810

***Brookhaven National Laboratory, Upton, NY 11973

ABSTRACT

The density of hydrogen in thin films or multilayers of metal hydrides can be inferred from an expansion of the host lattice as measured by conventional x-ray diffraction techniques. However, because hydrogen and deuterium have scattering lengths for neutrons that are comparable to those of most metal nuclei, unlike the corresponding case for x-ray atomic scattering amplitudes, the hydrogen density profile normal to the surface of a flat, thin film can be determined directly from neutron reflectivity measurements. The hydrogen (deuterium) density modulation in an artificial superlattice along the growth direction can also be determined in this manner. The thin film or multilayer host metal material need not even be crystalline. Furthermore, because relatively large, flat single crystal substrates such as Si or quartz are nearly transparent to neutrons, the substrate can serve as the incident medium and the reflectivities of films or multilayers in contact with liquid solutions can be obtained. Thus, in situ studies employing active electrochemical cells, for example, can be performed. In addition to discussing the sensitivity of the method, the results of some neutron reflectivity experiments on metal multilayers and films, electrolytically loaded in situ with deuterium, are reported in this paper.

INTRODUCTION

The neutron refractive index n for non-magnetic materials is given by [1] $n = 1 - \lambda^2 Nb/\pi$ where λ is the neutron wavelength, N the atomic density of the medium, and b is the coherent nuclear scattering length or amplitude for neutrons. For most materials the scattering density Nb is positive and, consequently, the neutron refraction index is less than unity and total external reflection at a glancing angle ϕ from a smooth, flat surface in vacuum will occur up to a characteristic critical angle ϕ_c . Because n is always very close to unity, the critical angle is usually a fraction of a degree. For example, for the naturally occurring isotopic mixture of Ni, $\phi_c = 0.1$ deg/Å. For most materials the neutron absorption cross section is negligible and b can be taken to be real. Furthermore, isotopes of the same element can have significantly different values of b . In particular, for hydrogen $b = -0.374 \times 10^{-12}$ cm whereas for deuterium, $b = +0.667 \times 10^{-12}$ cm. (In the case where absorption is not negligible, b must be written as a complex quantity).

If the reflectivity is measured as a function of glancing angle ϕ or wavevector transfer $|\vec{Q}| = \frac{4\pi}{\lambda} \sin\phi = |\vec{k}_f - \vec{k}_i|$ where \vec{k}_f and \vec{k}_i are the outgoing and incident neutron wavevectors, respectively, then the density profile $Nb = \rho = \rho(z)$ where z is an axis normal to the plane of the film or parallel to \vec{Q} , can be determined. A close analogy to ordinary optics is

possible [2] since the neutron can be described by a plane wave which is a solution of a one dimensional time-independent Schrödinger equation that can be solved in piece-wise continuous fashion by satisfying boundary conditions on the wave function and its derivative for slices of thickness dz [3]. It should be realized, however, that the neutron plane wave in effect sees a potential averaged over a relatively large lateral extent when $R(Q)$ is measured in a so-called $\theta:2\theta$ scan where the specular condition is always maintained. That is, on a microscopic scale an interfacial region may in actuality correspond to one of two very different pictures, e.g., interdiffusion or waviness, which give rise to nearly identical density profiles along z . In principle, in order to distinguish between such possibilities, transverse scans with some component of \vec{Q} parallel to the surface or interface can be done.

SENSITIVITY

To get an idea of the sensitivity for detecting hydrogen and deuterium in metal multilayers by measuring neutron reflectivity profiles, consider, for example, an idealized Pd-Al multilayer consisting of 150Å Pd and 50Å Al layers repeated 5 times in vacuum. It is assumed that the Pd and Al densities are those which occur in the bulk and that the Pd-Al interfaces are perfectly sharp. Figure 1 illustrates two neutron reflection profiles for this system with different atomic concentrations of H or D in the Pd layers only (the relatively small change in Pd density due to lattice expansion upon hydriding has been neglected). Neutron reflectivities down to 10^{-6} can be routinely measured. Concentration differences of a few percent can be accurately distinguished as shown in more detail in Figure 2 where the first order peak intensity is plotted as a function of H and D concentration. In fact, analysis of a measured neutron reflectivity profile can provide more detailed information, particularly regarding the profile of the interfacial region, if data of sufficiently high accuracy and at large enough values of Q are obtained [4].

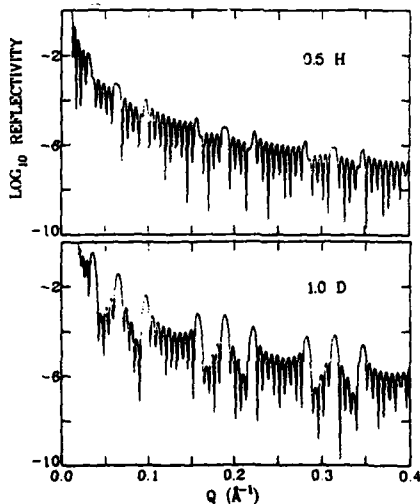


Figure 1. Neutron reflectivity profiles calculated for an idealized Pd-Al multilayer [(150Å Pd, 50Å Al) x 5] with different concentrations of H (or D) in the Pd layers. Principle maxima appear at multiples of 2π /bilayer thickness. Note that for 0.5H, the contrast between layers is significantly reduced because of the negative scattering length of hydrogen.

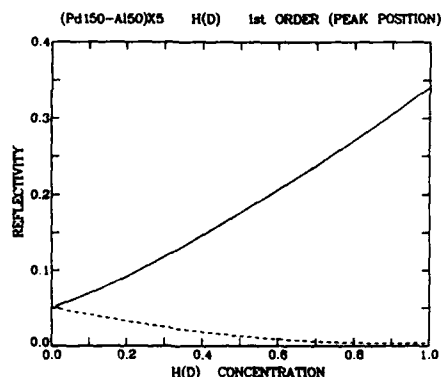


Figure 2. Calculated peak reflectivity of the first order principle reflection of the idealized (150Å Pd, 50Å Al) x 5 multilayer as a function of H (dashed line) and D (solid line). D concentrations to within a few percent or better can be accurately determined. Depending upon the scattering density of the metal host material, sensitivity to either H or D can differ significantly.

EXPERIMENT

It had been discovered previously by x-ray diffraction that the H concentration in solid solution is greatly enhanced in Nb films with diminishing film thickness below about 1200Å [5]. Again, the increased concentrations were inferred by the resultant expansion of the host metal lattice parameter. It is of interest to determine where the hydrogen actually goes in Nb and other thin metal films and multilayers. By combining neutron reflectivity and high angle x-ray and neutron diffraction data it is possible in principle to determine the absolute amount of hydrogen soluble in a given metal layer and whether the hydrogen occupies interstitial sites in the host lattice or resides in voids or in some mixture thereof.

Thus far, several multilayers and thin film systems have been investigated. Thin films of Pd (~1000Å) and multilayers composed of bilayers of Pd and Al, Pd and Cr, and Ni and Ti, each bilayer of the order of 200-300Å thick, were loaded either electrochemically or in a gas cell with deuterium. In all but the Ni-Ti multilayer case, the films either became significantly roughened or detached from the Si substrates on which they had been deposited by sputtering before any useful neutron reflectivity data could be obtained. In the case of the Ni-Ti multilayer, however, the film remained intact in an electrolytic cell containing an approximately 1.0 molar solution of LiOH·H₂O in 99.6% pure D₂O at currents up to 1.0 amp for several hours. A 4 inch diameter single crystal Si disc 3/16 inch thick and polished on the face on which the multilayer was deposited was pressed against a teflon reservoir holding the electrolytic solution. The multilayer served as one electrode and a Pt foil as the other. The neutron beam of wavelength = 4.05Å and of width 0.003" enters the edge of the Si so that for the reflection from the multilayer, Si is the incident medium. The divergence of the incident beam was -1 minute of arc with an energy resolution of 1% so that the instrumental Q-resolution varied from about 0.001Å⁻¹ to 0.002Å⁻¹ over a range of Q extending from 0.001 to 0.100Å⁻¹. A cooled Be filter preceding a pyrolytic graphite (002) monochromator was used to suppress higher order wavelength contamination. The Ni-Ti multilayer consisted of 20 bilayers with individual Ni and Ti layer thicknesses of the order of 95Å and 125Å, respectively, and was grown at Optoline Associates, Inc., Andover, MA. The neutron reflectivity, neutron diffraction, and x-ray diffraction measurements were performed at the National Institute of Standards and Technology, Gaithersburg, MD.

Starting at very low currents of about 0.001 amps and progressing to 1.000 amp over a period of several hours time, neutron reflectivity profiles

were measured. The current was increased every other scan until a change in the reflectivity profile was noticed. The current was then maintained at a constant level until no further change occurred, and then progressively increased. After several hours at 1.0 amp no additional change was observed. The final and initial reflectivity profiles are shown in Figure 3. In the initial profile, the first order peak at a $Q = 0.030\text{\AA}^{-1}$ is saturated with a reflectivity $R=1$. The broadening of the peaks, especially pronounced for the third order, can be explained by a non-uniform set of bilayer thicknesses. Total external reflection occurs up to about 0.022\AA^{-1} , characteristic of a 1000\AA Ni protective cap layer deposited over the multilayer. The appearance of a diminishing reflectivity below -0.013\AA^{-1} is a geometrical artifact. Inspection of the data shows that the 2nd and 3rd order peaks have shifted considerably to lower values of Q implying an expansion of the layer thickness in real space. It was expected that the deuterium would preferentially diffuse into the titanium, as is the case for ordinary bulk systems, and since Ti has a negative scattering length the deuterium, which has a positive scattering length, would result in an increased scattering density for the TiD_x layer and a corresponding decrease

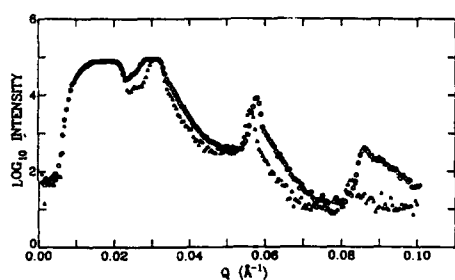


Figure 3. Final (solid triangles) and initial (open circles) neutron reflectivity data for Ni-Ti multilayer described in the text. Note that the 2nd and 3rd order peaks at -0.058 and -0.087\AA^{-1} in the initial scans have shifted to lower values of Q after deuteriding indicating an expansion in layer thickness. Other features and analysis are described in more detail in the text.

in reflectivity as observed. High angle x-ray diffraction experiments showed that after deuteriding only the Ti peaks were appreciably shifted to lower angles (both Ni and Ti Bragg peaks characteristic of the bulk structures were observed, indicating polycrystalline layer microstructure). However, attempts to fit the observed final reflectivity profile were not possible because it was (re)discovered that a significant preference for the uptake of one isotopic species, in this case hydrogen over deuterium, can exist in electrolytic charging processes. Even though the electrolytic solution contained $\sim 40\times$ more D than H the uptake of H can in some cases be favored by an order of magnitude or more. The ratio of D to H in the Ni-Ti multilayer after loading was simply not known. This problem became known to us during a related experiment on thin Pd sheet as will now be described.

The phase diagram of the palladium/hydrogen system is well known. At room temperature and low concentration of hydrogen (or deuterium) the system exists in the α -phase with a lattice constant very similar to that of pure palladium. At higher concentrations of H(D) there exists a β phase with a considerably expanded lattice where the H(D) atoms are located in the octahedral interstitial sites [6]. In situ neutron diffraction measurements on palladium in an electrochemical cell were done in order to investigate whether tetrahedral interstitial sites could be filled with D by the electrolysis process [7]. The electrolysis cell was constructed of thin walled teflon sheet. The electrolyte used was 0.1 M LiOH in D_2O (99.5%).

The palladium electrode was in the form of a sheet .4mm thick. The other electrode was a thin sheet of platinum placed above the neutron beam. During the diffraction data collection the cell was rotated $\pm 180^\circ$ to average out the effect of any preferred orientation of crystallites.

Figure 4 shows the neutron diffraction pattern (taken with 1.53 A neutrons) for Pd before electrolysis. All the Pd peaks are labelled in the figure. The other peaks are from the teflon cell. The Pd peak intensities (after correction for the Lorentz factors) are in good agreement with what is expected from pure fcc palladium. The palladium was first loaded with D by applying a current of 1 amp for 12 hrs before taking the diffraction data. The same current of 1 amp was maintained while collecting the diffraction data. The lower part of Figure 4 shows the diffraction pattern from D loaded Pd under the conditions described above. All of the peaks shift to lower angles due to expansion of the lattice. The even hkl peaks increased in intensity and all the odd hkl peaks decreased in intensity.

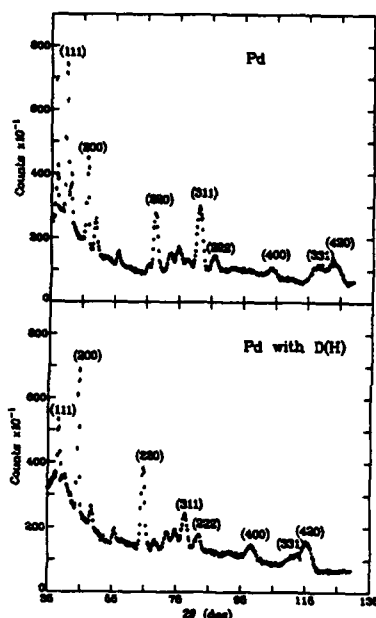


Figure 4. In-situ neutron diffraction patterns of Pd before and after electrolysis. The neutron wavelength used was 1.53 Å. Both Pd and Pd D(H) peaks are marked in the figure. The other peaks are from the teflon cell.

The lattice constant of the cell after electrolysis was found to be 4.035 Å. This is similar to what is reported for β -phase Pd-D(H) in the literature [6]. Our attempts to fit the data to a β -phase Pd-D cell, in which D atoms are located in octahedral sites, resulted in an octahedral site occupancy of only 0.32 as opposed to the known value of 0.7. The results of such a fit are shown in Table I. The rms displacement of D atoms was found to be 0.21 Å in very good agreement with earlier results [6]. Any attempts to fit the data by partially or fully filling the tetrahedral sites was unsuccessful.

An occupancy factor of only 0.32 for a D loaded sample points to the fact that there is a considerable amount of H along with D in the electrolysed palladium. Assuming a filling factor of 0.7 for octahedral sites, one can calculate the amount of H present in the D loaded Pd sample. This turns out to be H(0.35) and D(0.65) even though the electrolytes used contained at most 1-1.5% H. Higher solubility of H (as compared to D) in Pd under electrolysis is quite well known [8]. However, the separation factor

$$S_{\text{metal/liq}} = (H/D)_{\text{metal}} / (H/D)_{\text{liq}} \approx 35$$

that we obtain seems to be much higher than the highest values reported in literature (of the order of 10 - 13). A neutron activation analysis of the electrolysed Pd sample also confirmed our estimate of about 30% H in the sample [9].

TABLE I. Measured and calculated ratios of the integrated intensities of the observed peaks after the sample was loaded to those of the pristine sample. The calculated values were obtained using an octahedral site occupancy of 0.32 D/Pd and an rms displacement of 0.21 Å for the octahedral atoms.

Peak	Measured Ratio	Calculated Ratio
(111)	0.40 ± 0.03	0.48
(200)	1.68 ± 0.08	1.67
(220)	1.49 ± 0.07	1.52
(311)	0.47 ± 0.03	0.64
(222)	1.14 ± 0.17	1.41
(400)	1.44 ± 0.12	1.33
(331)	0.51 ± 0.07	0.76
(420)	1.11 ± 0.08	1.26

The electrolysis of Pd in nearly 99% deuterated electrolysis solution leads to substantial amounts of H isotope being incorporated in the Pd sample. Consequently, to determine the extent of any such preference for H over D in the electrolytically loaded Ni-Ti multilayer, we plan to repeat the experiment with pure H₂O solvent. Nonetheless, we believe these experiments illustrate the potential contribution of neutron reflectivity measurements in determining the microscopic structure of thin film metal-hydrogen systems.

ACKNOWLEDGEMENTS

Work at Brookhaven National Laboratory supported by the US Department of Energy under contract number DE-AC02-76CH00016.

REFERENCES

1. See, for example, V. F. Sears, Neutron Optics, (Oxford University Press, New York, 1989).
2. See, for example, M. Born and E. Wolf, Principles of Optics, (Pergamon, Oxford, 1975).
3. P. Croce and B. Pardo, *Nov. Rev. Opt. Appl.* **1**, 229 (1970).
4. S. H. Anastasiadis, T. P. Russell, S. K. Satija, and C. F. Majkrzak, *Phys. Rev. Letts.* **62**, 1852 (1989).
5. S. Moehelcke, C. F. Majkrzak, and Myran Strongin, *Phys. Rev. B* **31**, 6804 (1985).
6. J. E. Worsham, M. K. Wilkinson, C. G. Shull, *J. Phys. Chem Solids* **3**, 303 (1957).
7. S. K. Satija, D. A. Neumann, C. F. Majkrzak, J. J. Rush, D. Lashmore, C. Johnson, and R. M. Lindstrom, NBS Reactor: Summary of Activities July 1988 Through June 1989, NIST Technical Note, in press.
8. See, for example, F. A. Lewis, The Palladium-Hydrogen System, Academic Press (1967).
9. R. M. Lindstrom, unpublished result.

MAGNETOELASTICITY IN RARE-EARTH MULTILAYERS AND FILMS

R.W. ERWIN* J.J. RHYNE* J. BORCHERS** M.B. SALAMON** R. DU** and C.P. FLYNN**
 * National Institute of Standards and Technology, Gaithersburg, MD 20899
 ** University of Illinois at Urbana-Champaign, Urbana, IL 61801

ABSTRACT

The magnetic structure has been measured with neutron scattering and SQUID magnetometry for a number of epitaxial multilayers and films of the magnetic rare-earths dysprosium and erbium grown with non-magnetic yttrium. In almost all cases the first order ferromagnetic phase transitions are suppressed, although the Néel temperatures are within 5% of the bulk values. The observed critical fields are explained by including epitaxial constraints with the bulk theory of magnetoelasticity.

INTRODUCTION

The advancement of techniques for growing thin film and multilayer materials has made it commonplace to control structure on an atomic scale [1]. A principal *modus operandi* has been to grow one crystalline material layer on top of a different crystalline material. The proper growth technique and conditions can produce epitaxy between the dissimilar materials, resulting in intrinsic strains and new physical properties.

This paper presents an experimental investigation and a theoretical treatment of the effects of epitaxy on magnetic properties via magnetoelastic coupling. Using MBE techniques [2] to grow dissimilar rare-earth layers, we have observed a number of magnetic structures [3-7] that are different than in the bulk materials [8-12]. The rare-earths are particularly amenable for these investigations, since many of them attain magnetoelastic energies which are on the order of their exchange energies, they exhibit a wide range of lattice parameters, and their solubility is conducive to epitaxial growth. We have been able to explain many of the new structures by including epitaxial constraints with the bulk theory of magnetoelasticity. In some cases which do not fit the theory, the epitaxial constraints have been broken.

SAMPLES

The samples were films of Dy or Er and multilayers of Dy or Er interleaved with the non-magnetic rare-earth yttrium. The growth and characterization of these materials has been discussed [2-7]. The important points to recall are that the interfaces are interdiffused over approximately 4 to 7 atomic planes. The chemical coherence length along the growth direction is typically greater than 500 Å. The chemical coherence in the growth plane is limited by the formation of defects to relieve the lattice mismatch between the dissimilar rare-earths. A careful study of these defects would be useful. A single Bragg peak is observed for the growth plane reflections, indicating good epitaxy.

The layer thicknesses ranged from about 9 to 35 atomic planes (25Å to 100Å), and the total sample thickness was in the range of 0.3 to 0.5 microns. Most of the samples were grown on sapphire substrates with buffer layers of Nb and yttrium.

MAGNETIC STRUCTURES

Bulk Magnetic Structures

The bulk magnetic structures for Dy and Er have been measured using neutron and X-ray scattering [8-12]. The spins are aligned within each basal plane sheet of the hcp structure, and the magnitude or direction is modulated along the c-axis direction. Thus the structure is described by an effective temperature dependent turn angle, ω . The spin direction is in the basal plane for Dy and predominantly along the c-axis for Er. Both Dy and Er have a first order phase transition to a ferromagnetic state, which is primarily driven by magnetoelastic energetics [13-15].

Magnetic Structure in Rare-Earth Films and Multilayers

The magnetic structures in the films and multilayers have been measured with neutron scattering and SQUID magnetometry [3-7]. The temperature dependence of the neutron diffraction for a Dy film and a [Dy|Y] multilayer is shown in Fig. 1(a) and (b) respectively. The structure of the Dy film is identical to that of the bulk, except that the ferromagnetic transition has a broader temperature hysteresis and the ferromagnetic correlation length is only a few hundred Å. In contrast, the ferromagnetic transition in the [Dy|Y] multilayers is completely suppressed, and the temperature dependence of the turn angle is weaker than in the bulk. This behavior is also observed in Er films.

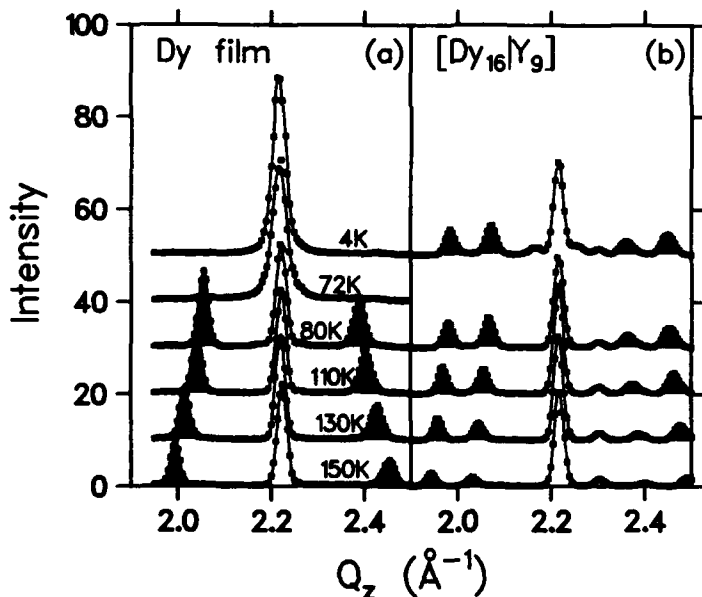


Fig. 1. The magnetic structure is determined for a Dy film(a) and a [Dy|Y] multilayer by scanning along (000 ξ). The film has a ferromagnetic transition where the magnetic intensity collapses onto the nuclear Bragg peak, while the multilayer does not. The helimagnetic intensity is shaded.

MAGNETOELASTICITY

The magnetoelastic free energy in Cartesian coordinates can be expressed as

$$f_{me} = \frac{1}{2} \sum_{\mu, \nu} c_{\mu\nu} \epsilon_{\mu\mu} \epsilon_{\nu\nu} - \sum_{\mu} K_{\mu} \epsilon_{\mu\mu} \quad (1)$$

The magnetoelastic coefficients appear in terms linear in the strains as they arise from derivatives of the exchange and single-ion energies with respect to the strains. The equilibrium strains satisfy the equations

$$\sum_{\nu} c_{\mu\nu} \bar{\epsilon}_{\nu\nu} = K_{\mu} \quad (2)$$

and the equilibrium magnetoelastic free energy is

$$\bar{f}_{me} = -\frac{1}{2} \sum_{\mu, \nu} c_{\mu\nu} \bar{\epsilon}_{\mu\mu} \bar{\epsilon}_{\nu\nu} = -\frac{1}{2} \sum_{\mu} K_{\mu} \bar{\epsilon}_{\mu\mu} \quad (3)$$

Magnetoelastic Energies in Bulk Dy and Er

Magnetoelastic energetics play a large role in the first order ferromagnetic transitions found in the rare earths. For example, in Dy this transition is accompanied by a 0.5% orthorhombic distortion of the basal plane and a 0.25% expansion of the c-axis of the hcp structure as the moments align along a single direction [16]. The magnetoelastic energy associated with this transition has been calculated according to eq.(3) for Dy[14] and Er[15]. The discontinuous decrease of the magnetoelastic energy drives the first order ferromagnetic transitions by overcoming the exchange energy difference between the ferromagnetic and antiferromagnetic states.

In Dy the γ -mode associated with an orthorhombic distortion in the basal plane provides the major part of the magnetoelastic energy which is responsible for the ferromagnetic transition, and this magnetoelastic energy can only be gained when the turn angle, ω , collapses to zero (the clamping effect) [14]. This mode provides a driving energy of about 3K/atom at 85K while the remaining modes make up approximately 1K/atom.

In Er the ferromagnetic alignment is along the c-axis so that there is no γ -mode distortion. The magnetoelastic driving energy is found to be 2.3 K/atom [15].

We shall attempt to apply the magnetoelastic coefficients of the bulk materials to the thin film materials. Care must be taken to correct for the magnetic structure dependence of the coefficients, since the structures are typically different in the layered materials compared to the bulk. For example, using eqs. (2) and (3) and symmetry arguments for the spin correlation functions[17], the magnetoelastic coefficients in the basal plane helimagnetic structure of Dy at T = 0 K are

$$K_{x,y}(T=0) = \pm 0.68 \delta_{\omega,0} - 0.06 (3 + \cos\omega)/4 \quad (10^3 \text{ K/atom}) \quad (4)$$

$$K_z(T=0) = 1.4 \cos\omega \quad (10^3 \text{ K/atom}) \quad (5)$$

The structural dependence of the magnetoelastic coefficients of Er is more complicated than in the case of Dy since there are two spin components, and the solution for the magnetoelastic coefficients can only be obtained by omitting the single-ion terms. The low temperature magnetoelastic coefficients are found to be

$$K_{x,y} = -0.427\beta\cos^2\theta + \sin^2\theta(1.34\cos\omega + 5.30) - 1.28 \quad (10^3 \text{ K/atom}), \quad (6)$$

$$K_z = 1.21\beta\cos^2\theta - \sin^2\theta(0.926\cos\omega) \quad (10^3 \text{ K/atom}). \quad (7)$$

Here $\tan\theta = \langle S^x \rangle / \langle S^z \rangle = 0.51$ at the ferromagnetic transition and $\beta = 1 - 2\omega/\pi$ is the nearest neighbor correlation function of the z spin components. Note that these coefficients are determined by oppositely signed terms, and in particular the last three terms in $K_{\mu\nu}$ nearly cancel. Furthermore, the relationship between β and ω leaves the coefficients only weakly dependent upon the magnetic structure except when β jumps from 1/2 to 1 at the ferromagnetic transition.

Modifications to Magnetoelasticity in Films and Multilayers

The elastic properties of films have been investigated extensively [18], and described by theories which take into account defects in the structure. However, we shall treat the magnetoelasticity by assuming perfect epitaxy, and then examine the agreement with experiments.

When a magnetic material is grown with a non-magnetic material in a film or multilayer additional elastic terms are added to the free energy. In the case that the strains in the growth plane are coherent the additional elastic energy from the non-magnetic material is

$$\bar{F}_{el} = \frac{1}{2} r_{\alpha} \sum_{\mu, \nu, \alpha} (\bar{c}_{\mu\nu} - \bar{c}_{\mu\alpha} \bar{c}_{\nu\alpha} / \bar{c}_{\alpha\alpha}) (\epsilon_{\mu\mu} - \bar{\epsilon}_{\alpha\mu}) (\epsilon_{\nu\nu} - \bar{\epsilon}_{\alpha\nu}) \quad (8)$$

The relative amount of non-magnetic material is represented by r . The $\bar{\epsilon}_{\mu\alpha}$ are the strains in the free non-magnetic material measured with respect to the non-magnetic strains in the free magnetic material. In other words they represent the non-magnetic lattice mismatch. This additional elastic energy has both quadratic and linear strain terms, so that the effective elastic coefficients for μ, ν, α are

$$\hat{c}_{\mu\nu} = c_{\mu\nu} + r_{\alpha} (\bar{c}_{\mu\nu} - \bar{c}_{\mu\alpha} \bar{c}_{\nu\alpha} / \bar{c}_{\alpha\alpha}) \quad (9)$$

and the effective magnetoelastic coefficients for μ, α are

$$\hat{K}_{\mu} = K_{\mu} + r_{\alpha} \sum_{\nu, \alpha} \bar{\epsilon}_{\alpha\nu} (\bar{c}_{\mu\nu} - \bar{c}_{\mu\alpha} \bar{c}_{\nu\alpha} / \bar{c}_{\alpha\alpha}) \quad (10)$$

FERROMAGNETIC TRANSITION IN RARE-EARTH FILMS AND MULTILAYERS

Neutron diffraction and SQUID measurements of the low temperature magnetization in two [Dy|Y] and two [Er|Y] multilayers is shown in Fig. 2. We would like to be able to explain the magnitude of the critical field necessary to induce the ferromagnetic state.

A first attempt to treat magnetoelastic effects in multilayers and films assumes that the basic exchange interactions and anisotropy energies can be transferred directly from the bulk magnetic materials. This assumption is likely to be incorrect at the interfaces, yet we shall see that it provides reasonable explanations for many of the experimental results. Consider the case that the layered rare-earth material is grown along the hcp c-axis. If we assume the elastic constants are equal in the magnetic and non-magnetic material then the magnetoelastic driving energy for the ferromagnetic transition, $\Delta = \bar{F}(\omega=0^{\circ}) - \bar{F}(\omega)$, can be calculated based on eqs. (9) and (10) and the known elastic and magnetoelastic constants. If the low temperature state of Dy has $\omega = 30^{\circ}$, then

$$\Delta = -1.25 - (3.95 - 91.0 r_{\alpha} \bar{\epsilon}_{\alpha ox, y}) / (1 + r_{\alpha}) \text{ K/atom.} \quad (11)$$

This magnetoelastic driving energy is plotted in Fig. 3(a) (in terms of an equivalent magnetic field acting on the magnetic moments of Dy) for r ranging from zero to infinity as a function of the lattice mismatch ϵ .

The conversion to a magnetic field is based on the assumption that the driving energy at a spontaneous ferromagnetic transition would correspond to zero field. The critical field data at 10K obtained from Fig. 2(a) and 2(b) are also plotted in Fig. 3(a) for comparison with the theory.

A similar calculation of the driving energy for Er c-axis growth multilayers is based on $\omega = 2\pi/7$ in the low temperature antiferromagnetic state. Thus the magnetoelastic driving energy for these multilayers is

$$\Delta_z = -1.56 - (0.86 - 553 r_z \bar{\epsilon}_{ox,y}) / (1 + r_z) \quad (\text{K/atom}). \quad (12)$$

This expression is plotted in Fig. 3(b) in terms of the equivalent field on the c-axis moments of Er. The dependence of the driving energy on the lattice mismatch is strong compared to the Dy case, and the observed critical fields in Fig. 2(c) and 2(d) of 16 to 17kOe correspond to large values of the parameter r . This also explains why critical field data[19] suggest that a several micron thick film of Er on yttrium is required before a low temperature ferromagnetic transition is obtained. Note also that for slightly negative values of ϵ , as might be achieved by growing Er on Lu, the ferromagnetic transition is expected to occur at a higher temperature than in the bulk.

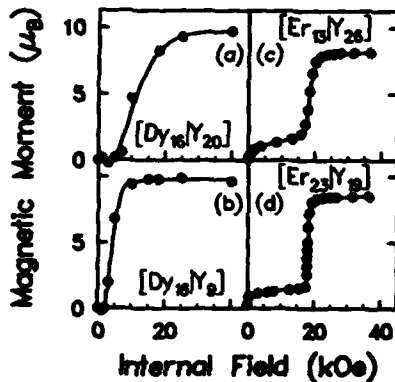


Fig. 2. The magnetization is plotted versus the internal field at 10K for [Dy|Y] (a,b) and [Er|Y] (c,d) multilayers. The critical field for ferromagnetism is determined qualitatively from where the magnetization first increases sharply towards saturation. The magnetization below about 15kOe in the erbium samples is due to ferrimagnetic states.

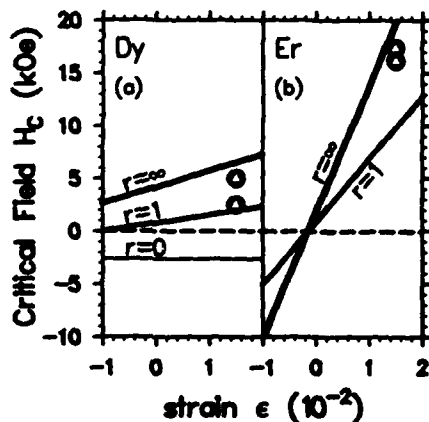


Fig. 3. The critical fields are calculated for Dy (a) and Er (b) c-axis materials as a function of the lattice mismatch ϵ , based on the perfect epitaxy model described in the text. The data points from Fig. 2 are shown for comparison. Note that for growth of erbium on a substrate with a smaller basal plane lattice parameter than erbium the ferromagnetic transition may occur at a higher temperature than in the bulk.

SUMMARY AND CONCLUSIONS

The critical fields required to induce ferromagnetism in [Dy|Y] and [Er|Y] multilayers and Er films are quantitatively explained by a simple model for the magnetoelasticity in these materials, which assumes perfect epitaxy and transfers the bulk elastic and magnetoelastic constants to the thin film materials. The model remains phenomenological by including all of the information about defects into the parameter r . However, r can be related directly to the observed growth plane strains, and this work is in progress. It is interesting that this model predicts that the ferromagnetic transition can be enhanced with the proper lattice mismatch, an effect which should be easily observed for Er.

ACKNOWLEDGMENTS

The work at Univ. of Illinois was supported through the National Science Foundation under NSF grant DMR 85-21616. We are indebted to Jens Jensen and Alan Mackintosh for useful reminders of the peculiarities of the exchange interactions in Er.

REFERENCES

- [1] J. Kwo, D.B. McWhan, M. Hong, E.M. Gyorgy, L.C. Feldman and J.E. Cunningham in Layered Structures, Epitaxy and Interfaces, edited by J.H. Gibson and L.R. Dawson (Mater. Res. Soc. Proc. **37**, Pittsburgh, PA 1985) pp 509.
- [2] S.M. Durbin, J.E. Cunningham and C.P. Flynn, *J. Phys. F* **12**, L75(1982).
- [3] J.J. Rhyne, R.W. Erwin, Shantanu Sinha, J. Borchers, M.B. Salamon, R. Du and C.P. Flynn, *J. Appl. Phys.* **61**, 4043 (1987).
- [4] M.B. Salamon, Shantanu Sinha, J.J. Rhyne, J.E. Cunningham, R.W. Erwin, J. Borchers and C.P. Flynn, *Phys. Rev. Lett.* **56**, 259 (1986).
- [5] R.W. Erwin, J.J. Rhyne, M.B. Salamon, J. Borchers, S. Sinha, R. Du, J.E. Cunningham and C.P. Flynn, *Phys. Rev. B* **35**, 6808 (1987).
- [6] J.J. Rhyne, R.W. Erwin, J. Borchers, M.B. Salamon, R. Du and C.P. Flynn, *Physica B* **152**, 111 (1989).
- [7] R.W. Erwin, J.J. Rhyne, J. Borchers, M.B. Salamon, R. Du and C.P. Flynn, *J. Appl. Phys.* **63**, 3461 (1988).
- [8] H.R. Child, W.C. Koehler, E.O. Wollan and J.W. Cable, *Phys. Rev.* **138**, A1655 (1965).
- [9] M.K. Wilkinson, W.C. Koehler, E.O. Wollan and J.W. Cable, *J. Appl. Phys.* **32**, 48S (1961).
- [10] J.W. Cable, E.O. Wollan, W.C. Koehler and M.K. Wilkinson, *Phys. Rev.* **140**, A1896 (1965).
- [11] M. Habenschuss, C. Stassis, S.K. Sinha, H.W. Deckman and F.H. Spedding, *Phys. Rev. B* **10**, 1020 (1974).
- [12] Doon Gibbs, Jakob Bohr, J.D. Axe, D.E. Moncton and K.L. D'Amico, *Phys. Rev. B* **34**, 8182 (1986).
- [13] B.R. Cooper, in Magnetic Properties of Rare-Earth Metals, edited by R.J. Elliot (Plenum, New York, 1972), p. 17.
- [14] W.E. Evenson and S.H. Liu, *Phys. Rev.* **178**, 783 (1969).
- [15] M. Rosen and H. Klimer, *Phys. Rev. B* **1**, 3748 (1970).
- [16] J.J. Rhyne and S. Legvold, *Phys. Rev.* **138**, A507 (1965).
- [17] E. Callen and H.B. Callen, *Phys. Rev.* **132**, A455 (1965).
- [18] for example, R. People and J.C. Bean, *Appl. Phys. Lett.* **47**, 322(1985).
- [19] J. Borchers, M.B. Salamon, R. Du, C.P. Flynn, R.W. Erwin and J.J. Rhyne, *J. Appl. Phys.* **61** (1987) 4050; *J. Appl. Phys.* **63** (1988) 3458.

THE MORPHOLOGY OF SYMMETRIC DIBLOCK COPOLYMERS AS
REVEALED BY NEUTRON REFLECTIVITY

S. K. Satija*, C. F. Majkrzak*, S. H. Anastasiadis** and T. P. Russell**

*National Institute of Standards and Technology, Gaithersburg, MD

**IBM Research Division, San Jose, CA

ABSTRACT

The specular reflectivity of neutrons has been used to characterize quantitatively the microphase separated morphology of symmetric, diblock copolymers of polystyrene, PS and polymethylmethacrylate, PMMA, as a function of the total molecular weight of the copolymer where either block is perdeuterated. It is shown that the hyperbolic tangent function, as opposed to a linear or cosine squared function, most closely describes the concentration gradient at the interface between the lamellar copolymer microdomains. The effective width of the interface is found to be independent of the molecular weight of the copolymer blocks and has a value of $50 \pm 3 \text{ \AA}$. This interface is also found to be identical to that of PS and PMMA, homopolymers. However, using measured values of the Flory-Huggins interaction parameter for PS and PMMA current theoretical treatments cannot describe the observed widths of the interface.

Recently, it has been shown that symmetric diblock copolymers of polystyrene (PS) and polymethylmethacrylate (PMMA) when prepared as thin films (5000 Å or less) on silicon substrates, exhibit a strong orientation of the lamellar microdomains parallel to the surface of the substrate [1,2]. This orientation occurs when the copolymer films are annealed at temperatures above the glass transition temperatures of the PS and PMMA blocks and results from the interactions of the two blocks with the air and substrate interfaces. PMMA, the more polar species, preferentially resides at the silicon (silicon oxide)/copolymer interfaces, whereas PS, the lower surface energy component, preferentially segregates to the air/copolymer interface. These interactions, coupled with the chemical connectivity of the PS and PMMA blocks, result in the observed multilayered structure.

In this report the details of the lamellar morphology for a series of PS and PMMA, symmetric diblock copolymers is reported where the molecular weight of the copolymer is varied. It is shown that neutron reflectivity provides the key means by which the detailed nature of the interface between the copolymer microdomains can be investigated. It is also shown that the interface between homopolymers of PS and PMMA is identical to that seen in the copolymers.

Symmetric, diblock copolymers of PS and PMMA, denoted P(S-b-MMA), were purchased from Polymer Laboratories and were prepared by a successive anionic polymerization process. The complete characterization of the copolymers is shown in table 1. As can be seen, the copolymers have narrow molecular weight distributions and styrene contents close to the desired 50%. It should also be noted that either the PS or PMMA block in the copolymer was perdeuterated which provided the contrast necessary for the neutron reflectivity studies.

Samples of the copolymers were prepared on 10 cm diameter, polished Si substrates. The substrates were ~ 5 mm in thickness to ensure that the substrate did not bow or bend when mounted in the sample holder. Solutions of the copolymer were prepared in toluene with the concentration being varied to produce the desired sample thickness. The substrates were fully coated with copolymer solutions and spun at 2000 rpm to produce a film with a uniform thickness. The spinning process also served to evaporate most of

the solvent in the film. The substrates were then placed under vacuum at 80 °C for 24 hrs. to remove the remaining solvent and then were heated to 170 °C for 72 hrs. to produce the oriented lamellar morphology. The specimens were then cooled to room temperature and investigated without further heating.

Neutron reflectivity measurements were performed on the BT-4 triple axis diffractometer at the NIST reactor. Details of the experimental geometry can be found elsewhere [7]. Experiments were performed with neutrons of wavelength $\lambda = 2.35$ Å over an angular range of $2\theta = 0^\circ$ to 1.7° . This translates into a neutron momentum, k_0 , range from 0 to -0.1 Å⁻¹

where $k_0 = (2\pi/\lambda) \sin \theta$. Under such condition reflectivities down to 10^{-6} could be measured which proved to be crucial to these studies [7,8].

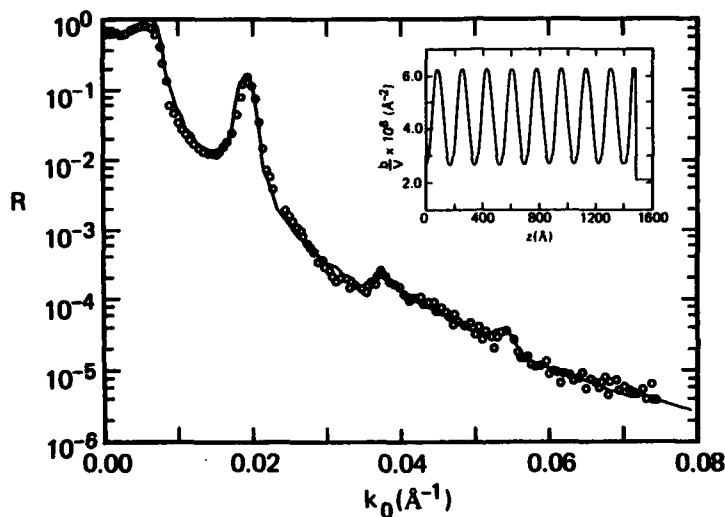


Figure 1. Neutron reflectivity profile of a P(S-b-d-MMA) diblock copolymer film annealed on a Si substrate for 72 hrs. at 170 °C where the total copolymer molecular weight is $\sim 30,000$. The points are the measured reflectivity profile whereas the solid line is the calculated reflectivity profile using the scattering length density profile shown in the inset.

The neutron reflectivity profile measured for the P(S-b-d-MMA) diblock copolymer, where the molecular weight of each block is $\sim 15,000$, after annealing at 170 °C for 72 hrs. is shown in figure 1. As can be seen at small values of the neutron momentum, total external reflection is seen below the critical angle. Above this the reflectivity drops by nearly two orders of magnitude whereupon a strong first order Bragg reflection at $k_0 = 0.0195$ Å⁻¹ is seen. This is followed by a further decrease in the reflectivity with the appearance of second and third order reflections at k_0 's of 0.0375 and 0.0540 Å⁻¹, respectively. The Bragg reflections are directly attributable to the layering of the lamellar morphology parallel to the surface of the film and the positions of the Bragg reflections yield

directly the period of the lamellar microdomain morphology. In this case the period is 175 Å which is comprised of a PS microdomain with a size of 91 Å and a PMMA microdomain of 84 Å. More importantly, the interface between the PS and PMMA microdomains is found to be 50 ± 3 Å. Using this model for the variation in the neutron scattering length density normal to the film surface, the calculated reflectivity profile, indicated by the solid line in figure 1, is obtained. The agreement between the calculated and measured reflectivity profile is very good over the entire k_0 range and over 5.5 orders of the reflectivity. Variation of the parameters outside of the stated values produces reflectivity profiles that do not agree with the experimentally measured profile. It must be emphasized that such precision on the width of the interface between the two microdomains was, heretofore, not attainable.

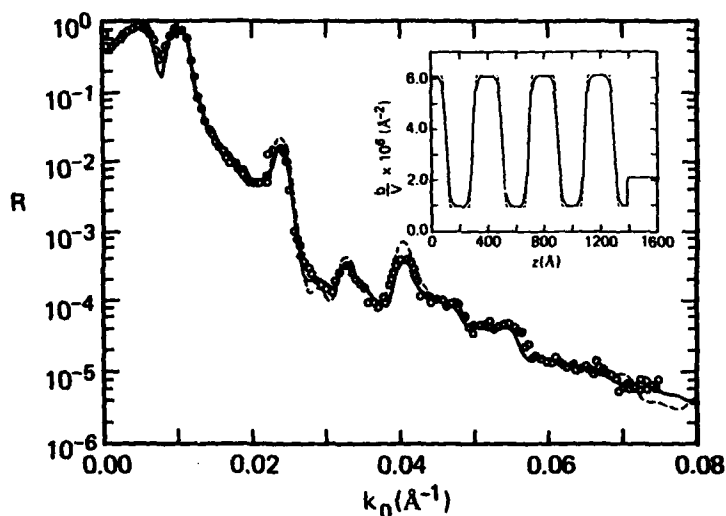


Figure 2. Neutron reflectivity profile of a P(d-S-b-MMA) diblock copolymer film on a Si substrate annealed for 72 hrs. at 170 °C where the total copolymer molecular weight is ~ 100,000. The points are the measured reflectivity profile the line is the calculated reflectivity profile using the hyperbolic tangent function to describe the interface between the copolymer microdomains and the dashed line is that calculated assuming a linear gradient between the microdomains. The models used to calculate the reflectivity profiles are shown in the inset.

Increasing the molecular weight of the blocks to ~ 50,000 per block produces dramatic changes in the neutron reflectivity profiles. Shown in figure 2 is the measured reflectivity profile of the P(d-S-b-MMA) diblock copolymer after annealing at 170 °C for 72 hrs. under vacuum. As with the lower molecular weight specimen, at small values of k_0 total external reflection. However, at higher k_0 at least five orders of Bragg reflections are evident which yield a period of 398 Å which is comprised of PS and PMMA microdomain sizes of 210 Å and 188 Å, respectively. As expected, the period of the lamellar morphology has increased with the increase in the molecular weight of the copolymer. The large number of Bragg reflections also provides a high sensitivity to the interface between the copolymer microdomains. Shown in figure 2 by the solid line is the calculated

reflectivity profile where the interface is described by a hyperbolic tangent function where the effective width of the interface is 50 ± 3 Å. This describes the observed reflectivity quite well over the entire measured k_0 range. Also shown in figure 2 as the dashed line, is the calculated reflectivity profile where a simple linear gradient of the neutron scattering length density was used to describe the concentration variation across the interface between the PS and PMMA microdomains. As can be seen, this model describes the data reasonable well over the entire k_0 range, but does not produce as good a fit to the data as the hyperbolic tangent function. Consequently, the neutron reflectivity results clearly show that whatever the functional form of the concentration gradient across the interface is, it must closely follow the hyperbolic tangent functional form. Such details on the morphology of block copolymers was previously unattainable by other techniques.

Similar studies have been performed on the P(S-b-d-MMA) diblock copolymer where the molecular weight of each block is - 50,000. In this case the neutron reflectivity profile yields a period of 512 Å comprised of a PS and PMMA microdomains with sizes of 268 Å and 244 Å. As with the P(d-S-b-MMA) copolymer the interface was well described by a hyperbolic tangent function with an effective width of 47 ± 4 Å. Thus, with the exception of the variation in the length of the period due to the increase in the molecular weight, these results are identical to the other cases.

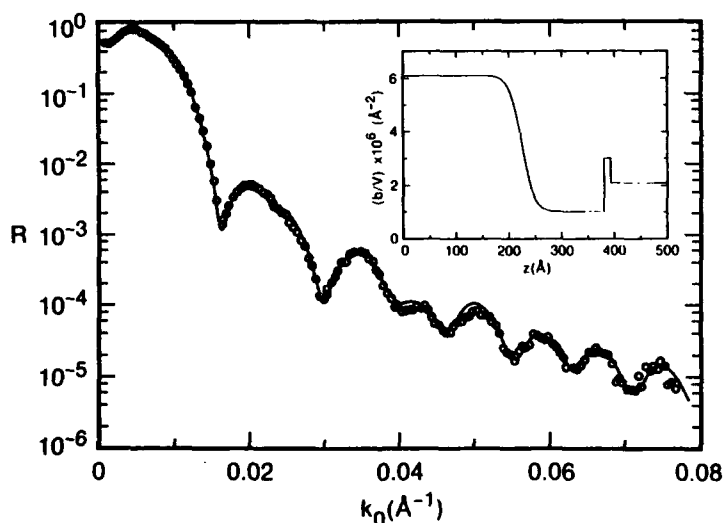


Figure 3. Neutron reflectivity profile for a P(d-S-b-MMA) diblock copolymer annealed for 240 hrs. at 170°C where the total molecular weight of the copolymer is - 300,000. The solid line is the calculated reflectivity profile using the scattering length density profile shown in the inset.

Finally, a P(d-S-b-MMA) diblock copolymer where the molecular weight of each block was - 150,000 was investigated. It has been found that the rate at which the copolymer microdomains orient parallel to the film surface depends strongly upon the molecular weight of the copolymer. For such high molecular weights the time required for the lamellar orientation is quite

long. Therefore, a copolymer film was prepared where the total thickness of the specimen corresponded to one-half of the period size. This specimen was annealed for 240 hrs. at 170 °C. The neutron reflectivity profile obtained from this specimen is shown in figure 3. As can be seen, periodic oscillations are seen in the data with at least two different characteristic frequencies. The frequencies correspond to the total thickness of the specimen and the thickness of the deuterated PS microdomain. The reflectivity results could be well described by the scattering length density profile shown in the inset of the figure. This model is comprised of a 225 Å layer of deuterated PS on top of a 156 Å layer of PMMA. The two layers are separated by an interface with a composition variation across the interface that is given by a hyperbolic tangent function with an effective width of 50 ± 4 Å.

Therefore, the clear picture that emerges from the combined results of these studies is that the period of the lamellar microdomain morphology increase with the molecular weight of the copolymer. If N is the total number of segments in the copolymer, then these results indicate that L , the period, varies with $N^{0.65}$ which agrees with theories describing copolymers in the strong segregation limit. The width of the interface is found to be independent of the copolymer molecular weight, and, for the P(S-b-MMA) copolymers, is found to be 50 Å. Independent studies on bilayers of PS and PMMA homopolymers [7,9] have shown that the interface between the homopolymers is well described by a hyperbolic tangent function (or other functions that closely follow this form) with an effective width of 50 Å in precise agreement with the copolymer results. From the measured values of the interaction parameter between PS and PMMA [10] and the values of the statistical segment lengths of PS and PMMA, the width of the interface can be calculated theoretically. These calculations yield a value of the interface of 30 Å. Annealing symmetric diblock copolymers of PS and PMMA above the glass transition temperature orients the lamellar microdomains parallel to the free surface of the film. The high resolution (~ 1 nm) of neutron reflectivity, in conjunction with the orientation of the lamellar microdomains parallel to the surface, has allowed a detailed study of the morphology of the copolymers as a function of the molecular weight.

It has been shown that the hyperbolic tangent function, as opposed to a linear or cosine squared function, most closely describes the concentration gradient at the interface between the copolymer microdomains. The effective width of the interface is found to be independent of the molecular weight of the copolymer blocks and has a value of $\sim 50 \pm 3$ Å. This interface has been shown to be identical to that between layers of PS and PMMA homopolymers. However, using measured values of the Flory-Huggins interaction parameter, current thermodynamic theories are not able to describe quantitatively the observed results.

Table 1.

Copolymer	M_{ps}	M_{PMMA}	M_w/M_n	Γ
P(S-b-d-MMA)	14,670	15,107	1.10	0.50
P(d-S-b-MMA)	52,900	48,000	1.07	0.50
P(S-b-d-MMA)	56,300	65,000	1.12	0.47
P(d-S-b-MMA)	169,500	131,900	1.08	0.53

References

- [1] Coulon, G.; Russell, T. P.; Deline V. R.; Green P. F. *Macromolecules* **22**, 2581 (1989).
- [2] Russell, T. P.; Coulon, G.; Deline, V. R.; Miller, D. C. *Macromolecules* (in press).
- [3] Helfand, E.; Wasserman, Z. R. *Developments in block copolymers - 1*. I. Goodman, ed. Applied Science Pub., New York (1982).
- [4] Meier, D. J. *Thermoplastic elastomers--research and development*. N. Legge, G. Holden, H. Schroeder, eds. Hanser Pub., Germany (1988).
- [5] Ohta, T.; Kawasaki, K. *Macromolecules* **19**, 2621 (1986).
- [6] Semenov, A. N. *Zh. Eksp. Teor. Fiz.* **88**, 1242 (1985).
- [7] Anastasiadis, S. H.; Russell, T. P.; Satija, S. K.; Majkrzak, C. F. *J. Chem. Phys.* (submitted for publication).
- [8] Anastasiadis, S. H.; Russell, T. P.; Satija, S. K.; Majkrzak, C. F. *Phys. Rev. Lett.* **62**, 1852 (1989).
- [9] Fernandez, M. L.; Higgins, J. S.; Penfold, J.; Ward, R. C.; Shackleton, C.; Walsh, D. J. *Polymer* **29**, 1923 (1988).
- [10] Russell, T. P.; Hjelm, R. P.; Seeger, P. A. *Macromolecules* (submitted for publication).

TEMPERATURE DEPENDENCE OF THE MORPHOLOGY OF THIN DIBLOCK
COPOLYMER FILMS AS REVEALED BY NEUTRON REFLECTIVITY

T. P. Russell*, S. H. Anastasiadis*, S. K. Satija** and C. F. Majkrzak**

*IBM Research Division, San Jose, CA

**National Institute of Standards and Technology, Gaithersburg, MD 20899

ABSTRACT

The order-disorder transition in thin films of symmetric diblock copolymers of polystyrene and polymethylmethacrylate has been investigated by neutron reflectivity. At temperatures above the order-disorder temperature, T_{MST} , a surface induced oscillatory segment density profile with an exponential decay length, ξ , is observed. The inverse of decay length $1/\xi$ is shown to vary as: $(\frac{1}{T_{MST}} - \frac{1}{T})^{1/2}$ in agreement with mean field predictions. For $T \leq T_{MST}$ a lamellar morphology oriented parallel to the surface propagates through the entire specimen.

Thin films of symmetric diblock copolymers on solid substrates have been shown to exhibit a strong orientation of the lamellar microdomains parallel to the surface of the substrate upon heating to temperatures above the glass transition temperature [1-4]. Specular neutron reflectivity measurements [3,4] clearly show that this orientation is parallel to the surface of the substrate over large lateral length scales. Consequently, the morphology produced by simply annealing the films above the glass transition temperature is that of a nearly perfect multilayer. This behavior is found provided the annealing temperature is below the microphase separation transition temperature (MST) where a transition from an ordered to a disordered morphology occurs. For perfectly symmetric diblock copolymers the MST occurs when $\chi N = 10.5$ where χ is the Flory-Huggins interaction parameter and N is the total number of segments in the copolymer chain. For thin films of symmetric diblock copolymers annealed at temperatures above the MST, recent neutron reflectivity studies [3] have shown that there is a preferential segregation of one of the components to the air/copolymer and the copolymer/substrate interfaces. Due to the connectivity of the blocks this excess surface concentration induces an oscillatory variation in the composition of the two components normal to the interface that is exponentially damped. This behavior has been shown to be in agreement with recent theoretical arguments [5].

In this report neutron reflectivity studies on the temperature dependence of the morphology of diblock copolymers in the vicinity of the MST are discussed. At temperatures below the MST the ordered multilayered lamellar morphology is found to penetrate through the entire specimen. At temperatures above the MST the periodic variation in the composition of the components is maintained but a clear dissipation of the order is found with increasing distance from either the air/copolymer or copolymer/substrate interfaces. An exponentially damped squared cosine function from both interfaces is found to well describe the reflectivity results. The characteristic decay length is found to decrease with increasing temperature in accordance with mean field arguments. Results from two different copolymers with two different molecular weights are found to fall on a straight line on a reduced temperature scale.

Symmetric, diblock copolymers of PS and PMMA, denoted P(S-b-MMA), were purchased from Polymer Laboratories and were prepared by a successive

anionic polymerization process. The P(S-b-d-MMA) copolymer, where the methacrylate block is perdeuterated, had a PS block molecular weight of 14,670 and a PMMA block molecular weight of 15,107. The total copolymer had an M_w/M_n of 1.1 and the fraction of PS in the copolymer was 0.5. The P(d-S-b-MMA) copolymer had a total molecular weight of 27,600 with $M_w/M_n = 1.08$ and a PS fraction of 0.43.

Samples of the copolymers were prepared on 10 cm diameter, polished Si substrates. The substrates were ~ 5 mm in thickness to ensure that the substrate did not bow or bend when being mounted in the sample holder. Solutions of the copolymer were prepared in toluene with the concentration being varied to produce the desired sample thickness. The substrates were fully coated with the copolymer solutions and spun at 2000 rpm to produce a film with a uniform thickness. The spinning process also served to evaporate most of the solvent in the film. The substrates were then placed under vacuum at 80 °C for 24 hours to remove the remaining solvent.

Neutron reflectivity measurements were performed on the BT-4 triple axis diffractometer at the NIST reactor experimental hall. Details of the experimental geometry can be found elsewhere [4]. Experiments were performed with neutrons of wavelength $\lambda = 2.35 \text{ \AA}$ over an angular range of $2\theta = 0^\circ$ to 1.7° . This translates into a neutron momentum k_0 range from 0 to

$$\sim 0.1 \text{ \AA}^{-1} \text{ where } k_0 = (2\pi/\lambda) \sin \theta.$$

Separate specimens were prepared for experiments above and below T_{MST} since it was found that long equilibration times were required to completely eradicate the order remaining from specimens heated first to $T < T_{MST}$ and then to $T > T_{MST}$. The samples were annealed at several temperatures for a period of at least 24 hours and then rapidly quenched to room temperature freezing in the structure at the annealing temperature.

The neutron reflectivity profile measured for the P(S-b-d-MMA) diblock copolymer, where the molecular weight of each block is ~ 15,000, at 120°C is shown in figure 1. As can be seen at small values of the neutron momentum total external reflection is seen below the critical angle. Above this the reflectivity is seen to drop by nearly two orders of magnitude where upon a strong first order Bragg reflection at $k_0 = 0.0195 \text{ \AA}^{-1}$ is seen. At higher values of k_0 a second order reflection and a diffuse third order reflection are evident. The solid line in the figure is the calculated reflectivity profile using the scattering length density profile shown in the inset where the period is 175 Å and the effective width of the interface between the PS rich and PMMA rich microdomains is 50 Å. For the P(S-b-d-MMA) copolymer investigated here the MST, calculated from the molecular weight of the copolymer and the temperature dependent interaction parameter [6], is 168 °C. Thus, at 120 °C the copolymer is below, but near, the MST. In keeping with this, the two microphases in the lamellar morphology are not pure PS or PMMA but are only rich in either component and the total fraction of the specimen that is occupied by the interface is ~ 0.65. Consequently, while the oriented lamellar morphology propagates through the entire specimen, it is very diffuse due to the proximity of the MST.

Reflectivity measurements on the copolymer for $T > T_{MST}$ are typified by the data for $T = 200^\circ\text{C}$ shown in Figure 2. Here it is seen that the first order reflection is retained but is significantly lower in intensity. The higher order reflections have become much more diffuse or completely lost. The best fit to the reflectivity profile, shown by the solid line, was obtained from the scattering length density profile shown in the inset.

Here the variation in the PS volume fraction, ϕ_{PS} , from the air/copolymer interface is given by $\phi_{PS}(z) = \phi_s e^{-z/\xi \cos^2 \frac{2\pi z}{L}} + \bar{\phi}_{PS}$ (1) where ϕ_s is the excess surface volume fraction of PS, $\bar{\phi}_{PS}$ is the average PS concentration, L is the bilayer period and ξ is the decay length.

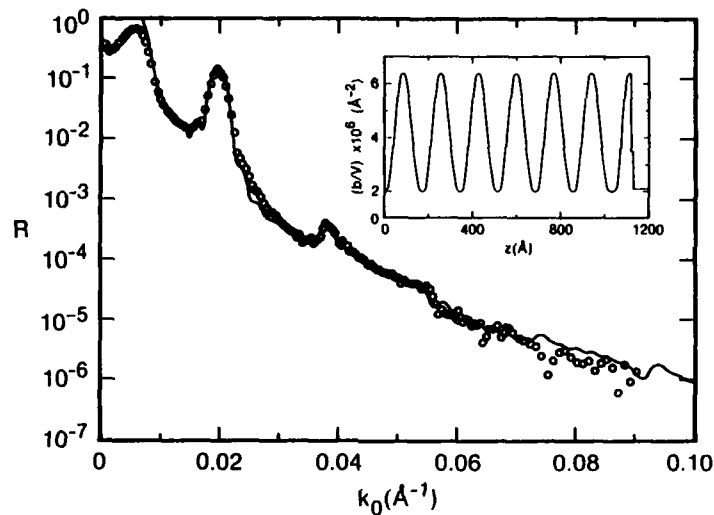


Figure 1. Neutron reflectivity profile of a P(S-b-d-MMA) diblock copolymer film on a Si substrate at 120 °C. The points are the measured reflectivity profile, the line is the calculated reflectivity profile using scattering length density profile shown in the inset.

Table 1

Copolymer Characteristics Above MST

T(°C)	L_{exp} (Å)	ξ (Å)	χ^\dagger	χ^*	$(\phi_s + \bar{\phi}_{PS})^*$	$(\phi_M + \bar{\phi}_{DPHMA})^*$
185	166	1100 ± 100	.0365	.0365	0.86	0.94
195	161	800 ± 75	.0363	.0365	0.84	0.94
200	162	600 ± 50	.0372	.0362	0.76	1.00

†Calculated value of χ from Ref. [6].

‡Calculated value of χ using the results found here.

*Total PS concentration at the air interface.

*Total d-PMMA concentration at the silicon interface.

The variation in the d-PMMA volume fraction from the Si/copolymer interface is given by an equation similar to the one above with ϕ_M being the excess surface volume fraction of d-PMMA at this interface. The model yielding the best fit to the data requires that ϕ_S and ϕ_M be different, giving the apparent asymmetry in the scattering length density profile shown in Figure 2. For $T = 200^\circ\text{C}$ at the air/copolymer interface $\phi_{PS} = 0.76$ and at the Si/copolymer interface $\phi_{d-PMMA} = 1.00$. We have assumed the decay length ξ to be the same from both interfaces, which turns out to be $\xi = 600 \pm 50\text{\AA}$ at 200°C . The difference in surface concentrations of PS at one interface and d-PMMA at the other interface agrees with our previous studies [3,4].

Results from reflectivity measurements at other temperatures ($T > T_{MST}$) are shown in Table 1. The surface excess of PS at the air interface decreases somewhat with temperature, whereas the temperature variation in ϕ_M at the Si interface is negligible. The decay length ξ , however, changes by nearly a factor of 2 with only a 15°C increase in temperature. It should be recalled that, in the bulk, for $T > T_{MST}$ the copolymer is phase mixed which would yield a constant scattering length density profile. Thus, these reflectivity results clearly show that the surface induces an ordering in copolymers above T_{MST} . The extent to which this ordering propagates into the specimen diminishes the farther one is from the T_{MST} .

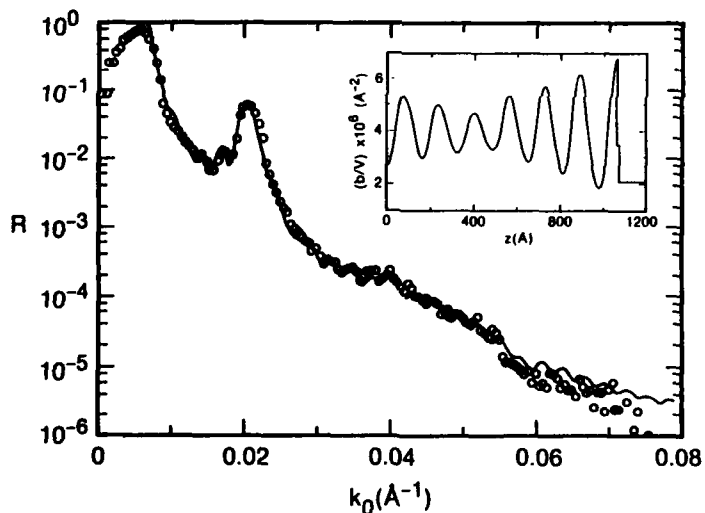


Figure 2. Neutron reflectivity profile for a P(S-b-d-MMA) diblock copolymer at 200°C . The solid line is the calculated reflectivity profile using the scattering length density profile shown in the inset.

These experimental results can be compared to the recent mean field predictions of Fredrickson [5] describing the surface induced ordering in diblock copolymers. From his arguments

$$\frac{1}{\xi} = \frac{6f(1-f)}{Nb^2} [(xN)_s - (xN)]^{1/2} \quad (2)$$

where b is the statistical segment length, N is the total number of segments in the copolymer chain, $(xN)_s$ is the value of xN at T_{MST} and f is the fraction of one component in the copolymer. As shown previously, [6] x is of the form $\alpha + \beta/T$. Therefore, Eq. (2) can take the form:

$$\frac{1}{\xi^2} = \frac{6f(1-f)\beta}{b^2} \left(\frac{1}{T_{MST}} - \frac{1}{T} \right) \quad (3)$$

Consequently, $\frac{1}{\xi^2}$ varies linearly with $1/T$ with a slope to intercept ratio of T_{MST} and a slope that yields β directly. Linear behavior was observed for such a plot where it was found that $T_{MST} = 179^\circ\text{C}$ and $\beta = 0.80\text{K}$. Independent neutron scattering measurements on a bulk specimen of P(S-b-d-MMA) yield a $T_{MST} = 175 \pm 5^\circ\text{C}$ in agreement with the result found here.

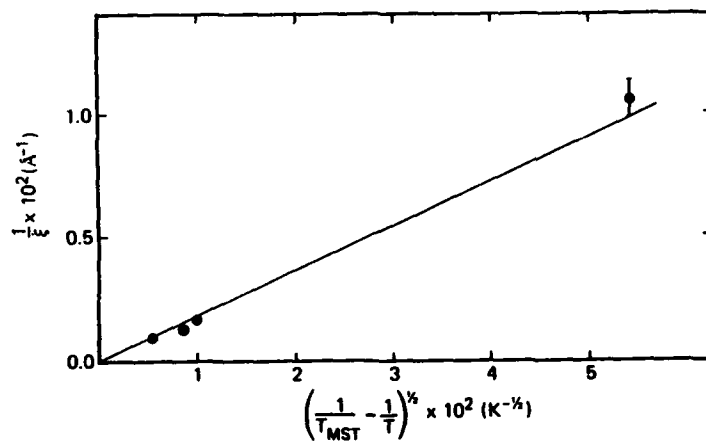


Figure 3. The inverse decay length, $1/\xi$, as a function of the $\left(\frac{1}{T_{MST}} - \frac{1}{T}\right)^{1/2}$ for P(S-b-d-MMA) and for P(d-S-B-MMA). The data are scaled to the P(S-b-d-MMA) results.

Previously [6], however, β was found to be $3.9 \pm 0.6\text{K}$ which is in disagreement with the value of 0.8 found here. The origin of this discrepancy lies in the weak temperature dependence of x and the limited range in temperature over which measurements can be performed. Using the temperature coefficient of x found in this study then $x = 0.0356 \pm (0.8 \pm 0.3)/T$. Values of x calculated from this equation were compared to those calculated from our previous results and are shown in

Table 1. As can be seen, over the temperature range studied, for any temperature, the difference in the χ values is less than 3% which is well within the error limits. It is not possible, using currently available techniques, to measure χ with better precision.

From Eq. (3) it should be possible to scale the results from a different, diblock copolymer to the results obtained here. If we consider our previous results on P(d-S-b-MMA) where $N = 263$, $f = 0.43$ and $\xi = 95 \pm 7 \text{ \AA}$ [3] at $T = 170^\circ\text{C}$, then multiplication of $1/\xi^2$ by the ratio of $f(1-f)$ for the two copolymers should be all that is required. A T_{MST} of -80°C , calculated from the temperature dependence of χ stated above, was used. A plot of $1/\xi$ as a function of $(\frac{1}{T_{\text{MST}}} - \frac{1}{T})^{1/2}$ for the P(d-S-b-MMA) and P(S-b-d-MMA) copolymers is shown in Figure 3. The data in Figure 3 are well described by a straight line passing through the origin with a slope of $(0.18 \pm 0.05) \text{ K}^{1/2} / \text{\AA}^{-2}$. When $T = T_{\text{MST}}$ an infinite decay length would be expected and is observed in that $\frac{1}{\xi} = 0$. This is also manifest in that the orientation of the lamellar microdomains parallel to the film surface propagates through the entire specimen at T_{MST} .

Thus, we have shown that the orientation of copolymer microdomains parallel to the film surface at temperatures above T_{MST} can be quantitatively described by simple mean field arguments. The transition from the disordered state is an ordinary transition where the modification of the thermodynamic potential by the surface induces an ordering at the surface at temperatures higher than that seen in the bulk. As T_{MST} is approached the ordering penetrates further into the bulk and at T_{MST} the ordering saturates the entire specimen. Full details of these experiments will be published elsewhere [7].

References

- [1] Coulon, G.; Russell, T. P.; Deline, V. R.; Green, P. F. *Macromolecules* **22**, 2581 (1989).
- [2] Russell, T. P.; Coulon, G.; Deline V. R.; Miller, D. C. *Macromolecules* (accepted for publication).
- [3] Anastasiadis, S. I.; Russell, T. P.; Satija, S. K.; Majkrzak, C. F. *Phys. Rev. Lett.* **62**, 1852 (1989).
- [4] Anastasiadis, S. H.; Russell, T. P.; Satija, S. K.; Majkrzak, C. F. *J. Chem Phys* (submitted for publication).
- [5] Fredrickson, G. H. *Macromolecules* **20**, 2535 (1987).
- [6] Russell, T. P.; Hjeltn, R. P.; Seeger, P. A. *Macromolecules* (submitted for publication).
- [7] Russell, T. P.; Anastasiadis, S. H.; Satija, S. K. and Majkrzak, C. F. *Phys. Rev. Lett.* (submitted for publication).

THE STUDY OF SURFACES AND INTERFACES ON THE REFLECTOMETER CRISP AT THE ISIS
PULSED NEUTRON SOURCE

J PENFOLD, Neutron Science Division, Rutherford Appleton Laboratory, Chilton,
Didcot, Oxon, OX11 0QX

ABSTRACT

The study of surfaces and interfaces using the specular reflection of neutrons on the reflectometer CRISP at the ISIS pulsed neutron source is discussed. The instrumentation, is briefly described, and the performance of the spectrometer being illustrated by some standard examples. Recent experimental results on the adsorption of surfactants at the air-water interface will be presented.

INTRODUCTION

Since the first observations of the total reflection of neutrons by Fermi and coworkers [1], specular neutron reflection has been extensively used in neutron polarisers [2] and neutron guides [3]. In recent years, however, attention has focused on the application of specular reflection of neutrons to study surface and interfacial problems. It was shown by Thomas and coworkers [4] that neutron reflection experiments give information about the neutron refractive index profile normal to the surface, and that a judicious use of hydrogen/deuterium contrast can provide unique information for a range of problems in surface chemistry. Due to the magnetic dipole interaction, magnetic materials exhibit a neutron spin dependent refractive index (this is the basis of neutron spin polarisers using critical reflection) and Felcher [5] has shown that the specular reflection of spin polarised neutrons is a particularly sensitive probe of surface magnetism.

The advent of dedicated spectrometers [6,7] has been accompanied by a rapid expansion in the scientific application of the technique to surface chemistry, surface magnetism and solid films.

DESCRIPTION OF REFLECTOMETER

The essence of a neutron reflection experiment is to measure the specular reflection over a wide range of wave vector transfers ($Q = 4\pi \sin\theta/\lambda$, θ is the glancing angle of incidence) perpendicular to the reflecting surface. The

wide Q range can be achieved either by using a monochromatic beam and scanning a larger number of angles, or by using the broad band neutron time-of-flight (TOF) method to determine λ at fixed Θ . As the critical glancing angles are small, narrow well collimated beams are required. To date, the majority of the reactor based measurements have been made using monochromatic long wavelength neutrons and a Θ - 2Θ angular scan (for example the D17 diffractometer at the Institute Laue Langevin). However, on a pulsed source, such as ISIS, the natural way to make the measurement is the white beam TOF method. The fixed sample geometry ensures a constant sample illumination, and the Q resolution (dominated by the $\Delta\Theta$ contribution) is essentially constant over the wide Q range available.

A schematic diagram of the CRISP reflectometer, on the ISIS pulsed neutron source, is shown in Figure 1.

Although the reflectometer has been described in detail elsewhere [6]; the important features are described here. It views the 20K hydrogen moderator giving an effective wavelength range 0.5 to 13Å. The beam is inclined at 1.5° to the horizontal (specifically for liquid surfaces), and a horizontal slit geometry is used giving typical beam dimensions 40 mm width and between 0.25 and 6 mm height, the beam size and divergence is variable and defined by two cadmium apertures (S1,S2). A single disc chopper (c) defines the wavelength band ($\delta\lambda$) and provides some frame overlap suppression. Additional suppression is provided by a series of frame overlap mirrors (F) which are set to reflect out of the main beam neutrons of wavelengths greater than 13Å.

The detector (D) (a single well shielded He³ detector, or a one dimensional multidetector with a positional resolution of < 1 mm) is located some 1.75 mm from the sample position.

The experimental arrangement is extremely flexible and solid films can be studied over a range of angles from 0.25° to 3°; liquid surfaces can be studied at angles less than 1.5° by the insertion of a supermirror. The Q range available is $\sim 4 \times 10^{-3}$ to 0.65 Å⁻¹. The limiting reflectivity is $\leq 10^{-6}$, and is sample dependent (for example; incoherent scattering from the bulk determines the background level for aqueous liquid surface).

Figure 2 shows the reflectivity from the surface of deuterium oxide, D₂O, measured over a wide range of Q at angles of incidence of 0.4, 1.0 and 1.5°. The flat background of 2.6×10^{-6} represents the incoherent scattering from the bulk liquid. The solid line is a calculated profile for Fresnel's law with an interfacial roughness of 2.8Å (rms value).

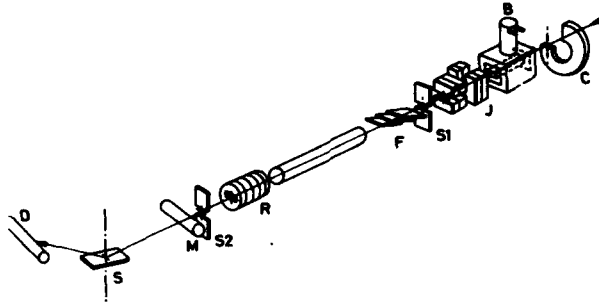


FIGURE 1

Schematic diagram of the CRISP reflectometer. C : Chopper, B : Beryllium filter, J : Coarse collimating jaws, S1, S2 : Collimating slits, F : Frame overlap mirrors, R : Downstream collimation, M : Neutron beam monitor, S : Sample and D : Detector.

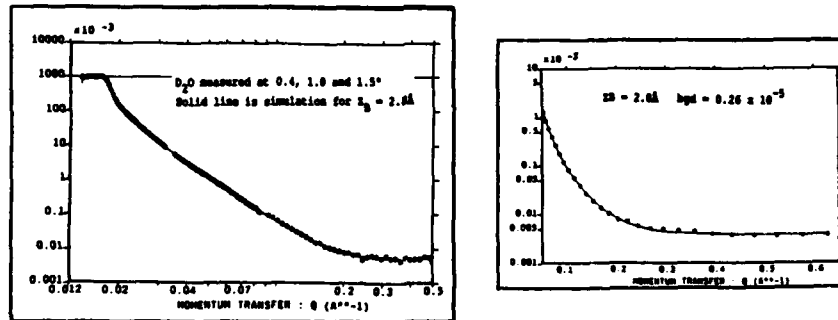


FIGURE 2

Reflectivity profile of D_2O measured at angles of incidence of 0.4, 1.0 and 1.5°. The solid line is a calculated profile for an interfacial roughness of 2.8Å , and a background of 2.6×10^{-6} .

The absolute reflectivity can be determined from the region of total reflection, or by reference to the incident neutron beam. An alternative scheme is normally used for the studies of adsorption at the air-liquid interface where the interesting region is only at high Q , and usually the low Q region which includes total region, is not measured. In such cases the absolute reflectivity is determined by reference to a standard and easily characterised liquid surface such as D_2O (see Figure 2).

SCIENTIFIC RESULTS

An extensive scientific programme [8] has emerged very quickly on CRISP, in surface chemistry, surface magnetism and solid films. The major part of the programme has been in surface chemistry, and much of the initial interest has been in the adsorption of surfactants, polymers and fatty acids at the air-liquid interface; more recently it has been successfully extended to the liquid-solid, and liquid-liquid interfaces.

Since neutron reflection is related to the refractive index profile normal to the surface, and since the refractive index profile is directly related to the composition profile, it is clear that the specular reflection technique can be used to obtain both the amount adsorbed and detailed structural information about the adsorbed layer. It is particularly important for the study of adsorption at the air solution interface due to the possibility of using isotopic substitution. As a majority of chemical systems contain some protons, and the scattering length protons and deuterons have opposite sign, hydrogen/deuterium substitution is used extensively to manipulate the refractive index profile. In the reflection experiment it is possible to choose the hydrogen/deuterium ratio for many solvents such that there is no specular reflection. In the case of surfactants, the solution will still be null reflecting even if the solute is fully deuterated. Any reflection will then of course result entirely from the surface adsorption of the surfactant, and so the technique will be specific to the adsorption of the solute. It is also possible to eliminate the reflection from the solute and determine the surface profile of the solvent. Isotopic substitution can also be used to highlight particular parts of a solute molecule by selective deuteration.

These features were used to some advantage in an early study on the adsorption of the surfactant decyltrimethyl ammonium bromide (DTAB) at the

air-solution interface [9], where it was possible to determine not only the surface excess but the detailed surface structure. It has also successfully been applied to the system tetramethylammonium dodecyl sulphate (TMDS) in water [10]. By selective deuteration of the tetramethyl ammonium counterion it was possible to obtain additional information about the degree of counterion binding, and the extent of the diffuse counterion layer.

Classically, the principle method to study surfactant adsorption is to combine measurements of the surface tension and of the activity of one of the components using the Gibbs equation. Neutron reflection determines not only the surface excess but can provide additional information on the surface structure. This is particularly true for concentrations of surfactant above the critical micellar concentration (cmc) when the Gibbs equation loses its effectiveness, and for mixed systems.

Specular neutron reflection has now been applied to study both mixed surfactant systems [11] and systems with a bulk concentration greater than the cmc [12].

The nature of adsorption from mixtures of surfactants has been relatively little studied because the Gibbs equation becomes rather cumbersome to apply. A classical problem in surface tension measurements is the minimum in the surface tension often observed in the sodium dodecyl sulphate (SDS) water system, which arises from the presence of small amounts of the impurity dodecanol.

Dodecanol is almost insoluble in water and on its own forms a close-packed monolayer on the surface. Thus a very small amount in an SDS solution below the cmc will preferentially adsorb at the surface. Above the cmc the SDS solubilizes the dodecanol and removes it from the surface. Since the surface free energy of a monolayer of SDS is greater than one containing a proportion of dodecanol, the surface tension will then rise at the cmc. In principle the Gibbs equation may be used to determine independently the surface excesses of SDS and dodecanol, but the determination of the activity of the latter is not easy. Figure 3 shows how easy it is to measure the dodecanol concentration by reflectivity.

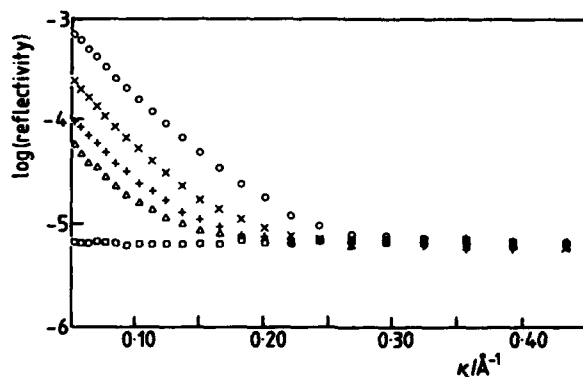


FIGURE 3

Reflectivity profiles of deuterated dodecanol/sodium dodecyl sulphate (SDS)/null reflecting water mixtures (background not subtracted). Circles show the profile of a spread monolayer of deuterated dodecanol on null reflecting water, squares show the reflectivity of 0.009M SDS in water. The remaining three profiles are for 1.25% dodecanol in SDS and a varying SDS concentration of 0.00675M (x), 0.009M (+) and 0.012M (o). The cmc of SDS is 0.008M.

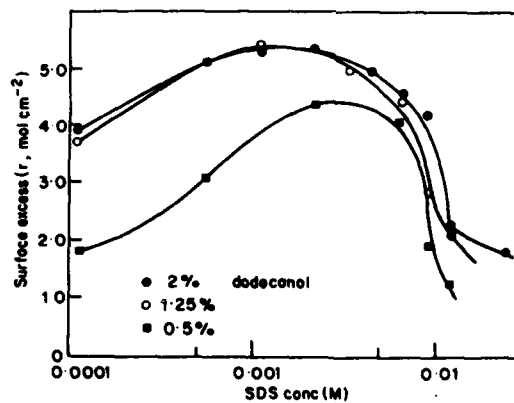


FIGURE 4

Adsorption isotherm for dodecanol in dodecanol/sds mixtures derived from reflectivity measurements.

The figure shows the reflectivity of SDS (protonated) in null reflecting water and, as would be expected, since both surfactant and water are contrast matched to air, there is no reflectivity. On the other hand the spread monolayer of pure deuterated dodecanol gives a strong reflected signal. The addition of a trace amount of deuterated dodecanol in the system leads to a significant increase in the reflectivity because the dodecanol displaces SDS from the monolayer. The actual amount has been determined over a wide range of conditions, leading to a set of isotherms for both dodecanol and SDS [12] (see Figure 4).

The preliminary analysis of recent results with either the dodecanol or the SDS deuterated and with protonated and deuterated subphases indicate that not only can the relative surface excesses be determined, but that the detailed surface structure of both components can be determined.

The dodecanol molecules are packed in an extended form within the mixed layer; the total width of the interfacial layer is larger than the fully extended molecule, with of the order of 20% of the chains in the headgroup region. This contrasts with the spread dodecanol layer which has a thickness corresponding to the fully extended molecule.

For the SDS molecules there is a higher degree of chain and headgroup intermixing, and the molecule is only extended to some 80% of its all trans configuration. The structure of the pure SDS surface layer is somewhat similar.

ACKNOWLEDGEMENTS

R C Ward, C Shackleton, J Herdman, W G Williams and R Felici have contributed to the development of CRISP.

The mixed surfactant measurements have been carried out in collaboration with R K Thomas, E Simister, E M Lee and A Rennie.

REFERENCES

- [1] E Fermi and W Zinn, Phys Rev 70, (1946) 103.
- [2] J B Hayter, J Penfold and W G Williams, J Phys E (1978) 11, 454.
- [3] H Maier-Leibnitz and T Springer, Reactor Sci & Tech, J of Nucl Energy, Parts A & B (1963) 17, 217.
- [4] J B Hayter, R R Highfield, B J Pulman, R K Thomas, A I McMullen and J Penfold, J Chem Soc Faraday, Trans 1 (1981) 97, 1437.
- [5] G P Felcher, Phys Rev B (1981) 24, 1995.
- [6] J Penfold, R C Ward and W G Williams, J Phys E (1987) 20, 1411.
- [7] G P Felcher, R D Hilleke, R K Crawford, J Haumann, R Kleb and G Ostroski, Rev Sci Inst, 58, 609 (1987).
- [8] J Penfold and R K Thomas, J Cond Matt Phys - in press.
- [9] E M Lee, R K Thomas, J Penfold and R C Ward, J Phys Chem (1989) 93, 381.
- [10] J Penfold, R K Thomas and E M Lee, Mol Phys 68, 33 (1989).
- [11] R K Thomas, A Rennie and J Penfold, to be published.
- [12] R K Thomas, E M Lee, E Sinister and J Penfold, J de Physique (in press)

PART IV

**Phase Transformations
and High T_c**

PHONONS AT MARTENSITIC PHASE TRANSITIONS OF
bcc-Ti, bcc-Zr AND bcc-Hf

W. PETRY*, A. HEIMING** AND J. TRAMPENAU**

* Institut Laue-Langevin, 156X, 38042 Grenoble Cedex, France

** Freie Universität Berlin, Fachbereich Physik, D-1000 Berlin, FRG

x Institut für Metallforschung, Univ. Münster, D-4400 Münster, FRG

ABSTRACT

Inelastic neutron scattering on in situ grown bcc single crystals of the group 4 metals Ti, Zr and Hf show a band of low energy and strongly damped phonons. Geometrical considerations show how these damped lattice vibrations achieve the displacements necessary for the two martensitic phase transitions from bcc to ω (under pressure) and from bcc to hcp (upon lowering the temperature). The low energy and temperature dependent phonons are precursor fluctuations of the hcp or ω phase within the bcc phase.

INTRODUCTION

All transition metals of group 3 to 6 exhibit over a certain temperature range and at normal pressure a stable bcc phase. Taking the range of existence and the melting temperature as a crude estimate of the stability of the bcc structure, its stability decreases when going from group 6 to group 3 (Fig. 1a). Whereas in group 6 and 5 the bcc phase is stable over the whole temperature range, group 4 metals Ti, Zr and Hf stabilize to the bcc (β) phase only in the upper third of the temperature range of the solid phase. For group 3 metals Sc, Y and La the stability range of the β phase narrows drastically, for instance Y crystallizes to bcc only during the last 40°C below the melting point. The relevant control parameter is the d-electron occupancy. All metals of group 3 and 4 transform martensitically upon lowering the temperature to hcp¹. For group 4 metals a second martensitic phase transition from bcc to the trigonal ω structure under typical pressures of 40 kbar at RT is known² (Fig. 1b).

Martensitic phase transitions (MT) in metals are of *1st order*.³ As such the amount of transformation is i) virtually independent of time and ii) is characteristic of temperature. The transformation is iii) very reversible, i.e. the same high temperature single crystal is obtained after a transformation cycle and there exists a iv) definite relation between the orientation of the original high temperature structure and the new structure at low temperature or at elevated pressure. v) No change in the chemical composition and almost no change in volume is observed after the transition. These are characteristics of *displacive* transitions which distinguish from diffusive transitions which are often continuous and of 2nd order.

In reality MTs in metals do not follow rigorously the rules of a strictly 1st order transition. Neutron scattering experiments on *metal alloys* show in a number of examples elastic as well dynamical precursor effects of the approaching MT. Their temperature dependence and location in Q-space reveals detailed information about the microscopic mechanism of the transformation. The well-known shape memory alloys Ni_{1-x}Ti_x (x ~ 0.5)⁴⁻⁶ and Ni_{1-x}Al_x (x = 0.35 - 0.5)^{7,8} and the ω -phase alloy Zr_{1-x}Nb_x (x = 0.2)⁹⁻¹¹ may serve as an illustration.

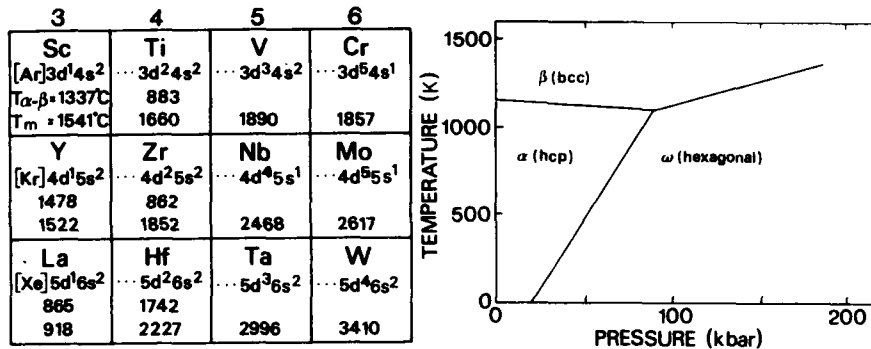


Fig. 1 a) Transition metals with bcc structure. b) Schematic P-T diagram for group 4 metals.

The high temperature phase of $\text{Ni}_{62.5}\text{Al}_{37.5}$ has the CsCl structure and transforms martensitically at the transition temperature $T_0 \sim 80$ K to the modulated 7R structure. $\text{Ni}_{50.5}\text{Ti}_{49.5}$ transforms from the high temperature ordered CsCl structure to an intermediate or pre-martensitic R phase at $T_0 \sim 320$ K. In both cases T_0 is very sensitive to compositional variations and to the thermal pretreatment. Both alloys show a remarkable softening of the $T_{1A}(\xi\xi 0)$ phonon branch at $\xi \sim 1/6$ and $\xi = 1/3$, respectively, when approaching T_0 . The phonons involved are those which achieve the displacements necessary to reach the new phase. It is important to note that the actual phase transitions occur at a finite phonon frequency, which distinguishes them definitely from soft mode transitions like in SrTiO_3 or KH_2PO_4 (KDP). In $\text{Zr}_{1-x}\text{Nb}_x$ ($x \geq 0.08$) the high temperature bcc phase can be quenched to room temperature. Again phonons of very low frequency were found at q vectors which are related to the MTs of bcc- $\text{Zr}_{1-x}\text{Nb}_x$ to hcp or to the ω structure. These phonons are no longer of a well defined frequency but extend over a broad range in energy up to zero energy transfer where additionally strong elastic scattering is found.

In contrast to the alloys, neutron scattering studies of precursor effects in pure metals yielded no or only a weak softening of particular phonons close to the MT. For instance in Li^{12-14} or Na^{15} - both transform to close packed structures at 74 K and 36 K, respectively - phonons at small q of the relevant phonon branch become even harder when T_0 is approached. In bcc-Tl¹⁶, which transforms to hcp at 507 K, low frequency phonons very similar to those of bcc $\text{Zr}_{0.8}\text{Nb}_{0.2}^{9,11}$ have been found. But none of them changes its frequency with decreasing temperature. No elastic precursors have been found in Na. Li and Co¹⁷ show strong satellites above T_0 . However, these have been explained by the coherent existence of the low temperature phase.

So, as a kind of conclusion of this difference between experimental observations on metallic alloys and pure metals one might ask to what extent phonon softening and central peaks are microscopic properties inherent to the martensitic phase transitions? Or, in other words, to what extent is the condensation of soft and damped phonons to a central peak driven by the point defects introduced by alloying? A series of theoretical investigations over the last four years¹⁸⁻²² support the view that dynamical and static precursors are inherent to MTs. Low frequency phonons at q -vectors which correspond to the

shuffling of the atoms into the low symmetry phase are predicted. Their frequency should decrease further but not go to zero when T_0 is approached. Furthermore, they predict areas of metastable domains of the new phase which have a relatively long lifetime. In a neutron scattering experiment the precursor effects should manifest themselves in *(over)damped* low frequency phonons while the second part should appear in a way similar to the central peak phenomena as scattering around $\hbar\omega = 0$. Within the energy resolution this appears as "elastic" scattering.

This in mind we have performed extensive studies of the phonon dispersion of the bcc phase of the group 4 elements Ti, Zr, and Hf²³⁻²⁶. The simple monoatomic structure of the bcc phase makes them to model cases to study eventually inelastic and elastic precursors of the new phases. These transitions occur at elevated temperatures (Fig. 1a) and thermal equilibrium is certainly achieved during the measurements. Because we deal with pure elements the attention is focussed on inherent properties of the bcc phase and phenomena induced by host-impurity interactions are expected to be of minor importance.

However, these elements are extremely difficult to obtain as bcc single crystals. It is the martensitic β to α transition, which prevents any quenching of the high temperature phase to room temperature. Rather they have to be grown in situ on the neutron spectrometer and to be kept at temperatures above the phase transition without intermediate cooling²⁷.

PHONON DISPERSION IN β -Ti, β -Zr AND β -Hf

With the exception of β -Zr^{28,29} the phonon dispersion of the bcc phase of the group 4 metals were not known. Measurements in β -Hf were particularly difficult because β -Hf is stable only at very high temperatures from 1740°C to 2223°C. Moreover its appreciable incoherent scattering cross-section $\sigma_{inc} = 2.6$ barn and its strong absorption $\sigma_{abs} (\lambda = 1.8 \text{ \AA}) = 104$ barn complicate the measurements. Figs 2 to 4 show our recent measurements on the triple axis instrument IN8 of the ILL of the phonon dispersion of the bcc phase of group 4 metals. The phonons as shown in Fig. 2 to 4 are the result of measurements on various crystals of each element, thus reducing systematic errors. This holds particularly true for phonons which show strong anharmonicity (see below). The full line in Figs. 2 to 4 represents a fit of the dispersion by a Born von Karman model taking into account force constants up to the fifth neighbour shell²³⁻²⁶. For all three elements additional phonon measurements have been performed in the whole temperature range of the bcc phase.

The dispersion of all three elements resemble very much to each other, i.e. they scale roughly with the square root of the mass and the lattice constant and thereby follow the homology rule. Most evidently the dispersion curves are dominated by a few unusual properties : i) At $q = 2/3(111)$ the $L[\xi\xi\xi]$ phonon branch shows a pronounced dip. As indicated by the dashed line intensity is measured in β -Ti and β -Zr down to zero energy transfer. ii) The whole $T_1[\xi\xi 0]$ phonon branch with $[1\bar{1}0]$ polarization is of low frequency when compared to the other transverse phonons. iii) The same holds true for the off symmetry $T_1[2\xi\xi]$ phonon branch.

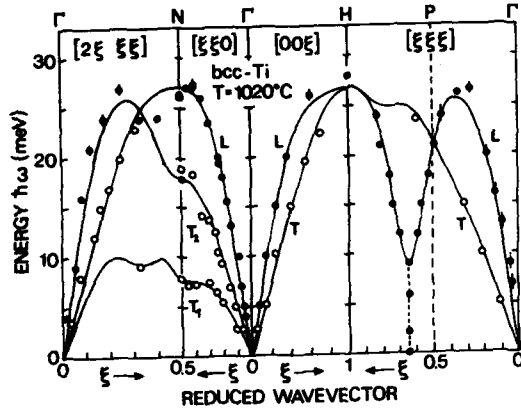


Fig. 2 Dispersion of bcc-Ti fitted by a Born von Karman model with force constants to the 5th neighbour shell²⁵.

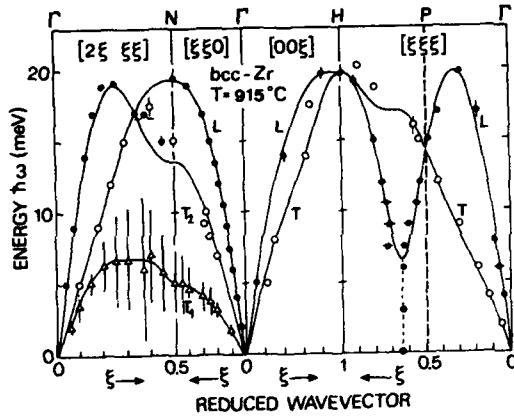


Fig. 3 Phonon dispersion of bcc-Zr fitted by a Born von Karman model with force constants to the 5th neighbour shell. Bars for the $T_1[2\xi\xi\xi]$ and $T_1[\xi\xi0]$ phonons indicate the width of the phonons as fitted by a damped harmonic oscillator²⁵.

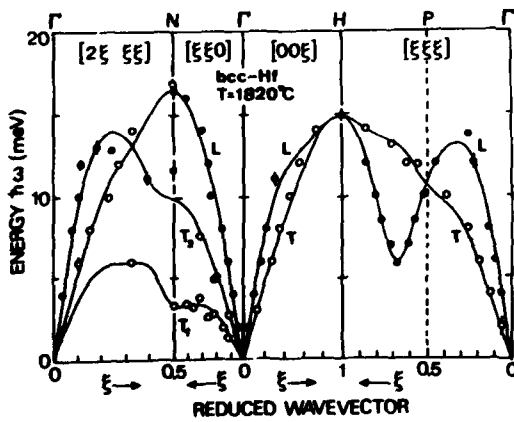


Fig. 4 Phonon dispersion of bcc-Hf fitted by a Born von Karman model with force constants to the 5th neighbour shell²⁵.

The $L2/3(111)$ phonon

As shown by de Fontaine and Buck²⁰ the atomic displacements achieved by a longitudinal phonon in $[\xi\xi\xi]$ direction with $\xi = 2/3$ have a particular crystallographic meaning in the bcc structure. For a stationary wave at $\xi = 2/3$ two of three neighbouring (111) planes move towards each other whereas every third plane stays at rest. When the two moving planes collapse together the ω structure is achieved. During the 2nd half of the wave the opposite motion is achieved and the moving planes approach to the plane at rest. Distortions in this direction are called anti- ω distortions. From symmetry it is evident that the restoring forces involved for distortions into the ω or anti- ω structure are different.

The ω lattice can be described with an hexagonal cell incorporating 3 atoms per cell with $A = \sqrt{2}a$ and $C = \sqrt{3}2a$, where a is the lattice constant of the bcc Bravais lattice. The C axis is along a (111) direction and the A axis along a (110) direction. Thus, the crystallographic relation between ω and β reads

$$(111)\beta // (00.1)\omega \quad \text{and} \quad [\bar{1}01]\beta // [01.0]\omega$$

There exists 4 possible variants for a given bcc structure to transform into the ω structure. ω Bragg peaks are expected at $Q = (n_1 \pm \eta, n_2 \pm \eta, n_3 \pm \eta)$ where (n_1, n_2, n_3) represent integers which obey the bcc selection rules of $\sum_{i=1}^3 n_i = \text{an even number}$. η is a shift in $[\xi\xi\xi]$ direction. Its ideal and commensurate value $\eta = 2/3$ and we refer to this position as the ω -point.

Representative for β -Ti and β -Zr constant energy scans at 1020°C for β -Ti around the ω -point are shown in Fig. 5a and illustrate what is meant with the dashed line in Figs. 2 and 3. *Coherent* intensity is measured down to zero (!) energy transfer; in particular the intensity measured at zero energy does not differ from the inelastic at for example 2 meV. For all three elements the position of this inelastic scattering is slightly incommensurate with $\eta = 0.65$. Coherent means that the neutron spectra shown in Fig. 5a have been corrected for the purely incoherent scattering contribution ($\sigma_{inc} = 2.7$ barn). In the elastic case this is of particular importance. For this correction the incoherent contribution has been measured directly by energy scans left and right of the ω -point at $Q = 1.1(111)$ and $1.6(111)$. By comparison of the incoherent scattering at other Q values it has been verified that the scattering at $Q = 1.1(111)$ and $Q = 1.6(111)$ is not contaminated by elastic coherent diffuse scattering. The incoherent scattering has then been subtracted from the spectra in Fig. 5a.

The importance of the incoherent elastic scattering is best illustrated by an energy scan at const. $Q = 1.35(111)$ on top of the intensity maxima of the phonon groups. As shown in Fig. 5b. The incoherent scattering is on top of a *broad shoulder* of inelastic scattering the intensity of which is symmetrically distributed over a range of almost 20 meV in energy gain and loss of the sample. The width in energy of the incoherent scattering peak is given by the instrumental resolution.

The crucial point to note is that within the time window of the method ($\leq 10^{-10}$ s) no stable ω embryo exist. We interpret the broad distribution of inelastic intensity in terms of (over)damped phonons, the scattering law of which reads as²¹

$$S(Q, \omega) = f(Q) \frac{1}{1 - e^{-\hbar\omega/k_B T}} \frac{\Gamma \omega}{(\omega^2 - \omega_0^2)^2 + (\Gamma \omega)^2} \quad (1)$$

with the damping Γ and the center frequency ω_0 . The full lines in Fig. 5b correspond to fits to Eqn.(1) convoluted with the measured resolution and the ω -dependent spectrometer sensitivity. Evidently Eqn.(1) accounts for the observed intensity distributions, in particular it gives a large scattering contribution at $\hbar\omega = 0$ without postulating a zero frequency. From the phonon width lifetimes of the fluctuations into ω -like deformations of 0.8×10^{-13} s, 1.4×10^{-13} s and 8×10^{-13} s for β -Ti, β -Zr and β -Hf, respectively, are calculated.

Whereas the L2/3(111) phonon is (over)damped in energy its width in q space is well defined (see Fig. 5a). From its width (fwhm) ~ 0.1 relative lattice units (r.l.u.) a correlation length of $r_c \sim 20 \text{ \AA}$ for the L2/3(111) excitation is estimated.

It is appealing to ask whether this weakness of the bcc lattice towards deformation into the ω phase is related to the β - α transition, i.e. how changes the L2/3(111) phonon upon changing the temperature. Fig. 5b shows measurements of the energy distribution at 895°C, 1025°C and 1430°C, i.e. measurements close to the β - α transition are compared to those near the melting point. Surprisingly the measurements over the whole temperature range (at normal pressure) of the bcc phase show no significant changes in the line shape of the vibrational spectra at $q = 2/3(111)$. An overall decrease of the intensity with increasing temperature can be fully explained by the Debye-Waller factor. Scans in q similar to Fig. 5a at 895°C and 1430°C yielded the

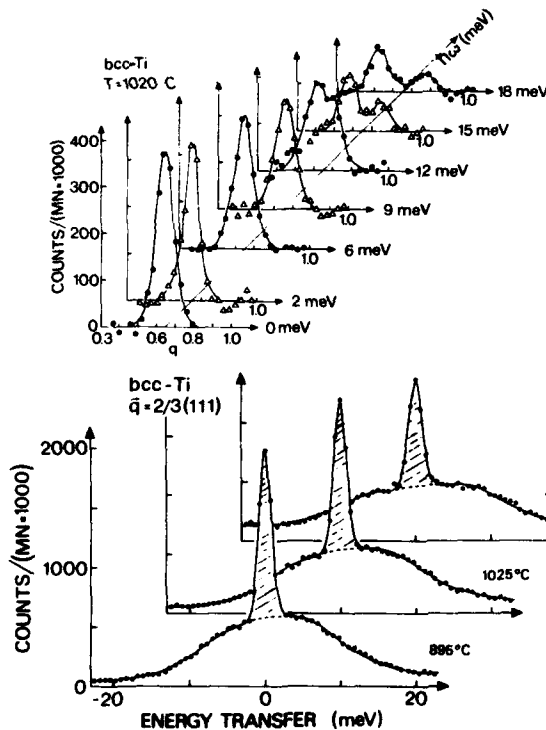


Fig. 5 a) Constant $\hbar\omega$ scans in β -Zr along $q // [\xi\xi\xi]$ for different neutron energy losses. For $\hbar\omega = 0$, the measured incoherent scattering has been subtracted. b) Uncorrected constant q scans in β -Ti at $Q = 1.35(111)$. All spectra fit to the same damped oscillator with $\hbar\omega_0 = 11(1) \text{ meV}$ and $\Gamma = 15(8) \text{ meV}$. The asymmetry of the spectra is purely instrumental. The shaded area indicates the elastic incoherent scattering.^{23,24}

same width of 0.1 r.l.u., i.e. no change in the correlation length r_c could be detected.

With respect to the degree of softening, the temperature is a less relevant parameter. This is in agreement with the pressure temperature phase diagram of group 4 elements (Fig. 1b). The ω phase is stable only under high pressure and therefore a further softening of the phonons at $q = 2/3(111)$ is expected under pressure.

From the experimental fact that the $L2/3(111)$ phonons do not change over the whole temperature region of the bcc phase we conclude that the weakness towards ω fluctuations is an intrinsic bcc property. This view is supported by (a) geometrical and (b) electronic arguments.

a) As depicted in Fig. 6 the rather open bcc structure is characterized by chains of nearest neighbour (NN) atoms in $[111]$ directions. Of all phonons in the $L[\xi\xi\xi]$ branch the phonon at $\xi = 2/3$ with $\lambda = \sqrt{3}/2 \cdot a$ is the only one which leaves the $[111]$ chains undisturbed. Thus atoms along $[111]$, i.e. the direction with shortest distances between the atoms and therefore strong restoring forces, do not alter their distance. The phonon frequency is determined by the weaker (because it does not compress the NN chains) restoring forces between the chains and therefore is low. All other modes with $[\xi\xi\xi]$ propagation will change the distances of the atoms along the chains and thus giving rise to extra restoring forces leading to higher phonon energies. Falter³² evaluated this geometrical effect in a proper mathematical formalism. By expanding the effective ion interaction around reciprocal lattice points he found that for purely geometrical reasons for the $L[\xi\xi\xi]$ mode at $\xi = 2/3$ structure stabilizing terms are switched off, i.e. the bcc lattice tends to destabilize at the ω -point. This purely geometrical argument is valid for all bcc structures and therefore cannot explain the difference in softening of the $L2/3(111)$ phonon in β -Ti and a very stable bcc metal like Cr. The latter one shows no softening in the $L[\xi\xi\xi]$ phonon branch at RT, only a flattening of the dispersion around $\xi = 2/3$ is observed.

b) It is the particular electronic screening which determines whether this

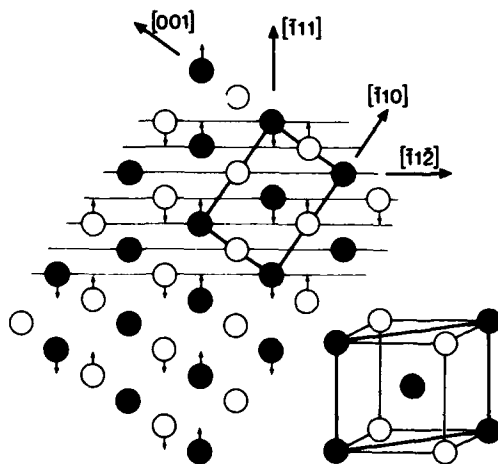


Fig. 6. Displacements of the atoms in a (110) plane due to a $L2/3(111)$ phonon. The same displacements are achieved by a $T_{1/3}(\bar{1}\bar{1}\bar{2})$ phonon with polarization in $[\bar{1}\bar{1}\bar{1}]$. Dark circles: atoms in the (110) plane, open circles: atoms in the (110) planes below and above.

general weakness of the bcc lattice towards the ω structure is enhanced or not. Frozen phonon calculations of Ho et al²³ which are based on the particular band structure reveal that in group 4 metals the charge density is concentrated in d-bonds and runs in chains along the [111] direction with very little interaction between neighbouring chains but strong interaction along a chain. Thus, the geometrical effects are amplified and the L2/3(111) phonons are of particular low frequency. Filling up the d-band the situation is inverted. For instance in group 6 metals it was found that d-bonds entangle the [111] chains and give rise to forces which oppose the shearing motion between neighbouring [111] chains²³. As a consequence the geometrical weakness is compensated and no softening of L2/3(111) phonons is observed in group 6 metals. This picture of the d-electron density as the relevant control parameter is illustrated by Fig. 7a where the degree of softening of the L2/3(111) phonon scales with the decreasing d-electron density.

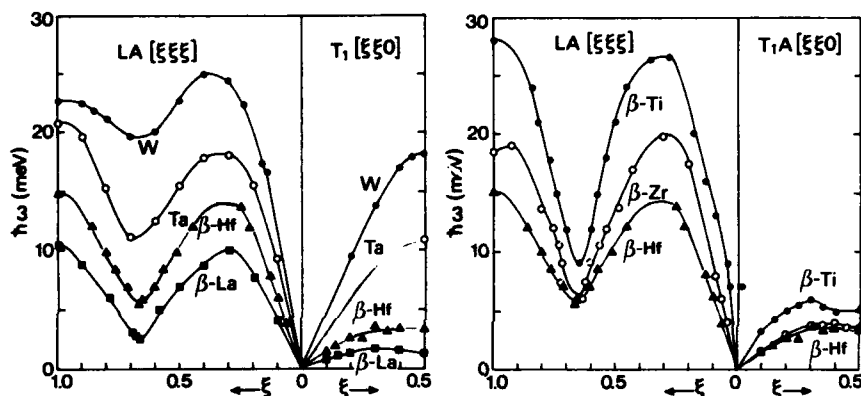


Fig. 7 Comparison of the L[$\xi\xi\xi$] and T_1 [$\xi\xi 0$] phonon branch for the bcc phase of a) metals with different d-electron density and b) for the group 4 metals with two d-electrons^{23,25,26,34,35}.

The calculations of Ho et al²³ for β -Zr predict an energy for the L2/3(111) phonon $\hbar\omega_0 = 7.9$ meV which compares well with the measured centre frequency of β -Zr²⁴ $\hbar\omega_0 = 7.6(5)$ meV. Qualitatively the recent calculations¹⁸⁻²² predict a broad band of low energy excitations at the ω -point but none of them delivers a quantitative description. As mentioned in the Introduction they all predict a kind of elastic precursor, which is in contradiction to the experimental findings at the ω -point in pure β -Ti, β -Zr and β -Hf^{23,26}.

These (over)damped phonons are the signature of strong anharmonicity at the ω -point. In a classical picture it is expected that the anharmonicity increases with increasing mass of the oscillator. The opposite is the case. Fig. 8 shows how the damping systematically decreases with increasing mass of the group 4 elements. Apparently inner shell contributions to the effective ion potential play an essential role in describing the anharmonicity of the L2/3(111) phonon.

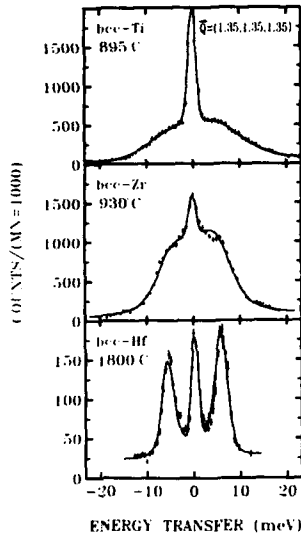


Fig. 8 Energy scans at constant $q = 2/3(111)$ for bcc-Ti, bcc-Zr and bcc-Hf. All spectra are fitted with a damped oscillator with centre energies $\hbar\omega_0 = 11(1)/7.5(5)/5.9(1)$ meV and $\Gamma = 15(8)/10(1)/1.6(2)$ meV for Ti, Zr and Hf, respectively.^{23,25,28}

The $T_{1\bar{1}0}[2(110)$ phonon)

The crystallographic relation for the β - α martensitic phase transition was established by Burgers²⁶.

$$(110)_\beta // (00.1)_\alpha \quad \text{and} \quad [\bar{1}11]_\beta // [\bar{2}1.1]_\alpha$$

The transformation can be achieved by the displacements of two phonons. The transverse zone boundary phonon $T_{1\bar{1}0}$ at the N-point with a displacement of neighbouring (110) planes in opposite $[\bar{1}\bar{1}0]$ directions by $\delta = \sqrt{2}/(12a)$ achieves the hcp stacking sequence. Two equivalent long wavelength shears - for instance $(\bar{1}\bar{1}2)[\bar{1}\bar{1}1]$ and $(\bar{1}\bar{1}2)[1\bar{1}\bar{1}]$ - squeeze the bcc octahedron to a regular hcp one, thereby changing the angle from 109.5°C to 120°C. These shears are roughly those given by the initial slope of the transverse $[2\xi\xi]$ phonon branch with almost $[\bar{1}\bar{1}1]$ polarization, a point which will be explained in the following paragraph.

The whole $T_{1\bar{1}0}[\xi\xi 0]$ phonon branch is of low energy (see Fig. 7b). Similar to the ω -phonon we deal with very broad phonon groups, the broadening increases with increasing q . Again, the appropriate lineshape is given by the Fourier transform of a damped oscillator. The $T_{1\bar{1}0}[\xi\xi 0]$ phonons have been measured over the whole temperature range of the bcc phase. On approaching T_0 the N-point phonon energy decreases considerably (Fig. 9) but the MT clearly occurs at finite frequency.

These observations may be compared to the results of frozen phonon calculations of the N-point phonon in Zr¹⁸ which have shown that the bcc phase is only stabilized by anharmonic contributions. For β -Zr at $T = 1123^\circ\text{C}$ the calculations yielded a phonon energy at the N-point of $\hbar\omega_N = 4.14(12)$ meV in

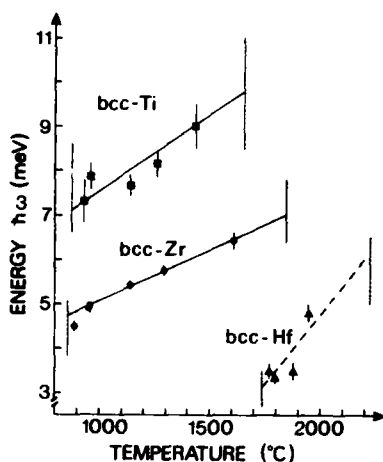


Fig. 9 Temperature dependence of the $T_{1/2}(110)$ phonon in β -Ti, β -Zr and β -Hf^{24,25,26}.

good agreement with our experimental result $\hbar\omega_N = 5.4(1)$ for $T = 1150^\circ\text{C}$. The temperature dependence of $\hbar\omega_N$ as calculated¹⁸, $d\hbar\omega_N/dT = 8 \times 10^{-3} \text{ meV/K}$, and our measurements (Fig. 9) $d\hbar\omega_N/dT = 3.4(4) \times 10^{-3} \text{ meV/K}$ do not agree so well. However, considering the problems of such calculations we regard this discrepancy as not so severe. A recent thermodynamic approach to the problem by the expansion of the free energy in terms of the dynamical displacements has independently suggested that a further small softening of the relevant low energy phonon is sufficient to produce a lower minimum of the free energy for the low temperature phase²⁰.

Similar to the case of the ω -phonon no condensation of the damped N-point phonon to an elastic superstructure peak around $q = 1/2(110)$ has been found.

Relation between the $L_{2/3}(111)$ and the $T_{1/2}(110)$ phonon

Two distinct regions of low energy phonons have been found in high symmetry directions of the bcc phase of the group 4 metals. The low energy and temperature dependent $T_1[\xi\xi 0]$ phonon branch is a precursor fluctuation of the martensitic β to α transition. The low energy $L_{2/3}(111)$ phonon reflects the intrinsic bcc property of a weak restoring force for displacements towards the ω phase. It is appealing to ask whether the two soft phonons are related to each other.

From Fig. 6 it can be seen that the displacements achieved by the $L_{2/3}(\bar{1}11)$ mode are identically to the displacements of a transverse phonon in $[\xi\xi \bar{2}\bar{2}]$ with a $[\bar{1}11]$ polarization and $\xi = 1/3$. Changing to equivalent indices we state that the $L_{2/3}(111)$ mode is equivalent to a $T_{1/3}(211)$ phonon with $[\bar{1}11]$ polarization. By similar arguments it can be shown that the $T_{1/2}(110)$ mode is identical to the $T_{1/2}(211)$ mode with $[\bar{1}10]$ polarization. In other words both low energy phonons lie in the same off-symmetry $T_1[2\xi \xi\xi]$ phonon branch. Furthermore the initial slope of this phonon branch is given by the long wavelength shear of

(211) planes in a direction close to $[\bar{1}11]$, i.e. the shear needed for the β - α transition. Because the propagation is in off-symmetry direction the polarization (or Eigenvector) changes with ω , for $\xi \rightarrow 0$ it is close to $[\bar{1}11]$, at $\xi = 1/3$ it is exactly $[\bar{1}11]$ and rotates to $[\bar{1}10]$ at $\xi = 1/2$.¹¹

It is evident that *all* phonons needed for the phase transitions in the group 4 metals lie on the same off-symmetry branch and it is anticipated that they are connected via a valley of low energy and (over)damped phonons on the Brillouin zone boundary along $[2\xi\xi\xi]$. This is best shown in the case of β -Zr in Fig. 3. Phonons along $T_1[2\xi\xi\xi]$ are of low energy and as indicated by the bars a valley of overdamped phonons connects the $T_1/3(211)$ (ω -point) phonon with the $T_1/2(211)$ (N-point) phonon.

A PICTURE OF THE LATTICE VIBRATIONS IN REAL SPACE

Summarizing where soft modes are observed in q space we state : along $[\xi\xi\xi]$ direction soft modes are observed in a narrow range around $\xi = 2/3$, i.e. indicating a correlation length in real space over roughly 20 Å along $[111]$. Perpendicular to $[111]$, namely in $[1\bar{1}0]$ and $[11\bar{2}]$ phonons propagate almost without dispersion, i.e. are more *localized*. So we end up with the following qualitative picture of the lattice vibrations of group 4 metals in real space : excitations propagate along $[111]$ chains. Excitations perpendicular to $[111]$ are to a certain extent localized. If a given $[111]$ chain vibrates along its direction neighbouring $[111]$ chains do not follow this motion. Along $[111]$ chains one has strong restoring forces whereas those perpendicular to $[111]$ are weak.

The soft phonons are located on the Brillouin zone surface. Different to long wavelength shear modes these large q modes achieve a maximum shift of neighbouring planes to each other, i.e. are best suited to achieve the displacement necessary for displacive or martensitic phase transitions.

DEFECT DRIVEN CONDENSATION OF SOFT AND OVERDAMPED MODES

With regard to the elastic precursors or central peaks all theoretical calculations¹⁸⁻²² discuss a freezing of the amplitudes of the low energy phonons which are related to the phase transition which then produce a kind of (quasi)elastic scattering. The elastic measurements on *high purity* β -Ti and β -Zr in various Brillouin zones and at various temperatures show, however, no intensity which could be interpreted in terms of elastic precursors of the transition. The precursor effects we find, namely the pronounced softening of overdamped phonons in the $T_1[\xi\xi0]$ branch, are of purely dynamical nature.

We suggest that the elastic precursors observed in metallic alloys on the basis of group 4 metals are defect driven. To prove that, we alloyed Ti and Zr with different impurities such as oxygen, nitrogen, Co, Nb or Cr.

Upon alloying in the order of 1 at% oxygen or nitrogen into β -Ti or β -Zr extremely temperature and sample dependent elastic peaks are found in different Brillouin zones²⁴. The width of these peaks never exceeds the instrumental resolution and their intensity increases exponentially upon approaching T_0 . Some additional tests unambiguously proved that these satellite peaks are only due to the coherent existence of α and β phase, caused by the alloying of interstitial impurities.

As stated before the elastic diffuse scattering in pure samples around the ω -point at $q = 2/3(111)$ is of purely inelastic nature (due to overdamped phonons). Careful analysis of this diffuse scattering in alloyed samples revealed an increase of this diffuse intensity, the intensity of which depends on the impurity and its concentration. Fig.10 shows this increase of diffuse elastic intensity with respect to the neighbouring inelastic phonon intensity for different β -Zr alloys. In all cases this *purely elastic* intensity does not alter significantly with temperature (with the exception of a Debye-Waller factor), i.e. turned out to be an intrinsic property of the bcc phase.

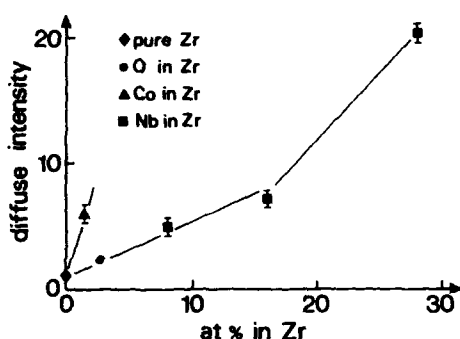


Fig. 10 Diffuse elastic intensity at $Q = 1.35(111)$ in units of the neighbouring $L2/3(111)$ phonon intensity for different solutes in β -Zr. The intensities refer to temperatures above T_0 , i.e. the alloys are in thermal equilibrium.

So, two effects occur upon alloying : i) Mainly interstitial impurities shift the sample at a given temperature in a two phase region of coherent existence of β and α phase. ii) The overdamped and soft ω -phonon freezes upon alloying substitutional and interstitial impurities to a static (within the time resolution of the method) displacement giving rise to an ω -like diffuse scattering.

SUMMARY

The phonon dispersion of the bcc phase of the *pure* group 4 metals Ti, Zr and Hf is dominated by a valley of anomalous low frequency and strongly damped phonons along $[2\frac{1}{2}\frac{1}{2}]$ propagation, which is related to the β to ω and β to α martensitic phase transitions. The low lying $L2/3(111)$ phonon does not change with temperature and is due to a bcc inherent weakness towards ω displacements. The $T_11/2(110)$ phonon decreases drastically upon approaching T_0 and is a precursor fluctuation of the β to α transition. Different to alloys the overdamped phonons, which achieve the displacements for the martensitic transition do not condensate to (quasi)static displacements.

ACKNOWLEDGEMENTS

Collaboration with C. Herzig and G. Vogl, and financial support given by Bundesministerium für Forschung und Technologie, FRG, under Project No. 03-HE2MUE-0 are gratefully acknowledged.

REFERENCES

1. La makes a certain difference. Its high temperature bcc phase transforms

- into two steps into different close packed structures. At 865°C, it transforms to fcc, which again at 336°C transforms to double hcp.
2. S. Sikka, Y.K. Vahra, and P. Chidambaram, *Progress in Material Science* **27**, 245 (1982).
 3. J.W. Christian, *Theory of Transformations in Metals and Alloys*, 2nd ed. (Pergamon Press, Oxford, 1975) p.12.
 4. S.K. Satija, S.M. Shapiro, M.B. Salamon and C.M. Wayman, *Phys. Rev. B* **29**, 6031 (1984).
 5. H. Tietze, M. Müllner and B. Renker, *J. Phys. C* **17**, L529 (1984).
 6. M. Müllner, H. Tietze, G. Eckold and W. Assmus, *Proc. Int. Conf. on Martensitic Transformations, ICOMAT 86*, Nara (Japan), ed. by I. Tamura (The Japan Inst. of Metals) p. 159 (1987).
 7. S.M. Shapiro, B.X. Yang, G. Shirane, Y. Noda and L.E. Tanner, *Phys. Rev. Lett.* **62**, 1298 (1989).
 8. R.J. Gooding and J.A. Krumhansl, *Phys. Rev. B* **39**, 1535 (1989).
 9. S.C. Moss, D.T. Keating, J.D. Axe, in *Phase Transitions*, ed. by L.E. Cross (Pergamon, New York) p. 179 (1973).
 10. J.D. Axe, D.T. Keating and S.C. Moss, *Phys. Rev. Lett.* **35**, 530 (1975).
 11. Y. Noda, Y. Yamada and S.M. Shapiro, *Phys. Rev. B* **40**, 5995 (1989).
 12. G. Ernst, C. Artner, O. Blaschko and G. Krexner, *Phys. Rev. B* **33**, 6465 (1986).
 13. H.G. Smith, *Phys. Rev. Lett.* **58**, 1228 (1987).
 14. R.J. Gooding and J.A. Krumhansl, *Phys. Rev. B* **38**, 1695 (1989).
 15. O. Blaschko and G. Krexner, *Phys. Rev. B* **30**, 1667 (1984).
 16. M. Iizumi, *J. Phys. Soc. of Japan* **52**, 549 (1983).
 17. O. Blaschko, G. Krexner, J. Pleschiutchnig, G. Ernst, C. Hitzenberger, H.P. Karnthaler and A. Korner, *Phys. Rev. Lett.* **60**, 2800 (1988).
 18. Y.-Y. Ye, Y. Chen, K.-M. Ho, B.N. Harmon and P.-A. Lindgard, *Phys. Rev. Lett.* **58**, 1769 (1987).
 19. Y. Chen, K.-M. Ho and B.N. Harmon, *Phys. Rev. B* **37**, 233 (1988).
 20. P.-A. Lindgard and O.G. Mouritsen, *Phys. Rev.* **57**, 2458 (1986).
 21. J.A. Krumhansl and R.J. Gooding, *Phys. Rev. B* **39**, 3047 (1989).
 22. W.C. Kerr and A.R. Bishop, *Phys. Rev. B* **34**, 6295 (1986).
 23. W. Petry, T. Flottmann, A. Heiming, J. Trampenau, M. Alba and G. Vogl, *Phys. Rev. Lett.* **61**, 722 (1988).
 24. A. Heiming, W. Petry, J. Trampenau, M. Alba, C. Herzig, and G. Vogl, *Phys. Rev. B* (1989), in press.
 25. A. Heiming, W. Petry, J. Trampenau, M. Alba, C. Herzig, H.R. Schober and G. Vogl, to be published.
 26. J. Trampenau, W. Petry, A. Heiming, M. Alba, C. Herzig, W. Miekele and H.R. Schober, to be published.
 27. T. Flottmann, W. Petry, R. Serve and G. Vogl, *Nucl. Instrum. & Methods. A* **280**, 165 (1987).
 28. C. Stassis, J. Zarestky and N. Wakabayashi, *Phys. Rev. Lett.* **41**, 1726 (1978).
 29. C. Stassis and J. Zarestky, *Solid State Comm.* **52**, 9 (1984).
 30. D. de Fontaine and O. Buck, *Phil. Mag.* **27**, 967 (1973).
 31. S.W. Lovesey, *Theory of Neutron Scattering from Condensed Matter*, Vol. 1 (Oxford Science Publ., Oxford, 1986) p. 299.
 32. C. Falter, *Physics Reports* **164**, 1 (1988).
 33. K.-M. Ho, C.-L. Fu and B.N. Harmon, *Phys. Rev. B* **28**, 6687 (1983); **29**, 1575 (1984).
 34. H.R. Schober and P.H. Dederichs in *Landolt-Börnstein*, New Series, Group III, Vol. 13a (Springer Verlag, Berlin, 1981) and references therein.
 35. C. Stassis in J.D. Axe and R.M. Nicklow, *Physics Today*, Jan. 1985, p. 27.
 36. W.G. Burgers, *Physica* **1**, 561 (1934).

POLARIZATION RELAXATION IN KDP-ISOMORPH FERROELECTRICS

VICKI HOMER* AND RONALD EDGE**

*University of South Carolina, Dept. of Physics, Columbia, SC 29208

**University of South Carolina, Dept. of Physics, Columbia, SC 29208

ABSTRACT

The two-dimensional position sensitive detector at IPNS was used to probe the splitting of a single Bragg peak of the ferroelectric KD₂PO₄ (DKDP) at temperatures below the Curie point. The (440) peak was split into four components as the crystal itself divided into four domains. When the crystal was subjected to electric fields of sufficient strength and duration, these peaks would change in relative intensity, thus displaying the rearrangement of the domain structure as the crystal changed its level of polarization. Even at temperatures 15-20K below the Curie point, the polarized crystal was observed to relax back to an almost completely unpolarized state upon removal of the applied electric field. This indicates that the true coercive field for the crystal at this temperature was much smaller than values previously reported [1]. Low frequency dielectric constant studies using a capacitance bridge have since been conducted, which confirm and expand on these results.

INTRODUCTION

Neutron scattering has been used to observe the domain splitting of the ferroelectric KH₂PO₄ (and some of its isomorphs) since the early 1950's [2]. Recent work done at the Joint Institute for Nuclear Research at Dubna, USSR, [1] used a time-of-flight position sensitive detector to monitor the polarization of (DKDP) as electric fields of increasing intensity were applied to the crystal. Their crystals were taken from a completely depolarized to a fully polarized state in four steps of applied electric field. At each stage, the changes in the contour map of the split peaks showed the corresponding changes in the crystal's polarization structure. Their results established that, given an instrument of sufficient resolution, it should be possible to observe at least qualitative changes in the crystal's polarization state as it is subjected to electric fields of different durations and intensities. However, it was not clear from their published data how sensitive this technique is to relatively small changes in the crystal's polarization state.

EXPERIMENT

In order to determine whether this technique could be used to probe other aspects of ferroelectric behavior, and to test the plausibility of obtaining quantitative results, we conducted similar experiments on the single crystal diffractometer at Argonne National Laboratory, using time-of-flight with a two-dimensional position sensitive detector. The crystals we used were 95% pure DKDP obtained from Lasermetrics, cut to 3x3x1.5 cu.mm. and polished with glycol-wetted silk; gold/chromium electrodes were then evaporated on the crystal surfaces perpendicular to the ferroelectric axis. The electric fields were applied in one of two ways: in square wave pulses of 533 V/cm lasting 33 msec each, with the data collected after the pulses had been applied, or by applying a DC voltage across the crystal while the data was being collected.

When DKDP is cooled below the Curie point (T_c), the lattice divides into four domains. Two have positive polarization (with piezoelectric strain developed along axes orthogonal to each other and to the ferroelectric axis), and the other two have negative polarization, with corresponding strain orientations. The symmetry of the strains causes the Bragg peaks in the (hk0) planes in reciprocal lattice space to be split into four components equally

spaced about the point $(kk0)$. The fractional volume of scattering intensity of each domain peak measures the fraction of total crystal volume having the sublattice associated with that domain. The relative peak heights of these split peaks roughly corresponds to this fractional volume (as long as the contributions to the peak height from its neighbors are taken into consideration). By observing these changes in relative peak height, we obtain a first approximation of the corresponding changes taking place within the crystal itself.

DISCUSSION AND RESULTS

The four components of the split Bragg peak we examined, the (440) peak, are far from being completely resolved. In the limited beam time available for our initial experiment, we chose to concentrate on the response of the crystal to different modes of applied electric field, rather than focus on the problem of determining the peak shape sufficiently well to assign numbers to the fraction of crystal volume corresponding to the four domain types. Nevertheless, we did make the following observations:

- i) the position of the domain peaks are readily determined from the contour spectra (see fig. 1): they are correctly oriented, and their observed degree of splitting indicates the crystal underwent "24" of piezoelectric strain;
- ii) the peak shape appears to be the same for all four domains (as expected by symmetry),
- iii) the wings of each domain peak fall essentially to zero within twice the distance between them, which will greatly facilitate future convolution algorithms,
- iv) crystals exposed to similar conditions exhibit similar patterns of domain structure, and
- v) a rough estimate of the peak shape led to good agreement between expected values for peak heights and our observed results, for different runs with the same crystal at the same temperature.

From the above observations, it is reasonable to suppose that when more spectra are collected at the opposing extremes of fully polarized crystals (monodomain), and completely unpolarized crystals (four identical domains), the task of determining the peak shape, and thus quantifying the data, will become relatively straightforward. [This will be one of our first priorities when we return to Argonne in January.]

First the electric field was applied to the crystal in square pulses of 533 V/cm, lasting 33mseconds each. These values were chosen to match the experimental parameters of related studies of domain reversal which had been conducted at the University of South Carolina, using electron spin resonance to monitor the domain switching [3]. Although we chose temperatures closer to those used by the Russian group in their experiments (~200K) than the temperatures used in the experiments at South Carolina (~130K), we were far enough below the Curie point (~218K for our crystals) for it to be reasonable to assume that the crystals would be subject to little back-relaxation. (This is equivalent to the assumption that a significant coercive field would be required to depolarize the crystals, once we had put them in a polarized state.) However, repeated attempts to polarize the crystal in such a manner clearly failed (fig. 2(a,b), and numerous other spectra not shown, almost identical to these). We had to assume that either the duration of the pulse was too brief, that the amount of field being applied was inadequate, or that the crystal was undergoing back-relaxation too quickly to be able to monitor the polarization.

To test the circuit itself, and to ensure that the crystal really did become polarized, we then applied DC fields across the crystal, and collected data while the field was being applied. The initial value of field chosen, 333 V/cm, was not strong enough to polarize the crystal (fig. 2c). However, application of 1,300 V/cm (fig. 2d) brought the crystal to nearly complete polarization. At this point, the field was removed and another data set immediately taken (fig. 2e). It is clear from the spectra that the crystal had relaxed back to a nearly completely depolarized state, merely by removing the applied electric field, thus indicating that the 'equilibrium' coercive field for the crystal at this temperature must be quite small. To check this result, another crystal was examined, under slightly different conditions. This second crystal was brought to nearly complete polarization with a field of 4 kV/cm, at 210K (fig. 3a), and then brought down to 180K while the field was still on. When the field was removed and data collected (fig. 3b), the spectra shows that once more the crystal had nearly completely depolarized, in the absence of any opposing applied field, at a temperature $>35K$ below the Curie point!

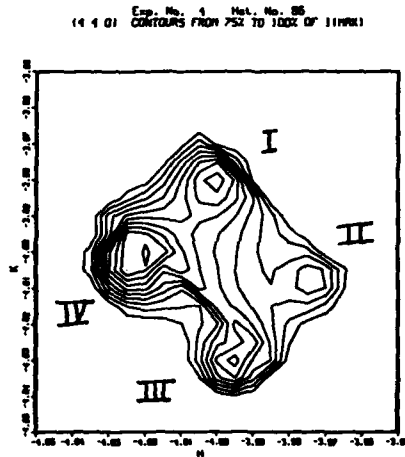


FIG 1: Peaks I and III represent domains having strain along the tetragonal a-axis; peaks II and IV show domains having strain along the b-axis. Peaks III and IV are polarized up. Peak IV is the most intense; peaks I, II, and III have intensities of 93%, 80%, and 95%, respectively, of peak IV.

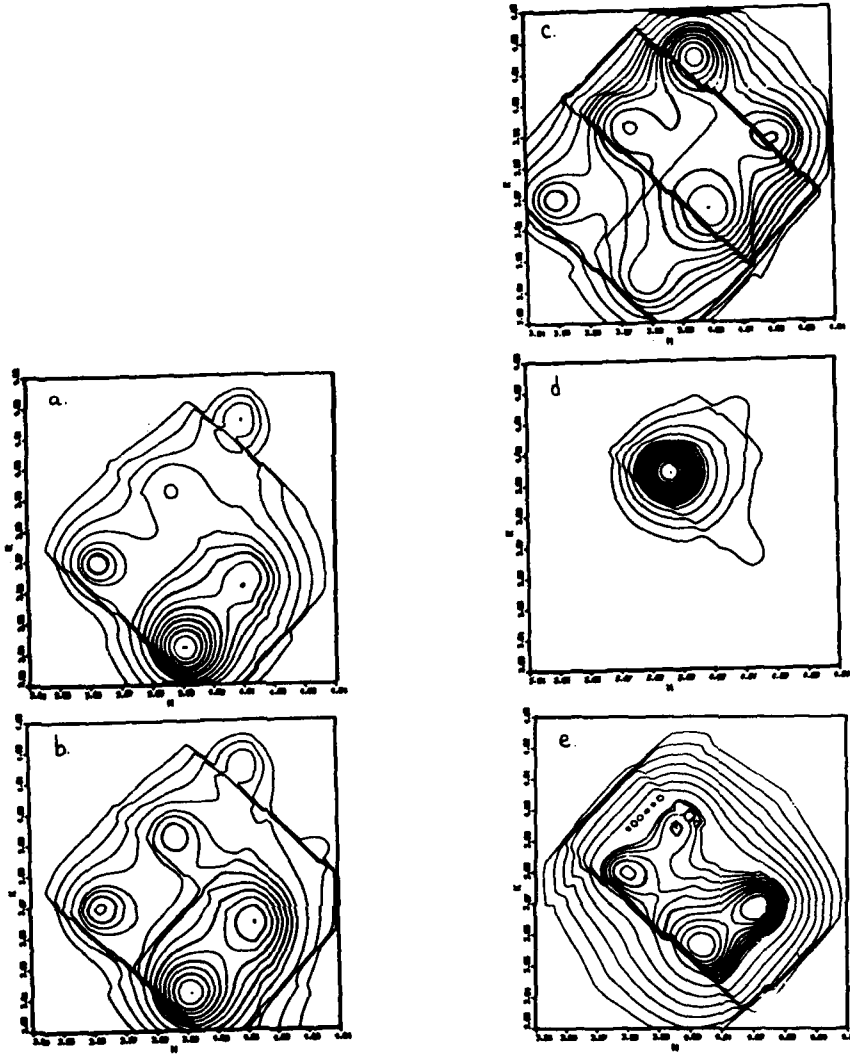


FIG 2: (a) no field applied
(b) 150 pulses (533 V/cm) applied
(c) 333 V/cm DC applied
(d) 1,300 V/cm DC applied
(e) 0.5 hr after removal of the electric field used in (d)

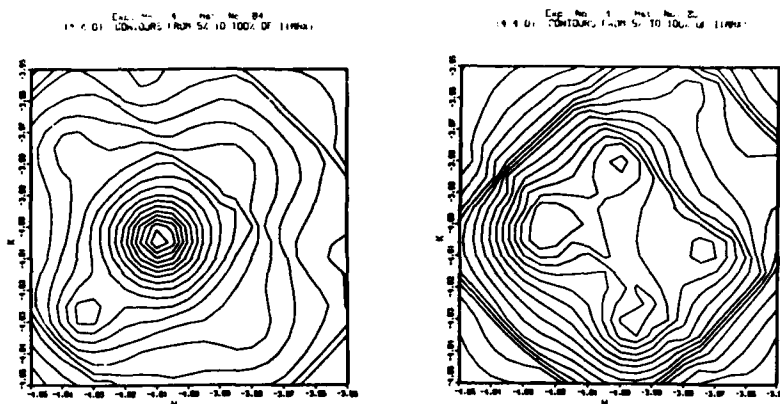


FIG 3: (a) Crystal polarized by 4 kV/cm electric field.
 (b) Crystal 0.5 hr after removal of the field in (a).

These results indicated that DKDP has domains that are far more mobile than had previously been supposed [1]. Low frequency dielectric constant studies were then conducted to test the responsiveness of the dielectric constant as a function of temperature, for a range of temperatures from a few degrees above the Curie point (T_c) to temperatures well below T_c . At the same time, because the crystals that had been used in the ESR study of domain switching had necessarily been 'doped' with 5% KH_2AsO_4 , and then irradiated with x-rays, in order to create the paramagnetic centers needed to use ESR, we also looked at the low frequency dielectric constant behavior for irradiated DKDP, irradiated KDP, pure KDP, doped KDP, and doped, irradiated KDP. (These results will be presented in detail elsewhere.)

One of the principal results from these experiments was that DKDP has highly mobile domain walls for 30-40K below the transition temperature, where it then appears to undergo a 'freezing' process much like that observed for KDP. Indeed, by using the real part of the dielectric constant (ϵ') at T_c as an indicator of the domain structure at its most fluid and most highly mobile state, and then looking at the ratio of $\epsilon'(T)$ to $\epsilon'(T_c)$, it can be shown that DKDP loses very little of its domain mobility for a considerable temperature range below T_c . Interestingly, doped KDP that has not been irradiated, and irradiated KDP and DKDP that have not been doped, all maintain a reasonably high level of domain mobility (as characterized by high ratios of $\epsilon'(T)$ to $\epsilon'(T_c)$) for a considerable temperature region below T_c . It is only when KDP is both doped and irradiated that $\epsilon'(T)$ drops within 3-5 degrees below T_c to only a small fraction of its maximum value at T_c . This strongly suggests that it is the creation of the AsO_4 free radicals caused by the radiation that quite possibly creates the pinning centers that inhibit domain mobility.

SUMMARY

We have explored how technical improvements in neutron scattering methods can be exploited to yield increasingly subtle and detailed information about the polarization behavior of the ferroelectric DKDP as its responds to the introduction (and removal) of applied electric fields. One significant observation was that DKDP has highly mobile domain walls, which maintain their mobility at temperatures far below the Curie point. This leads to the existence of considerable backrelaxation of the polarization upon removal of the applied electric field, as later verified in independent studies of the low frequency dielectric constant.

ACKNOWLEDGEMENTS

It is a pleasure to acknowledge the helpful discussions with Robert Nicklow at Oak Ridge National Laboratory, the unending patience, suggestions, and assistance of Art Schultz at Argonne, and the translations of technical Russian, as well as the different point of view provided by a theoretician, Lev Vaidman.

REFERENCES

1. A.M. Balagurov, I.D. Damm, B.N. Savenko, and L.A. Shuvalov, *Sov. Phys. Solid State* 22, 1595 (1980).
2. G.E. Bacon and R.S. Pease, *Proc. R. Soc. London Ser. A* 230, 359 (1955).
3. R.D. Truesdale, H.A. Farach, and C.P. Poole, *Phys. Rev. B* 28, 5268 (1983).

[This work has benefited from the use of the Intense Pulsed Neutron Source at Argonne National Laboratory. This facility is funded by the U.S. Department of Energy, BES-Materials Science, under Contract W-31-109-Eng-38.]

STRUCTURE OF $\text{ErBa}_2\text{Cu}_3\text{O}_x$ IN THE COMPOSITION RANGE $6.1 \leq x \leq 7.0$

E. PÖRSCHKE*, P. MEUFFELS* AND B. RUPP**

* Institut für Festkörperforschung, KFA Jülich, D-5170 Jülich, Fed. Rep. Germany

** Lawrence Livermore National Laboratory, Livermore, CA 94550, USA

ABSTRACT

The structure of a series of homogeneous $\text{ErBa}_2\text{Cu}_3\text{O}_x$ powder samples ($6.1 \leq x \leq 7.0$) has been determined by elastic neutron scattering using the Rietveld method of profile refinement. All samples were prepared in the same way using a defined absorption-desorption method.

By removing oxygen the c axis expands, whilst the Cu2-Cu2 and the Ba-Ba distances contract. Accordingly, the most significant changes in atomic distances occur between the Cu2-O2,3 planes and the Cu1-O4-Cu1 chains. With decreasing oxygen content the distance between the Cu-O planes and the Cu-O-Cu chains increases and the oxygen (0, 0, z) apex atom O1 moves closer to the Cu-O-Cu chains withdrawing from the Cu-O planes. The O1-plane and O1-chain distances are monotonic functions of the oxygen content, but the x dependence of these bonding lengths seems to be much stronger below $x < 6.5$. The change of the interatomic distances can be correlated to the suppression of superconductivity which clearly occurs within the orthorhombic phase.

INTRODUCTION

Various groups have replaced Y in the 123-compound by a Rare Earth atom which carries a magnetic moment to investigate crystal field effects [1] or magnetic superstructures [2]. Substituting Y by most of the Rare Earths only slightly affects the superconducting properties [3]. These are, however, strongly influenced by the amount of oxygen in $\text{YBa}_2\text{Cu}_3\text{O}_x$ which can be varied between 6.0 and 7.0 [4]. $\text{YBa}_2\text{Cu}_3\text{O}_x$ has a defect perovskite structure within this range of oxygen concentrations. At oxygen contents < 6.32 the crystal structure is tetragonal at room temperature [5]. At oxygen contents > 6.32 it becomes orthorhombic as a result of oxygen ordering driven by repulsive O-O interactions [6, 7, 8]. The transition temperature to superconductivity, T_c , which is 92 K for $x = 7$ decreases with decreasing x in a steplike manner until at $x \approx 6.4$ the material is no longer a superconductor. Cava et al. showed that there is no direct correlation between the loss of superconductivity and the structural transition from orthorhombic to tetragonal [9].

In the $\text{ErBa}_2\text{Cu}_3\text{O}_x$ system, the orthorhombic-to-tetragonal (O-T) phase transformation at room temperature occurs at a lower oxygen content ($x \approx 6.25$ [10]) than in $\text{YBa}_2\text{Cu}_3\text{O}_x$ [5]. Hence we chose to study $\text{ErBa}_2\text{Cu}_3\text{O}_x$ to see more clearly the effects of structure on the electronic properties. Qualitatively, the results are not strongly influenced by the Er ions and should also be valid for $\text{YBa}_2\text{Cu}_3\text{O}_x$.

EXPERIMENTAL

The $\text{ErBa}_2\text{Cu}_3\text{O}_x$ starting material was produced from stoichiometric amounts of Er_2O_3 , BaCO_3 and CuO powders by the following standard sintering process. The powders were thoroughly mixed, pressed to pellets and then fired twice under flowing oxygen gas up to a temperature of 950°C. Between the two firing processes the material was reground to enhance the sample homogeneity. The material prepared in this way was single phased with $T_c \approx 92$ K.

The oxygen content, x, of 12-gr batches of $\text{ErBa}_2\text{Cu}_3\text{O}_x$ powder was then adjusted in a volumetric system by a temperature and time controlled oxygen desorption-absorption process [5]. First, the samples were degassed under vacuum at 750°C to attain a common reference state for the subsequent absorption of oxygen. The reference state is the equilibrium state of $\text{ErBa}_2\text{Cu}_3\text{O}_x$ at 750°C under an oxygen pressure of $\approx 1.5 \times 10^{-5}$ mbar. Then at 750°C a defined amount of oxygen gas was introduced to the chamber containing the sample. Upon cooling to room temperature at a rate of 0.75°C/min all the oxygen gas was absorbed by the sample.

To estimate the oxygen contents of the samples in the reference state, the $\text{ErBa}_2\text{Cu}_3\text{O}_7$ sample was produced with an excess amount of oxygen gas in the sample chamber. It absorbed $0.94(\pm 0.02)$ mole of O_2 per two moles of $\text{ErBa}_2\text{Cu}_3\text{O}_x$. Thus taking into consideration an oxygen content of $x = 6.06(2)$ in the reference state we prepared seven samples with final concentrations of $x = 6.06, 6.30, 6.50, 6.62, 6.75, 6.87$ and 7.0 (with an absolute error of about $\pm 0.02 - 0.03$). The oxygen concentration x can also be obtained from the neutron diffraction data adding the site occupation factors of all the oxygen sites. Since the site occupation factors are an absolute measure, the x values as derived from the neutron scattering data have been used to characterize the samples: $x = 6.11(2), 6.34(2), 6.53(2), 6.64(2), 6.78(2), 6.87(1)$ and $7.02(2)$.

After preparation, the samples were placed in vanadium containers (10 mm diameter, 50 mm height) which were sealed under helium using indium wire gaskets. Neutron diffraction data were collected in the 2θ angular range $3^\circ - 130^\circ$ on the multidetector powder diffractometer DMC at the SAPHIR reactor in Würenlingen, Switzerland (liquid-nitrogen-cooled Si filter, vertically focusing Ge(311) monochromator, collimation $10'/-12'$) at a temperature of 20 K. At this temperature all samples showing superconductivity were in the superconducting state. The wavelength used for all experiments was $1.7060(5)\text{Å}$ as calibrated from spectra of pure silicon. The diffraction patterns were evaluated by a Rietveld refinement [11] using a modified code of Hewat [12, 13] that includes the refinement of anisotropic temperature factors.

RESULTS AND DISCUSSION

All neutron spectra could be indexed on the basis of the oxygen-deficient triple perovskite cell. No extra peaks larger than 3 estimated standard deviations (e.s.d.'s) of background due to additional phases or superstructure were observed.

We started refining 165 reflections of the $\text{ErBa}_2\text{Cu}_3\text{O}_7$ sample in the orthorhombic space group Pmmm (No. 47, D_{2h}^1). The input parameters for this refinement were taken from a neutron study on $\text{YBa}_2\text{Cu}_3\text{O}_7$ at 10 K [14]. In the first runs only the scale factor, the zero point, the profile parameters U, V, W and the cell constants a, b, and c were allowed to vary. After the refinement stabilized, the z parameters were opened to refinement and in subsequent refinement cycles the temperature factors were determined. The site occupation factor of the O4 chain atoms was opened during all the final runs. All other atoms, including the oxygen apex atom O1 and the Cu-O plane atoms O2 and O3, showed only insignificant over or under occupation (O1, O2 and O3 site occupation factors were 1.0 ± 0.02 to ± 0.03) so that they were fixed to 1.0 in all runs to reduce excessive parameter freedom. The temperature factor of the O4 atom, when refined in an isotropic model, was unusually large. The refinement was significantly improved by using anisotropic B factors. This was indicated by the decrease of the reliability factors as well as proved by implementation of a significance test [15] searching for differences in the model predictions. In the final refinement cycles all profile, lattice, and structural parameters were varied simultaneously until the weighted reliability factor R_w differed by less than 1/1000 in two successive runs.

The refinements for the oxygen deficient samples were carried out in the same way for the succession of samples with decreasing oxygen content, always using the results of the preceding calculation as starting input parameters. The refinement of the $\text{ErBa}_2\text{Cu}_3\text{O}_{6.11}$ data in the Pmmm space group gave equal cell constants a and b and equal occupations of the O5 (1/2, 0, 0) and O4 sites. The use of anisotropic B factors did not improve the fit. The spectrum was thus refined in the $P4/mmm$ space group (No. 123, D_{4h}^1) fitting 100 reflexions with 19 parameters. Attempts to refine $\text{ErBa}_2\text{Cu}_3\text{O}_{6.34}$ in the $P4/mmm$ space group were not successful. The cell constants a and b did not refine to equal values. If oxygen was forced onto the O5 site the temperature factor increased to physically unrealistic values. If we used a fixed B factor with the same value as for the O4 atom the O5 site occupation factor was calculated to 0 ± 0.03 . The same result was found for all samples refined in the Pmmm space group.

In all cases the peak profiles were described well by a Gaussian function. The profile parameters U, V and W were in the range usually observed for intermetallic powders (using the same spectrometer configuration). They did not indicate any anomaly in the diffraction peak width. The results of our refinements are listed in Table I including lattice and structural parameters as well as the reliability factors, R, for all refinements (assigning

TABLE I. Structural parameters of $\text{ErBa}_2\text{Cu}_3\text{O}_x$ at 20 K. For refined parameters the e.s.d.'s of the last significant digit are given in parentheses. The reliability factors were evaluated following the procedure of Young, Prince and Sparks [16]. $\text{ErBa}_2\text{Cu}_3\text{O}_x$, space group Pmmm [No. 47, D_{2h}^1 , $x=6.34, 6.53, 6.64, 6.78, 6.87, 7.02$; Er: 1h, Ba: 2t, Cu1: 1a, Cu2, O1: 2q, O2: 2s, O3: 2r, O4: 1e] or $P4/mmm$ [No. 123, D_{4h}^1 , $x=6.11$; Er: 1d, Ba: 2h, Cu1: 1a, Cu2, O1: 2g, O2=O3: 4i, O4: 2f]. Neutron wavelength 1.7060(5)Å. Units for temperature factors B: Å². Form of the temperature factors is isotropic: $\exp(-B_{\text{iso}} \sin^2 \theta / \lambda^2)$ and anisotropic: $\exp[-(h^2 a^2 B_{11} + k^2 b^2 B_{22} + l^2 c^2 B_{33})]$

Atom	Param.	6.11	6.34	6.53	6.64	6.78	6.87	7.02
Er	B	0.20(9)	0.32(8)	0.27(7)	0.32(8)	0.46(10)	0.22(7)	0.21(6)
Ba	B	0.02(9)	0.28(9)	0.19(9)	0.19(9)	0.07(11)	0.41(8)	0.30(6)
	s	0.1951(4)	0.1935(3)	0.1899(3)	0.1882(4)	0.1864(5)	0.1852(4)	0.1838(3)
Cu1	B	0.21(9)	0.20(8)	0.27(8)	0.12(8)	0.14(10)	0.10(7)	0.00(6)
Cu2	B	0.01(6)	0.10(5)	0.08(5)	0.11(6)	0.34(7)	0.04(5)	0.07(4)
	s	0.3610(3)	0.3609(3)	0.3584(3)	0.3575(3)	0.3567(4)	0.3565(2)	0.3552(2)
O1	B	0.35(9)	0.62(8)	0.41(8)	0.39(9)	0.39(12)	0.16(8)	0.30(7)
	s	0.1532(4)	0.1536(4)	0.1559(4)	0.1569(4)	0.1578(5)	0.1584(3)	0.1586(4)
O2	B	0.13(6)	0.05(22)	0.11(9)	0.04(9)	0.01(10)	0.13(7)	0.29(6)
	s	0.3797(3)	0.3828(6)	0.3802(5)	0.3796(5)	0.3782(6)	0.3785(4)	0.3779(3)
O3	B		0.34(6)	0.31(8)	0.17(9)	0.21(11)	0.18(7)	0.24(6)
	s		0.3792(2)	0.3770(3)	0.3770(5)	0.3770(6)	0.3789(4)	0.3790(3)
O4	B	1.5(9)						
	B ₁₁		6.3(1.8)	2.9(9)	3.8(9)	4.7(9)	2.4(4)	1.0(3)
	B ₂₂		0.2(1.2)	1.7(7)	1.4(7)	0.5(6)	1.1(4)	1.0(3)
	B ₃₃		6.4(2.0)	3.2(1.2)	2.7(1.1)	2.1(1.0)	1.3(4)	1.7(3)
	n	0.11(2)	0.34(2)	0.53(2)	0.64(2)	0.78(2)	0.87(1)	1.02(2)
		Cell constants (Å)						
a		3.846(2)	3.844(1)	3.823(1)	3.820(1)	3.817(2)	3.812(1)	3.803(1)
b			3.851(1)	3.865(1)	3.869(1)	3.874(3)	3.877(1)	3.873(1)
c		11.792(6)	11.760(5)	11.694(5)	11.676(5)	11.653(6)	11.650(5)	11.620(4)
		R values						
R _i		4.15	4.54	3.66	5.01	6.71	4.10	4.09
R _{wp}		10.02	9.06	8.19	9.09	10.96	7.69	7.50
R _e		4.18	4.03	4.20	4.53	5.03	4.17	3.92

the apex atom O1 and the Cu-O chain atom O4, we adopt the nomenclature of the ILL group [17] which corresponds to the Argonne description [18] if O1 and O4 are interchanged).

The concentration dependence of some relevant bond distances projected in the z direction is shown in Fig. 1. The changes occurring in the inner cube of the triple perovskite cell together with the change of the Ba-(Er)-Ba distance are sketched in Fig. 1a. Fig. 1b shows the x dependence of the distance between the Cu-O chains and this inner cube and in Fig. 1c we present the relative shifts of the oxygen apex atom O1 which occupies a bridging position between the Cu-O chains and the Cu-O planes. With decreasing oxygen content the distance between the Cu-O planes as well as the Ba-(Er)-Ba distance decrease, contrary to the x dependence of the cell axis c. As the contraction of the inner cube is less than the increase of the Cu-O chain Cu-O plane distance the c axis increases with decreasing oxygen content. The strongest changes of atomic distances are observed between the Cu-O planes and the Cu-O chains. The O1 atom changes its relative position: the Cu2-O1 and Ba-O1 (along z) distances increase, whereas the O1 atom Cu-O chain distance — the shortest bonding length in the cell — decreases further.

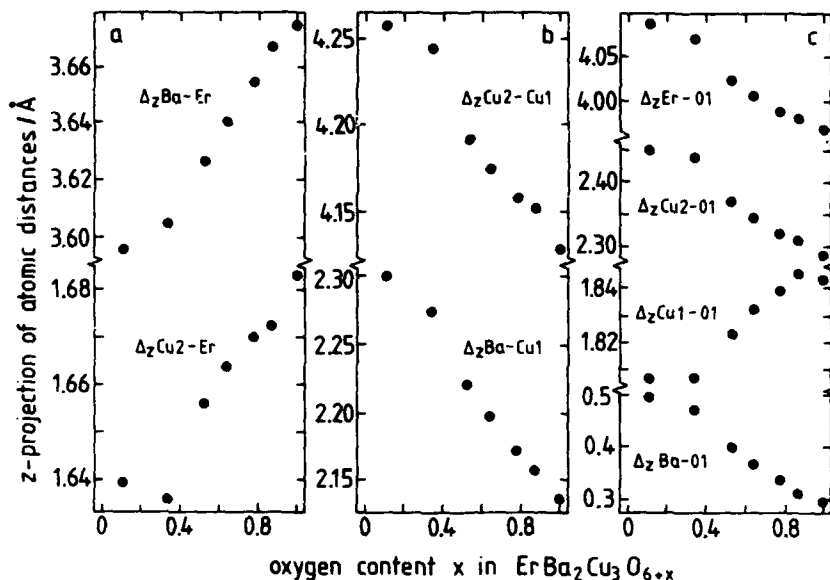


Fig. 1. Interatomic distances in $\text{ErBa}_2\text{Cu}_3\text{O}_{6+x}$: (a) changes occurring in the inner cube of the triple perovskite cell; (b) distances between the Cu-O chains and the inner cube; (c) distances, representing the position of the O1 apex atom relative to the Cu-O chains and Cu-O planes. (The error of the interatomic distances is about $\pm 0.005 \text{ \AA}$, which is a worst case estimate also accounting for errors like individual background subtraction, errors of the cell constants and errors of wavelength.)

An interesting feature of the bond lengths plotted in Fig. 1c is their enhanced composition dependence in the region $6.3 < x < 6.5$. To examine whether this behaviour is correlated to the suppression of superconductivity we prepared a series of smaller samples with a finer gradation of the oxygen content. Fig. 2 shows the cell parameters of these samples measured by x-ray diffraction [10] together with their transition temperatures. The T_c 's were determined from the onset of the Meissner signal measured by the field-cooling procedure in 20 Oe by means of a SQUID susceptometer (S.H.E. model 800) [19]. It can be clearly seen from Fig. 2 that in the concentration range $6.3 < x < 6.5$ the samples are still orthorhombic but that T_c decreases drastically with decreasing x . Superconductivity is suppressed totally at oxygen contents $x \leq 6.33$.

Similar observations in the $\text{YBa}_2\text{Cu}_3\text{O}_x$ system led to speculations about charge redistributions between the Cu-O chains and the Cu-O planes. It was suggested that this mechanism is responsible for the loss of superconductivity [9, 20, 21]. In current theories of high- T_c superconductivity the number of holes in the Cu-O planes plays an important role [22]. The changes in the bond lengths relative to the O1 atom might be correlated to an electron transfer from the chains to the planes when oxygen is removed from the Cu-O chains. This leads to a decrease of the hole concentration in the Cu-O planes and thus causes the disappearance of superconductivity. The x dependence of the Ba-O1 separation (see Fig. 1c) also suggests the concept of negative charge transfer from the chains to the planes and can be explained in terms of electrostatics as a reaction on the altering internal electric field. The Ba atom is attracted by the increasing amount of negative charges in the planes whereas the O1 atom moves toward the Cu-O chains. Thus the Cu-O chains only play the role of a charge reservoir for the Cu-O planes. The fact that the superconductivity decays more rapidly with decreasing x in the same concentration range, where a

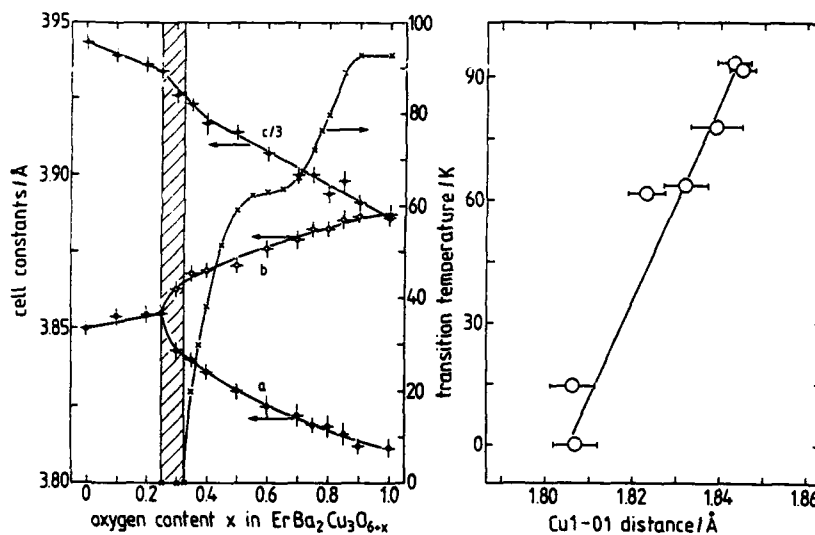


Fig. 2. (left side) Cell constants a , b and c of $\text{ErBa}_2\text{Cu}_3\text{O}_x$ at room temperature measured by x-ray diffraction, together with the transition temperatures obtained from dc susceptibility measurements. The hatching marks the region of non-superconducting but still orthorhombic samples.

Fig. 3. (right side) Transition temperatures of $\text{ErBa}_2\text{Cu}_3\text{O}_x$ as a function of the Cu1-O1 bond length.

stronger shift of the O1 atoms from the planes towards the chains is observed, is a striking argument that the model described is reasonable.

In Fig. 3 we have plotted T_c versus the Cu1-O1 distance. As expected from the above discussion, we find a nearly linear dependence of T_c on this bond length. Similar results are reported by Ashkenazi and Kuper [23]. From the plot we estimate a limiting distance of 1.805(5) Å between the apex oxygen atom and the Cu-O chains for the occurrence of superconductivity in $\text{ErBa}_2\text{Cu}_3\text{O}_x$.

CONCLUSIONS

We have shown that a clear relation exists between structural changes and changes in the superconducting properties of $\text{ErBa}_2\text{Cu}_3\text{O}_x$ upon oxygen deintercalation. At the crossover from superconductivity to non-superconductivity the apex oxygen atom O1 approaches the Cu-O chains and withdraws from the Cu-O planes. This shift of the O1 atom together with the observed changes in the Ba-O1 distance support a charge transfer model which describes the transition to non-superconducting behaviour. Furthermore, T_c was found to depend almost linearly on the O1 Cu-O chain distance. Recently, similar relations between bonding lengths and superconductor properties were found for $\text{YBa}_2\text{Cu}_3\text{O}_7$ [24]. In this case, however, the bonding lengths were affected by applying a hydrostatic pressure.

ACKNOWLEDGEMENT

We would like to thank P. Fischer and P. Allenspach for their support during our stay at the PSI, Villigen and H. Maletta for the performing of SQUID measurements.

REFERENCES

1. A. Furrer, P. Brüesch, and P. Unternährer, *Phys. Rev. B* **38**, 4616 (1988)
2. T. Chattopadhyay, P.E. Brown, D. Bonnenberg, S. Ewert, and H. Maletta, *Europhys. Lett.* **5**, 363 (1988)
3. J.M. Tarascon, W.R. McKinnon, L.H. Greene, G.W. Hull, and E.M. Vogel, *Phys. Rev. B* **36**, 226 (1987)
4. P.K. Gallagher, H.M. O'Bryan, S.A. Sunshine, D.W. Murphy, *Mat. Res. Bull.* **22**, 995 (1987)
5. P. Meuffels, B. Rupp, and E. Pörschke, *Physica C* **156**, 441 (1988)
6. H. Bakker, J.P.A. Westerveld, D.M.R. Lo Cascio, and D.O. Welch, *Physica C* **157**, 25 (1989)
7. A. Berera and D. de Fontaine, *Phys. Rev. B* **39**, 6727 (1989)
8. R. Kikuchi and J.-S. Choi, *Physica C* **160**, 347 (1989)
9. R.J. Cava, B. Batlogg, K.M. Rabe, E.A. Rietman, P.K. Gallagher, and L.W. Rupp, *Physica C* **156**, 523 (1988)
10. E. Pörschke and P. Meuffels in *High T_c Superconductors, Part A* edited by P.F. Boegers, C. Schlenker, and B. Stritzker (*J. Less-Common Met.* **150**, E-MRS Fall Conference, Strasbourg 1988) pp. 153-158
11. H.M. Rietveld, *J. Appl. Cryst.* **2**, 65 (1969)
12. A.W. Hewat, Atomic Energy Research Establishment Report No. AERE-R7350, 1973 (unpublished)
13. B. Rupp, MS-DOS microcomputer version, 1988 (unpublished)
14. F. Beech, S. Miraglia, A. Santoro, and R.S. Roth, *Phys. Rev. B* **35**, 8778 (1987)
15. E. Prince, *Acta Crystallogr., Sect. B* **38**, 1099 (1982)
16. R.A. Young, E. Prince, and R.A. Sparks, *J. Appl. Cryst.* **16**, 357 (1982)
17. A.W. Hewat, J.J. Capponi, C. Chailout, M. Marezio, and E.A. Hewat, *Solid State Commun.* **64**, 301 (1987)
18. J.D. Jorgensen, B.W. Veal, W.K. Kwok, G.W. Crabtree, A. Umezawa, L.J. Nowicki, and A.P. Paulikas, *Phys. Rev. B* **36**, 5731 (1987); J.D. Jorgensen, M.A. Beno, D.G. Hinks, L. Soderholm, K.J. Volin, R.L. Hitterman, J.D. Grace, I.K. Schuller, C.U. Segre, K. Zhang, and M.S. Kleefisch, *ibid.*, 3608 (1987)
19. H. Maletta (private communication)
20. P.F. Miceli, J.M. Tarascon, L.H. Greene, P. Barboux, F.J. Rotella, and J.D. Jorgensen, *Phys. Rev. B* **37**(10), 5932 (1988)
21. M.-H. Whangbo, M. Evain, M.A. Beno, U. Geiser, and J.M. Williams, *Inorg. Chem.* **27**, 467 (1988)
22. B.K. Chakraverty, M. Avignon, and D. Feinberg in *High T_c Superconductors, Part A* edited by P.F. Boegers, C. Schlenker, and B. Stritzker (*J. Less-Common Met.* **150**, E-MRS Fall Conference, Strasbourg 1988) pp. 11-31
23. J. Ashkenazi and C.G. Kuper, in *Studies of High Temperature Superconductors*, edited by A.V. Narlikar (NOVA Science, New York, 1989) p. 1
24. E. Kaldis, P. Fischer, A.W. Hewat, E.A. Hewat, J. Karpinski, and S. Rusiecki, *Physica C* **159**, 668 (1989)

NEUTRON POWDER DIFFRACTION STUDY OF THE
STRUCTURES OF $\text{La}_{1.9}\text{Ca}_{1.1}\text{Cu}_2\text{O}_6$ and $\text{La}_{1.9}\text{Sr}_{1.1}\text{Cu}_2\text{O}_{6+\delta}$

A. Santoro*, F. Beech*, and R. J. Cava**

*National Institute of Standards and Technology, Reactor Division,
Gaithersburg, MD 20899

**Bell Laboratories, 600 Mountain Ave., Murray Hill, N.J. 07974

ABSTRACT

The title compounds are structurally isomorphous and crystallize with the symmetry of space group $I4/mmm$. The lattice parameters are $a = 3.8248(1)$, $c = 19.4286(5)\text{Å}$ for $\text{La}_{1.9}\text{Ca}_{1.1}\text{Cu}_2\text{O}_6$ and $a = 3.8601(1)$, $c = 19.9994(5)\text{Å}$ for $\text{La}_{1.9}\text{Sr}_{1.1}\text{Cu}_2\text{O}_{6+\delta}$. The structure can be easily derived from that of La_2CuO_4 by substituting the layers of composition CuO_2 present in La_2CuO_4 with a block of three layers having composition and sequence $(\text{CuO}_2) - (\text{R}) - (\text{CuO}_2)$, where R is Ca, Sr, and/or La. Although the general structural configuration is the same for the Ca and the Sr compounds, the distribution of the metal atoms is different in the two cases. More specifically, in $\text{La}_{1.9}\text{Ca}_{1.1}\text{Cu}_2\text{O}_6$ the perovskite-type layers form blocks with sequence $(\text{CuO}_2) - (\text{Ca}) - (\text{CuO}_2)$, and are separated by rock-salt blocks of two layers $(\text{LaO}) - (\text{LaO})$. In $\text{La}_{1.9}\text{Sr}_{1.1}\text{Cu}_2\text{O}_{6+\delta}$, on the other hand, the perovskite-type blocks have composition and sequence $(\text{CuO}_2) - (\text{R}) - (\text{CuO}_2)$ and they are separated by blocks $(\text{NO}) - (\text{NO})$, where both R and N are about 65%La and 35%Sr.

INTRODUCTION

In all the superconducting copper oxides there are CuO_2 planes separated by either charge reservoir layers or by rare-earth oxide layers which can be doped by aliovalent ions to induce superconductivity. These compounds can be described as members of a large family derived from stacking blocks having the rock-salt and perovskite-type structure [1]. Most commonly, the electronically active CuO_2 layer has copper in square-pyramidal coordination.

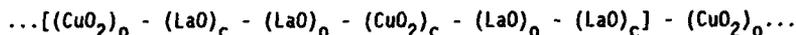
There are members of this family, strongly related to the structure of La_2CuO_4 and $\text{Ba}_2\text{YCu}_3\text{O}_7$, which have never been made superconducting, that is the compounds with 3:2 stoichiometry, $\text{La}_{2-x}\text{M}_{1+x}\text{Cu}_2\text{O}_{6+\delta}$ ($M = \text{Ca}, \text{Sr}$) [2]. In spite of similarities to known compounds, these materials apparently cannot be doped with holes by the usual M^{2+}/M^{3+} substitution to an extent sufficient to induce even metallic conductivity. Small substitutions ($0.0 \leq x \leq 0.15$) are, however, possible.

In this paper, we present the results of our structural studies of $\text{La}_{1.9}\text{M}_{1.1}\text{Cu}_2\text{O}_{6+\delta}$ ($M = \text{Ca}, \text{Sr}$) by neutron powder profile analysis carried out to find structural clues that would shed light on the surprising lack of superconductivity in this structural type.

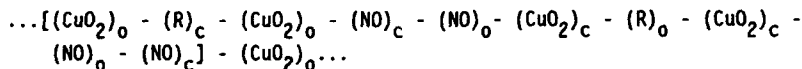
EXPERIMENTAL

The compounds $\text{La}_{1.9}\text{Ca}_{1.1}\text{Cu}_2\text{O}_6$ and $\text{La}_{1.9}\text{Sr}_{1.1}\text{Cu}_2\text{O}_6$ were prepared as described in ref. [2]. The neutron diffraction measurements were performed

on the high-resolution five-counter diffractometer at the reactor of the National Institute of Standards and Technology, using a neutron wavelength of 1.553(1)Å. The structures were refined with the Rietveld method [3] adapted to the multicounter diffractometer and modified to include the background parameters [4]. Peak shapes were described by Gaussian functions. The neutron scattering amplitudes used in the refinements were $b(\text{La}) = 0.827$, $b(\text{Ca}) = 0.490$, $b(\text{Sr}) = 0.702$, $b(\text{Cu}) = 0.772$ and $b(\text{O}) = 0.581 \times 10^{-12} \text{cm}$. The structure is built by substituting the layers $(\text{CuO}_2)_{\text{o,c}}$ present in the structure of La_2CuO_4 [5] with blocks of three layers - $(\text{CuO}_2)_{\text{o,c}} - (\text{R})_{\text{c,o}} - (\text{CuO}_2)_{\text{o,c}}$ -, where R can be Ca, Sr, or La (in this description a layer is specified by a chemical symbol giving the composition of the layer, and by a subscript o or c indicating if the cation is, respectively, at the origin or at the center of the mesh of the layer [1]). Thus, from the sequence



describing the structure of La_2CuO_4 , we obtain the sequence



which describes the structure of $\text{La}_2\text{MCu}_2\text{O}_6$ and where N and R can be Ca, La, and/or Sr and where the square brackets include the content of a unit cell of the structure. This atomic configuration has true or approximate tetragonal symmetry and is based on a body-centered lattice of approximate lattice parameters $3.8 \times 3.8 \times 19 \text{Å}^3$. The initial positional parameters obtained from the model were therefore refined in space group $I4/mmm$. A few weak reflections, observed in the powder patterns of both compounds, could not be indexed in terms of the adopted unit cell or in terms of multiple cells and were, therefore, attributed to impurities and excluded from all subsequent calculations. In the final refinements all the structural, lattice, and profile parameters were varied simultaneously with the only constraint that the positions 2a and 4e of the R and N atoms, respectively, be fully occupied. The results of these calculations are given in Tables I and II. The relevant bond distances are shown in Table III and a schematic representation of the structure is illustrated in fig. 1.

TABLE I. Refined Structural Parameters of $\text{La}_{1.9}\text{Ca}_1\text{Cu}_2\text{O}_6$

Space group: $I4/mmm$		$a = 3.8248(1)$	$c = 19.4286(5)\text{Å}$	$v = 284.22(2)\text{Å}^3$		
Atom	Position	x	y	z	$B(\text{Å}^2)$	n
La	2a $4/mmm$	0	0	0	1.0(1)	0.014(6)
Ca	2a $4/mmm$	0	0	0	1.0(1)	0.236(6)
La(1)	4e $4mm$	0	0	0.17578(9)	0.47(5)	0.47(1)
Ca(1)	4e $4mm$	0	0	0.17578(9)	0.47(5)	0.03(1)
Cu	4e $4mm$	0	0	0.58503(9)	0.32(4)	0.5
O(1)	8g mm	0	1/2	0.08230(9)	0.74(5)	1.005(8)
O(2)	4e $4mm$	0	0	0.7046(2)	1.52(8)	0.506(6)
O(3)	2b $4/mmm$	0	0	1/2	0.7	0.008(2)

$$R_n = 4.58 \quad R_D = 5.96 \quad R_w = 8.54 \quad R_e = 4.34 \quad \chi = 1.97$$

Formula obtained from refinement: $\text{La}_{1.94(5)}\text{Ca}_{1.06(5)}\text{Cu}_2\text{O}_{6.08(4)}$

TABLE II. Refined Structural Parameters of $\text{La}_{1.9}\text{Sr}_{1.1}\text{Cu}_2\text{O}_{6+\delta}$

Space group: $I4/mmm$		$a = 3.8601(1)$	$c = 19.9994(5)\text{Å}$	$v = 298.00(2)\text{Å}^3$		
Atom	Position	x	y	z	$B(\text{Å}^2)$	n
La	2a $4/mmm$	0	0	0	0.78(8)	0.17(2)
Sr	2a $4/mmm$	0	0	0	0.78(8)	0.08(2)
La(1)	4e $4mm$	0	0	0.1792(1)	0.53(6)	0.31(3)
Sr(1)	4e $4mm$	0	0	0.1792(1)	0.53(6)	0.19(3)
Cu	4e $4mm$	0	0	0.5924(1)	0.62(4)	0.5
O(1)	8g mm	0	1/2	0.08603(8)	1.00(4)	1.00
O(2)	4 $4mm$	0	0	0.7024(2)	1.84(6)	0.5
O(3)	2b $4/mmm$	0	0	1/2	0.7	0.035(2)

$$R_n = 6.29 \quad R_p = 6.13 \quad R_w = 8.28 \quad R_e = 5.23 \quad \chi = 1.58$$

Formula obtained from refinement: $\text{La}_{1.9(2)}\text{Sr}_{1.0(2)}\text{Cu}_2\text{O}_{6.14(1)}$

TABLE III. Relevant bond Distances in $\text{La}_{1.9}\text{Ca}_{1.1}\text{Cu}_2\text{O}_6$ and $\text{La}_{1.9}\text{Sr}_{1.1}\text{Cu}_2\text{O}_{6+\delta}$

$\text{La}_{1.9}\text{Ca}_{1.1}\text{Cu}_2\text{O}_6$		$\text{La}_{1.9}\text{Sr}_{1.1}\text{Cu}_2\text{O}_{6+\delta}$	
Ca-O(1) x 8	2.493(1)	LaSr-O(1) x 8	2.586(1)
La-O(1) x 4	2.638(1)	LaSr-O(1) x 4	2.683(1)
La-O(2) x 4	2.7619(6)	LaSr-O(2) x 4	2.769(1)
La-O(2) x 1	2.324(3)	LaSr-O(2) x 1	2.368(5)
Cu-O(1) x 4	1.9132(1)	Cu-O(1) x 4	1.9340(2)
Cu-O(2) x 1	2.323(3)	Cu-O(2) x 1	2.196(5)

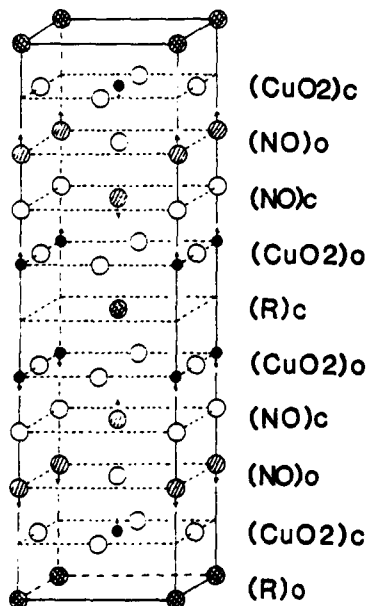
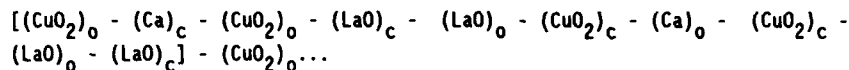


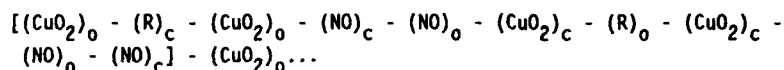
Fig. 1. Schematic representation of the structure of $\text{La}_{1.9}\text{M}_{1.1}\text{Cu}_2\text{O}_{6+\delta}$. Small full circles are copper atoms, large open circles oxygen atoms, hatched circles N atoms and cross-hatched circles R atoms (R and N are Ca and La, respectively, in $\text{La}_{1.9}\text{Ca}_{1.1}\text{Cu}_2\text{O}_6$ and La + Sr in $\text{La}_{1.9}\text{Sr}_{1.1}\text{Cu}_2\text{O}_{6+\delta}$). The oxygen atoms near the copper layers are labeled O(1) in Tables I and II and those near the layers of N and R, O(2) and O(3), respectively. The arrows indicate the direction of displacement of the cations relative to the planes of the oxygen atoms.

DISCUSSION

The results of Table I show that the structure of $\text{La}_{1.9}\text{Ca}_{1.1}\text{Cu}_2\text{O}_6$ determined in this study agrees closely with that previously determined by Izumi *et al.* [6] for the same composition. Although the general structural features for the Ca and Sr compounds are the same, the distribution of the metal atoms in the crystallographic sites is different in the two cases. This may be easily seen by representing the two structures as sequences of layers in the following way:



for $\text{La}_2\text{CaCu}_2\text{O}_6$, and

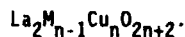


for $\text{La}_2\text{SrCu}_2\text{O}_6$. In this case, N and R are both $-65\%\text{La} + 35\%\text{Sr}$ and, as before, the content of a unit cell of the structure is enclosed in square brackets. The above schemes show that the (CuO_2) layers are separated by

(Ca) layers in $\text{La}_{1.9}\text{Ca}_{1.1}\text{Cu}_2\text{O}_6$ with Ca^{2+} in eight-fold and La^{3+} in nine-fold coordination. In $\text{La}_{1.9}\text{Sr}_{1.1}\text{Cu}_2\text{O}_{6+\delta}$, on the other hand, both sites are occupied by La^{3+} and Sr^{2+} in a disordered fashion and in proportions consistent with the stoichiometry of the compound. The interatomic distances and the lattice parameters of the two structures reflect the fact that the ionic radius of Sr^{2+} is larger than that of Ca^{2+} .

The coordination of copper in La_2CuO_4 is bipyramidal with the bipyramid of oxygen atoms considerably elongated along the c-axis [5]. The replacement of the (CuO_2) layers of La_2CuO_4 with $(\text{CuO}_2) - (\text{R}) - (\text{CuO}_2)$ to produce $\text{La}_2\text{MCu}_2\text{O}_6$ has the effect of changing the polyhedron surrounding the copper atom into a pyramid in which the Cu-O distances within the layer (CuO_2) are much shorter than the Cu-O distance with the oxygen atom at the apex (1.913 versus 2.323Å in $\text{La}_{1.9}\text{Ca}_{1.1}\text{Cu}_2\text{O}_6$). The same kind of situation has been found in other compounds [7]. The copper atoms are slightly removed from the plane of the oxygen atoms towards the interior of the pyramid. This shift, however, is considerably smaller in the title compounds than in $\text{Ba}_2\text{YCu}_3\text{O}_{6+x}$ [7] (0.05 and 0.13Å in the Ca and Sr compounds, respectively, versus 0.27 and 0.22Å in $\text{Ba}_2\text{YCu}_3\text{O}_7$ and BaYCu_3O_6) and, as a consequence, the buckling of the (CuO_2) layers is less pronounced.

La and N atoms ($N = \text{La} + \text{Sr}$) are nine-coordinated to oxygen in the same way found in La_2CuO_4 . The coordination polyhedron is a capped antiprism and the cation is shifted from the center towards the capped face. The oxygen atoms O(2) (fig. 1) are removed from the planes of the cations by 0.56Å in the calcium compound and by 0.46Å in the strontium compound. The La-O and N-O bond lengths are virtually identical to those found in La_2CuO_4 . The eight-coordinated cations (Ca and R in the calcium and strontium compounds, respectively) are located at the center of square prisms. This type of coordination is possible only for $n \geq 2$ in the homologous series



As shown in Tables I and II, the refined composition is in excellent agreement with the nominal stoichiometry, with all components within two standard deviations of the expected values in both compounds. Due to large correlations in the refinements of the occupancy factors in

$\text{La}_{1.9}\text{Sr}_{1.1}\text{Cu}_2\text{O}_{6+\delta}$, the standard deviations on the La:Sr ratio are larger than those for the calcium compound, allowing for considerable ambiguity.

The most significant differences between the Ca and Sr analogs are in the nature of the cation in the eight-coordinated site between the copper pyramids (primarily Ca in $\text{La}_{1.9}\text{Ca}_{1.1}\text{Cu}_2\text{O}_6$ and primarily R = 65%La + 35%Sr in $\text{La}_{1.9}\text{Sr}_{1.1}\text{Cu}_2\text{O}_{6+\delta}$), and in the occupancy of the oxygen interstitial site

O(3) associated with that cation. As expected, for the small Ca^{2+} ion the preferred coordination with oxygen is eight and no significant presence of oxygen is found in this site in the Ca compound. For the Sr analog, however, a coordination larger than eight is possible, and this favors the partial occupancy of site O(3) which we actually observe. The disruptive presence of this interstitial oxygen has often been proposed as being responsible for the lack of superconductivity in $\text{La}_{1.9}\text{Sr}_{1.1}\text{Cu}_2\text{O}_{6+\delta}$, and our observations are in support of this view. For the Ca analog, however, this cannot be the case. Although the band structures of these materials have not been calculated to our knowledge, the relative flatness of the CuO_2 plane in $\text{La}_{1.9}\text{Ca}_{1.1}\text{Cu}_2\text{O}_6$ is in considerable contrast to the puckered planes found in the hole doped superconductors, and suggests a somewhat different distribution of charge among the bonds within the CuO_5 pyramids, which may affect the ability of the planes to accept a significant amount of hole doping.

The compounds analyzed in this study are terms of the homologous series $\text{La}_2\text{M}_{n-1}\text{Cu}_n\text{O}_{2n+2}$ with $n = 2$. This series may be considered as a particular case of a more general class of compounds of formula $(\text{AO})_x(\text{BO})_y(\text{M})_{n-1}(\text{CuO}_2)_n$ having a structural type in which blocks of $(\text{AO})_x(\text{BO})_y$ with the rock-salt structure alternate with blocks having a defective perovskite configuration. The condition of equality between cation and anion valences requires that $2(2n + x + y) = px + qy + s(n+1) + mn$ where p , q , s and m are the valences of A, B, M and Cu, respectively. If we assume that $m = s = 2$ (case of Ca^{2+} and Cu^{2+}), we have $x(p-2) + y(q-2) = 2$ and, for $y = 0$ and $p = 3$ (case of La^{3+}) we obtain the formula $(\text{AO})_2(\text{M})_{n-1}(\text{CuO}_2)_n$ i.e., $\text{A}_2\text{M}_{n-1}^{3+}\text{Cu}_n\text{O}_{2n+2}$ which is the homologous series of the title compounds. Note that for $q = 2$, y may assume any value. For $y = 2$ we obtain $(\text{AO})_2(\text{BO})_2(\text{M})_{n-1}(\text{CuO}_2)_n$ i.e., $\text{A}_2\text{B}_2\text{M}_{n-1}\text{Cu}_n\text{O}_{2n+4}$ which is the homologous series of the well known compounds $\text{Bi}_2\text{Sr}_2\text{Ca}_{n-1}\text{Cu}_n\text{O}_{2n+4}$ and $\text{Tl}_2\text{Ba}_2\text{Ca}_{n-1}\text{Cu}_n\text{O}_{2n+4}$. The above formulas not only show how $\text{La}_2\text{MCu}_2\text{O}_6$ is related to compounds of the same homologous series, but also how it is connected with materials belonging to the more general class with the same structural type, formed by block of layers with the rock-salt structure alternating with blocks with the perovskite configuration.

REFERENCES

1. A. Santoro, F. Beech, M. Marezio and R. J. Cava, *Physica C* 156, 693 (1988).
2. N. Nguyen, L. Er. Rakho, C. Michel, J. Choisnet and B. Raveau, *Mat. Res. Bull.* 15, 891 (1980).
3. H. M. Rietveld, *J. Appl. Cryst.* 2, 65 (1969).
4. E. Prince, U. S. Tech. Note 1117 (F. J. Shorten, Ed.) p. 8.
5. J. M. Longo and P. M. Raccah, *J. Sol. State Chem.* 6, 526 (1973).
6. F. Izumi, E. Takayama-Muromachi, Y. Nakai and H. Asano, *Physica C* 157, 89 (1989).
7. S. Miraglia, F. Beech, A. Santoro, D. Tran Qui, S. A. Sunshine and D. Murphy, *Mat. Res. Bull.* 22, 1733 (1987).

NEUTRON DEPOLARIZATION BY FLUX LATTICES IN HIGH- T_c MATERIALS

S. J. PICKART*, A. C. NUNES*, M. L. CROW*, BO FU*, T. R. MCGUIRE**, S. SHINDE**, AND S. A. SHIVASHANKAR

* University of Rhode Island, Department of Physics, Kingston, RI 02881

** IBM Thomas J. Watson Research Center, Yorktown Heights, NY 10598

ABSTRACT

We have recently reported[1] neutron depolarization measurements on an $\text{YBa}_2\text{Cu}_3\text{O}_{7-\delta}$ composition exhibiting a transition from a low temperature state which caused depolarization ($P=0.76\pm.02$) to one at high temperatures ($T=55\text{K}$) where depolarization was absent. Since this temperature is well below the measured superconducting transition at 86K , we speculated that the transition was a dynamic one corresponding to flux lattice melting[2] or to formation of a glassy state[3]. We have now extended these depolarization measurements to two specimens of $\text{Bi}_{2.2}\text{Sr}_{1.7}\text{CaCu}_2\text{O}_{8+\delta}$, prepared and characterized[4] at IBM, which showed superconducting transitions at 80K with weak tails extending to 110K . The two samples have critical current densities, as determined by the Bean expression[5], that differ by 50%.

Data were taken at temperatures down to 10K and in applied fields up to 2000 oe , with cooling and field application sequences exactly the same as with the $\text{YBa}_2\text{Cu}_3\text{O}_{7-\delta}$. Surprisingly, the sample with higher current density shows only a small amount of depolarization ($P=.988\pm.003$), while the other shows no depolarization. We therefore conclude that the flux lattice arrangement and/or stability is qualitatively different in these compositions as compared with $\text{YBa}_2\text{Cu}_3\text{O}_{7-\delta}$, perhaps due to extrinsic properties such as grain size (suggested by photomicrographs), or to the intrinsic nature of pinning forces. Further experiments are in progress to sort out these questions.

1. M.L. Crow, R.J. Goyette, A.C. Nunes, S.J. Pickart, T.R. McGuire, S. Shinde, and T.M. Shaw, *J. Appl. Phys.* **64**, 5815 (1988); *Proc. 34th Conf. on Magnetism and Magnetic Mats.* (to be published).
2. D.R. Nelson, *Phys. Rev. Lett.* **60**, 1973 (1988); P.L. Gammel, L.F. Schneemeyer, J.V. Waszczak, and D.J. Bishop, *Phys. Rev. Lett.* **61**, 1666 (1988).
3. M.P.A. Fisher, *Phys. Rev. Lett.* **62**, 1415 (1989).
4. T.R. McGuire, S.A. Shivashankar, S.J. LaPlaca, G.V. Chandrashekar, R.F. Boehme, T.M. Shaw, D.S. Yee, M.W. Shafer, and J.J. Cuomo, *J. Appl. Phys.* **64**, 5792 (1988).
5. C.P. Bean, *Phys. Rev. Lett.* **8**, 250 (1962).

USE OF NEUTRON DIFFRACTION IN DETERMINING STRAINS IN HIGH-TEMPERATURE SUPERCONDUCTING COMPOSITES*

D. S. Kupperman, J. P. Singh, and S. Majumdar, Materials and Components Technology Division, R. L. Hitterman, Materials Science Division, Argonne National Laboratory, Argonne, Illinois 60439-4838
J. Faber Jr., Amoco Research, Naperville, Illinois

ABSTRACT

The Argonne Intense Pulsed Neutron Source and General Purpose Powder Diffractometer have been used to study high T_c metal oxide composites composed of yttrium barium copper oxide and silver. Neutron diffraction techniques were applied to composites with 15, 20 and 30% silver content by volume. We have observed that after hot pressing, the 30% Ag specimens contained both orthorhombic high T_c and tetragonal, non-superconducting phases near the center of the specimens but only tetragonal near the surface. The relationship of shifts in Bragg peaks to strains of the constituents is discussed.

INTRODUCTION

Since the discovery of superconducting materials with relatively high transition temperatures (T_c), there has been a considerable effort both to understand the reason for the high T_c and to improve the mechanical properties, which limit the practical applications. The $\text{YBa}_2\text{Cu}_3\text{O}_{7-\delta}$ (YBCO) compounds have received considerable attention [1-3], because of their high T_c and high upper critical magnetic field. Additions of silver have recently been shown [4] to improve the mechanical properties (toughness and strength) of these compounds. Furthermore, the addition of the Ag can improve the conductive path between grains of superconducting YBCO and possibly help reduce the "weak-link" effect [5]. Note that whereas the addition of a low-volume fraction of silver does not adversely affect the superconductivity the introduction of transition metals to YBCO can have a detrimental effect on the superconducting properties. Also, the addition of silver has a minimal affect on the stress free lattice spacing. During fabrication of YBCO/Ag composites, differential thermal expansion upon cooling can lead to potentially troublesome residual stresses. Since the Ag contracts more than the YBCO, good bonding between the ceramic and silver could lead [6] to tensile stresses in the silver and compressive stresses in the YBCO for relatively small percentages of Ag. The mechanical properties and life expectancy of components made from this material may depend on the residual stresses. An understanding of the nature and magnitude of these stresses will help improve the design of these composites.

Neutron diffraction is a powerful method for measuring bulk residual strains, from which residual stresses can be calculated [7,8]. Neutrons can provide a bulk measurement because they can penetrate deeper than X-rays. In the present work, the Intense Pulsed Neutron Source (IPNS) and General Purpose Powder Diffractometer (GPPD) at Argonne National Laboratory were used to measure the residual thermal strains in YBCO composites.

Sample Preparation

Samples discussed here are fabricated from a mixture of YBCO and Ag powders, with 0, 15, 20, and 30% Ag by volume [8]. The phase composition of YBCO powder was confirmed by X-ray analysis. The Ag powder had a particle size range of 2-3.5 μm , as indicated by the supplier. Both YBCO and composite powders were formed into rectangular bars, (~5.1 x 0.6 x 0.3 cm) by uniaxial pressing in a steel die at 150 MPa. Rectangular bars of composite YBCO/Ag were sintered in flowing O_2 at 930°C for 4 h and then annealed for 8 h from 435 to 380°C. Examination of polished surfaces of sintered YBCO/15% Ag bar specimens by SEM showed that the Ag phase was randomly distributed in discrete globules. Furthermore, little or no preferred orientation of Ag was observed next to the YBCO. The density of the sintered specimens was observed to increase with increasing Ag content. A density of 95% theoretical was obtained at 30 vol% Ag content. The increase in density probably occurs because the Ag acts as a sintering aid. Examination of the fracture surface of a sintered specimen of YBCO/20% Ag showed a typical grain size of 15 μm . These grains are about twice as large as those for YBCO specimens without any Ag addition. This increase in grain size is believed to be due to the presence of a liquid phase formed as a result of Ag addition. The resistivity was measured by a conventional four-probe technique. The critical current density values were determined with a criterion of 1.0 $\mu\text{V}/\text{cm}$ at 77 K and zero magnetic field.

Neutron Diffraction Using the Intense Pulsed Neutron Source

In the experiments described here, Bragg's Law is used first to determine the lattice spacing d for a particular hkl reflection from both YBCO and Ag averaged over a volume of the strain-free powder. The stressed composite fabricated from these powders is examined next. The lattice strain associated with the hkl plane of a given phase in the composite is given by

$$e = (d - d_0)/d_0, \quad (1)$$

where d_0 is the unstrained hkl spacing (powder) and d is the spacing for the composite.

Lattice spacings can be measured to an accuracy of $\pm 0.0002 \text{ \AA}$. The main advantage of the pulsed source is that many diffraction peaks can be measured at the same time in different spatial directions. Results reported here combine the data from the 90° and 148° detectors.

EXPERIMENTAL RESULTS

Figure 1 shows the average bulk strain at room temperature in the Ag as a function of volume percent Ag in the composite and the crystallographic direction. The Ag diffraction peaks for which data are presented are clearly isolated from the YBCO diffraction peaks. The potentially complex loads and the relatively large error in absolute measurement of strain makes it difficult to reach any conclusions by comparing strains in

various crystallographic directions. However, there is a trend toward decreasing Ag strain as the Ag volume fraction increases (the relative error in strain between samples of varying Ag content is about half the uncertainty in the absolute values). The strain, however, is expected to be proportional to the difference between the thermal expansion coefficient of Ag and that of the composite (which increases with increasing Ag) [9]. It is unlikely that Y, Ba, Cu or O can change the Ag spacing chemically. The difference between the thermal expansion coefficients of Ag and YBCO is about $2 \times 10^{-6}/^{\circ}\text{C}$. An increase in Ag content from 15% to 30% should increase the composite coefficient of expansion by about 2%. The observed decrease in strain is much larger than can be explained by the ~2% change in thermal expansion coefficient. It is possible that the strain is relieved by creep. Analysis of the diffraction peak full-width-at-half-maximum (FWHM) shows insignificant broadening (<10%), which is consistent with little or no yielding. The Ag hydrostatic stress calculated from the strain values and the Ag bulk modulus ranges from 130 ± 65 MPa for 30% Ag to 229 ± 65 MPa for 15% Ag. These relatively low values also support the conclusion that no yielding of the Ag occurs.

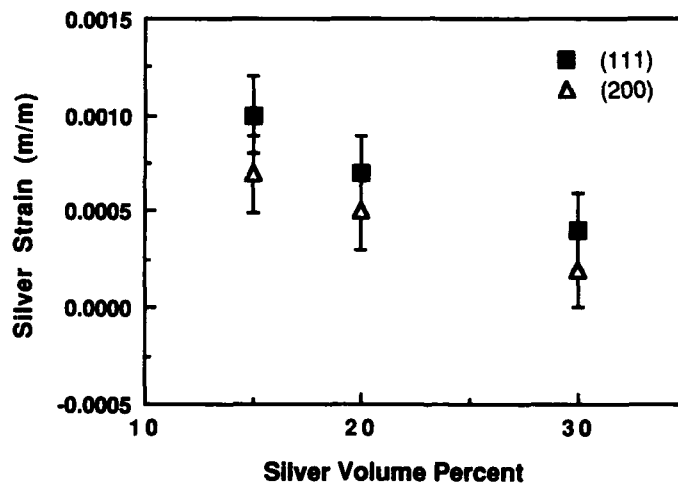


Fig. 1. Room-temperature tensile strain in Ag as a function of Ag content in YBCO/Ag composite and crystallographic direction.

Measuring strains in the YBCO is difficult because the stoichiometry can change with Ag content. Thus the shifts in YBCO diffraction peaks may not be solely the result of strain. Figure 2 shows the change in the diffraction pattern with Ag content for several Ag and YBCO peaks. The pattern for the 30% Ag composite is clearly different from the others and indicates a nearly tetragonal structure. Destructive analysis, combined with X-ray diffraction analysis of sections of a 30% Ag sample [4], shows that the stoichiometry for the 30% sample changes gradually from $\delta = 0.1$ at the outer surface (orthorhombic superconducting phase) to $\delta = -0.8$ near the center of the specimen (non-superconducting tetragonal phase). This

finding is consistent with the observation that the 30% Ag sample shows a dramatic decrease in critical current density as compared with samples with 0, 15, and 20% Ag content.

Since the lattice spacings for the three principal directions of YBCO are known as a function of stoichiometry, it is possible to estimate the diffraction peak shift resulting from strain (for some diffraction lines) by correcting for stoichiometry. For example, since the (111) diffraction peak is a single peak and the shifts are unambiguous, we can predict the change in the spacing of the (111) plane as a function of stoichiometry from the relationship

$$1/d_{111} = 1/a^2 + 1/b^2 + 1/c^2, \quad (2)$$

where the values of a , b , and c as a function of δ are determined by neutron diffraction [10]. The value of δ for YBCO in the present composites was estimated by comparing relationships that are primarily due to stoichiometry and not strain with those of materials with known δ (Fig. 2). Strains determined from lattice parameter estimates for strain-free YBCO (111) as a function of Ag content are presented in Fig. 3. We have assumed that the addition of 15% Ag does not significantly change the stoichiometry of YBCO. The stoichiometry of the 30% Ag sample is assumed to be nearly tetragonal (bulk average), and the 20% Ag sample is assumed to be intermediate in stoichiometry between 15% and 30% Ag samples [11]. These assumptions are consistent with Fig. 2. The lattice parameter is predicted to increase as the stoichiometry approaches the tetragonal phase (with increasing Ag content). However, experimentally, the spacing for the (111) planes decreases as the Ag content increases from 15% to 20%, indicating an average compressive stress in the YBCO (Fig. 3). This result is in qualitative agreement with expectations, since the Ag strain is tensile. At 30% Ag, the difference between measured and stress-free lattice spacing indicates negligible YBCO strain. This finding is consistent with the low strain measured for Ag in the YBCO/30% Ag composite, and is probably a result of additional creep of the composite which can vary with stoichiometry [12].

DISCUSSION

We have shown that neutron diffraction techniques can be applied to YBCO composites to measure residual strains in the constituent parts caused by differential thermal contraction after fabrication, and to determine the effect of Ag on stoichiometry (and thus on the critical current density). We have observed residual tensile strains in Ag as a function of crystallographic direction; these strains range from as high as 0.085% in 15% and 20% Ag samples to as low as about 0.02% in a 30% Ag sample. Compressive strains in the YBCO (111) crystallographic direction were estimated by correcting for the diffraction peak shift due to changes in stoichiometry with Ag content. The estimated compressive-strain values vary from 0.04% (15% Ag) to 0.09% (20% Ag) to 0.01% (30% Ag), with an uncertainty of about 0.03%. The decrease in strain in YBCO is consistent with the decrease in Ag strain and may be due to vari

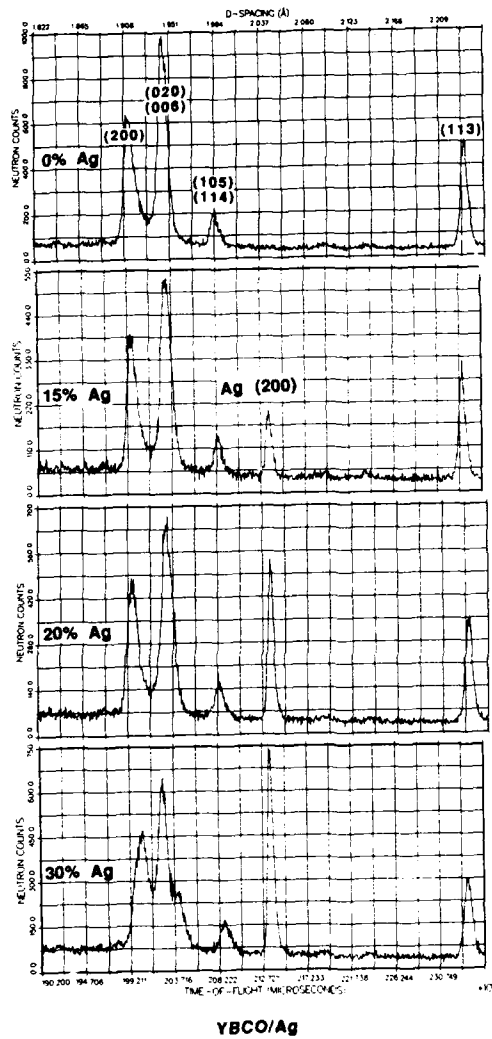


Fig. 2. Neutron diffraction spectrum of YBCO/Ag as Ag volume fraction varies from 0 to 30%. The YBCO (200), (020)/(006), (105)/(114), and (113) lines and the Ag (200) lines are shown.

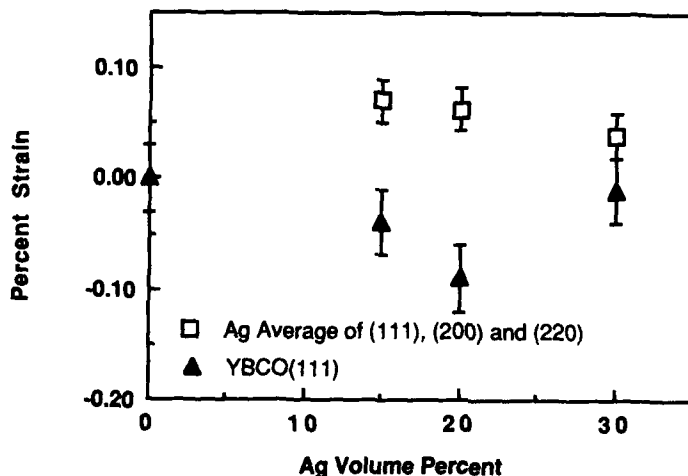


Fig. 3. Ag strain and calculated and experimentally measured strains for the YBCO (111) plane as a function of stoichiometry.

ation in creep properties of the composite which is sensitive to stoichiometry (11). The presence of significant average tensile strain in the Ag, particularly for 15 and 20% Ag samples, indicates good interface bonding between YBCO and Ag.

Strains were also measured at liquid nitrogen temperatures for the 15%Ag sample. Only small changes in strain detected. The largest increase in strain was observed for the YBCO (111) plane. The compressive strain increased about 0.04%. The absence of any relaxation of strain suggests little or no cracking occurred as the temperature was lowered to superconducting transition.

ACKNOWLEDGMENTS

The authors wish to thank J. D. Jorgensen, and H. Shaked for helpful discussions and B. Tani for X-ray diffraction data. This work has benefited from the use of the Intense pulsed Neutron Source at Argonne National Laboratory.

REFERENCES

1. J. G. Bednorz and K. A. Muller, *Z. Phys.* B64, 189 (1986).
2. J. M. Liang, R. S. Liu, L. Chang, P. T. Wu, and L. J. Chen., *Appl. Phys. Lett.* 53, 1434 (1988).
3. O. Kohno, Y. Ikeno, N. Sadakata, and K. Goto, *Jpn. J. Appl. Phys.* 27, L77 (1988).

4. J. P. Singh, H. J. Leu, E. Van Voorhees, G. T. Gondey, K. Winsley and D. Shi, unpublished information.
5. S. Jin, T. H. Tiefel, R. C. Sherwood, M. E. Davis, R. B. Van Dover, G. W. Kammlott, R. A. Fastnacht, and H. D. Keith, *Appl. Phys. Lett.* 52, 2074 (1988).
6. S. Majumdar, D. Kupperman, and J. Singh, *J. Am. Ceram. Soc.* 71(10), 858 (1988).
7. A. J. Allen, M. T. Hutchings and C. G. Windsor, *Advances in Physics*, 34(4) 445 (1985).
8. D. S. Kupperman, J. P. Singh, J. Faber, Jr. and R. L. Hitterman, *J. Appl. Phys.*, 66(7), 3396 (1989).
9. J. Selsing, *J. Amer. Ceram. Soc.* 44, 419 (1961).
10. J. D. Jorgensen (private communication).
11. H. Shaked (private communication).
12. A. W. von Stumberg, Nan Chen, K. C. Goretta and J. Routbort, *J. Appl Phys.* 66 (5), 2079 (1989).

*Work supported by the U.S. Department of Energy, Office of Energy Storage and Distribution.

Conservation and Renewable Energy, under Contract W-109-31-Eng-38. This work has benefited from the use of the Intense Pulsed Neutron Source at Argonne National Laboratory.

HIGH RESOLUTION NEUTRON POWDER DIFFRACTION STUDIES OF THE FERROELASTIC PHASE TRANSITION IN LaNbO_4

W I F DAVID, Rutherford Appleton Laboratory, Chilton, Didcot, Oxon, OX11 0QX, UK

ABSTRACT

Analysis of high resolution neutron powder diffraction data of ferroelastic LaNbO_4 indicates a monoclinic to tetragonal structural phase transition that is accompanied by anomalous line broadening. The origins of this line broadening have been investigated using a novel modification of the Rietveld technique. The results show that strain broadening is associated with the ferroelastic phase transition both above and below the transition temperature. This anomalous 'microstrain' is well-described by a second rank strain tensor, the principal axes of which are collinear with the spontaneous lattice strain. This phenomenon may be a general feature of proper ferroelastic phase transitions.

INTRODUCTION

Lanthanum niobate (LaNbO_4) is a ferroelastic material that undergoes a structural phase transition from a monoclinic (space group $I2/a$ (C^6_{2h})) to tetragonal structure (space group $I4_1/a$ (C^6_{4h})) [1,2]. A striking characteristic of this second-order phase transition is the absence of a soft optic mode [3]. Indeed, the transition is driven by a soft acoustic mode and thus LaNbO_4 is a rather unusual example of a proper ferroelastic material in which the order parameter may be regarded as the lattice spontaneous strain. High resolution neutron powder diffraction data presented in this paper exhibit unusual line-broadening behaviour. Such behaviour has also been observed in another proper ferroelastic material, arsenic pentoxide (As_2O_5), that does not possess a soft optic mode at the ferroelastic phase transition [4]. It is speculated that the anomalous strain broadening observed in LaNbO_4 and As_2O_5 is a general feature of proper ferroelastics that have displacive structural phase transitions.

EXPERIMENTAL PROCEDURE AND DATA ANALYSIS

High resolution neutron powder diffraction data were collected at a series of temperatures from a 1 cm^3 sample of LaNbO_4 on the High Resolution Powder Diffractometer (HRPD) at the spallation neutron source ISIS [5]. Each run lasted for

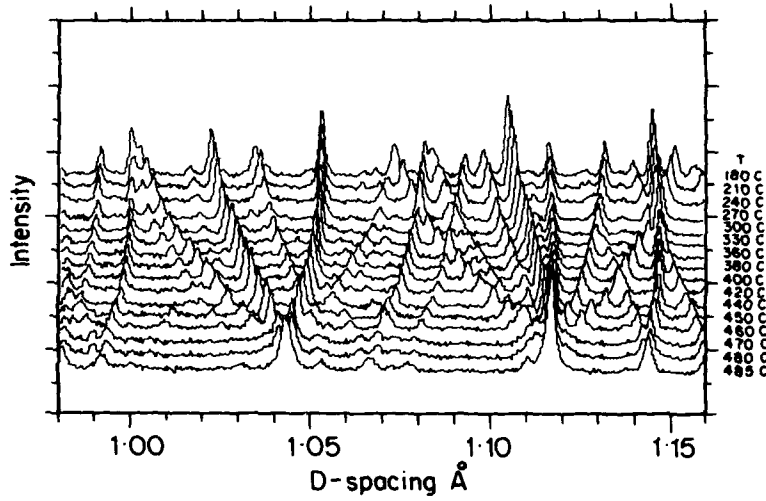


Figure 1. Multiple diffraction patterns from a 1 cm^3 sample of LaNbO_4 recorded as a function of temperature. The peak splitting associated with the ferroelastic phase transition is evident.

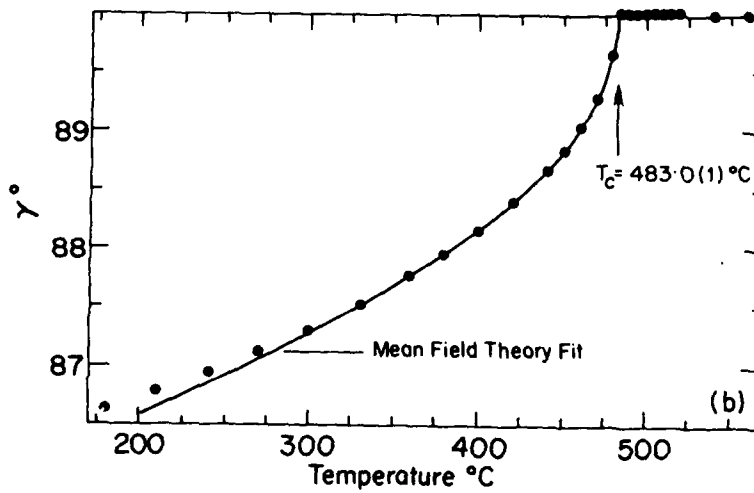


Figure 2. The variation of the monoclinic angle as a function of temperature. Least square fitting confirms a mean-field behaviour and a transition temperature of $483.0(1)^\circ\text{C}$.

approximately 30 minutes. A small portion of the range of d-spacings surveyed is shown in Figure 1. There is clear evidence of a structural phase transition. Indeed, the refined lattice parameters indicate a large monoclinic distortion that collapses in a mean-field manner at the transition temperature. The monoclinic shear angle is displayed in Figure 2.

Close examination of the diffraction data collected at temperatures near the phase transition reveals significant broadening, particularly of some $hk0$ reflections. Standard Rietveld profile refinement of data obtained below 180°C and above 540°C proceeded routinely. However, at intermediate temperature the refinements became progressively worse on approaching the phase transition. Indeed, differences between diffraction patterns recorded at room temperature and the transition temperature were extremely pronounced. As the origin of the line broadening was initially unknown a modified Rietveld profile refinement (SAPS - Structures And Peak Shape Refinement) was employed [5]. SAPS permits simultaneous analysis of the crystal structure and the hkl -dependent broadening in a model-independent manner. The principal difference is that instead of describing peak widths as a function of time of flight, all peak widths may be refined as independent variables. Structural parameters for LaNbO_4 were thus obtained that were unbiased by an imposed peak broadening model. A selection of the (Lorentzian) peak width components so refined are presented in Table I.

Table I. Part of one of the output files from SAPS. This contains Miller indices hkl , along with peak intensities, I , and standard deviations, $\sigma(I)$. If $I/\sigma(I)$ is greater than a predetermined value (12 in this particular case) then peak widths may be refined. For $I/\sigma(I) < 12$, peak widths are fixed (note zero standard deviations for some Γ). In this example the usual TOF functional form for σ was refined: all individual Gaussian widths were fixed.

h	k	l	I	$\sigma(I)$	Γ	$\sigma(\Gamma)$	σ	$\sigma(\sigma)$
0	1	5	663.8	20.5	25.3	3.9	51.8	0.0
1	0	5	540.2	20.6	43.1	5.3	51.9	0.0
-1	1	4	3646.5	37.8	49.7	1.7	55.9	0.0
1	1	4	3460.5	38.5	45.5	1.7	56.2	0.0
-1	2	1	715.1	24.2	112.5	8.5	56.7	0.0
-2	1	1	2443.0	31.0	40.7	2.1	57.1	0.0
1	2	1	2192.0	28.3	38.5	2.2	57.3	0.0
2	1	1	836.2	26.5	97.4	6.6	57.7	0.0
0	2	2	461.3	29.5	89.7	10.3	59.0	0.0
2	0	2	579.9	30.7	58.2	6.5	59.6	0.0
0	2	0	10.3	35.4	42.2	0.0	64.9	0.0
-2	0	0	0.7	35.7	42.8	0.0	65.8	0.0
0	0	4	121.4	43.7	45.9	0.0	70.6	0.0
0	1	3	361.6	45.4	49.6	0.0	76.2	0.0
1	0	3	303.1	30.3	49.8	0.0	76.5	0.0
-1	1	2	9352.3	89.6	114.4	2.7	77.0	0.0
1	1	2	10061.0	98.0	93.5	2.3	77.7	0.0

These peak widths were then analysed to determine the origin of the line broadening. Refinements at various temperatures revealed a pronounced temperature dependence that diverges around T_c . The anomalous Lorentzian broadening of the 220, $\bar{2}20$ and 112, $\bar{1}12$ reflections are displayed in Figure 3. The ratio of the slopes above and below T_c is 2:1 within experiment error as predicted by mean-field theory. The predominant nature of the Lorentzian broadening is consistent with strain effects described by a second rank tensor. Accordingly, anisotropic Lorentzian strain and particle size effects described by a second rank tensor formulation were added in convolution to the standard time-of-flight peak shape. The full width at half maxima formulae used were

$$\Gamma_{\text{strain}} = \eta d^2; \quad \Gamma_{\text{size}} = \eta d^3$$

where

$$\eta^2 = \Gamma_{11}h^2a^*2 + \Gamma_{22}k^2b^*2 + \Gamma_{33}l^2c^*2 + 2[\Gamma_{23}klb^*c^*\cos\alpha^* + \Gamma_{13}hla^*c^*\cos\beta^* + \Gamma_{12}hka^*b^*\cos\gamma^*]$$

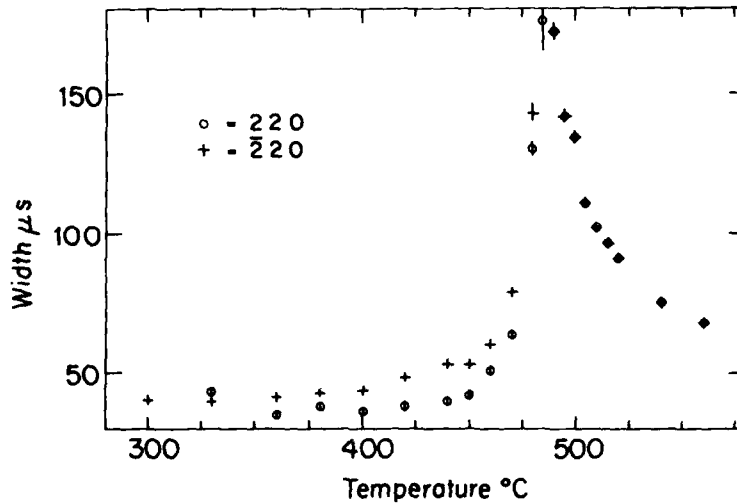


Figure 3. Refinement of individual peak widths reveals a pronounced temperature dependence that diverges around T_c . The distinction between 220 and $\bar{2}20$ (similarly 112 and $\bar{1}12$) peak widths is consistent with strain effects described by a second rank tensor.

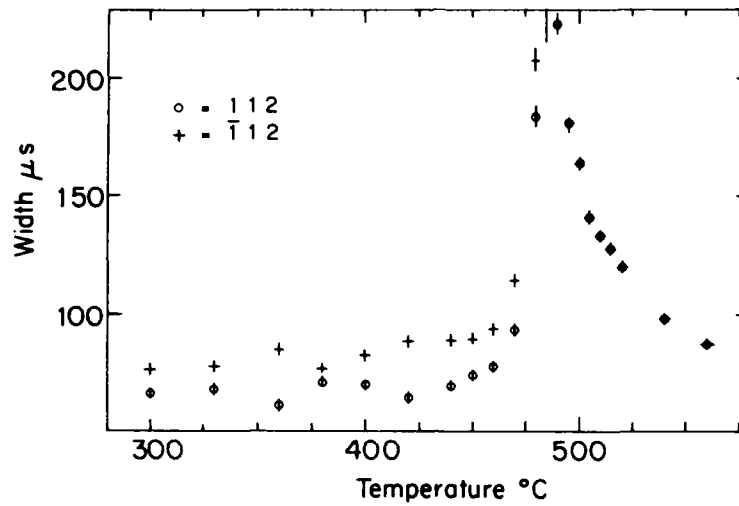


Figure 3 (Continued)

Rietveld refinement at a number of different temperatures indicated that the anisotropic broadening resulted from strain rather than size effects. This anomalous behaviour is restricted to the *ab* plane: no extra broadening is associated with the *c* axis. The refined values shown in Table II clearly indicated strain anisotropy within the *ab* plane.

Table II. Refined anisotropic strain broadening terms

T(°C)	Γ_{11}	Γ_{22}	Γ_{12}
240	205(15)	402(20)	600(300)
270	198(15)	366(20)	900(300)
300	183(15)	392(20)	1600(300)
330	227(20)	378(20)	1500(300)
360	190(15)	447(25)	2500(400)
380	214(20)	462(25)	2300(400)
400	257(20)	417(25)	2600(500)
420	266(20)	598(30)	3900(600)
450	400(25)	676(30)	6500(1000)
460	460(40)	770(40)	8700(1500)
470	840(40)	1320(50)	15300(3000)
480	2200(200)	3800(250)	36000(5000)

The anisotropic broadening of the Bragg peaks (microstrain) in LaNbO_4 may, as with the monoclinic lattice distortion (macrostrain), be described in terms of a second rank tensor. The principal axes of the ellipsoid representing the microstrain broadening is rotated by 21° from a^* . This agrees to within experimental error ($\sim 2^\circ$) with the orientation of the principal axes of the spontaneous macrostrain hyperbola for all data sets collected between $(T_c - 50^\circ)$ and T_c (see Figure 4).

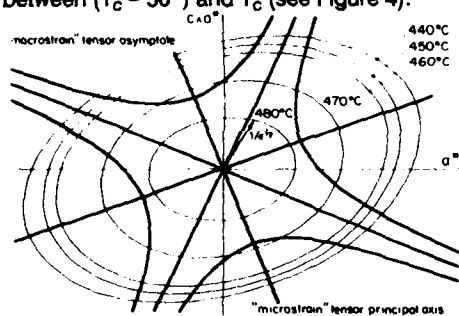


Figure 4. The representation quadrics for spontaneous lattice strain (hyperbola) and microstrain broadening (ellipsoids) in the low temperature monoclinic phase are coincident to within experimental error.

The coincidence of the orientation of microstrain (obtained from line broadening considerations) and macrostrain (calculated from peak splittings associated with monoclinic symmetry) was unexpected and is at present unexplained, although the strain broadening is probably associated with crystal imperfections such as dislocations. It indicates, perhaps unsurprisingly, that unit cell and unit cell contents play a coherent role with respect to the phase transition. The importance of strain in the driving mechanism is associated with the fact that LaNbO_4 is a proper ferroelastic material – there is a soft acoustic mode but no observed soft optic mode. Further analysis of this phase transition using the structural information is currently underway.

REFERENCES

1. S. Tsunekawa and H. Takei, *Mater. Res. Bull.* **12**, 1087 (1977)
2. W. I. F. David, D. Phil. Thesis, University of Oxford, 1981
3. M. Wada, Y. Nakayama, A. Sawada, S. Tsunekawa and Y. Ishibashi, *J. Phys. Soc. Japan*, **47**, 1575 (1979)
4. S. A. T. Redfern and E. Salje, *J. Phys. C: Solid State Phys.* **21**, 277 (1988)
5. W. I. F. David, D. E. Akporiaye, R. M. Ibberson and C. C. Wilson, Rutherford Appleton Laboratory Report No. RAL-88-103, 1988

PART V

Alloys

NEUTRON SCATTERING FROM LATTICE DEFECTS

JOHANN PEISL, HELMUT DOSCH and STEFAN KIRCHNER
Sektion Physik, Ludwig-Maximilians-Universität, 8000 München 22,
FRG

ABSTRACT

For O in Nb the experimental scattering distribution can be described by a so-called 3-force model. The scattering pattern exhibits close similarity to the one observed for the ω -phase in some bcc alloys. It is shown that the lattice distortion calculated from the proposed 3-force model contains static fluctuation of the ω -phase. The ω -phase is closely related to the minimum in the LA 2/3 (111) phonon dispersion branch. With decreasing temperature the frequency of this phonon decreases, whereas the elastic diffuse scattering at the same position increases. This "softening" of the lattice, together with an increasing "central peak", gives an equivalent description of the situation.

1. INTRODUCTION

The real structure of a solid can be described in most cases by a picture of a perfect crystal lattice containing defects. In the following discussion we consider only point defects like impurities on substitutional or interstitial sites. They may be unavoidable defects or deliberately introduced dopants. Defects produced by irradiation are self-interstitials, vacancies and small agglomerates formed by these defects. These defects can be studied in a neutron diffraction experiment by detection of the scattering from the defects themselves and the scattering from defect-induced displacements of the lattice atoms.

For an undistorted crystal lattice the neutron (or X-ray) scattering intensity distribution from the atoms in the lattice is zero except for the case that all the atoms scatter in phase, i.e. whenever the scattering vector \mathbf{K} is equal to a reciprocal lattice vector \mathbf{G} . For $\mathbf{G} = \mathbf{K}$ narrow Bragg peaks are observed and contain information about the periodic arrangement of the atoms in the crystal lattice. The wide range of \mathbf{K} values between \mathbf{G} vectors contains intensity from sources of incoherent and inelastic scattering in the neutron case, Compton and thermal diffuse scattering in the X-ray case and scattering due to defects in the crystal lattice.

Neutron scattering methods are superior to X-ray scattering in a great number of problems where light interstitials like H, C, N and O, which in metals play an important role for the properties of materials, can hardly be detected with X-rays. Small defect concentrations and/or defects with low scattering length contrast can be studied by neutron scattering because the background scattering can be extremely low. Thermal diffuse scattering background which is inelastic can be suppressed in an elastic scat-

tering experiment. Unlike X-ray scattering there is no Compton background and incoherent scattering can be separated in some cases by using polarized neutrons and polarization analysis.

2. NEUTRON SCATTERING FROM LATTICE DEFECTS

Lattice defects in solids are described by their lattice location and the lattice distortions caused by the defects. Defects at lattice positions \mathbf{r}_d may have a different scattering length b_d and the lattice atoms are shifted from their regular sites \mathbf{r}_m to new positions $\mathbf{r}_m' = \mathbf{r}_m + \mathbf{u}_m$. All defects contribute to the displacements \mathbf{u}_m by their individual displacement field \mathbf{u}_m^d . The scattering distribution changes accordingly. The Bragg peaks are shifted due to a change Δa of the average lattice parameter a . Deviations from this average lattice decrease the amount of positive interference that gives rise to the Bragg peaks. This attenuation of the scattered intensity is described by a static Debye-Waller factor $\exp(-2L)$. Between the Bragg peaks the scattered waves are no longer interfering destructively to zero and a defect-induced diffuse scattering intensity is observed.

The defect-induced scattering intensity for a low concentration c of randomly distributed defects is obtained by properly subtracting the scattering intensity for a defect-free crystal [1].

$$I_d(\mathbf{K}) = c \exp(-2L) \exp(-2M) \left\{ b_d \exp(i\mathbf{K} \cdot \mathbf{r}_d) + b \sum_m \exp(i\mathbf{K} \cdot \mathbf{r}_m) \cdot (\exp(i\mathbf{K} \cdot \mathbf{u}_m) - 1) \right\}_p^2 \quad (1)$$

b is the scattering length of the crystal atoms. Within this single defect approximation the diffuse scattering intensity, neglecting static DWF effects (see below), is just c times the scattering intensity from a single defect and the corresponding lattice distortions. If the defects are correlated in clusters or special defect distributions, then the scattering amplitudes have to be summed up properly and c has to be replaced by the Fourier transform of the concentration fluctuations.

The first factors in equation (1) are the static and thermal Debye-Waller factors. The first term in the carats is the scattering contribution of the defect, the so-called Laue scattering. The phase factor includes the defect location \mathbf{r}_d . The second term is the scattering contribution from the lattice distortions \mathbf{u}_m . The average denoted by $\langle \quad \rangle_p$ is over all possible defect sites. In order to calculate model scattering distributions and compare them with the experimentally observed ones, one describes the displacement field of the defects by a force distribution. These so-called Kanzaki forces \mathbf{f}^n on the lattice atoms at \mathbf{r}^n give the same displacements as the ones caused by the defects. Lattice statics allow us to calculate \mathbf{u} using these forces and the lattice Green's function G_{ij}^{m-n} available from experimental phonon dispersion curves. The before-mentioned force dipole tensor is $P_{ij} = \sum_n \mathbf{f}_i^n r_j^n$. The advantage of this parametrization of the long

ranged displacement field lies in the appreciable reduction of free parameters. Usually Kanzaki forces with radial components on the next neighbours of the defect site are sufficient.

3. EXPERIMENTAL RESULTS

The neutron scattering experiments have been carried out on a three-axis spectrometer. In order to reject all inelastic scattering processes the spectrometer is run in an elastic mode. The neutrons, which are scattered from the sample without energy change, were selected by the analyzer crystal. The incoherent scattering and some weak inelastic scattering close to Bragg reflections were subtracted experimentally by measuring the corresponding intensities of a pure reference sample. For more experimental details the reader is referred to the literature [2, 3].

3.1 Elastic diffuse scattering from NbO_x

The force dipole tensor of O in Nb has been determined by Huang diffuse scattering of X-rays [4].

$$P_{ij}^O = \begin{pmatrix} 12.4 & 0 & 0 \\ 0 & 5.1 & 0 \\ 0 & 0 & 5.1 \end{pmatrix} \text{ eV}$$

The coherent elastic diffuse scattering far away from Bragg peaks could be observed by neutron scattering. Fig. 1(a) shows, as an example, iso-intensity plots as observed from $\text{NbO}_{0.020}$ [5].

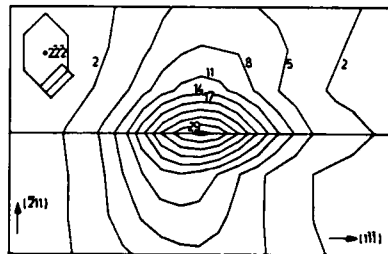
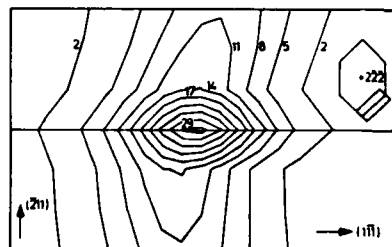


Fig. 1: Elastic diffuse neutron scattering distribution from $\text{NbO}_{0.02}$ at $T = 270$ K. Iso-intensity contours are shown in the vicinity of the (222) Brillouin zone boundary.

- a) Measured distribution
b) Calculated distribution with the 3-force model



In Fig. 1(b) corresponding model calculations are shown. Oxygen is assumed to occupy the octahedral interstitial sites in the bcc niobium lattice. Possible sets of Kanzaki forces have to be consistent with the experimentally determined force dipole tensor P_{ij}^O . It turns out that one needs radial forces on defect neighbours which extend to the third-nearest Nb neighbour (3f model). Table 1 shows the

Kanzaki forces and lattice displacements which give a good quantitative agreement between calculated and measured intensity distributions for oxygen in niobium.

Table 1. Kanzaki forces f_i ($i = 1, 2, 3$) and lattice displacements u_j ($j = 1, 2, 3, 4$) used to describe the lattice distortions due to O in Nb [6]

Kanzaki forces ($\text{eV } \text{\AA}^{-1}$)	$f_1 = 2.80$	$f_2 = -0.27$	$f_3 = 0.54$
Lattice displacements (\AA)	$u_1 = 0.42$	$u_2 = -0.13$	$u_3 = 0.06$
	$u_4 = 0.07$		

It has been pointed out by several authors that the intensity distributions like the ones shown in Fig. 1 show the same characteristic features as observed if an ω -phase is formed. Dosch et al. [6] have followed this point into great detail and show that the local defect-induced displacements from the Kanzaki force model are interrelated with static fluctuations of the ω -phase. Especially the displacement u_2 towards the defect is directly correlated to the structure of the locally condensed ω -phase fluctuations in the bcc lattice. The general instability of bcc lattices towards ω -phase formation is important. ω -phase fluctuations due to hydrogen on tetrahedral interstitial sites in bcc lattices have, however, not been observed. The defect location and details of the interaction between the defect and the host lattice atoms seem to be important.

Fig. 2 shows a projection of the calculated lattice displacement $u_{1,2}$ on a $(2\bar{1}\bar{1})$ plane which contains the (111) direction in which the ω -fluctuations occur. The undistorted bcc lattice is

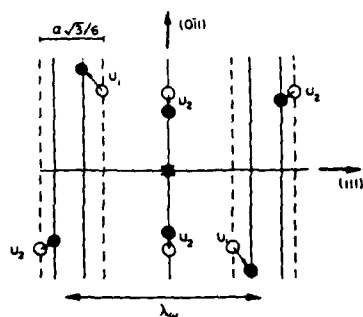


Fig. 2: Projection on a $(2\bar{1}\bar{1})$ lattice plane of the displacements of the Nb atoms (open symbols: undistorted, full symbols: distorted) close to an oxygen impurity (star). The dashed lines denote the (111) planes in the undistorted lattice (bcc). The full lines denote the same planes as shifted by the static displacements u_1 and u_2 (rumpled ω -phase). (Lattice distances and lattice distortions are not on scale).

shown by open circles and equidistant dashed lines. The full circles and full lines show the position of the atoms and the (111) planes after introduction of the defect (O or N). The distorted lattice shows clear similarities to a rumpled ω -phase [6]. In order to learn more about this close connection between the bcc

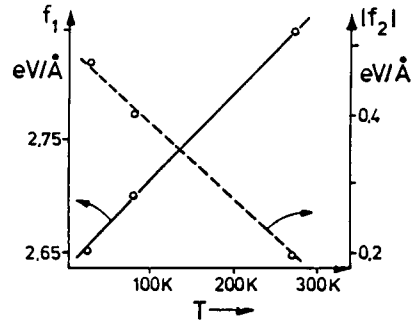


Fig. 3: Temperature dependence of the Kanzaki forces f_1 and f_2

inherent instability towards an ω -phase and the local lattice distortions the latter were studied at various temperatures and oxygen concentrations [5].

Fig. 3 shows the temperature dependence of the Kanzaki forces f_1 and f_2 on first and second next neighbours of O in Nb. f_1 increases, whereas f_2 decreases with increasing temperature. f_3 shows a slight decrease with temperature (not shown in Fig. 3). The corresponding lattice displacements for two temperatures (270 K and

Table 2. Lattice displacements u_j ($j = 1, 2, 3, 4$) of the four neighbouring atom shells around O in Nb at 270 K and 25 K

displacements (\AA)	u_1	u_2	u_3	u_4
270 K	0.421	-0.113	0.0573	0.0693
25 K	0.405	-0.144	0.0751	0.0667

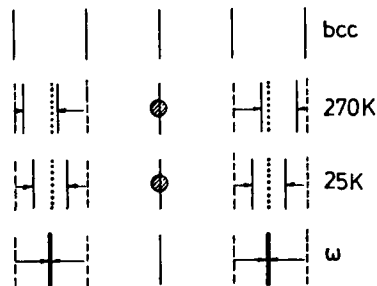


Fig. 4: Defect-induced lattice displacements for various temperatures schematically denoted by (111) planes

25 K) are listed in Table 2 and again shown in Fig. 4 in a projection on the $(2\bar{1}\bar{1})$ plane like in Fig. 2. At lower temperatures (25 K) the ω -phase like distortion is even more pronounced.

Thus the idea that defects like O and N on interstitial sites induce lattice distortions which show a similarity to the ω -phase is supported once more. It is then no longer surprising that at low temperature, where in the "defect-free" alloys like $Zr_{1-x}Nb_x$ the ω -phase was originally observed [7, 8], this tendency is more pronounced.

3.2 Inelastic scattering from NbO_x

The occurrence of the ω -phase in bcc metals and its structure are intimately related to the instability of the bcc structure against lattice strains in the [111] direction, which manifests itself in the well-known minimum of the LA [111] phonon dispersion curve at $q = 2/3 (1,1,1)$. It is generally accepted that this phonon mode is responsible for the displacements of the (111) planes which leads, when frozen in as the static displacement $u = \pm \sqrt{3}/12 (111)$, to the trigonal ω -phase. In this connection the question arises whether this phonon itself is altered when impurities nucleate ω -fluctuations.

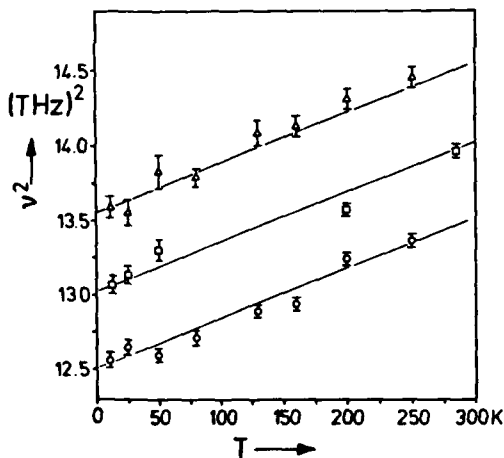


Fig. 5: Square of the ω -phonon frequency v^2 as a function of temperature and oxygen concentration

circles: pure Nb; squares: $NbO_{0.01}$
triangles: $NbO_{0.02}$

increases only slightly with increasing temperature but increases with oxygen concentration. The linear connection between v^2 and T stems from the same relation between the phonon frequencies and

We have measured [5] in an inelastic neutron scattering investigation the dependence of the LA $2/3 (111)$ phonon (" ω -phonon") on temperature and oxygen concentration. The results are shown in Fig. 5. The square of the measured frequencies is plotted versus temperature for pure Nb, $NbO_{0.01}$ and $NbO_{0.02}$. The pure Nb sample shows a decrease of the frequency with decreasing temperature. Increasing oxygen concentration increases the frequency whereby the temperature dependence remains almost the same. The energy width of the phonon scattering peaks

the force constants. Thus we have to conclude that for the lattice as a whole, oxygen impurities increase the ω -frequency and the force constants.

4. CONCLUSIONS

The elastic diffuse scattering induced by the defects can be described by a temperature-dependent 3-force-model. The displacements in the vicinity of the defects as calculated from the forces via lattice statics show at lower temperature increasingly more similarities with the displacements leading to the ω -phase. The Nb lattice with decreasing temperature shows an increased instability towards an ω -phase. This is connected with the "softening" of the relevant " ω -phonon" at $q = 2/3$ (111). At the same time the elastic diffuse scattering at $q = 2/3$ (111) increases. This reminds one of the "central peak" phenomenon. We have demonstrated here that in our case the central peak is caused by the static lattice distortions induced by interstitial defects. A series of questions arises :

- How does this behaviour depend on the defect location in the lattice and the defect strength?
- Does the increase of the ω -phonon frequency with defect concentration finally lead to a stabilization of the lattice against ω -phase formation ?
- How is this behaviour changed in metals where the ω -phonon frequency is lower (Zr) or higher (Mo) in the defect-free crystal ?

ACKNOWLEDGEMENT

This work was supported by the Bundesministerium für Forschung und Technologie under contract no. 03-PE1LMU-2.

REFERENCES

- [1] For details see e.g. M.A. Krivoglaz, Theory of X-Ray and Thermal Neutron Scattering by Real Crystals (Plenum, New York, 1969)
- [2] H. Dosch and J. Peisl, Phys. Rev. B **32**, 623 (1985)
- [3] H. Dosch, J. Peisl and B. Dorner, Z. Phys. B - Condensed Matter **63**, 479 (1986)
- [4] U. Schubert, H. Metzger and J. Peisl, J. Phys. F **14**, 2467 (1984)

- [5] S. Kirchner, Diploma Thesis, University of Munich 1988
- [6] H. Dosch, A.v. Schwerin and J. Peisl, Phys. Rev. B 34, 1654 (1986)
- [7] R. Currant and R. Pynn, in Neutron Scattering in Material Science, edited by G. Kostorz (Academic, New York, 1979)
- [8] S.C. Moss, D.T. Keating and J.D. Axe, Phase transformations (Pergamon, Oxford, 1973)

SHORT-RANGE ORDER IN α -BRASS

L. REINHARD* **, B. SCHOENFELD*, G. KOSTORZ* AND W. BUEHRER***

*Angewandte Physik, ETH Zürich, CH-8093 Zürich, Switzerland

**now at Physics Department, University of Houston, Houston, TX 77204-5504

***Lab. f. Neutronenstreuung der ETHZ, CH-5303 Würenlingen, Switzerland

ABSTRACT

Quenched equilibrium states of Cu-31.1 at.% Zn and Cu-22.4 at.% Zn single crystals (prepared with the Cu-65 isotope) were investigated by elastic diffuse neutron scattering. The diffuse intensity showed maxima which are attributed to the flat portions of the Fermi surface in the $\langle 110 \rangle$ directions. Short-range order parameters and linear displacement parameters were obtained from a fit to the measured data. Pair interaction energies were determined based on the inverse Monte-Carlo method. An ordered low-temperature phase Cu_3Zn with the DO_{23} structure is suggested.

INTRODUCTION

The Cu-Zn system has been the subject of many theoretical investigations which have tried to relate the stability regions of the observed phases to the electronic properties of the alloy (see [1] for a brief survey). In this connection, the question of short-range order in the α -phase arises. Indications of short-range order have been found in measurements of the electrical resistivity [2], the Zener relaxation [3] and the Mössbauer spectrum [4]. However, a prior attempt to detect short-range order in α -brass by neutron scattering failed [5].

In the present work, neutron scattering was used to study short-range order in single crystals of α -Cu-Zn. Compared with X-rays, the scattering contrast for neutrons is considerably higher and can be further increased by using the Cu-65 isotope.

From the short-range order scattering of a sample representing a state of thermodynamic equilibrium, effective interatomic pair potentials (m is a label for the type of neighbouring site)

$$V_m = \frac{1}{2}(V_m^{AA} + V_m^{BB} - 2V_m^{AB}) \quad (1)$$

can be obtained, e.g. by the approximation-free inverse Monte-Carlo algorithm [6]. These interactions can be used to predict low-temperature ordered structures and to calculate phase diagrams. Furthermore they offer a valuable link to electronic structure calculations, based on the KKR-CPA-GPM method (Korringa-Kohn-Rostoker-coherent-potential approximation, generalized perturbation method; see ref. [1,7] and references therein).

For a given scattering vector Q the elastic diffuse scattering from a solid solution contains contributions due to short-range order (I_{SRO}) and static displacements of the atoms from the positions of the mean periodic lattice. For small atomic displacements one obtains a linear approximation for the 'size effect':

$$I_{\text{Diff}}(Q) = I_{\text{SRO}}(Q) + I_{\text{SE}}(Q) \quad (2)$$

where (in Laue units for a binary alloy), see e.g. [8]:

$$I_{\text{SRO}}(\underline{Q}) = \sum_m \alpha_m \exp(i\underline{Q} \cdot \underline{r}_m) ; I_{\text{SE}}(\underline{Q}) = \sum_m \underline{Q} \cdot \underline{\pi}_m \exp(i\underline{Q} \cdot \underline{r}_m). \quad (3)$$

The α_m are the Warren-Cowley short-range order parameters, and $\underline{\pi}_m = (\pi_m^x, \pi_m^y, \pi_m^z)$ are the linear displacement parameters for the interatomic distances \underline{r}_m .

EXPERIMENTS AND RESULTS

Two single-crystalline α -brass samples were prepared by the Bridgman method using isotopically pure [99.2(2)%] Cu-65 and 99.9999% pure Zn. The concentrations as determined by chemical analysis were 31.1(2) at.% Zn (sample 1) and 22.4(3) at.% Zn (sample 2). The mosaic spread (FWHM) for the 200 reflection was 1.6° and 1.2° for sample 1 and 2, respectively. After homogenization the samples were annealed (sample 1 for 160 h at 473 K, sample 2 for 270 h at 493 K) and water quenched. This heat treatment was chosen to obtain, and safely freeze-in, equilibrium atomic distributions: for the zinc concentrations and annealing temperatures involved, the relaxation times are ~ 1000 s [2].

The scattering experiments (for details see [9]) were performed at the triple-axis spectrometer R5 at the LNS, Würenlingen. With both samples, the (001), (011) and (111) reciprocal-lattice planes were investigated using neutrons with wavelengths of 2.44 Å and 4.15 Å. The accessible range for the scattering vector was $0.3 < h < 2.3$ reciprocal-lattice units ($Q = 2\pi h/a$). About 950 data points were measured in each plane, with a mesh of $\Delta h = 1/30$. The data were converted to absolute units by measuring the incoherent scattering from a vanadium sample.

The diffuse scattering intensity in the (001) plane (Fig.1) shows maxima between the Bragg positions indicating short-range order. The particular arrangement of diffuse 'satellites' around the 110 position is typical for many copper-based alloys and has been attributed to flat portions of the Fermi surface in the $\langle 110 \rangle$ direction [10]. In the framework of a one-electron theory, singularities of the static dielectric function $\epsilon(\underline{Q})$ lead to minima of the Fourier-transformed pair potential $V(\underline{Q}) \propto 1/\epsilon(\underline{Q})$ and thus to

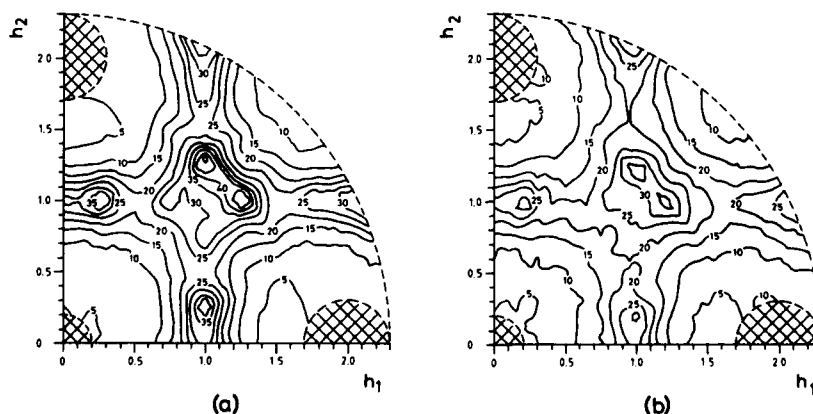


Figure 1. Diffuse scattering intensity (in 0.1 Laue units) for the (001) plane: (a) sample 1, (b) sample 2.

maxima of the short-range order scattering $I_{SRO}(Q)$ for $Q = 2k_F$ (k_F being the Fermi vector perpendicular to a flattened portion of the Fermi surface) [11,12]. In a more fundamental approach based on the KKR-CPA method '2 k_F singularities' have also been obtained for the short-range order scattering in the Cu-Pd system [13].

The magnitudes of the Fermi vectors k_F as obtained from the positions of the maxima are $1.38(2) \text{ \AA}^{-1}$ (sample 1) and $1.34(2) \text{ \AA}^{-1}$ (sample 2). These values agree satisfactorily with the value $1.40(2) \text{ \AA}^{-1}$ found in positron annihilation measurements for a Cu-30 at.% Zn crystal [14] and with $k_F = 1.37(1) \text{ \AA}^{-1}$ from CPA calculations for Cu-20 at.% Zn [15].

Short-range order and atomic displacements

For each sample, 71 α_m and 40 α_m^i values were obtained by a weighted least-squares fit to the experimental data. Fig.2 shows the I_{SRO} and I_{SE} intensities as recalculated from the Fourier coefficients. The short-range order intensity exhibits four symmetric maxima around 110; the asymmetry of the measured diffuse pattern (Fig.1) is due to the displacement scattering.

Both alloys show a very similar variation of the short-range order parameters (Fig.3) as a function of the interatomic distance. However, the α_m for sample 2 - with the lower Zn concentration - have smaller absolute values in accordance with the weaker modulations of the diffuse intensity for this sample. The short-range order parameter α_{110} is negative, indicating a preference for unlike atoms in the nearest-neighbour shell. As the α_{200} are positive and the $\alpha_{(2n-1)110}$ are negative, there is a tendency for atoms of the same kind to form chains along $\langle 100 \rangle$ directions. Fig.4 compares a (001) plane of a model crystal fitted to the set of α_m values of sample 1 (a) with a plane from a crystal with a random arrangement of atoms at the same concentration (b). The higher abundance of nearest-neighbour Cu-Zn bonds as well as chains of Zn atoms along $\langle 100 \rangle$ are visible in Fig.4a. From the measured α_m , the individual atomic displacements were estimated to be less than 0.01 of the lattice parameter.

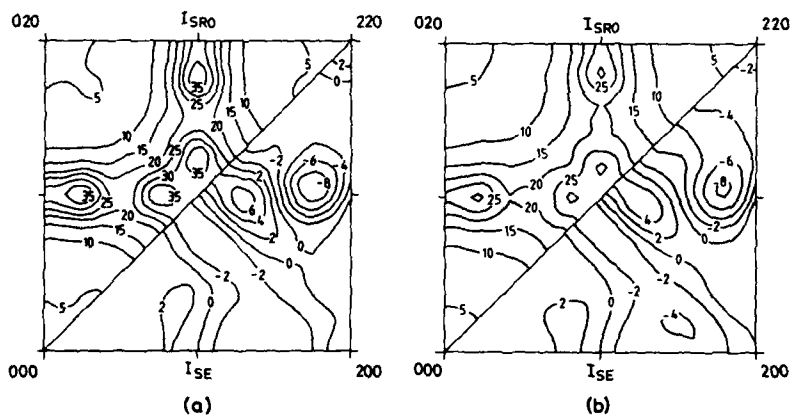


Figure 2. Short-range order scattering I_{SRO} and linear displacement scattering I_{SE} (in 0.1 Laue units) for the (001) plane: (a) sample 1; (b) sample 2.

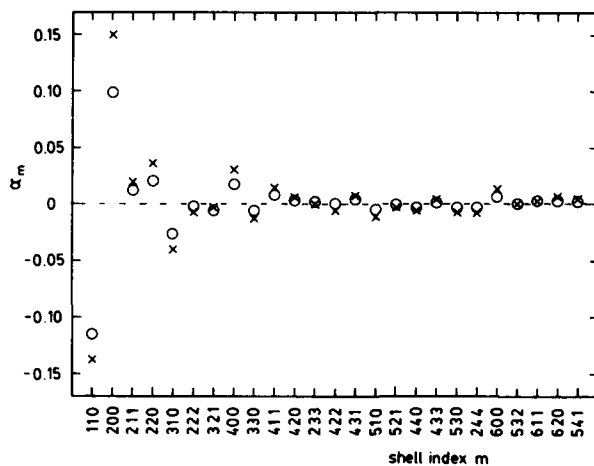


Figure 3. The first 25 short-range order parameters for sample 1 (x) and sample 2 (o).

Pair potentials

From the experimental values for the α_m , 20 pair potentials have been determined by the inverse Monte-Carlo method (Fig.5). For both Zn concentrations the nearest-neighbour potential $V_{110} \approx 20$ meV is dominant. There is no oscillatory behaviour and no slower decrease of the V_m in $\langle 110 \rangle$ direction, as might be expected from a Friedel potential and the flatness of the Fermi surface perpendicular to $\langle 110 \rangle$ [16]. Nevertheless, the fourfold splitting of the diffuse intensity around the 110 position is reproduced if one recalculates I_{SP0} from the pair potentials by the Monte-Carlo method [17]. As V_{110} dominates, the Fourier transform $V(Q)$ has extended and rather weakly modulated minima along $(1,q,0)$, which means that ordered structures

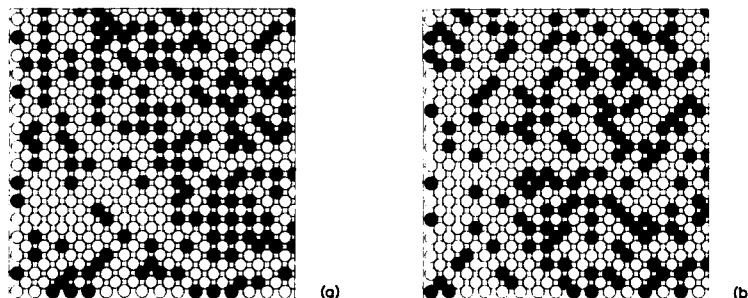


Figure 4. (001) plane of a modelled short-range ordered Cu-31.1 at.% Zn alloy (a) and of a random arrangement with identical composition (b): Cu (o) atoms, Zn (e) atoms.

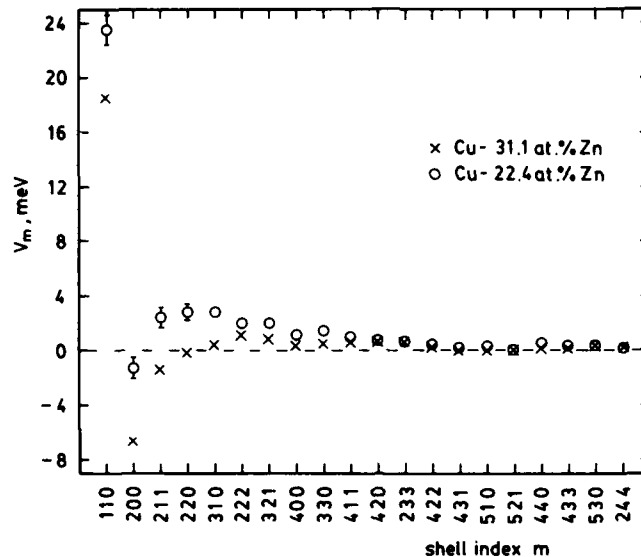


Figure 5. Pair potentials as obtained by the inverse Monte-Carlo method: (x) sample 1, (o) sample 2.

with superstructure reflections located on the line (1,q,0) are good candidates for the $T = 0$ K ground-state. For the Cu_2Zn stoichiometry, the configuration energies of $L1_2$ -related superstructures with antiphase boundaries were calculated using the pair potentials [the structures considered were $L1_2$ ($M = \infty$), DO_{22} ($M = 1$), DO_{23} ($M = 2$) and the long-periodic structure with $M = 3$]. With both sets of V_m , the DO_{23} structure has the lowest energy, the energy differences between the various structures being of the order of 1 meV per atom. A DO_{23} structure might actually be expected from the I_{SPD} plot (Fig. 2) because the locations of the short-range order maxima are close to the $1/2$ superlattice peaks of DO_{23} . In order to stabilize DO_{23} , rather long-ranged interactions are needed; DO_{23} becomes the energetically favorable structure only if at least eleven V_m values of sample 1 or thirteen V_m values of sample 2 are used. A Monte-Carlo simulation was used to estimate the critical temperature for the order-disorder transition, leading to a value of about 330 K.

REFERENCES

1. G.M. Stocks, M. Boring, D.M. Nicholson, F.J. Pinski, D.D. Johnson, J.S. Faulkner, and B.L. Gyorffy, in *Noble Metal Alloys*, edited by T.B. Massalski, W.B. Pearson, L.H. Bennett, and Y.A. Chang (Proceedings of the Metallurgical Society of AIME Annual Meeting, 1985), p. 27.
2. W. Pfeiler, R. Reihnsner, and D. Trattner, *Scripta Metall.* **19**, 199 (1985).

3. M. Halbwachs, D. Beretz, and J. Hillairet, *Acta Metall.* 27, 403 (1979).
4. Th. Obenhuber, W. Adlassnig, U. Narger, J. Zankert, W. Potzel, and G.M. Kalvius, *Europhys. Lett.* 3, 989 (1987).
5. D.T. Keating, *Acta Metall.* 2, 885 (1954).
6. V. Gerold and J. Kern, *Acta Metall.* 35, 393 (1987).
7. M. Sluiter, P.E.A. Turchi, D.M. Nicholson, G.M. Stocks, D.D. Johnson, and F.J. Pinski, this symposium.
8. L.H. Schwartz and J.B. Cohen, *Diffraction from Materials*, 2nd ed. (Springer, Berlin, 1987), p. 402.
9. L. Reinhard, B. Schonfeld, G. Kostorz, and W. Buhrer, to be published in *Phys. Rev. B*.
10. S.C. Moss, *Phys. Rev. Lett.* 22, 1108 (1969).
11. P.C. Clapp and S.C. Moss, *Phys. Rev.* 142, 418 (1966).
12. S.C. Moss and R.H. Walker, *J. Appl. Cryst.* 8, 96 (1975).
13. B.L. Gyorffy and G.M. Stocks, *Phys. Rev. Lett.* 50, 374 (1983).
14. M. Haghgoie, S. Berko, and U. Mizutani, in *Proceedings of the Fifth International Conference on Positron Annihilation*, edited by R.R. Hasiguti and K. Fujirawa (Japan Institute of Metals, Sendai, 1979), p. 291.
15. R. Prasad, S.C. Papadopoulos, and A. Bansil, *Phys. Rev. B* 23, 2607 (1981).
16. L.M. Roth, H.J. Zeiger, and T.A. Kaplan, *Phys. Rev.* 149, 519 (1966).
17. K. Binder, in *Monte Carlo Methods in Statistical Physics*, edited by K. Binder (Springer, Berlin, 1979), p. 1.

A FIRST-PRINCIPLES STUDY OF SHORT RANGE ORDER IN Cu-Zn

M. SLUITER^{1,2}, P.E.A. TURCHI², D.D. JOHNSON³, F.J. PINSKI⁴, D.M. NICHOLSON⁵, G.M. STOCKS⁵

¹ Lawrence Berkeley Laboratory, Materials and Chemical Sciences Department, Berkeley, CA 94720, USA. ² Lawrence Livermore National Laboratory, P.O. Box 808, Condensed Matter Division L-268, Livermore, CA 94550, USA. ³ Sandia National Laboratory, Div. 8341, P.O. Box 969, Livermore, CA 94551-0969, USA. ⁴ University of Cincinnati, Dept. of Physics, Cincinnati, OH 45221, USA. ⁵ Oak Ridge National Laboratory, Metals and Ceramics Div., P.O. Box 2008, Oak Ridge, TN 37831, USA.

Recently, measurements of short-range order (SRO) diffuse neutron scattering intensity have been performed on quenched Cu-Zn alloys with 22.4 to 31.1 atomic percent (a/o) Zn, and pair interactions were obtained by Inverse Monte Carlo simulation [1]. These results are compared to SRO intensities and effective pair interactions obtained from first-principles electronic structure calculations. The theoretical SRO intensities were calculated with the Cluster Variation Method (CVM) in the tetrahedron-octahedron approximation with first-principles pair interactions as input. More generally, phase stability in the Cu-Zn alloy system is discussed, using ab-initio energetic properties.

Phase stability in the Cu-Zn system has long been explained in terms of phenomena related to the electronic bandstructure [2]. Methods that provide a formal, first-principles connection between electronic structure and phase stability in alloys have become available only in the last decade. The quest for these methods has been motivated by two factors: i) statistical mechanical models, such as the Monte Carlo and the CVM, are highly successful in the description of ordering or segregation in substitutional alloys over wide concentration ranges and at finite temperatures; and ii) first-principles electronic total energy methods based on the local density approximation are able to accurately predict the ground state properties of alloys. A number of approaches have been proposed, such as the concentration functional theory, developed by Gyorffy and Stocks [3], the embedded cluster method of Gonis et al. [4], and the Generalized Perturbation Method (GPM) by Ducastelle and Gautier [5]. In this paper, we will use the latter method, the GPM applied to the Korringa-Kohn-Rostoker multiple scattering formulation of the Coherent Potential Approximation (KKR-CPA-GPM) [6]. With this method the energetic properties of phase stability, such as the energies of mixing and effective cluster interactions, can be computed from first-principles. When these energetic properties are used in statistical mechanical methods, such as Monte Carlo simulations or the CVM, a complete description of the thermodynamics and hence the phase stability of alloys at non-zero temperatures can be obtained. Moreover, other properties, such as SRO diffuse scattering, can be predicted.

Previously, the GPM has been used extensively within the tight-binding approximation (TBA), and it has been shown that, at least as far as tendencies are concerned, reliable predictions of phase stability can be made [7,8,9]. Preliminary calculations of phase diagrams based on the use of TBA-CPA-GPM effective interactions to describe the ordering energy on the one hand and the CVM to calculate the configurational equilibrium free energy on the other hand indicate that the main features of coherent and non-coherent phase diagrams can be obtained [10].

The GPM is based on a perturbative treatment of a reference medium which is close to any particular configuration c of the alloy. The most natural choice for such a reference medium is the completely disordered state, as the one described by the CPA. For each configuration of the alloy, specified by a set of occupation numbers $\{p_n^i\}$, (p_n^i takes the value 1 if site n is occupied by an atom of type i , and equals 0 otherwise), the total energy is written as a sum of two terms: the concentration dependent energy of the CPA medium, $E_{CPA}(c)$, and a configuration and concentration dependent ordering energy, $E_{ord}(\{p_n^i\})$. The ordering energy can be written as an expansion in terms of concentration dependent l^{th} -order effective cluster interactions, $V_{n_1, n_2, \dots, n_l}^{(l)}$. For example, by defining $\delta c_n = p_n^B$ for a binary alloy, the total energy for a given configuration, $E_{tot}(\{\delta c_n\})$, can be expressed as:

$$E_{tot}(\{\delta c_n\}) = E_{CPA}(c_B) + \frac{1}{2} \sum_{n_1, n_2} V_{n_1, n_2}^{(2)}(c_B) \delta c_{n_1} \delta c_{n_2} + \frac{1}{3} \sum_{n_1, n_2, n_3} V_{n_1, n_2, n_3}^{(3)}(c_B) \delta c_{n_1} \delta c_{n_2} \delta c_{n_3} + \dots, \quad (1)$$

where the sums run over distinct consecutive sites. The concentration dependent effective cluster interactions have been shown to exhibit rapid convergence [11]. It must be noted that the above expression is not a simple transcription of the Ising Hamiltonian. The main difference is that in expression (1) the random (CPA) medium can not be represented by a sum over a limited number of clusters and corresponding interactions. Often, it is convenient to define an "energy of mixing" (E_{mix}), defined as the CPA-energy minus a linear part, given by:

$$E_{mix}^{\alpha}(c) = E_{CPA}^{\alpha}(c) - cE_B^{\alpha} - (1-c)E_A^{\alpha}, \quad (2)$$

where $E_{A(B)}$ designates the total energy of pure A (B), and α indicates the lattice (fcc or bcc), and c represents the concentration of the B species.

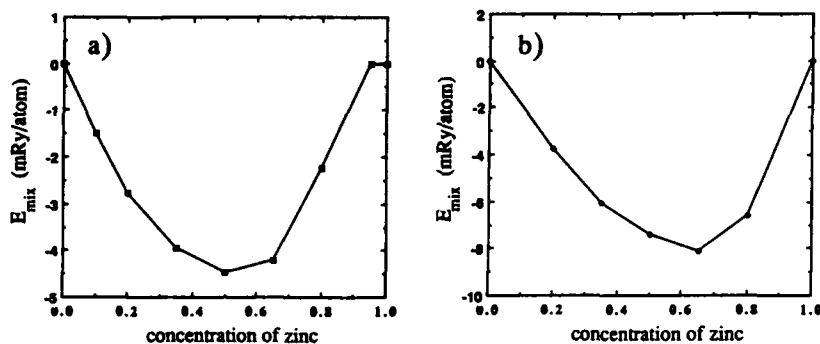


Fig. 1. The energy of mixing (E_{mix}) as a function of composition in mRy/atom as computed with the KKR-CPA-GPM, a) on the fcc lattice, b) on the bcc lattice.

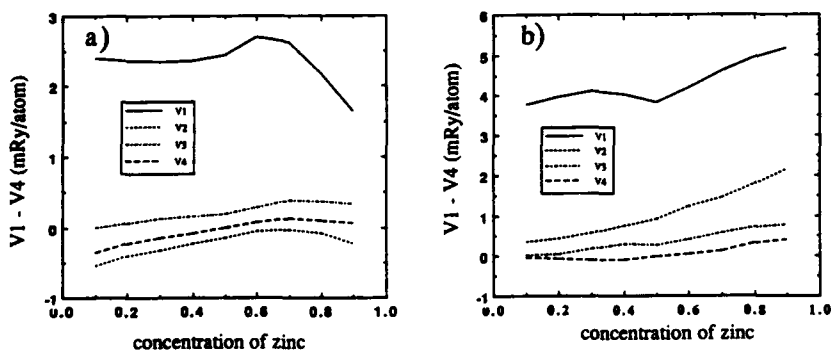


Fig. 2. Effective pair interactions as a function of composition in mRy/atom as computed with the KKR-CPA-GPM, a) on the fcc lattice, b) on the bcc lattice.

The results for fcc and bcc Cu-Zn alloys are shown in figs. 1 and 2, and table I. The energy of mixing (E_{mix}), is negative in both the fcc (fig. 1a) and the bcc (fig. 1b) based alloys, indicating a strong tendency toward phase formation. The ordering tendencies are confirmed by the effective pair interactions (fig. 2a for the fcc lattice, fig. 2b for the bcc lattice), which are predominantly positive. The strong concentration dependence, especially of the more distant pair interactions is readily apparent: the first neighbor pair interaction is 1 to 2 orders of magnitude larger than the third and fourth neighbor pair interactions. Pair interactions beyond the fourth neighbor shell are all less than 0.1 mRy/atom. Hence, a fast convergence of the pair expansion for the ordering

Table I. Lattice parameter (a), energy of mixing (E_{mix}), and pair interactions (V_i) for the four neighbor shells on the fcc and bcc lattice as a function of zinc concentration (c_{Zn}), as computed with the KKR-CPA-GPM. The lattice parameter is given in atomic units, the energetic properties are expressed in mRy/atom.

lattice	c_{Zn}	a	E_{mix}	V_1	V_2	V_3	V_4
fcc	0.0	6.760	0.0				
	0.1	6.800	-1.506	2.39	-0.56	-0.01	-0.36
	0.2	6.838	-2.772	2.37	-0.41	0.06	-0.23
	0.35	6.897	-3.955	2.36	-0.30	0.14	-0.12
	0.5	6.943	-4.480	2.43	-0.16	0.18	-0.01
	0.65	7.025	-4.213	2.72	-0.02	0.36	0.11
	0.8	7.105	-2.238	2.17	-0.09	0.36	0.09
	1.0	7.250	0.0				
bcc	0.0	5.3500	0.0				
	0.2	5.3971	-3.772	3.95	0.44	0.02	-0.08
	0.35	5.4765	-6.083	4.13	0.62	0.26	-0.12
	0.5	5.5559	-7.495	3.82	0.90	0.26	-0.03
	0.65	5.5559	-8.116	4.40	1.30	0.49	0.07
	0.8	5.6350	-6.578	4.93	1.77	0.69	0.31
	1.0	5.7500	0.0				

energy is obtained. The interactions on the fcc lattice indicate the L_{12} and L_{10} as ground states. However, the anti-phase boundary (APB) energy, given by:

$$E_{APB-(100)} = \frac{2V_2 - 8V_3 + 16V_4 + \dots}{a^2} \quad (3)$$

where a represents the (fcc) lattice parameter and V_i is the pair interaction with the i^{th} neighbor shell, is only of the order of 12 mJ/m^2 in Cu_3Zn . This APB energy is, for all practical purposes, effectively nil. This means that the L_{12} structure is energetically barely more stable than phases which contain structural [100] APBs, such as DO_{22} and DO_{23} . The theoretical order-disorder temperatures computed with the CVM in the tetrahedron-octahedron approximation for the L_{10} and the $\text{Cu}_3\text{Zn}-L_{12}$ phases are 300 K and 288 K, respectively. The interactions on the bcc lattice indicate a stable B2 phase, and an only barely stable DO_3 phase at the composition Cu_3Zn . A stable B2 phase is indeed experimentally observed at temperatures below 740 K around the equiatomic composition. The theoretically predicted ordering energy of the B2 phase at stoichiometry, given by:

$$\Delta E_{ord}^{B2} = V_1 - \frac{3}{4}V_2 - \frac{3}{2}V_3 + 3V_4 + \dots, \quad (4)$$

is about 2.7 mRy/atom (3.5 kJ/mol), which lies between two values extracted from experimental data: 1.3 kJ/mol from a phase diagram assessment [12], and 4.6 kJ/mol from a compilation of data [13]. Moreover, the theoretical order-disorder temperature of 770 K, as computed with the CVM in the tetrahedron approximation, compares very well with the experimentally observed order-disorder temperature. It is interesting to note that the experimentally observed martensitic transformation occurring at room temperature in near-equiatomic CuZn alloys seems to be suggested by a softening of the first neighbor pair interaction (see fig. 2b), and by the L_{10} order-disorder temperature of 300 K.

To completely model the Cu-Zn phase diagram, one must compare the stability of fcc and bcc based structures, that is, the differences in structural stability of the fcc and bcc modifications of both pure Cu and pure Zn must be known. Work is currently under way to accurately compute these energy differences.

First- and second neighbor pair interactions on the bcc lattice have also been obtained by fitting to experimental results [13,14]. These empirical interactions do not reproduce the known phase boundaries in the phase diagram accurately [13], and differ significantly from our theoretical

results. The empirical interactions are: $V_1 = 6.04$ mRy/atom, $V_2 = 3.39$ mRy/atom; to be compared with the theoretical effective pair interactions at equiatomic composition in table I. Ignoring the concentration dependence of the interactions in the "fit" is a possible cause for the disparity. Other methods for obtaining pair interactions from experimental data are the Krivogiaz-Clapp-Moss method, the inverse Monte Carlo (IMC) and the inverse CVM. In these methods one attempts to match the Warren-Cowley parameters as determined experimentally and as generated with an Ising-like Hamiltonian in which the interactions serve as adjustable parameters. Usually, a Hamiltonian is chosen that contains pair interactions only. An important limitation of these techniques is that the energy of mixing can not be extracted from SRO intensity data. For systems that display ordering only, that may not hamper the possibility of computing a realistic phase diagram, but when phase segregation occurs, the disordered energy plays a crucial role in the appearance of the miscibility gap in the phase diagram [8,15]. In the case of segregation, it should in general be impossible to compute an accurate phase diagram with the interactions obtained from SRO data as input only. In addition, the neglect of many-body interactions can be unjustified in some alloy systems. However, ignoring many-body interactions is well justified in Cu-Zn, as our computations have shown.

Recent diffuse neutron scattering measurements and IMC simulations on Cu-rich fcc Cu-Zn solid solutions by Reinhard et al. [1] provide an opportunity for a comparison of interactions based on experimental results and effective interactions derived from first-principles. Our results for fcc $\text{Cu}_{0.69}\text{Zn}_{0.31}$ indicate the possibility of ground states with structural [100] APBs, such as the DO_{22} and DO_{23} phases, and indeed, the IMC results [1] show that at low temperatures a DO_{23} phase might form. This is clearly visible in fig. 3, where the SRO diffuse scattering intensity, computed with the CVM using interactions from ref. [1] (sample 1), exhibits maxima at $[1, \frac{1}{4}, 0]$ positions. As to be expected, the CVM SRO intensity, computed in the tetrahedron-octahedron approximation [16,17,18] with a Bragg-Williams extension for the interactions beyond the second neighbor shell, clearly reproduces the experimental result [1]. Our study indicates that the first neighbor pair interaction is much larger than the other interactions, and that the more distant pair interactions are all below 0.1 mRy/atom, in excellent agreement with the IMC results [1]. The fact that the GPM does not univocally predict the DO_{23} as ground state comes as no surprise. A systematic ground state study [19] has indicated that contributions from interactions as distant as the 8th neighbor and beyond are required to stabilize a DO_{23} phase. These distant pair interactions are extremely small and enter the expression for the ordering energy with coefficients both positive and negative, so that many contributions almost cancel. This means that in order to accurately predict a DO_{23} phase in a real-space approach, interactions must be obtained with extreme accuracy, even in very distant shells, and in addition, these interactions should be so well behaved that their errors

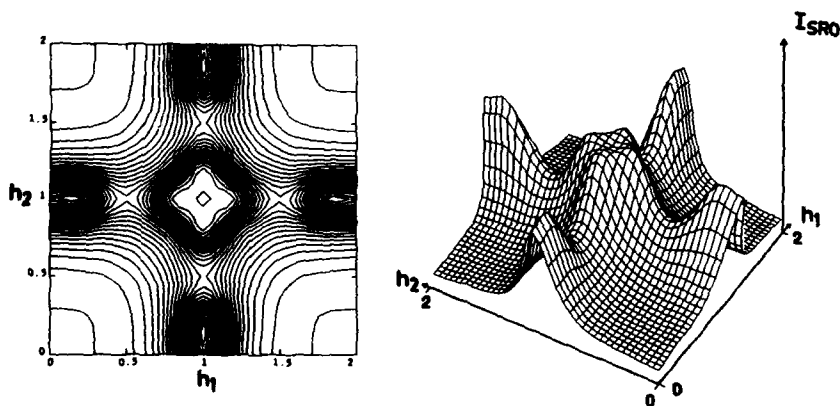


Fig. 3. SRO diffuse scattering intensity in the $[h_1, h_2, 0]$ plane at 500 K in a $\text{Cu}_{0.69}\text{Zn}_{0.31}$ alloy, as computed with the CVM in the tetrahedron-octahedron approximation with interactions from reference [1].

do not significantly accumulate in the appropriate expressions for the ordering energy. This appears an almost impossible task for a real-space method. A reciprocal-space approach, such as the concentrational functional theory [3], is likely to be more successful when long range interactions are crucial. The extreme sensitivity to distant pair interactions is also apparent from the fact that SRO diffuse scattering intensities computed with the CVM with up to fourth neighbor interactions, exhibit maxima at the $\{100\}$ positions only, irrespective whether GPM (fig. 4a) or IMC (fig. 4b) interactions are used.

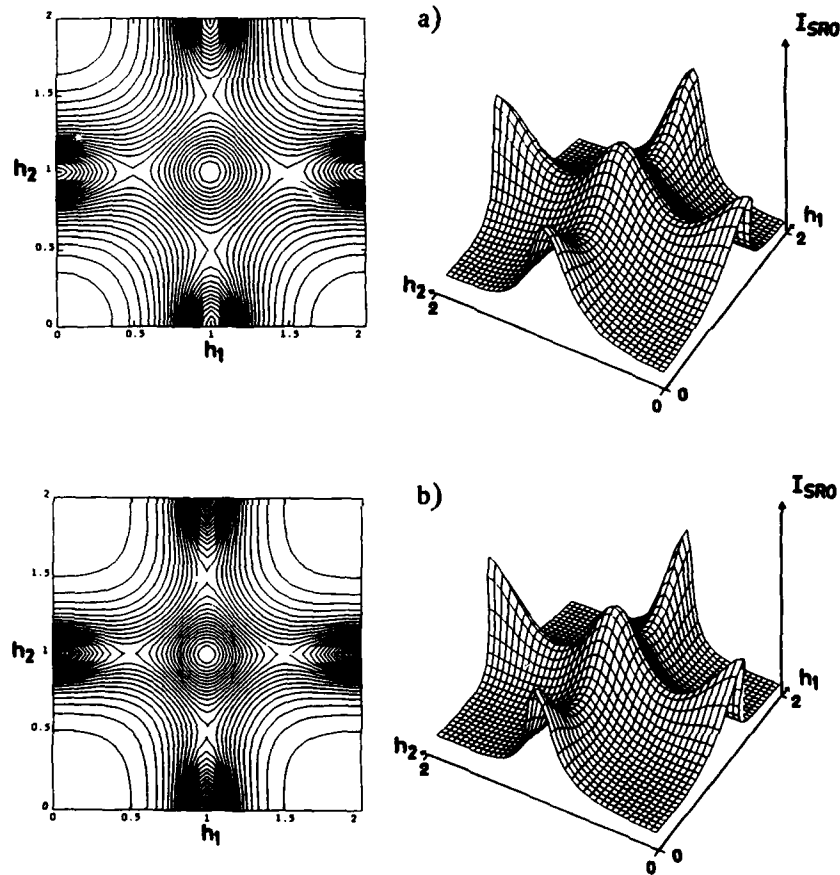


Fig. 4. As fig. 3, but with only four neighbor interactions taken into account, a) interactions computed with the KKR-CPA-GPM, b) interactions from the IMC work of [1].

Summarizing, it can be stated that the KKR-CPA-GPM produced some remarkably accurate results, such as the order-disorder temperature of the B2 phase, and the extremely small APB energy in Cu_3Zn . Moreover, the SRO intensities predicted from first-principles are about as good as one might hope with the number of interactions considered. A full analysis of the phase formation in Cu-Zn will be given in a forthcoming paper.

Work performed under the auspices of the U.S. Department of Energy by the Lawrence Livermore National Laboratory and the Lawrence Berkeley Laboratory under contract No. W-7405-ENG-48 (M.S. and P.T.). Additional support was received from: the Ohio Supercomputer Center (F.P.), and from the U.S. department of Energy, Basic Energy Sciences, Division of Materials Science, under contracts: DEAC05-84OR21400 at Oak Ridge National Laboratory with Martin Marietta Energy Systems Inc. (G.S. and D.N.), and DEAC05-76DP00789 at Sandia National Laboratory with AT&T (D.J.).

References

- 1 L. Reinhard, B. Schoenfeld, G. Kostorz, and W. Buehrer, this symposium, and L. Reinhard, Ph.D. Thesis ETH, unpublished, Zurich, Switzerland (1989).
- 2 W. Hume-Rothery, P.W. Reynolds, and G.V. Raynor, *J. Inst. Metals* **66**, 191 (1940)
- 3 B.L. Gyorffy and G.M. Stocks, *Phys. Rev. Lett.* **50**, 374 (1983).
- 4 A. Gonis, X.G. Zhang, A.J. Freeman, P. Turchi, G.M. Stocks, and D.M. Nicholson, *Phys. Rev. B* **36**, 4630 (1987).
- 5 F. Ducastelle and F. Gautier, *J. Phys. F* **6**, 2039 (1976).
- 6 P.E.A. Turchi, G.M. Stocks, W.H. Butler, D.M. Nicholson, and A. Gonis, *Phys. Rev. B* **37**, 5982 (1988).
- 7 A. Bieber and F. Gautier, *Acta Metall.* **34**, 2291 (1986).
- 8 P.E.A. Turchi, M. Sluiter, and D. de Fontaine, *Phys. Rev. B* **36**, 3161 (1987).
- 9 C. Sigli, M. Kosugi, and J.M. Sanchez, *Phys. Rev. Lett.* **57**, 253 (1986).
- 10 M. Sluiter, P. Turchi, Fu Zezhong, and D. de Fontaine, *Phys. Rev. Lett.* **60**, 716 (1988).
M. Sluiter, Ph.D. Thesis, unpublished, University of California, Berkeley (1988).
- 11 A. Bieber and F. Gautier, *J. Phys. Soc. Jap.* **53**, 2061 (1984).
- 12 P.J. Spencer, *Calphad* **10**, 175 (1986).
- 13 M. Ahlers, *Prog. Mat. Sci.* **30**, 135 (1986).
- 14 G. Inden, *Z. Metallkunde* **66**, 648 (1975).
- 15 M. Sluiter and P.E.A. Turchi, to be published.
- 16 J. M. Sanchez, *Physica* **111A**, 200 (1982).
- 17 A. Finel, These de doctorat d'Etat, unpublished, University Pierre et Marie Curie, Paris (1987).
- 18 T. Mohri, J.M. Sanchez, and D. de Fontaine, *Acta Metall.* **33**, 1463 (1985).
- 19 J. Kanamori and Y. Kakehashi, *J. Phys. (Paris)* **38**, C7-274 (1977).

ORDERING MECHANISM IN Ni-Cr ALLOYS: THEORY AND EXPERIMENT

P.E.A. TURCHI¹, F.J. PINSKI², R. H. HOWELL¹, A.L. WACHS¹, M.J. FLUSS¹,
D.D. JOHNSON³, G.M. STOCKS⁴, D. M. NICHOLSON⁴, and W. SCHWEIKA⁵

1. Lawrence Livermore National Laboratory, L-268, Livermore, CA 94550
2. Department of Physics, University of Cincinnati, Cincinnati, OH 45221
3. Theoretical Division, Sandia National Laboratories, Livermore, CA 94550
4. Metals and Ceramics Division, Oak Ridge National Laboratory, Oak Ridge, TN 37831
5. IFF-KFA, GmbH, Postfach 1913, D-5170, Jülich, FRG

ABSTRACT

Recently, short range order (SRO) parameters have been extracted from the neutron diffuse scattering intensities on Ni-Cr alloys with 11 to 25 at. pct. chromium. These data were analyzed using inverse-Monte Carlo simulations to extract atomic interactions and the results suggested the existence of a well defined, flat sheet of Fermi surface normal to the [110] direction. In this paper, this suggestion is investigated with a series of calculations which are based on the first-principles Korringa-Kohn-Rostoker-coherent-potential-approximation (KKR-CPA). We calculate the electronic structure and the Bloch spectral function at the Fermi energy. We then proceed to calculate the effective cluster interactions using the generalized perturbation method (GPM) and compare them with the above-mentioned experimentally deduced interactions. In addition, we present preliminary results of two-dimensional angular correlation of positron annihilation radiation (2D-ACPAR) measurements, which probe the fermiology of this alloy system. The positron experiments demonstrate the existence of well-defined features in the Fermi surface of Ni₈₉Cr₁₁ but our calculations still have not yet established the origin of SRO in this system.

INTRODUCTION AND METHODOLOGY

Ordering processes are known to be of major importance to the understanding of phase stability relationships and of most physical properties in substitutional alloys. When using a microscopic description of phase stability, one needs to combine the electronic structure calculations with statistical studies, each possessing a high degree of accuracy. One way to achieve this goal is to design a reference system which is as close as possible to any ordered state of the alloy within a given crystalline structure. We use the completely configurationally disordered state since it is both free of predetermined biases and amenable to calculations, i.e. using the CPA. The GPM uses the CPA medium as a reference state and includes fluctuations of the local concentration, which are omitted in the CPA. In the GPM, the internal energy is obtained in terms of a rapidly convergent expansion, whose coefficients are also known as effective cluster interactions. This formalism has been used to justify the study of the properties of alloys via the three-dimensional Ising model, and therefore to calculate the correlations and entropic contributions at arbitrary temperatures. In the present study, the electronic structure of the reference medium will be obtained within the first-principles framework of the KKR-CPA [1], which is based on a multiple scattering approach. A condensed description of the KKR-CPA-GPM can be found in [2]. The cluster interactions, as calculated within the GPM, depend on the geometrical characteristics of the clusters (topology and size), as well as on the alloy parameters: concentration and atomic numbers.

Hence, for a binary alloy, $A_{1-c}B_c$, the ordering energy, i.e. the difference between the totally ordered and disordered states, takes the form

$$\Delta E_{\text{ord}}(\{\delta c_n\}) = \sum_{k=2}^{\infty} \frac{1}{k} \sum_{n_1, \dots, n_k} V_{n_1, \dots, n_k}^{(k)} \delta c_{n_1} \delta c_{n_2} \dots \delta c_{n_k}, \quad \delta c_n = p_n - c \quad (1)$$

for any specific configuration specified by the set of occupation numbers (p_n), with p_n equal to zero or one if the site is occupied by an A or B atom, respectively. The cluster interactions are denoted by V ; in particular $V_{nm}^{(2)}$ is the second-order pair interaction between sites n and m , and given by $V_{nm}^{(2)} = V_{nm}^{AA} + V_{nm}^{BB} - 2V_{nm}^{AB}$. It should be noted that the underlying Ising model differs from the standard one in two ways. First, this model is only written for the ordering part of the internal energy. And second, the interactions depend on concentration.

These pair interactions can be compared with those extracted from neutron or X-ray diffuse scattering studies. Indeed, from the measured Warren-Cowley parameters, the pair interactions can be extracted using so-called "inverse" techniques based on Monte Carlo or other schemes such as the cluster variation method. Moreover, these interactions implicitly contain information about the electronic structure and the features of the Fermi surface which are responsible for the ordering processes. On the other hand, the Fermi surface itself can be directly probed by 2D-ACPAR which measures the two-dimension angular correlation of gamma rays produced by positrons when they annihilate in the alloy.

Hence, a consistent scheme exists which, in principle, addresses and solves the problem of ordering in substitutional alloys, with comparison between theory and experiment being possible on many levels, as summarized in figure 1. In this paper, we are concerned with the Ni-Cr alloy system. We will first show the results of our calculations of the electronic structure, including a discussion of the density of states and Bloch spectral functions, the latter describing the Fermi surface topology. We will continue with a presentation of the calculated interatomic interactions and then discuss the implications of preliminary results from the 2D-ACPAR experiments.

ELECTRONIC STRUCTURE RESULTS

The anomalous behavior of nickel-rich Ni-Cr alloys has attracted attention from experimentalists for a long time [3]. More recently, measurements of the neutron SRO-diffuse scattering intensities clearly indicate that for alloys with 11% to 25% chromium [4,5,6] the SRO diffuse intensities peak at $(1, 1/2, 0)$. The pair interactions [4,5] deduced from these experiments were interpreted as oscillatory

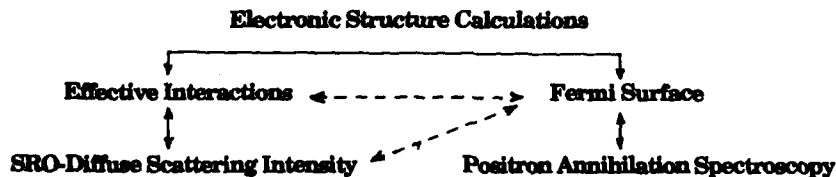


Figure 1. Schematic of the interrelations between theory and experiment in the study of alloy phase stability.

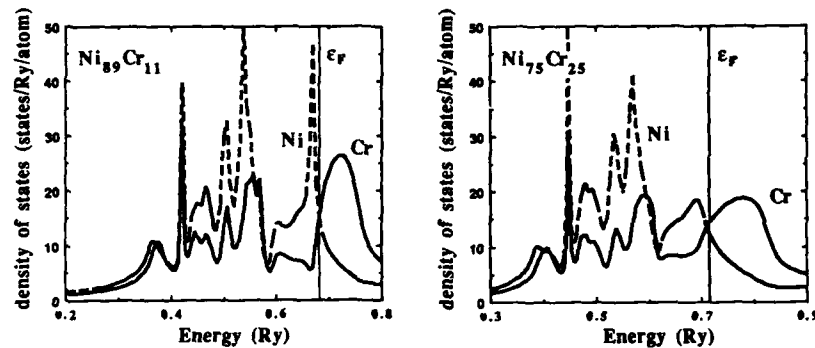


Figure 2. Density of states for $\text{Ni}_{89}\text{Cr}_{11}$ and $\text{Ni}_{75}\text{Cr}_{25}$. The density of states averaged over each site, $n_{\alpha}(\epsilon)$, for both nickel and chromium is denoted by the dashed and solid line respectively.

and long-ranged and caused by the existence of flat sheets of the Fermi surface normal to the [110] direction and with a value of k_F of approximately 10 nm^{-1} [4]. Because the experiments on alloys seem to indicate that the pair interactions vary significantly with concentration [4,5,6], we have performed calculations of the electronic structure of these alloys using the self-consistent KKR-CPA including angular momentum contributions up to a maximum of $l=3$ at each selected concentration (11, 20 and 25 at. pct. Cr). The partial densities of states (site-restricted average), $n_{\alpha}(\epsilon)$, displayed in figure 2 for $\text{Ni}_{89}\text{Cr}_{11}$ and $\text{Ni}_{75}\text{Cr}_{25}$, show the split-band nature of the alloy and the strong disorder broadening. There is an accompanying 0.17 electron transfer from the chromium which is almost independent of concentration. The charge transfer onto the nickel is much smaller and depends on the concentration. A useful quantity for describing the electron structure of an alloy is the Bloch spectral function, $A_B(\mathbf{k}, \epsilon)$, which describes the probability of finding an electron with crystal momentum in the range $(\mathbf{k}, \mathbf{k}+d\mathbf{k})$ and within the energy range $(\epsilon, \epsilon+d\epsilon)$. In an ordered crystal,

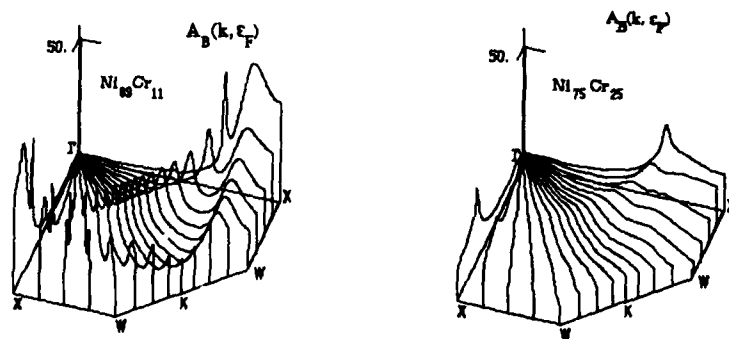


Figure 3. Bloch spectral function, $A_B(\mathbf{k}, \epsilon_F)$, as calculated for $\text{Ni}_{89}\text{Cr}_{11}$ and $\text{Ni}_{75}\text{Cr}_{25}$.

$A_B(\mathbf{k}, \epsilon)$ is a set of Dirac delta functions whenever the dispersion relation is satisfied, $A_B(\mathbf{k}, \epsilon) = \sum \delta(\epsilon - \epsilon_{\mathbf{k}\alpha})$. Even though, in the disordered alloy, the underlying symmetry is not preserved by the random occupation of sites, \mathbf{k} can be a reasonably good quantum number, and the delta functions are then simply broadened due to the finite electron lifetimes. At the Fermi energy ϵ_F , this spectral function gives a representation of the Fermi surface. In figure 3, we have plotted $A_B(\mathbf{k}, \epsilon_F)$ for the disordered alloys $\text{Ni}_{89}\text{Cr}_{11}$ and $\text{Ni}_{75}\text{Cr}_{25}$. In the 11% alloy, one can easily recognize features of the nickel Fermi surface [8], especially the flat sheet perpendicular to the ΓK direction, with k_F approximately 9.4 nm^{-1} . At the higher concentration of chromium, the features are substantially smeared, the 20% and 25% alloys being very similar.

EFFECTIVE PAIR INTERACTION RESULTS

For three concentrations of the paramagnetic fcc Ni-Cr alloys, effective cluster interactions were calculated within the KKR-CPA-GPM. The second-order terms in the cluster expansion are the dominant contributions to the effective pair interactions. As seen in table I, these interactions converge rapidly after the fourth neighbor except in the [110] direction. The higher order terms, such as the triplet, are all small (not displayed). Both of these effects can be attributed to the combination of a large amount of d-character at the Fermi energy with strong disorder.

The variation of the pair interactions (as a function of concentration) is particularly notable because the values for V_1 in the 20% and 25% alloys are not even the same sign as those extracted from experiment, i.e. a weak clustering tendency has been deduced from these calculations, as well as from previous work which was based on a semi-phenomenological tight-binding model [9]. Several factors which we have not handled, or handled incorrectly, may contribute to this discrepancy. The most prominent possibilities are effects due to charge transfer, to magnetic fluctuations, or to errors which shift the Fermi energy. The charge transfer away from chromium is, as noted above, not small and almost constant in these three alloys. The resulting Madelung terms, which have been omitted, will have the largest effect on the nearest-neighbor pair interaction. Second, magnetic fluctuations will shift the spin-up and spin-down Fermi levels in opposite directions, and due to the strong energy dependence of V_1 , a significant contribution may be generated. This energy dependence is illustrated in figure 4, where the interactions for $\text{Ni}_{80}\text{Cr}_{20}$ are displayed as a function of energy (assuming frozen potentials). Thirdly, this large energy

Table I. Lattice parameter a , Fermi energy ϵ_F and second order terms of the effective pair interactions (mRy. per atom) for the three Ni-Cr alloy calculations.

	$\text{Ni}_{89}\text{Cr}_{11}$	$\text{Ni}_{80}\text{Cr}_{20}$	$\text{Ni}_{75}\text{Cr}_{25}$
a in a.u.	6.60	6.60	6.60
ϵ_F in Ry	0.682	0.706	0.717
V_1 (110)	0.44	-2.31	-2.35
V_2 (200)	0.80	-2.74	-2.83
V_3 (211)	0.65	0.11	0.18
V_4 (220)	3.13	2.44	2.12
V_6 (222)	-0.08	-0.31	-0.23
V_8 (400)	0.34	0.06	0.04
V_9 (330)	-0.49	-0.59	-0.62
V_{10} (411)	0.09	0.03	0.03

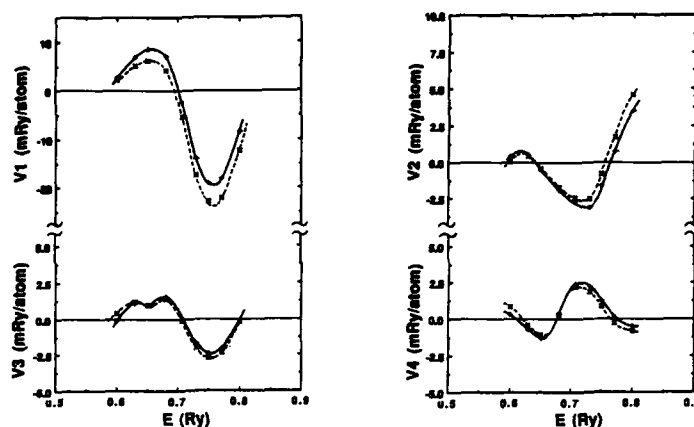


Figure 4. Second-order effective pair interactions, up to fourth neighbors for $\text{Ni}_{80}\text{Cr}_{20}$, plotted as a function of energy: total (—) and d-contribution (---).

dependence shows the sensitivity of our calculations to small errors in determining the Fermi energy: even a small change in ϵ_F will substantially alter our result for V_1 . Hence, the origin of the discrepancy still remains to be determined.

FERMI SURFACE STUDY BY 2D-ACPAR

The 2D-ACPAR technique is useful for probing the electronic momentum density of solids and has been successfully used in studies of the Fermi surface, particularly in disordered alloys [10] where it has become the major source of information. Using the ACPAR technique, one obtains a measurement of the momentum density $\rho^2\gamma(\mathbf{p})$ of electrons in the crystal, as modulated by the positron momentum distribution and by screening effects. It is convenient to partition the contributions to the angular correlations into two cases, from electrons in either fully or partially filled bands. In the former case, the correlations are continuous throughout the Brillouin zone, while in the latter, the sharp cutoff in the momentum at the Fermi surface leads to observable structure. As an illustration, we present in figure 5 a contour plot of projected momentum densities (as measured) for $\text{Ni}_{89}\text{Cr}_{11}$ integrated along [100] and [110], with the corresponding Fermi-surface projections, obtained from KKR-CPA calculations. A careful examination of the second derivatives of the experimental spectra indicate the existence of well defined features, however, a full three-dimensional reconstruction is necessary before a more detailed comparison can be made. Work is in progress on such a reconstruction and will be published later.

CONCLUSION

In summary, these electronic structure calculations have shown that the Fermi surfaces of Ni-Cr alloys possess a flat sheet which broadens with increasing chromium concentration, and that a weak tendency towards clustering exists for Ni-Cr alloys with 20 or more at. pct. Cr. We have shown that the GPM expansion for the ordering energy converges rapidly and confirmed the

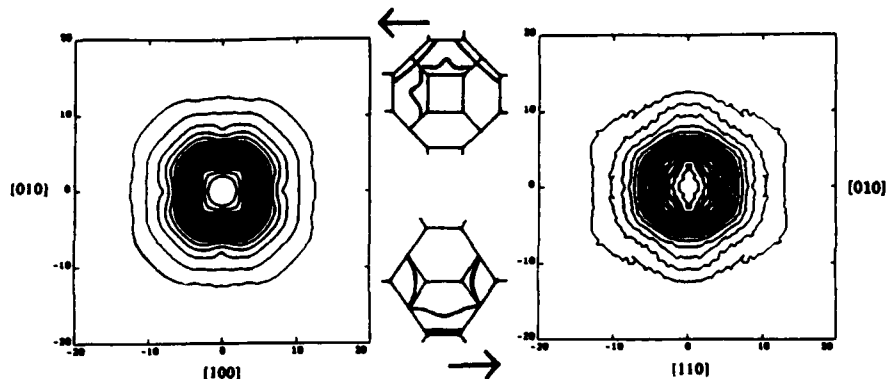


Figure 5. Two dimensional electron-positron momentum distributions with the p direction of integration along $[001]$ (left) and $[110]$ (right), and corresponding projected Fermi surface. p_x and p_y are given in units of $10^{-3} mc$ ($\sim 2.5 \text{ nm}^{-1}$).

long-range nature of the interactions along the $[110]$ direction as well as the size of the fourth-neighbor pair interaction. Finally, we displayed positron spectra which demonstrated the existence of well-defined features in the Fermi surface of $\text{Ni}_9\text{Cr}_{11}$.

This work was performed under the auspices of the U.S. Department of Energy by the Lawrence Livermore National Laboratory under contract No. W-7405-Eng-48, by the Oak Ridge National Laboratory under contract No. DE-AC05-84OR21400 with Martin Marietta Energy Systems Inc., and by Sandia National Laboratory under contract No. DE-AC05-76DP00789 with A.T.T. One of us (F.J.P.) thanks the Ohio Supercomputer Center for its generous support of this work and acknowledges support from Lawrence Livermore National Laboratory.

REFERENCES

- [1] B.L. Gyorffy, D.D. Johnson, F.J. Pinski, D.M. Nicholson, and G.M. Stocks in *Alloy Phase Stability*, G.M. Stocks and A. Gonis, editors, NATO ASI Series E, No. 163 (Kluwer, Norwell, 1989), p. 421 and references cited therein.
- [2] P.E.A. Turchi, G.M. Stocks, W.H. Butler, D.M. Nicholson, and A. Gonis, *Phys. Rev. B* **37**, 5982 (1988), and references cited therein.
- [3] A. Marucco and B. Nath, *J. of Mater. Sci.* **23**, 2107 (1988).
- [4] W. Schweika and H.-G. Haubold, *Phys. Rev. B* **37**, 9248 (1988).
- [5] B. Schönfeld, L. Reinhard, G. Kostorz and W. Bührer, *Phys. Stat. Sol. (b)*, **148**, 457 (1988).
- [6] R. Caudron, F. Ducastelle, F. Solal and A. Finel, Technical Report ONERA, No. 16/1221M, June 1989 and private communication.
- [7] J.S. Faulkner and G.M. Stocks, *Phys. Rev. B* **21**, 3222 (1980); and S.L. Gyorffy, in *Transition Metals 1980*, Inst. of Phys. Conf. Ser. No. 55, P. Rhodes, editor, (Inst. of Phys., London, 1980), ch. 2, p. 89.
- [8] C.S. Wang and J. Callaway, *Phys. Rev. B* **15**, 298 (1977).
- [9] N.C. Teo, M. Kosugi, and J.M. Sanchez, *Acta Metall.* **37**, 121 (1989).
- [10] S. Berko, in *Positron Solid State Physics*, W. Brandt and A. Dupasquier, editors, (North Holland, Amsterdam, 1983); J.H. Kaiser, P.A. Walters, C.R. Bull, A. Alam, R.N. West, and N. Shiotani, *J. Phys. F* **17**, 1243 (1987).

PHONON DISPERSION AND KOHN ANOMALIES IN THE ALLOY $\text{Cu}_{0.84}\text{Al}_{0.16}$

Henry Chou, S. M. Shapiro
Physics Department, Brookhaven National Laboratory, Upton, N.Y. 11973

S. C. Moss
Physics Department, University of Houston, Houston, Texas 77204-5504

and

Mark Mostoller
Solid State Division, Oak Ridge National Laboratory, Oak Ridge, TN 37831

ABSTRACT

We have made detailed measurements of phonon frequencies along all high-symmetry directions on a large single crystal of $\text{Cu}_{0.84}\text{Al}_{0.16}$ at room temperature. Phonon frequencies were ascertained to better than ± 0.03 meV. Inter-atomic force constants and vibrational density of states were calculated by performing a Born-von Karman analysis on the complete set of phonon dispersion curves. In contrast to the case of pure Cu, no evident Kohn anomaly (neither in the phonon dispersion itself nor in the derivatives) was observed near the expected wave vector $q=2k_F$. The absence of Kohn anomalies in the present system could be due either to a smeared out Fermi surface or to the possibility that the electron-electron interaction which screens the inter-ionic potential is not the dominant interaction in the system; i.e. the existence of Kohn anomalies in these alloys may depend mainly on the details of the electron-phonon interaction.

I. INTRODUCTION

By considering the screening effect of a free electron gas on a fluctuating charge distribution such as a lattice vibration, Kohn[1] predicted that there should be lines in reciprocal space through which the dispersion surfaces of the lattice vibrations will have infinite slopes. At the simplest level, for a spherical Fermi surface of radius k_F , this can be understood from the fact that lattice vibrations (phonons) of wave vector $q \leq 2k_F$ can cause virtual excitations of the electrons with conservation of momentum, while phonons with $q > 2k_F$ cannot. This effect has become known as the Kohn anomaly and, in pure metals, has been observed in Pb by Brockhouse et al.[2,3], in Cu by Nilsson and Rolandson[4], and in Nb by Sharp[5].

The strength of the anomaly is influenced by the geometry of the Fermi surface. This can be seen by considering the static dielectric function $\epsilon(q,0)$ in the random phase approximation via the polarizability $\alpha(q,0) = 1 + 4\pi\alpha(q)$ as

$$\alpha(q) = \frac{e^2}{q^2} \sum_{\mathbf{k}} \frac{f(\mathbf{k} + \mathbf{q}) - f(\mathbf{k})}{E_{\mathbf{k}} - E_{\mathbf{k} + \mathbf{q}}} \quad (1)$$

where $f(\mathbf{k})$ is the probability of occupation of state \mathbf{k} . The only contributions come from terms for which state \mathbf{k} is occupied and state $\mathbf{k} + \mathbf{q}$ is empty, or vice versa, and the largest contributions clearly occur when $E_{\mathbf{k}} = E_{\mathbf{k} + \mathbf{q}}$. For a spherical Fermi surface, both of the above conditions are satisfied only when $q \leq 2k_F$. At $q = 2k_F$, one observes a sudden decrease of the static dielectric function, i.e. an abrupt decrease of the ability of the electrons to screen the embedded charge distribution. But since the change in $f(\mathbf{k} + \mathbf{q}) - f(\mathbf{k})$ is slow near $q = 2k_F$, the dielectric function remains continuous and only the derivative shows a logarithmic singularity. Other shapes of the Fermi surface, such as cylindrical (2-D) and flat parallel sections (1-D), enhance the singularity by enhancing the number of singular contributions in the sum of

Eq. (1)[6]. It should also be pointed out that the strength of the Kohn anomaly is related in turn to the details of the electron-phonon interaction in a more complicated fashion than is supposed in Eq. (1)[7].

The pair interaction potential $V(r)$ of the ions in a solid is screened by the electrons, with Fourier transform $V(q) \sim \frac{e}{q^2 \epsilon(q)}$, and the singularity in the dielectric function is thus directly reflected in $V(q)$. In the case of alloys, $V(r)$ is usually taken as the sum over a set of pairwise interactions between an origin ion and its several neighbors. Krivoglaz[8] has discussed how the diffuse scattering of X-rays, neutrons and electrons from an alloy above the order-disorder transition is related to this pair interaction, where the screening effect is treated self-consistently by the introduction of the dielectric function. By extending this idea of Krivoglaz, Moss[9] noted that the shape of the Fermi surface in Cu-Au alloys was indeed imaged in the diffuse scattering via the singularity in $\epsilon(q=2k_F)$. Fig. 1(a) shows a Kohn construction of the satellite positions when k_F is known for the (001) plane of an FCC lattice. Conversely, given the satellite positions, one could deduce the magnitude of the Fermi wave vector along the appropriate direction.

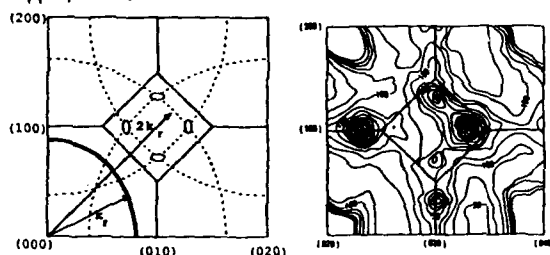


Fig. 1: The [001] zone in reciprocal space of a FCC lattice schematically showing (a) Kohn construction of the diffuse satellite positions given k_F in the (110) direction. (b) the diffuse scattering as observed by Borie and Sparks,¹⁴ the asymmetry in the satellite intensity is caused by atomic displacements arising from unequal atom sizes.

Scattergood, Moss and Bever[10] measured the X-ray diffuse satellite positions in Cu-Al alloys of various concentrations and deduced that $k_F(110)/0.74 = n^{1/3}$, and $k_F(100)/0.84 = n^{1/3}$, where $n = x_{Cu} + 3x_{Al}$ is the average number of conduction electrons per atom in the Cu-Al alloy. They also showed that these were consistent with positron annihilation determinations of k_F . Recently, Pinski[11] has calculated the Fermi surface for $Cu_{0.85}Al_{0.15}$ and found good agreement with the measured satellite positions. The phonon anomalies in the region of $2k_F$ have, however, remained unstudied. In this paper, we explore the Kohn anomalies in the phonon dispersion in the alloy $Cu_{0.84}Al_{0.16}$, with particular attention to the [100] and [110] directions.

II. EXPERIMENTAL DETAILS

Phonon frequencies were measured on the triple-axis spectrometer H7 at the HFBR of Brookhaven National Laboratory. The sample was a single crystal of $Cu_{0.84}Al_{0.16}$ in the shape of a cylinder approximately 2 cm in diameter and 5 cm in length. It is a FCC lattice with lattice parameter $a^* = 2\pi/a = 1.714 \text{ \AA}^{-1}$ (in pure Cu, $a^* = 1.741 \text{ \AA}^{-1}$). The sample has a mosaic spread of 40 minutes. Pyrolytic graphite was used as both monochromator and analyzer. A pyrolytic graphite filter was used before the analyzer to eliminate the higher order contamination in the beam. Constant-Q scans were made with either fixed final energy $E_f = 3.56 \text{ THz}$ (14.7 meV) or 7.38 THz (30.5 meV), depending on where in reciprocal space we chose to measure the phonon frequencies. The collimations before monochromator, before and after

sample, and after analyzer were 20, 20, 20, 40 minutes, respectively. With $E_f=3.56$ THz the energy resolution is in the range 0.12-0.36 THz (0.5-1.5 meV) and with $E_f=7.38$ THz, it is in the range 0.24-0.6 THz (1.0-2.5 meV), depending on the energy transfer. All measurements were made at room temperature.

III. RESULTS AND DISCUSSION

A. SHORT RANGE ORDER

The observation of diffuse scattering in alloys has chiefly been used to study short-range order[8,12-13]. Borie and Sparks[14] made an extensive study of diffuse scattering in an alloy $\text{Cu}_{0.84}\text{Al}_{0.16}$, which was in fact a slice of the sample we studied. Fig. 1(b) shows the measured diffuse satellites in the [001] zone from Borie and Sparks[14]. We observed elastic diffuse scattering at the same positions along [1 ζ 0] and [ζ 10] directions. As short-range order is not the main purpose of our present study, we have not investigated it further. It is, however, important to note that the origin of the diffuse satellites is not in the dynamical response of the crystal (i.e., the phonons).

B. PHONON SPECTRUM

Phonon frequencies were measured along all the high-symmetry directions [ζ 00], [$\zeta\zeta$ 0], [$\zeta\zeta\zeta$] and [1 ζ 0]. Observed phonon peaks were fitted to a damped harmonic oscillator function convoluted with the instrumental resolution function. Although the energy resolution of the instrument is on the order of 0.24 THz (1.0 meV), the peak positions can be determined with a standard deviation better than 0.007 THz (0.03 meV) in most cases by such a fitting procedure.

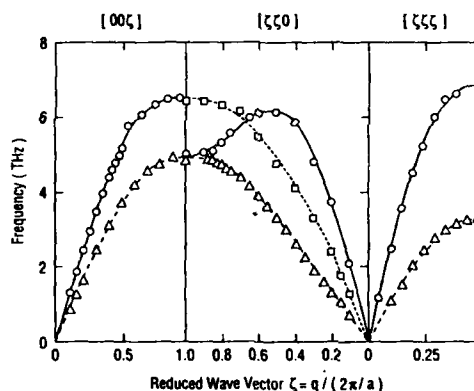


Fig. 2: Phonon dispersion curves of $\text{Cu}_{0.84}\text{Al}_{0.16}$. The lines represent a 5th nearest-neighbor Born-von Karman fit.

Fig. 2 is a plot of the measured phonon dispersion. The lines through the data points represent a fifth-nearest-neighbor Born-von Karman fit of the standard form

$$M\omega_{\alpha}^2(\mathbf{q}) = \sum_{l', \alpha'} \Phi_{\alpha\alpha'}(l') \exp(i\mathbf{q} \cdot \mathbf{R}) u_{\alpha'}(\mathbf{q}) \quad (2)$$

where $\Phi_{\alpha\alpha'}$ is the restoring force exerted on atom l in the direction α when atom l' is moved a unit distance in direction α' , and $\mathbf{R}_{ll'}$ is the vector distance. The standard error of the overall

fit improves with the number of nearest neighbors N used for fitting. $N=6$ is just marginally better than $N=5$, at which $S=0.068$. The inter-atomic force constants and vibrational density of states were deduced from the Born-von Karman fit. The errors on all except the largest few force constants are of the same order of magnitude as the force constants themselves. As Brockhouse[2] emphasized in his work on Pb, the errors are introduced by cutting off at the N -th neighbor while the inter-atomic forces are long-range in nature. The fifth neighbor forces are treated as axially symmetric because data along the high-symmetry directions is insufficient to determine general tensor forces[16].

In comparing the phonon frequencies measured in the present sample with those measured in pure Cu[15], we note that the high frequency phonons near the zone-boundaries in $\text{Cu}_{0.84}\text{Al}_{0.16}$ are lower in energy than the corresponding phonons in pure Cu by as much as 15%. Nicklow et al[16] have observed high-frequency local modes in the alloy $\text{Cu}_{0.96}\text{Al}_{0.04}$ which they interpreted as localized vibrations of the lighter Al atom in a Cu cage. This was confirmed by Kaplan and Mostoller[18] who showed that the neutron scattering from the local mode was reproduced well by mass defect coherent potential calculations. The suppression of the high-frequency phonons in our sample could be due to mode repulsion between this high-frequency local mode and the lattice modes.

C. KOHN ANOMALY

The Fermi surface of pure Cu (and, by implication, Cu-rich alloys) has a flat portion perpendicular to the $\langle 110 \rangle$ direction[20]. Nilsson and Rolandson[4] observed Kohn anomalies in pure Cu by studying small deviations in the slope of the measured phonon dispersion from that of a Born-von Karman fit. They found a systematic deviation in the $\langle 100 \rangle$ -LA branch at the wave vector $q=(0.35 \pm 0.02)2\pi/a$.

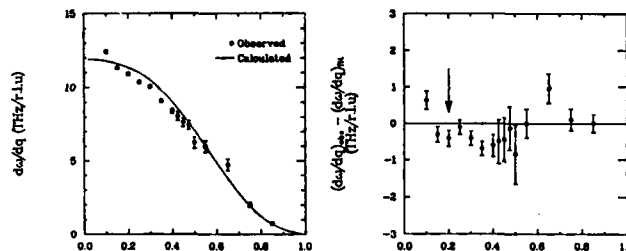


Fig. 3: $d\omega/dq$ for the (100)-LA branch of $\text{Cu}_{0.84}\text{Al}_{0.16}$. The arrow indicates position of $2k_F$ as derived from the position of the diffuse satellite.

We carried out the same analysis for $\text{Cu}_{0.84}\text{Al}_{0.16}$ in the $\langle 100 \rangle$ -LA and $\langle 110 \rangle$ -T1 branches where we have the most complete data. According to the interpretation of the diffuse scattering data by Scattergood et al.[10], the $2k_F$ position in $\text{Cu}_{0.84}\text{Al}_{0.16}$ should be at wave vectors equivalent to $q \sim 0.2(2\pi/a)$ along the $\langle 100 \rangle$ direction and $q \sim 0.85(2\pi/a)$ along the $\langle 110 \rangle$ direction. Figs. 3 and 4 plot the local slope of the phonon dispersion along $\langle 100 \rangle$ -LA and $\langle 110 \rangle$ -T1 respectively. For $\langle 100 \rangle$ -LA, there seems to be some systematic deviation near $q=0.4(2\pi/a)$ rather than the expected $q=0.2(2\pi/a)$. For $\langle 110 \rangle$ -T1, there is a clear depression in the slope at $q=0.2(2\pi/a)$, the origin of which we do not understand.

We also studied the linewidths of phonons measured along $\langle 100 \rangle$ -LA and $\langle 110 \rangle$ -T1. Since the frequency shift (real part of the phonon self-energy) and the width (imaginary part of the phonon self-energy) are related by the Kramers-Kronig relation, the Kohn anomaly could also be manifested in the phonon linewidths. In Fig. 5 we plot the resolution corrected phonon linewidths along the $\langle 100 \rangle$ and $\langle 110 \rangle$ directions. In general, a phenomenological treatment[3] including damping forces in the lattice dynamics would give a linewidth increasing with wave-vector as $\Gamma \sim \sin^2[q/(2\pi/a)]$. This is roughly what is observed in the

$\langle 100 \rangle$ -LA branch (Fig. 5a), but for the $\langle 110 \rangle$ -T1 branch (Fig. 5b), there is an apparent suppression of the linewidth at $q \sim 0.8(2\pi/a)$, which is in contradiction with a suppression of phonon frequency expected in the Kohn anomaly.

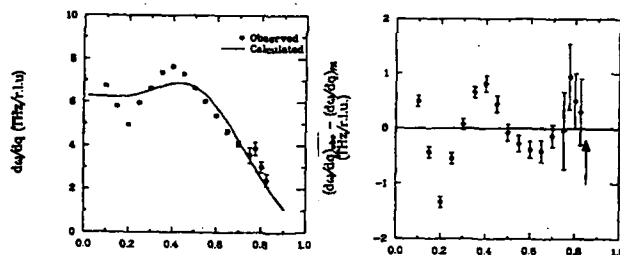


Fig. 4: $d\omega/dq$ for the (110) -T1 branch of $\text{Cu}_{0.84}\text{Al}_{0.16}$. The arrow indicates position of $2k_F$ as derived from the position of the diffuse satellite.

It is also interesting to look at the linewidths of those phonons whose wave vectors are exactly at the positions of diffuse satellites. These phonons are expected to be scattered (damped) by the locally ordered regions associated with these satellites. We observed an increase in phonon width along the $[1\bar{1}0]$ direction between $\zeta = 0.2-0.3$, which coincides with the diffuse scattering maxima (Fig. 1). We believe the increase in the observed width is related to the diffuse scattering and expect there to be a concomitant shift of phonon frequency to a lower value.

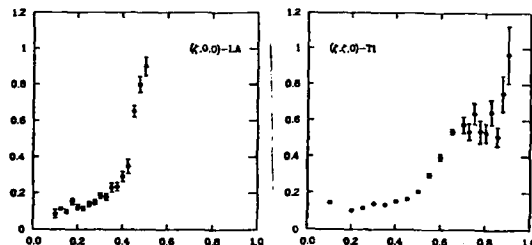


Fig. 5: Resolution-corrected phonon width of $\text{Cu}_{0.84}\text{Al}_{0.16}$ as a function of reduced wave-vector for the (100) -LA and (110) -T1 branches.

IV. CONCLUSION

In conclusion, our phonon data on $\text{Cu}_{0.84}\text{Al}_{0.16}$ does not indicate any strong Kohn anomalies. As noted earlier, Pinski[11] has made Fermi surface calculations for the composition $\text{Cu}_{0.85}\text{Al}_{0.15}$ which give a smeared-out Fermi surface, with the Fermi wave vector along $[110]$ in good agreement with the value deduced from the diffuse satellite positions. The smeared Fermi surface may in part be responsible for our negative result. The same calculation for the alloy $\text{Cu}_{0.85}\text{Pd}_{0.15}$ indicates a sharp Fermi surface[11,21]. It would be interesting to study the Kohn anomalies in the Cu-Pd system, especially as prominent diffuse satellites have also been calculated in that system[21].

As we discussed above, the strength of the Kohn anomaly, revealed by singularities in the denominator in the dielectric response (Eq. 1), also involves details of the electron-phonon interaction[7] which introduces electron-phonon matrix elements in the numerator that are not considered in Eq. (1). The electron-phonon coupling in turn depends on the

details of the Fermi surface. It could be the dominant effect determining Kohn anomalies in this system, in which case we would need to make a more sophisticated analysis of where to expect the singularities in Eq. (1). The existence of the diffuse satellites, however, seems to require some flatness at $2k_F$ in the [110] direction.

ACKNOWLEDGEMENT

We would like to thank C. J. Sparks for providing the sample, H. G. Smith for pointing out the relevance of the local mode in Cu-Al, and F. Pinski for helpful discussions and information about the Fermi surface. The work at Brookhaven National Laboratory was supported by Division of Material Science, U.S. Department of Energy under contract DE-AC02-76CH00016. SCM acknowledges support through NSF DMR 8603662 and DMR8903339. The work at Oak Ridge National Laboratory was supported by the U.S. Department Energy under contract No. DE-AC05-84OR21400 with Martin Marietta Energy Systems, Inc.

REFERENCES

1. W. Kohn, *Phys. Rev. Lett.* **2**, 393 (1959)
2. B. N. Brockhouse, T. Arase, G. Caglioti, K. R. Rao and A. D. B. Woods, *Phys. Rev.* **128**, 1099 (1962)
3. B. N. Brockhouse, T. Arase, G. Caglioti, M. Sakamoto, R. N. Sinclair and A. D. B. Woods in *Inelastic Scattering of Neutrons in Solids and Liquids*, (International Atomic Energy Agency, Vienna, 1961)
4. G. Nilsson and S. Rolandson, *Phys. Rev.* **B9**, 3278 (1974)
5. R. I. Sharp, *J. Phys.* **C2**, 432 (1969)
6. C. Kittel in *Solid State Physics* **22**, 1 (1968) edited by H. Ehrenreich, D. Turnbull and F. Seitz (Academic Press, New York & London)
7. C. M. Varma and W. Weber, *Phys. Rev. Lett.* **39**, 1094 (1977)
8. M. A. Krivoglaz, *Theory of X-Ray and Thermal Neutron Scattering by Real Crystals*, Plenum Press, New York, 1969
9. S. C. Moss, *Phys. Rev. Lett.* **22**, 1108 (1969)
10. R. O. Scattergood, S. C. Moss and M. B. Bever, *Acta Metal.* **18**, 1087 (1970)
11. F. Pinski, private communication
12. J. B. Cohen and J. E. Hilliard, *Local Atomic Arrangements Studied by X-Ray Diffraction* (Gordon and Breach, 1962)
13. W. Buhner, L. Reinhard, B. Schonfeld and G. Kostorz, preprint, 1989
14. B. Borie and C. J. Sparks, Jr., *Acta Cryst.* **17**, 827 (1964)
15. Landolt-Bornstein, NS III/13a, p. 44
16. R. J. Birgeneau, J. Cordes, G. Dolling and A. D. B. Woods, *Phys. Rev.* **136**, 1356 (1964)
17. R. M. Nicklow, P. R. Vijayaraghavan, H. G. Smith, and M. K. Wilkinson, *Phys. Rev. Lett.* **20**, 1245 (1968)
18. T. Kaplan and M. Mostoller, *Phys. Rev.* **B9**, 353 (1974)
19. R. M. Nicklow, G. Gilat, H. G. Smith, L. J. Raubenheimer, and M. K. Wilkinson, *Phys. Rev.* **164**, 922 (1967)
20. B. Segall, *Phys. Rev.* **125**, 109 (1962)
21. B. L. Gyorffy and G. M. Stocks, *Phys. Rev. Lett.* **50**, 374 (1983)

PHASE DIAGRAMS AND DIFFUSE NEUTRON SCATTERING

RENE CAUDRON**, MAURICE SARFATI**, ALPHONSE FINEL* AND
FRANCINE SOLAL***

*ONERA, B.P. 72, 92322 Chatillon Cedex, France

**ONERA and Laboratoire Leon Brillouin, CEN Saclay, 91191 Gif
sur Yvette Cedex, France

***Lawrence Livermore Laboratory Dept. of Materials Science ,L-268,
PO BOX 808 Livermore, CA 94550, U.S.A

The order or segregation properties of compounds or solid solutions are important ingredients of the phase diagrams. If the order can be described as an atomic distribution on an underlying lattice, and if the interactions can be expressed in terms of pairs and other multiplet potentials between the atomic species, phase diagrams should be deducible from these potentials, along with other properties, such as antiphase boundaries, core structures of the dislocations in ordered compounds... This approach, i.e. the very existence of the potentials, is legitimated by electronic structure calculations for or alloys of normal [1] and transition metals [2]. The G.P.M. (General perturbation Method) allows indeed to develop the order energy in terms of interatomic potentials, the reference state, namely the random alloy, being calculated within the C.P.A. (Coherent Potential Approximation). For transition alloys, this procedure, within the Tight Binding Approximation, leads to simple and general results:

-The pair potentials are dominant versus the other multiplet interactions, i.e. the order energy writes:

$$H = \sum_m \sigma_m \sigma_n J_{mn} + h \sum_n \sigma_n \quad (1)$$

the σ 's are spin-like operators taking -1 or 1 values depending on the species sitting on the sites m and n, the J's are the corresponding pair potentials and h is the chemical potential.

2) The interactions between the 2d, 3d and 4th neighbors are of the same order of magnitude, and generally small compared to the first neighbor interaction. Further interactions are negligible.

Experimentally, our purpose is to obtain interaction potentials through the measurements of the short range order parameters, in order to check them against the calculated orders of magnitude and, ultimately, to build phase

diagrams. As an example, we describe our diffuse neutron scattering measurements at high temperature on single crystals of Pd₃V, Ni₃V and Ni₃Cr. The high temperature phase of these alloys is a disordered FCC solid solution. At 815 and 1045°C respectively, Pd₃V and Ni₃V exhibit a first order transition from the disordered FCC solid solution to DO₂₂, a FCC based superstructure. Ni₃Cr is not known to order. However, for the Ni-Cr system, the only known ordered structure is Ni₂Cr, a Pt₂Mo - like structure, built on (1 1/2 0) concentration waves, and then of the same family as DO₂₂. The order-disorder transition temperature of this compound is 580°C.

The measurements were performed at the L.L.B, on a specially built 2 axis spectrometer, equipped with a furnace and a time of flight analysis allowing the rejection of the inelastic scattering. Pd₃V has been investigated at 835°C and Ni₃V at 1100 and 1200°C, Ni₃Cr at 600°C. For each composition and temperature, we explored the (100) and the (110) planes of the reciprocal space. We submitted the intensities measured in both planes to a linear least squares fitting procedure, using a model including 10 to 25 chemical short range order parameters $\alpha(R)$ and first order displacement parameters. The values of the parameters are displayed on table I.

TABLE I : SHORT RANGE ORDER PARAMETERS

	Pd ₃ V T=840°C	Ni ₃ V T=1100°C	Ni ₃ V T=1200°C	Ni ₃ Cr T=600°C
011	-0.16 ±0.02	-0.18 ±0.02	-0.12 ±0.01	-0.039±0.005
002	+0.17 ±0.01	+0.11 ±0.015	+0.055±0.015	+0.077±0.007
112	+0.015±0.01	+0.04 ±0.015	+0.035±0.005	+0.033±0.002
022	+0.03 ±0.01	-0.01 ±0.01	-0.015±0.005	-0.038±0.002
013	-0.04 ±0.01	-0.035±0.015	-0.03 ±0.005	-0.026±0.007
222	0.0 ±0.01	-0.05 ±0.015	-0.05 ±0.005	-0.027±0.007
123	-0.01 ±0.01	-0.01 ±0.01	0.0 ±0.002	0.00±0.002
004	+0.07 ±0.01	+0.03 ±0.01	+0.015±0.002	+0.014±0.005
114	+0.01 ±0.01	+0.01 ±0.005	0.0 ±0.002	0.00±0.002
033	-0.01 ±0.01	-0.01 ±0.005	0.0 ±0.002	+0.027±0.002
024	+0.01 ±0.005	+0.01 ±0.002		
233	+0.015±0.005	+0.005±0.002		
224	-0.01 ±0.005	-0.005±0.002		

The reconstructed (100) maps of the intensity due to the chemical order are shown on fig.1. For Ni₃V, and Ni₃Cr, the diffuse maxima occur at

the expected $(1 \frac{1}{2} 0)$ positions, the known ordered structures belonging to the $(1 \frac{1}{2} 0)$ family. For Pd_3V , they surprisingly occur at (100) positions.

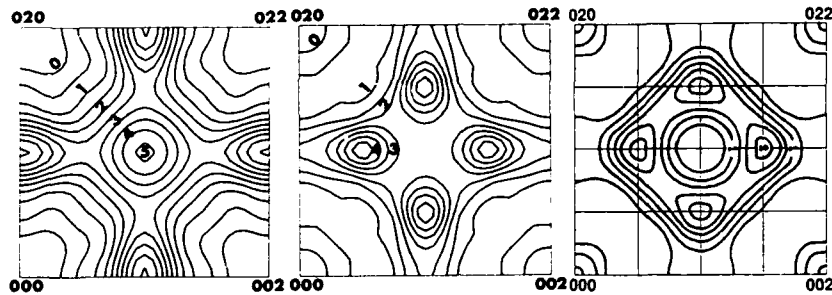


Fig.1: Short range order intensities in the (100) plane for Pd_3V at 840°C , Ni_3V at 1100°C and Ni_3Cr at 600°C . Laue units.

First, let us briefly discuss the case of Pd_3V and its comparison with Ni_3V , which has already been explained elsewhere [3]. In a 2 potential model (J_1 and J_2), the DO_{22} structure is stabilized as a ground state for $J_1 > 0$ and $0 < J_2/J_1 < 1/2$, whereas L_{12} is stabilized when $J_2 < 0$. In the mean field approximation, the regime of $J_2 > 0$ corresponds to diffuse intensity maxima located at $(1 \frac{1}{2} 0)$ positions, whereas the regime of $J_2 < 0$ leads to maxima located at $(1 0 0)$ [4]: the mean field theory leads to a correct prediction for Ni_3V , but not for Pd_3V . To explain this discrepancy, we first performed CVM calculations, in the tetrahedron-octahedron (T.O.) approximation, including the potentials J_1 and J_2 . The resulting phase diagram shows a narrow region ($J_2/J_1 < 0.08$), where the DO_{22} structure disorders towards a short range ordered FCC phase with diffuse maxima located at the (100) positions - (100) regime-, corresponding to the Pd_3V situation, whereas the Ni_3V pertains to the $(1 \frac{1}{2} 0)$ regime ($J_2/J_1 > 0.08$) where the DO_{22} structure disorders towards a $(1 \frac{1}{2} 0)$ disordered state. This is a qualitative success of the model. To reach a more quantitative account of the measured intensity distribution, further interactions are needed, at least up to the fourth neighbour, in agreement with recent electronic structure calculations [2]. Then, provided that the first neighbor interaction is dominant, this phase diagram should remain qualitatively valid when changing J_2 into the antiphase energy $\xi = J_2 - 4J_3 + 4J_4$. In order to determine the interactions up to the fourth neighbors, we used an inverse C.V.M. algorithm based simultaneously

on two clusters: the FCC cube (14 points) and a point surrounded by its 12 nearest neighbours (13 points). This procedure leads to the potentials displayed on table II [5]. For both systems, J_1 is far stronger than the three other potentials, which are all of the same order of magnitude. The different aspects of the diffuse maps of Pd_3V and Ni_3V are accounted for by the discrepancy of the antiphase boundary energies ξ : they are effectively small for Pd_3V , which belongs to the (100) regime, and much stronger for Ni_3V which belongs to the $(1\ 1/2\ 0)$ regime.

TABLE II : PAIR POTENTIALS EXTRACTED
FROM TABLE I PARAMETERS

J(meV)	Pd_3V	Ni_3V	Ni_3Cr
011 (J_1)	47.	27.	3.1.
002 (J_2)	-1.5	-5.	-9.8.
112 (J_3)	5.9	-1.3	-2.5
022 (J_4)	6.9	3.5	5.2
ξ	2.4 ± 2	15 ± 3	21 ± 2

At variance with the Ni_3V case, fig.1 shows that, for Ni_3Cr , the intensity, starting from the maximum at $(1\ 1/2\ 0)$, decreases steeply and nearly falls to zero at the (100) points. The lines are also much broader in the perpendicular direction, i.e. along the lines $(1/2\ \xi\ 0)$. This is consistent with the much lower α_{110} value calculated by the least squares fit (table I). On the other hand, the order of magnitude of the other order parameters is the same as for the two other samples: the first parameter only has been strongly reduced.

The order parameters have been submitted to the same treatment as for the other samples to obtain the potentials J_1, J_2, J_3 and J_4 : they are displayed on table II and fig.2, together with the values found by authors of recent work on the same system.[6]. The same conclusions are reached as for the order parameters when we compare the potentials for Ni_3Cr and those found on the other alloys: the first potential is strongly depressed and the orders of magnitude of the other potentials remain the same. This low level of the first potential compared to others is expected when the diffuse intensity is spreaded along the lines $(1/2\ \xi\ 0)$. The decrease of the first potential is consistent with the trends of the first principle calculations shown on fig.3:

for Ni as B element, $N_B=9$; for Cr or V as A element, $\Delta N_e=4$ or 5 respectively. Fig.3a indicates a decrease of the potential.

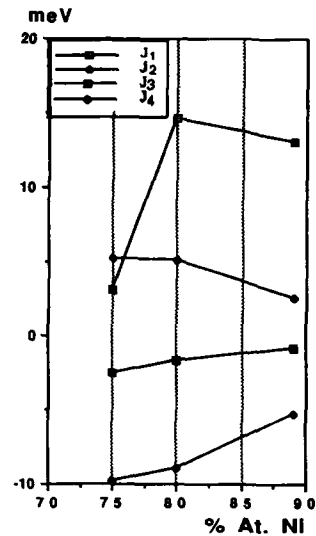


Fig.2: comparison of our potentials with the values found by other authors [6] for the Ni-Cr system

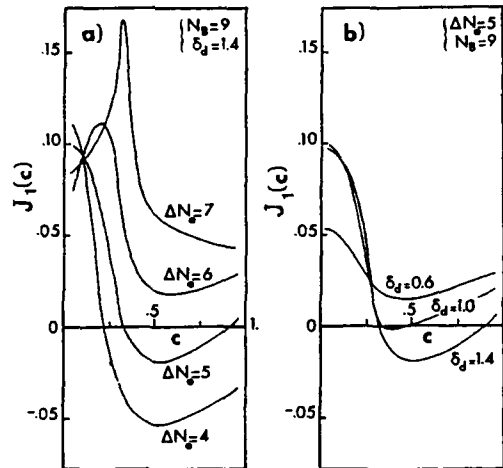


Fig.3: Calculations of the potential J_1 using the TB/CPA/GPM approximations. J_1 is plotted as a function of the concentration c . It also depends on the electronic concentration N_B of the B element, the differences ΔN_e in electronic concentration and δ_d in electronic potential between the two components.[7]

We have compared the experimental transition temperatures with the theoretical estimates obtained from our sets of potentials: by a Monte Carlo method, we obtain 600°C for Pd_3V instead of 815°C experimentally; for Ni_3V , we obtain 985°C instead of 1045°C and, for Ni_3Cr , the transition temperature is lower than 150°C . Fig.2, comparing our results with those of other authors obtained at different compositions, shows a noticeable decrease of the first potential with decreasing nickel concentration, the other potentials remaining similar. This raises a question: if the potentials were to stay at this low level, there would probably be no way for Ni_2Cr to remain ordered up to 580°C . We then expect an interesting behavior of the potentials as a function

of the concentration. Therefore, the study of the diffuse scattering at the Ni₂Cr composition would be of great interest.

Références

1. J. Hafner, From hamiltonians to Phase Diagrams, n°70 of Solid State Science series, Springer 1977
2. F. Ducastelle et F. Gautier, J. Phys. F., 6, 2039 (1976)
A. Bieber et F. Gautier, Acta Metall., 34, 2291 (1986)
A. Bieber et F. Gautier, Acta Metall., 35, 1889 (1987)
F. Ducastelle : La Recherche Aéronautique 4, 11 (1986)
3. F. Solal, R. Caudron, A. Finel, Physica B 156-157, 75 (1989)
F. Solal, R. Caudron, F. Ducastelle, A. Finel and A. Loiseau, Phys. Rev. Lett. 58, 2245 (1987)
4. P.C. Clapp et S.C. Moss, Phys. Rev. 171 (1968) 754
5. A complete analysis shows that the conditioning of the inverting procedure is so poor in the Pd₃V case that the J's are exceedingly sensitive to *small errors on the α 's*. However, the antiphase energy is not sensitive at all to the α errors. So, we can safely compare the antiphase energies of the two alloys.
6. B. Schonfeld, L. Reinhardt and G. Kostorz, Phys. Stat. Solidi (b) 147, 457 (1988)
W. Schweika and H.G. Haubold, Phys. Rev. B37, 9240 (1988)
7. P. A. Turchi, Thesis, Paris (1984)

DIFFUSE NEUTRON SCATTERING STUDY
OF SHORT-RANGE ORDER IN $\text{Fe}_{0.8}\text{Al}_{0.2}$ ALLOY

WERNER SCHWEIKA

KFA Jülich, Institut für Festkörperforschung, D-5170 Jülich, Federal Republic of Germany

ABSTRACT

Diffuse neutron scattering experiments have been performed on a single crystal $\text{Fe}_{0.8}\text{Al}_{0.2}$ at $T=1013\text{K}$. The data are analysed in terms of short-range order and lattice displacements. Effective pair-interactions have been determined by the inverse Monte Carlo method. Further measurements of the temperature dependence of the diffuse scattering reveal a long-range ordered phase with the $B32$ structure below $T \sim 650\text{K}$. This new phase is related to the influence of the magnetism on the chemical ordering in the iron-aluminum alloys.

INTRODUCTION

In some alloys, states of magnetic and compositional order coexist. If the ordering energies are comparable, magnetic and chemical order may be strongly coupled, giving rise to rising physically and technologically interesting phenomena^{1,2}. Recently, a few theoretical studies using the Monte Carlo^{3,4} and Cluster Variation⁵ methods have treated the ordering phenomena in FeAl, including also the chemical and magnetic interactions explicitly^{3,5}. The description of ordering in binary systems, like alloys, using the Ising model is quite attractive because of the basic, microscopic concept and its possible links to results of modern electronic band theory. However, if the interaction parameters are fitted to experimental phase diagrams, such calculations have not much predictive power.

Precise measurements of the short-range order of an alloy in thermal equilibrium are particularly interesting, since it has been demonstrated that the characteristic atomic interactions can be determined in a straightforward fashion using the inverse Monte Carlo method^{6,7}. Previous diffuse x-ray experiments^{8,9,10} on quenched α -FeAl have already shown the existence of short-range order, reflecting the ordering tendency of the alloy to the known FeAl and Fe_3Al phases. Furthermore, lattice displacements due to the different atomic sizes have been found. FeAl is an attractive system for both x-rays and neutrons. However, an essential advantage of neutrons is that the elastic and inelastic scattering can be measured separately. This is especially important for in-situ studies at high temperatures, which are necessary if the interesting equilibrium structure can not be obtained during a quench. Recent neutron scattering experiments¹¹ have shown that the short-range order intensity exhibits an unusual temperature dependence. Instead of an increase of the short-range order peak, almost no change has been observed in a large interval around the Curie temperature. A qualitative explanation was given in terms of the competition between the Fe-Al interaction, with its tendency to order with unlike neighbors, and the ferromagnetic coupling of the Fe moments, favouring the formation of Fe-Fe pairs.

In this paper we present first results of the diffuse scattering from a $\text{Fe}_{0.8}\text{Al}_{0.2}$ single crystal above the Curie temperature. The equilibrium short-range order has been measured at $T=1013\text{K}$, where the influence of the magnetic interactions is expected to be small and the local atomic order is mainly determined by the effective atomic pair-interactions. We also describe the diffuse scattering at lower temperatures, where a phase transition into a new ordered phase has been observed.

EXPERIMENT

The diffuse scattering experiments were carried out at the new external neutron guide hall at the Jülich research reactor. The instrument used is especially designed for such studies. It is a time-of-flight instrument, with a modest resolution but high flux and low background. The monochromatic flux at the sample position is $10^7 \text{ n/cm}^2 \text{ s}$ at $\lambda = 0.33 \pm 0.015 \text{ nm}$. 64 ^3He detectors are arranged around the sample at 0.8 m distance. The background scattering from the furnace is eliminated by a radial collimation in front of the detector system.

The sample is a single crystal Fe-20at%Al, grown by Bridgeman technique at the MPI Düsseldorf. It has a cylindrical shape with 5 mm diameter and 4 cm length. The axis is close to a [100] direction. The ends have been cut parallel to a (211) and a (110) plane respectively.

Diffuse neutron scattering at $T=1013\text{K}$

The measurements at $T = 1013\text{K}$ were done for three different orientations in order to collect data in the (100), (211) and (110) planes. The sample was therefore rotated in the furnace in steps of 4° degrees. The measuring time has been less than one day for each plane. Thus 5600 time-of-flight spectra have been measured. A typical set of TOF-spectra, measured for one sample position, is shown in fig.1.

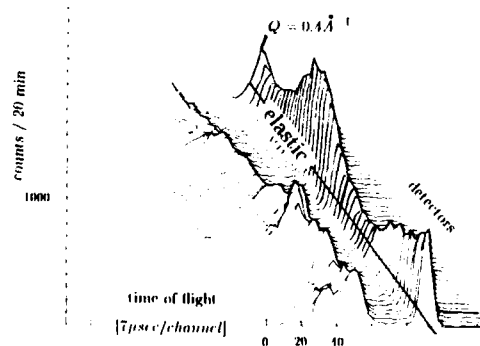


Fig.1 Time-of-flight spectra measured at $T=1013\text{K}$.

The elastic intensities have been determined by fitting to gaussians appropriate to the instrumental resolution. The calibration was done by a vanadium reference measurement. A further correction assuming equal Debye-Waller factors for Fe and Al atoms has been applied. The small, incoherent background scattering has been subtracted. The coherent diffuse elastic structure factor $S(\vec{Q}) = I(\vec{Q})/I_{\text{Lam}}$ is given by the intensity normalized by the Laue-scattering $I_{\text{Lam}} = c_{\text{Fe}}c_{\text{Al}}(b_{\text{Al}} - b_{\text{Fe}})^2$ and is displayed in contour plots in fig.2. Within the approximation $Q \cdot a \ll 1$ the diffuse structure factor of a binary substitutional disordered system can be written as

As can be seen, it is easy to distinguish between inelastic phonon scattering and the diffuse elastic scattering. It is worthwhile to mention that the background due to the quasielastic paramagnetic scattering should have a width in the order of $k_B T_c \approx 80 \text{ meV}$, whereas the energy resolution is 0.8 meV (FWHM). However, the quasielastic width vanishes in the limit of $\vec{q} = 0$, and in order to separate the critical magnetic scattering in the vicinity of T_c , such good energy resolution is rather favourable.

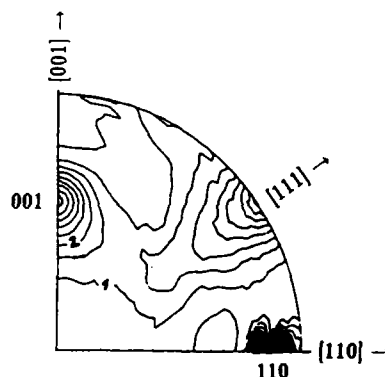


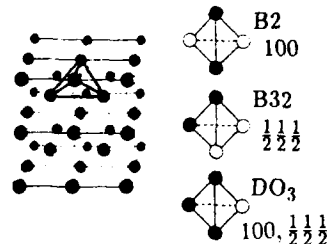
Fig.2 $S(\vec{Q})$ of $\text{Fe}_{0.8}\text{Al}_{0.2}$ at $T=1013\text{K}$ in the (110) plane.

$$S(\vec{Q}) = \alpha(\vec{q}) + i\vec{Q} \cdot \vec{\gamma}(\vec{q}) - \frac{1}{2}Q^2 \epsilon(\vec{q}) \dots$$

The first term describes the short-range order contribution, the subsequent terms are related to the lattice displacements $\langle \vec{u} \rangle$ and to $\langle \vec{u}^2 \rangle$ respectively. The Fourier analysis of the scattering functions $\alpha(\vec{q})$, $\vec{\gamma}(\vec{q})$ and $\epsilon(\vec{q})$ yields the real space parameters, which will be discussed further below. From symmetry arguments, we note some important features: The diffuse maxima at $\{100\}$ is related to the short-range order (even functions) while its asymmetry is due to the first order displacement scattering (odd functions).

The peak at $\{100\}$ reflects the tendency of the alloy to form the long range ordered B2 phase (fig.3). There is almost no enhanced intensity at $\frac{1}{2}\{111\}$, the additional ordering wave vector of the DO_3 phase, i.e. the ordered Fe_3Al .

Fig.3 Bcc lattice, ordered structures and ordering wave vectors



Temperature dependence of the intensity and B32-ordering

Earlier measurements have shown that the intensity of the 100 peak remains almost unaltered in the temperature range from $550^\circ C$ up to $750^\circ C$ ¹¹. At lower temperatures we have observed now a phase transition below approx. $380^\circ C$ (fig.4).

The ordering wave vector is $\frac{1}{2}\{111\}$ but not $\{100\}$. Hence the ordering is of the B32 type instead of DO_3 , which is a new observation in the Fe-Al system. An indication for another ordered phase occurring in the iron-rich part of the phase diagram is also found in measurements of the thermal expansion etc.¹² In a recent phase diagram^{12,13} a new phase K_1 is suggested and related to the so-called "K"-state¹⁴. This term has been used for alloys, whose residual electrical resistivity increases towards lower temperatures presumably due to (short-range) ordering.

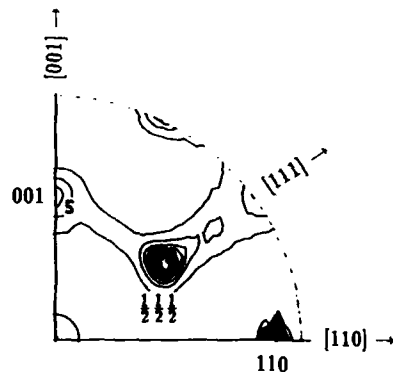


Fig.4 $S(\vec{Q})$ of $Fe_{0.8}Al_{0.2}$ at R.T. in the (110) plane.

RESULTS AND DISCUSSION

Short range order and lattice displacements at $T=1013$ K

The diffuse elastic scattering measured at 1013 K has been analysed according to eq. 1 in terms of short-range order and lattice displacements. Therefore a linear least squares analysis has been applied. The short-range order parameters α_{lmn} , which are obtained are given in fig.5.

Just as in reciprocal space, where the short-range order peak indicates the alloy's favour of the $B2$ structure, the real space parameters reveal the $B2$ character of the existing short range correlations. Within the small error bars, all α parameters with odd indices are negative and those with even ones are positive. Hence, there is the same alternation in sign as in perfectly ordered $B2$. The first short-range order parameter $\alpha_{111} = -0.124 \pm 0.002$ says that the probability of unlike nearest neighbors is enhanced by 12% relative to the random configuration in $Fe_{0.8}Al_{0.2}$. The error bars of the following parameters are even smaller.

It is interesting to compare these results with recent data obtained from x-ray diffuse scattering of a single crystal with rather the same composition but quenched from $T=823$ K¹⁰. Compared to the present case, the ordering tendency towards the $B2$ phase has significantly decreased in the ferromagnetic state. A paradoxical situation, if the role of the magnetism would be neglected.

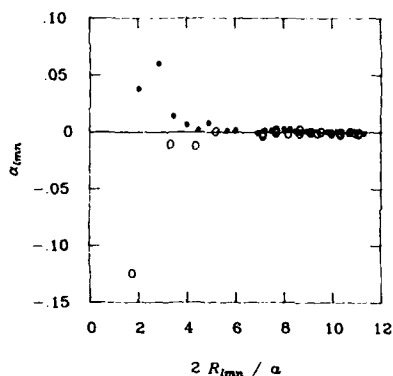


Fig.5 Short-range order parameters α_{lmn} (●) even and (○) odd indices.

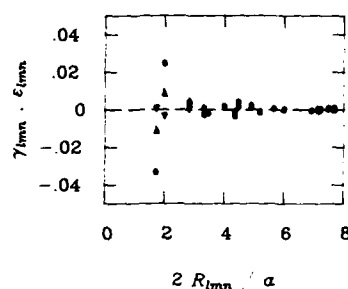


Fig.6 Lattice displacement parameters (●) γ_{lmn} and (○) ϵ_{lmn} .

The asymmetry of the short-range order peak at $\{100\}$ indicates that there are significant lattice distortions in this alloy. The lattice displacement parameters $\tilde{\gamma}_{lmn}$, displayed in fig.6, are linear combinations of the three different displacements between Al-Al, Al-Fe and Fe-Fe atoms.

The displacement parameters describe the mentioned asymmetry and also the minima at the low Q side of the Bragg peaks. These features are consistent with a positive lattice parameter change due to the Al defects in the Fe-rich matrix and the concept of Al being larger in size than Fe^{7,11}. Because of the limited Q -range of this measurement, $Q_{max} = 34.5 \text{ nm}^{-1}$, the contribution from the second order displacement term $\epsilon(\vec{q})$ is small, which means also, that the data offer only weak information about the second order displacement parameters ϵ_{lmn} .

Effective pair-interactions

Effective pair-interactions have been determined by the inverse Monte Carlo method^{6,7}. It has been shown¹⁵, that possible small many-body interactions can be accurately described by only effective pair-interactions which then would have a specific intrinsic dependence on concentration and temperature. In the inverse Monte Carlo method, a model crystal with the measured short-range order parameters is first generated. The

interactions are then calculated employing detailed balance. There is one important assumption, which has implicitly been made: the effect of the ferromagnetic interactions on the measured chemical short-range order has been neglected. This may be justified, since the measurement has been performed at $T = 1013\text{K}$ in the paramagnetic state, where this effect is at least weaker than in the ferromagnetic alloy.

The results are shown in fig.7. The interactions are defined by the Ising Hamiltonian

$$H = -\frac{1}{2} \sum_{i,j} V_{ij} s_i s_j$$

where $s_i = \pm 1$ denotes the site occupation and the interactions V_{ij} between sites with the same distance $\vec{r}_i - \vec{r}_j$ are described by one parameter V_{lmn} . The negative nearest neighbor interaction V_{111} describes the preference for unlike neighbors and is important for the phase stability of the *B2* phase in *FeAl* alloys. The negative value of $V_{2(11)}$ and the positive V_{220} offer an explanation for the existing *DO3* phase (*Fe3Al*). Such ground state considerations also indicate that the system is not far from the boundary of stability between *B2* and *B32*; in particular, additional ferromagnetic interactions are in favour of the *B32* structure.

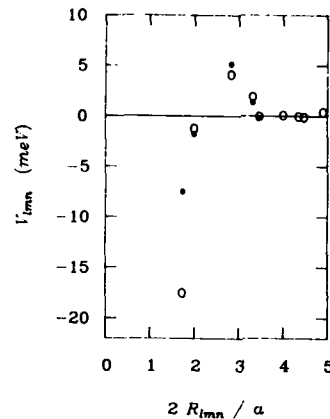


Fig.7 Inverse Monte Carlo result for the effective pair-interactions. (o) $T=1013\text{K}$; (•) $T=823\text{K}$, calculated from SRO-data¹⁰.

For comparison the effective interactions related to the short-range order measured at $T=823\text{K}$ ¹⁰ have also been calculated by the inverse Monte Carlo method. Both results agree nicely, except for the nearest neighbor interaction. Apparently the ferromagnetic interaction has reduced the effective interaction parameter V_{111} .

This influence can be further illustrated by Monte Carlo simulations of the short range order in a magnetic alloy, when an additional magnetic interaction J is included. The temperature dependence of the short range order parameter α_{111} is altered due to the magnetism as shown in fig.8. At high temperatures in the paramagnetic phase the influence of the magnetic interaction on the chemical short range order is vanishing, but closer to the ferromagnetic transition temperature T_c this influence is increasing. Although the model parameters used in this earlier calculation are different from the ones of the present study, there is the interesting qualitative feature of an inflection point at T_c in the temperature dependence of the short range order, which has also been observed in the scattering experiment¹¹. From this Monte Carlo simulation we can also conclude that the effective interactions determined from the short range order at $T = 1013\text{K}$ ($T_c = 950\text{K}$) is still reduced by a small ferromagnetic contribution.

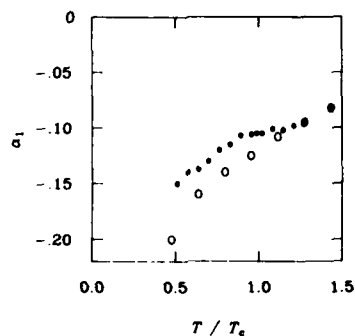


Fig.8 Monte Carlo simulation of α_1 . $V_1 = -1$, $V_2 = \frac{1}{2}$; (•) $J_1 = 1$, (o) $J_1 = 0$

FINAL REMARKS

A more detailed description of this work will be published elsewhere. The *B32* phase has also been observed using transmission electron microscopy¹⁶. A certainly surprising fact is the large deviation from stoichiometry of the *B32* phase being found. Further studies should clarify the region of stability for the *B32* phase. It is also possible that the magnetism is involved in the transformation to a suggested, but unknown phase "*K₂*"^{12,13}. One might further speculate, whether the interesting spin glass behaviour in *FeAl* alloys is also related to the competition between chemical and magnetic order. The present result also raises the question, as to whether the *B32*, and not the *B2* phase is the real ground state of *FeAl* alloys. This can be answered if the magnetic interactions would be known better. However, even if *B32* would be the stable low temperature phase for *FeAl*, since during cooling the phase transformation to the *B2* phase is precurring, a possible further transformation to *B32* is rather unlikely.

References

1. Magnetism and Metallurgy, eds. A. E. Birkowitz and E. Kneller (Academic, New York, 1969) Vol.II
2. D. D. Johnson, F. J. Pinski, J. B. Staunton, B. L. Györfy, G. M. Stocks, SANDIA REPORT ; to be published in Physical Properties of Low-Expansion (INVAR-type) Alloys, ed. Ken Russel, Mater. Res. Soc.,(1989)
3. B. Dünweg and K. Binder, Phys. Rev. B **36**, 6935 (1987)
4. H. Ackermann, thesis, MPI Düsseldorf & Dortmund University 1988
5. D. A. Contreras-Solorio, F. Mejia-Lira, J. L. Moran-Lopez and J. M. Sanchez, Phys. Rev. B**38**, 4955 (1988); Phys. Rev. B**38**, 11481 (1988); J. De Physique C**8** **49**,105 (1988).
6. V. Gerold and J. Kern Act. Metall. Vol.**35**, 393-399 (1987).
7. W. Schweika and H. G. Haubold, Phys. Rev. B**36**, 6935 (1987).
8. J. E. Epperson and J. E. Spruiell, J. Phys. Chem. Solids **30** 1733 (1969).
9. S. V. Semenovskaya, Phys. Status Solidi B**64**, 291 (1974).
10. V. Pierron-Bohnes, thesis, Strasbourg University, 1988
11. W. Schweika, M. Monkenbusch, H. Ackermann, Physica B**156&157**, 78-80 (1989).
12. W. Köster and T. Gödeke, Z. Metallkde **71**, 765 (1980)
13. O. Kubashewski (ed.), Iron - Binary Phase Diagrams, (Springer 1982) p. 5-9
14. H. Thomas, Z. Metallkde. **41**, 185 (1950)
15. W. Schweika and A. E. Carlsson, Phys. Rev. B**40**, 4990-4999 (1989).
16. W. Jäger and W. Schweika, to be published

LATTICE MISFIT AND DECOMPOSITION IN NI-AL-MO ALLOYS

HECTOR CALDERON AND GERNOT KOSTORZ
 Angewandte Physik, ETH Zürich, CH-8093 Zürich, Switzerland

ABSTRACT

The effect of lattice mismatch δ between the α -matrix and α' -precipitates on the decomposition process of Ni-Al-Mo alloys has been investigated. The results show that for $\delta = 0$ spherical precipitates are formed without any orientational correlation. For $\delta > 0$ non-spherical particles, aligned along $\langle 100 \rangle$, are produced. The kinetics of the α - α' decomposition becomes slower as δ is reduced to zero.

INTRODUCTION

In many Ni-rich alloys, α' -precipitates [essentially Ni₃(Al,Ti), L₁ structure] coherent with the fcc α -matrix form after suitable thermal treatment. In the case of Ni-Al, the decomposition takes place via nucleation, growth and coarsening [1]. Atom-probe field ion microscopy shows α' -precipitates (Ni₃Al) from the beginning of decomposition [2]. Although this decomposition process has been extensively investigated, the effect of lattice mismatch [$\delta = (a_{\alpha'} - a_{\alpha})/a_{\alpha}$ where a is the lattice constant] and elastic strains upon nucleation and phase separation, though clearly recognized, has not yet been fully examined. The theoretical work of Larai et al. [3] and Kawasaki and Enomoto [4] on the effect of stress-induced interactions on the coarsening of precipitates and on the thermodynamics of stressed solids, indicates the way toward a more realistic treatment of particle evolution. Reliable experimental data on the simplest possible systems are required, too. In Ni-Al alloys the mismatch δ is positive but it can be reduced by alloying with elements that primarily increase the lattice constant of the α -phase, e.g., refractory metals. Thus, this investigation has been conducted to obtain information, via small-angle neutron scattering (SANS), regarding the evolution of particle shape, size and elastic strains during the α - α' decomposition process.

ALLOYS AND EXPERIMENTAL PROCEDURE

The SANS experiments were carried out at the Institut Laue-Langevin, Grenoble (France), using the D11 facility. Four monocrystalline specimens were aged 'in beam' and had the compositions and lattice misfits given in Table I. Alloy 4 was aged at 883 K because of the relatively slow kinetics of the α - α' decomposition in this alloy. The other alloys were aged at 833 K. The specimens were cut along the (110) plane, and the incident neutron beam was perpendicular to these faces. The sample to detector distance employed for the measurements was 1.5 m, and the wavelength was 0.66 ± 0.06 nm. The samples were aged in a vacuum better than 8×10^{-4} Pa which resulted in a negligible oxidation.

Table I: Alloy Compositions and Lattice Misfits

Alloy	Composition	Lattice misfit (%)
1	Ni-12 at.% Al	1.2
2	Ni-10.3 at.% Al-5.5 at.% Mo	0.6
3	Ni-6.5 at.% Al-9.6 at.% Mo	0
4	Ni-6.1 at.% Al-9.4 at.% Mo	0

EXPERIMENTAL RESULTS

The scattering patterns obtained for the alloys under analysis are characteristic of the mismatch value δ . As Fig.1a shows, the particles in alloy 1 produce anisotropic patterns with sharp peaks along $\langle 100 \rangle$. As the value of δ decreases (alloy 2), the anisotropy as well as the intensity of the peaks along $\langle 100 \rangle$ are reduced. For both alloys, the scattering patterns suggest that the particles are not spherical and that there is a spatial particle correlation along $\langle 100 \rangle$. The anisotropic shape of the pattern is observed from the beginning of the $\alpha-\alpha'$ decomposition. In contrast, when $\delta = 0$ (alloys 3 and 4), the scattering pattern is "isotropic" (Fig.1b), and no peaks are observed. In this case, a spherical particle morphology and a random particle distribution are expected.

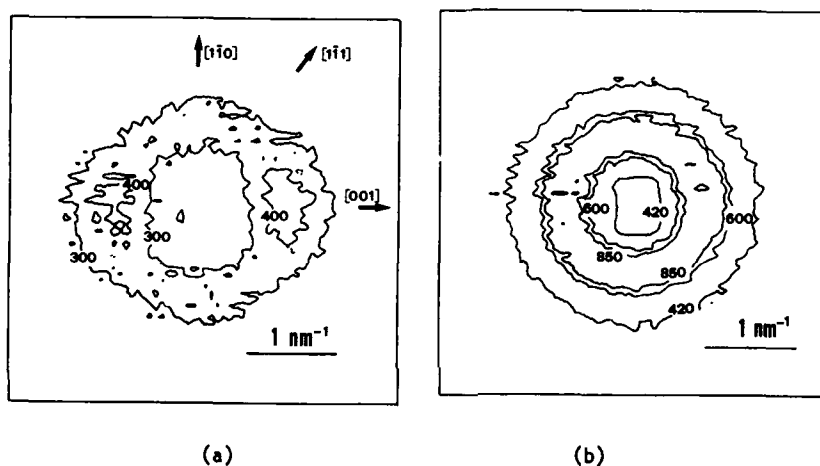


Figure 1. Isointensity plots (counts in 20 min) of SANS spectra. (a) Alloy 1 after 35 min at 833 K. (b) Alloy 4 after 3.9 h at 883 K.

The absolute scattering cross-sections have been obtained as a function of aging time by using four averaging techniques for the two-dimensional detector, i.e. annular (labelled isotropic) and in sectors $\pm 15^\circ$ from [001], [110], [111] and [111]. Fig.2 illustrates the results obtained for the case of alloy 2 ($\delta = 0.6\%$) and alloy 4 ($\delta = 0\%$). In all cases, with increasing aging time, the intensity maxima produced by interparticle interference move toward the center of the detector, and in particular for the alloys with a measurable lattice mismatch, the anisotropy of the pattern increases. Thus in alloys 1 and 2, as the interparticle distance and particle size increases with aging time, the shape of the particles deviates more and more from spherical. On the other hand, the particle shape in alloys 3 and 4 ($\delta = 0$) remains spherical during the time of observation.

The averages along different crystallographic directions reflect the development of both the anisotropy of the scattering pattern and the spatial correlation of the particles, i.e. the intensity maxima are located at different values of the scattering vector and their absolute values depend on the orientation. This feature may be used to represent, in a semiquantitative manner, the evolution of the scattering pattern with aging time. Fig. 3 shows the variation of the ratio I_{100}/I_{111} as a function of aging time for each alloy under analysis, I_{111} and I_{100} representing the values of the

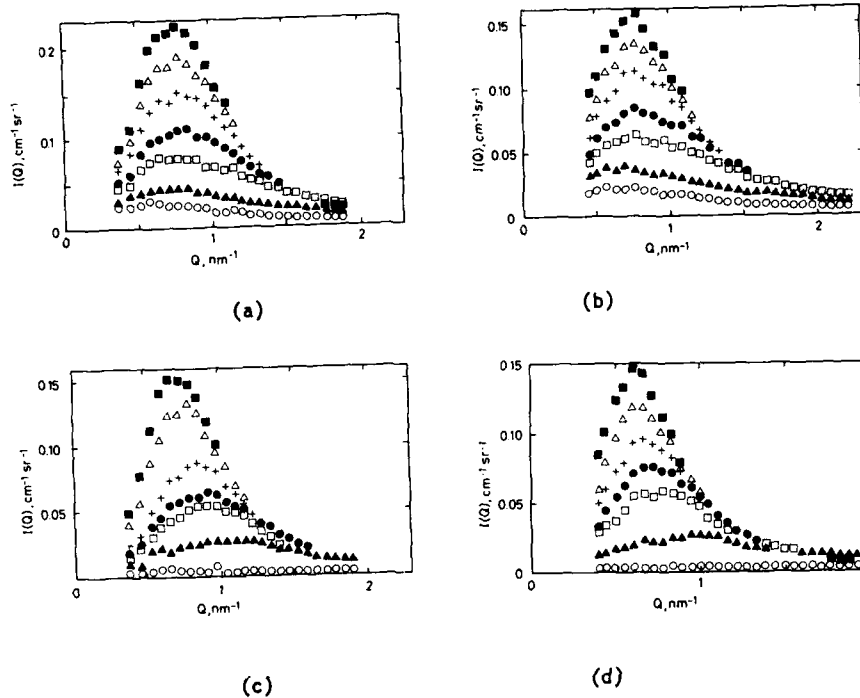


Figure 2. Time evolution of the SANS intensity. (a) Alloy 2 along $\langle 001 \rangle$ (o: quenched, Δ : 0.1 h, \square : 1.6 h, \circ : 3 h, $+$: 4.9 h, \triangle : 6.6 h, \blacksquare : 8.2 h). (b) Same as (a), along $\langle 111 \rangle$. (c) Alloy 4 along $\langle 001 \rangle$ (o: quenched, Δ : 0.5 h, \square : 1.4 h, \circ : 2 h, $+$: 2.5 h, \triangle : 3.4 h, \blacksquare : 4.2 h). (d) Same as (c), along $\langle 111 \rangle$.

absolute intensity maxima obtained after averaging along the $[001]$ and $\langle 111 \rangle$ directions, respectively. The strong anisotropy of the scattering pattern and its evolution during aging for alloy 1 can be clearly seen in Fig. 3. On the other hand, changes in the scattering pattern of alloy 2 are much subtler than those for alloy 1. This may be interpreted as a direct consequence of the reduction of lattice mismatch through the addition of Mo, as discussed below. For alloys 3 and 4, the ratios I_{100}/I_{111} are close to one as expected.

The kinetics of the σ - σ' decomposition is apparently affected by the different values of δ . An analysis based on the evolution of the radius of gyration, R_G (see, e.g., [5]), shows that for aging times longer than 15 min, R_G^3 tends to vary linearly with aging time in all cases. This can be interpreted as coarsening in agreement with the classical Lifshitz-Slyozov-Wagner (LSW) theory [6]. Fig. 4 shows the results of this analysis. The slopes of the lines, which represent the coarsening kinetics rate constants K according to the LSW theory, are given in Table II. The values of K show that by decreasing the lattice mismatch δ from 1.2% (alloy 1) to 0% (alloy 3), the coarsening kinetics is slowed down by a factor of 23 (K_1/K_3).

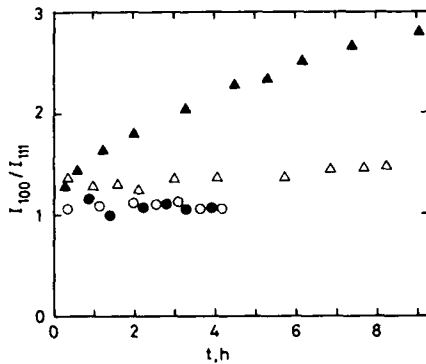


Figure 4. Cube of the radius of gyration R_G as a function of aging time t . Alloy 4 aged at 883 K, all others at 833 K. (\blacktriangle : Alloy 1, \triangle : Alloy 2, \bullet : Alloy 3, \circ : Alloy 4).

Figure 3. Ratio I_{100}/I_{111} as a function of aging time t . I_{100} and I_{111} represent the values of the maximum intensity along $\langle 001 \rangle$ and $\langle 111 \rangle$, respectively. (\blacktriangle : Alloy 1, \triangle : Alloy 2, \bullet : Alloy 3, \circ : Alloy 4).

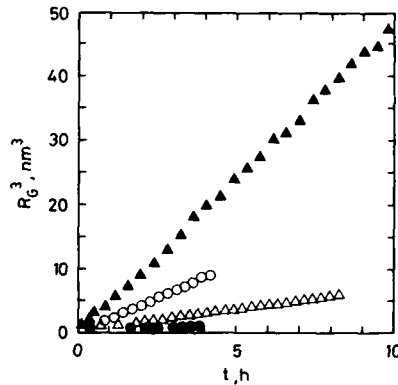


Table II: Coarsening Kinetics Rate Constants K

Alloy	K (nm ³ /h)	δ (%)
1	4.7	1.2
2	0.7	0.6
3	0.2	0
4	2.2	0

The volume fraction f_v of the alloys under study was calculated from the integrated intensity Q_v . The values reported here were obtained after a circular average of the recorded intensities. The integrated intensities were calculated according to the technique introduced by Gerold [7] in which the experimental data are used until a given scattering vector q_{max} and the remaining integration is calculated by using Porod's law (see, e.g., [5]). By changing q_{max} it is possible to select the minimum value of Q_v . In all cases after a period of instability, the values of Q_v become approximately constant with respect to the aging time. These values were used to calculate f_v and are given in Table III. Because of counting statistics and other measuring errors, the estimated accuracy of Q_v is only $\pm 8\%$. The calculated values f_v are also given in Table III together with the corresponding uncertainties. The volume fractions in alloys 1 and 3 are very similar but nevertheless, the decomposition kinetics are considerably different.

Table III: Integrated intensity and volume fractions

Alloy	$Q_0/4\pi$ (10^{28} m^{-4})	$\Delta\rho$ (10^{13} m^{-2})	f_v (%)
1	1.42 ± 0.11	9.2	9.5 ± 1.0
2	1.96 ± 0.16	7.8	19.0 ± 2.0
3	1.07 ± 0.09	6.86	13.0 ± 1.0
4	1.10 ± 0.09	6.86	13.7 ± 1.0

DISCUSSION

The differences in the decomposition kinetics of α' are basically related to the lattice mismatch δ . One of the possible disadvantages of adding Mo to the binary Ni-Al is that the undercooling, ΔT , with respect to the solvus temperature might be changed. A smaller undercooling can result in a slower rate of decomposition. However, analysis of the known sections of the ternary Ni-Al-Mo [8] indicates that the undercooling tends to be higher if Mo is added to Ni-Al (up to 10 at.% Mo). Furthermore, the volume fraction of α' in the alloys containing Mo is higher than in the binary alloy (Table III). This can be partially explained by the observed tendency of ΔT . A larger ΔT will produce a large f_v if the shape of the solvus line for the Mo-concentration used is not drastically different from that of the binary alloy, which is apparently the case.

A linear relation between R_G^3 and t is found in agreement with the LSW theory [6]. According to this model, the coarsening rate is directly proportional to the product of σC_0 , where σ is the interfacial energy, D the diffusivity and C_0 the solubility of the rate controlling species. The LSW theory is a classical treatment that does not consider the effects of elastic stresses. According to Cahn and Larché [11], two interfacial stresses in addition to σ are necessary to describe a solid-solid interface. Thus, a reduction of δ is expected to reduce σ or the interfacial stresses, which produces a reduction of the coarsening rate. Larai et al. [3] have demonstrated that the kinetics of coarsening are altered by the elastic stresses basically through the coupling of misfit and interfacial stress. These researchers also suggest that the sign of δ is important. In the present study the reduction of the coarsening rate by means of a reduction of a positive δ was possible. Alloys with negative δ are necessary in order to test completely Larai et al.'s predictions. On the other hand, the effects of D and C_0 on the coarsening rate are difficult to assess due to the lack of experimental information. Nevertheless, analysis of the known sections of the ternary Ni-Al-Mo phase diagram does not support the possibility of a great change of C_0 for the Mo contents used.

The shape of the particles in the binary alloy is not spherical from the beginning of the decomposition at 833 K. TEM investigations [9,10] indicate that α' -particles smaller than 3 nm in Ni-12 at.% Al are spherical. The higher sensitivity of the SANS technique to detect deviations from spherical shape for small particles is evident. Beddoe et al. [1] have suggested that an ellipsoidal shape simulated best their SANS intensity patterns for Ni-Al alloys.

No special orientational arrangement of the particles in the alloys with $\delta = 0$ is observed. By reducing the elastic strains between particles, the particle alignment observed in binary Ni-Al is suppressed. This is not due to a change in the elastic anisotropy of the Mo-containing alloy. Measurements of the anisotropy ratio A [$2C_{44}/(C_{11}-C_{12})$] show that in the binary alloy A equals 2.9 while in the alloy containing 9.6 at.% Mo, A becomes 3.0. Whether the value of A changes drastically at high temperature is not known.

Kawasaki and Enomoto [4] have predicted that attractive interaction between particles counteract coarsening, while repulsive interactions for α'

accelerate coarsening from a $t^{1/3}$ to a $t^{1/2}$ tendency. No changes of the time exponent have been observed in this investigation but new data obtained at longer aging times are currently under analysis.

CONCLUDING REMARKS

The use of SANS to monitor 'in situ' the σ - σ' decomposition in Ni-Al-Mo alloys at 833 K shows that in a binary alloy the particles arrange along $\langle 100 \rangle$ and have a non-spherical shape. Decreasing the lattice mismatch to zero by Mo addition produces randomly distributed and spherical particles. A reduction in the decomposition kinetics by a factor of 23 is also related to the change in δ .

ACKNOWLEDGMENTS

The authors would like to thank R. Baker, R.E. Ghosh, R. May and C. Rey for their help at the Institut Laue-Langevin during data collection, and Ms. Bänninger and E. Fischer for their skilful experimental assistance.

REFERENCES

1. R.E. Beddoe, P. Haasen, and G. Kostorz, in Decomposition in Alloys: the early stages, edited by P. Haasen, V. Gerold, R. Wagner, M.F. Ashby (Pergamon Press, Oxford, 1984), p. 233.
2. H. Wendt and P. Haasen, *Acta Metall.* 31, 1649 (1983).
3. V.J. Lari, W.C. Johnson and P.W. Voorhees, to be published.
4. K. Kawasaki and Y. Enomoto, *Physica A150*, 463 (1988).
5. G. Kostorz, in Neutron Scattering, edited by G. Kostorz (Vol.15, A Treatise in Materials Science and Technology, edited by H. Herman, Academic Press, 1979), p. 227.
6. I.M. Lifshitz and V.V. Slyozov, *J. Phys. Chem. Sol.* 19, 35 (1961); C. Wagner, *Z. Elektrochem.* 65, 581 (1961).
7. V. Gerold, *Phys. Stat. Sol.* 1, 37 (1961).
8. V. Ya Markiv, V.V. Burnashova, L.I. Prgahina, and K.P. Mgasnikova, *Metally* 5, 180 (1969).
9. M.E. Fine, J.R. Weertman, and J.G. Conley, in Phase Transformations 87', edited by G.W. Lorimer (The Institute of Metals, Cambridge, 1987), p. 501.
10. F. Ernst, S.G. Xiao, F. Haider and P.-J. Wilbrandt, *Scripta Metall.* 21, 1189 (1987).
11. J.W. Cahn and F. Larché, *Acta Metall.* 30, 51 (1982).

INFLUENCE OF INTERSTITIAL OXYGEN ON THE LATTICE PARAMETERS OF
SOLUTION-TREATED AND AGED Ti-8.6 wt% Al ALLOYS

G. T. GRAY III AND A. C. LAWSON

Los Alamos National Laboratory, Materials Science and Technology Division, Los Alamos,
New Mexico 87545

ABSTRACT

Neutron powder diffraction data have been obtained on Ti-8.6wt.% Al alloys with three different oxygen contents (500, 1000, and 2000 ppm) in the solution-treated and aged condition (containing α_2) to investigate possible oxygen and aluminum ordering and lattice parameter variations. The lattice parameters "a" and "c" were found to depend on the oxygen content and heat-treatment condition. Consistent with the literature lattice parameter data on pure Ti, the "a" lattice parameter of the solution-treated Ti-8.6Al material is relatively insensitive to the oxygen content while the "c" parameter increases with increasing oxygen. Following aging to precipitate the ordered α_2 , the "c" lattice parameter in the Ti-8.6Al alloys still exhibits a positive dependence on oxygen content with aging and a slight "c" increase over the solution-treated condition. The "a" lattice parameter following aging is observed to be lower than the solution-treated value, particularly for the 1000 and 2000ppm alloys. The diffraction data will be discussed in light of parallel electron microscopy results and literature data.

Introduction

Interstitial oxygen has long been known to have a pronounced influence on the structure and mechanical properties of titanium and titanium alloys, particularly those containing the ordered Ti₃Al (hereafter α_2) phase[1-5]. Recent interest on titanium-based alloys for aerospace applications has in particular focused on the effect of ternary and interstitial additions on the titanium intermetallic alloys TiAl and Ti₃Al because of their attractive strength and modulus values, especially when normalized by their relatively low density. Systematic studies on binary Ti-Al alloys have suggested that oxygen stabilizes α_2 in addition to α by raising the $\alpha / \alpha + \beta$ and $\alpha / \alpha + \alpha_2$ phase boundaries; this has also been qualitatively linked to an increased tendency for inhomogeneous slip in alloys containing >6 wt% Al[2,3]. In alloys containing < 6 wt% Al, increased oxygen has also been suggested to increase the tendency for planar slip due to the enhanced degree of short-range order. The restriction of plastic flow to narrow slip bands (causing high stress concentrations) favors crack nucleation and fracture at low macroscopic plastic strains and a fracture mode transition from ductile rupture to cleavage-like fracture[7,8]. This fracture mode transition is thought to be related to the combined effects of two factors: 1) increasing the oxygen content increases the volume fraction of ordered α_2 precipitates, leading to slip intensification in planar slip bands and 2) the effect of oxygen is additive to that of Al in solid solution in promoting planar slip in the titanium matrix[7]. The role of oxygen is therefore manifest in promoting slip localization by inhibiting dislocation pileup relaxation due to slipband broadening by double cross slip (between the α_2 particles)[7].

Recent Transmission Electron Microscopy (TEM) work[9] on the influence of oxygen on the structure / property relationships of Ti-6Al-2V with 0.65 wt% oxygen (alpha alloy) found dislocations occurring in superdislocation pairs following solution treatment and quenching where there was no diffraction evidence of detectable α_2 . Since oxygen ordering is known to occur at oxygen concentrations greater than or equal to 3 wt%, this observation raises the question whether the dislocation pairs are due to crystallographic ordering of the aluminum. This is considered possible because oxygen reduces the solubility of aluminum in titanium. In addition, it has been determined that enlarged octahedral holes exist in α_2 , making preferential uptake of oxygen in α_2 likely[10]. This theory is consistent with experimental observations that oxygen promotes α_2 formation[2,6,9,11]. TEM investigation of Ti-8.6Al alloys with various oxygen contents has shown that following constant temperature and time aging the volume fraction of α_2 increases with oxygen content [11]. However, when the Ti-6Al-2V

alloy is aged such that diffraction evidence of α_2 was observed, superdislocation pairs were not observed, suggesting evidence of oxygen-ordering[9]. However, experiments on the influence of oxygen content on the structure of Ti-8.6 wt% Al found dislocations to still be in pairs in the presence of detectable α_2 [11].

The object of the present study was to investigate systematically the effect of interstitial oxygen and α_2 precipitate formation on the structure of Ti-8.6 wt% Al alloys using neutron diffraction. Neutron diffraction has the advantage of penetrating bulk specimens, and the time-of-flight technique gives excellent d-spacing precision. The primary goal of the study was to assess possible oxygen and aluminum ordering in Ti-8.6 Al alloys as a function of interstitial content. In addition, we have examined the effect of oxygen content, thermal aging, and α_2 formation on the lattice parameters of a titanium binary alloy.

Experimental Procedure

This investigation was performed on Ti-8.6 wt.% Al (14.3 atomic %), hereafter called Ti-8.6 Al, alloys supplied by Timet containing 0.044, 0.103, and 0.209 wt. pct. oxygen (hereafter labeled 500, 1000, and 2000 ppm). The Ti-8.6 Al alloys were cross-rolled in multiple passes from ~40 to ~8 mm thickness at 950°C, recrystallized in an argon atmosphere at 950°C for 24 hours, and then water-quenched (hereafter called the solution-treated "ST" condition). To assess the affect of the presence of α_2 , some of the alloy samples were subsequently aged to precipitate the ordered and coherent α_2 phase as follows: 500°C/4h/ air cooled - samples machined to dimension, then - 500°C/20 h/ air cooled (hereafter called the ST +AGED or just STA condition). All the alloys exhibited an equiaxed grain structure with an ~110 μm grain size and a strong texture, with the basal planes lying close to the rolling plane. The final sample dimensions were 18 mm in width x 35 mm in height x 6 mm thick. TEM of the STA Ti-8.6Al alloys containing 500, 1000, and 2000 ppm oxygen showed that aging for a constant temperature and time resulted in differences in α_2 precipitation in the three alloys. Dark-field TEM images obtained from $(1101)_{\alpha_2}$ reflection in a $[1120]_{\alpha}$ zone axis for two oxygen content alloys are shown in Figure 1. The α_2 is observed to have nucleated uniformly in the matrix, with the size and volume fraction of the α_2 precipitates increasing with increasing oxygen. Based on dark-field TEM images of the aged Ti-8.6Al alloys, as in Figure 1, it is qualitatively observed that the volume fraction and size of the α_2 in the 1000 and 2000 ppm oxygen alloys are similar and display a significantly higher size and volume fraction of α_2 than in the 500 ppm alloy. X-ray diffraction measurements of the bulk Ti-8.6Al samples' integrated $(1011)_{\alpha_2}$ and $(1011)_{\alpha}$ peak intensities similarly supported this observation.

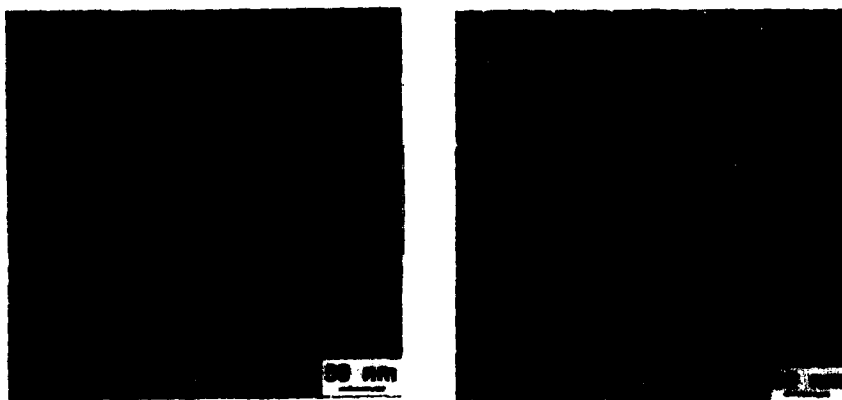


Fig. 1: TEM dark-field images showing the effect of oxygen content increasing the size and volume fraction of α_2 in Ti-8.6Al. (a) 500 ppm oxygen and (b) 2000 ppm oxygen.

Neutron powder diffraction data were obtained at 305K on the High Intensity Powder Diffractometer (HIPD) at the Manuel Lujan, Jr., Neutron Scattering Center (LANSCE) at Los Alamos National Laboratory. Diffraction data were obtained with the rolling plane of the Ti-8.6Al samples normal to the incident beam (beam size = 12mm x 25mm), so that most of the incident flux could be used. This choice of geometry was the best that could be made given the morphology of the samples, as it allowed very reproducible positioning of the samples, consistent with the precision inherent in time-of-flight diffraction (0.3% for HIPD). Data from the $\pm 153^\circ$ and $\pm 90^\circ$ detector banks were co-refined via Rietveld analyses using the Generalized Structure Analysis System (GSAS) developed by Larson and Von Dreele[12]. Unfortunately, it was impossible to make an exact refinement of the preferred orientation, since the assumption presently made in GSAS is that the (single) preferred orientation axis is normal to the diffraction plane. However, it was found that the use of the existing preferred orientation correction (even though improperly formulated for our experiment) allowed a great improvement of the refinements, and this correction was used on an empirical basis. In principle, and as verified by refinement of synthetic data, the failure to use a completely accurate preferred orientation correction can result in slight errors in the refined lattice constants. However, the texture of all the samples and their orientation with respect to the diffractometer were held constant throughout these experiments, so that the trends reported here are expected to be valid.

Results and Discussion

The lattice parameter "a" and "c" data for Ti-8.6Al as a function of oxygen content and heat treatment condition are shown in Figures 2 and 3, respectively. The "a" lattice parameter of the ST/Ti-8.6Al material is seen to be relatively insensitive to oxygen, exhibiting a small negative dependence within the experimental scatter, while the "c" lattice parameter increases with increasing oxygen content.

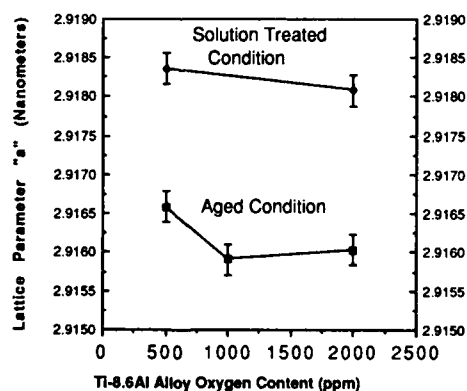


Figure 2: The effect of oxygen content on the "a" lattice parameter of Ti-8.6Al.

The lattice parameter trends in the ST/Ti-8.6Al alloys as a function of oxygen content are seen to be consistent with the previous results of Clark[13] on the influence of oxygen or nitrogen additions on the lattice parameters of high-purity titanium. In the pure Ti case, the addition of oxygen to titanium was observed to expand the lattice in the "c" direction much more than in the "a" direction[13]. The ST/Ti-8.6Al, 500 ppm oxygen alloy displays lattice parameters consistent with the reduced "a" and "c" parameters due to the predominant influence of aluminum alloying.

The "c/a" ratio of the Ti-8.6Al alloy as a function of oxygen content as shown in Figure 4. As expected, the ST condition "c/a" data reflects the marked "c" lattice parameter dependency on oxygen. The significant influence of aluminum content on the lattice parameters of titanium

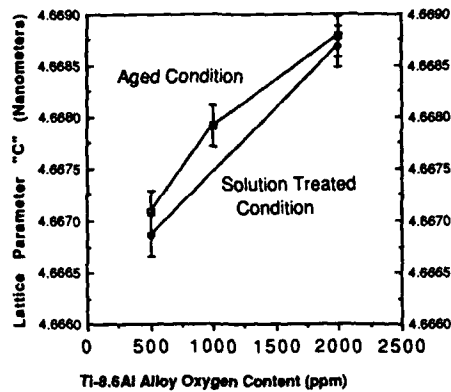


Figure 3: The effect of oxygen content on the "c" lattice parameter of Ti-8.6 Al.

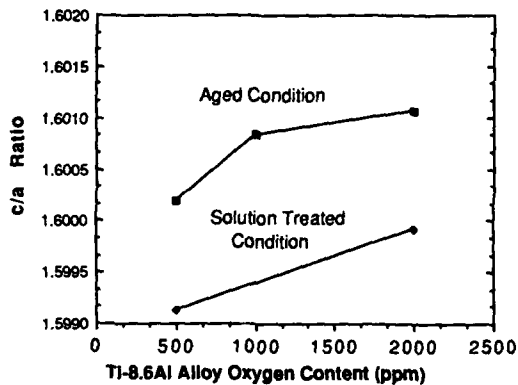


Figure 4: The effect of oxygen content and heat-treatment on the "c/a" ratio of Ti-8.6Al.

are additionally reflected in the differences of the "c/a" of the zero oxygen extrapolated Ti-8.6Al value compared to the "c/a" of pure Ti of 1.587. Extrapolation of the ST / Ti-8.6Al condition "c/a" ratio to zero oxygen content gives a "c/a" of ~1.5988 which is comparable to the "c/a" value for the binary Ti-15at.% Al alloy value (alloy actually containing 150 ppm oxygen) of ~1.594 studied by Clark et.al.[14].

Upon aging the Ti-8.6Al alloys to precipitate α_2 , the "c" lattice parameter still exhibits a positive dependence on oxygen content with aging and a slight "c" parameter increase compared to the solution-treated material. The "a" lattice parameter of the STA / Ti-8.6Al alloys however show decreased "a" values compared to the ST-alloys and a decrease in the aged "a" parameter value between the 500 ppm and the higher oxygen content alloys. The volume fraction of α_2 in the Ti-8.6Al alloys as a function of oxygen content was also estimated from the neutron diffraction data to be: 500ppm alloy contains 11 ± 3 vol.% α_2 , 1000 ppm alloy contains 32 ± 8 vol.% α_2 , and the 2000ppm alloy contains 36 ± 4 vol.% α_2 . These volume fraction values are consistent with our TEM observations showing the overall effect of oxygen content on α_2 formation in this alloy and the similarity between the 1000 and 2000 ppm alloy volume fractions.

To understand the lattice parameter data of the aged Ti-8.6Al alloys as a function of oxygen

content, in particular the "a" lattice parameter, we must consider the literature concerning the precipitation of α_2 in alpha alloys, the α_2 volume fraction data in the Ti-8.6 Al alloys, and the TEM observations. Given the lattice parameters of pure Ti ("a" = 2.9511, "c" = 4.6843) and α_2 ("a" = 5.782, "c" = 4.629) it appears that the promotion of α_2 in Ti-8.6Al with increasing oxygen is consistent with several of the measured changes in the lattice parameter of the α -Ti-8.6Al alloys. In the aged Ti-8.6Al alloys the "c" parameter increases slightly over the ST-condition, independent of oxygen content, which is consistent with the fact that the matrix will see a decreasing aluminum content in the matrix upon precipitation of the α_2 . Based on the potent aluminum lattice parameter effect, the only slight increase in the "c" lattice parameter with aging appears is somewhat surprising considering significant the decrease in the matrix aluminum concentration, particularly in the high oxygen alloys where ~30 wt.% α_2 precipitates[14]. The very slight change in the "c" lattice parameter with aging is however consistent with the fact that the "c" lattice spacing in the α and α_2 are very close, as noted by Clark et.al.[14]. Consideration of the small aluminum effect upon aging must however also be considered if oxygen may directly affect the "c" values. Unfortunately, no data exists to our knowledge concerning the combined effects of aluminum and oxygen on the lattice parameters of titanium. It has been speculated that the large octahedral holes in the α_2 may have a sizable effect on the solubility of interstitials in α_2 [10]. If the α_2 preferentially absorbs oxygen upon precipitation, only slight increases in the "c" parameter may be expected. While decreasing aluminum levels during α_2 precipitation will favor increasing the "c" lattice parameter, decreasing the matrix oxygen content, due to the preferential α_2 uptake, will favor decreasing the "c" values. This interpretation suggests a strong synergistic effect between the oxygen and the aluminum on the titanium lattice parameters.

The decrease in the "a" lattice parameter in Ti-8.6 Al with aging is inconsistent with the arguments applied to the aged "c" values, in particular the effect of aluminum. Aluminum removal from the matrix, with α_2 precipitation, should be expected to result in an increase in the "a" values, based on the Ti-Al lattice data[14], which is directly opposite to that observed. The lattice parameter data of Clark et.al.[14] however noted that the lattice parameter values between 12 and 25 at.% Al exhibited a number of interesting features. In this composition range the lattice parameters, in particular the "a", were no longer independent of aging and quenching temperatures. X-ray diffraction line broadening effects in a Ti-14.8 at.% Al alloy suggest strong evidence for a considerable degree of short-range order in a slow quench prior to definitive identification of the presence of α_2 [14]. Further, the Clark data found a split in the "a" parameter data at aluminum concentrations above ~12 at.% aluminum which was prescribed to differences in the disordered and ordered alloys[14]. The "a" lattice parameter data in the current study on Ti-8.6 Al alloys supports differences in the "a" values between the ST and aged conditions; the magnitude of this change paralleling the volume fraction of α_2 measured and observed in the TEM.

Based on the strong link between α_2 precipitation and the oxygen content [2,6,9,11], the differences in the "a" lattice parameters in the aged Ti-8.6 Al alloys are thought to indicate movement of the oxygen between the titanium lattice and the α_2 and also suggest an enhanced influence of oxygen on the "a" lattice parameter of titanium in Ti-Al alloys. The presence of substitutional aluminum additions to titanium are known to cause a localized distortion of the octahedral sites which destroys the isotropic nature of the available sites for oxygen[15]. This fact may lead to an enhanced affect of oxygen on the lattice spacings in Ti-Al alloys, compared to elemental titanium. Upon aging to precipitate α_2 this condition will be altered and will then place different constraints on the oxygen. Further experiments on lower aluminum content alloys, in which α_2 will not form, are clearly necessary to determine the independent effect of oxygen content on the "a" lattice parameter of Ti. It is interesting to note however that the pronounced effect of oxygen on the precipitation of α_2 strongly suggests that more than a simple uptake of oxygen into the α_2 is occurring. The marked link between oxygen content and α_2 formation in aluminum containing Ti-alloys may in fact suggest either: 1) preferential oxygen clustering near the α_2 to reduce the lattice mismatch jump between the α_2 (a=5.782) and the α (a=2.9511) or 2) direct chemical interaction between the oxygen and the α_2 , perhaps in the form of a Ti_3AlO_x . Since interstitial oxygen is known to expand the titanium lattice 0.13 cubic angstroms per atomic % oxygen, the expansion of the unit cell is significant and therefore a lattice mismatch argument may be a plausible explanation. This interpretation and particularly the chemical interaction postulate poses the question of whether α_2 precipitation would occur at all in a titanium-aluminum alloy with extremely low oxygen content. A thorough investigation of the TiAlO system will be required to decide these questions.

Conclusions

Based on a study of the influence of oxygen content on the lattice parameters of Ti-8.6Al in a solution-treated and aged heat-treatment condition, the following conclusions can be drawn:

- 1) Increasing oxygen content increases the "c" lattice parameters of Ti-8.6Al alloys while not significantly altering the "a" lattice values.
- 2) The lattice parameters of Ti-8.6Al, in particular the "a" values, are different between the ST and aged conditions due to the effects of α_2 precipitation on the matrix aluminum concentration, and the possible relocation of oxygen in the titanium and α_2 lattice.

Acknowledgement

This work was supported under the auspices of the United States Department of Energy. The Manuel Lujan, Jr., Neutron Scattering Center is a national user facility funded by the United States Department of Energy, Office of Basic Energy Science. The authors are indebted to John O'Rourke for conducting the X-ray studies and to R.B. Von Dreele and the late Art Williams for their assistance with the neutron experiments.

References

1. N.E. Paton, J.C. Williams, and G.P. Rauscher, in Titanium Science and Technology, edited by R.I. Jaffee and H.M. Burte (Plenum Press, New York, Vol. 2, 1973), p. 1049-69.
2. J.Y. Lim, C.J. McMahon, Jr., D.P. Pope, and J.C. Williams, Metall. Trans. **7A**, 139 (1976).
3. J.C. Williams, A.W. Sommer, and P.P. Tung: Metall. Trans. **3**, 2979 (1972).
4. M.J. Blackburn and J.C. Williams, Trans. ASM **62**, 398 (1969).
5. H. Conrad, Prog. Mater. Sci. **26**, 123 (1981).
6. D.J. Truax and C.J. McMahon, Jr., Mater. Sci. Eng. **13**, 125 (1974).
7. J.C. Williams and G. Luetjering, in Titanium '80 - Science and Technology, edited by H. Kimura and O. Izumi (AIME, New York, Vol. 1, 1980), p. 672-681.
8. G. Luetjering and S. Weissman, Acta Metall. **18**, 785 (1970).
9. Z. Liu and G. Welsch, Metall. Trans. **19**, 527 (1988).
10. P.C. Gehlen, in The Science, Technology, and Application of Titanium, edited by R.I. Jaffee and N.E. Promisel (Pergamon Press, New York, 1970), p. 349-357.
11. G.T. Gray III, G. Luetjering, and J.C. Williams: "The Influence of Oxygen on the Structure, Fracture, and Fatigue Crack Propagation of Ti-8.6Al", Metall. Trans., in press (1989).
12. A.C. Larson and R.B. Von Dreele, "Generalized Structure Analysis System", Los Alamos National Laboratory, LAUR-86-748 (1986).
13. H.T. Clark, Jr., Trans. AIME **185**, 588 (1949).
14. D. Clark, K.S. Jepson, and G.I. Lewis, J. Inst. Metals **91**, 197 (1962-63).
15. D. Gupta and S. Weing, Acta Metall. **10**, 292(1962).

IN-BEAM SMALL-ANGLE SCATTERING STUDIES OF PHASE SEPARATION
IN NI-TI SINGLE CRYSTALS

ALBERTO CERRI^{*,**}, BERND SCHOENFELD^{*}, GERNOT KOSTORZ^{*} AND ALBERT F. WRIGHT^{***}

^{*} Angewandte Physik, ETH Zürich, CH-8093 Zürich, Switzerland

^{**} now at Festkörperphysik, University of Vienna, A-1090 Wien, Austria

^{***} Institut Laue-Langevin, BP 156X, F-38042 Grenoble-Cedex, France

ABSTRACT

Phase separation of quenched supersaturated Ni-(9.5-12.0)at.% Ti single crystals was followed by small-angle neutron scattering during in-beam aging at 773, 813 and 853 K. With the incident beam along $\langle 110 \rangle$, scattering maxima in $\langle 100 \rangle$ directions were observed from the earliest stages of decomposition. While the results obtained at 773 K may be compatible with the general features of spinodal decomposition, a two-phase model with homogeneous precipitation in a depleted matrix is more appropriate at 813 and 853 K. Though scaling may be shown to hold, the aging kinetics is considerably slower than expected, which is related to a stabilizing effect of elastic coherency stresses.

INTRODUCTION

During the decomposition of supersaturated alloys obtained by quenching from a homogeneous equilibrium state at some higher temperature, metastable states may be reached before a finally stable state, depending on the kinetics of competing processes. In nickel-rich supersaturated Ni-Ti alloys aged at intermediate temperatures, the metastable, coherent σ' -phase (L1 structure) appears first, while the final decomposition product is the incoherent hexagonal η -phase (DO₂₄ structure) [1].

The formation of σ' is accompanied by order, and conflicting observations have been reported on the sequence of ordering and decomposition (see [2] for a summary). A combination of wide-angle and small-angle scattering techniques using the same samples, shows that both, ordering and local compositional changes occur from the beginning of the aging treatment [2]. Details of the mechanisms involved and of the influence of supersaturation/undercooling, quench-rate, lattice strains etc., however, remain to be investigated. During later stages of σ' -precipitation, coherency strains are known to influence the morphology and spatial correlations of the precipitates, as shown, e.g., by Ardell [3] using transmission electron microscopy. Precipitates exceeding a size of ~ 6 nm are cuboidally shaped and align preferentially along $\langle 100 \rangle$.

Small-angle neutron scattering (SANS) is a very sensitive tool for the study of small-scale inhomogeneities (see, e.g. [4]). As the SANS intensity depends on the square of the difference in scattering lengths b_i of the two components of a decomposing binary alloy, Ni-Ti is ideally suited, because $b_{Ni} = 10.3$ fm and $b_{Ti} = -3.30$ fm [5] provide for a large scattering contrast. Thus, earlier stages of decomposition may be studied, and, within a reasonable concentration and temperature range, in-beam decomposition studies become possible. In the following, SANS results on several crystals decomposing in-beam are presented and interpreted.

SAMPLES

Starting from 4-9 Ni and 3-9 Ti, an alloy was prepared by induction-melting Ni in high vacuum and adding Ti. Cylindrical rods of Ni-12 at.% Ti were then cast in a nickel-plated copper mould. Single crystals about 6 cm long and 10 mm in diameter were grown from these rods by the Bridgman technique in a soft MgO crucible. The Ti concentration was determined from

chemical and x-ray fluorescence analyses and was found to be between 9.5 and 12.0 at.% in or near the sections of the crystals used for experiments, with gradients of ~ 0.5 at.%/cm along the rod axis. Samples for SANS were slices about 2.5 mm thick, cut by spark erosion, with $\{110\}$ faces. After solution treatment at 1373 K in purified Ar, the samples were quenched in water. SANS was used to check the homogeneity of the sample and those displaying no measurable sign of decomposition were selected for further study.

SANS MEASUREMENTS AND EVALUATION

Quenched single crystals were mounted in a vacuum furnace designed to fit the D11 instrument at the ILL Grenoble. In-beam decomposition was studied for about 20 h at 773 K and 813 K and for 10 h at 853 K. The incident neutron wavelengths λ were 0.6 and 0.66 nm, selected with a helical-slit selector with $\Delta\lambda/\lambda \approx 10\%$. Multiple Bragg scattering was thus avoided. The distance from sample to detector was 1.7 m, corresponding to a maximum observable modulus of the scattering vector Q of $Q (= 4\pi\sin\theta/\lambda$ with $\theta =$ half the scattering angle) $\approx 2 \text{ nm}^{-1}$.

The measuring temperatures were reached within 10 min starting from room temperature and were kept constant during the SANS measurements. The scattering patterns with the two-dimensional position-sensitive detectors (64 cm x 64 cm, pixel size 1 cm^2) were stored initially for intervals of 2 min and progressively longer intervals later. As soon as a SANS signal exceeding the flat incoherent scattering became visible (after a few minutes), a strong dependence of this coherent scattering intensity on the direction of Q was also evident (see Fig.1 for an early stage).

Measured intensities were corrected for background, and absolute macroscopic differential scattering cross-sections were calculated using the incoherent scattering of a vanadium single crystal for calibration. "Anisotropic" cross-sections along $\langle 100 \rangle$ and $\langle 110 \rangle$ were obtained by averaging intensities per detector element for given Q intervals ($\Delta Q \approx 0.05 \text{ nm}^{-1}$) over sectors including cells within $\pm 15^\circ$ around these directions. An "isotropic" average for rings of constant Q was also determined. Fig.2 shows the results for an experiment at 813 K. For comparison with some current theories on the evolution of decomposing systems, and for the integrated SANS intensity, average scattering curves for all crystal orientations are appropriate. Detailed analysis (see [6]) and experimental tests (sample rotation) show that the "isotropic" average in the $\{110\}$ plane deviates only little (a few percent) from a hypothetical polycrystalline average. An important quantity in the two-phase model is the integrated SANS intensity \bar{Q} given by

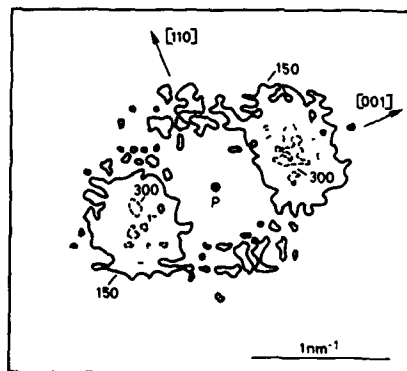


Figure 1. Scattering pattern of a Ni-10 at.% Ti single crystal aged at 813 K for 15 min. Lines of equal intensity show pronounced peaks in $\langle 100 \rangle$ direction.

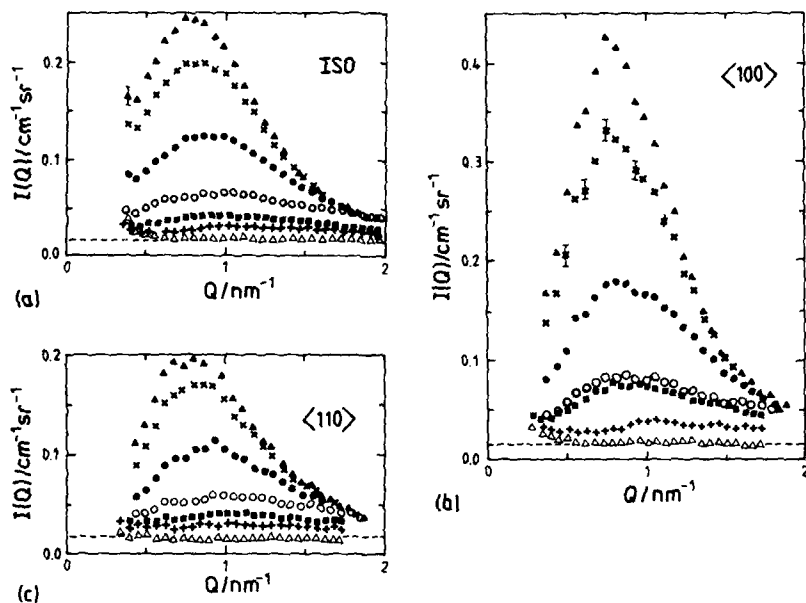


Figure 2. Coherent SANS cross-sections for a Ni-10.5 at.% Ti single crystal aged at 813 K.
 (a) "isotropic" average, (b) $\langle 100 \rangle$, (c) $\langle 110 \rangle$.
 Δ : as quenched, +: 2.6 min, •: 43 min, ○: 108 min,
 \circ : 377 min, ×: 750 min, \blacktriangle : 986 min at 813 K.
 Broken lines indicate the calculated Laue scattering for a Ni-10.5 at.% Ti solid solution.

$$\bar{Q} = \int I(Q) dQ \quad (1)$$

where the integration includes the whole reciprocal space. The orientationally averaged data were used to test the validity of the Porod law

$$I(Q) = A Q^{-4} + B \quad (2)$$

with A, B constants, which holds for large enough values of Q ($QR \geq 2.5$, where R is the radius of the scattering object). Fig. 3 shows a Porod plot (IQ^4 vs. Q^4) for the aging of Ni-10.5 at.% Ti at 813 K (cf. Fig. 2). The Porod law is well followed within the accessible Q range after six hours. After the constant A has been determined (eq. 2), \bar{Q} may be fully calculated.

A reduced scattering (= "structure") function $S(Q, t)$ may be obtained by dividing the orientationally averaged curves $I(Q)$ by the integrated intensity. This function is analyzed for scaling which is said to hold if

$$S(Q, t) = L^3(t) F(x) \quad (3)$$

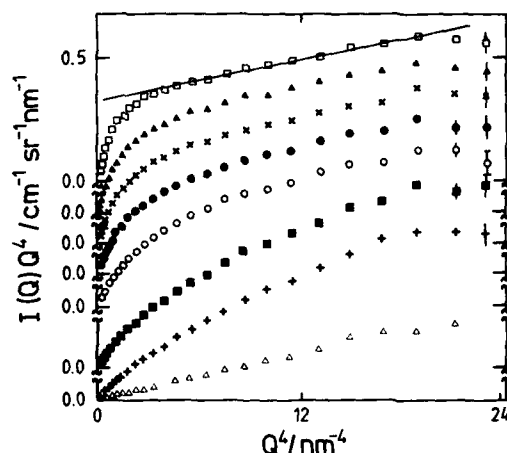


Figure 3. Porod plots for Ni-10.5 at.% Ti aging at 813 K.

Δ: as quenched,
 +: 118 min, ■: 212 min,
 ○: 360 min, ●: 513 min,
 ×: 648 min, ▲: 750 min,
 □: 986 min.

with a time-independent "scaling function" $F(x)$, $x = QL(t)$, and a time-dependent characteristic length scale of the system, $L(t)$. For $L(t)$, the reciprocal of the first moment of $S(Q,t)$, given by $M_1 = \int QS(Q,t)dQ / \int S(Q,t)dQ$, may be used, but the reciprocal of the position of the scattering maximum, Q_M , or the radius of gyration, R_G , obtained from Guinier's law, $\ln(I/I_0) = -R_G^2 Q^2 / 3$ are also used (see, e.g., [7], [8] for reviews). In this study, all three possibilities have been used and compared.

RESULTS AND DISCUSSION

The most striking feature of the scattering is its anisotropy (cf. Fig. 2) which would, of course, not be visible for polycrystalline samples. A preferred alignment of decomposition products along $\langle 100 \rangle$ is expected if elastic coherency stresses intervene [9]. The SANS maxima are most pronounced along $\langle 100 \rangle$, but the Q value of the maximum intensity is (within the experimental resolution and with some deviation at 773 K) independent of orientation, facilitating the "isotropic" averaging. Fig. 4 shows the averaged maximum intensity I_M as a function of aging time for the three different temperatures. It is obvious that no simple power law $I_M \propto t^a$ is followed, but may be approached at 813 and 853 K. The asymptotic exponent is 0.55–0.6, but not equal to one, as expected for Ostwald ripening. The time dependence of the position of the maximum, Q_M , may also be tested for a power law, $Q_M \propto t^{-a'}$. The peak position does not change with time at 773 K during about 20 h. At 813 K, a' is very small (0.08 ± 0.05), while at 853 K, $a' = 0.23 \pm 0.04$ is found. Scaling was tested for all aging sequences, using the three differently defined characteristic lengths (Fig. 5). The scattering curves coincide best if M_1^{-1} is used as scaling length. While the deviations for R_G may be attributed to the very approximate character of this quantity (as size and distance distributions interfere in the scattering range where R_G is determined), the lack of correspondence between Q_M^{-1} and M_1^{-1} indicates that some caution is necessary before any type of "universality" may be evoked. Nevertheless, $F(x)$ is very similar at 853 K, whereas at 773 K, its shape is clearly different, indicating another mechanism.

An analysis of the SANS results at 773 K follows the general trends of the non-linear spinodal theory of Langer et al. [10]. For aging at 813 K and 853 K, the integrated intensity tends to reach a plateau after several hours (Fig. 6). Although the absolute errors are large (involving uncertainties from

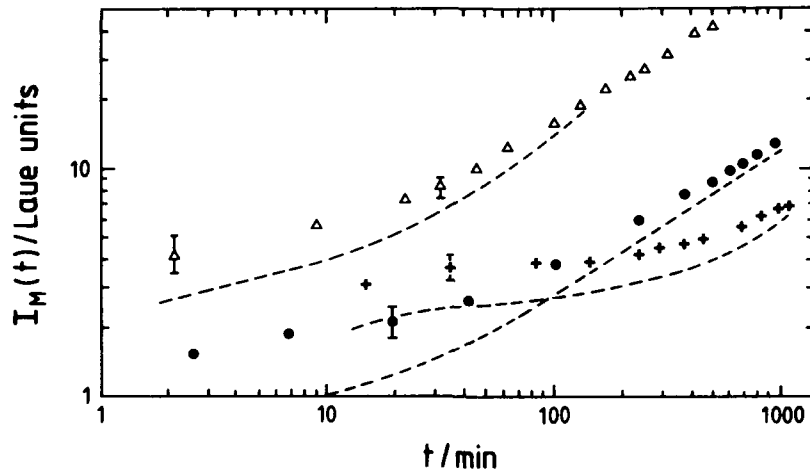


Figure 4. Maximum intensity I_M as a function of aging time. Broken lines are obtained after subtraction of the constant B (cf. eq.2).
 \triangle : 11.5 at.% Ti/773 K, \bullet : 10.5 at.% Ti/813 K,
 \times : 11.5 at.% Ti/853 K.

calibration and extrapolation), at least the behavior at 853 K suggests that the coarsening regime is reached and that the matrix is fully depleted for this (metastable) precipitation process. Recent theoretical studies [11,12] indicate that strong coherency stresses due to the lattice mismatch between matrix and particle ($> 0.1\%$ per % Ti) may reduce the exponents a and a' , as was found here. If the two-phase model is used, \bar{Q} may be written as

$$\bar{Q} = (2\pi)^3 f_V (1-f_V) (\Delta\rho)^2 \quad (4)$$

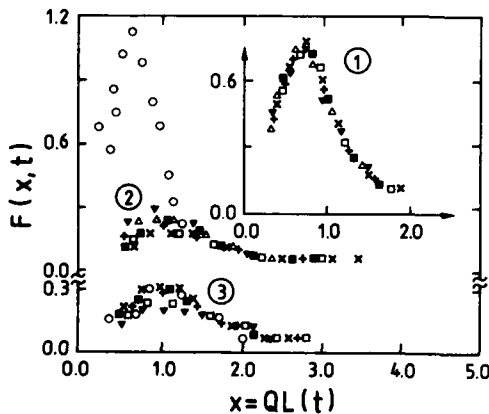


Figure 5. Scaled structure function $F(x,t)$ for Ni-10.5 at.% Ti aging at 813 K.
 \circ : 43 min, ∇ : 276 min,
 \triangle : 360 min, $+$: 513 min,
 \blacksquare : 648 min, \square : 750 min,
 \times : 986 min.

① M_1^{-1} , ② R_G , ③ Q_M^{-1} .

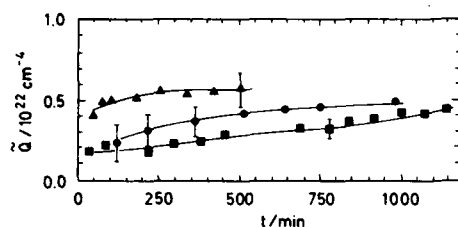


Figure 6. Integrated intensity Q as a function of aging time.
 ■: Ni-11.5 at.% Ti/773 K
 ●: Ni-10.5 at.% Ti/813 K
 ▲: Ni-11.5 at.% Ti/853 K

where $\Delta\rho$ is the difference in scattering length density between particle and matrix and f is the volume fraction of precipitates. Using $c_m = 8.6$ at.% Ti for the matrix at 853 K [13], one obtains $c_p = (16 \pm 3)$ at.% Ti^m for the precipitates. This value is much lower than expected for the ordered σ' -phase (25%), which may again be caused by coherency stresses [14]. The possibility of a transitional ordered phase has already been proposed by Ben Israel and Fine [15] and others [16,17], but opposing views have also been advanced (see, e.g., a recent atom-probe field-ion microscopy study on Ni-12 at.% Ti aged at 823 K [18]). More elaborate small- and large-angle scattering experiments on single crystals, combined with high-resolution electron microscopy, are planned to further investigate this point.

ACKNOWLEDGEMENTS

The authors are grateful to R. Baker, R.E. Ghosh, R. May, C. Rey at the Institut Laue-Langevin for valuable help during the SANS measurements and data processing, and to Ms. R. Bänninger and E. Fischer for experimental assistance.

REFERENCES

1. T.B. Massalski, Binary Alloy Phase Diagrams (ASM, Metals Park, Ohio, 1986).
2. A. Cerri, G. Kostorz, R. Schmelzger, B. Schönfeld, and P. Schwander, in Phase Transformations '87, edited by G.W. Lorimer (The Institute of Metals, London, 1988), p. 592.
3. A.J. Ardell, Metall. Trans. **1**, 525 (1970).
4. G. Kostorz, in Physical Metallurgy, 3rd ed., edited by R.W. Cahn and P. Haasen (North-Holland, Amsterdam, 1983), p. 793.
5. V.F. Sears, Thermal-Neutron Scattering Lengths and Cross-Sections for Condensed-Matter Research (Atomic En. of Canada, Chalk River, 1984).
6. A. Cerri, Dr.sci.nat. Dissertation, ETH Zürich (1988).
7. J.D. Gunton, M. San Miguel and P.S. Sahni, in Phase Transitions, Vol.8, ed. by C. Domb and J.L. Lebowitz (Academic Press, London, 1983), p.290.
8. H. Furukawa, Adv. Phys. **34**, 703 (1985).
9. F.C. Larché and J.W. Cahn, Acta Metall. **33**, 331 (1985).
10. J.S. Langer, M. Bar-on, and H.D. Miller, Phys. Rev. A **11**, 1417 (1975).
11. J. Gayda and D.J. Srolovitz, Acta Metall. **37**, 641 (1989).
12. W.C. Johnson, P.W. Voorhees, and D.E. Zupon, Metall. Trans. A **20**, 1175 (1989).
13. P.K. Rastogi and A.J. Ardell, Acta Metall. **17**, 595 (1969).
14. W.C. Johnson and P.W. Voorhees, Metall. Trans. A **18**, 1213 (1987).
15. D.H. Ben Israel and M.E. Fine, Acta Metall. **11**, 1051 (1963).
16. K. Hashimoto and T. Tsujimoto, Trans. Jap. Inst. Metals **19**, 77 (1978).
17. H. Yoshida, M. Arita, A. Cerri, and G. Kostorz, Acta Metall. **34**, 1401 (1986).
18. R. Grüne, Acta Metall. **36**, 2797 (1988).

SANS MEASUREMENT OF DEUTERIUM-DISLOCATION CORRELATION IN PALLADIUM

BRENT J. HEUSER, G.C. SUMMERFIELD, J.S. KING, and J.E. EPPERSON*

University of Michigan, Ann Arbor, MI
*Argonne National Laboratory, Argonne, IL.**ABSTRACT**

Small angle neutron scattering (SANS) measurements have been made on deformed polycrystal palladium samples with and without deuterium dissolved in the solution phase (α) at room temperature. Concentrations were held constant during SANS experiments by an equilibrium gas pressure cell. The difference scattering cross section for the same sample with and without deuterium loading has a $1/Q$ behavior ($Q=4\pi/\lambda \sin\theta/2$) at intermediate values of Q . At very low values of Q the dependence is much stronger than $1/Q$. The $1/Q$ behavior is attributed to deuterium trapping close to long dislocation cores forming rod-like scattering structures.

Introduction

Small angle neutron scattering (SANS) from edge dislocations in deformed metals has been the subject of several studies since the early work of Atkinson and Hirsch¹ in 1958. Their model cross section varies as Q^{-3} (where $Q=4\pi/\lambda \sin\theta/2$ and θ is the scattering angle) and this has apparently been confirmed by several authors²⁻⁵ for Cu and Al, both single and polycrystal. A natural extension is to look for the spatial correlation between deuterium impurities and these dislocations. Success depends on detecting the weak cross sections expected. We report here an attempt to observe this correlation in deformed Pd polycrystals.

Hydrogen can be diffused into metal hosts easily if the enthalpy of solution is negative. Particular attention has been given to Pd because hydrogen can be readily accepted in dilute solution near room temperature without significant dislocation recovery. It has been shown by Flanagan and coworkers,⁶⁻⁸ and by Kirchheim,⁹ that the hydrogen solubility of an undeformed sample of Pd follows the equilibrium law of Sievert,¹⁰ but after deformation the same sample shows an enhanced solubility depending on the degree of cold work. There is apparent agreement that this enhancement is due to the attraction to induced dislocations and not to other possible defects, including grain boundaries.⁷ The solubility enhancement factor is typically 1.25 to 1.50 for dilute solutions. Hence, for a SANS experiment with deuterium loaded Pd samples, we expect a Pd lattice in which 20% to 33% of the deuterium atoms are correlated with dislocations and 80% to 67% are distributed at random octahedral sites in the bulk of the lattice. Only the correlated fraction would be visible in a coherent scattering experiment.

Experimental

We have prepared and examined many polycrystal Pd wafers for solubility. As-grown 99.95% pure ingots¹¹ are cut into wafers, cold rolled to 60% cw, then annealed in flowing argon at 1000°C

for 10 hours. This produces dislocation free wafers with a reasonably controlled grain size of about 100μ . Separate wafers are then deformed by one of two methods: cross rolled at room temperature to approximately 70% cw (samples cw 1 and cw 2); or given a hydride-dehydride cycle in a vacuum/gas manifold (samples $(\alpha/\beta/\alpha)_1$ and $(\alpha/\beta/\alpha)_2$). The $(\alpha/\beta/\alpha)$ samples are subjected to total deuterium pressures of 200-300 torr over a period of 48-72 hours at room temperature. This procedure results in complete hydriding of the samples ($H/Pd=0.6$). The deuterium is removed by heating to 100°C in vacuum for 12 hours. The measured deuterium solubility enhancement factor for a typical $(\alpha/\beta/\alpha)$ sample is 1.50, in agreement with Lynch *et al.*⁸, and is attributed to dislocations created in the hydride-dehydride cycle. Both cw and $(\alpha/\beta/\alpha)$ samples are then cut into sample discs 1.0 cm in diameter x 0.135 cm thick. After surface polishing and cleaning, a stack of three wafers are reintroduced to the manifold, and heated to 180°C for 1 hour in a vacuum of 10^{-6} torr. After cooling down to room temperature the manifold is isolated from the pumps and deuterium gas, at a pressure of approximately 17 torr, is introduced into the manifold. The dissolved deuterium atom density is monitored by the pressure fall-off of an absolute capacitance manometer pressure gauge. Typical bulk deuterium densities are 5500 ppm.

When equilibrium is reached, the wafer stack is quickly transferred to an evacuated gas cell, backfilled with the equilibrium deuterium pressure and one atmosphere of nitrogen. The gas cell is valved off and transferred to the SANS spectrometer sample stage. The cell windows are single crystal silicon 0.32 cm thick and the empty cell showed a transmission greater than 98% at 5.0\AA . SANS measurements were made on the small angle diffractometer (SAD) at the Argonne National Laboratory time of flight source, IPNS. Because of strong multiple Bragg scattering only data from wavelengths greater than 4.5\AA could be used. Deformed sample runs took approximately 10 hours. When finished, the wafer stack is reinserted in the vacuum manifold, brought to a temperature of 140°C and pumped free of deuterium for 1-2 hours. The stack is then reinserted in the gas cell and a second 10 hour SANS run made. Additional runs are made to obtain sample transmission, empty gas cell background, dark current background, and an absolute calibration from a standard polystyrene wafer. Finally, an undeformed Pd polycrystal was also measured. The net macroscopic scattering cross section is defined here as the difference in scattered intensities for the same deformed sample, with and without deuterium loading. This difference removes unwanted contributions such as incoherent scattering and scattering events not produced by the presence of the deuterium.

Results and Discussion

Figure 1 gives the macroscopic scattering per steradian from the $(\alpha/\beta/\alpha)_1$ sample, with and without deuterium, plotted on a $\ln\text{-}\ln$ scale to include the full Q span measured, which ranged from 0.006\AA^{-1} to 0.090\AA^{-1} . Its thickness was 0.356 cm, which, for 5.0\AA neutrons, gave a transmission of 0.653 with deuterium loading and 0.660 without deuterium loading (the difference is well within statistical uncertainty and not considered significant). The difference scattering for this $(\alpha/\beta/\alpha)$ sample is replotted in Figure 2, together with a linear least square slope fit. As can

be seen, the statistics from point to point are only fair, and the net difference becomes difficult to define at lowest Q . We defer comment on this Q region until later. What is clear is a trend at higher Q : The intensity varies as Q^{-1} .

Figure 3 shows the equivalent difference scattering result for the cw 1 sample. The degree of cold-work was 70%, and the stack thickness and transmissions are similar to the $(\alpha/\beta/\alpha)$ values. The solubility enhancement factor was 1.24. The statistics are marginal, making the high Q region slope fit less certain. The poorer statistics here are due to the lower enhancement factor, as we will see below. Nevertheless, the difference scattering shows the same Q^{-1} intensity variation as that for the $(\alpha/\beta/\alpha)$ sample. Note that in all figures the macroscopic differential scattering cross section is given in absolute units.

Based on the Q^{-1} scattering behavior in both Figures 2 and 3, we are observing the Fourier transform peculiar to a random, non-interacting array of rod-like scattering structures. If we further assume these rods are lines of deuterium atoms lying close to the cores of dislocations, the macroscopic cross section for such a system can be calculated. It is given by the simple relation

$$\frac{d\Sigma}{d\Omega} = \frac{\pi b^2 N_D^2}{Q \rho_d} \quad (1)$$

where N_D is the density for the total enhanced fraction of the dissolved deuterium, ρ_d is the volume average dislocation density, in cm/cm^3 , and b is the bound atom coherent neutron scattering length for the deuteron. The cross section is a strong function of N_D . Using the measured cross sections from Figures 2 and 3, the measured enhanced fraction of deuterons dissolved, and known b , we can determine the dislocation density ρ_d . We can also determine the number of deuterons, per Pd atom, trapped near a dislocation core by assuming a core radius. The ratio of trapped deuterons per Pd atom we call N_D/N_{Pd} . Values are given in Table I for the $(\alpha/\beta/\alpha)$ and cw samples. These are evaluated at a Q value of 0.03\AA^{-1} , and for a core radius of two Burgers vectors. b is $0.667 \cdot 10^{-12}$ cm, and the Burgers vector length, B , is 2.75\AA .

TABLE I
Dislocation Densities and Core-Trapped
Deuterium Densities from Equation (1)

sample ID	$d\Sigma/d\Omega$ (cm^{-1})	N_D (cm^{-3})	ρ_d ($\cdot 10^{11}$ cm/cm^3)	N_D/N_{Pd} ($2B$)
$(\alpha/\beta/\alpha)1$	0.0244	$1.86 \cdot 10^{20}$	6.6 ± 0.7	0.4
$(\alpha/\beta/\alpha)2$	0.0138	$1.13 \cdot 10^{20}$	4.3 ± 0.7	0.4
cw 1	0.0103	$0.93 \cdot 10^{20}$	3.9 ± 0.9	0.4
cw 2	0.0064	$1.07 \cdot 10^{20}$	8.3 ± 2.7	0.2

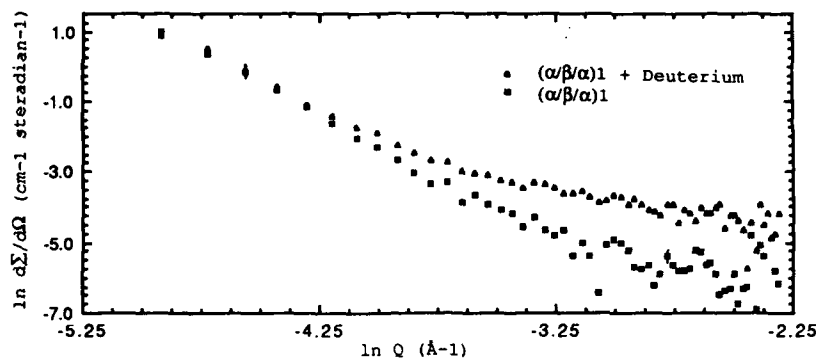


Figure 1. $\ln d\Sigma/d\Omega$ vs. $\ln Q$ for $(\alpha/\beta/\alpha)1$ sample with and without deuterium loading.

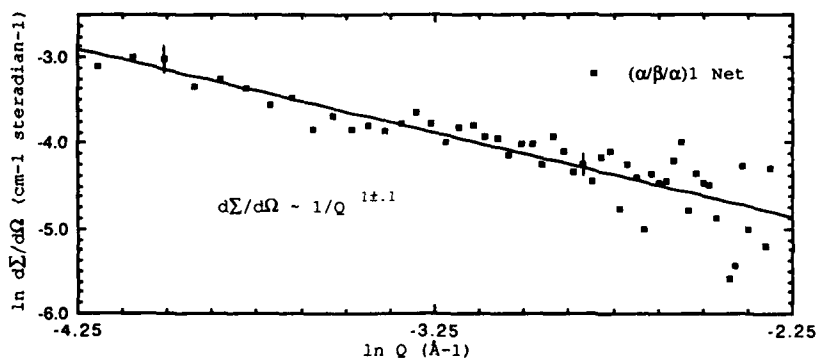


Figure 2. Net $\ln d\Sigma/d\Omega$ vs. $\ln Q$ for $(\alpha/\beta/\alpha)1$ sample.

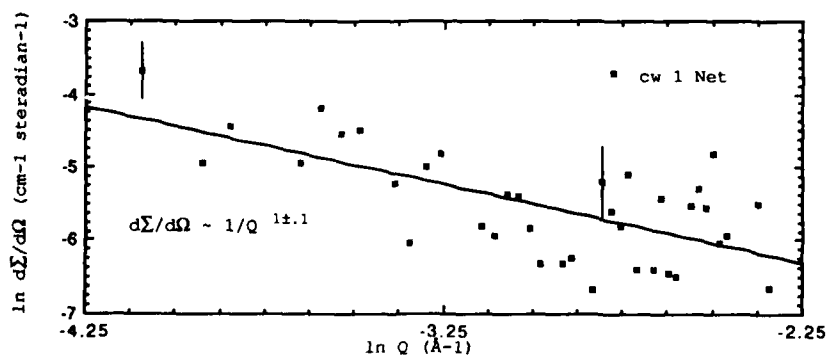


Figure 3. Net $\ln d\Sigma/d\Omega$ vs. $\ln Q$ for cw 1 sample.

The limits of large Q over which we can evaluate equation (1) are 0.015\AA^{-1} to 0.08\AA^{-1} . It is of some interest that within experimental error ρ_d is the same for both sample types although the scattering cross sections differ by almost a factor of 4, and the dislocation networks are quite different. Preliminary TEM investigations show a high degree of dislocation cellularization in the cw samples, but an approximately uniform spacing of dislocations in the $(\alpha/\beta/\alpha)$ samples. The trapped deuterium densities seem to be independent of this variation in dislocation cell structure.

These values for ρ_d , where the errors are derived from the uncertainty of a best-fit line slope, are very reasonable. The $(\alpha/\beta/\alpha)$ samples deserve special attention. During the preparation of $(\alpha/\beta/\alpha)_2$ only 66% of the bulk was converted to hydride and back again. Since dislocations are created in the $(\alpha/\beta/\alpha)$ samples as the phase boundary propagates through the lattice, we expect the dislocation density in $(\alpha/\beta/\alpha)_2$ to be roughly 66% of $(\alpha/\beta/\alpha)_1$, which was completely cycled. Table I shows this is the case. These dislocation densities may be compared to the volume average magnitude $5.0 \cdot 10^{11}$ cm/cm³ estimated by Lynch⁸ and $2.0 \cdot 10^{12}$ cm/cm³ postulated by Wise¹² for hydrided-dehydrided Pd polycrystals. It must be emphasized that Q^{-1} scattering behavior is peculiar to line or thin rod composition fluctuations; it cannot be invoked for surface or grain boundary layers, vacancy clusters, voids, etc. Finally, it is to be noted that the average Pd density discontinuity itself at the dislocation core is small enough to be an insignificant contribution.

Net scattering was also observed at low Q , between 0.006\AA^{-1} and 0.015\AA^{-1} , with a Q dependence of Q^{-3} to Q^{-4} . The statistical uncertainties are too large to justify any interpretation of these results. If a significant fraction of the deuterium is distributed according to the long range stress field of edge dislocations we would expect to see the scattering cross section vary as Q^{-3} at low Q .

An observation, repeated numerous times for both single crystal and polycrystal Pd (without deuterium loading), is the low Q intensity from undeformed samples is actually larger than the intensity from the deformed samples. That is, dislocation scattering alone has not yet been observed by us for Pd, as it has been for Cu single crystal as well as polycrystal samples by others^{2,3}. As yet we do not have a definitive explanation.

Conclusions

1.) Both target types show a net Q^{-1} dependence over a large Q range, which can only be attributed to the trapping of deuterium in a rod-like structure close to long dislocation core lines. The data are only sufficient to place an upper bound of 30-40Å on the radial dimension of these rods, although the deuterium may be trapped much tighter to the dislocation cores.

2.) Our assumption that all of the enhanced fraction of dissolved deuterium is trapped in this rod geometry gives dislocation densities from equation (1) of very realistic magnitudes. If instead a significant fraction is distributed

according to the long range stress field underlying Atkinson's Q^{-3} cross section, ρ_d from equation (1) will drop.

3.) A net deuterium scattering contribution is observed in the lowest Q regime that could fulfill a Q^{-3} law, but the present data are not adequate to quantify this component. A Q^{-3} component could be evidence of Cottrell cloud type deuterium correlations. A distance scale of 100Å, found by Guinier analysis of SANS data from deuterium-loaded deformed Pd, has been reported by Kirchheim *et al*¹³.

4.) Dislocation scattering alone has not been observed by us in Pd single crystals or polycrystals. Both deformed and undeformed samples show a suspiciously similar Q dependence, and this data is not of pure Q^{-3} slope.

"Work supported by the U.S. Department of Energy, BES-Materials Sciences, under contract W-31-109-ENG-38."

References

1. H.H. Atkinson and P.B. Hirsch, *Phil. Mag.* **3**, 213 (1958).
2. J.E. Epperson, G. Kostorz, C. Ortiz, P. Fürnrohr, and K.W. Gerstenberg, *Acta Metall.* **27**, 1363 (1979).
3. J. Christ, *Phys. Stat. Sol.* **7**, 557 (1964).
4. W. Schmatz, T. Springer, J. Schelten, and K. Ibel, *J. Appl. Cryst.* **7**, 96, (1976).
5. E. Taglauer, *Phys. Stat. Sol.* **29**, 259 (1968).
6. T.B. Flanagan, J.F. Lynch, J.D. Clewley, and B. von Turkovich, *Scripta Metall.* **9**, 1063 (1975).
7. T.B. Flanagan and S. Kishimoto, Electronic Structure and Properties of Hydrogen in Metals, edited by P. Jena and L.B. Satterthwaite (NATO Conference Series. VI, Materials Science; V. 6, Richmond, Va 1982), p. 623.
8. J.F. Lynch, J.D. Clewley, T. Curran, and T.B. Flanagan, *J. Less-Common Metals* **55**, 153 (1977).
9. R. Kirchheim, *Acta Metall.* **29**, 835 (1981); **29**, 845 (1981).
10. E. Fromme and H. Jehn, Solubility of Hydrogen in the Elements, *Bulletin of Alloy Phase Diagrams* **5** (3), 324 (1984).
11. *Materials by Metron*, Allamuchy, NJ.
12. M.L.H. Wise, J.P.G. Farr, I.R. Harris, and J.R. Hirst, (*L'Hydrogène Dans les Métaux*, Tome 1, Editions Sciences et Industrie, Paris 1972).
13. R. Kirchheim, X.Y. Huang, H.-D. Carstanjen, and J.J. Rush, Chemistry and Physics of Fracture, (NATO ASI Series, Series E, No. 130, Fed. Rep. Ger. 1987), p. 580.

PART VI

**Residual Stress and
Analytical Techniques**

RESIDUAL STRESS ANALYSIS WITH NEUTRONS

Aaron D. Krawitz, Dept. of Mechanical and Aerospace Engineering, University of Missouri, Columbia, MO 65211

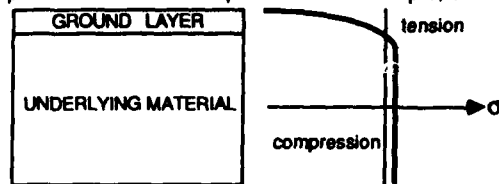
ABSTRACT

The use of neutrons for the measurement of stress is complementary to and extends traditional x-ray diffraction methods to new types of problems. This is due to the lower absorption of neutrons compared to x-rays by most engineering materials, which increases the sampling depth from microns to millimeters. It is particularly suitable for triaxial macrostress gradients through the depth of engineering components and volumetric microstresses in composites. In addition, applied stress studies may also be performed. This paper briefly describes the nature of residual stresses, the use of diffraction for stress measurements, experimental aspects of the use of neutrons, and illustrative applications.

INTRODUCTION

Residual stresses in solids are stresses present in the absence of an external force. Such stresses are common and originate from three basic physical sources, all of which are differential in character: plastic flow, thermal contraction, and volume change. Differential plastic flow occurs in the near-surface region due to the machining of a part. Differential thermal contraction arises during the non-uniform cooling of a large part, in the heat-affected zone of a weldment, and between two phases with different thermal expansion coefficients cooled from an elevated temperature. Differential volume change is a common result of solid state precipitation. Residual stress states are subject to an internal force balance over the volume of the part.

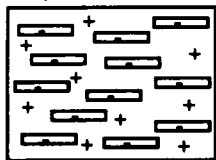
Residual stress states are of two types: macro- and microstress [1]. Macro stresses are long-range relative to the scale of the microstructure, i.e. they are on the scale of the sample. Common sources are machining, heat treatment, and welds. Macro stresses are the most commonly studied as they can affect the service performance of a component. For example, a machined or ground surface is often



placed in compression due to the frictional drag of the operation. A thin surface layer is plastically extended, then thrown into compression by the undeformed material beneath. Thus a stress gradient is created through the depth which is strongly

compressive in the near-surface region and is counter-balanced by a weak tensile stress below, as indicated in the insert. Such a stress state can dramatically prolong the fatigue life of a part in service. Fatigue, the application of cyclic stress or load, usually leads to failure through the growth of surface flaws under the action of repeated tensile stress. If a compressive residual stress is present at the surface, it acts to vectorially reduce the applied stress, creating a net stress of lower magnitude. Indeed, critical regions of parts subject to fatigue loading are deliberately treated to create compressive residual stresses.

Residual microstresses are short-range relative to the scale of the sample, i.e. are on the scale of the microstructure. They tend to occur in multiphase alloys and composites due to differences in thermal expansion coefficients between phases.



For example, an aluminum alloy matrix composite containing SiC fibers for reinforcement is produced at elevated temperature and cooled. The Al alloy matrix has a much greater coefficient of thermal expansion and thus shrinks more relative to the refractory SiC phase. This results in compressive stresses in the SiC fibers and tensile stresses in the Al alloy matrix, as indicated in the insert. Another possible source of microstresses is plastic anisotropy. Cold-

worked zirconium alloys are hexagonal close-packed and are therefore plastically anisotropic. Some grains will readily yield while others do not, creating a range of tensile and compressive stresses that vary from grain to grain. Microstress states are inherently volumetric in nature.

The principal virtue of neutrons for stress measurements is their greater penetration relative to x-rays in most engineering materials [2]. This may be seen through a comparison of values of the depth below the surface from which 50% of the diffracted beam originates for neutrons vs. x-rays [3]; see Table I. It is clear that neutrons penetrate on the order of millimeters compared to microns for x-rays.

Table I. Linear absorption coefficients (μ) and depths from which 50% of the diffracted beam originates ($G_{50\%}$) for 1.3 Å neutrons and Cu K_{α} x-rays at a diffraction angle $2\theta = 90^\circ$.

Elements	Neutrons		X-Rays	
	μ (cm^{-1})	$G_{50\%}$ (mm)	μ (cm^{-1})	$G_{50\%}$ (μm)
Al	0.10	24.5	131	19
Ti	0.45	5.4	938	2.6
Fe	1.12	2.2	2424	1.0
Ni	1.86	1.3	407	6.0
W	1.05	2.3	3311	0.74

Diffraction is the principal non-destructive means of measuring residual stresses. The basis of the use of diffraction for the measurement of residual or applied stress may be illustrated in the following example. Suppose a steel sample is subjected to a tensile stress $\sigma = 200$ MPa. The resultant parallel elastic strain is given by Hooke's law, $\epsilon_{\text{para}} = \sigma/E$, and the transverse elastic strain by $\epsilon_{\text{trans}} = -\nu\sigma/E$, where E is Young's modulus and ν is Poisson's ratio. For steel, $E = 200$ GPa and $\nu = 0.28$. Thus, $\epsilon_{\text{para}} = 0.001$ and $\epsilon_{\text{trans}} = -0.00028$. The position of a diffraction peak at 2θ will shift with a change in d-spacing according to $\Delta(2\theta) = -2(\Delta d/d)\tan\theta$, which is obtained by differentiating Bragg's law. If a peak is at 90° 2θ in the unstressed steel, it will shift by -0.115° 2θ if the diffraction vector, Q , is parallel to the tensile axis and by $+0.0321^\circ$ 2θ if it is normal to it, i.e. parallel to the transverse direction. The geometry is shown in Fig. 1.

Two main ideas are involved. First, if a residual stress (strain) is present in a sample, the interplanar spacings are altered relative to the unstressed state, causing shifts in the position of diffraction peaks. Second, a given stress state is resolved

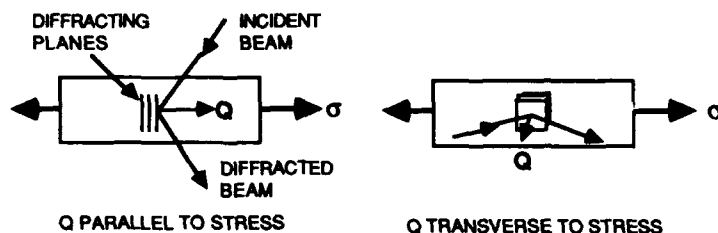


Figure 1 Diffraction measurement of parallel and transverse strain in uniaxially loaded tensile sample.

differently in different physical directions in the sample so that the peak position generally changes with sample orientation. Because engineering materials are polycrystalline, there will be grains oriented to diffract in any sample orientation for a given peak. Residual stress states are measured by systematically changing the sample orientation, observing the shifts in peak position, then converting the shifts first to strains, then to stresses, using elasticity theory.

These ideas lead to a number of problems and studies particularly appropriate for neutron methods: 1) The measurement of macrostress gradients in components [4-12]. 2) The measurement of microstresses in composites and multiphase alloys [13-17]. 3) The study of microstrain/stress distributions due to particle shape effects [15,18]. 4) The study of applied stress problems, such as anisotropic diffraction elastic constants and differential yield [19-21].

In the next section, a general description of the analytical treatment of triaxial stress states is presented. This is followed by a discussion of experimental aspects for the use of neutrons. Finally, some examples of the technique are presented.

ANALYTICAL

The following treatment is based on ref. 1. The general elastic strain state at a point is given by:

$$\epsilon = l^2\epsilon_{11} + m^2\epsilon_{22} + n^2\epsilon_{33} + 2lm\epsilon_{12} + 2mn\epsilon_{23} + 2nl\epsilon_{31} \quad (1)$$

where ϵ_{ii} are normal strains, ϵ_{ij} are shear strains, and l , m , and n are direction cosines. The coordinate systems used for the application to diffraction are shown in Fig. 2. The S_1 define the specimen system, with S_1 and S_2 in the surface of the specimen. The L_1 define the laboratory system such that L_3 is in the direction of the normal to the diffracting planes. L_2 is in the S_1 - S_2 plane and makes an angle ϕ with S_2 . The angle ψ is between S_3 and L_3 . For a given diffraction peak, the lattice spacing d_{hkl} is obtained from the peak position and the strain along L_3 is obtained from the formula

$$\langle \epsilon_{33} \rangle_{\phi\psi} = \frac{d_{\phi\psi} - d_0}{d_0} = \frac{\sin\theta_{\phi\psi}}{\sin\theta_0} - 1 \quad (2)$$

where the carats represent the strain averaged over the irradiated volume, d_0 is the unstressed lattice spacing and θ^0 is the diffraction angle of the unstressed planes.

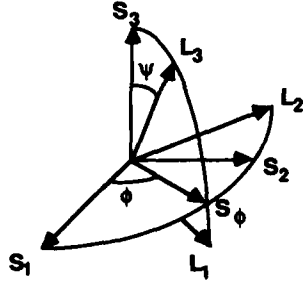


Figure 2 Axial convention used in stress measurements. S_i , L_i are the sample and laboratory systems, respectively, and are related by ϕ and ψ . The diffracting planes are normal to L_3 .

In terms of the angles ϕ and ψ , the strain relation in eqn. (1) is

$$\langle \epsilon_{\phi\psi} \rangle = [\langle \epsilon_{11} \rangle \cos^2\phi + \langle \epsilon_{12} \rangle \sin 2\phi + \langle \epsilon_{22} \rangle \sin^2\phi] \sin^2\psi + [\langle \epsilon_{13} \rangle \cos\phi + \langle \epsilon_{23} \rangle \sin\phi] \sin 2\psi + \langle \epsilon_{33} \rangle \cos^2\psi \quad (3)$$

If plots of $\langle \epsilon_{\phi\psi} \rangle$ vs. $\sin^2\psi$ are linear, i.e. do not show splitting for positive and negative ψ tilts, then $\langle \epsilon_{13} \rangle = \langle \epsilon_{23} \rangle = 0$. The intercept for such plots at $\phi = 0$ and 90° is $\langle \epsilon_{33} \rangle$ and the slopes are $\langle \epsilon_{11} \rangle - \langle \epsilon_{33} \rangle$ and $\langle \epsilon_{22} \rangle - \langle \epsilon_{33} \rangle$, respectively. For cylindrical symmetry, i.e. no shift in peak position with ϕ rotation, $\langle \epsilon_{11} \rangle = \langle \epsilon_{22} \rangle$.

The measured strains can also be expressed in terms of the stresses:

$$\langle \epsilon_{\phi\psi} \rangle = (S_2/2)[\langle \sigma_{11} \rangle \cos^2\phi + \langle \sigma_{12} \rangle \sin 2\phi + \langle \sigma_{22} \rangle \sin^2\phi] \sin^2\psi + (S_2/2)\langle \sigma_{33} \rangle \cos^2\psi + S_1[\langle \sigma_{11} \rangle + \langle \sigma_{22} \rangle + \langle \sigma_{33} \rangle] + (S_2/2)[\langle \sigma_{13} \rangle \cos\phi + \langle \sigma_{23} \rangle \sin\phi] \sin 2\psi \quad (4)$$

where $S_2/2$ is $(1+\nu)/E$, S_1 is $-\nu/E$, E is Young's modulus and ν is Poisson's ratio for the diffracting planes. In general, six measurements are required to extract all the stress components. Another approach is to define two terms:

$$a_1 = \frac{d_{\phi\psi+} + d_{\phi\psi-}}{2d_0} = (S_2/2)[\sigma_{11} \cos^2\phi + \sigma_{12} \sin 2\phi + \sigma_{22} \sin^2\phi] \sin^2\psi + (S_2/2)\sigma_{33} \cos^2\phi + S_1[\sigma_{11} + \sigma_{22} + \sigma_{33}] \quad (5a)$$

$$a_2 = \frac{d_{\phi\psi+} - d_{\phi\psi-}}{2d_0} = (S_2/2)[\sigma_{13} \cos\phi + \sigma_{23} \sin\phi + \sigma_{22} \sin^2\phi] \sin 2\psi \quad (5b)$$

The stresses σ_{11} , σ_{12} , σ_{22} , and σ_{33} may be obtained from the slope and intercept of a_1 vs. $\sin^2\psi$ for $\phi = 0, 45,$ and 90° . The stresses σ_{13} and σ_{23} may be obtained from the slope of a_2 vs. $\sin|2\psi|$ for $\phi = 0$ and 90° .

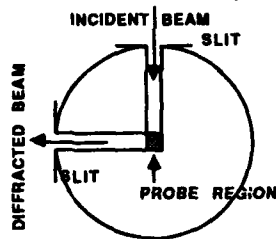
In the general case of a component containing a triaxial macrostress gradient, the analysis described above must be applied at each point from which data are collected. Many problems can be simplified from symmetry due to sample shape or considerations of elasticity theory, e.g. heat-treated cylinders or plates. However, a weld may be complex and even the principal stress directions may be unknown.

Microstresses in multiphase alloys or composites are measured with larger beams, essentially as in conventional powder diffraction. For composites, the stress state in the matrix or reinforcement will often be hydrostatic. However, for oriented fiber composites, the stresses generally vary with direction and have principal axes parallel and normal to the direction of fiber alignment. Finally, it is noted that systems containing both macro- and microstresses can also be analyzed [22,23].

EXPERIMENTAL

Probe regions and measurement angle

The creation of probe regions for the profiling of subsurface residual stress gradients is accomplished through the use of slits or apertures in the incident and diffracted beams, as indicated in the insert. The shape of the probe region is a function of the diffraction angle; see Fig. 3. For a plate oriented as shown, the probe region is extended parallel to the surface for diffraction angles less than $\theta = 45^\circ$ and in the direction of the depth for θ greater than this value. The geometry shown is for



$\psi = 0^\circ$, i.e. in the normal powder diffraction orientation. The dimensions of the probe region as a function of slit width and diffraction angle are indicated in the figure. The shape of the probe region is most symmetric at $90^\circ 2\theta$, so that workers try to find peaks near this angle. Another reason for working in this region is that, due to the geometrical optics of neutron spectrometers, peaks begin to substantially broaden at higher angles. Ninety degrees is substantially below the diffraction angles used in x-ray stress measurement, which are often at about $150^\circ 2\theta$. This is because the Bragg's law

sensitivity to changes in interplanar spacing increases with $\tan\theta$. For a given change in d-spacing, the angular shift at $150^\circ 2\theta$ is 3.7 times greater than at 90° . However, many such measurements have been made with neutrons. Some of the loss in sensitivity is, in effect, recovered because neutron diffraction peaks can generally be fit with greater accuracy than for the x-ray case.

Sample positioning, alignment, and determination of peak positions

For depth-profiling experiments, sample positioning and alignment are best accomplished using a table with x-y and rotational motion controls, and adjustable sample height. Special sample fixturing is generally required to handle parts of odd shape. The front surface can be located with accuracy by driving the sample into

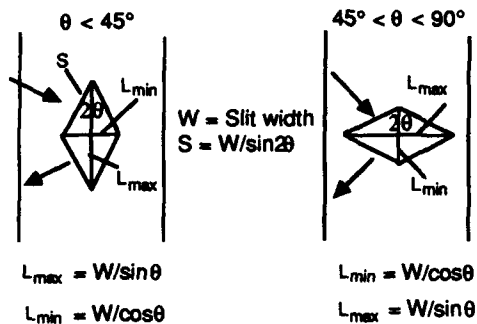


Figure 3 Probe region geometry for $\psi = 0^\circ$ for a flat plate sample.

the beam in small steps while sitting on a diffraction peak and noting when the counts reach a maximum.

Neutron diffraction peaks are largely Gaussian in shape. Whole peaks can be fit to high accuracy with Gaussian, pseudo-Voigt, or more sophisticated routines. Statistical fitting accuracy should be in the range of 0.003 to $0.006^\circ 2\theta$, with overall experimental reproducibility of at least $\pm 0.01^\circ 2\theta$.

The requirements for a specific experiment obviously depend on the peak shifts obtained, which in turn depend on the magnitude of the stresses and the elastic constants of the material. Residual stress experiments can usually be well modelled prior to making measurements.

Spectrometer and detector considerations

To date, depth measurements of macrostress gradients have been made using steady state sources. Both conventional powder and triple axis spectrometers have been employed. Triple axis instruments offer certain advantages, namely the ability to readily select wavelengths, i.e. to move peaks of interest near to diffraction angles of $90^\circ 2\theta$, and to make energy scans so that sample motion is not required, which can be useful for strongly textured or oddly shaped samples. However, such instruments are usually not optimized for resolution.

A powder spectrometer optimized for stress measurements should have a monochromator take-off angle in the 60 to 90° range; a soller collimator (10 to $30'$) in front of the monochromator (α_1); a collimator between the monochromator and sample (30 to $50'$); and, a large as possible sample-to-detector distance. This combination provides a good balance of intensity and resolution.

Three kinds of detectors have been successfully employed. Conventional BF_3 detectors with receiving slits, linear position-sensitive detectors (PSD), and, for horizontal instruments, a vertical row of detector tubes, forming a position-sensitive multi-detector. Assuming that peaks of interest are 2° wide at the base and that step scans are made in 0.1° increments, conventional detectors require 20 measurements per scan. The advantage of PSDs is that the throughput is greatly enhanced, i.e. the whole peak is collected simultaneously. However, linear PSDs can be somewhat unstable along the length of the tubes, introducing uncertainty in

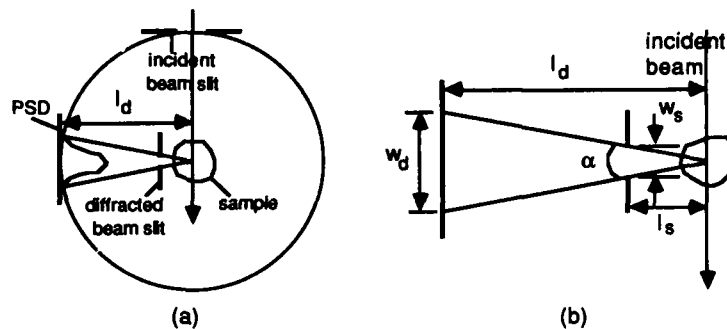


Figure 4. Geometry for depth probe measurements with position-sensitive

peak positions. Furthermore, much of the tube length is not used for single peak measurements. A multi-PSD, with tubes stacked vertical to the diffraction plane, removes the source of instability and can be designed to span only one peak. For either PSD system, receiving slit geometry is complicated by the need to place the diffracted beam slit close to the sample in order to properly define the probe volume; see Fig. 4. The working parameters are related by [24]

$$\tan(\alpha/2) = w_d/2l_d = w_s/2l_s \quad (6)$$

Steady state vs. pulsed sources

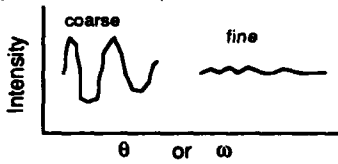
Macrostress gradient (and applied stress) measurements have been made at steady state sources while most microstress studies have been conducted at pulsed sources, for the following reasons. Control of beam size, sample positioning and orientation is more readily accomplished at steady state reactors because the sample stage is physically accessible, whereas at pulsed sources it must be placed in an evacuated and shielded chamber. On the other hand, the excellent resolution of pulsed sources, the ability to simultaneously collect diffraction peaks over a wide range of d-spacing (0.5 to 5 Å at IPNS), and the high diffraction angles employed (up to $150^\circ 2\theta$) are great advantages for microstress studies. These differences arise from the fact that steady state (reactor) spectrometers operate at constant wavelength while pulsed sources are time-of-flight instruments, i.e. operate at fixed diffraction angle (the general purpose powder diffractometer at the Argonne Intense Pulsed Neutron Source has detector banks at 60° , 90° , and $150^\circ 2\theta$ [25]) and collect a wide range of energies (wavelengths).

Problems

Three major problems can be encountered: the need for stress-free d-spacings, large grain sizes, and texture. Triaxial stress measurements require accurate values of stress-free d-spacings in order to convert shifts in peak position to strains. A number of approaches have been taken. A stress-free region of the sample or a separate piece of stress-free material can be used as long as there are no compositional differences. Another approach for alloys is to deduce the stress-

free value from equilibrium requirements during data analysis. For composites, it is often possible to use powders of the reinforcement phase. The matrix is itself an alloy or can take some of the reinforcement in solution. If it does not, a reinforcement-free matrix sample can be produced using the same procedure as for the composite, leading to the same composition as in the composite. For ceramics, this is also possible.

Large grain sizes (greater than about $50\ \mu\text{m}$) can cause inaccuracies in peak positions, the "spottiness" observed on x-ray Debye-Scherrer films. The sample can



be checked for this problem by performing rocking-curve type measurements, i.e. positioning the detector at the diffraction angle of the peak and making a θ or ω scan with the sample stage over a range of, say, $\pm 10^\circ$; see insert. Model samples can sometimes be processed to refine the grain size, however, this is not feasible for actual material. A rotational or translational oscillation of the sample acts to

smooth the pattern. If all else fails, a decision must be made either to live with the errors or abandon the experiment.

Texture (preferred grain orientation) can affect measurement accuracy and the conversion of strain to stress. The main effect is to alter the effective elastic constants. Texture can be investigated by obtaining full pole figures or, at the least, analyzing the relative powder pattern intensities. Ideally, diffraction elastic constants should be measured on the same material.

ILLUSTRATIVE APPLICATIONS

Macrostress gradient through an aluminum alloy bar

A stress gradient was measured through the central cross-section in a 25.4 mm square bar of 2024-T86 aluminum alloy machined into a U-shape [4]. A combined load through the central cross-section was generated by applying a 5.235 KN load at the ends of the legs; see Fig. 5a. The stress state was calculated and measured for the tangential (σ_θ) and radial (σ_r) components. The stress was measured through the depth using both the 311 and 333/511 diffraction peaks. Slit widths of 1.83 and 3.86 mm for the 311 and 333/511 peaks, respectively, were employed. The results for σ_θ are shown in Fig. 5b. The 311 and 333/511 peaks were at about 64 and $112^\circ 2\theta$, respectively; the neutron wavelength was $1.293\ \text{\AA}$. Measurements were made on a powder diffractometer at the University of Missouri Research Reactor (MURR). The unstressed d -spacings were obtained from the unloaded sample in this test case.

Anisotropic microstress in a SiC/Al composite

Measurements were made on a cylindrical sample (1.8 cm diameter by 4.3 cm in height) of a 20 vol. % SiC whisker-1100 aluminum alloy matrix composite, with whiskers aligned in the axial direction [26]. The matrix 311 peak was used and data was collected for $\psi = \pm 0, 30, 45, 60$ and 90° , and $\phi = 0$ and 90° using a full circle diffractometer at MURR. Stress-free d -spacings were obtained from an unreinforced alloy cylinder produced in the identical manner as the composite. The grain size

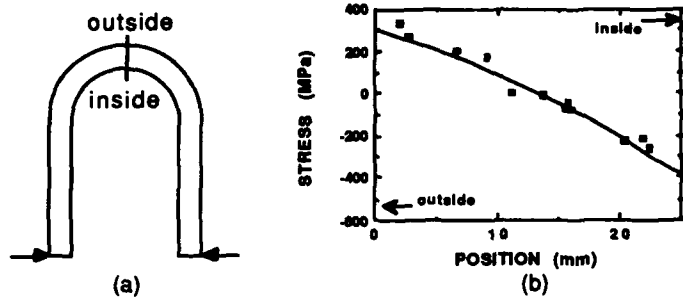


Figure 5 (a) Al alloy U-bar sample, (b) Calculated (solid line) and measured tangential stress σ_{θ} using 311 (solid squares) and 333/511 (open squares) diffraction peaks.

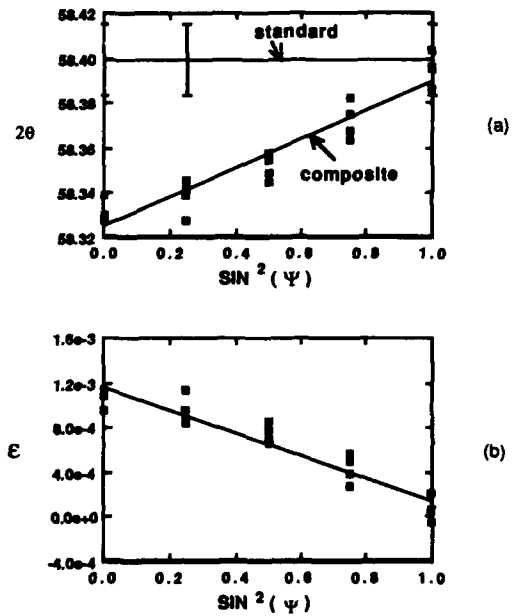


Figure 6 Aligned 20 vol. % SiC whisker 1100 aluminum alloy matrix composite. (a) 2θ vs. $\sin^2\psi$, (b) ϵ vs. $\sin^2\psi$.

was rather large, as observed in rocking curves, giving rise to scatter in the reference d-spacing, as indicated in Fig. 6a. Neither ψ -splitting nor a dependence on ϕ rotation was observed. Thus, the stress state is free of measurable shear stresses and is cylindrically symmetric. Fig. 6b shows strain (ϵ) vs. $\sin^2\psi$. The axial ($\langle\sigma_{33}\rangle$) and radial ($\langle\sigma_{11}\rangle = \langle\sigma_{22}\rangle$) stress values obtained were 136 and 83 MPa, respectively, in agreement with analytical calculation and the known value of matrix yield stress (about 150 MPa).

Microstress and stress/strain distribution in WC/Ni cemented carbide composites

Measurements were made on WC-Ni cemented carbide (particulate) composites with low (6%) and high (26%) Ni binder content [27]. The samples were in the form of 6x6x50 mm bars. Data were collected on the general purpose powder diffractometer at the Argonne Intense Pulsed Neutron Source at 100, 200, 300, 500, 700, and 900°K. Identical measurements were made on stress-free WC powder. The cell parameters of the HCP WC phase were determined and are shown in Fig. 7, as a function of temperature. It is seen that the WC is in compression and that the magnitude is greater for the higher binder content, i.e. the lower WC content. The WC particles are plate-like with the thickness direction parallel to the c-axis. This shape effect causes the strain to be greater in the a-axis direction [28].

Fig. 8 shows the stresses for both the WC and Ni. Because the Ni phase takes W into solution during sintering it is not easy to directly determine the stresses in this

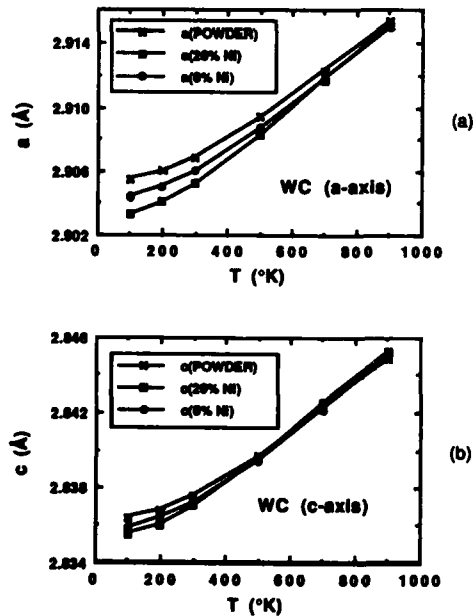


Figure 7 Cell parameters for (a) a-axis and (b) c-axis of WC phase in stress-free powder and the high and low binder composites.

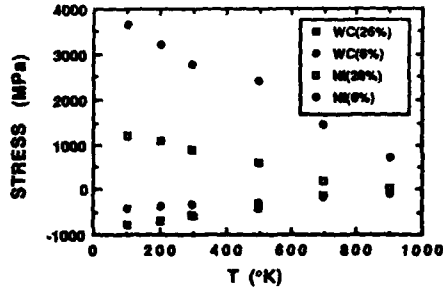


Figure 8 Residual thermal stresses in the WC and Ni phases of the high and low binder composites.

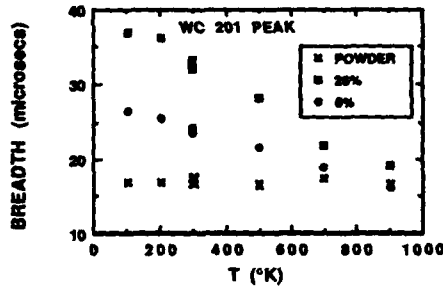


Figure 9 WC peak breadths (in time-of-flight units) for the composites and powder.

phase; they are calculated from the requirement of equilibrium. The stresses approach zero as the set-up temperature (900-1000°K) is approached.

These composites show striking peak breadth effects. The WC peaks increasingly broaden, relative to the stress-free powder, as the temperature decreases. This is shown in Fig. 9, for the WC 201 peak, in terms of time-of-flight units. The broadening has two components. A stress distribution is present due to the angular shape of the particles. A strain distribution is present due to a range of particle aspect ratios in the composites. Quantitative separation of the two effects is difficult.

CONCLUSIONS

The application of neutron diffraction to residual stress studies complements and extends x-ray diffraction methods. The greater penetration of neutrons enables new problems to be addressed, in particular, macrostress gradients, microstresses, and microstress/strain distributions.

ACKNOWLEDGEMENT

The assistance of Mr. K. Seol is gratefully acknowledged.

REFERENCES

1. I. C. Noyan and J. B. Cohen, *Residual Stress*, Springer Verlag, New York, 1987.
2. G. E. Bacon, *Neutron Diffraction*, 3rd ed., Oxford Univ. Press, 1975.
3. B. D. Cullity, *Elements of X-Ray Diffraction*, 2nd ed., Addison-Wesley, 1978.
4. M. J. Schmank and A. D. Krawitz, *Metall. Trans.*, **13A**(1982)1069-1076.
5. L. Pintschovius, V. Jung, E. Macherauch and O. Vohringer, *Matis. Sci. and Engrg.*, **61**(1983)43-50.
6. H. J. Prask and C. S. Choi, *J. Nuc. Matis.*, **136**(1984)124-131.
7. T. M. Holden, B. M. Powell, G. Dolling and S. R. MacEwen, *Proc. 5th Riso Intl. Symp. on Metallurgy and Matis. Sci.*, 1984, pp. 291-294.
8. R. A. Holt, G. Dolling, B. M. Powell, T. M. Holden and J. E. Winegar, *Proc. 5th Riso Intl. Symp. on Metallurgy and Matis. Sci.*, 1984, pp. 295-300.
9. A. J. Allen, M. T. Hutchings, C. G. Windsor, and C. Andreani, *Adv. in Phys.*, **34**(1985)445-473.
10. L. Pintschovius, E. Macherauch and B. Scholtes, *Matis. Sci. and Engrg.*, **84**(1986)163-170.
11. A. J. Allen, M. T. Hutchings and V. S. Rainey, *Non-Destructive Testing*, *Proc. 4th European Conf.*, Pergamon Press, 1987, pp. 1808-1817.
12. D. J. Smith, R. H. Leggatt, G. A. Webster, H. J. MacGillivray, P. J. Webster and G. Mills, *J. Strain Analysis*, **23**(1988)201-211.
13. S. R. MacEwen, J. Faber and A. P. L. Turner, *Acta Metall.*, **31**(1983)657-676.
14. A. D. Krawitz, R. Roberts and J. Faber, *Science of Hard Materials*, *Inst. of Physics Conf. Series No. 1*, 75, 1986, pp. 577-589.
15. A. D. Krawitz, D. G. Reichel and R. L. Hitterman, *Matis. Sci. and Engrg.*, **A119**(1989), in press.
16. S. Majumdar, D. Kupperman and J. Singh, *J. Am. Ceram. Soc.*, **71**(1988)858-863.
17. S. Majumdar and D. Kupperman, *J. Am. Ceram. Soc.*, **72**(1989)312-313.
18. A. D. Krawitz, M. L. Crapenhoft, D. G. Reichel and R. Warren, *Matis. Sci. and Engrg.*, **A105/106** (1988) 275-281.
19. A. J. Allen, M. Bourke, M. T. Hutchings, A. D. Krawitz and C. G. Windsor, *Residual Stresses in Sci. and Tech.*, Eds. E. Macherauch and V. Hauk, DGM Verlag, Vol. 1, 1987, p. 151.
20. P. J. Rudnik, A. D. Krawitz, D. G. Reichel and J. B. Cohen, *Adv. in X-Ray Anal.*, Vol. 31, Plenum, 1988, pp. 245-253.
21. B. D. Butler, B. C. Murray, D. G. Reichel and A. D. Krawitz, *Adv. in X-Ray Anal.*, Vol. 32, Plenum Press, 1989, pp. 389-395.
22. J. B. Cohen, *Powder Diffraction*, **1**(1986)15-21.
23. P. Predecki, A. Abuhasan and C. S. Barrett, *Adv. in X-Ray Anal.*, Vol. 31, Plenum, 1988, pp. 231-243.
24. A. D. Krawitz, B. Butler, P. Rudnik and J. B. Cohen, *Adv. in X-Ray Anal.*, Vol. 29, Plenum, 1986, pp. 163-172.
25. J. Faber and R. L. Hitterman, *Adv. in X-Ray Anal.*, Vol. 29, Plenum, 1986, pp. 119-130.
26. A. D. Krawitz and R. J. Arsenault, unpublished research.
27. K. Seol, unpublished research.
28. S. Majumdar and A. D. Krawitz, *J. Matis. Sci. and Engrg.*, in press.

RESIDUAL STRESS MEASUREMENTS BY MEANS OF NEUTRON DIFFRACTION

H. J. PRASK and C. S. CHOI¹
 Reactor Radiation Division, MSEL, National Institute of Standards and
 Technology, Gaithersburg, MD 20899

ABSTRACT

Energy-dispersive neutron diffraction has been developed at the NIST reactor as a probe of sub- and near-surface residual stresses in technological samples. Application of the technique has been made to a variety of metallurgical specimens which includes the determination of tri-axial stresses as a function of depth in a number of uranium-3/4wt%Ti samples with different thermo-mechanical histories, and in two types of 7075-T6 aluminum "ogives"- of interest to the Army. Preliminary results have been obtained for an induction-hardened steel shaft, a fatigue lifetime test specimen for the SAE.

INTRODUCTION

To our knowledge, the first references to the use of neutron diffraction to solve engineering problems was in 1979, and was in the area of crystallographic texture characterization [1]. The first description of the application of neutron diffraction to the measurement of residual stress gradients for engineering problems was in 1981 [2]. Since then the field has expanded enormously, as evidenced by the scope of contributions to this sub-session. In the following we report on a portion of the neutron diffraction residual stress work that has taken place at the NBSR, chosen to illustrate the variety of applications. Some of the results have been presented elsewhere [3].

METHODOLOGY

A unique advantage of neutron diffraction arises from the different relative scattering cross-sections and penetration of neutrons relative to x-rays. This is illustrated in Table I in which $t_{1/2}$, the thickness at which half the beam intensity is lost through scattering and absorption processes, is listed for selected metals. The values are based on cross-sections from standard references and the difference in wavelengths used for neutrons(1.08Å) and x-rays(1.54Å) is not significant.

Table I. X-Ray/Neutron Comparison

Element(At. No.)	$t_{1/2}$ (X-rays)	$t_{1/2}$ (Neutrons)
Al (13)	0.0530 mm	71.0 mm
Ti (22)	0.0076	15.9
Fe (26)	0.0027	6.1
Cd (48)	0.0035	0.057
W (74)	0.0021	6.5
U ²³⁸ (92)	0.0015	13.6

The $t_{1/2}$ values clearly show that neutrons in the normal diffraction wavelength range are several orders-of-magnitude more penetrating than x-rays. Also, the penetration does not decrease monotonically with atomic number as with x-rays but is, essentially, a random function of atomic number. It is clear from the Table that both depleted uranium and aluminum are very good materials for neutron examination, while steel is less so.

The properties of neutrons presented the possibility of measuring sub-surface residual stress gradients by employing tight collimation and -90°

¹Guest scientist from ARDEC, Picatinny Arsenal, NJ.

scattering geometry (i.e. "depth-profiling") [2,3]. In our measurements, we have made use of the fact that Bragg-condition resonances (at $\lambda=2d\sin\Omega/2$), can also be observed at fixed scattering angle, Ω , with varying wavelength, λ . With the scattering angle fixed the examined volume, ΔV , remains the same throughout each scan. Also in this mode, the intensity profile distortion which occurs when part of the ΔV is outside the sample may be lessened compared to angle-dispersive scans [4].

The instrument that we use for energy-dispersive neutron diffraction (EDND) is a triple-axis spectrometer. Crystals of known d-spacing are placed before (monochromator) and after (analyzer) the sample; the Bragg relation is then used to select and step the wavelength incident on the sample. In principal, the analyzer crystal - which we step at the identical wavelength as the monochromator - is not needed. However, for a given scattering configuration, utilization of the analyzer significantly enhances instrumental resolution. Instrumental details are given elsewhere [3].

The relation between stress and strain applicable to diffraction measurements has been presented, for example, by Evenschor and Hauk [5]. With reference to Figure 1, r , θ , and z are specimen-fixed axes, and the strain $\epsilon'_{\phi\psi}$ is measured along \tilde{L}'_3 ; then

$$\epsilon'_{\phi\psi} = (d_{\phi\psi} - d_0) / d_0 \quad (1)$$

where $d_{\phi\psi}$ is the lattice spacing along \tilde{L}'_3 and d_0 is the unstressed lattice spacing. The stresses are related to the measured strains through

$$\epsilon'_{\phi\psi} = \frac{1}{2} S_2(hkl) [\sigma_{11} \cos^2\phi \sin^2\psi + \sigma_{22} \sin^2\phi \sin^2\psi + \sigma_{33} \cos^2\psi + \sigma_{12} \sin 2\phi \sin^2\psi + \sigma_{13} \cos\phi \sin 2\psi + \sigma_{23} \sin\phi \sin 2\psi] + S_1(hkl) [\sigma_{11} + \sigma_{22} + \sigma_{33}]. \quad (2)$$

The $S_i(hkl)$ are diffraction elastic constants ("XEC") for the (hkl) reflection which, in general, depend on the material and the reflection examined. For an elastically isotropic solid the XEC are given by

$$\frac{1}{2} S_2(hkl) = (1+\mu)/E \text{ and } S_1(hkl) = -\mu/E \quad (3)$$

where μ , E are Poisson's ratio and Young's modulus, respectively. Since the determination of residual stress in technological samples by means of Eq. 2 depends directly on measurement of strain values, a precise value for the unstressed d-spacing, d_0 , is essential. Often d_0 can be obtained from powders or stress-free samples, but this is not always possible. Alternatively, we utilize the overall equilibrium conditions required by elasticity theory to determine d_0 . That is, since the body is static with no external force applied, residual stresses normal to any plane must balance such that in cylindrical geometry:

$$\int \sigma_{zz} r dr d\theta = 0 \text{ and } \int \sigma_{\theta\theta} dr dz = 0 \quad (4)$$

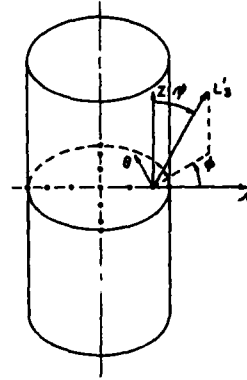


Figure 1. Coordinate system for cylindrical samples and measurement mesh for the 2.5 cm diameter by 10 cm long U-3/4Ti samples. The solid circles represent the centers of the 4 mm X 4 mm X 4 mm ΔV s examined.

and at any surface the stress orthogonal to that surface must vanish. Stresses inferred from measured strains can be adjusted, by adjusting d_0 , to fulfill the equilibrium conditions.

RESULTS

U-0.75wt%Ti ("U-3/4Ti")

Two different types of U-3/4Ti samples were studied. Starting with 3.3 cm diameter stock, all material was γ -phase solutionized at 800°C, water quenched, and rotary straightened. Of these, two were machined to the final 2.4 cm diameter. Additional cold working was performed on two of the samples before final machining: after turning to ~2.9 cm diameter, both were swaged in a single pass (7% R.A.); one of the two was then swaged in three additional passes to a final 31% R.A. Both were then turned to the final diameter. In all cases aging after quenching was 1-2 hours at 400°C or less. For convenience, the residual stress determinations were made on 10 cm long pieces cut from the mid-point of 46 cm long rods.

One difficulty with U-3/4Ti material prepared as described above is that it is not single-phase. Very rapidly cooled material consists of a single martensitic phase, α' -U, whereas slowly cooled material consists of α -U (containing some dissolved Ti) and U_2Ti . α - and α' -U are orthorhombic and almost identical in structure [6], and 3.3 cm U-3/4Ti rods of the above type are ~88 vol% α' -U at the surface, ~67% at the centerline after quenching and aging [7]. The machined and cold-worked samples examined with neutrons were estimated to be 85 or (for the 31% swaged sample) 87 vol% α' -U at the surface.

Utilizing the {112} reflection we have determined d-spacings in the midpoint r - θ plane of each sample for the measurement grid shown in Fig. 1. Determination of stresses was made using eqns. 2-4 and isotropic elastic constants [8], simply averaged according to composition at each point. Two d_0 's were determined for each sample from eqn. (4), with the effect on d of compositional gradients taken into account. Stress distributions for the two unswaged samples and the 7% swaged sample have been presented elsewhere [3]. The results for the unswaged samples were in excellent quantitative agreement with measurements made on similar samples by the Sach's boring-out technique (references cited in [3]).

An internal check of the utilization of eqn. 4 to determine d_0 is possible as follows. The d_0 's obtained from the σ_{zz} - and the $\sigma_{\theta\theta}$ -balance conditions, if the procedure is correct, should be approximately equal (assuming that $\sigma_{\theta\theta}$ at any r is essentially constant along the length of the cylinder). In Table II a summary of results for four U-3/4Ti samples is presented. The d_0 's obtained for the swaged and unswaged pairs differ because scattering angles in the two cases were not determined absolutely. The agreement between d_{0z} and $d_{0\theta}$ is excellent for each sample except the 31% swaged material. The d_0 's for each unswaged sample are also in excellent agreement, whereas the d_0 's of the two swaged materials are significantly different from each other.

Table II. U-3/4Ti Summary

Sample	Q(nom.)	$d_{0z}(r=0)$	$d_{0\theta}(r=0)$	$\sigma_{\theta\theta}(r=0)$	$\overline{\sigma_{\theta\theta}}(r=R)$
Ind. heat/spray	100°	1.79094A	1.79104A	297±15MPa	-314±12MPa
Vac. heat/bath	100°	1.79095	1.79091	250±12	-327±14
7% RA swaged	90°	1.78551	1.78551	-113±12	84±13
31% RA swaged	90°	1.78676	1.78600	(-71±13)	(-16±14)

The measured textures of these several samples show that both of the swaged samples possess fiber texture ([072] fiber axis), with the (112)

poles aligned perpendicular to the cylinder axis; the unswaged samples are essentially untextured. The degree of orientation is ~2.5 times as great in the 31% swaged as the 7% swaged sample. Since the U-3/4Ti specimens are in fact three-phase materials, we speculate in the following way. We assume that microstrains have been produced in the cylinder-axis direction in either the α - or U_2Ti phases by severe plastic deformation, leading to d_{α}, d_{U_2Ti} . To correct for this we add a uniform Δd to all measured d 's until eqns. (4) are fulfilled. Two interesting results come out of this: first, the d_0 which balances stresses in both directions is 1.78560Å, in quite good agreement with the 7% swaged sample; secondly, the Δd (-0.0022Å) is comparable to $d_1(112) - d_2(112)$ (-0.0031Å) measured for a 1cm long x 1cm diam. texture specimen taken from the center of the 31% swaged sample. Some representative, measured residual stress values are shown in Table II; those for the 31% swaged sample are after the empirical correction.

7075-T6 Ogives

In the past few years several ogive failures have occurred during ballistic acceptance testing of the 155 mm M483A1 projectile. The ogive is manufactured from 7075-T6 aluminum and is pictured in Figure 2. Production ogives are manufactured by two different suppliers who use somewhat different manufacturing methods. Manufacturer B produces the ogives by cold forging the cavity to finished dimensions, heat treating, and machining the outside dimensions. Manufacturer A produces a preform by forging at 332°-382°C, machines the cavity, heat treats, then finish machines the outside dimensions. Both suppliers use ALCOA aluminum. In full-scale tests the primary failure mode, exclusive to the B-type ogive, is a circumferential fracture at the first loaded thread.

Several material characterization studies, including X-ray and hole-drilling residual stress measurements with layer removal, and simulation tests have been conducted (summarized in ref. 3). No substantial material property differences, including residual stresses, were observed. The results of a simulation study, in which ogives were sealed and a charge exploded within, showed substantial differences in behavior. The B-ogives failed at the thread at containment pressures substantially below that which is required to fail A-ogives. Furthermore, these tests showed that the A-ogives failed by ductile rupture with the crack running in the longitudinal direction.

In our work one ogive of type B and one of type A were studied by EDND. Six 4x4x4mm³ beam-spot positions along a diameter in the plane of the potential failure site were used. Axial-direction equilibrium (eqn. 4) was used to determine $d_0(200)$, assuming that the average of the 0° and 180° data was representative of the full circumference. The d_0 's arrived at to balance σ_{xx} stresses were in reasonable agreement for both types of ogives. The diffraction elastic constants used in the stress/strain calculations were the theoretical values of Bollenrath et al [9].

In Figure 3, final absolute residual stress values are shown for both ogive types for 0° and 180° positions at the first thread position. In

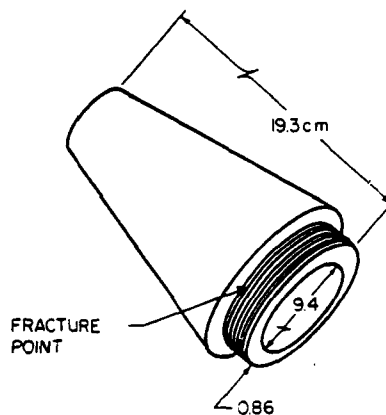


Figure 2. M483A1 ogive with forward end at upper left. The region of interest is under the most forward thread, as indicated.

contrast to previous measurements, the nondestructive EDND stress determination indicates very significant differences in the two ogive types. In the A-type ogive it is found that near the thread root ("OD") the σ_{zz} stresses are about -30 MPa (compressive) whereas the B-type show +13 to +45 MPa (tensile) stresses. In contrast, σ_{zz} and $\sigma_{\theta\theta}$ near the ID of the A-type ogive are zero or somewhat tensile, but in the B-type are clearly compressive at this position. These results are consistent with the observed failure modes for the two ogive types.

Steel Fatigue-test Specimen

Recently, a feasibility study was made for the SAE Fatigue Design and Evaluation Committee to determine the applicability of the neutron diffraction technique to residual stress determination in a multi-axial fatigue lifetime prediction project. Test spindles, shown in Figure 4, will be tested for fatigue life, characterized for materials properties - including residual stress, and modeled by finite element techniques. Some depth-profiling of residual stresses has been done by x-ray diffraction with layer removal [10].

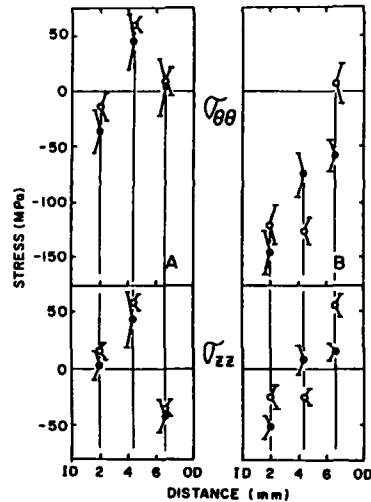


Figure 3. Stress distributions of the A and B type ogives. "OD" is the thread-root position. The open and closed circles correspond to measurements made 180° apart.

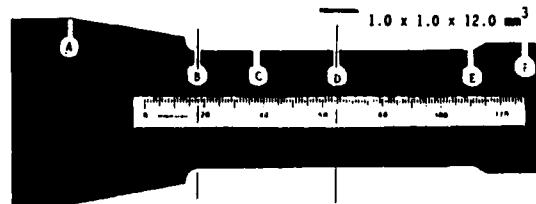


Figure 4. Schematic of SAE 1045 steel shaft. Overall length is 36cm, diameter at "D" is 4.0cm.

For the initial neutron measurements, a simplified procedure was employed in which $d(110)$ -spacings were measured only for probe directions in the $r-\theta$ plane, i.e. with Q perpendicular to the cylinder axis. The beam-spot employed was $1 \times 1 \times 12 \text{ mm}^3$ in size, oriented such that the long dimension was always parallel to the cylinder axis. Measurements were made with the center of the 1 mm^2 cross-section at 1.3, 3.3, and 6.3mm below the 40mm diameter surface, which allows a relatively quick determination of $(\sigma_{rr} - \sigma_{\theta\theta})$ but not any of the individual stress components. Measurements at several angles were made at each of the three depths along single radii with the center of the 12 mm length at positions "B" and "D" of Figure 4 (-50mm

separation). Results of a finite element analysis (FEA) were available at these positions [11]. XEC for iron were used to determine stresses [9].

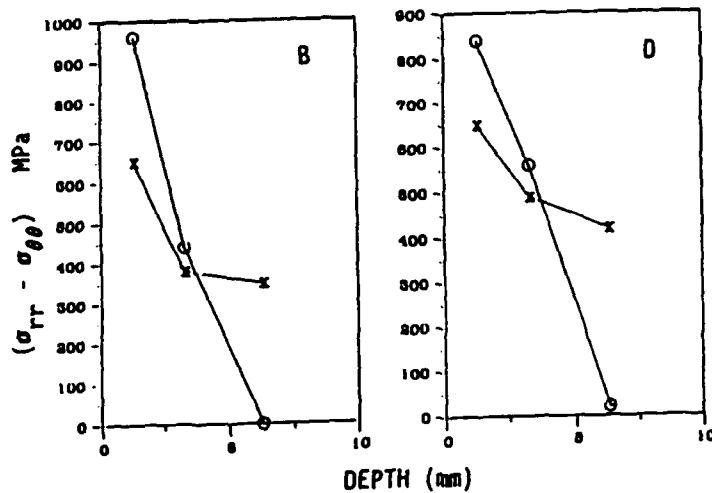


Figure 5. Measured [X] and calculated [O] $(\sigma_{rr} - \sigma_{\theta\theta})$ at "B" and "D" of the shaft of Figure 4.

Neglecting stress gradients in the axial direction, a $(\sigma_{rr} - \sigma_{\theta\theta})$ can be obtained from the three calculated stress components which can be compared to the neutron results (Figure 5). It is clear that the calculated $(\sigma_{rr} - \sigma_{\theta\theta})$ changes much more sharply with depth than the measured values for both positions. It is worth noting that both the x-ray and the neutron results are in reasonably good agreement, and in poor agreement with the FEA calculations. However, the results provide a new starting point for further calculations. Determination of the triaxial stress state at selected points in the shaft is planned for the near future.

REFERENCES

1. C.S. Choi, H.J. Prask, S.F. Trevino, H.A. Alperin, and C. Bechtold, NBS Tech. Note 995, 34-39 (1979); C.S. Choi, H.J. Prask, and S.F. Trevino, J. Appl. Cryst. 12, 327-331 (1979).
2. A.D. Krawitz, J.E. Brune, and M.J. Schrank, in *Residual Stress and Stress Relaxation*, edited by E. Kula and V. Weiss (Plenum Press, New York and London, 1982) pp. 139-155; L. Pintschovius, V. Jung, L. Maucherauch, R. Schäfer, and O. Vöhringer, *ibid.*, pp. 467-482.
3. H.J. Prask and C.S. Choi, in *Residual Stress in Design, Process and Materials Selection*, edited by W.B. Young (ASM International, 1987) pp. 21-26.
4. H.J. Prask (unpublished).
5. P.D. Evenshor and V. Hauk, Z. Metallkde. 66, 167-8 (1975).
6. C.S. Choi, H.J. Prask, and G.M. Ludtka, J. Nucl. Matis. 150, 85 (1987).
7. K.H. Eckelmeyer (unpublished).
8. G.H. Llewellyn et al., Oak Ridge Y-12 Plant Report No. Y-2397, 1989.
9. F. Bollenrath, V. Hauk, and E. Muller, Z. Metallkde. 58, 76-82 (1967).
10. P. Prevey et al. (unpublished).
11. J.K. Ochsner (unpublished).

RESIDUAL STRESS ANALYSIS BY NEUTRON TIME-OF-FLIGHT AT A REACTOR SOURCE

H.G. PRIESMEYER* AND J. SCHRÖDER**

*Institut für Reine und Angewandte Kernphysik, Universität Kiel

**Institut für Werkstofforschung, GKSS-FORSCHUNGSZENTRUM GEBSTHACHT,
Federal Republic of GermanyABSTRACT

Non-destructive neutron diffractometry for stress analysis will be a powerful experimental tool in material science research performed at the GKSS 5 MW reactor FRG-1. Arguments which show the advantages of the time-of-flight method are given and a suitable high-resolution neutron-efficient type of spectrometer is introduced. First results derived from this method are presented.

Introduction

Neutron diffraction is being used increasingly to determine residual stresses in polycrystalline materials. The positions of LAUE-BRAGG reflection peaks from strained volume elements are compared to those for the unstrained equilibrium case. For most materials of interest the penetrability of neutrons is considerably higher than for x-rays. This allows three-dimensional measurements such as strain depth profiling or tensor determination to be achieved non-destructively.

The most common neutron sources - like synchrotron x-ray sources - provide a white spectrum, which is a smooth function of the neutron wavelength. They are generally less intense than x-ray sources, so that beam cross-sections are wider and measuring times longer for neutron measurements. Nuclear reactors produce a polychromatic thermal neutron spectrum shaped like a Maxwellian corresponding to a velocity of 2200 m/sec. The typical integrated neutron flux is 10^{13} to 10^{14} n/cm² sec, from which a flux of 10^8 to 10^9 n/cm² sec can be extracted for experiments by neutron guide techniques.

To observe the wavelength-dependent elastic neutron scattering from a material, two methods are known: one can either use monochromatic neutrons produced by a crystal monochromator or work with a pulsed "white" neutron source and perform time-of-flight analysis. Lattice spacings d are determined from the well-known BRAGG law, written as either

$$(A) \quad d_{hkl} = \frac{\lambda}{2 \sin \theta_{hkl}}$$

or

$$(B) \quad d_{hkl} = 1.978 \cdot 10^{-3} \cdot \frac{t_{hkl}}{L \cdot \sin \theta}$$

λ = neutron wavelength [Å]
 2θ = scattering angle
 t = flight time [μs]
 L = flight path [m]
 hkl = Miller indices

Case (A) requires a spectrometer that can measure the scattered fraction of the incoming flux by moving sample and detectors by very precise

angular steps about the main scattering direction 2θ . Typically about 1% of the available primary spectrum is selected by the monochromator and care must be taken to avoid background contributions from higher-order reflected neutrons. Wavelength resolution is determined by the quality of the monochromator-crystal and the scattering geometry. It is in general wavelength dependent.

Conventional time-of-flight measurements (Case B) at a steady-state reactor require a neutron shutter in order to define a limited time interval during which the complete neutron source spectrum is allowed to enter an evacuated flight path. After this short time interval the shutter must close again in order to let neutrons from the individual bursts spatially separate according to their velocity dispersion. Time-of-flight methods of this kind also use typically about 1% of the incoming beam intensity. Resolution in time-of-flight is largely determined by the width of the neutron burst and therefore closely related to the neutron intensity per pulse: high resolution requires short bursts that necessarily contain fewer neutrons. At steady-state reactors the Fourier- and the binary pseudorandom-correlation choppers have been developed, which use the available neutron spectrum in a much more economic way. In this case resolution and intensity are decoupled from each other, as will be explained in this paper.

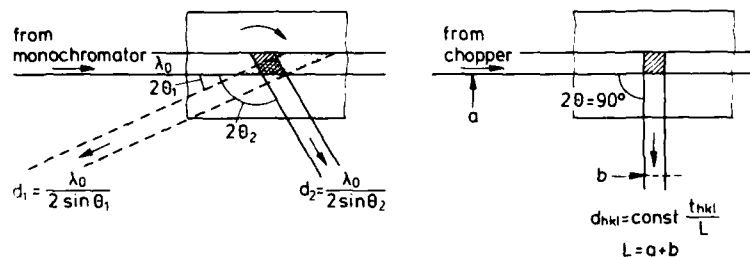
The Neutron Time-Of-Flight Method in Non-destructive Strain Measurements

Time-of-flight spectroscopy has several features that make it attractive for strain measurements. They can be summarized as follows:

The whole "white" neutron spectrum emerging from a moderator can be used so that several individual reflections can be investigated simultaneously, whereas crystal spectrometry allows only for one peak at a time. This is an important feature considering the fact that microscopic elastic constants are orientation dependent and that grain size distribution or likely texture will change the intensity of certain BRAGG reflections. The wavelength range of the neutron spectrum extends from 1 Å to about 5 Å and covers the elastic scattering from most of the materials of technical interest.

Neutron time-of-flight spectrometry has no constraints concerning the angle between the incoming and scattered neutron beams, since there are always neutrons available with wavelengths required by the BRAGG scattering law for any fixed angle. Therefore a fixed scattering angle of 90° may be chosen, by which the smallest and with regards to strain-tensor determination best defined scattering volume may be attained. (Fig. 1)

Fig. 1: Principal Setups for Strain Determinations from BRAGG-Peak-Position



(A) Neutron Crystal Diffractometry

(B) Neutron Time-of-Flight Diffractometry

The fixed geometry eases the setup of samples under investigation as opposed to a θ - 2θ precision scan necessary for crystal spectrometry. Time-of-flight methods need a flight path to allow the measurement of neutron velocities. This distance separates the sample position from the rest of the spectrometer. It is then easier to design a sample positioner to meet special requirements as for heavy samples, samples under external loads, samples in operating conditions or in hot or cold environments. Since neutrons are isotropically scattered, a fixed geometry allows for several detectors which look at the sample from different directions at the same time. This reduces measurement times for strain tensor determinations, for which the sample must be tilted at least six times in the ordinary case.

Time-of-flight spectrometry is not spoiled by background contributions from neutrons whose wavelength is different from that corresponding to the measured flight times, provided the shutter completely cuts off the incoming neutron flux.

Generally with time-of-flight spectrometers a higher resolution $\Delta d/d$ can be achieved than with crystal spectrometers.

Neutron-Efficient Correlation Time-Of-Flight Methods

The advantages of time-of-flight measurements for strain determination outlined in the last section can only be fully exploited when neutron-economic methods are employed. The common way to do time-of-flight experiments at a steady-state neutron source employs the so-called Fermi chopper, i.e. a rotating disk of a neutron-absorbing material with a slit system to produce short neutron pulses. The disadvantage in this case is a considerable reduction in neutron intensity, necessitating long measuring times, if high resolution is to be attained. Therefore methods have been developed which use the available neutron flux in a more economic way without the need to reduce the resolution [2, 3]. They have become known as correlation spectroscopy using either Fourier or pseudorandom beam modulation. The Fourier-chopper is the instrument of choice in our case, because one may adjust the neutron beam cross section to the problem under investigation.

As is known from Fourier analysis, any spectrum can be composed of a series of groundwave and higher-order Fourier components. In order to be able to determine the parameters in this series, the primary neutron flux must be modulated in a sinusoidal way and amplitudes and corresponding phase relations, i.e. neutron intensities and their phase relative to the chopper modulation, have to be measured. A Fourier chopper consists of a disk equipped with equidistant alternating neutron absorbing and neutron transparent fields around its periphery, rotating in front of a similar stator. This setup generates a triangular intensity pattern which can be assumed to be approximately sinusoidal.

The Fourier method has been improved by the ingenious idea of triggering the time-of-flight analyser by the detected neutrons instead of by the rotor position. This results in an on-line correlation determination of the diffraction pattern when the rotor is driven at continuous frequencies from zero up to a maximum f_{\max} . The method is known as reverse-time-of-flight Fourier spectroscopy and has been extensively investigated by the Finnish group, who developed the system [4, 5, 6]. An RTOF spectrometer has been implemented at the Russian 16 MW research reactor in Gatchina [7]. It is known that a general disadvantage of the method is its inferior response to very small peaks in neutron powder diffraction spectra. But this feature is of little interest in strain determination, where only prominent peaks are used for the analysis.

The Fourier Strain Spectrometer FSS at the 5 MW Swimmingpool-Reactor FRG 1

The Fourier beam modulator consists of a titanium disk of 60 cm outer diameter which contains around its outer edge 1024 equally spaced strips of neutron absorbing gadolinium, each 0.25 mm thick, 0.7 mm wide and 35 mm long. The disk can be rotated with up to 9000 rpm. The titanium thickness is 5 mm in order to reduce neutron losses between the Gd strips. A stationary section having the same neutron absorber pattern is positioned at 6 mm behind the rotor. The position of the stator can be controlled remotely during an experiment. By rotating the disk the intensity of the entire incoming neutron beam of $15 \times 10^8 \text{ mm}^2$ cross-section is modulated in a quasi-sinusoidal way. The beam modulation frequency is 1024 times the rotational frequency of the disk, resulting in a maximum frequency of 153.6 kHz.

Generally time-of-flight resolution is composed of several contributions, the two most important being the time spread of the neutron pulse and the flight path uncertainty due to a finite detector thickness. The relative uncertainty in determining the lattice spacing d is given by

$$\frac{\Delta d}{d} = \left\{ \left(\frac{\Delta t}{505.6 \cdot L \cdot d \cdot \sin\theta} \right)^2 + \left(\frac{\Delta L}{L} \right)^2 \right\}^{1/2} \quad \begin{array}{l} \Delta L, L \text{ [m]} \\ \Delta t \text{ [\mu s]} \end{array}$$

If the time uncertainty Δt is estimated as the reciprocal of the maximum modulation frequency, it will be 6.4 μsec . A neutron with a velocity of 2200 m/sec will move about 14 mm during this time. If all flight path uncertainties are kept well below this value, the relative uncertainty in $\Delta d/d$ will be determined predominantly by the maximum modulation frequency. An important flight path uncertainty can be inferred by the detector thickness. A Li-6 glass-scintillator detector of 2 mm thickness has been chosen to meet the requirement of being 100 % efficient to detect the fastest neutrons in the diffraction spectrum. For a total flight path of $L = 23 \text{ m}$ the d -resolution is less than 1×10^{-3} .

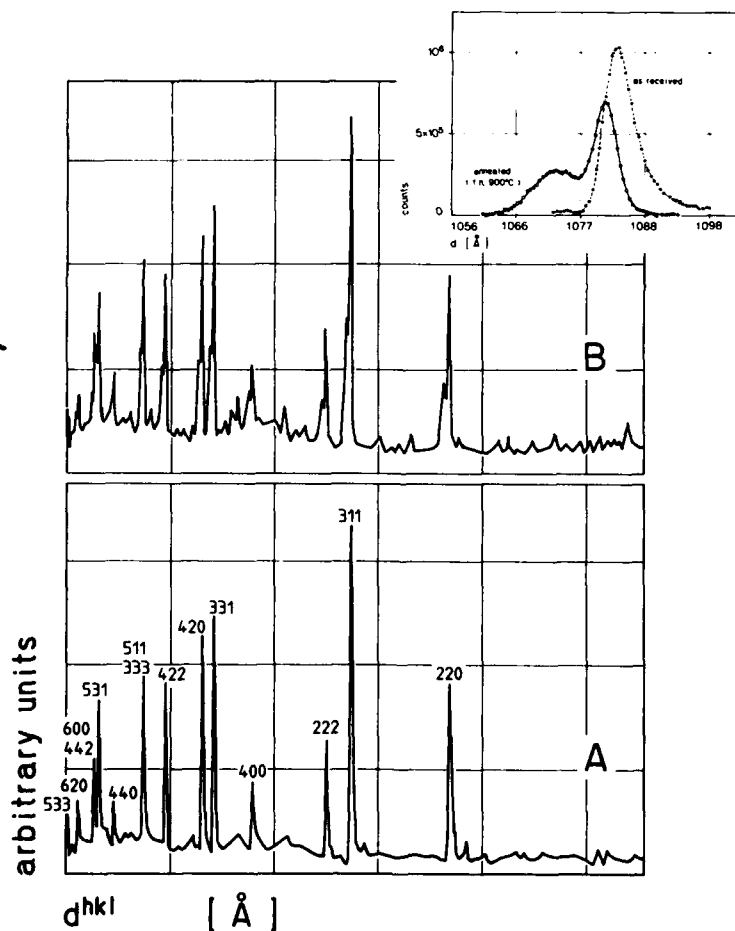
The flight path over a distance of 21 m is defined by a neutron guide tube with a curvature of 3000 m and a characteristic wavelength $\lambda^* = 1.83 \text{ \AA}$, in order to avoid intensity losses due to geometrical spreading. The beam can be collimated down to $2 \times 2 \text{ mm}^2$. Its intensity was measured to be $1.2 \times 10^7 \text{ n/cm}^2 \text{ sec}$. The sample is viewed by one detector in 90° scattering geometry, but provisions are made to install more detectors later, in order to reduce measuring times for strain tensor depth profiling.

The correlation electronics are commercially available from [8]. Two personal computers support the experiment, one for control and the other one for data acquisition and evaluation.

First Strain Measurement Results using the Fourier Method

Since FSS at Geesthacht is in the final stage of being set up, we present data collected at the similar MINISFINKS instrument in Gatchina, the resolution of which is lower by a factor of two, compared to FSS. Figure 2 shows diffraction spectra of 1.7 cm³ of plasma-sprayed Ni-base superalloy (WASPALLOY) powder. Due to the rapidly-quenching process involved the powder particles contain internal stresses. This becomes obvious after a subsequent aging treatment (1 h/900 °C), by which each originally single peak splits up into a double-humped structure (cf. insert). With reference to an almost stress-free WASPALLOY bulk sample the shift of the original peaks of the powder introduced after aging can be primarily attributed to the internal stress relief. The measurement was supervised by Dr. Heikki Pöyry, whose help is gratefully acknowledged.

Fig. 2: High-resolution powder diffractograms of WASPALLOY
(A : as received, B : aged for 1 h at 900 °C)



References

- [1] A. J. Allen, M. T. Hutchings, C. Windsor, C. Andreani
Advances in Physics 34 (1985), 445-473
- [2] J. F. Colwell, S. R. Lehman, P. H. Miller, Jr., W. L. Whittemore
Nucl. Instr. Meth. 76 (1969), 135-149
Nucl. Instr. Meth. 77 (1969), 29-39
- [3] F. Gompf, W. Reichardt, W. Gläser, K. H. Beckurts
IAEA Symposium Neutron Inelastic Scattering, Copenhagen 1968,
paper SM-104/67 p. 417-428
- [4] P. Hiismäki,
IAEA Conference Neutron Inelastic Scattering, Grenoble 1972,
paper SM-155/F-10 p. 803-807
- [5] A. Tiitta
Technical Research Center of Finland Publication # 27 Espoo
1980
- [6] H. Pöyry
Nucl. Instr. Meth. 156 (1978), 499-514
Nucl. Instr. Meth. 156 (1978), 515-528
- [7] P. Hiismäki et al.
IAEA Conference Neutron Scattering in the Nineties, Jülich 1986,
paper CN-46/35P
- [8] VTT
Technical Research Center of Finland
Reactor Laboratory
Otakaari 3A
SF-02150 ESPOO, Finland

NON-DESTRUCTIVE MEASUREMENT OF RESIDUAL STRESSES
IN U-0.8 WT% TI BY NEUTRON DIFFRACTION

A. SALINAS-RODRIGUEZ, J.H. ROOT, T.M. HOLDEN, S.R. MACEWEN AND G.M. LUDTKA*
Chalk River Nuclear Laboratories, Atomic Energy of Canada Ltd., Chalk River,
Ontario, Canada K0J 1P0.
*Martin-Marietta Energy Systems, Inc., Oak Ridge Y-12 Plant, Oak Ridge,
Tennessee, USA 37831.

ABSTRACT

The macroscopic residual stress distribution in γ -quenched and stress levelled U-0.8wt% Ti alloy tubes was studied using neutron diffraction techniques. Residual strains were evaluated from the difference in d-spacings measured in the tubes and in small reference samples machined from each tube. Residual stresses were calculated with the isotropic bulk values of the elastic constants for polycrystalline α -U. Quenching from the γ field resulted in a nearly equi-biaxial stress state at every point across the wall thickness of the tube. The magnitude of the radial stress was very small compared with that of the axial and hoop stresses which were compressive at the surfaces and tensile in the interior. Stress levelling relieved almost completely the hoop residual stress without affecting the radial stress. The axial residual stress becomes tensile through the wall thickness and remains constant at about 20% of its magnitude in the as-quenched condition.

INTRODUCTION

Residual stresses are frequently introduced into uranium and uranium alloys as a result of the thermo-mechanical treatments employed during fabrication. Large residual stresses impair manufacturability and performance. Effects such as centre-line bursting of solid bars, stress corrosion cracking and distortion during machining are all consequences of the presence of residual stresses. Mechanical relaxation methods of measuring residual stresses have been applied to uranium alloys since the early 1960's to estimate machining and quenching stresses in solid and hollow cylinders [1]. The main disadvantage of these methods is that they are destructive. Moreover, it is implicitly assumed that the stress distribution is symmetric about the cylinder axis and can only give average stresses as a function of radial distance from the axis. This is a reasonable assumption for the case of solid cylinders but implausible for the case of tubes.

X-ray diffraction methods are usually unsuitable for measuring residual stresses in uranium alloys because of the low penetrating power of x-rays into the sample. The diffracted radiation usually originates from within 1 μm of the specimen surface.

Neutron scattering is a particularly suitable technique for the study of residual stresses in uranium alloys due to the high penetrability of neutrons. This allows the non-destructive measurement of bulk residual stresses in large and complex engineering components without much effort. Prask and Choi [2] have applied an energy dispersive method to estimate residual stresses in solid U-0.75wt% Ti rods. In the present work, the θ -2 θ neutron diffraction technique was employed to examine the residual stress distributions existing in depleted U-0.8wt% Ti tubes which had different thermomechanical histories.

EXPERIMENTAL

The U-0.8wt% Ti tubes examined had the following dimensions: 108 mm height, 151 mm outside diameter and 17 mm wall thickness. Martin-Marietta

provided four batches of tubes (three tubes per batch), each in a different metallurgical condition. However, in this paper only the results obtained in tubes γ -quenched and stress levelled are reported. The tubes were solution heat treated at 1073 K for 4 hours prior to quenching which was carried out by rapid immersion into a water bath. Stress levelling was carried out after quenching by imposing a compressive axial strain of 1.5%.

Detailed mapping of residual stresses was performed in one tube out of each batch. This included measurement of strain components along the three principal tube directions as a function of position through the wall thickness. Since the tubes were significantly distorted from a perfectly cylindrical shape, this exercise was repeated at three different positions around the circumference and at two axial positions along the length of the tube. To evaluate the variation of residual strains within a given batch, the distribution of axial strain along the length of the tubes was measured along half the total length of each tube. In this paper only the through-wall variation of residual stresses at the position of maximum diametral distortion will be presented.

The residual strains were determined by measuring the d-spacings of the (110), (111) and (112) crystal planes of the α' phase. The experiments were carried out at the L3 triple-axis spectrometer located at the NRU reactor. The (113) planes of a Ge crystal were used to monochromate the neutron beam coming out of the reactor. The collimations of the incident and scattered beams were 0.1° and 0.2° , respectively. Wavelength calibration was performed using standard Si powder and the wavelength of the incident neutron beam was $2.6133 \pm 0.0001 \text{ \AA}$. The slits in the incident and scattered beams were arranged using absorbing Cd masks and designed such that the gauge volume, the diamond-shaped region of overlap between the incident and scattered beams, had dimensions (3.0 x 1.7 mm), (2.6 x 1.8 mm) and (2.1 x 2.2 mm) for the (110), (111) and (112) reflections, respectively. The tubes were mounted on a computer-controlled rotary table on top of an X-Y translator table. In this way, any point in the sample could be brought into the gauge volume with a precision of $\pm 0.1 \text{ mm}$. The rotary table permitted rotation of the tube about its own axis so that any point on the circumference could be accessed.

The values for the Bragg angles, $2\theta_{hkl}$, of the various diffraction peaks were obtained by least squares fitting a Gaussian line-shape on a sloping background to the experimental data of recorded counts versus scattering angle. The precision with which $2\theta_{hkl}$ can be measured depends on the line-width of the diffraction peak. For these uranium alloy experiments, the measured line-width was approximately twice the instrumental line-width and this effectively limited the precision with which the lattice spacing could be determined. Typically, the angular uncertainties in the measurements of the (110), (111) and (112) diffraction peaks were $\pm 0.007^\circ$, $\pm 0.010^\circ$ and $\pm 0.009^\circ$, respectively. This in turn implies errors of $\pm 0.0003 \text{ \AA}$, $\pm 0.0003 \text{ \AA}$ and $\pm 0.0001 \text{ \AA}$ in the measurements of the (110), (111) and (112) interplanar spacings, respectively. Because of the intrinsic line-width, no increase of experimental resolution would substantially improve the accuracy of the measured interplanar spacing. The effective transmission at the wavelength of the experiment is $I = I_0 e^{-0.697t}$, where t is the path length in cm. Typical values of I/I_0 for measurement of axial, hoop and radial strain components were 22%, 2% and 5%, respectively. In addition, the absorption process generates fast neutrons in U_{235} which easily penetrate the Cd mask in the scattered beam and increase the background at the detector. These factors make the experiment on uranium more than twice as difficult as on, for example, a steel tube. Typical values of the errors involved in the estimation of the residual strains were within the range 3×10^{-4} to 5×10^{-4} . These errors are 3 to 5 times greater than those usually associated with similar strain measurements in other materials.

RESULTS AND DISCUSSION

A typical Intensity vs. 2θ scan for the α' phase in U-0.8wt% Ti is illustrated in Fig. 1. As can be seen, the (110), (111) and (112) peaks can be resolved readily in angle from other reflections and this is partly why they were selected to estimate residual strains in the present material. The residual strain component, ϵ_r , in the direction of the normal to a crystal plane (hkl) with interplanar spacing d is given by,

$$\epsilon_r = (d - d_0)/d_0 \quad \dots (1)$$

The interest in the present tubes is in determining the macroscopic stresses generated by the various thermo-mechanical treatments. The values of d_0 employed in Eq. (1) were determined by machining small cylindrical samples from the tubes and measuring the interplanar spacings for the (111), (110) and (112) planes with the scattering vector aligned parallel to the radial direction of the tube where the lowest residual stresses were expected. These specimens were not annealed so as not to alter the microstructure of the material. Thus, the reference d_0 's do not correspond to a stress-free state. Since, residual microstresses, such as grain-interaction stresses, are not relieved when the specimens are machined from the tube. However, the d_0 's do provide a reasonable approximation to a state of zero macroscopic residual stress. The d_0 's for the (110), (111) and (112) planes in the γ -quenched condition were 2.5691, 2.2825 and 1.7865 ± 0.0002 Å, respectively. In the stress levelled condition the d_0 's were 2.5680, 2.2811 and 1.7849 ± 0.0002 Å for the (110), (111) and (112) planes, respectively.

Residual Stresses in γ -Quenched Tubes

The residual stress distribution across the wall thickness of one of the γ -quenched tubes is shown in Fig. 2. The stresses were calculated using the following expression,

$$\sigma_i = [E/(1+\nu)] * (\epsilon_i + [(\nu/(1-2\nu)) * (\epsilon_1 + \epsilon_2 + \epsilon_3)]) \quad \dots (2)$$

where E and ν are the bulk (isotropic) values of Young's modulus and Poisson's ratio, respectively ($E=195$ GPa, $\nu=0.209$). σ_i and ϵ_i are the principal components of the residual stress and strain tensors, respectively. The strains used in Eq. (2) were obtained by averaging the strains from the three different planes. This procedure was preferred since the strains calculated from the individual (hkl) d -spacings at a given location were all equal within the experimental error. The texture of the tubes was measured using neutron diffraction and the results indicated no significant degree of preferred orientation. Therefore, the residual stresses calculated assuming polycrystalline isotropy should be accurate to a first approximation.

Fig. 2 indicates that the axial (σ_A) and hoop (σ_H) components of the residual stress are both tensile and equal within the accuracy of the measurements. The error in the reported stress values is ± 50 MPa. σ_A and σ_H increase from about 200 MPa at 2 mm from the internal surface to a maximum of about 550 MPa near the centre of the tube wall thickness. They decrease continuously towards the external surface of the tube until at about 5 mm from the external wall become compressive and reach a maximum of about -600 MPa 3 mm from the external surface. It is noteworthy that the variation of σ_A and σ_H through the wall thickness is not symmetric around the tube axis. The magnitude of the radial component of the stress (σ_R) remains within ± 100 MPa through the wall thickness with a maximum tensile stress of about 75 MPa near the centre of the tube wall. σ_R is compressive in the regions between 0 and 4 mm from the internal surface and between 0 and 6 mm from the external surface.

Fig. 3 gives the variation of the axial component of residual strain along the length of the tube. This gives a clear indication of the variation of residual stresses along the length of the tube which would be very difficult to evaluate using mechanical relaxation methods.

The observed residual stress field resulting from γ -quenching is due to

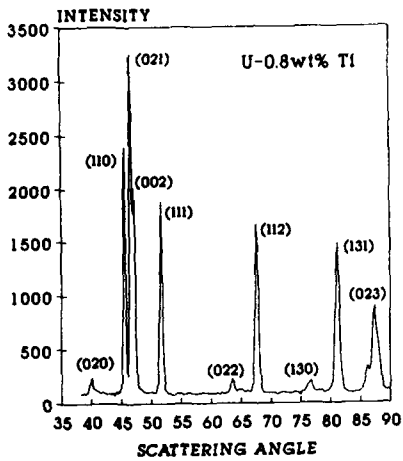


Fig. 1 Neutron diffraction pattern for U-0.8wt% Ti (wavelength: 1.9896 Å)

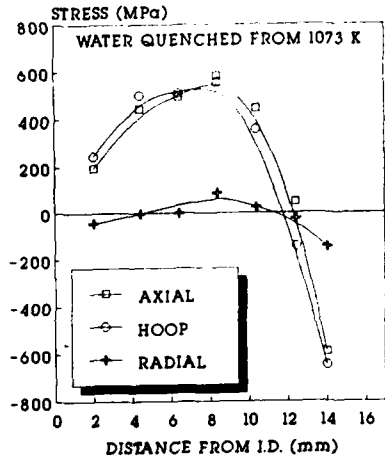


Fig. 2 Residual stresses induced by quenching in U-0.8wt% Ti tubes.

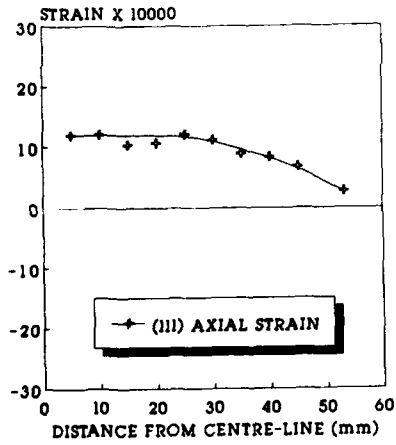


Fig. 3 Longitudinal variation of the axial strain component at mid-thickness in quenched U-0.8wt% Ti tubes.

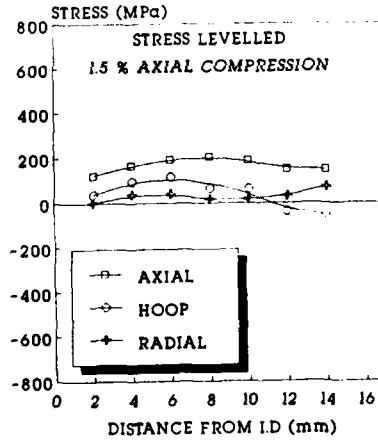


Fig. 4 Effect of axial stress levelling on the residual stresses present in quenched U-0.8wt% Ti tubes.

the interaction between: (i) thermal stresses, introduced by inhomogeneous changes in volume across the tube wall due to the temperature and cooling rate gradients and, (ii) transformation stresses, generated by the volume changes and lattice distortions associated with the $\gamma \rightarrow \alpha'$ phase transformation. The $\gamma \rightarrow \beta$ phase transformation is suppressed due to the fast cooling rates which promote phase transformation by a martensitic mechanism. Annealing at 1073 K eliminates any pre-existing stresses in the material and, therefore, the residual stresses after γ -quenching do not depend on the previous state of the material.

The evolution of thermal stresses can be understood qualitatively by considering that the cooling rate at the surfaces of the tube is greater than at the center of the wall. Thus, material in the surface layers contracts faster and more severely than the material in the interior. Due to the mutual constraints that develop because of the inhomogeneous volume changes, transient tensile stresses are generated at the surfaces and, because of equilibrium requirements, compressive stresses are produced in the interior. The yield strength of α' is about 20 times larger than that of the γ phase, [3], thus, plastic relaxation takes place more easily in the partially transformed interior than in the fully transformed surface regions and, therefore, the transient compressive stresses at the centre do not build up very much. As the temperature continues to decrease the cooling rate gradient changes sign and the centre contracts faster than the surfaces. The situation is now reversed and transient compressive stresses develop at the surfaces while the centre is in tension. At the lower temperatures the local yield strength only depends on the local temperature since most of the material has transformed to martensite. As cooling progresses the transient stresses generated by the temperature and cooling rate gradients can no longer be relieved by local plastic deformation. As the tube tends to thermal and dimensional equilibrium at room temperature, the transient stress state evolves into a state of residual macroscopic stresses in which the tube surfaces are in compression while the material within the central region is in tension. It should be pointed out that the final magnitude of the residual stresses depends on the magnitude and distribution of plastic strain during the quenching operation.

On quenching, the shape change associated with the $\gamma \rightarrow \alpha'$ transformation is accommodated by a 0.6% volume contraction [3] and local plastic deformation. The evolution of transformation stresses as the γ phase transforms to α' is then completely analogous to that observed in the absence of the phase transformation, as described above. The state of residual stresses in the tube after quenching is, therefore, a result of the additive contributions of thermal and transformation stresses. Recent analytical parametric studies using finite element techniques [3] have shown that transformation stresses account for less than 20% of the overall residual stresses in γ -quenched U-0.8wt% Ti tubular components.

Residual Stresses in Stress-Levelled Tubes

The residual stress field across the wall thickness of a stress-levelled tube is illustrated in Fig. 4. The position of measurement corresponds to maximum diametral distortion at half way along the length of the tube. Compressive deformation largely relieves the residual stresses generated by γ -quenching. The three principal components of stress are approximately constant between 2 and 14 mm from the internal surface. σ_r and σ_θ are both within 50 MPa of zero while σ_A attains a value of about 180 MPa. Equilibrium requires the σ_A to be compressive at regions near the surfaces of the tube. Assessment of this condition requires a modification of the experimental set up to increase the spatial resolution by decreasing the dimensions of the gauge volume. The scope of this investigation did not allow for verification of this condition and further work is required to clarify this subject. The present results indicate that although axial compression significantly

relieves the magnitude of σ_A , axial residual stresses as high as 20% of their value in the γ -quenched condition still remain after stress levelling. The significance of this finding is that the distortion observed after machining stress levelled solid and hollow cylinders can be attributed to the effect of the axial residual stress left after the stress levelling operation.

The considerable stress relieving effect caused by axial compressive deformation can be attributed to the anisotropy of plastic deformation exhibited by α -U at room temperature. Slip usually takes place on the (010)[100] system [4]. Since this system is unique, in the sense that there is only one variant in the orthorhombic structure, unfavourably oriented crystals must find other ways to accommodate the imposed strains.

Mechanical twinning is by far the most common deformation mechanism in α -U at room temperature. Frequently observed twinning systems in α -U are (130)[3 $\bar{1}$ 0] and (1 $\bar{7}$ 2)[312] [4]. Twinning is an effective mechanism of stress relaxation since it produces large lattice reorientations which can bring the crystals to more favourable orientations which then allow the activation of other deformation mechanism leading to lower stresses.

A further room temperature mechanism of plastic relaxation in α -U is kinking [4]. When the orientation of a grain is such that compressive strains must be accommodated parallel to the [100] direction, slip and twinning cannot relieve the stress which then builds up elastically. The slip planes then "collapse" so that a grain becomes divided into several wedge-shaped regions with the slip direction inclined at various angles to the compression direction. While this process accommodates the required compressive strain, the local lattice reorientation facilitates the activation of easier deformation modes which relieve the high elastic stresses generated when the grains cannot deform plastically. It is thought that the stress relieving produced by uniaxial compression can be attributed to the twinning and kinking processes that take place when α -U is plastically deformed.

CONCLUSIONS

Neutron diffraction provides a unique method of evaluating non-destructively residual stresses fields in thermomechanically treated uranium alloy products.

The residual stress distribution through the wall thickness of γ -quenched U-0.8wt% Ti is nearly equi-biaxial with compressive hoop and axial stresses at the surfaces and tensile stresses in the middle of the tube wall. The magnitudes of these stress components reach values as high as $0.75\sigma_y$. The residual stress state arises from the additive contributions of thermal and transformation stresses developed during quenching.

Effective stress relieving of γ -quenched U-0.8wt% Ti tubes can be achieved mechanically by imposing axial compressive strains. The hoop and radial stresses are approximately uniform at ± 50 MPa through most of the thickness of the tubes. Axial residual stress components with magnitudes of about 20% of that in the γ -quenched condition can still be observed after stress levelling. It is suggested that these can be responsible for the distortion observed after machining operations in stress-levelled tubes.

REFERENCES

- 1.- K.H. Eckelmeyer, SAND85-1427, Sandia National Laboratories, 1985.
- 2.- H.J. Prask and C.S. Choi, J. Nucl. Mater., 126, 124 (1984).
- 3.- G.M. Ludtka, Private communication, 1989.
- 4.- R.W. Cahn, Acta Metall., 1, 49 (1953)

NEUTRON MEASUREMENT OF RESIDUAL STRESSES IN A USED RAILWAY RAIL

P.J. WEBSTER*, K.S. LOW*, G. MILLS* AND G.A. WEBSTER**

*Department of Civil Engineering, University of Salford,
Salford, M5 4WT, UK**Department of Mechanical Engineering, Imperial College, London,
SW7 2AZ, UK

ABSTRACT

The high resolution neutron diffraction technique has been applied to determine, non-destructively, the residual stress distribution developed in the head of a railway rail after normal service.

Measurements were made, using the neutron strain scanner at the Institut Laue Langevin, Grenoble, on a transverse slice of rail 12mm thick taken from a section of straight track. The rail head was scanned in the three principal orientations in a series of parallel traverses sufficiently close to enable a two-dimensional matrix of data to be accumulated and vertical, transverse and longitudinal residual stress contours to be drawn.

Substantial residual compressive and tensile stresses and steep stress gradients were observed related to the depth below the top surface, distance from the running line and shape of the rail head. The highest stresses and stress gradients were observed in transverse and vertical directions but significant stresses were also retained in the longitudinal (12mm thick) direction of the rail.

The results demonstrate the effectiveness and unique characteristics of the neutron technique to determine non-destructively and continuously the residual stresses inside engineering components.

INTRODUCTION

Residual stresses and rails

Residual stresses can be an important factor influencing the failure processes and service lives of engineering components. These stresses may be introduced deliberately or incidentally during the manufacturing process or they may develop during service, usually as a result of non-uniform plastic strain. They may be beneficial in reducing total stresses if they are opposed to applied stresses or detrimental if they add to them. Examples of beneficial residual stresses deliberately introduced into engineering components are those induced in surface layers by shot peening or to deeper depths into the interior of cylindrical pressure vessels by autofrettage [1]. In both of these cases the stresses induced parallel or tangential to the surface are compressive and have the effect of inhibiting crack propagation from surface defects. The compressive stresses near the surface must, however, be balanced by tensile stresses within the body of the component and these can be detrimental if there are internal imperfections at which cracks can initiate or if surface cracks have propagated a significant distance into the component.

The manufacture of railway rails involves repeated hot rolling to produce the required rail profile, followed perhaps by

a variety of heat-treatments, cooling and then straightening as necessary. The steel composition and fabrication processes are chosen to produce high surface hardness to resist wear, and high flow stress to resist plastic deformation, but also combine to induce residual stresses within the rails [2].

In service the residual stresses that were present initially due to the production process are modified by what is known as "shakedown". Subsequently a characteristic and substantial residual stress pattern evolves which is related to track parameters, train speeds, axle loads and cumulative service load. In service the wheel flange may scrub the gauge corner, particularly on tight curves, resulting in abrasive wear. Also, with axle loads perhaps in excess of 30 tonnes, the load will plastically deform the rail head in the vicinity of the region of the running line. This repetitive loading can result in rolling contact fatigue which together with the residual stresses and any material defects in the rail and the effects of braking, accelerating and skidding, can lead to wheelburns, flaking, shelling, squats and tache ovaies. These defects, the residual stresses and abrasive wear will ultimately increase the risk of rail fracture and possible derailment [3,4].

Residual stress measurement

Most traditional engineering methods for determining residual stresses involve the use of a number of surface mounted strain gauges to measure the relaxations that occur when a component is drilled or cut [5]. The techniques are destructive, are limited in the number of measurements which may be made and require calculations which become uncertain for all but relatively simple shaped components.

In the high resolution neutron diffraction method residual stresses are calculated from measurements of the small changes in the angles at which Bragg reflections occur when a crystalline lattice is strained [1,3,6,7]. Bragg reflections occur at angles 2θ relative to the incident beam direction given by the equation:

$$2d\sin\theta = \lambda \quad (1)$$

where d is the interplanar spacing and λ is the neutron wavelength. Differentiation of equation (1) at a constant wavelength gives:

$$\delta\theta = -\tan\theta \cdot \delta d/d \quad (2)$$

The lattice strain ϵ , in the direction of the scattering vector Q , is thus given by:

$$\epsilon = \delta d/d = -\delta\theta \cdot \cot\theta \quad (3)$$

Strains at different points within a component may be determined by measuring the relative shift in Bragg angle that occurs as the component is scanned by translating it through the small sampling volume that is defined by precise masking and is irradiated by a collimated beam of monoenergetic neutrons. Components of the strains in different directions may be obtained by rotating the component to align the specified direction along the scattering vector. In general it requires at least six

measurements in different directions to obtain the full strain state but, for plane stress conditions, or if the principal stress directions are known, measurements in three orthogonal directions will usually suffice. Stresses are calculated from the measured strains in the usual manner using the appropriate Young's Modulus and Poisson's Ratio [1,2,5,6].

EXPERIMENTS

Measurements were made on a transverse section of railway rail 12mm thick, taken from a straight section of British Rail track, using the D1A high resolution neutron diffractometer at the Institut Laue Langevin, Grenoble. The diffractometer had been adapted for use as a strain scanner using the Salford/Imperial "Engineering Package" comprising a specimen translator/rotator, precise neutron beam definition and "UTOPIA" software.

Scans were made in the three principal orientations, X, Y and Z, corresponding to longitudinal, transverse and vertical directions in the rail, respectively, using a 2mm cubic sampling volume. Data, for the (211) reflection using a wavelength 0.19nm, were collected in a series of parallel Z traverses from the top of the rail, $z = 0$, to a depth of 40mm into the head at locations $y = 0, \pm 8, \pm 16, \pm 24$ and ± 30 mm from the centre line as indicated in figure 1. The angular positions, widths and integrated intensities of the reflections were determined using a Gaussian peak fitting routine and strains were then calculated for the three orientations X, Y and Z from the peak shifts. The data were subsequently combined to calculate the corresponding stresses. Typical accuracies were ± 25 MPa.

RESULTS

Two-dimensional stress contours were computed from the matrix of measured longitudinal, transverse and vertical stresses using an interpolation routine. The results are shown in figures 2-4. The gauge side of the rail is indicated by negative values of y and the gauge corner is seen to be the more rounded. The centre of the running line was at $y = 6$ mm, to the outer side of the rail as indicated in figure 1.

The specimen of rail investigated was a transverse slice 12mm thick taken from a long straight section of track. It is to be expected that the cut slice would retain most of the vertical and transverse stresses of the original long rail but that the longitudinal stresses would be substantially relaxed. This appears to be shown in the figures 2,3, and 4.

The measured longitudinal stresses exceed -75MPa compression and 100MPa tension, with a tensile region below the running line. Compression, shown shaded on the figures, is highest at a depth below the top surface of about 5mm. Below this there is a broad tensile region stretching across the centre of the rail head which changes to compression near the bottom corner of the head.

The measured transverse stresses vary between -225MPa and +275MPa with a marked compressive region extending from the top surface to a depth of about 6mm to 10mm where the stress gradient is very steep. A broad tensile region then extends to a depth of about 35mm with the highest tensions located in two regions

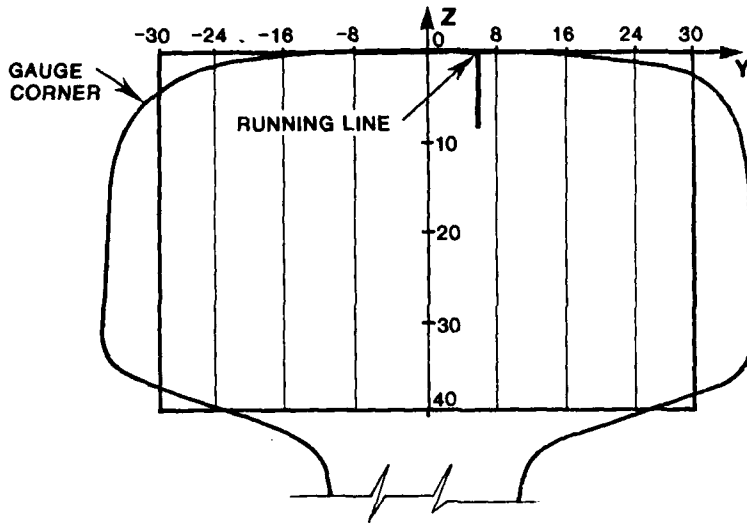


Fig 1. Transverse section through the rail head showing the measuring grid in mm and position of the running line.

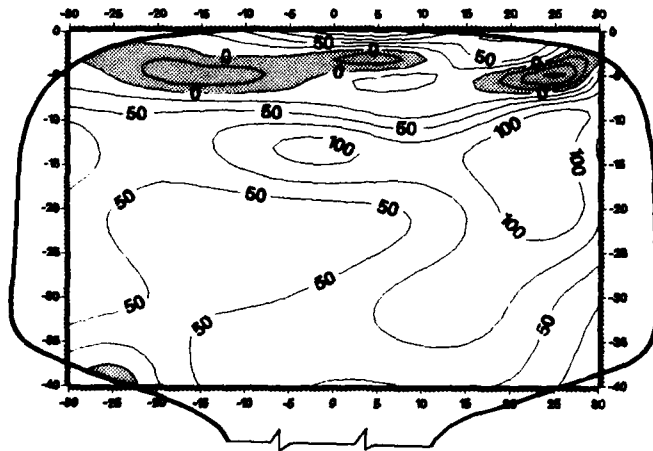


Fig 2. Longitudinal residual stresses in a rail head (MPa)

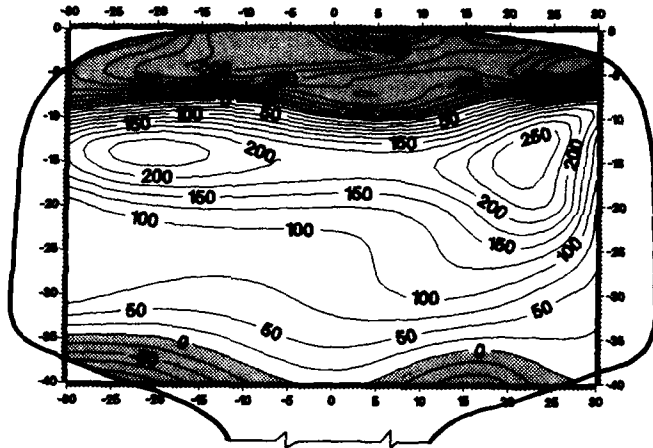


Fig 3. Transverse residual stresses in a rail head (MPa)

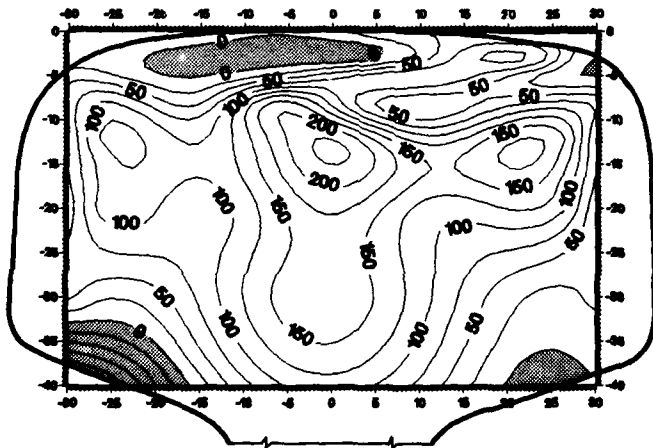


Fig 4. Vertical residual stresses in a rail head (MPa)

either side of the running line at a depth of about 14mm.

The vertical stress pattern shows an outer low stress or moderately compressive region surrounding a central T-shaped tensile region where maxima exceed +225MPa, again at a depth of about 14mm, but extending further vertically down the centre line towards the web. There is an asymmetry to all the patterns which is clearly related to the position of the running line.

DISCUSSION

If it is assumed that the measured, partially relaxed, longitudinal stresses may be scaled up, in accordance with other evidence, to values similar to those measured in the transverse and vertical directions a good picture is obtained of the residual stresses present in the long rail. The combined patterns show features that suggest that residual stresses similar to those measured could play a large role, in particular circumstances, in inhibiting or furthering the development of defects such as squats, in which horizontal cracks propagate a few millimetres below the running surface, and of taches ovales, which occur when the cracks descend at a steep angle into the tensile region of the head.

The results demonstrate the effectiveness and unique characteristics of the neutron technique to determine non-destructively, continuously and accurately the residual stresses inside engineering components.

REFERENCES

1. A. Stacey, H.J. MacGillivray, G.A. Webster and K.R.A. Ziebeck, *J. Strain Analysis* **20** 93-100 (1985).
2. F.D. Fischer, E. Hinteregger and F.G. Rammerstorfer in International Conference on Residual Stresses ICRS2, edited by G. Beck, S. Denis and A. Simon (Elsevier Applied Science, London, 1989) pp. 467-472.
3. G.A. Webster, M.A.M. Bourke, H.J. MacGillivray, P.J. Webster, K.S. Low, D.F. Cannon and R.J. Allen, International Conference on Residual Stresses ICRS2, edited by G. Beck, S. Denis and A. Simon (Elsevier Applied Science, London, 1989) pp. 203-208.
4. C. Urashima, S. Nishida and K.S. Yawata in International Conference on Residual Stresses ICRS2, edited by G. Beck, S. Denis and A. Simon (Elsevier Applied Science, London, 1989) pp. 912-918.
5. C.G. Schilling and G.T. Blake, United States Steel Report No. R-477, 1981.
6. A.J. Allen, M.T. Hutchings and C.G. Windsor, *Adv. Phys.* **34** 445-473 (1985).
7. D.J. Smith, R.H. Leggatt, G.A. Webster, H.J. MacGillivray, P.J. Webster and G. Mills, *J. Strain Analysis* **23** 201-211 (1988).

NEUTRON DIFFRACTION MEASUREMENT OF THE STRESS FIELD DURING
FATIGUE CYCLING OF A CRACKED TEST SPECIMEN

M.T. HUTCHINGS, C.A. HIPPSLEY AND V. RAINEY
Materials Physics and Metallurgy Division, Harwell Laboratory, Didcot,
OX11 0RA, United Kingdom.

ABSTRACT

The triaxial stress field has been measured along the centre line of a compact tension specimen in the direction of cracking. The specimen had been subjected to $\sim 60,000$ cycles at $\Delta K=31$ and $K_{\max}=34$ MPa mm $^{3/2}$ and was bolted open at maximum stress. The field was remeasured after the stress had been fully relaxed. The results are discussed in terms of expectations from fracture mechanics calculations.

INTRODUCTION

Neutron diffraction enables the absolute full stress tensor within a metallic sample to be measured nondestructively [1]. Stresses which have previously only been determined by theoretical methods can now be tested experimentally. In this paper we report the initial results from the measurement of the triaxial stress field along the line of cracking of a compact tension, fatigue test, specimen which had been subjected to fatigue cycling.

SPECIMEN

The specimen of ferritic steel, BS 4360, had overall dimensions of 31.5 mm high (Oz), 49.6 mm along the crack direction (Ox), and 13.1 mm thick (Oy). A threaded hole enabled a bolt to be screwed in to maintain a determined stress level. It was designated W1, and is illustrated in the inset of figure 1, where the axes are defined relative to an origin at the geometric centre of the specimen. As all the values of x in this paper are negative, the sign is omitted. The notch, 2.6 mm high at the edge, ended at x = 9.1 mm, and the crack ran from x = 9.1 mm to 12.7 mm at the centre of the specimen and to x = 11.7 mm at the outside. The edge of the sample was at x = 24.8 mm.

The specimen had been cycled $\sim 60,000$ times to induce a crack of inner length 3.6 mm, with a stress intensity level varying between minimum of $K=3$ and maximum $K=34$ MPa mm $^{3/2}$. The fatigue cycling was stopped at the maximum level, and the bolt screwed in place to maintain the stress during stage one of the measurements. The manner in which the bolt was tightened, however, caused the load to increase above the maximum cycling load, subjecting the specimen to plastic strain over a large volume from the crack tip to the edge of the specimen (x = 24.8mm). The yield stress of the material is $\sigma_{yld} = 375$ MPa. As this was exceeded, the J integral was calculated, and found to be 29.2 kN/m at the maximum load. From this value an effective $K_{eff} = 78$ MPa mm $^{3/2}$ can be calculated, corresponding to what it would have been if linear elastic theory had held during the extra loading.

The J-integral value was used together with a finite element stress analysis for the compact tension specimen geometry to calculate the peak stress at the crack tip. Assuming plane strain, this was found to be 1400 MPa, or 3.73 times the σ_{yld} , located at 0.065 mm from the crack tip. If the

extra load had not been applied, this distance would have been smaller but the crack tip maximum stress would have been similar.

The main consequence of the large plastic strain of the sample is that when the bolt was removed for the second stage of measurements, the crack was not compressed to as great an extent by the elastic relaxation of surrounding material as would have been the case if no extra loading had taken place. Hence a smaller compressive principal (crack-growing) stress, σ_z , is expected.

A 'stress free' sample was used to determine the reference Bragg angles. This sample, designated W4, was a piece cut from a similar specimen, $\sim 13 \times 11 \times 14.5 \text{ mm}^3$ in size, and was heat treated by annealing in air at 850 C for one hour followed by a slow cool.

THEORY

The elastic lattice macrostrain, e , is measured along the direction of the scattering vector $\vec{Q} = (\vec{k}_i - \vec{k}_f)$, where \vec{k}_i and \vec{k}_f are the incident and scattered neutron wavevector respectively, with wavelength $\lambda = 2\pi/k$. It is given by

$$e = (d - d_0)/d_0 = -(\phi - \phi_0) \cdot (\cot(\phi/2)) / 2 \quad (1)$$

where $\phi = 2\theta$ is the scattering angle of the Bragg reflection from the sampled volume under stress, and $\phi_0 = 2\theta_0$ is the scattering angle of the same reflection from a 'stress-free' sample. d and d_0 are the corresponding lattice plane spacings, so that $2d \sin\theta = \lambda$.

The strain is measured along 3 perpendicular principal directions, here assumed to lie along O_x, O_y, O_z in figure 1, to give e_x, e_y, e_z . The stress in these directions, i , is then given by

$$\sigma_i = \frac{E}{(1+\nu)} e_i + \frac{\nu E}{(1+\nu)(1-2\nu)} (e_x + e_y + e_z) \quad (2)$$

For mild steel $E=207 \text{ GPa}$ and $\nu=0.28$, and these values apply well to strains measured by the (112) reflection [2]. A spreadsheet programme allowed e_i and σ_i , with errors, to be readily calculated from the measured ϕ and ϕ_0 .

EXPERIMENTAL PROCEDURE

The strain measurements were made using the D1A diffractometer at ILL Grenoble. The incident neutron beam of 1.905Å wavelength from a vertically bent Ge(115) monochromator was carefully defined using the high precision system developed by P Webster and kindly loaned for this experiment. Masks in the diffracted beam, at $\sim 109^\circ$ scattering angle from the ferritic steel (112) reflection, were also carefully positioned between the specimen and soler in front of the counter.

The specimen was placed on a platform capable of being translated in three perpendicular directions, the assembly being mounted on the sample table of the diffractometer. The translations were along the scattering vector \vec{Q} , perpendicular to \vec{Q} , and vertical. By rotating about the sample table vertical axis, the position on the platform of the axis, through which the beam passed, could be determined using a needle viewed by a theodolite. The vertical height of the beam relative to the platform could also be determined by the theodolite, which was used to carefully position the sample in the vertical plane. The whole translation assembly could be rotated by the sample table axis. In this way measurement of the strain along two

perpendicular directions, e_x and e_y , could be measured automatically at a series of values of x . Measurements of e_z were made with the sample turned so that the notch and Ox were vertical, varying x by the vertical slide.

The beam from the monochromator on the D1A diffractometer is vertically focussed on to the sample position, and therefore masking to give the necessary small sampling volume at the specimen position is difficult. Apertures of 4x4 mm and 1x1 mm at ~60 mm and 10 mm before the sample in the incident beam, and 1x52 mm at about 80mm after the sample and 4x80 mm before the soller-detector system in the scattered beam, defined a sampling volume of ~1 mm³ in the specimen. This was verified by a photograph at the specimen position. The resolution volume along Q was therefore ~1.5 mm and vertically it was 1 mm. This gave a suitable compromise between count rate and volume resolution. Counting times were typically between 5 and 15 min. depending on the path length of the beam in the sample. Throughout the measurements the monochromator was isolated so that λ was fixed.

The scattering angles ϕ ~109.4° were determined from the profile of intensity against counter angle using the standard routine PKFIT, which gave a typical accuracy of $\pm 0.007^\circ$ and widths of 0.350°. Only where the strain varied rapidly with position x were peaks observed which were broader than this resolution width. The scattering angle from the stress-free block W4 in three orientations gave $\phi_s = 109.496 \pm 0.005$, in good agreement with that from a corner of the specimen W1 where the stress is expected to be zero.

Measurements of e_x , e_y and e_z were made at close intervals of x , of ~0.25mm, near the position of the crack tip, and of 2mm in the region well away from the tip. Positioning was judged to be to 0.2mm or better. The stress was calculated from equation (2), and where all three strain values were not measured at the same value of x interpolated values were used. The stress variation for the sample held at maximum stress at the crack tip, stage 1, is shown in figure 1, and in the relaxed state, stage 2, in figure 2. Typical error bars are shown.

DISCUSSION AND CONCLUSION

The measurements show that along its centre line the specimen was neither in a state of plane strain nor plane stress at either stage. In the bolted state the peak measured stress of $\sigma_z = 500$ MPa, is much less than the 1400 MPa calculated, and in plane strain one would expect ($\sigma_z - \sigma_x$) to be equal to σ_{yld} [3]. In fact this is also less by ~ 1/3. This difference from the expected values could be partly due to the effects of volume resolution, as the strains were averaged over ~1.5 mm. These resolution effects are currently being investigated.

On relaxing the specimen, stage 2, the peak value of σ_z moves out by ~2 mm from the crack tip, and the values of σ_z and σ_x are only slightly compressive at the tip. This is a result of the large plastic strain on bolting the specimen, without which one would have expected a compressive stress at the tip of equal magnitude to the tensile stress under maximum K.

The movement of the peak stress during load cycling has important implications for the modelling of stress-driven solute segregation during fatigue crack growth. Nakasa et al [4] propose a model for hydrogen diffusion to a growing fatigue crack tip based on motion of the peak stress region towards the crack tip on unloading. The current measurements in fact indicate motion in the opposite direction. In either case embrittling solutes such as hydrogen, at low temperature [4], or sulphur, at high temperature [5], would be driven by a moving stress peak during fatigue

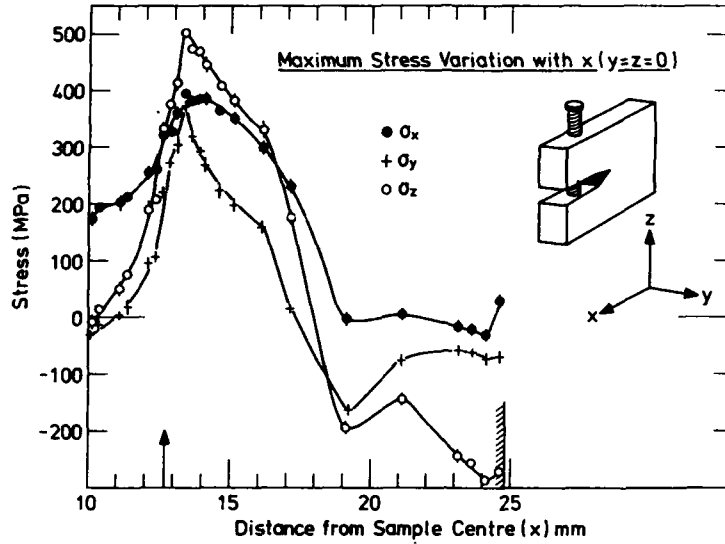


Figure 1 Triaxial stress variation with position x , with the specimen in the bolted, maximum crack-tip stress, stage one, configuration. The arrow denotes the position of the crack tip on the specimen centre line, and the shaded line the outer edge of the specimen.

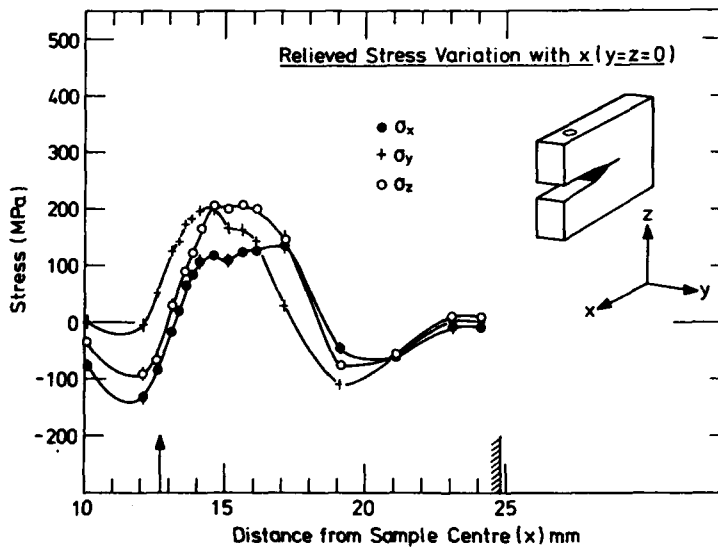


Figure 2 Triaxial stress variation with position x , with the specimen in the relaxed state, stage two.

fracture, and calculations of crack tip solute enrichment must take this into account.

It is clear that better experimental volume resolution would improve the comparisons made in order to test theory, and that this would be best accomplished using a larger specimen of the same width as it is unlikely that sufficient diffraction intensity would be given by a smaller sampling volume. Further experiments are planned to measure the stress field without the excess load on bolting, when a comparison with the present data will indicate the effects of crack opening on the stress field.

ACKNOWLEDGEMENTS

We are grateful to Dr. P. Webster of Salford University for the loan of his beam masking system at I.L.L Grenoble. The work was undertaken as part of the Underlying Research Programme of the U.K.A.E.A.

REFERENCES

- [1] A.J.Allen, M.T.Hutchings, C.G.Windsor, A.Andreani, *Adv. in Phys.* 34, 445 (1985).
- [2] A.J.Allen, M.Bourke, W.I.F.David, S.Dawes, M.T.Hutchings, A.D.Krawitz, C.G.Windsor, *Proc. ICRS-2, Nancy, France*, Ed.G.Beck et al (Elsevier, Amsterdam, 1989) p78.
- [3] J.F.Knott, *Fundamentals of Fracture Mechanics* (Butterworths, London, 1973).
- [4] K.Nakasa, H.Takei, K.Kajiwara, *Eng. Fract. Mech.* 14, 507 (1981).
- [5] P.Bowen, C.A.Hippesley, J.F.Knott, *Acta Metall.* (to be published 1990).

THE MEASUREMENT OF BORON AT SILICON WAFER SURFACES BY NEUTRON DEPTH PROFILING

R.G. DOWNING*, J.P. LAVINE**, T.Z. HOSSAIN**, J.B. RUSSELL**, AND
G.P. ZENNER**

*Center for Analytical Chemistry, National Institute of Standards and
Technology, Gaithersburg, MD 20899

**Research Laboratories, Eastman Kodak Company, Rochester, NY
14650-2008

Abstract

The thermal neutron reaction $^{10}\text{B}(n,\alpha)^7\text{Li}$ is used to measure the boron concentration on the surface of silicon wafers. The technique, referred to as neutron depth profiling (NDP), requires no special sample preparation. Boron is determined on the as-received wafers at a level of 10^{12} to 10^{13} atoms/cm². A boron level of about 2×10^{12} atoms/cm² is found at the wafer surface after oxidation, epitaxial, or polycrystalline silicon deposition. Additional measurements are given from SIMS measurements of multilayer structures on silicon also showing the presence of boron. Ambient air appears to be a significant source of the boron.

Introduction

Neutron absorption reactions with boron and a few other low-Z elements exhibit exoergic nuclear reactions that yield charged particle reaction products. Those reactions which also have high thermal neutron capture cross sections are fundamental to the technique of neutron depth profiling (NDP). The basics of the technique, typical applications, and descriptions of the NDP facilities within the U. S. have been described at two recent conferences and elsewhere in the literature [1-3]. NDP is often the technique of choice for the determination of boron at the surface, at an interface, or within a near-surface region as the method is not sensitive to the chemical structure of the material but only the atomic environment. Furthermore the neutron depth profiling (NDP) technique requires no special sample preparation before the analysis. The specific reaction of $^{10}\text{B}(n,\alpha)^7\text{Li}$ is used by NDP to accurately determine the concentration and the spatial distribution of boron in many of the principle materials used in the fabrication of silicon semiconductor devices [3]. In this study the presence of boron at the surface of intrinsic silicon and at the interface of processed silicon wafers is shown using NDP and secondary ion mass spectrometry (SIMS).

Low levels of boron have been detected previously at the surface of crystalline silicon wafers after processing. Boron is observed after a vacuum anneal [4], after various types of cleaning [5,6], and after silicon molecular beam epitaxy [7-11]. Additional discussion is given by Robbins et. al. [10]. The boron is detected by spreading resistance [4] or by SIMS [5-11]. Generally boron is measured after a high temperature processing step thus diffusing the boron into the silicon. Slusser and MacDowell [5] deposit a polysilicon layer to enable the use of SIMS without a high temperature treatment. However, even this introduces additional processing that may complicate the isolation of the source of a surface contaminant such as boron. The thermal neutron-induced nuclear reaction $^{10}\text{B}(n,\alpha)^7\text{Li}$ is used in this work to provide a direct quantitative

determination of the presence of boron at the surface of as-received wafers without further preparation of the wafers. In addition, wafers with an oxide, polysilicon layers, and an epitaxial silicon layer are analyzed for boron. The resulting observations provide direct evidence for the suggestion of Iyer et al. [7] and Kubiak et al. [8] that some boron contamination occurs upon exposure of the wafers to air and further substantiate Casel et al. [9] experimental results that indicate air is a source of boron contamination.

Experimental and Discussion

The thermal NDP facility at the NIST was used for these measurements. The facility uses a thermal neutron beam of ~1 cm in diameter from the 20 MW nuclear research reactor to analyze materials. Because of the low energy (~10⁻² eV) of the individual neutrons used in the analysis and their uncharged state, the material under investigation is left virtually undamaged. The nuclear reaction $^{10}\text{B}(n,\alpha)^7\text{Li}$ occurs with the production of monoenergetic and isotropically emitted alpha particles of energy 1.47 MeV or 1.78 MeV. A charged particle detector, placed normal to the surface of the wafer at a distance of a few cm, detects and measures the residual energy of the alpha particles. For example, alpha particles originating at the wafer surface will show the full 1.47 or 1.78 MeV of energy, but particles originating from within the near surface of the wafer will have lost some of their energy in exiting the wafer. Therefore, the count versus the measured energy spectrum provides information about the depth distribution of the boron within a sample [3]. Figure 1 shows both the nuclear decay scheme for the ^{10}B reaction and the resulting particle energy spectrum versus number of particles detected for the case when all the boron lies at the sample surface. The width of the peaks is due to detector and system resolution and the energy scale is partitioned into 1024 channels. In a typical analysis of the 1.47 MeV alpha particle, the decreasing energy for the detected alpha particles corresponds to about 5 nm in depth of silicon per channel. Depth increases to the left in the spectrum.

Figure 2 gives the NDP results for the total front surface boron of 100 mm diameter n-type Czochralski wafers from three different vendors. The wafers were removed from the sealed as-received boxes at the time of measurement for vendors B and C. Approximately three minutes elapsed between the opening of a box until the wafer was in the vacuum (~10⁻² Pa) of the NDP chamber. The box of wafers from vendor A had been opened several weeks earlier. The electrical resistivity and interstitial oxygen concentration was determined by the vendor. In order to optimize the detection limit for boron by NDP the charged particle detector was placed about 1 cm from the sample, however this configuration precludes the determination of a depth distribution for the boron [12,13]. The measured ^{10}B signal was converted to a total boron surface concentration by assuming normal isotopic abundance. The highest boron level is seen on the wafer from vendor C. The back surface of this wafer is shown to have the approximately same level of boron as the front surface. The vendor-to-vendor variation seen in figure 2 indicates that wafer processing is likely responsible for part of the observed boron and recent work supports this suggestion [9,14].

The NDP system boron background was measured at about 1.5×10^{11} atoms/cm² and is shown in figure 2. The boron background of the NDP system was determined by placing a piece of 7.5 μm thick polyimide film over a silicon wafer during one of the analysis. It is possible that the background is overestimated using this procedure should the polyimide be contaminated with traces of boron, however no cleaner surface was available at the time of the

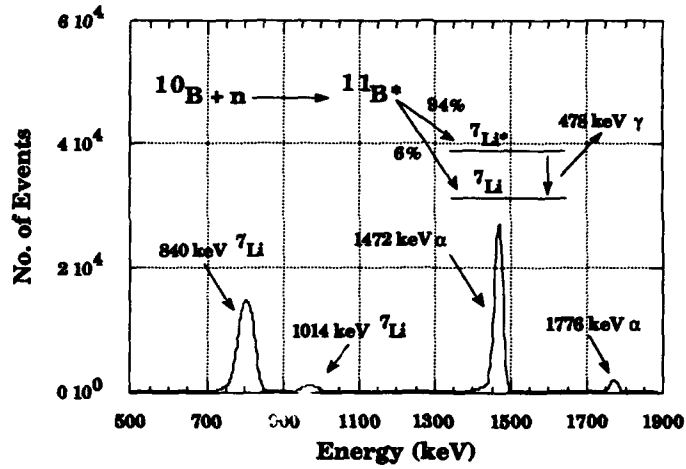


Figure 1. Energy spectra for particles emitted from the reaction of ^{10}B with thermal neutrons where boron lies only at the surface of the sample. Also shown is the nuclear decay diagram for the nuclear reaction.

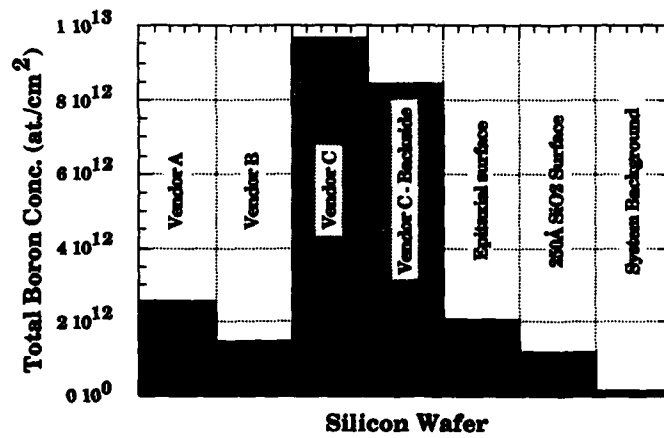


Figure 2. Total surface boron as determined by NDP for a series of silicon wafers. See text for discussion of sample.

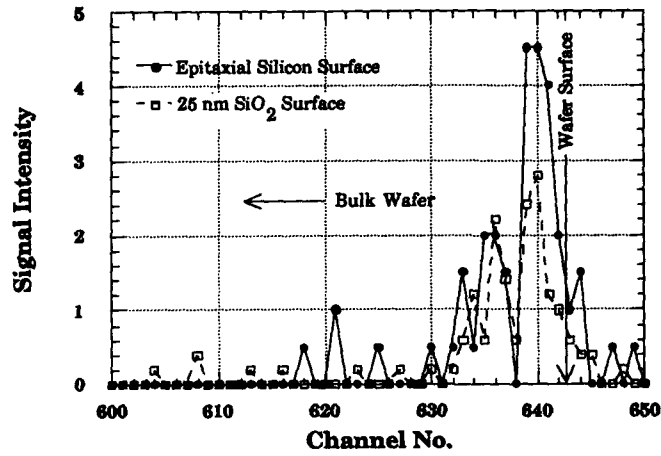


Figure 3. NDP spectrum of boron signal. The solid line (—) is for a silicon wafer covered with an epitaxial silicon layer and the dashed line (- -) is for a wafer covered with a thermally-grown oxide. The sample surface is indicated.

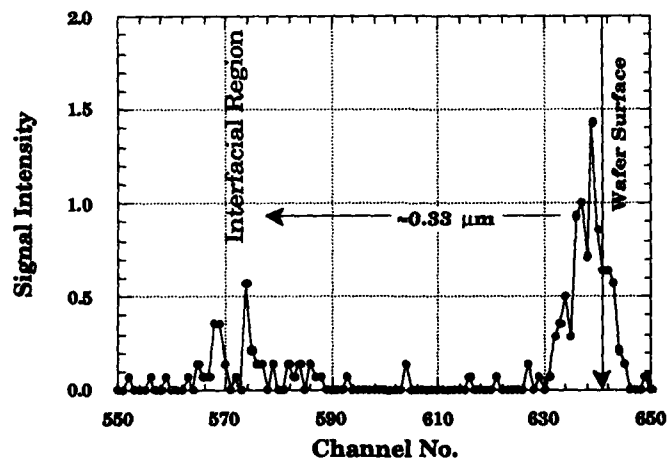


Figure 4. NDP spectrum of boron signal for a silicon wafer with about $0.33 \mu\text{m}$ of polysilicon layer over a thermal oxide. The surface is indicated.

analysis. The background contribution to the boron observed on the wafers has been subtracted from concentration shown for the wafers given in figure 2. Because the observed boron signal is near the detection limit for the analysis time used in these measurements, the total uncertainty on the boron concentration for these wafers is estimated at 15%.

Boron is also found on the surface of a silicon epitaxial layer. The substrate underwent intrinsic gettering before the deposition of a 10 μm arsenic-doped silicon layer. Figure 2 shows that the total surface boron is similar to that observed for the wafers from vendors A and B. The boron spectrum for the epi wafer is shown in figure 3. Boron is also seen on the surface of and throughout an oxide grown during an intrinsic gettering procedure. Figure 2 shows that the minimum amount of boron appears on this wafer and figure 3 presents the boron spectrum. Figure 4 shows the presence of two boron peaks on a wafer with polysilicon deposited over thermal oxide at 620° C. The first peak is at the silicon dioxide/polysilicon interface and the boron distribution in the oxide resembles that of the oxide-coated wafer in figure 3. There is also a boron peak at the top surface of the polysilicon layer.

The direct boron measurements of figures 2, 3 and 4 show a boron containing layer at the surfaces. While there is usually a low level of boron distributed throughout a silicon wafer, the heat treatments used in this study could not produce $\sim 10^{12}/\text{cm}^2$ by surface gettering boron from the wafer interior. Even if all the boron in an n-type wafer diffused to the wafer surfaces during the heat treatments, this amounts to only $2.5 \times 10^{11}/\text{cm}^2$ at each surface for an assumed boron bulk wafer concentration of $1 \times 10^{13}/\text{cm}^3$. There does not appear to be evidence for higher bulk boron concentrations in n-type wafers. The measured boron levels at the surface of silicon wafers exceed this by an order of magnitude. Moreover, the low temperature polysilicon deposition step cannot bring the boron at the silicon dioxide surface to the polysilicon surface by normal diffusion processes. Thus, the simplest explanation of figures 2, 3 and 4 is that there is a common external source for the observed boron.

Exposure to air is common to all the samples and can explain the surface peaks of figure 3 and the double peak of figures 4. The epi sample was measured weeks after epitaxial deposition while the polysilicon sample was measured only days after its deposition. Therefore the amount of surface boron does not seem to be correlated to the length of time the wafer was exposed to air. Perhaps the native oxide that forms on silicon provides a limited number of sites for boron atoms to be incorporated. Casel et al. [9] show that the presence of the native oxide is essential for boron to be found in the quantities seen by the present measurements. Further support for the central role of the native oxide is found in the work of Robbins et al. [10] and Grunthaler et al [11]. During the formation of the native SiO_2 layer on the surface of the wafer, it is quite possible that a related chemical reaction that produces oxides of boron takes place, since the formation of borated glass is well known. This hypothesis is supported by the presence of boron in the air as has been found in atmospheric gas phase and aerosol studies [15,16]. Atmospheric gas phase boron has a nominal concentration of 10-100 ng/m^3 and is probably in the chemical form $\text{B}(\text{OH})_3$. Further investigations of the chemical nature of the surface boron on the wafer may illuminate the mechanism responsible for the appearance of boron on the wafer surface.

Two wafers from a different lot of the material from vendor C were analyzed by secondary ion mass spectrometry (SIMS) for the presence of boron. Polysilicon was deposited upon each silicon wafer in two discrete processing steps. The first wafer was exposed to room air between the polysilicon deposition steps. Figure 5a shows three boron peaks in a depth profile by SIMS. The deepest peak is at the polysilicon-silicon interface, the middle peak is at the

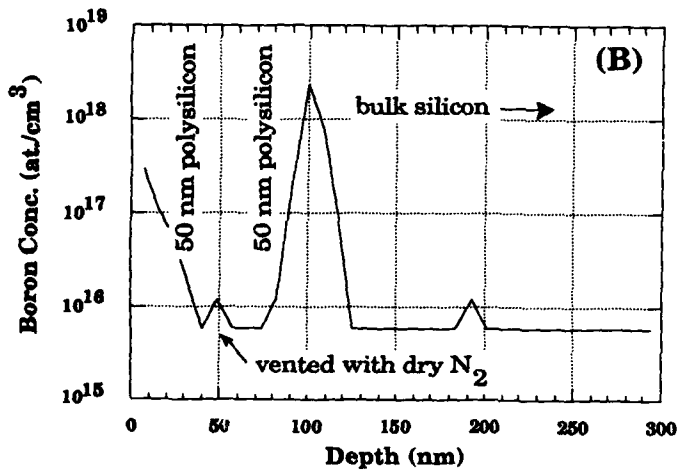
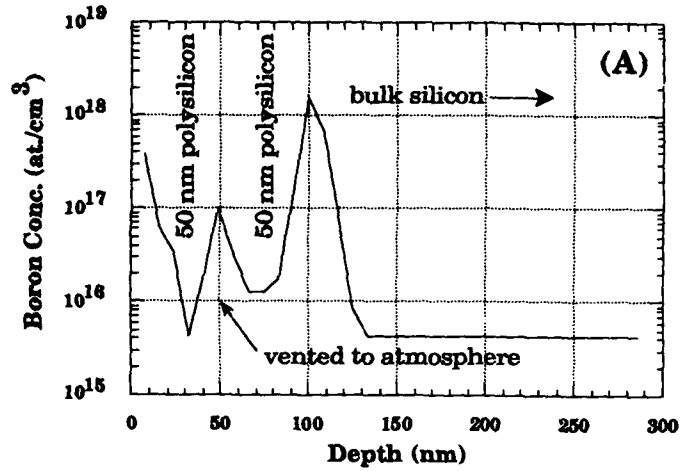


Figure 5. Boron concentration vs. depth by SIMS. (A) The silicon wafer was exposed to room air between polysilicon depositions. (B) The silicon wafer was left in the deposition tube in a dry nitrogen ambient between polysilicon depositions.

polysilicon layer 1-polysilicon layer 2 interface, and the surface peak is from the surface of polysilicon layer 2. The integrated boron concentration in the two peaks are 2×10^{12} and $9 \times 10^{10}/\text{cm}^2$. Figure 5b presents the SIMS depth profile for a second wafer which remained in the deposition tube under a dry nitrogen ambient between the layer depositions. No boron peak is observed at the interface between the polysilicon layers for this sample, and the integrated boron concentration at the polysilicon-silicon interface is $2 \times 10^{12}/\text{cm}^2$. This dose is consistent with the result for the first wafer as is the presence of the boron peak at the surface of polysilicon layer 2. As with the NDP measurements, the SIMS spectra of these two wafers suggest that boron arrives at the silicon surface during exposure to air.

Conclusions

By using NDP it is shown that boron adsorbs or chemisorbs onto the silicon wafer surface and perhaps is incorporated into the native oxide found on silicon. As suggested by figure 2, the initial wafer preparation processes may also leave boron as a result of chemical or mechanical cleaning and polishing. This assumes the atmospheric boron concentration is roughly the same in the various wafer preparation facilities. However, the surface boron seen after polysilicon or epitaxial silicon deposition requires that the boron source be in the ambient air itself. The present direct measurements of boron with thermal neutrons do not require pretreatment for sample analysis. Thus, unequivocal support is provided for the earlier suggestion of Iyer et al. [7] and Kubiak et al. [8] that the atmosphere is at least one source and likely the most common source for the observed boron surface contamination.

Acknowledgements

We thank Dr. Gilbert Declerck of Interuniversitair Micro-Elektronica Centrum VZW, Dr. David L. Anderson of the United States Food and Drug Administration, and Dr. Richard S. Hockett of Charles Evans and Associates for helpful conversations and references. The SIMS work was done at Charles Evans and Associates.

References

1. Workshop on the Utilization of Cold Neutron Beams for Prompt Gamma Activation Analysis (PGNAA) and Neutron Depth Profiling (NDP), Rockville, MD, May 22-23, 1989.
2. Proceeding of the American Nuclear Society Winter Meeting, November 15-19, 1987, Los Angeles, CA, Materials Characterization Using Neutron Depth Profiling, **55**, 207 (1987).
3. R.G. Downing, J.T. Maki, and R.F. Fleming, in Microelectronics Processing: Inorganic Materials Characterization, edited by L.A. Casper (ACS Symposium Series No. 295, Washington, D.C., 1986) p. 163.
4. M. Liehr, M. Renier, R.A. Wachnik, and G.S. Scilla, *J. Appl. Phys.* **61**, 4619 (1987).
5. G.J. Slusser and L. MacDowell, *J. Vac. Sci. Technol.* **A5**, 1649 (1987).

6. H.T. Yang and P.M. Mooney, *J. Appl. Phys.* **58**, 1854 (1985).
7. S.S. Iyer, S.L. Delage, and G.J. Scilla, *Appl. Phys. Lett.* **52**, 486 (1988).
8. R.A.A. Kubiak, W.Y. Leong, M.G. Dowsett, D.S. McPhail, R. Houghton, and E.H.C. Parker, *J. Vac. Sci. Technol* **A4**, 1905 (1986).
9. A. Casel, E. Kasper, H. Kibbel, and E. Sasse, *J. Vac. Sci. Technol.* **B5**, 1650 (1987).
10. D.J. Robbins, A.J. Pidduck, J.L. Glasper, and I.M. Young, *Appl. Phys. Lett.* **55**, 1229 (1989).
11. P.J. Grunthaner, F.J. Grunthaner, R.W. Fathauer, T.L. Lin, F.D. Schowengerdt, B. Pate, and J.H. Mazur, in Proceedings of the 2nd International Symposium on Silicon MBE, edited by J.C. Bean and L.J. Schowalter (Electrochemical Society, Pennington, N.J. 1988), Vol. 88-8, p. 375.
12. J.T. Maki, R.F. Fleming, and D.H. Vincent, *Nucl. Instr. Meth.* **B17**, 147 (1986).
13. R.G. Downing, R.F. Fleming, J.K. Langland, and D.H. Vincent, *Nucl. Instr. Meth. Phys. Res.* **218**, 47, 1983.
14. K. Takami, Y. Iwamoto, R.A. Craven, and R.W. Shaw, Abstract 3-p ZG-8, Spring 1989 Meeting of the Japanese Society for Applied Physics.
15. M.E. Kitto, Receptor Modelling of Atmospheric Particles and Acidic Gases, Ph.D. dissertation, University of Maryland (1987).
16. M.E. Kitto and D.L. Anderson, in The Chemistry of Acid Rain: Sources and Atmospheric Processes, edited by R.W. Johnson, G.E. Gordon, W. Calkins, and A. Elzermann, ACS Symposium Series (American Chemical Society, Washington, D.C., 1987), pp. 84-92.

**NEUTRON DEPTH PROFILES OF BORON
IMPLANTED SEMICONDUCTORS**

ROBERT C. BOWMAN, JR., JOHN F. KNUDSEN AND R. GREGORY DOWNING*
The Aerospace Corporation, Laboratory Operations, P.O. Box 92957, Los Angeles, CA 90009

*National Institute for Standards and Technology, Center for Analytical Chemistry, Gaithersburg, MD 20899

ABSTRACT

The nondestructive neutron depth profile (NDP) technique has been used to measure boron (^{10}B) distributions in Si and $\text{Hg}_{0.7}\text{Cd}_{0.3}\text{Te}$ after multiple energy ion implants. The NDP results are compared with simulations generated by TRIM and SUPREM computer codes. The influence of SiO_2 films on the boron profiles was examined and the effects of thermal anneals are also described.

INTRODUCTION

The implantation of boron ions into silicon wafers is extensively used during the fabrication of various electronic devices. In addition, boron implants into $\text{Hg}_{1-x}\text{Cd}_x\text{Te}$ produce n-p junctions for photovoltaic infrared detectors [1]. In order to optimize device performances, multiple energy implants are often used to produce more uniform dopant profiles over larger depths than are possible with single energy implants. Such implants often occur through passivation films grown by thermal oxidation [2] or photochemical vapor deposition [3]. In order for the implanted boron atoms to become electrically active, annealing treatments at elevated temperatures are normally required [4,5]. The distributions of the implanted species between the semiconductor and the passivation film as well as changes induced by the anneals are important parameters that can influence the behavior of processed devices. While these distributions can be predicted by various numerical models such as the Monte Carlo simulation with the well-known TRIM computer codes [6,7], direct experimental determinations provide verifications for these models or can explicitly point out their limitations.

The capture of thermal neutrons by the light boron isotope (^{10}B) via the reaction $^{10}\text{B}(n,\alpha)^7\text{Li}$ provides a novel and non-destructive method to measure boron distributions in a variety of materials [8]. Among its advantages, neutron depth profiling (NDP) gives quantitative determinations of isotopic concentrations with few interferences. Although NDP is not as sensitive as secondary ion mass spectrometry (SIMS), it can be used across oxide-semiconductor interfaces without the complications inherent for the SIMS analyses [2,9].

The present paper summarizes several representative NDP evaluations of boron ion implanted silicon and $\text{Hg}_{0.7}\text{Cd}_{0.3}\text{Te}$ samples that illustrate the types of information provided by this technique. In particular, the NDP measured boron profiles compare quite favorably with the predicted curves for the various simulations.

* Certain commercial equipment, instruments, or materials are identified to specify experimental procedures. Such identification does not imply recommendation or endorsement by the National Institute of Standards and Technology.

TABLE I. SUMMARY OF BORON ($^{10}\text{B}^+$) ION IMPLANT CONDITIONS

Implant Series (Label)	Target Temp. (K)	Materials (Substrate)	Ion Energies (keV)	Ion Dose at Each Energy ($10^{15}/\text{cm}^2$)	Ion Beam Current ($\mu\text{A}/\text{cm}^2$)
A-100	298	Si, SiO ₂ , HgCdTe	100	2.0	0.19
A-250	298	HgCdTe	250	2.0	0.12
B	298	Si, HgCdTe	50	5.0	0.09
			100	10.0	0.12
C	298	Si, HgCdTe	100	2.5	0.25
			200	2.5	0.22
			300	2.5	0.17
			400	2.5	0.04
E	78	HgCdTe	100	0.5	0.037
			200	0.5	0.044
			300	0.5	0.044
			400	0.5	0.036

EXPERIMENTAL DETAILS

Implants of $^{10}\text{B}^+$ ions were done using a model 400 MPR-Veeco/Al ion implanter with the samples mounted 7° off-axis to reduce channeling contributions. The ion beam currents were kept low enough to avoid excessive heating during the implants. The conditions for the implants are summarized in Table I. The silicon samples were phosphorus doped single-crystal wafers with (100) or (111) polished faces. Most of the nominal $\text{Hg}_{0.7}\text{Cd}_{0.3}\text{Te}$ samples were liquid phase epitaxially grown layers on (111)-CdTe substrates; however, some bulk single crystals were also implanted with no discernible differences being found. SiO₂ films were deposited on a few samples by low-temperature photo-enhanced deposition methods that were previously described [3].

The NDP experiments were performed with the 20-MW research reactor at the National Institute for Standards and Technology. The general analytical procedures have been reported previously [8]. The energy spectra for the charged particles emitted from the implanted silicon samples were analyzed with a silicon surface barrier detector. However, rather severe "pulse pile-up" effects arose when fully depleted detectors were used for $\text{Hg}_{1-x}\text{Cd}_x\text{Te}$ samples [3] that lead to distorted boron profiles. Consequently, partially biased transmission silicon detectors with nominal 40 μm thicknesses have been used to obtain the present boron profiles for the $\text{Hg}_{0.7}\text{Cd}_{0.3}\text{Te}$ samples with 50 nm full-width half-maximum resolution.

RESULTS AND DISCUSSIONS

The boron distributions in Si for the Series B and C implants are presented in Fig. 1 where the NDP results are compared with predictions from TRIM-86 models [6,7] and the SUPREM II model developed at Stanford University [10]. The NDP measured profiles agree fairly well with the theoretical curves for as-implanted conditions shown in Figs. 1a and 1b.

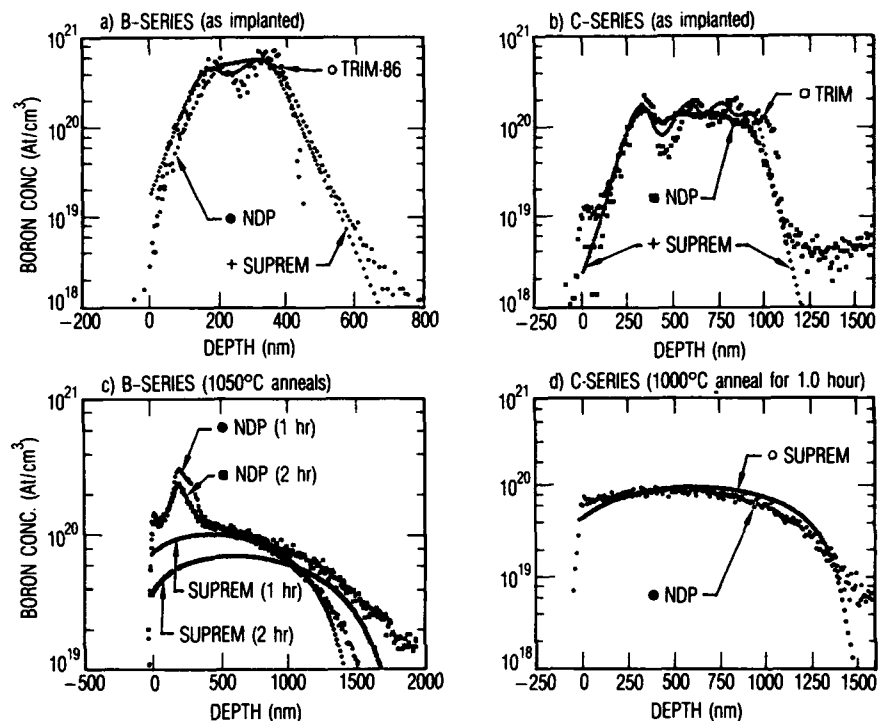


Fig. 1. Boron distributions for Series B and C multiple energy implants into (100)-Si. The measured NDP profiles are compared to predictions from TRIM and SUPREM II models for as-implanted and annealed conditions.

However, some minor discrepancies are found. Although two and four peaks are evident in the NDP results for the Series B and C implants, respectively, they are not as pronounced as predicted by the models. The nominal 25 nm instrumental resolution for NDP should not be a significant factor in these differences. Since the TRIM curves were generated by summing the separate profiles for each implant energy and dose, they do not properly account for mixing effects during the sequential multiple-energy implants. Hence, these TRIM-86 profiles should have somewhat sharper profiles than the experimental boron distributions. It should be noted that SUPREM II, which had estimated the profiles in sequential manner, produces more shallow dips in the boron profiles that correspond better to the NDP curves. Furthermore, SUPREM II predicts the total shapes of the NDP curves rather well over the entire range of boron concentration. NDP data points for negative depths are due to finite instrumental resolution, while tails below 1100 nm can arise from energy overlap of the secondary decay process of the boron reaction [8].

Electrical activation of the boron implanted into silicon requires post-implant anneals [4,5]. Although annealing temperatures around 600°C will essentially remove all of the lattice damage [5], much higher temperatures are necessary for activation of boron on their substitutional lattice sites [4]. Our previous NDP studies [3] of ^{10}B implanted Si as well as other measurements showed no change in boron profiles for anneals

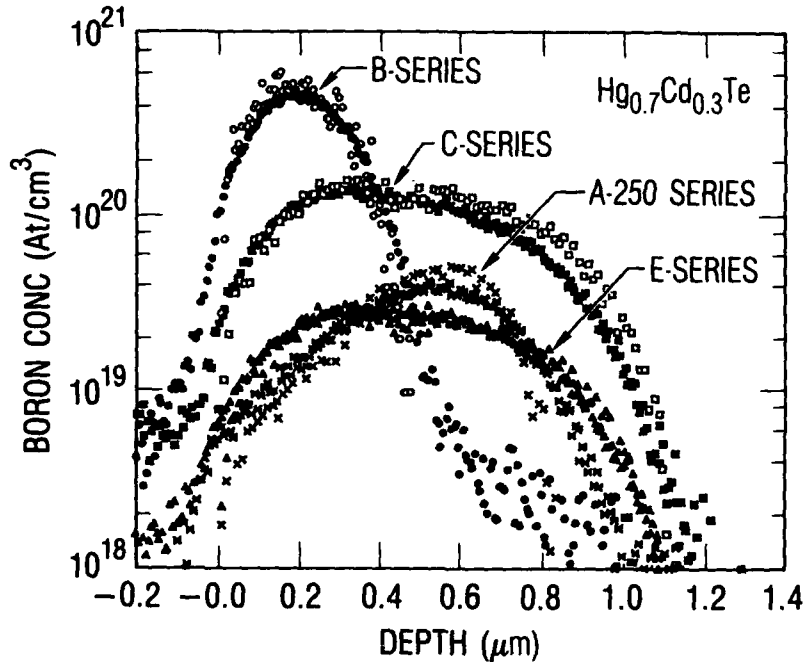


Fig. 2. Comparison of boron profiles in $\text{Hg}_{0.7}\text{Cd}_{0.3}\text{Te}$ from NDP measurements and TRIM calculations for as-implanted conditions. Filled symbols correspond to NDP data.

at temperatures up through 600°C . In Fig. 1 the influence of 1000°C (Series C) and 1050°C (Series B) anneals under flowing nitrogen are presented in Figs. 1d and 1c, respectively. The NDP boron profile after the 1 hr 1000°C anneal of the Series C implanted sample is extensively broadened compared to the as-implanted distribution. Through the solution of appropriate diffusion equations, the SUPREM II program predicts the redistribution of boron as a function of time and temperature. Since the maximum boron concentration for the Series C implant does not exceed the 10^{20}cm^{-3} limit [11], the SUPREM II model gives good agreement with the NDP measured profile. After the 1 hr and 2 hr anneals at 1050°C , peaks are found on the NDP curves for the Series B implanted Si samples as indicated in Fig. 1c. Ryssel, et al. [11] have reported very similar peaks to those in Fig. 1c after 1000°C anneals of Si wafers that had been implanted with 120 keV 10B^{+} to doses above $5 \times 10^{15}\text{cm}^{-2}$. For the very high boron concentrations (Table I) after the Series B implants, the solid solubility limits [11] have been exceeded for the 1050°C anneals (see, Figs. 1a and 1c). Consequently, this excess boron apparently forms precipitates [11] of boron-rich impurity phases which will not become

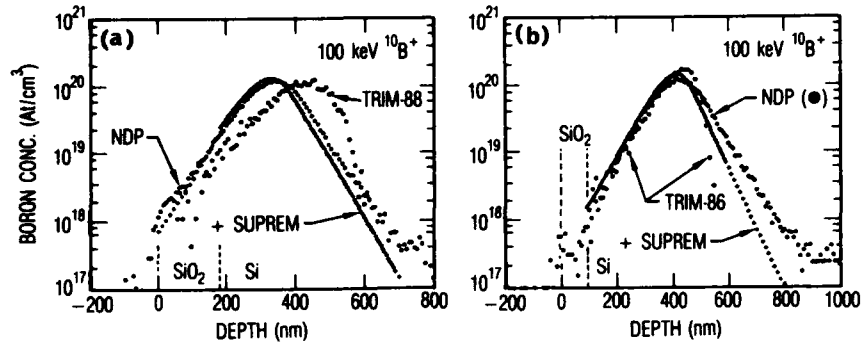


Fig. 3. Boron profiles for implants in silicon wafers with photochemically deposited SiO_2 films: (a) 100 keV $^{10}\text{B}^+$ implant (Series A-100) through a 186 nm film and (b) after post-implant deposition of a 94 nm film on a Series A-100 implanted bare wafer surface.

electrically active [4]. While the SUPREM II model qualitatively predicts the broadening of the Series B profiles following the 1050°C anneals, SUPREM II does not account for boron concentrations which exceed the solid solubility limits. Therefore, NDP should be regarded as the more reliable indicator of the boron profiles after annealing.

The ^{10}B depth profiles observed in $\text{Hg}_{0.7}\text{Cd}_{0.3}\text{Te}$ after four different implant series are compared in Fig. 2. As we have reported previously [12], the NDP and TRIM-86 profiles consistently show good agreement for this material. Through the use of transmission detectors, distortions from pulse-pile up during the NDP measurements [3,12] have been greatly reduced. However, examinations of the NDP curves in the surface region reveal that some minor distortions still remain (e.g., the finite boron concentrations external to the crystal surface). Nevertheless, the overall shapes and absolute concentrations measured by NDP now correspond more closely to the TRIM-86 predictions than were seen in previous studies [3]. The boron distributions in $\text{Hg}_{0.7}\text{Cd}_{0.3}\text{Te}$ exhibit the behavior expected for the various implant energies and ion doses. The four-energy implants (i.e., Series C and E) produced reasonably flat boron concentration profiles to a depth approaching a micrometer, in contrast to the much more asymmetric profile from a single energy implant (e.g., 250 keV for Series A-250).

Fig. 3 illustrates the boron profiles obtained from silicon wafers with photochemically deposited [3] SiO_2 films. For a 100 keV $^{10}\text{B}^+$ implant through a 186 nm thick oxide (i.e., Fig. 3a), the NDP measurements do not show any discontinuities at the SiO_2 -Si interface, which has been noted previously [2,3]. Both the TRIM-88 and SUPREM II simulations also indicated little or no significant disruption in the boron content at this interface and ion dose. The TRIM-88 model predicts the boron peak to lie about 100 nm deeper than the NDP measured value; however, TRIM-86 calculations for this implant (not shown in Fig. 3a) do overlay with both the leading edge and the boron peak positions obtained by NDP and SUPREM II. These results are also consistent with the profile predictions from TRIM-86 for the implant condition in Fig. 3b. Furthermore, the TRIM generated boron profiles fall off much more steeply than either the NDP or the SUPREM II curves, although the front side is similar. The overall prediction of the boron profile by SUPREM II corresponds quite closely to the NDP results, except for slightly faster decrease beyond the peak for

this simulation, which is primarily due to NDP instrumental resolution of these depths. In Fig. 3b the boron profile obtained after a 100 keV $^{10}\text{B}^+$ implanted wafer had been coated with a 94 nm SiO_2 film is shown. Consequently, the low boron concentration implied by the NDP data for the first 100 nm inside the surface are again due to finite instrumental resolution. The TRIM-86 and SUPREM II results correspond to 100 keV $^{10}\text{B}^+$ into bare silicon that were shifted 94 nm inwards to account for the deposited SiO_2 film. Although the simulations both give reasonable representations for the NDP data in front of the concentration maximum, they decrease more rapidly (with TRIM falling more rapidly) at the deeper depths. While the implants were performed in a manner that should minimize the channeling contributions to the projected boron range, the NDP measurements suggest a deeper profile than predicted by the models.

CONCLUSIONS

Neutron depth profiling is a convenient and useful method to assess boron (^{10}B) distributions in semiconductors after multiple energy ion implants. The behavior of post-implant anneals on the boron profiles can be readily determined by NDP and non-ideal effects that are not predicted by simulation models can be identified. NDP also permits assessment of boron between oxide films and semiconductor in a straightforward fashion.

ACKNOWLEDGMENTS

This work was partially supported by The Aerospace Corporation Research Sponsored Program. We appreciate the assistance of Robert C. Cole (Aerospace), Steven C. Moss (Aerospace), and G. Lamaze (NIST) with some of the model calculations.

REFERENCES

1. H. Ryssel, G. Lang, J.P. Biersack, K. Muller, and W. Kruger, IEEE Trans. Electron Devices **27**, 58 (1980).
2. W. Vandervorst, F.R. Shepherd, and R.G. Downing, J. Vac. Sci. Technol. A **3**, 1318 (1985).
3. R.C. Bowman, Jr., J. Marks, R.G. Downing, J.F. Knudsen, and G.A. To., Mat. Res. Soc. Symp. Proc. **20**, 279 (1987).
4. D. Fink, J.P. Biersack, H.D. Carstanjen, F. Jahnel, K. Muller, H. Ryssel, and A. Osei, Rad. Effects **77**, 11 (1983).
5. R. C. Bowman, Jr., and D.N. Jamieson, Symp. Proc. SPIE **322**, 31 (1987).
6. J.P. Biersack and L.G. Haggmark, Nucl. Instrum. Methods **174**, 257 (1980).
7. J.F. Ziegler, J.P. Biersack, and A. Littmark, The Stopping and Range of Ions in Solids, (Pergamon, New York, 1985)
8. R.G. Downing, J.T. Maki, and R.F. Fleming, in Microelectronic Processing: Inorganic Materials Characterization, edited by L.A. Casper (Am. Chem. Soc., Washington, D.C., 1986) p. 163.
9. V.R. Deline, N.M. Johnson, and L.A. Christel, in Mat. Res. Symp. Proc. **25**, 649 (1984).
10. D. A. Antoniadis, S. E. Hansen, and R. W. Dutton, "SUPREM II -- A Program for IC Process Modeling and Simulation", SEL 78-020, Stanford Electronics Labs, Stanford University, June 1978.
11. H. Ryssel, K. Muller, K. Habberger, R. Henkelmann, and F. Jahnel, Appl. Phys. **22**, 35 (1980).
12. R. C. Bowman, Jr., J. F. Knudsen, R. G. Downing, and R. E. Kremer, Mat. Res. Soc. Symp. Proc. **126**, 89 (1989).

TOF MEASUREMENTS OF PULSED NEUTRONS FOR TEXTURE ANALYSIS OF LOW SYMMETRY MATERIALS

Allen C. Larson*, Phillip J. Vergamini* and Hans-Rudolf Wenk**

*Manual Lujan, Jr. Neutron Scattering Center, LANSCE, Los Alamos National Laboratory, Los Alamos, NM

**Department of Geology and Geophysics, University of California, Berkeley, CA

ABSTRACT

The single crystal diffractometer at LANSCE, SCD, provides an ideal capability for the study of preferred orientation in geological samples by time-of flight (TOF) measurement of pulsed neutrons. The 2-d position sensitive neutron detector with the large wave length range allows one to measure the complete distribution of intensities for several poles very quickly. Each histogram covers about $\pi^2/16$ radians of reciprocal space and contains information from all possible poles visible with the wave length range used, usually about 0.5 to 5.0Å. With this method complete pole figures of many lattice planes can be constructed from only 12 to 20 sample orientations as compared to over 1000 sample settings per lattice plane using conventional diffractometers.

Pole figures from measurements of experimentally deformed standard samples of calcite and quartzite with a known history of deformation provide information about deformation mechanisms and their temperature/strain history. This information can be applied to interpret preferred orientation of naturally deformed rocks.

INTRODUCTION

In many of the rocks composing the Earth's crust, mantle and core, mineral crystals display a preferred orientation distribution or texture. Among various origins of texture such as growth, flow of rigid particles in a rigid medium, recrystallization and dislocation glide, the latter is by far the most important mechanism. Rotations of crystals due to slip produce strong preferred orientation during tectonic deformation of the crust or during convection in the mantle. An understanding of texture development by plastic deformation helps us to understand dynamic processes within the earth. Also texture development produces anisotropy, eg. of seismic wave propagation, which needs to be taken into account for a quantitative interpretation of the earth's structure. One prerequisite in using textures for indicators of the geological history and structure is a need for quantitative texture measurements.

Traditionally X-ray diffraction has been used and this is sufficient for many applications. However neutron diffraction has some unique advantages for quantitative texture determinations. Weak absorption allows integration over sample volumes rather than surfaces. Also complete pole figures can be measured without

intensity corrections. With position sensitive detectors large ranges of the 2θ spectrum can be scanned at once and many poles recorded simultaneously. The time-of-flight measurements of pulsed neutrons combined with a 2D position sensitive detector offer the additional advantage of being able to scan large pole figure sectors of many pole figure simultaneously. We illustrate applications of this technique with experimentally produced quartz and calcite textures and the texture of a fluorapatite sample from a dinosaur bone.

EXPERIMENTAL PROCEDURE

The single crystal instrument at LANSCE is shown in Figure 1 [1]. This unique instrument uses a 2D position sensitive area counter positioned such that the θ axis makes an angle of 45° with the ω axis and the χ axis permanently set at 60° . Use of this instrument for pole figure measurement is described by Wenk, et al.[2].

This instrument can be used to examine about 80% of a sphere of reciprocal space. Only a small region on the bottom of the sphere is occluded. The reciprocal space coverage in the radial direction is illustrated in Figure 2 and Figure 3 shows the coverage of reciprocal space normally used for complete pole figures. Each histogram covers an area about 25° parallel to θ and about 50° perpendicular to θ .

The best way to handle the variation in detector efficiency, the geometric correction over the face of the detector and the variation in intensity due to the thermal neutron spectrum is to measure an isotropic sample and use its intensity data to calibrate or normalize the data. This can be approximated by summing the pole figure data from all histograms to obtain a self calibration. The only requirement in this is that the features in the pole figure be broad enough to provide a reasonable average value for all points on the detector.

Since the samples being examined on SCD are about 10 mm^3 in volume and the entire sample is placed in the incident beam, no corrections are needed for changes in the sample volume due to the angle of the incident and diffracted beams with respect to the sample surface. In addition no unusual background should arise and for samples lacking a strong incoherent scatterer the background is negligible,

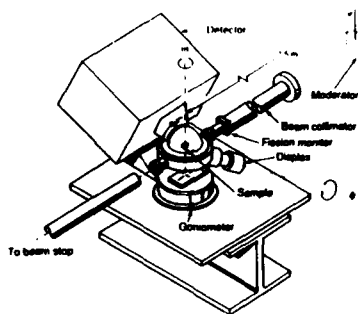


Figure 1. Schematic diagram illustrating the experimental setup of the SCD instrument at LANSCE. The sample is mounted on a two circle goniometer with a fixed χ -angle and the detector centered at $2\theta=90^\circ$ with the θ -axis tilted 45° from the ω -axis. Sample to the $25 \times 25 \text{ cm}$ detector distance is 25cm.

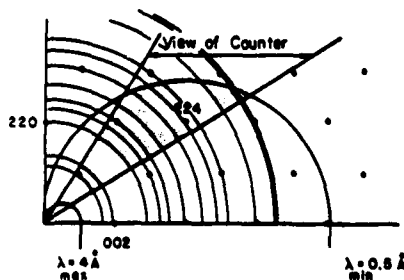


Figure 2. Diagram of a FCC reciprocal lattice showing traces of powder lines from lattice points and coverage of a histogram with the SCD detector.

as is the absorption for most geological materials.

The d-resolution obtainable on the LANSCE SCD instrument is dependent on the detector to sample distance, and in the setup usually used is $\Delta d/d = \text{ca. } 0.01$. The major contribution to $\Delta d/d$ is the detector resolution and the effect of this can be easily improved by moving the detector from 25cm to 50cm. This however causes a decrease in pole figure coverage by a factor of about four. At 50cm the detector contribution to $\Delta d/d$ is ca. 0.005. With this resolution and a good peak to background ratio, measurements of pole figures for low symmetry geological materials having many closely spaced and weak diffraction peaks should be feasible.

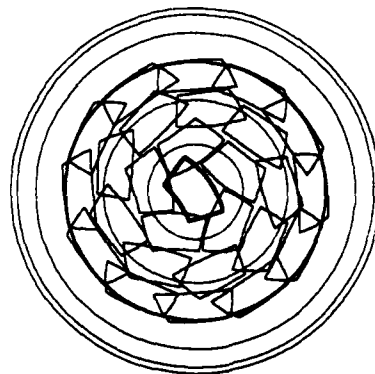


Figure 3. SCD detector coverage used to collect complete pole figures. An equal area plot.

RESULTS

The first example is an experimentally deformed limestone, CaCO_3 . Deformation of 35% was in pure shear, at 400°C . The sample used in the texture analysis was a cube 0.8 cm on the side. The diffraction pattern of this trigonal mineral is considerably complex with five diffraction peaks in the range of interest between $d=1.75$ and 4.5\AA (Figure 4). This sample is currently used as a "round robin" to determine the reliability of neutron diffraction pole figure determinations [3]. In Figure 5 LANSCE pole figure results are compared with measurements at ILL Grenoble with monochromatic neutrons and a 1-d position sensitive detector. Apart from a rotation difference which is due to a different sample orientation, pole figures are virtually identical, even for the very weak pole figure 110 for which counting statistics are poor.

The second sample is a mixture of 75% quartz and 25% muscovite, experimentally compressed by 60%. The quartz diffraction pattern is similar in complexity to calcite (Figure 6). Notice the weak diffraction peaks for muscovite which are barely above the background. Due to the axial symmetry of the deformation experiment and correspondingly of the pole figures, intensity profiles from parallel to perpendicular to the common axis are all that is necessary to describe the preferred orientation. With the detector window of 25° by 50° and ten sample settings we covered a large range (Figure 7). This was

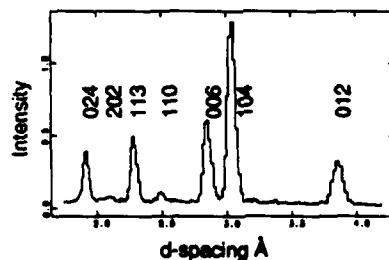


Figure 4. d-spectrum for limestone standard sample, K433, experimentally deformed by H. Kern, Kiel.

useful to establish an overall axial symmetry, also to note local deviations over which we were able to average. Texture profiles for quartz and muscovite are shown in Figure 8. From six partial pole figures we then calculated an inverse pole figure of the compression direction with the WIMV algorithm [4] which we present in Figure 9. The pole figure inversion shows good resolution with error values of less than 0.5% and is consistent with earlier observations [5]. With texture determinations on 4 samples of different composition and different degrees of deformation we could document that preferred orientation of quartz increases moderately in strength with increasing strain and is attenuated by interspersing muscovite in the sample.

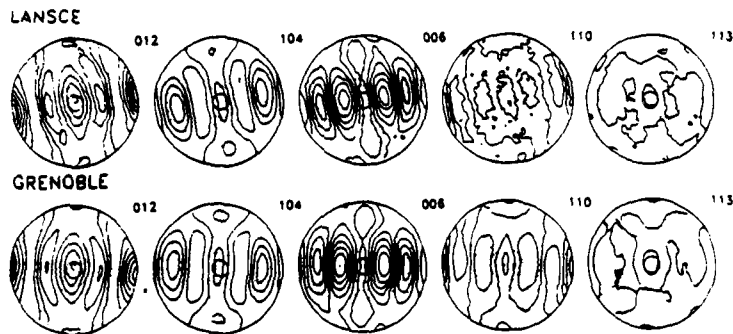


Figure 5. Comparison of five pole figures for experimentally deformed limestone, K433. Top was measured by TOF at LANSCE, bottom by monochromatic neutrons at ILL, Grenoble. Contours are in multiples of a random distribution, contours interval is 0.2, dotted regions are below 1 m.r.d., equal area projection.

A third geological sample is of biological origin. A fossil bone from a dinosaur found in the Seismosaurus locality in the southeastern San Juan Basin, Sandoval County, New Mexico shows a strong fabric of fluorapatite, $\text{Ca}_5\text{F}(\text{PO}_4)_3$ with c axes aligned in a single maximum, Figure 10, (002), and a and b axes distributed uniformly in a girdle perpendicular to the c axis maximum, Figure 10, (310). The example demonstrates that the original bone structure and the alignment of crystallites is still preserved after 140 million years.

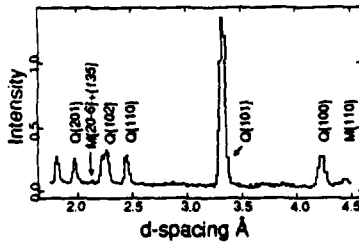


Figure 6. d-spectrum of a 75% quartzite, 25% muscovite mixture, Q505, deformed experimentally by J. Tullis, Brown. Notice weak peaks for muscovite.

CONCLUSIONS

The SCD and TOF neutron measurements at LANSCE were used to measure preferred orientation of geological materials with complex diffraction patterns. The method is efficient (about one hour per histogram), particularly for low symmetry compounds where the whole of reciprocal space is covered and should therefore also be attractive for ceramics such as high temperature superconductors [6]. At this point the experimental method could still be improved by allowing for larger samples and detectors with a wider coverage, e.g. of cylindrical shape. The data analysis should be extended to enable integration and deconvolution of overlapping peaks. Also measuring time could be reduced by sparser coverage of the pole figures which will require modifications of the algorithms to calculate the orientation distributions.

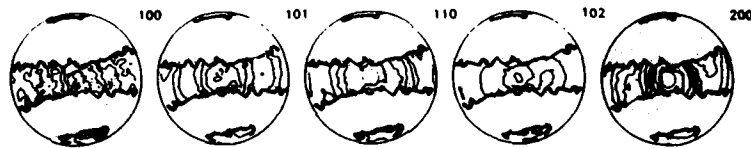


Figure 7. Partial pole figure coverage documenting approximate axial symmetry, equal area projection.

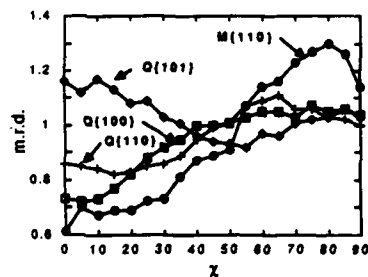


Figure 8. Pole density profiles for quartz from parallel to perpendicular to the compression axes for selected diffraction peaks in m.r.d. The profiles were averaged from pole figures in Fig. 7.

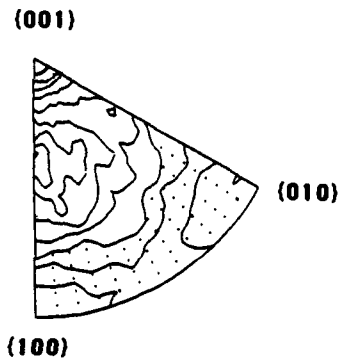


Figure 9. Inverse pole figure for quartz in experimentally deformed quartz-muscovite aggregate. Contours are in multiples of a uniform distribution.

Acknowledgements

We are appreciative for access to the LANSCE and support through IGPP Los Alamos and NSF EAR 870 9378. Hartmut Kern, Kiel and Jan Tullis, Brown University kindly provided the samples which were in this study.

This work was performed under the auspices of the US Department of Energy, Office of Basic Energy Sciences.

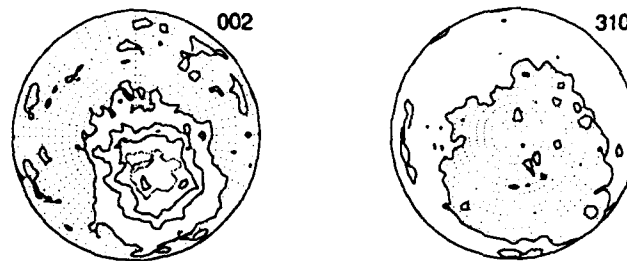


Figure 10. Pole figures of fluorapatite composing fossil bone of *Seismosaurus*. Contours at 0.2 m.r.d with regions below 1.0 dotted. Equal area projection.

REFERENCES

1. P.J. Vergamini, G.G. Christoph, R.W. Alkire and A.C. Larson, (Unpublished) (1987).
2. H.R. Wenk, P.J. Vergamini and A.C. Larson, *Textures and Microstructures* 8&9, 443-456 (1988)
3. H.R. Wenk, H. Kern, J. Pannetier, S. Höfer, W. Schäfer, G. Will and H.G. Brokmeier, *Proceed. Int. Conf. Textures of materials*, 8, 229-234. TMS, Warrendale. (1987)
4. J. S. Kallend and H.R. Wenk, *Am. Soc. Metals, Annual Meeting* (abstr.) (1989).
5. J. Tullis, J.M. Christie and D.T. Griggs, *Geol. Soc. Am. Bull.* 84, 294-314 (1973)
6. H.R. Wenk, J. Pannetier, G. Bussod and A. Pechenick, *J. Appl. Phys.* 65, 4070-4072 (1989).

PART VII

Disordered Systems

STRUCTURE AND DYNAMICS OF GLASSES AND LIQUIDS

DAVID L. PRICE

Argonne National Laboratory, Materials Science Division, Argonne, IL 60439

INTRODUCTION

Neutron scattering has proved to be a powerful tool in the study of glasses and liquids: structures are investigated by *neutron diffraction*, and dynamics by *inelastic neutron scattering*. Evidence of current interest in this field is provided by the new instruments for diffraction from amorphous systems being constructed at IPNS¹, ISIS² and the R2-reactor at Studsvik³, in addition to existing instruments such as the D4B diffractometer at ILL⁴.

Structure

This is the simpler case and we discuss it first. A typical diffraction measurement is shown schematically in Fig.1. We describe an incident neutron by \mathbf{k}_0 , a vector in the direction of the beam with magnitude $2\pi/\lambda_0$ where λ_0 is the mean wavelength, and a scattered neutron by a wave vector \mathbf{k}_1 . A typical scattering event is described by the scattering vector

$$\mathbf{Q} = \mathbf{k}_0 - \mathbf{k}_1. \quad (1)$$

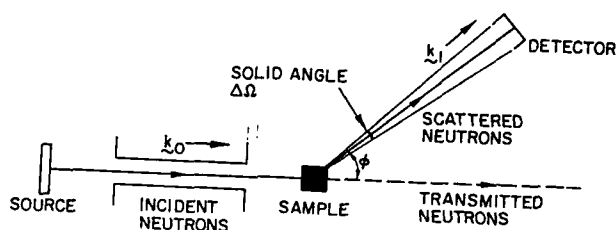


Figure 1
Schematic diagram of a neutron scattering measurement.

The count rate in the detector is given by the differential cross section $d\sigma/d\Omega$ multiplied by some trivial experimental factors. For neutron diffraction, $d\sigma/d\Omega$ is very simply related to the *static structure factor* $S(\mathbf{Q})$ which is a fundamental property of the sample, independent of the details of the scattering experiment:

$$\frac{d\sigma}{d\Omega} = \overline{b^2} S(\mathbf{Q}) + (\overline{b^2} - \overline{b}^2), \quad (2)$$

where \bar{b} and $\overline{b^2}$ are the mean and mean square scattering amplitudes of the nuclei comprising the sample. We generally assume that the scattering is mainly elastic, $k_1 \sim k_0$, and so only one quantity, k_0 or k_1 or some combination of the two, needs to be measured. In practice this is only an approximation and "Placzek corrections" have to be applied to take care of this fact⁵, especially when light atoms are involved.

$S(Q)$ can be written simply in terms of the particle density operators in reciprocal space

$$\rho(Q,t) = \sum_i e^{iQ \cdot R_i(t)} \quad (3)$$

where $R_i(t)$ is the position of particle i at time t :

$$S(Q) = \frac{1}{N} \langle \rho(-Q,0)\rho(Q,0) \rangle \quad (4)$$

where $\langle \rangle$ represents a thermal average,

$$= \frac{1}{N} \sum_{i,j} e^{iQ \cdot (R_i(0) - R_j(0))}. \quad (5)$$

Thus, $S(Q)$ represents the instantaneous correlations in particle density, averaged over the system.

A convenient starting point for considering the structure of disordered systems is the concept of dense random packing of hard spheres (DRPHS)⁶. The structure factor describing the arrangement of spheres of diameter d_s is uniquely determined by the packing fraction

$$\eta = \left(\frac{\sigma}{d_s}\right)^3 \quad (6)$$

where $\rho_0^{-1} = (\pi/6)d_s^3$ is the volume per particle. Dense random packing corresponds to the maximum value $\eta=0.637$, or $d_s = 1.162 \sigma$. $S(Q)$ can be evaluated by numerical methods, or analytical approximations such as the Percus-Yevick method, for such a system, and turns out to be an excellent approximation for most simple liquids, including rare gases and metals, as well as many metallic glasses. As an example, Fig. 2 compares the $S(Q)$ measured for liquid Rb with the DRPHS model⁷: $\sigma=4.3 \text{ \AA}$ was chosen to give the best fit, while η corresponds to the measured value of the number density ρ_0 through Eq. (6). The main peak is seen to be at $Q \sigma = 6.5$, a typical value for a hard sphere close to the dense random packing limit.

Most glasses have two or more components, which introduces a complication in that an n -component system is described by $n(n+1)/2$ partial structure factors S_{ab} given by

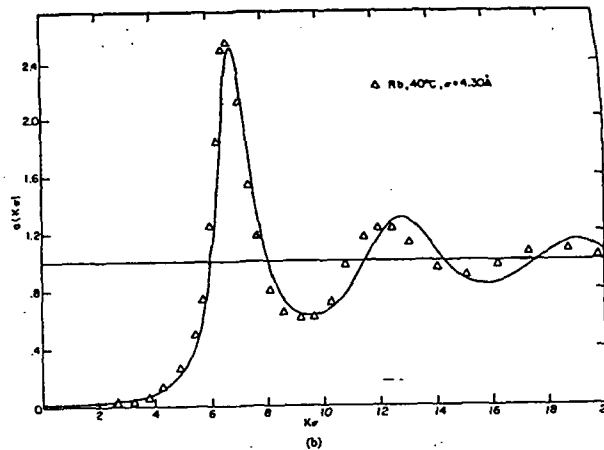


Figure 2
DRPHS model (line) fitted to experimental data (points) for $S(Q)$ of liquid Rb at 40°C (from Ref. 7).

$$S_{ab}(Q) = \frac{1}{\sqrt{N_a N_b}} \langle \rho_a(-Q, 0) \rho_b(Q, 0) \rangle. \quad (7)$$

The measured differential cross section is then an average of the S_{ab} , weighted by the appropriate products of scattering lengths. In many cases, it turns out that the DRPHS model is still a good description if the hard sphere diameters are chosen appropriately for the two components. In some cases, however, an additional peak in the structure is observed at smaller Q , especially when there is an appreciable difference in the scattering lengths of the two components. Fig. 3 shows an example of this case for glassy TiZr (ref. 8), where there is a peak in the structure factor $S_{CC}(Q)/c_1 c_2 = (c_2 S_{11} + c_1 S_{22} - 2(c_1 c_2)^{1/2} S_{12})$ at $Q=2.0 \text{ \AA}^{-1}$ in contrast with the main peak in the structure factor $S_{NN}(Q) = (c_1 S_{11} + c_2 S_{22} + 2(c_1 c_2)^{1/2} S_{12})$ at $Q=3.0 \text{ \AA}^{-1}$ which represents the

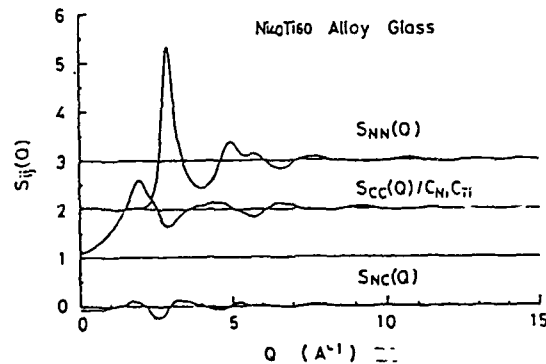


Figure 3
Partial structure factors S_{NN} , S_{CC} and S_{NC} for $\text{Ni}_{40}\text{Ti}_{60}$ alloy glass (Ref. 8).

DRPHS peak. The peak at lower Q represents the effects of chemical short-range order (CSRO) and has a similar origin to the first peak observed in liquid alkali halides, for example, when the two scattering lengths are appreciably different. Typically, the pre-peak is observed at Q values given by $Q r_1 \sim 5$, where r_1 is the nearest-neighbor distance ($\sim \sigma$ for the DRPHS model).

In many glasses and liquids we observe a peak at still smaller Q . An example is given in Fig. 4 where the structure factors for both glassy and liquid GeSe_2 reveal a peak at $Q \sim 1 \text{ \AA}^{-1}$, or $Q r_1 \sim 2.5$. This "first sharp diffraction peak" (FSDP) is observed in many glasses and complex liquids, usually at very similar values of $Q r_1$.¹⁰ It is characterized by anomalous behavior in several properties, compared with the remainder of the structure factor, including dependence on temperature, pressure, components and thermal treatment¹¹.

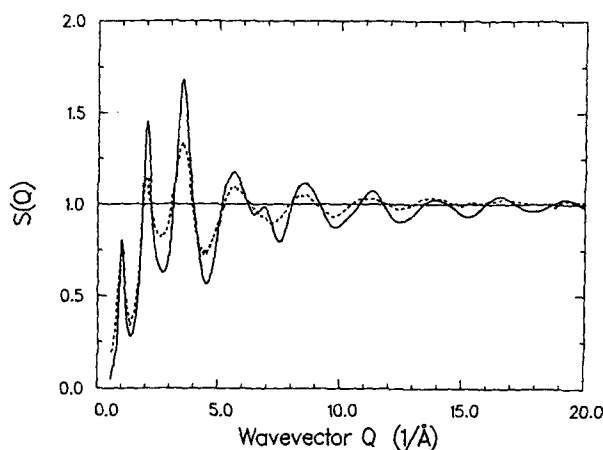


Figure 4
Structure factors $S(Q)$ for glassy (solid line) and liquid (dashed line) GeSe_2 (Ref. 9).

Fig. 5 shows the Q values for significant peaks in the structure factors of several glasses and liquids scaled with respect to r_1 and d_s . The figure shows the grouping into the three classes of peaks discussed above, namely DRPHS, CSRO and FSDP.¹⁰

The physical origin of the FSDP raises interesting questions. In molecular glasses and liquids, it can be understood in terms of the random packing of molecules or other structural units, for which the structure factor is given by¹²

$$S(Q) = f_1(Q) + f_2(Q) [S_c(Q) - 1] \quad (8)$$

where $S_c(Q)$ is the DRPHS solution for spheres circumscribing the structural units and f_1, f_2 are form factors for the units themselves. Usually $S_c(Q)$ is rising sharply and the $f(Q)$'s falling sharply where the two functions cross, giving rise to a sharp peak in $S(Q)$ that is very sensitive to small changes in structure. For network glasses, such as GeSe_2 and SiO_2 , the interpretation is

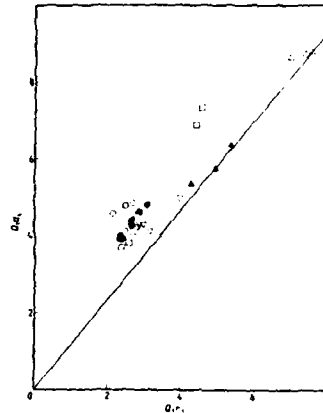


Figure 5
Wavevectors Q_1 of peaks in the structure factors of some liquids and glasses, scaled by nearest-neighbor distance r_1 and mean atomic spacing d_s . The full line represents the limit for dense random packing, $d_s = 1.162 r_1$ (from Ref. 10).

not so clear. It is possible that the same picture holds with regard to intermediate-range structural entities such as large rings in the network. Support for this view comes from Molecular Dynamics (MD) computer simulation¹³ of GeSe_2 , where it is found that Ge-Ge correlations in the range of 10 Å are primarily responsible for the peak. The MD results also explain the anomalous temperature dependence, namely that the decrease in available volume in cooling frustrates the formation of intermediate-range order and leads to a decrease in the peak height.

Dynamics

We now investigate whether dynamic properties, measured for example by inelastic neutron scattering, can shed light on the problem of intermediate-range order and other aspects of glass and liquid structure. In inelastic scattering measurements we no longer assume that $k_1 \sim k_0$ but measure directly the energy transfer

$$E = \frac{\hbar^2 k_0^2}{2m} - \frac{\hbar^2 k_1^2}{2m} \quad (9)$$

In this case the count rate is measured as a function of two variables, Q and E , and is given by the double differential cross section

$$\frac{d^2\sigma}{dQdE} = \frac{k_1}{k_0} \left[\bar{b}^2 S_c(Q,E) + (\bar{b}^2 - \bar{b}^2) S_i(Q,E) \right], \quad (10)$$

where $S_c(Q,E)$ and $S_i(Q,E)$ are the coherent and incoherent scattering functions. Here we are interested in the coherent function, which tells us about the time development of the correlations in particle density:

where $S_c(Q,E)$ and $S_i(Q,E)$ are the coherent and incoherent scattering functions. Here we are interested in the coherent function, which tells us about the time development of the correlations in particle density:

$$S_c(Q,E) = \frac{1}{2\pi\hbar N} \int \langle \rho(-Q,0) \rho(Q,t) \rangle e^{-i E t/\hbar} dt. \quad (11)$$

For solids, whether crystalline or amorphous, $S(Q,E)$ is dominated by elastic scattering in which the neutron recoils from the sample as a whole, without measurable loss of energy. For a harmonic solid, this is given by

$$S_{c,el}(Q,E) = S_{el}(Q) \delta(E) \quad (12)$$

where the elastic structure factor is

$$S_{el}(Q) = \frac{1}{N} \sum_{i,j} e^{-(W_i + W_j)} e^{i Q \cdot (j - i)} \quad (13)$$

and i, j represent the equilibrium positions of particles i and j . The first factor after the summation sign in Eq. (13) is the Debye-Waller factor, a slowly varying function of Q , expressing the effects of thermal displacements about the equilibrium positions. We see that the total and elastic structure factors, Eqs. (5) and (13), are similar in form but mean different things. Sometimes this difference can be exploited¹⁴.

In Fig. 6 we show an example of $S_c(Q,E)$, measured for α -GeSe₂¹⁴. The scattering is clearly dominated by the elastic scattering, which has a somewhat similar profile to the $S(Q)$ shown in Fig. 4.

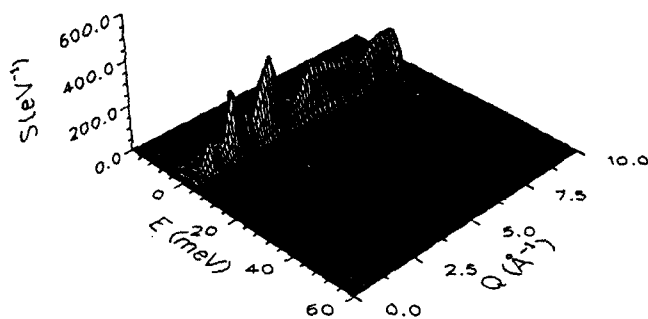


Figure 6
Scattering function $S(Q,E)$ for α -GeSe₂ at 13K (Ref. 14).

The inelastic scattering for an amorphous system described by a continuous and in general slowly varying function of Q and E . For most solids it is dominated by the one-phonon scattering

$$S_{c,\pm 1}(Q,E) = \sum_{\lambda} S_{c,\lambda}(Q) \delta(E \pm \hbar\omega_{\lambda}) . \quad (14)$$

The coherent one-phonon structure factor for the mode λ is given by

$$S_{c,\lambda}(Q) = \frac{1}{2N} \sum_{ij} (\text{same factors as } S_{cl}) \frac{\hbar(Q \cdot e_i^{\lambda})^* (Q \cdot e_j^{\lambda}) \langle n_{\lambda} + 1 \rangle}{(M_i M_j)^{1/2} \omega_{\lambda}} \quad (15)$$

where ω_{λ} , e_i^{λ} and n_{λ} represent the frequency, displacement vectors and thermal population for the mode λ . The phase factor (see Eq. (13)) and scalar products in Eq. (15) give $S_{c,\lambda}(Q)$ a characteristic Q variation for a given λ .

Fig. 7 shows the inelastic scattering measured for a-GeSe₂¹⁴. Structure can be observed, varying with both E and Q . To investigate this in detail, we investigate the scattering over a range in Q (2.0 - 7.5 Å⁻¹) to obtain the effective *one-phonon density of states* shown in Fig. 8.

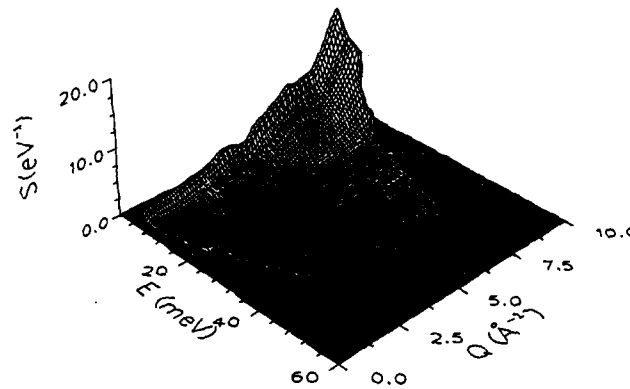


Figure 7
Scattering function $S(Q,E)$ for a-GeSe₂, with the elastic region suppressed to highlight the inelastic scattering (Ref. 14).

The symbols ν_{λ} identify the vibrational modes of the Ge(Se_{1/2})₄ tetrahedron which is the basic building block of this glass. The identification of each mode λ can be confirmed by calculating $S_{c,\lambda}(Q)$ for that mode and comparing it with the variation in Q of the scattering observed at $E = \hbar\omega_{\lambda}$. This is done in Fig. 9 for the breathing mode at $E = 26$ meV (ν_1) and excellent agreement is seen to be obtained.

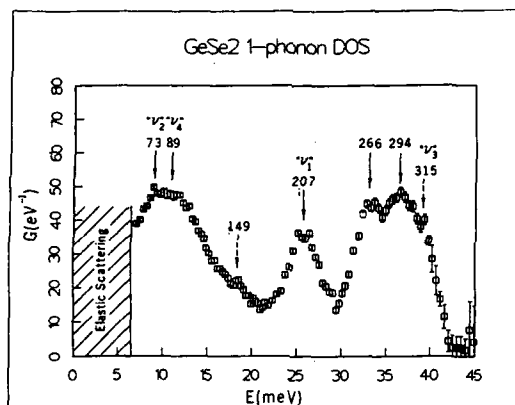


Figure 8
One-phonon effective density of states for α -GeSe₂. The labels attached to various features give the frequency in cm⁻¹; the symbols ν_λ , $\lambda=1-4$, give assignments in terms of a Ge(Se_{1/2})₄ tetrahedron (Ref. 14).

We should like to proceed further to identify the two components in this mode resolved by recent Raman scattering and ascribed to intermediate range order¹⁵; at present this appears extremely difficult to do.

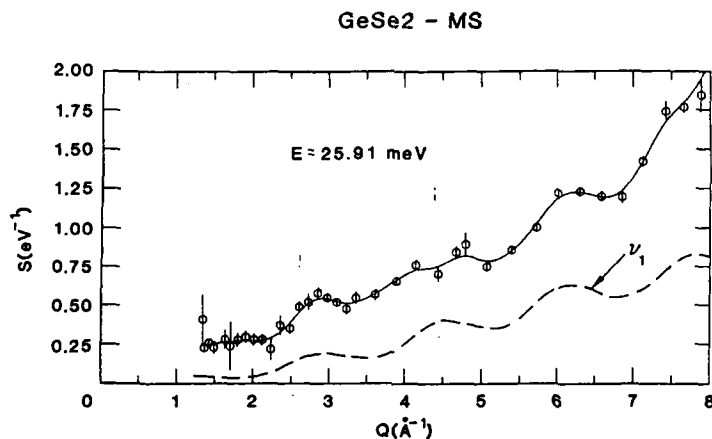


Figure 9
One-phonon structure factor $S_{c,\lambda}(Q)$ for the breathing mode ν_1 in α -GeSe₂.
Circles: measurement at $E=25.91$ meV; solid line: cubic spline fit to measured data; dashed line: calculation for an isolated Ge(Se_{1/2})₄ tetrahedron (Ref. 14).

Conclusions

Neutron diffraction is a powerful tool for investigating the atomic structure of amorphous systems. In particular, the various types of ordering - hard-sphere packing, chemical short-range order and intermediate-range order caused by the presence of structural units, can be identified. The origin of the intermediate-range order in certain amorphous solids, for example oxide and chalcogenide glasses, is a controversial question. The measurement of phonon densities of states and structure factors with inelastic neutron scattering may shed some light on this problem, coupled with computer simulation techniques such as molecular dynamics.

ACKNOWLEDGEMENTS

I wish to acknowledge the contributions of my coworkers to the results and concepts discussed in this paper, including R.J. Dejus, M.-L. Saboungi, S. Susman, K.J. Volin, U. Walter, I. Ebbsjö, R. Kalia, P. Vashishta, S.C. Moss and A.C. Wright. The work was supported by the U.S. Department of Energy (BES - Materials Sciences) under Contract No. W-31-109-ENG-38.

References

- [1] R. K. Crawford, D. L. Price, J. R. Harrmann, R. Kleb, D. G. Montague, J.M. Carpenter, S. Susman and R. J. Dejus, Proc. Xth Intl. Coll. on Advanced Neutron Sources, to be published (1989).
- [2] A. K. Soper, "Future Perspectives for Liquids and Amorphous Materials Diffraction at ISIS," to be published (1989).
- [3] R.G. Delaplane, U. Dahlborg, M. Sandström and K. Sköld, in: Neutron Scattering in the Nineties (IAEA, Vienna, 1985), p.469.
- [4] Neutron Research Facilities at the ILL High Flux Reactor (Institute Laue-Langevin, Grenoble, France, 1986).
- [5] P.A. Egelstaff, in: Neutron Scattering, Ed. D.L. Price and K. Sköld, Methods of Experimental Physics, Vol.23, Part B (Academic, San Diego, 1987), p. 405 (see pp. 428 - 442).
- [6] R. Zallen, The Physics of Amorphous Solids (Wiley, New York, 1983) P.49.
- [7] N.W. Ashcroft and I. Lekner, Phys.Rev. 145, 83(1966).
- [8] T. Fukunaga, N. Watanabe, and K. Suzuki, J.Non-Cryst.Solids 61/62, 343(1984).
- [9] S. Susman, K.J. Volin, D.G. Montague, and D.L. Price, to be published.
- [10] D.L. Price, S.C. Moss, J. Reijers, M.-L. Saboungi and S. Susman, J. Phys: Condensed Matter 1, 1005 (1989).

- [11] S.C. Moss and D.L. Price, in Physics of Disordered Materials, ed. D. Allen, H. Fritzsche and S.R. Orshinsky (Plenum, New York, (1985), p. 77.
- [12] P.A. Egelstaff, An Introduction to the Liquid State (Academic, London and New York, (1967), p. 75.
- [13] P. Vashishta, R.K. Kalia, G.A. Antonio and I. Ebbsjö, Phys.Rev.Letters **62**, 1651(1989); P. Vashishta, R.K. Kalia and I. Ebbsjö, Phys.Rev. **39**, 6034(1989).
- [14] U. Walter, D.L. Price, S. Susman and K.J. Volin, Phys.Rev.B**37**, 4232(1988).
- [15] S. Sugai, Phys. Rev. **B35**, 1345 (1987).

DYNAMICS OF WEAKLY CONNECTED SOLIDS: SINTERING OF POLYMERIC
AEROGELS

D. W. SCHAEFER*, D. RICHTER**, B. FARAGO**, C. J. BRINKER*,
C. S. ASHLEY*, B. J. OLIVIER*, AND P. SEEGER***

*Sandia National Laboratories, P. O. Box 5800, Albuquerque, NM
87185

**Institut Laue-Langevin, 38042 Grenoble, France

***Los Alamos National Laboratory, Los Alamos, NM, 87545

ABSTRACT

A combination of small angle scattering (SAS) and neutron spin-echo (NSE) spectroscopy is used to characterize the structure and dynamics of polymeric silica aerogels during sintering. The SAS data indicate that densification at short length scales precedes the densification at longer scales (comparable to that of the pore structure). Interpreted within the fracton model, the NSE data are consistent with an initial decrease in connectivity during relatively early stages of densification.

INTRODUCTION

It has recently become clear that weakly connected porous solids display unusual low-energy vibrational excitations [1-5]. The concept of fractons first advanced by Alexander and Orbach [4], stands as the most reasonable model for the origin of these excitations. Fractons occur in fractal structures and are the analog of phonons in ordered systems.

By studying a series of aerogels synthesized by different pathways, we have associated the frequency dependence of low-energy excitations in aerogels with connectivity [6]. In particular, highly branched systems display large spectral (or fracton) dimensions, approaching three for dense compact materials. As the connectivity is decreased, however, (say by removing bonds in a random network) the spectral dimension decreases. Fracton analysis, therefore, provides a means of measuring the connectivity of a network.

In this paper we analyze both the structure and connectivity of a polymeric silica aerogel during sintering to a dense solid. We use small angle x-ray and neutron scattering to assess positional correlations and neutron spin-echo spectroscopy to assess connectivity via the density of states associated with the low-energy excitations described above. We observe unusual features in the dynamics of polymeric aerogels that suggest the connectivity actually decreases during the early stage of sintering.

GROWTH AND STRUCTURE OF POLYMERIC AEROGELS

We are particularly interested in porous solids which have a unique polymer-like structure. In general, however, it is difficult to make a porous solid from a polymeric precursor

because during the drying process even branched polymers lack sufficient rigidity to resist collapse. In general, therefore, porous solids are always quite dense and compact on short length scales. The exception to this rule occurs when certain polymeric aerogels are made from highly branched precursor monomers [7,8]. Aerogels are made by solution polymerization of a soluble monomeric silicate followed by super-critical solvent extraction from the resulting gel.

By manipulating the synthetic protocol in the precursor gel phase, it is possible to prepare polymeric aerogels with sufficient branching (ramification) on a short length scale to resist collapse during drying. Polymeric materials can be prepared by a two-stage synthetic process [8,9], first reacting the monomeric silicate under acid catalysis and subsequently under base catalysis. Branched polymer molecules are formed under acid catalysis via cluster-cluster aggregation. The clusters lack sufficient rigidity to form aerogels. By switching to base catalysis in the second stage, however, the small precursor clusters densify sufficiently to impart adequate local rigidity. Under basic conditions there is an initial prejudice toward a monomer cluster growth leading to short scale compaction of the growing clusters. When all the monomers are exhausted, however, the system converts to a cluster-cluster process leading to branched polymer structures [10].

Figure 1 includes the small-angle x-ray scattering curves for two-stage polymeric aerogels. The limiting slope of -2.2 indicates branched polymeric structures for spatial dimensions between 10 and 100\AA .

STRUCTURAL CHANGES UPON SINTERING

Figure 1 shows the changes in the small-angle scattering profile during sintering

at 950°C . After four hours the scattering curve is nearly unchanged except for a slight enhancement of the intensity and a somewhat steeper slope at high Q . The enhanced intensity is probably due to an increase in scattering length density as the organics are burned off yielding pure SiO_2 . The crossover to steeper slope at large Q (not very evident below $Q = 0.1\text{\AA}^{-1}$) is consistent with the formation of compact structure on the 10\AA length scale. A limiting slope of -4 indicates a sharp interface at the pore surfaces.

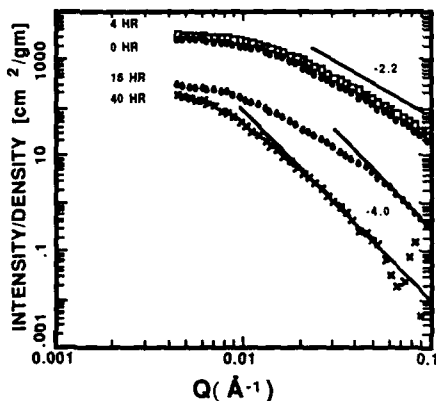


FIG 1: CHANGE OF SMALL ANGLE PROFILE DURING SINTERING OF POLYMERIC AEROGEL

After sixteen hours, there is distinct evidence of compact structures on length scales approaching 50Å. In addition, the increased slope at intermediate length scales signals an increased fractal dimension of the polymer-like network.

As sintering proceeds, the entire scattering curve changes character leading to a limiting slope of -4. At this point, there is no evidence of any residual polymer structure so the structure should be simply viewed as an interconnected solid consisting of fully dense SiO₂ and unoccupied pores with smooth interfaces between them.

The general evolution of the scattering curve is consistent with the conventional ideas concerning sintering [11]. Short length-scale structure disappears first by forming compact droplets. The droplets develop by "chewing up" density fluctuations at longer and longer length scales until the network structure evolves into a conventional glassy phase. The final stage of sintering (not studied) then involves the surface-tension-driven elimination of internal surfaces.

VIBRATIONAL DYNAMICS AND SINTERING

We have studied the development of the vibrational dynamics in polymeric aerogels via neutron spin-echo spectroscopy. In this method one measures the self-intermediate scattering function, $S(Q,t)$. For coherent scattering in the harmonic approximation, $S(Q,t)$ is directly related [12] to the vibrational density of states $g(\omega)$.

$$S(Q,t)/S(Q,0) = \exp[2W(Q)S(Q)(1-\gamma(t))] \quad (1)$$

where

$$\gamma(t) = \int d\omega \omega^{-1} n(\omega) g(\omega) \exp(i\omega t) \quad (2)$$

where $n(\omega)$ is the Bose factor, $2W(Q) = Q^2\gamma(0)$ is the Debye-Waller factor.

The form of $g(\omega)$ depends on the nature of excitations. $g(\omega)$ goes like ω^2 for phonon excitations and ω^{d-1} for fractons [4] where d is the spectral dimension.

The spectral dimension d is sensitive to the connectivity of the sample and provides information that is distinct from the fractal dimension D . The former is related to network topology whereas the latter is related to positional correlations. For example, ideal gaussian chains and lattice animals are both described by $D = 2.0$. The former, however, has linear connectivity leading to $d = 1.0$ whereas the latter is branched leading to $1 < d < 3$.

Figure 2 shows the measured dynamic structure factors where the lines represent a simple model involving phonon excitations at long times and fracton excitations at shorter times. The data were fit to the empirical function given by Eq. (3), which is consistent with a phonon-fracton crossover

This function is also found to fit the data for non-fracton excitations as well:

$$g(\omega) = \frac{\omega^2}{[\omega_0^2 + \omega^2]^{(3-d)/2}} \quad (3)$$

The fits of equations (1-3) to the data in Fig. 2 reveal an interesting development during the course of the sintering. The measured spectral dimension for the unsintered sample, $d = 1.5$, is consistent with a branched topology. After pyrolysis for 2 hr at 500°C, d decreases to 1.2. After sintering for 20 hrs, low-energy modes disappear completely.

What is surprising is that the measured spectral dimension decreases when the organics are pyrolyzed by treatment of the

virgin sample at 500°C for two hours. Within the fracton model, the decreased value of d implies decreased branching. It should be recognized that this decrease in branching relates to very large scale structures, an order of magnitude larger than the SiO_2 molecular building blocks [6].

Unfortunately, we do not have data at intermediate levels of sintering. It is possible that the system passes through a rigidity threshold [13]. At a critical value of d , low-energy excitations would be strongly suppressed as the network becomes rigid.

In the latest stages of sintering, curve C of figure 2, low-energy excitations completely disappear consistent with the dense, fully connected structure of SiO_2 .

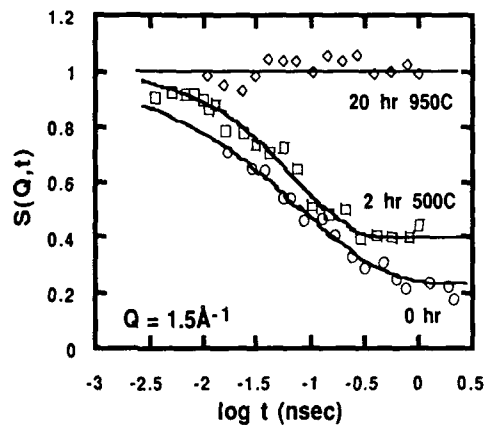


FIG 2: NEUTRON SPIN ECHO DATA FOR VIRGIN AND PYROLYZED AND SINTERED POLYMERIC AEROGELS

Figure 3 shows the small-angle neutron scattering profiles of the actual materials used in the dynamics study. Although the development of the data is similar to Fig. 1, the virgin aerogel was fully deuterated and had a fractal dimension of 2.5, somewhat larger than the sample used in Fig. 1. The differences arise because the final value of D depends sensitively on the degree of aging prior to supercritical extraction.

The pyrolyzed (2 hr 500°C) and sintered (20 hr 950°C) samples in Fig. 3 were protonated aerogels. The curves in Fig. 3 are shifted in the ordinate for clarity.

CONCLUSION

A combination of small-angle and NSE data shows that sintering occurs via the formation of compact structures first at short length scales then proceeding to larger scales. During the initial development, however, this system shows a lower spectral dimension consistent with a more weakly connected structure. We speculate that the early compact short range structure develops at the expense of weak links in the network. As NSE is sensitive to long-range network excitations, the data reveal that this long range network becomes less connected as the system densifies at the shortest length scale. This general development is consistent with the concept of Ostwald ripening where weak links between clusters would be sacrificed in favor of enhanced bonding at short length scales.

Although we have no data between 4 and 16 hours sintering, it is reasonable to believe that the structure would develop from a polymeric to a colloidal microstructure. We have shown that aerogels with a colloidal microstructure show unphysical negative values of d corresponding to a peak in the density of states [6]. We can speculate then that empirical parameter d in Eq. (3) changes smoothly during the sintering process from about 1.5 to a value less than 1. This transition involves first the sacrifice of weak links in the polymeric network to form the colloidal microstructure. Compacting of the colloidal structure then eliminates the low energy excitations altogether consistent with curve C of figure 2. Clearly, a full analysis of this problem requires substantially more data during the intermediate stages of sintering

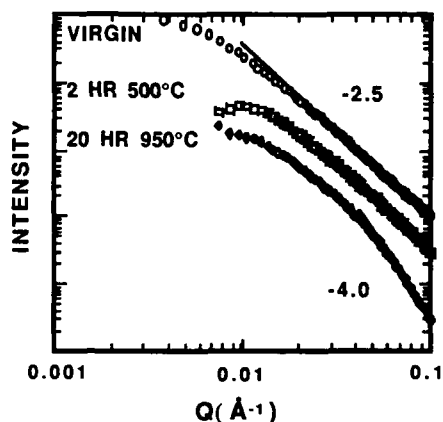


FIG. 3: SMALL ANGLE SCATTERING PROFILES FOR SAMPLES USED IN NEUTRON SPIN-ECHO EXPERIMENTS.

ACKNOWLEDGMENT

Work performed at Sandia National Laboratories was supported by the U. S. Department of Energy under contract DE-AC04-76DP00789 for the Office of Basic Energy Sciences, Division of Materials Science. This study resulted from discussions with Alan J. Hurd. We thank Steve Spooner and Rex Hjelm for contributions in collection of the SAXS and SANS data.

REFERENCES

1. A. Boukenter, B. Champagnon, E. Duval, J. Dumas, J. F. Quinson and J. Serughetti, *Phys. Rev. Lett.* **57**, 2391 (1986).
2. E. Courtens, J. Pelous, J. Phalippau, R. Vacher, and T. Woignier, *Phys. Rev. Lett.* **58**, 128 (1987).
3. Y. Tsujimi, E. Courtens, J. Pelous and R. Vacher, *Phys. Rev. Lett.* **60**, 2757 (1988).
4. S. Alexander and R. Orbach, *J. Phys (Paris)* **43**, L-625 (1982).
5. H. Conrad, J. Fricke and G. Reichenauer, *J. Phys. Colloque (Paris)*, **24**, C4-157 (1989).
6. D. W. Schaefer, C. J. Brinker, D. Richter, B. Farago and B. Frick, to be published.
7. D. W. Schaefer, *J. Phys. Colloque, (Paris)*, **24**, C4-121 (1989).
8. D. W. Schaefer, C. J. Brinker, J. P. Wilcoxon, D.-Q. Wu, J. C. Phillips, and B. Chu, in Better Ceramics Through Chemistry III, edited by C. J. Brinker, D. E. Clark and D. R. Ulrich. (*Mater. Res. Soc. Proc.* **121**, Pittsburgh, PA 1988) pp. 691-696.
9. C. J. Brinker, K. D. Keefer, D. W. Schaefer and C. S. Ashley, *J. Non-Cryst. Solids* **48**, 47 (1982).
10. D. W. Schaefer and K. D. Keefer, in Better Ceramics Through Chemistry II, edited by C. J. Brinker, D. E. Clark and D. R. Ulrich. (*Mater. Res. Soc. Proc.* **73**, Pittsburgh, PA 1986) pp 277-288.
11. W. D. Kingery, H. K. Bowen and D. R. Uhlmann, Introduction to Ceramics, (New York, Wiley-Interscience, 1976).
12. D. Richter, B. Farago, B. Frick, D. W. Schaefer and C. J. Brinker, to be published.
13. M. F. Thorpe, *J. Non. Cryst. Solids* **57**, 355 (1983)

VIBRATIONAL SPECTRA FOR HYDROGENATED AMORPHOUS SEMICONDUCTORS

W. A. KAMITAKAHARA*, R. BISWAS[†], A. M. BOUCHARD^{**}, F. GOMPF^{**},
AND J. B. SUCK^{**}

*Ames Laboratory, Iowa State University, Ames, IA 50011

[†]Microelectronics Research Center, Iowa State University, Ames,
IA 50011^{**}Kernforschungszentrum Karlsruhe, Institut für Nukleare
Festkörperphysik, D-7500 Karlsruhe, Federal Republic of Germany

ABSTRACT

Hydrogen vibration spectra have been measured by neutron scattering for several amorphous semiconductor materials, including a-Ge:H and a-SiC:H samples containing about 10 at. % H. The data for a-Ge:H are compared in detail with the results of realistic computer simulations.

INTRODUCTION

The inclusion of hydrogen plays a key role in improving the electronic properties of amorphous semiconductors, making them suitable for photovoltaic device applications by passivating defects intrinsic to the unhydrogenated materials. Vibrational spectroscopy has often been used to characterize the local bonding configurations of the H atoms in materials such as a-Si:H and a-Ge:H. The most commonly employed methods are infrared (IR) absorption and Raman scattering, although their interpretation is complicated by complex transition probabilities whose effects are frequently ignored. Neutron scattering offers the significant advantage that these effects are absent, directly yielding a physically relevant vibrational density of states which can readily be compared with theoretical calculations.

In this paper, we report measurements of the vibrational spectra of a-Ge:H and a-SiC:H, obtained by time-of-flight neutron spectroscopy. The results are compared with calculations based on realistic computer-generated structural models. Most prior theoretical calculations have used simplified models involving Bethe lattices, or random network models with small numbers of atoms. Our calculations employ models containing several hundred atoms, obtained by molecular dynamics methods.

EXPERIMENT

The samples of a-Ge:H and a-SiC:H, produced by reactive rf sputtering in an Ar/H₂ atmosphere, contained 10-12 at. % H. The H content was determined by comparing NMR signals with a standard H₂O sample. The neutron measurements were carried out at room temperature, mainly on the IN4 time-of-flight (TOF) spectrometer at the Institut Laue-Langevin, Grenoble. Additional data were obtained on the TOF spectrometer operated by the Karlsruhe neutron scattering group at the Melusine reactor of the Centre d'Études Nucléaires de Grenoble.

Hydrogen has a large scattering cross section (about 80 barns/atom) for neutrons, while those of Ge (8.4 barns), C (5.6 barns) and Si (2.1 barns) are much smaller. The weighting of the partial densities of states for each atomic species when measured by neutron scattering is proportional to the scattering cross section divided by the atomic mass, so that, in an integral sense, the measured densities of states are totally dominated by the H contributions when the H concentrations are as high as 10 at. %. However, most of the H spectral densities appear above 50 meV where major bond-bending and bond-stretching modes appear. Below this energy, the H atoms tend to be passive "riders" on the modes of the heavier atoms. What this implies is that for our a-Ge:H sample, the Ge scattering is comparable in strength to the H scattering below 35 meV (near the maximum Ge frequency), but is negligible at higher energies.

The spectrum obtained for a-Ge:H is shown in Fig. 1. The quantity shown is the "neutron-weighted", i.e., cross-section and inverse-mass-weighted, density of states which can be readily extracted from the observed inelastic neutron scattering. The data have been carefully corrected for multi-phonon scattering. As discussed above, the spectrum is essentially the H partial density of states, except below 35 meV, where the Ge scattering is appreciable. The dominant peak at 70 meV comprises most of the H motions of Ge-H bond-bending character. Its substantial width (7 meV, compared with a resolution of about 3 meV in this region) suggests considerable variation in the local H-bonding geometry. In the lower frequency range, the peaks at 12 and 32 meV are the analogues of the TA and TO peaks in the unhydrogenated a-Ge material. The weak feature at 14 meV is the Cardona local mode [1-3], which has been studied in detail by Raman and IR spectroscopy.

The most noteworthy features in Fig. 1 lie between 40 and 58 meV (322 and 468 cm^{-1}), where two unexpected weak peaks occur.

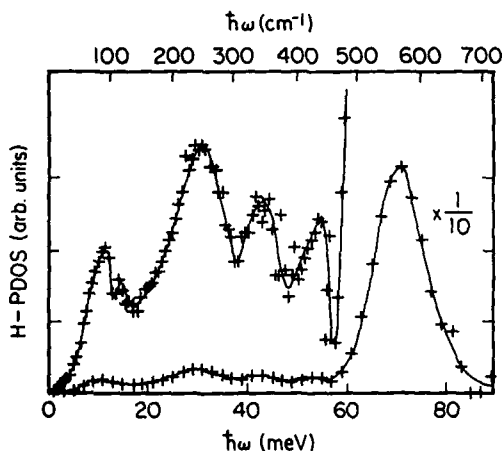


Fig. 1. Experimentally measured partial vibrational density of states for H modes (H-PDOS) in a-GeH_{0.11}.

The existence of these features was checked by making two separate measurements on different instruments with different incident neutron energies. We believe that this is the first observation of structure in this region. In the following section, an interpretation of these features will be given in connection with our a-Ge:H model calculations. The features occur in a window of energies between the highest Ge vibrations at 37 meV and the 60 meV lower edge of the H bond-bending peak. Such a window does not occur for a-Si:H, where the higher-frequency Si vibrations extend nearly to the bottom edge of the H bond-bending band. We have previously reported [4] neutron measurements on a-Si:H. The qualitative appearance of the a-Si:H spectrum is similar to that of a-Ge:H, except in the 40-58 meV window region.

The partial density of states measured for H modes in a-SiC:H is shown in Fig. 2. In this case, one obtains unusually clear structural information which is not dependent on interpretation via model calculations. The dominant peaks at 80 and 120 meV are, respectively, the features associated with Si-H and C-H bond-bending motions. Because the peaks are of roughly equal strength, one can conclude that, in this particular sputtered sample, H is bonded in roughly equal amounts to C and H atoms. This is an example of how the absence of complex transition probability effects in neutron scattering can facilitate the interpretation of vibrational spectra.

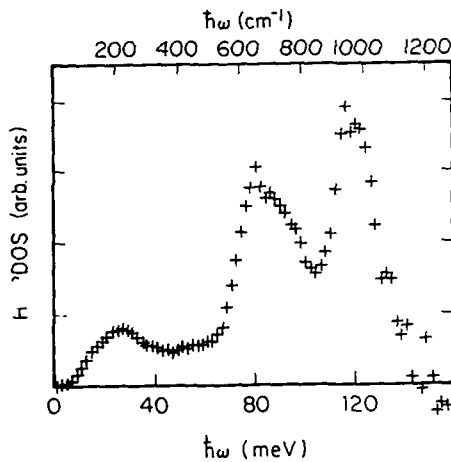


Fig. 2. Experimentally determined partial density of states for H modes in a-SiC:H, containing about 10 at. % hydrogen.

COMPUTATIONAL METHODS

The calculations proceed in several steps. The first and most difficult step is the generation of large, realistic structural models of a-Si and a-Ge via molecular dynamics simulations of quenching liquid Si or Ge from the melt. These simulations were performed with separable two- and three-body potentials developed by Biswas and Hamann [5], yielding N-atom structures ($N=512$ and 2000), with periodic boundary conditions,

as described in detail [6] by Biswas, Grest, and Soukoulis (BGS). The bond length, bond angle, and dihedral angle distributions are similar to those of the Wooten, Winer, Weaire (W3) model [7], which was generated by Monte Carlo methods. The vibrational densities of states for a-Si, calculated from the BGS models, are in very good agreement with neutron measurements, and reveal some novel localization behavior at low frequencies [8].

A characteristic feature of the BGS models is the presence of coordination defects consisting of two-, three-, and five-coordinated atoms (1, 34, and 52 in number, respectively, in the 512-atom network). The presence of the dangling bond sites provided a natural way of incorporating H into the network, yielding an amorphous network with 5.3 at. % H ($N_H=29$, $N_{Ge}=512$). This small number of H atoms led to considerable statistical variation in the calculations of the H partial density of states. In order to improve statistics and to mimic known structural features of sputtered amorphous Ge, we incorporated more H by introducing spherical voids in the the a-Ge networks, leading to many dangling bonds and consequently H sites at the void surfaces. H atoms were placed at the dangling bond sites so that H-Ge distances had the known value of 1.54 Å, and were as close as possible to a tetrahedral position vis-a-vis the Ge-Ge back bonds. H atoms which were less than 1 Å from other H atoms, or less than 2 Å from other Ge atoms, were removed, thus leaving some dangling bonds in the network. Finally, by breaking Ge-Ge bonds at monohydride sites and introducing H atoms, the number of dihydride configurations (two H atoms bonded to the same Ge atom) was increased. The resultant network had 21.8 at. % H ($N_H=103$, $N_{Ge}=370$), of which 59 and 44 H atoms were in monohydride and dihydride configurations, respectively.

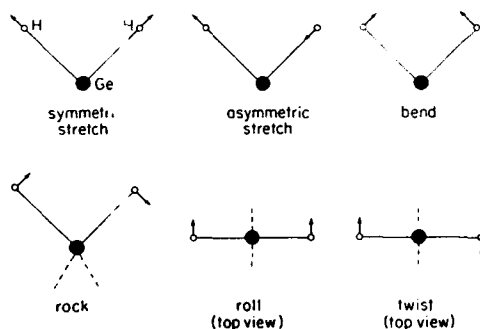


Fig. 3. The fundamental vibrational modes for the Ge-H₂ dihydride group, assuming only H motion.

The entire network was relaxed with the Keating potential, which is particularly convenient for calculations of vibrational properties. The Ge-Ge force constants were taken from our earlier studies [8]. The Ge-H force constants were fitted to the experimental positions for the Ge-H bond-stretching and bond-bending modes, including the scissor-bending mode at 840 cm⁻¹. The six fundamental modes of the Ge-H₂ dihydride configuration are schematically shown in Fig. 3. The Ge-H stretching force constant was taken to be slightly larger for dihydride than for monohydride configurations.

RESULTS

Diagonalizing the dynamical matrix for the network, using the Keating potential and counting the zone center frequencies of the periodically repeated structure, resulted in the H density of states shown in Fig. 4. The mode eigenvectors were used to calculate a very useful measure of mode localization, the inverse participation ratio [9] $1/p$, for each mode. $1/p$ can be thought of as the inverse of the number of atoms moving in a vibrational mode (Fig. 5).

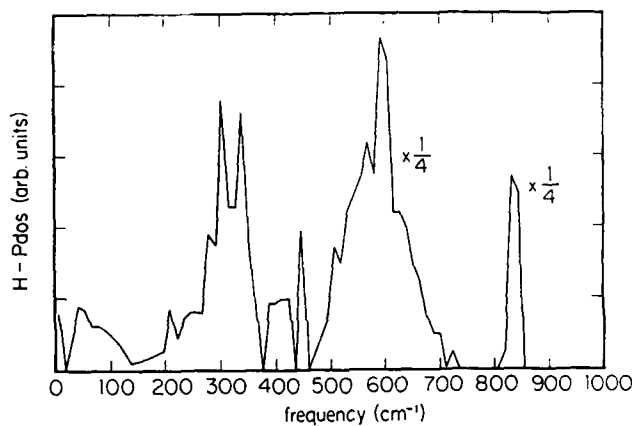


Fig. 4. Calculated partial density of states for H modes in a-Ge:H. The amorphous network contains 22 at.% H, of which 42 % are in dihydride configurations.

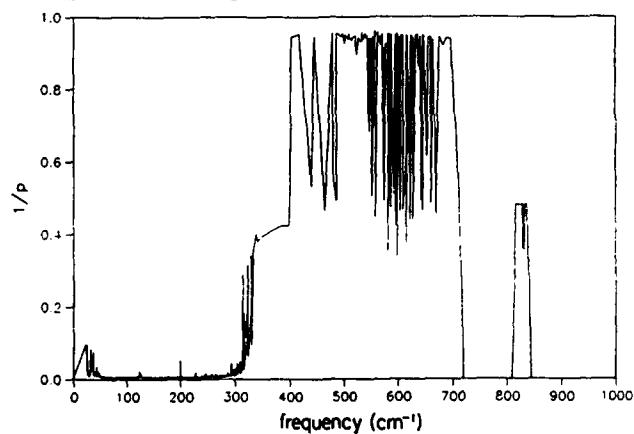


Fig. 5. Calculated inverse participation ratios for the modes in a-Ge:H. Values of $1/p$ around 0.9 arise from monohydride H modes, while dihydride modes have values around 0.5.

The broad peak between 480 and 710 cm^{-1} consists of (i) bending modes of monohydride species that have $1/p$ values greater than 0.9, and (ii) both the rock and twist modes of the dihydride species that have $1/p$ values between 0.4 and 0.6, i.e., two H atoms are involved in the vibrational mode. We have verified this interpretation by detailed examination of the eigenvectors. The scissor modes appear at 830 cm^{-1} , with $1/p$ values appropriate to dihydride modes.

Our calculations indicate that there are indeed H modes in the 370-480 cm^{-1} region, as observed in the neutron experiment. These have $1/p$ values between 0.35 and 0.6, and are thus dihydride modes. Examination of a number of eigenvector patterns indicated that these are rock modes of the dihydride species, with eigenvector patterns very similar to those shown in Fig. 3. The calculated H density of states (Fig. 4) is qualitatively similar to the experimental data in the range 350 to 450 cm^{-1} . We interpret the new features at 350 and 430 cm^{-1} as dihydride rocking mode peaks. This assignment is consistent with the value of 380 cm^{-1} for the dihydride rock suggested by Cardona [1]. The presence of dihydride configurations in our sample of a-Ge:H was independently supported by IR absorption measurements which showed both a scissor mode peak at 890 cm^{-1} and a two-peak structure in the stretch-mode feature at 1900 cm^{-1} .

ACKNOWLEDGMENTS

The Ames Laboratory is operated by Iowa State University for the U.S. Dept. of Energy (USDOE) under contract no. W-7405-eng-82. This research was supported by the Office of Basic Energy Sciences, Division of Materials Sciences, USDOE. Research at the Microelectronics Research Center was supported by the Air Force Office of Scientific Research and by the Electric Power Research Institute.

REFERENCES

1. M. Cardona, *Phys. Stat. Solidi* **118**, 463 (1983).
2. E. Martinez and M. Cardona, *Phys. Rev. B* **28**, 880 (1983).
3. D. Bermejo and M. Cardona, *J. Non-Cryst. Solids* **32**, 405 (1979).
4. W. A. Kamitakahara, H. R. Shanks, J. F. McClelland, U. Buchenau, F. Gompf, and L. Pintschovius, *Phys. Rev. Lett.* **52**, 644 (1984).
5. R. Biswas and D. R. Hamann, *Phys. Rev. B* **36**, 6434 (1987); *Phys. Rev. Lett.* **55**, 2001 (1985).
6. R. Biswas, G. S. Grest, and C. M. Soukoulis, *Phys. Rev. B* **36**, 7437 (1987).
7. F. Wooten, K. Winer, and D. Weaire, *Phys. Rev. Lett.* **54**, 1392 (1987).
8. R. Biswas, A. M. Bouchard, W. A. Kamitakahara, C. M. Soukoulis, and G. S. Grest, *Phys. Rev. Lett.* **60**, 2280 (1988).
9. P. Dean, *Rev. Mod. Phys.* **44**, 127 (1972); R. J. Bell, *Rep. Prog. Phys.* **35**, 1315 (1972).

**INELASTIC NEUTRON SCATTERING STUDIES OF NONLINEAR OPTICAL MATERIALS:
p-NITROANILINE ADSORBED IN ALPO-5**

JACQUELINE M. NICOL*, TERRENCE J. UDOVIC**, J.J. RUSH**, SHERMAN D. COX***
AND GALEN D. STUCKY***

* University of Maryland, College Park, MD 20742 and National Institute of Standards and Technology, Gaithersburg, MD 20899¹.

** National Institute of Standards and Technology, Gaithersburg, MD 20899.

*** University of California, Santa Barbara, CA.

† Address for correspondence

ABSTRACT

Inelastic neutron scattering has been used to characterize the vibrational spectroscopy below 220 meV of para-nitroaniline adsorbed in the molecular sieve ALPO-5. Samples at loadings of both 3 and 13 weight %, which represent the onset of and the maximum in the nonlinear optical properties respectively, were studied. The torsional vibration of the amino (NH₂) group has been identified at ca. 50 meV. The splitting and structure of this mode is sensitive to the loading level. This can be related to differences in the nature of the hydrogen bonding in these materials.

INTRODUCTION

The inclusion of a guest species into a host framework is a relatively new method by which nonlinear optical materials for second harmonic generation (SHG) can be synthesized [1-3]. The search for new nonlinear optical materials for SHG is constrained primarily by the bulk hyperpolarizability tensor, which in the second order case is sensitive to symmetry restrictions. Thus for a material to exhibit SHG, the crystal structure must be noncentrosymmetric. In inclusion chemistry, this symmetry restriction may be imposed on a guest molecule by an acentric host or created through guest-host interactions. Therefore by careful size and shape selection of the host and guest, the inclusion of a guest molecule in a host framework can result in molecular alignment and optimization to create a system whose nonlinear optical properties are very different from those of either the individual guest molecules or the host framework.

The first nonlinear optical materials generated by inclusion were organic molecules included within an organic host, e.g. p-nitroaniline in β -cyclodextrin [1]. More recently, the use of inorganic hosts, in particular large pore molecular sieves, has been reported [2,3]. Inorganic hosts have the advantages over organic hosts of increased rigidity, thermal stability and chemical inertness, which are important in many applications. The wide variety of pore structures, sizes, shapes and charge densities available in the molecular sieves makes this group of hosts particularly promising for matching the guest to the host to optimize the nonlinear optical properties. In particular, molecular sieves possessing a one-dimensional pore structure have considerable potential for molecular alignment.

Recently, the adsorption of para-nitroaniline (p-nitroaniline) into the channels of the molecular sieve ALPO-5 has been shown to produce SHG effects substantially larger than that of any previously reported organic or organometallic inclusion complex [2,3]. (For pure p-nitroaniline, SHG = 0). The acentric molecular sieve ALPO-5 [4] is composed of alternating AlO₄ and PO₄ tetrahedra linked by oxygen bridges to form a neutral array of one-dimensional 12-ring channels, into which p-nitroaniline is adsorbed and aligned.

In this paper, we report the preliminary results of an incoherent inelastic neutron scattering (IINS) study to characterize the vibrational spectroscopy below 220 meV of p-nitroaniline adsorbed in ALPO-5. Two p-nitroaniline loadings of 3 and 13 wt % were investigated, which represent the onset of and the maximum in the nonlinear optical properties, respectively. In addition, the spectra of p-nitroaniline and ALPO-5 were obtained for comparison.

EXPERIMENTAL

The IINS scattering data were obtained at the Neutron Beam Split-core Reactor (NBSR) at the National Institute of Standards and Technology, Gaithersburg, MD, using the BT-4 (triple-axis) spectrometer with either a liquid-nitrogen-cooled Be or Be-graphite-Be filter analyzer. A Cu (220) monochromator with 40'-40' collimation before and after it was used to cover the energy range 32-220 meV with a combination of both analyzers. The energy resolution using the Be-graphite-Be analyzer over the 35-100 meV range was between 1.9-4 meV, while for the Be analyzer in the 32-200 range it was 5-6 meV below 90 meV and $\approx 6\%$ above 90 meV. A fast neutron background was measured and subtracted from the spectra.

The samples of p-nitroaniline adsorbed in ALPO-5 were prepared by a vapor-phase loading method [2]. Desired portions of predried ALPO-5 and p-nitroaniline (purified by sublimation followed by recrystallization from 95 % ethanol) were placed into an ampoule connected to a vacuum stopcock, in a dry atmosphere. The ampoule was evacuated and the stopcock closed off. The sample was thoroughly mixed and heated at 373K overnight. For the IINS experiments, the samples were transferred to aluminum sample cans in a He dry box. All measurements were made with the samples cooled to 80 K.

RESULTS AND DISCUSSION

The p-nitroaniline molecule, which has a chemical formula of $\text{NO}_2\text{-C}_6\text{H}_4\text{-NH}_2$, is composed of a ring of six carbon atoms, with a nitro (NO_2) and amino (NH_2) group attached to carbon atoms 1 and 4. Normal mode analysis shows that the p-nitroaniline molecule, with symmetry C_{2v} , possesses 3N-6=42 internal vibrational modes, none of which are degenerate. Of these, 6 are associated with the stretching vibrations of the C-H and N-H bonds and will be of energy greater than 300 meV. Consequently these will not be observed in our IINS data, which is limited to the spectral region below 220 meV. Further, as the IINS data will be dominated by the vibrational modes associated with the hydrogen nuclei (the scattering cross-section of hydrogen being much greater than the other nuclei), the 6 vibrational modes of the nitro group are unlikely to be observed unless coupled to the hydrogen atoms. Thus, the IINS spectrum of p-nitroaniline will be dominated by modes associated with vibrations of the carbon ring and its attached hydrogen atoms and of the amino group. Illustrated in figures 1 and 2 are representative spectra of the IINS data obtained for p-nitroaniline adsorbed in the channels of ALPO-5 molecular sieve. These spectra show a large number of well-resolved and intense features due to the adsorbed p-nitroaniline. Assignment of the observed peaks to a particular mode is complex due to the fact that some of the normal modes have very similar energies, which results in the IINS intensity being due to the sum of these modes. We have started a preliminary analysis of the data, and are at the present time performing normal coordinate analysis calculations to further refine these assignments. Here we report preliminary results.

The IINS spectra depicted in figures 1 and 2 show the data obtained in the energy region above 32 meV for p-nitroaniline adsorbed in ALPO-5 at loadings of 3 and 13 wt %, which represent the onset of and the maximum in

the nonlinear optical properties respectively. Also shown are the background spectra of dehydrated ALPO-5 molecular sieve. Data collected in the spectral region below 32 meV and the spectra of pure crystalline p-nitroaniline are not illustrated here, but will be reported elsewhere [5]. Consider first the spectra of dehydrated ALPO-5 shown in figures 1a and 2a. The weak scattering features observed at ca. 140, 86 and 55 meV may be associated with the asymmetric and symmetric T-O stretching and T-O-T rocking motions of the ALPO-5 framework respectively (T = Al,P). Similar modes were observed in the IINS spectrum of Na,Cs-Rho zeolite due to framework vibrations [6]. The low overall scattering intensity of ALPO-5 is attributed to the low scattering cross-section of the elements which form the framework. Thus, the spectra of p-nitroaniline adsorbed in ALPO-5 will be dominated by the vibrational modes of the adsorbate that involve hydrogen

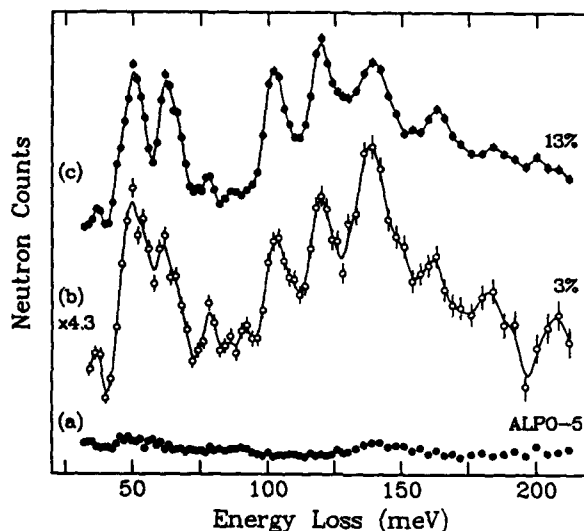


Figure 1. Low resolution IINS spectra of p-nitroaniline adsorbed in ALPO-5 molecular sieve. (a) Dehydrated ALPO-5; (b) 3 wt % p-nitroaniline; (c) 13 wt % p-nitroaniline. The solid line represents a guide to the eye.

motion. However, it is possible that coupling of the adsorbate to the framework vibrations will enhance the contribution of the framework vibrations in the spectra of the adsorbed p-nitroaniline, resulting in their observation.

The data in Figure 1 depict the low resolution spectra obtained using the Cu (220) monochromator and the Be filter analyzer. In this figure, the spectrum of 3 wt % sample has been rescaled by a factor of 4.3, the ratio of hydrogen nuclei in the 3 and 13 wt % samples. Overall, the spectra of the 3 and 13 wt % p-nitroaniline loadings are very similar when compared to the spectrum of pure crystalline p-nitroaniline, indicating that the internal vibrational modes of adsorbate are perturbed only slightly by adsorption. Comparison of the spectra of the 3 and 13 wt % p-nitroaniline shows higher relative intensities in the features at ca. 140, 86 and 51 meV for the 3 wt % sample. This additional intensity can be accounted for by the coupling of the p-nitroaniline to the vibrations of the ALPO-5 framework discussed above. All the observed features of the adsorbed p-nitroaniline, except the

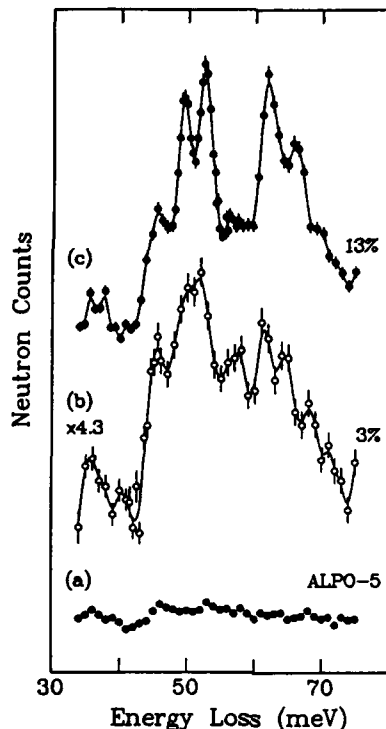


Figure 2. High resolution IINS spectra of p-nitroaniline adsorbed in ALPO-5 molecular sieve. (a) Dehydrated ALPO-5; (b) 3 wt % p-nitroaniline; (c) 13 wt % p-nitroaniline. The solid line represents a guide to the eye.

peak at 50 meV, can be associated with the stretching vibrations of the carbon ring, and the deformation and bending modes of the ring, C-H groups and amino group. In particular, the deformation modes of the amino group are observed in the spectral region above 180 meV. At the present time a more precise assignment of these features is not available, but awaits the normal coordinate analysis results. The intense feature observed at 50 meV may be assigned to the torsional mode of the amino group. This value is in good agreement with Raman scattering data, where the torsional mode of the amino group was assigned a value of 52.9 meV [7].

The torsional mode of the amino group has been investigated further using the higher resolution Be-graphite-Be filter analyzer. Figure 2 illustrates this data in the 35-75 meV energy range. The torsional mode of the amino group at ca. 50 meV is seen to have additional structure. In the case of the 13 wt % sample, this mode is now resolved into a doublet, with features centered at 49 and 52 meV. On the other hand, the spectrum of the 3 wt % sample shows one broad peak centered at ca. 51 meV. In addition, a feature is now observed at 46 meV, which can be assigned to a framework mode of the ALPO-5, enhanced in intensity by coupling to the adsorbate.

The observed differences in the shape and splitting of the torsional mode of the amino group in the 3 and 13 wt % samples can be related to

differences in the intermolecular hydrogen bonding and the arrangement of the p-nitroaniline molecules in the channels of ALPO-5. Structural data [7] for crystalline p-nitroaniline show that the molecules form chains which are linked together by hydrogen bonding between the amino hydrogen and the nitro oxygens. When p-nitroaniline is included in the channels of ALPO-5 molecular sieve, Cox et al [3] have shown from infrared measurements of the N-H stretching vibration that this chain structure is disturbed by inclusion. At loading levels below 3 wt %, they observe a shift in the N-H band of ca. 5 meV, relative to solid p-nitroaniline, that is very similar to the value observed for p-nitroaniline in chloroform solution. This indicates that at low loading levels essentially, all hydrogen bonding is lost. Above 5 wt %, the value of N-H stretching vibration is found to be intermediate between that observed in solution and in the crystal, indicating that there is weak intramolecular hydrogen bonding. From these results it was concluded that weak intermolecular hydrogen bonding plays an important role in SHG production for p-nitroaniline adsorbed in ALPO-5. The IINS data are supportive of these conclusions. The splitting of the torsional mode in the case of the 13 wt % sample, where the channels are filled with p-nitroaniline molecules, is similar to that observed for pure solid p-nitroaniline. This suggests a non-symmetrical torsional mode, a result of hydrogen bonding between one of the amino group hydrogens and a nitro group oxygen in an adjacent molecule. In the case of the 3 wt % sample, we observe that the torsional mode is broad and asymmetric, and is most probably composed of a number of components. This suggests that we may be observing two kinds of p-nitroaniline molecules in the low loading sample. At this loading level, some p-nitroaniline molecules will be independent as the channels are only partially filled, while others may be able to hydrogen bond to adjacent molecules. As a result, the observed torsional peak could be due to a combination of free and hydrogen bonding p-nitroaniline molecules. Such a conclusion is also supported by the infrared data for the 3 wt % sample, where the observation of a shoulder on the N-H mode can be taken as evidence for two kinds of p-nitroaniline molecules in the 3 wt % samples.

SUMMARY

The IINS spectra of p-nitroaniline adsorbed at two different loadings in the channels of ALPO-5 molecular sieve have been measured. The torsional mode of the amino group has been identified at ca. 50 meV. At 13 wt %, the peak is resolved into a doublet, whereas at 3 wt %, a broad asymmetric band is observed. These results, coupled with published infrared data [3], indicate that whereas all molecules appear to be hydrogen bonded in the 13 wt % sample, this is not the case in the 3 wt % sample. In this latter case, the results suggest that some molecules are independent, while others are associated by hydrogen bonds. The IINS data are being further analyzed with the aid of normal coordinate analysis calculations to refine the assignments of the spectral features.

ACKNOWLEDGEMENTS

S.D.C. and G.D.S. acknowledge the Office of Naval Research and E. I. du Pont for support of this work.

REFERENCES

1. S. Tomaru, S. Zembutsu, M. Kawachi and M. Kobayashi, *J. Incl. Phenom.* **2**, 885 (1984); *J. Chem. Commun.* **1984**, 1207.

2. S. D. Cox, T. E. Gier, G. D. Stucky and J. Bierlein, *J. Am. Chem. Soc.*, **110**, 2986 (1988).
3. S. D. Cox, T. E. Gier, G. D. Stucky and J. Bierlein, *Solid State Ionics* **32/33**, 514 (1989).
4. J. M. Bennet, J. P. Cohen, E. M. Flanigen, J. J. Pluth and J. V. Smith, in *Intrazeolite Chemistry*, Edited by G. D. Stucky and F. G. Dwyer, (ACS Symposium Series 218, American Chemical Society, Washington D.C., 1983) pp. 109-118.
5. J. M. Nicol, T. J. Udovic, J. J. Rush, S. D. Cox and G. D. Stucky, to be published.
6. M. J. Wax, R. R. Cavanagh, J. J. Rush, G. D. Stucky, L. Adams and D. R. Corbin, *J. Phys. Chem.*, **90**, 532 (1986).
7. M. Harrand, *J. Raman. Spectrosc.* **4**, 53 (1975).
8. K. N. Trueblood, E. Goldish and J. Donohue, *Acta. Cryst.*, **14**, 1009 (1961).

DIFFUSE NEUTRON SCATTERING FROM EXCESS OXYGEN IN $UO_{2.13}$

J.P. GOFF*, M.T. HUTCHINGS*, K. BROWN*, W. HAYES**, AND H. GODFRIN†

*Materials Physics & Metallurgy Division, Harwell Laboratory, Didcot, OX11 0RA, UK

**The Clarendon Laboratory, Parks Road, Oxford, OX1 3PU, UK

†Institut Laue Langevin, BP156X, Grenoble 38042, France

ABSTRACT

Coherent diffuse neutron scattering from single crystal $UO_{2.13}$ has been investigated at temperatures up to 2100K. Above 850K the crystal has a single phase and the excess anions give rise to a characteristic pattern of elastic diffuse scattering. This can be interpreted in terms of uncorrelated simple clusters of defective anions first postulated by Willis. The intensity distribution changes with temperature increase but no quasielastic scattering has yet been resolved. On cooling to 293K a strong hysteresis is exhibited.

INTRODUCTION

Uranium dioxide is the most extensively used nuclear fuel today, and is found in PWR, AGR and CANDU type reactors. It has the fluorite crystal structure $Fm\bar{3}m$, and a high melting temperature, of $T_m = 3120K$, for the stoichiometric compound. Like several other actinide oxides it can deviate considerably from stoichiometry while still retaining the fluorite structure. Hyperstoichiometric uranium dioxide UO_{2+x} , with $0 < x < 2.17$ exists as a mixture of UO_2 and U_4O_9 at ambient temperature but transforms to a single phase UO_{2+x} above a transition temperature which increases with x . For $UO_{2.13}$ this temperature is in the region 800 - 900K. The thermophysical properties of oxidised UO_{2+x} are not well established, but are important for estimating the fuel behaviour under hypothetical fault conditions in oxidising environments.

This paper reports the initial stages of an investigation of oxidised UO_2 using neutron elastic and quasielastic diffuse scattering to obtain information on the nature of the disorder and on the dynamical behaviour of the excess oxygen as the temperature is varied. These techniques have proved very informative in studying the thermally induced disorder in stoichiometric fluorite compounds including UO_2 [1-4]. Recently they have been used [5] to study the behaviour of excess anions in YCl_3 doped $SrCl_2$, a case in which the excess chlorine ions scatter both incoherently and coherently and so provide information respectively on the individual ions behaviour and on their correlated behaviour. In the present analogous example the oxygen ions scatter only coherently.

Following their original application in the interpretation of coherent diffuse scattering from thermally induced disorder at temperatures $T > 0.7T_m$ in the stoichiometric fluorites PbF_2 , $SrCl_2$ and CaF_2 [1], defect cluster models have been successfully used to interpret data from anion excess fluorides [6] and YCl_3 doped $SrCl_2$ [5]. In the former case the model is used to describe an average instantaneous picture of the diffusing ions and their distortion field, whereas in the anion excess systems the disorder is static at ambient temperature. The transition from static clusters to dynamic behaviour as the temperature is raised has recently been observed in YCl_3 doped $SrCl_2$, where the coherent diffuse scattering becomes quasielastic [5]. $UO_{2.13}$ has been

studied previously by diffraction at $\sim 1073\text{K}$ by Willis [7], who postulated a 2:2:2 type cluster to explain the mean occupation of lattice sites given by the data. Other more complex clusters have also been suggested [8].

THEORY

In the defect cluster model used here, the cations are assumed to remain on their regular lattice sites and the excess anion interstitials are located at positions (I) displaced from the mid-point of nearest neighbour (n.n.) anion sites along a $\langle 110 \rangle$ direction into an empty anion cube. The n.n. anions are relaxed to sites (R) in $\langle 111 \rangle$ directions towards empty cube centres, leaving vacancies (V) on their regular sites. Next n.n. (n.n.n.) anions may also be relaxed. One can thus form 2:1:2 or 8:1:8, and 2:2:2 or 8:2:8 clusters, with one or two interstitials respectively, where the numbers denote the V:I:R occupation. A good estimate of the magnitude of relaxation is given by the hard sphere model. The 2:2:2 cluster is shown in figure 1.

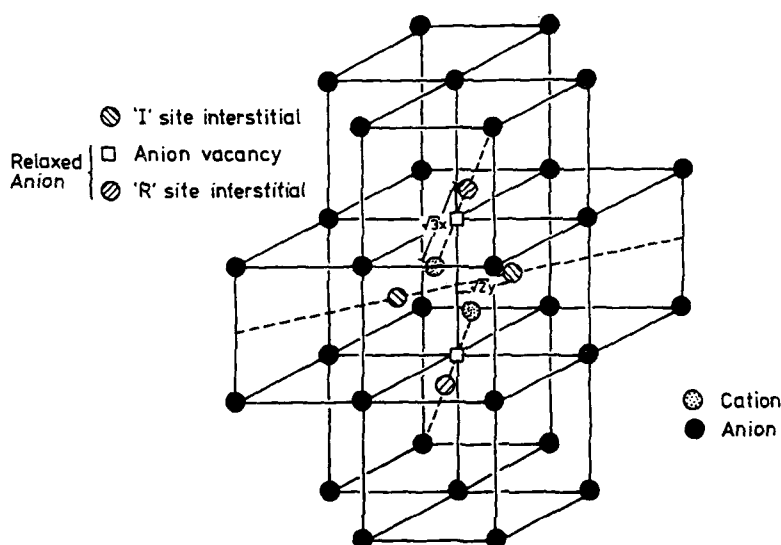


Figure 1 The 2:2:2 defect cluster in fluorite.

The structure factor of such a cluster is simply

$$F_I(Q) = \sum_{\mathbf{R}_I} b_A e^{i\mathbf{Q} \cdot \mathbf{R}_I} - \sum_{\mathbf{R}_V} b_A e^{i\mathbf{Q} \cdot \mathbf{R}_V} \quad (1)$$

The summation is made over all interstitials and vacancies, irrespective of whether their origin is a true interstitial or a relaxed ion. The vectors \mathbf{R}_I and \mathbf{R}_V give their site locations relative to the cluster centre, and b_A is the anion scattering length.

The scattering per defective anion, $Y(Q)$, is defined by

$$Y(Q) = \frac{1}{N_d N_0} \sum_{i=1}^{N_0} F_i(Q) F_i^*(Q) \quad (2)$$

where N_d is the number of defective ions in the cluster and N_0 is the number of possible orientations of the cluster.

For a given defect cluster we can calculate the experimentally determined coherent diffuse scattering function, $S_d(Q)$, by

$$S_d(Q) = n_d Y(Q) e^{-2W}$$

where n_d is the fraction of anions off their regular sites, and W is the Debye-Waller factor.

For elastic or quasielastic scattering within the instrumental resolution, scans of $S_d(Q, \omega = 0)$ give $S_d(Q) = \int S_d(Q, \omega) d\omega$, where the integral excludes the phonon contribution. Here $Q = k_i - k_f$, and $\hbar\omega = E_i - E_f$, where k_i (k_f) and E_i (E_f) are the wavevector and energy of the incident (scattered) neutron respectively.

EXPERIMENTAL PROCEDURE AND RESULTS

Two single crystals of ~ 1 cc volume were aligned and cut ultrasonically into cylinders with a $\langle 110 \rangle$ axis and encapsulated under vacuum in molybdenum cans. They were oxidised to a hyperstoichiometry of $UO_{2.13}$. The cans were mounted in specially designed furnaces capable of a maximum temperature of ~ 2100 K. The temperature was measured by W-W/Rh thermocouples. The measurements were made using the triple axis spectrometer in the PLUTO reactor at Harwell, and IN12 at the Institut Laue Langevin, Grenoble.

At 293 K both UO_2 and U_4O_9 phases were initially present, with no diffuse scattering detectable. As the temperature was raised the U_4O_9 satellite peaks decreased in intensity and diffuse scattering with a characteristic pattern built up. The exact temperature at which the U_4O_9 peaks disappeared, in the region 800-900 K, depended on the thermal history of the sample. The coherent diffuse scattering, $S(Q)$, from sample 1 at 858 K is shown in figure 2. It is seen that there is a strong peak, centred along the $[00\zeta]$ direction just beyond the (002) point, and a weaker peak along $[\zeta\zeta\zeta]$. Scans of intensity along $[00\zeta]$ were made at a number of temperatures between 858 K and 2100 K. The broad diffuse peak decreases in intensity and its centre shifts towards (002) as the temperature increases. The scattering was elastic at all temperatures within the instrumental resolution of 0.25 meV.

On cooling sample 1 for the first time, the diffuse scattering was present even at 293 K with only a slight intensity drop, indicating retention of the UO_{2+x} phase. After 8 days at 293 K, with no incident neutron beam, the sample was found to have reverted mainly back to $UO_2 + U_4O_9$. The measurements of $S(Q)$ shown in figure 2 were made on a second cycle of temperature up to 2100 K. The intensity of diffuse scattering fell sharply at the highest temperature and it is possible that some oxygen was lost from the sample above 1800 K.

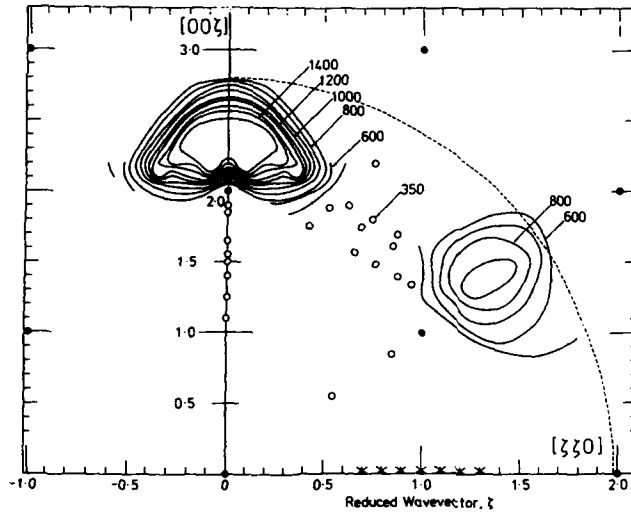
COHERENT DIFFUSE SCATTERING FROM $UO_{2.13}$ AT 858K

Figure 2 Measured coherent diffuse scattering from $UO_{2.13}$ at 858K in the (110) plane (arbitrary scale).

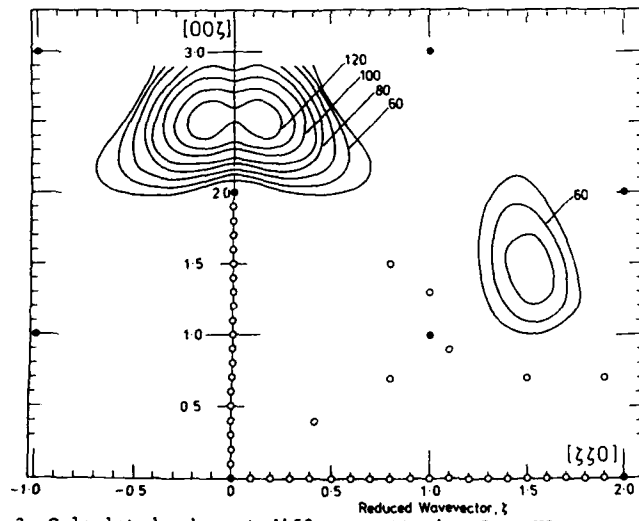
 $S(Q)$ CALCULATED FROM AN 8:2:8 CLUSTER

Figure 3 Calculated coherent diffuse scattering from $UO_{2.13}$ assuming an 8:2:8 cluster as described in text.

INTERPRETATION

The main features of the diffuse scattering can be reproduced using an 8:2:8 cluster model, with relaxations calculated from a hard sphere model giving I at $y = 0.16$, R(n.n) at $x = 0.34$, and R(n.n.n) displaced by $x = 0.04$ (see figure 1). The calculated S(Q) is shown in figure 3. The data have yet to be put on an absolute scale, but there is generally good agreement in the relative intensities of the two peaks. Indeed the quality of the data is such that it should be possible to fit the parameters in the theory to the data. Alternative cluster configurations do not fit the data as well, although the sensitivity to the presence of one or two interstitial ions is not great. The cubooctahedral cluster configuration used by Bevan et al [8] in several fluorite structures can be positively excluded.

CONCLUSION

The diffuse scattering from single phase $\text{UO}_{2.13}$ at 858K indicates that the excess oxygen ions form uncorrelated clusters of the 8:2:8 type, consistent with those postulated by Willis from diffraction data. Measurements at higher temperatures are planned, where changes in the nature of the scattering should reflect the increasing mobility of the oxygen ions, and enable estimates of the oxygen diffusion coefficient to be made.

Acknowledgement

This work was performed as part of the Underlying Research Programme of the UKAEA. It was supported in part by GNSR of the UKAEA.

References

- [1] M.T. Hutchings, K. Clausen, M.H. Dickens, W. Hayes, J.K. Kjems, P.G. Schnabel, C. Smith, *J. Phys. C* **17**, 3903 (1984).
- [2] K. Clausen, W. Hayes, J.E. Macdonald, R. Osborn, M.T. Hutchings, *Phys. Rev. Lett.* **52**, 1238 (1984).
- [3] M.T. Hutchings, *J. Chem. Soc., Farad. Trans. 2*, **83**, 1083 (1987).
- [4] M.T. Hutchings, *Crystal Lattice Defects and Amorphous Materials* **18**, 205 (1989).
- [5] J.P. Goff, W. Hayes, S. Hull, M.T. Hutchings, J. Godfrin, R. Ward (private communication).
- [6] N.H. Andersen, K. Clausen, J.K. Kjems, J. Schoonman, *J. Phys. C* **19**, 2377 (1986).
- [7] B.T.M. Willis, *Acta Cryst.* **A34**, 88 (1978).
- [8] D.J.M. Bevan, I.E. Grey, B.T.M. Willis, *J. Solid State Chem.* **61**, 1 (1986).

COMPARISON OF NEUTRON ELASTIC AND INELASTIC SCATTERING FROM
FUSED QUARTZ, CAB-O-SIL AND AEROGEL

JOHN H. ROOT^{*}, WILLIAM J. L. BUYERS^{*}, JOHN H. PAGE^{**}, DALE W.
SCHAEFER^{***} AND C. J. BRINKER

^{*}Atomic Energy of Canada Ltd., Chalk River, Ontario,
Canada, K0J 1J0

^{**}University of Manitoba, Winnipeg, Manitoba, Canada, R3T 2N2

^{***}Sandia National Laboratories, Albuquerque, NM 87185

ABSTRACT

Neutron scattering experiments have been performed to study the structure and dynamics of three preparations of silica: a dense glass (fused quartz), a flame-hydrolyzed aggregate (Cab-O-Sil, grade M5) and a polymeric aerogel. The experiments were performed on the three materials at temperatures selected from 300, 77 and 4.2 K. Neutron inelastic scattering was measured at $Q = 2.5, 2.9$ and 4.0 \AA^{-1} .

The elastic scattering indicates a systematic decrease in positional correlations on progressing from fused quartz through Cab-O-Sil to aerogel. The inelastic scattering was analyzed with the Buchenau model [1] to obtain the sample, Q and temperature dependences of the density of states, $g(\nu)$. In the aerogel $g(\nu)$ increases with temperature at frequencies greater than 1.5 THz and is enhanced at $Q = 2.5 \text{ \AA}^{-1}$. Thus a complete explanation of the inelastic scattering from aerogels must account for multiphonon processes, local antiphase motions and anharmonic effects.

INTRODUCTION

Silica may be prepared through a number of fabrication routes to produce a rich variety of structural forms. These include polycrystalline aggregates of quartz, high density glass and low density networks created by flame hydrolysis or hypercritical drying of gels. The unique structures and dynamics of the low density materials lead to applications in radiation detectors, high efficiency transparent insulators, and high surface area catalyst substrates.

In glassy forms of silica the fundamental structural unit is an SiO_4 tetrahedron. The local environment of each tetrahedron varies due to the statistical nature of configurations in the vitreous state. Buchenau et al investigated the neutron inelastic scattering from vitreous silica [2,3]. These authors analyzed the mixed coherent and incoherent scattering from silica by an intuitively appealing expression,

$$d^2\sigma/d\Omega d\nu \propto Q^2 S(Q,0) n(\nu) g(\nu)/\nu \quad (1)$$

where ν is the vibrational frequency, $g(\nu)$ is the density of states, $S(Q,0)$ is the elastic scattering intensity and $n(\nu)$ is the thermal population factor, $1 + [\exp(h\nu/kT) - 1]^{-1}$. The expression is expected to be valid for vibrational modes which are harmonic, have a wavenumber much less than Q and consist of in-phase motions of neighbouring atoms as occurs in sound waves and librational motions.

The present experiment is a comparison of neutron elastic and inelastic scattering from three samples of silica: fused quartz, Cab-O-Sil (grade M5) and a polymeric aerogel. Measurements at three convenient temperatures, 300 K, 77 K and 4.2 K and at Q values 2.5, 2.9 and 4.0 \AA^{-1} were made to search for anomalous variations in the density of vibrational states in the range 0.3 to 6.0 THz. These experimental conditions most readily yield structural and dynamical information which is dominated by interactions on molecular length scales and therefore complement recent neutron scattering experiments that attempt to investigate large scale "fractal" structures and dynamics of silica aggregates [4-8].

EXPERIMENTS

The fused quartz specimen was in the form of a tube of diameter 25 mm, wall thickness 1 mm and height 60 mm. The Cab-O-Sil (M5) specimen was prepared as a slurry in D₂O which was subsequently dried in vacuum at 120 C. This treatment compacts the sample by a factor of about three and is designed to exchange surface hydrogen with much less strongly scattering deuterium. The aim was to collect neutron scattering information from silica and not from the surface water and bound hydroxyl groups that are present in untreated specimens. The sample was contained in an aluminum can of diameter 62 mm, height 60 mm and wall thickness 0.2 mm. The polymeric aerogel sample was prepared by a two-stage protocol [9] in which tetraethoxysilane was first hydrolyzed in acid solution and then condensed under basic conditions. It was contained in a can similar to that of the Cab-O-Sil but having a diameter of 25 mm. A cycle of evacuation at 120 C and flushing with D₂O vapour was repeated three times to minimize the signal from surface water and hydroxyl groups. All sample cans were backfilled with helium to facilitate thermal equilibration.

The neutron scattering experiments were conducted on the N5 triple axis spectrometer at the NRU reactor of Chalk River Nuclear Laboratories. Soller slits set the beam divergence to 0.6°. The monochromator and analyzer were silicon crystals oriented to scatter from (111) planes. For most measurements the spectrometer was operated in constant Q mode with fixed scattered energy 3.52 THz and a graphite filter in the scattered beam. Thus the beam was free of second and third order contamination. For small angle elastic scattering the collimation was reduced to 0.2°, the graphite filter was replaced by a beryllium filter before the monochromator and the neutron wavelength was fixed at 4.09 \AA . The beam was 50 mm wide and illuminated a large volume of sample but scattering from the analyzer suppressed the fast neutron contribution to the beam width and we could reach a Q of 0.02 \AA^{-1} .

For a sample at a given temperature we first measured the elastic scattering, $S(Q,0)$, to obtain structural information and the normalizing factor required in equation (1). Then we measured $S(Q,\nu)$, the variation of intensity with frequency, on the neutron energy loss side at a selection of Q values including 4.0, 2.9 and 2.5 \AA^{-1} . Temperatures were set by filling the cryostat with liquid helium (4.2 K) or liquid nitrogen (77 K) or by leaving it empty (300 K).

DATA AND ANALYSIS

Small angle scattering from the Cab-O-Sil sample was consistent with smooth surfaced primary particles of diameter 130 Å. The particle cores are thought to have an equilibrium glass intermolecular structure but a less well defined structure at the surface with randomly distributed OH- or O= terminations of SiO₄ tetrahedra [10]. Small angle scattering from the aerogel indicates mass fractal structure over a limited range of length scales. For $0.03 \leq Q \leq 0.1 \text{ \AA}^{-1}$ the slope of a log-log plot of intensity versus Q is -2.40 ± 0.03 , consistent with other experiments [11] and with predictions for reaction limited cluster-cluster aggregation followed by partial collapse on drying. The transition from the fractal region to the Porod limit is incomplete so one concludes there are no smooth primary particles or that the structure is fractal down to molecular length scales.

Figure 1 presents a comparison of $S(Q,0)$ for the three

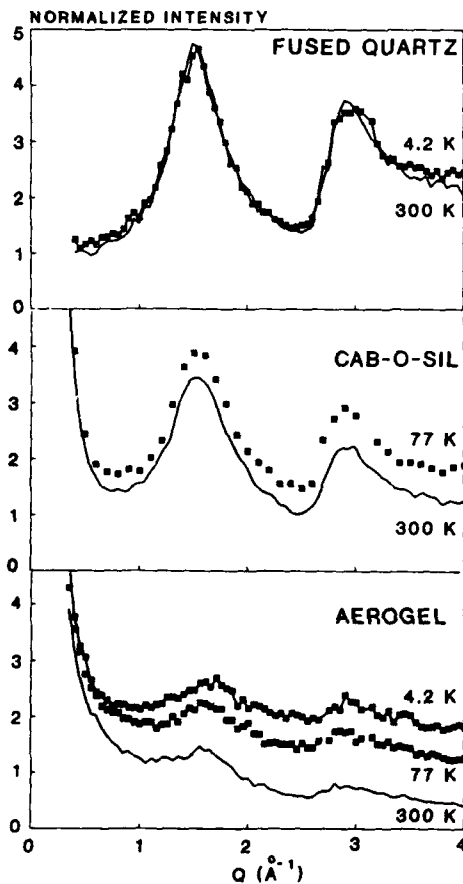


Figure 1.

Elastic scattering in different forms of silica. The intensity scale is in arbitrary units, but data sets have been normalized by equation (2).

samples at all temperatures investigated. The intensities have been internormalized to within 5% by the requirement

$$\sum_{\nu=0}^{\nu_m} S(Q, \nu) \Delta \nu = \text{Constant} \quad (2)$$

at $Q = 4.0 \text{ \AA}^{-1}$ which is near a node in the oscillatory structure of silica glass. The upper bound ν_m is 6 THz, sufficiently high that the integral yields the same value for a given sample at all three temperatures. There is a decrease in amplitude of the oscillations in $S(Q, 0)$ and an increase in the Q range of the small angle scattering tail on traversing the series fused quartz through Cab-O-Sil to aerogel. In aerogel the decrease in elastic scattering intensity by a factor of five at $Q = 4.0 \text{ \AA}^{-1}$ between 4.2 K and 300 K indicates a much stronger temperature dependence than in fused quartz where only minor differences are observed at the two temperature extremes.

Figure 2 presents a comparison of the inelastic neutron scattering from the three materials. The data have been corrected by eq. 1 to obtain an effective density of states or DOS, $g(\nu)$. This spectrum has not been corrected for multiphonon or multiple scattering effects. For fused quartz at 300 K we find excellent agreement with data analyzed similarly by Buchenau et al [2]. At 300 K the inelastic scattering in Cab-O-Sil beyond 2 THz is about twice as intense as in the fused quartz while in aerogel the factor is about twenty. Below 1.5 THz the DOS seems nearly to be independent of temperature but at larger frequencies in the aerogel there is a systematic rise with each temperature. Figure 3 shows the Q dependence of the DOS in the aerogel at 300 K. The spectra are practically identical at 2.9 and 4.0 \AA^{-1} but at 2.5 \AA^{-1} , near a minimum in the structure factor, there is an enhancement by a factor of 2 near 1 THz and by 30% beyond 2 THz.

DISCUSSION

On the length scales of molecules and SiO_4 tetrahedra the three materials are distinguished by the breadth of configuration space available to the fundamental structural units. To gain a detailed understanding of the structures and dynamics of amorphous materials one generally needs to perform computer simulations with reliable intermolecular potentials. Without such assistance a physical picture can still be formed. In the condensed glass the range of molecular orientations and separations is limited by packing constraints and the potential surface experienced by a given molecule or tetrahedron has well defined minima. The observed loss of 20% in the amplitude of oscillations in the elastic scattering between Cab-O-Sil and fused quartz may be explained as a volume fraction of silica in a high degree of disorder. One envisions an outer shell of molecules within about 7 \AA of the surface of the 130 \AA particles in Cab-O-Sil. These molecules have reduced packing constraints and randomly terminated silicon bonds, experience broad, ill-defined minima in the intermolecular potential and hence exhibit configurational disorder. A broadened potential surface permits wider vibrational amplitudes and correspondingly stronger damping of the elastic scattering with increased temperature as observed in $S(Q, 0)$ at larger Q . It

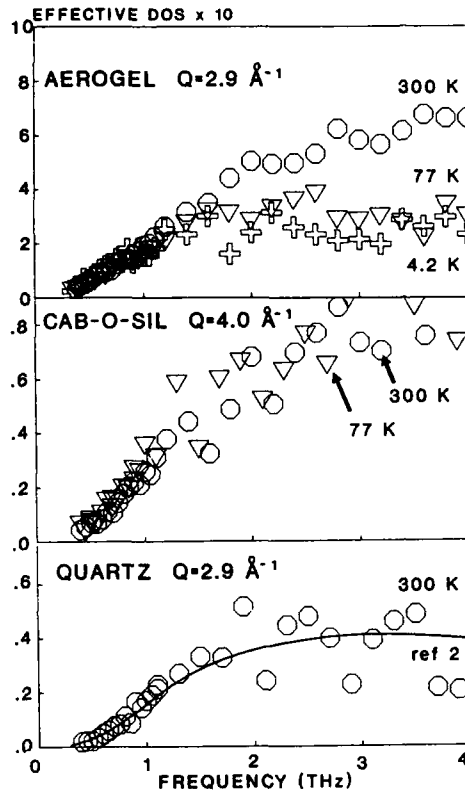


Figure 2

Effective density of states in silica samples as labelled in each frame. The intensity scale is in units of THz⁻¹. The continuous line is a spline fit to data from ref. 2. Data at two temperatures for Cab-O-Sil were not obtained at Q = 2.9 Å⁻¹ but the results at 4.0 Å⁻¹ may be compared to the aerogel which yields the same intensities at either value of Q. Note that for aerogel the intensity scale is greater by a factor of ten.

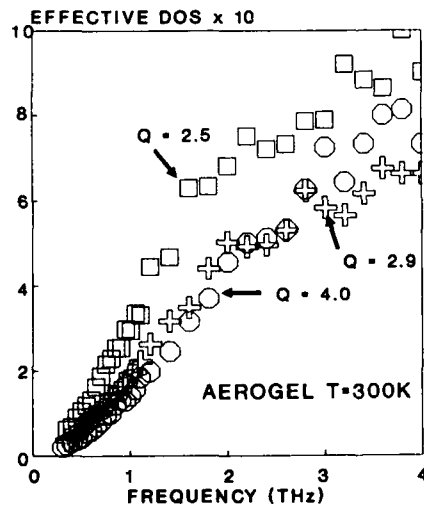


Figure 3

Effective density of states in aerogel at 300 K and three Q values.

also increases the density of vibrational modes at lower frequencies as we observe in the inelastic scattering.

The very low amplitude of oscillations and strong temperature dependence in $S(Q,0)$ for the aerogel is reminiscent of the structures observed in dense molecular gases except that the positions of the peaks are not strongly temperature dependent. Thus there are wide positional fluctuations about fixed equilibrium positions in the aerogel. Below 1 THz the overlap of results suggests a constant velocity of sound but the increase of intensity with temperature at frequencies greater than 1.5 THz shows that the vibrational spectrum is changing. This might be explained as multiphonon scattering [8] which enhances scattered intensity at larger frequencies and has little influence at lower frequencies, as observed. However multiphonon enhancements increase with Q while the reverse is observed in our data. While eq. 1 assumes only in-phase vibrations of neighbouring molecules, antiphase oscillations are quite conceivable in the highly branched aerogel. The unusual Q and T dependences of the aerogel DOS may also arise because low packing constraints permit molecules to sample anharmonic features of the potential energy surface and eq. 1 assumes only harmonic excitations.

CONCLUSION

Fused quartz, Cab-O-Sil and aerogel form a series of materials with increasing fractions of molecules in configurational disorder and having wide amplitudes of thermal vibration. The density of states in the aerogel cannot be obtained directly by analysis of the scattering data through eq. 1.

REFERENCES

1. U. Buchenau, Z. Phys. **B58**, 181 (1985).
2. U. Buchenau, M. Prager, N. Nücker, A.J. Dianoux, N. Ahmad and W.A. Phillips, Phys. Rev. **B34**, 5665 (1986).
3. U. Buchenau, H.M. Zhou, N. Nücker, K.S. Gilroy and W.A. Phillips, Phys. Rev. Lett. **60**, 1318 (1988).
4. J.K. Kjems, T. Freltoft, D. Richter and S.K. Sinha, Physica **136B**, 285 (1986).
5. T. Freltoft, J. Kjems and D. Richter, Phys. Rev. Lett **59**, 1212 (1987).
6. J.H. Page, W.J.L. Buyers, G. Dolling, P. Gerlach and J.P. Harrison, Phys. Rev **B39**, 6180 (1989).
7. R. Vacher, T. Woignier, J. Pelous, G. Coddens and E. Courtens, Europhys. Lett. **9**, 161 (1989).
8. G. Reichenauer, J. Fricke and U. Buchenau Europhys. Lett. **9**, 415 (1989).
9. D.W. Schaefer, C.J. Brinker, J.P. Wilcoxon, D.Q. Wu, J.C. Phillips and B. Chu, MRS Symp. Proc. **121**, 691 (1988).
10. D. Richter, L. Passell, Phys. Rev **B26**, 4078 (1982).
11. D.W. Schaefer, C.J. Brinker, D. Richter, B. Farago and B. Frick, preprint.

THERMAL EXPANSION OF GRAPHITE AND HNO_3 -GRAPHITE INTERCALATION COMPOUNDS,
A NEUTRON DIFFRACTION STUDY

HAIM PINTO*, MORDECHAI MELAMUD*, AND HAGAI SHAKED**

*Physics Department, Nuclear Research Centre - Negev, P.O. Box 9001,
84190 Beer-Sheva, Israel

#Physics Department, Ben-Gurion University of the Negev, P.O. Box 653,
84120 Beer-Sheva, Israel

ABSTRACT

The temperature dependent lattice parameter, $c(T)$, was determined for samples of graphite, and HNO_3 -graphite intercalates stage 3 and stage 4, using neutron diffraction. The temperature range studied is 12 to 300 K. The stage 3 and stage 4 intercalates exhibit a strong two-step discontinuity at the temperature of their structural phase transition (≈ 260 K). A stage-independent, temperature-dependent lattice parameter for the intercalant layer is extracted from the observed lattice parameters for graphite, stage 3, and stage 4 intercalates. The graphite and the intercalant lattice parameters are calculated using one-dimensional Debye theory in the framework of the Grüneisen relation. The Debye temperatures that yield best fits to the observed lattice parameters of the graphite and the intercalant are 500 K and 421 K, respectively. Using these values, thermal expansion coefficients for graphite, the intercalates and the intercalant are derived.

INTRODUCTION

HNO_3 forms intercalation compounds with graphite. These HNO_3 -graphite intercalation compounds (GIC) can be formed in different stages [1-4]. As the HNO_3 -GIC is cooled below room temperature, it undergoes (at ≈ 260 K) a structural phase transition, which is characterized by two phenomena [2-5]: a. The intercalant (i.e. HNO_3) layer "freezes" as evidenced by the emergence of incommensurate Bragg rods [5], and b. The graphite blocks slide to new positions with respect to each other [3,4].

The low temperature structure of the intercalant layer has not yet been solved, whereas, the low temperature structure of the graphite blocks was solved for stage 3 [3] and stage 4 [4] GIC. The transition is accompanied by a large discontinuity in the lattice parameter, c . While studying this discontinuity, we have measured the lattice parameters of graphite, stage 3, and stage 4 GIC, in the temperature range 12 to 300 K. In the present paper we report the results of these measurements. We are able to show that the temperature dependence of the lattice parameters fits a one-dimensional Debye function in the framework of the Grüneisen relation. We also find that the contributions of the graphite blocks and of the intercalant layers to the lattice parameter of the intercalates are stage independent.

EXPERIMENTAL

The temperature dependence of the lattice parameter, c , was determined from the value of the Bragg angles of $\{00l\}$ reflections as a function of temperature. The measurements were performed on the KANDI-III diffractometer at the IRR-2, using a neutron wavelength of 2.4 \AA . Samples of graphite, stage 3, and stage 4 HNO_3 -GIC were mounted in a DISPLEX cryostat [6]. The graphite was a 3.5° highly-oriented pyrolytic graphite (HOPG), and the GIC were prepared from similar HOPG [3,4]. The samples were cooled in steps of ≈ 1 K and were held ≈ 1 hour at each step, thus ensuring stabilization of the

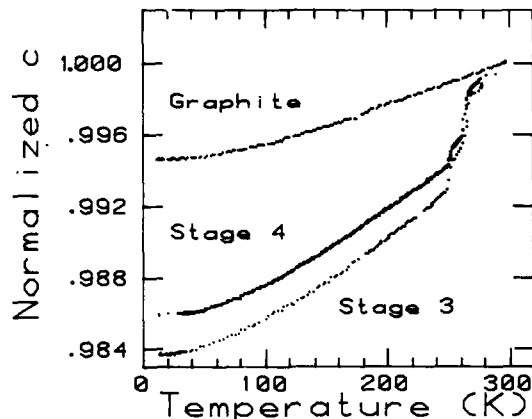


Figure 1 : Observed lattice parameters vs. temperature for graphite, stage 3 GIC and stage 4 GIC. The normalization factors are equal to the corresponding room temperature values of the lattice parameters, i.e. 6.696, 29.025 and 53.57 Å, respectively.

temperature (± 0.2 K). The highest accessible scattering-angle reflections (92° - 96°) were chosen in order to maximize sensitivity to changes in d -values. This led to $\{00l\}$ lines with $l = 4, 18,$ and 33 for graphite, stage 3 and stage 4 respectively. Upon cooling from 300 to 12 K, the shifts in Bragg scattering-angles were 0.7° , 2.1° and 1.8° for graphite, stage 3 and stage 4, respectively. The Bragg angles of the $\{00l\}$ reflections at each step were taken at the "center of mass" of the reflection. The observed lattice parameters, $c(T)$, were determined from these Bragg angles using the Bragg law. The observed temperature dependence of the lattice parameters for the graphite, stage 3 GIC, and stage 4 GIC are shown in Fig. 1. The two GIC samples exhibit a strong discontinuity in $c(T)$ at ≈ 260 K. The temperature dependences of these lattice parameters were fitted to fourth order polynomials of the form :

$$c(T) = P_0 + P_1T + P_2T^2 + P_3T^3 + P_4T^4 \quad (1)$$

Excellent fits were obtained, and the appropriate coefficients for these fits are listed in Table I. These polynomials were used to represent the observed lattice parameters in the data analysis (see next section).

Table I : Coefficients of fitted polynomials, valid for 12 to 300 K for graphite, and 12 to 250 K for the other three samples. R is defined in [7].

Compound	P_0	$10^5 P_1$	$10^6 P_2$	$10^8 P_3$	$10^{11} P_4$	R (%)
Graphite	6.6600 ₂	-2.7 ₃	1.00 ₄	-0.21 ₂	0.15 ₄	0.003
Stage 3	28.553 ₂	-20 ₅	11.2 ₇	-4.1 ₄	6.6 ₈	0.005
Stage 4	52.821 ₁	-57 ₃	18.6 ₄	-5.2 ₂	5.8 ₄	0.003
Intercalant	4.287 ₁	-10 ₂	4.2 ₃	-1.5 ₂	2.3 ₃	—

ANALYSIS AND DISCUSSION

The stacking sequences for the stage 3 and stage 4 GIC are given [4] by ABA/ACA/... and ABAB/BCBC/CACA/..., respectively, where A,B,C stand for graphite planes and / stands for an intercalant plane [4]. The lattice parameters of these intercalates can be expressed in terms of the graphite lattice parameter, c_G , and the intercalant lattice parameter, c_{Ij} ($j = 3,4$ representing the thickness of the intercalant layer in stages 3 and 4 respectively [3]), as follows :

$$c_3 = 3c_G + 2c_{I3} \quad (2a)$$

$$c_4 = 6c_G + 3c_{I4} \quad (2b)$$

The temperature dependence is omitted for convenience. From these equations we obtain :

$$c_{I3} = (c_3 - 3c_G)/2 \quad (3a)$$

$$c_{I4} = (c_4 - 6c_G)/3 \quad (3b)$$

Using these equations it was found to a good approximation that $c_{I3} \approx c_{I4}$. Hence, we have used a single c_I given by :

$$c_I = (c_{I3} + c_{I4})/2 = (c_3 + 2c_4/3 - 7c_G)/4 \quad (4)$$

The observed lattice parameters c_G and c_I are shown (square symbols) in Fig. 2(a) and 2(d), respectively, as a function of temperature.

According to the Grüneisen relation [8] in the one-dimensional Debye approximation [9] the lattice parameter is given (see appendix) by :

$$c(T) = \{c(0) - c_0\} f(T/\theta) + c_0 \quad (5)$$

where :

$$f(T/\theta) = 1 + 4(T/\theta)^2 \int_0^{\theta/T} \frac{x}{e^x - 1} dx \quad (6)$$

θ is the Debye temperature and c_0 is equal to the lattice parameter at $T=0$.

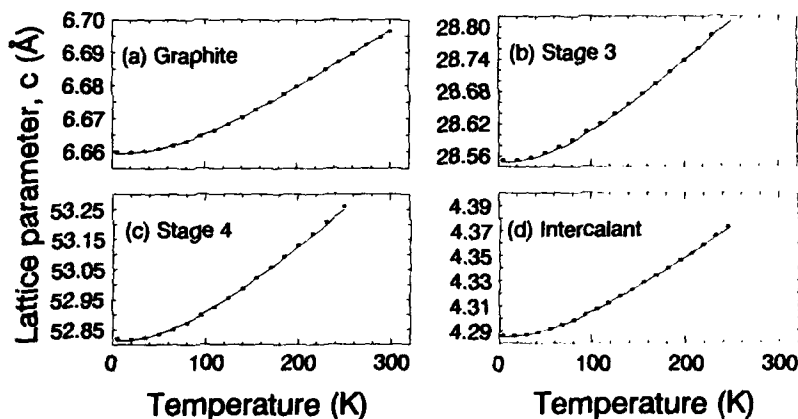


Figure 2. : Observed (square symbols) and calculated (solid line) lattice parameters of (a) graphite, (b) stage 3 GIC, (c) stage 4 GIC, and (d) intercalant layer.

with no zero-point energy. The parameters $c(0)$, c_0 , and θ were refined so that $c(T)$ gave the best fit (least squares) to the observed $c_G(T)$ and $c_I(T)$. The refined parameters are listed in Table II. The calculated $c_G(T)$ and

Table II : The refined parameters for equation (5).

Material	$c(0)$ (Å)	c_0 (Å)	θ (K)	R (%)
Graphite	6.659 ₆	6.635 ₃	500 ₅	0.382
Intercalant	4.285 ₄	4.228 ₂	421 ₈	0.373

$c_I(T)$ are shown (solid lines) in Fig. 2(a) and 2(d). The calculated lattice parameters $c_3(T)$ and $c_4(T)$ were reconstructed using eqns 2 with $c_{Ij} = c_I$ and are shown (solid lines) in Fig. 2(b) and 2(c).

The coefficient of thermal expansion

$$\alpha(T) = \frac{1}{c(T)} \frac{dc(T)}{dT} \quad (7)$$

was calculated (see appendix) for the graphite and the intercalant from the best fitted Debye functions :

$$\alpha(T) = \frac{1}{\theta} \frac{2}{T/\theta} \frac{f(T/\theta) - \coth(1/\{2(T/\theta)\})}{f(T/\theta) + c_0 / (c(0) - c_0)} \quad (8)$$

The coefficients for the stage 3 and stage 4 were calculated using :

$$\alpha_3 = (3c_G\alpha_G + 2c_I\alpha_I)/c_3 \quad (9a)$$

$$\alpha_4 = (6c_G\alpha_G + 3c_I\alpha_I)/c_4 \quad (9b)$$

The resulting $\alpha_j(T)$ ($j = G, 3, 4, I$) are shown in Fig. 3.

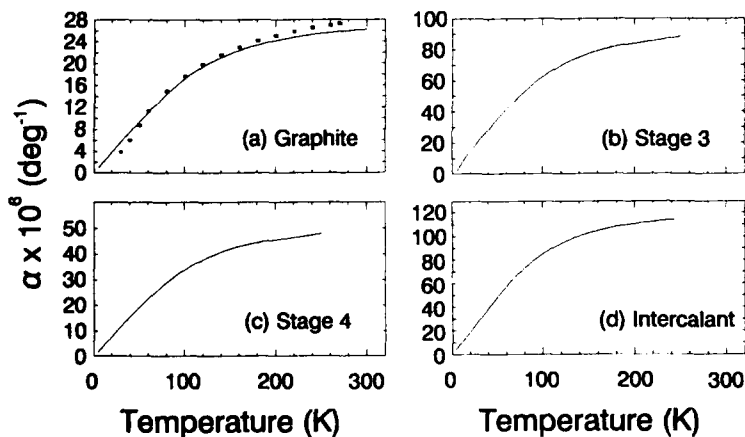


Figure 3. : Thermal expansion coefficients, calculated from the fits of the one-dimensional Debye model to the observed lattice parameters for (a) graphite, (b) stage 3 GIC, (c) stage 4 GIC, and (d) the intercalant layer. Results from Ref. 11 are shown in (a) (square symbols) for comparison.

The $c(T)$ discontinuity in temperature for stage 3 and stage 4 GIC (Fig. 1) is stage independent. It appears at the structural transition temperature where incommensurate Bragg rods emerge [5]. At the transition, the intercalate layer "freezes" [5] and the graphite blocks slide to new positions [3,4]. A careful examination shows that the $c(T)$ discontinuity consists of two steps, about 10 K apart (Fig. 1). It is tempting to relate these two steps to the two structural processes (i.e. "freeze" and slide). The refined Debye temperature for graphite is 500 K (Table II), in good agreement with the previously reported value of $\theta = 494$ K of Trucano and Chen [10]. The thermal expansion coefficient found for graphite (Fig. 3(a)) is in fair agreement with Bailey and Yates [11] (square symbols in Fig. 3(a)). The temperature dependent lattice parameter of the intercalate, is a weighted sum of the lattice parameters for graphite and the intercalant (eqns. (2)). In other words, the lattice parameter of the graphite block, and the lattice parameter of the intercalant layer, are independent of the intercalate stage. Our results show that the intercalant layer is much softer than the graphite and its temperature dependent lattice parameter fits a Debye model with $\theta = 421$ K (Table II). The coefficient of thermal expansion for the intercalant layer is about 5 times larger than the corresponding coefficient for graphite (Fig. 3) throughout the whole temperature range.

ACKNOWLEDGEMENT

The authors wish to thank Mr. Hanania Etedgui for his skilful help in performing the experiments.

APPENDIX

The volume thermal expansion, $\delta V/V$, is related to the total free energy of the crystal, U , through the Grüneisen relation [8] :

$$\delta V/V = k \tau U(T) \quad (A1)$$

where k and τ are the compressibility and the Grüneisen constant, respectively, for the crystal. In the case of graphite, the thermal expansion in the basal plane is negligible compared to the thermal expansion along the c axis. Hence, we consider the one-dimensional problem where

$$\delta c/c = \delta V/V \quad (A2)$$

and using the one-dimensional Debye model [9] :

$$U(T) = \frac{1}{2} \frac{\theta k_B}{c} \{1 + 4(T/\theta)^2 \int_0^{\theta/T} \frac{x}{e^x - 1} dx\} = \frac{1}{2} \frac{\theta k_B}{c} f(T/\theta) \quad (A3)$$

where $f(T/\theta)$ is defined by this equation ($f(0) = 1$), k_B is the Boltzmann constant, and θ is the Debye temperature. Substituting (A2) and (A3) into (A1) yields :

$$\delta c = \frac{1}{2} k \tau \theta k_B f(T/\theta) \quad \text{where : } \delta c = c(T) - c_0 \quad (A4)$$

and c_0 is the lattice parameter at $T = 0$ and with no zero-point energy. From (A4) evaluated at T and at $T = 0$ we obtain an expression for the temperature dependent lattice parameter :

$$c(T) = \{c(0) - c_0\} f(T/\theta) + c_0 \quad (A5)$$

The coefficient of thermal expansion

$$\alpha(T) = \frac{1}{c(T)} \frac{dc(T)}{dT} \quad (A6)$$

is obtained through differentiation of equation (A5) :

$$\alpha(T) = \frac{1}{\theta} \frac{2}{T/\theta} \frac{f(T/\theta) - \coth(1/\{2(T/\theta)\})}{f(T/\theta) + c_0 / (c(\theta) - c_0)} \quad (A7)$$

In conclusion, by applying the Grüneisen relation and the one-dimensional Debye theory we have obtained analytic expressions for the temperature-dependent lattice parameter (A5) and coefficient of thermal expansion (A7).

REFERENCES

1. D. E. Nixon, G. S. Parry, and A. R. Ubbelohde, Proc. Roy. Soc. Ser. A 291, 324 (1966).
2. G. S. Parry, Mater. Sci. Eng. 31, 99 (1977).
3. H. Shaked, H. Pinto, and M. Melamud, Synthetic Metals 26, 321 (1988).
4. H. Shaked, H. Pinto, and M. Melamud, Phys. Rev. B 35, 838 (1987).
5. H. Shaked, M. Melamud, H. Pinto, R. Hitterman, and J. Faber, in Research Laboratories Annual Report 1985, Report IA-1421 (Israel Atomic Energy Commission, Tel-Aviv, 1986), p. 69; in IPNS Progress Report 1985-1986, edited by F. J. Rotella (Argonne National Laboratory, Argonne, Illinois, 1986), Chap. 10, p. 23.
6. DISPLEX is a brand name of a closed cycle He cooler made by Air Products.
7. The residual, R(%), is defined by: $R = 100 \{ \sum (c_{obs} - c_{calc})^2 / \sum c_{obs}^2 \}^{1/2}$, summing over all the experimental data points.
8. J. M. Ziman, Principles of the Theory of Solids (University Press, Cambridge, 1965), p. 64.
9. J. S. Blakemore, Solid State Physics (W. B. Saunders Co., Philadelphia, 1970), p. 106.
10. P. Trucano and R. Chen, Nature 258, 136 (1975).
11. A. C. Bailey and B. Yates, J. Appl. Phys. 41, 5088 (1970).

CHARACTERIZATION OF SOL-CLAY COMPOSITES
BY SMALL-ANGLE NEUTRON SCATTERING

AHMAD MOINI*, THOMAS J. PINNAVAIA*, AND P. THIYAGARAJAN**

*Department of Chemistry and Center for Fundamental Materials
Research, Michigan State University, East Lansing, MI 48824

**IPNS Division, Argonne National Laboratory, Argonne, IL
60439

ABSTRACT

Silica-clay composites were prepared by reacting a 40 Å silica sol with aqueous clay suspensions. The clays which were studied included Na⁺-montmorillonite, fluorohectorite, and the synthetic clay Laponite. The aggregation mechanism of the sol particles and the degree of dispersion of the clay layers were monitored by small-angle neutron scattering. The data for powdered silica-montmorillonite products showed the presence of highly dispersed clay platelets and spherical sol particles. The results suggest that the interaction between these two components inhibits the sol aggregation process. Studies on the products prepared from other types of clays, however, showed that this interaction is highly dependent on the morphology and charge density of the clay platelets.

INTRODUCTION

Pillared clays form a unique class of microporous catalysts in which thermally stable cations, or metal oxide aggregates, behave as molecular props in the gallery space between the clay platelets.[1-4] The size and composition of these pillars play important roles in the properties of the final three-dimensional networks. In pursuit of larger "pillaring agents," we have carried out exploratory studies on the interaction of clay platelets with colloidal particles.[5] These new sol-clay composites have been found to form irregular networks of spherical sol particles and two-dimensional clay platelets.

A large portion of our studies have focused on a commercially available silica sol (Nalco 1115) with an approximate particle diameter of 40 Å. The reaction of this sol with Na⁺-montmorillonite resulted in the formation of highly porous composites. We have made extensive use of small-angle neutron scattering (SANS) for the characterization of these materials. The differences in the shape and particle size range of the two components, i.e. spherical particles less than 100 Å which interact with platelets larger than 1 μ, make this system ideally suited for SANS studies.

Our previous SANS results[6] on the Nalco 1115 silica sol showed that, upon acid hydrolysis, the sol formed a partially aggregated network containing 73 Å particles. On the other hand, studies on silica-montmorillonite composites provided preliminary evidence for the formation of sol-clay networks in which the clay layers were delaminated and the sol aggregation process was impeded. We now present preliminary results on the effects of clay type on the formation of sol-clay composites.

Experimental

Natural Wyoming Na⁺-montmorillonite (< 2 μ, ~ 80 meq/100 g) was obtained from the Source Clay Minerals Repository, Columbia, Missouri. Fluorohectorite (>> 2 u, ~ 120 meq/100 g) was obtained from Corning Glass, Corning, NY. The synthetic clay Laponite (200-500 Å, ~ 48 meq/100 g) was obtained from Laporte Industries, Widnes, England. Prior to use, the montmorillonite clay was suspended in water, and the impurities were removed by sedimentation. The other clays were used as received. The silica sol (Nalco 1115, 40 Å particles) was a gift from Nalco Chemical Company, Oak Brook, Illinois.

The synthesis of silica sol-clay complexes involved the dilution of the silica sol with water to approximately 1 wt. %, followed by the addition of small amounts of dilute HCl to adjust the pH to approximately 3. The latter step ensured the presence of positively charged silica particles for interaction with the negatively charged clay layers. After several minutes, a 1 % aqueous suspension of the clay was added, and the mixture was stirred for 24 h. The final product was dried in air.

Small angle neutron scattering data were obtained on the Small Angle Diffractometer (SAD) at the Intense Pulsed Neutron Source, Argonne National Laboratory.[7] The data were collected over a Q range of 0.006 to 0.25 Å⁻¹ where the momentum transfer Q is defined in Eq. 1,

$$Q = (4\pi \sin \theta) / \lambda \quad (1)$$

in which λ is the wavelength, and θ is half of the scattering angle. Routine data treatment including Porod analysis was carried out on the background-corrected data.

RESULTS

The SANS data for a 4:1 silica-montmorillonite complex are presented in Figure 1a. Two power-law regimes are clearly observed in this log (I) vs. log (Q) plot. The slope in the low-Q region (0.00582-0.02378 Å⁻¹), due to scattering from clay particles, is -1.79(3) corresponding to nearly 2-dimensional

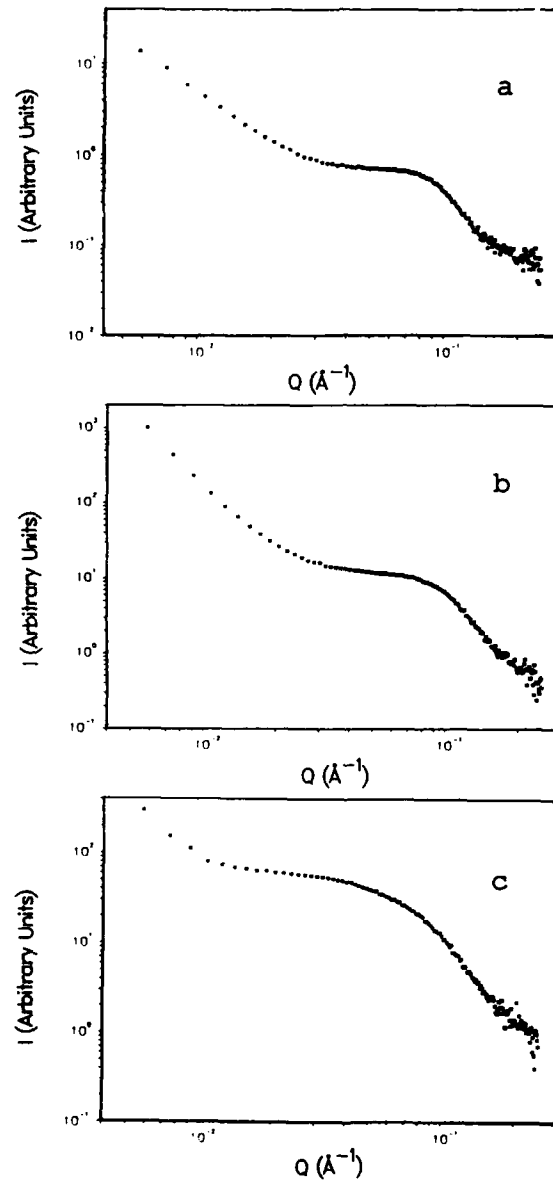


Figure 1. Plots of $\log(I)$ vs. $\log(Q)$ for (a) 4:1 silica-montmorillonite, (b) 10:1 silica-fluorohectorite, and (c) 4:1 silica-Laponite.

platelets. This result suggests the presence of delaminated clay layers in the sol-clay composite. In comparison, scattering from pure Na^+ -montmorillonite gives a slope of $-3.23(1)$. In the pure clay, the layers are expected to be highly stacked and forming nearly 3-dimensional particles, thus giving rise to slopes close to -4 . The high-Q (0.10218 - 0.15118 \AA^{-1}) scattering for the 4:1 silica-montmorillonite complex, which is due to the silica sol particles, has a slope of $-3.25(7)$. This value corresponds to nearly spherical particles with rough surfaces.[8-9]

The scattering data for a 10:1 silica-fluorohectorite complex is shown in Figure 1b. The shape of the scattering curve is similar to the curves obtained for silica-montmorillonite complexes. The high-Q scattering from silica particles is in close agreement with the above data; a slope of $-3.64(4)$ is obtained in the Q range 0.08095 - 0.11852 \AA^{-1} . On the other hand, the low-Q scattering is considerably different from the results obtained for the silica-montmorillonite species. In the Q range 0.00582 - 0.02215 \AA^{-1} , a log-log slope of $-2.82(1)$ is obtained. This value is very close to the range of slopes expected for highly aggregated or stacked clay platelets. We speculate that the sol particles do not separate the clay layers as effectively in the case of fluorohectorite.

The data for a 4:1 silica-Laponite product appears in Figure 1c. This scattering curve is clearly different from those obtained for complexes of montmorillonite and fluorohectorite. The slope in the high-Q region (0.08095 - 0.15118 \AA^{-1}) of the scattering curve is $-3.22(4)$. Furthermore, the scattering in the low-Q region is very similar to curves which have been obtained for globular or glassy networks.[8-9] Attempts to subtract the clay scattering from these data made little change in the overall shape of the curve, confirming that most of the scattering is from the silica particles.

CONCLUSIONS

The results obtained for silica-montmorillonite complexes clearly show the presence of strong interaction between the sol and clay particles. The portion of the scattering curve which is associated with clay scattering gave slopes indicative of very anisotropic particles. It should be mentioned that, in a previous control study[6], data were collected on a heterogeneous mixture of hydrolyzed sol and air-dried Na^+ -montmorillonite. The results showed that the silica particles had a very small effect on the scattering in the low-Q region, confirming that the slopes in this region are determined mainly by the scattering from clay.

Comparison of the SANS data obtained for silica-montmorillonite complexes with those prepared using

fluorohectorite and Laponite shows that the degree of sol-clay interaction is highly dependent on the nature of the clay particles. The results for the fluorohectorite products suggest that a considerable amount of the platelets form stacked or aggregated arrangements despite the presence of silica particles. This type of behavior may be associated with the large particle size and perhaps the high charge density of the layers. On the other hand, the scattering data for silica-Laponite products show that the small Laponite platelets do not segregate the silica particles in an efficient manner thus resulting in a highly aggregated silica product.

It is clear that small-angle scattering is an effective tool for studying the texture of these disordered microporous systems. Work is currently in progress on sol-clay suspensions and solids prepared under varying pH conditions.[10]

ACKNOWLEDGMENTS

We thank the National Science Foundation, Division of Materials Research (DMR-8903579), and the Michigan State University Center for Fundamental Materials Research for financial support. We acknowledge the Intense Pulsed Neutron Source at Argonne National Laboratory, which is funded by the U. S. Department of Energy, BES-Materials Science under contract W-31-109-Eng-38.

REFERENCES

1. R. M. Barrer, Zeolites and Clay Minerals as Sorbents and Molecular Sieves, (Academic Press, New York, 1978).
2. T. J. Pinnavaia, *Science*, 220, 365 (1983).
3. D. E. W. Vaughan, in Perspectives in Molecular Sieve Science, ACS Symposium Series No. 368, edited by W. H. Flank, and T. E. Whyte, Jr., (American Chemical Society, Washington, D. C., 1988), pp. 308-323.
4. F. Figueras, *Catal. Rev. Sci. Eng.*, 30, 457 (1988).
5. A. Moini and T. J. Pinnavaia, *Solid State Ionics*, 26, 119 (1988).
6. A. Moini, T. J. Pinnavaia, P. Thiyagarajan, and J. W. White, *J. Appl. Crystallogr.*, 21, 840 (1988).
7. J. E. Epperson, P. Thiyagarajan, and T. E. Klippert, *SAD Manual*, Argonne National Laboratory, 1988.

8. D. W. Schaefer and K. D. Keefer, *Phys. Rev. Lett.*, 56, 2199 (1984).
9. D. W. Schaefer, K. D. Keefer, J. H. Aubert, and P. B. Rand, in Science of Ceramic Chemical Processing, edited by L. L. Hench, and D. R. Ulrich, (Wiley, New York, 1986), pp. 140-147.
10. A. Moini, P. Thiyagarajan, and T. J. Pinnavaia, *J. Phys. Chem.*, to be published.

**NEUTRON SCATTERING STUDY OF LAYERED SILICATES
PILLARED WITH ALKYLAMMONIUM IONS**

D. A. NEUMANN,* J. M. NICOL,** J. J. RUSH,* N. WADA,*** Y. B. FAN,****
H. KIM,**** S. A. SOLIN,**** T. J. PINNAVAIA,**** AND S. F. TREVINO*****

* *Materials Science and Engineering Laboratory, National Institute of Standards and Technology (NIST), Gaithersburg, MD 20899*

** *University of Maryland, College Park, MD 20742 & NIST, Gaithersburg, MD*

*** *Department of Physics, Colorado School of Mines, Golden, CO 80401*

**** *Michigan State University, East Lansing, MI 48824*

***** *ARDEC, Picatinny Arsenal, NJ & NIST, Gaithersburg, MD 20899*

ABSTRACT

Incoherent, inelastic neutron scattering has been used to study the vibrational spectra of tetramethylammonium montmorillonite and trimethylammonium vermiculite in the energy range 20-140 meV. For both systems peaks are observed due to the internal modes of the intercalate and to the excitations of the hydroxyl groups within the host layers. For the montmorillonite sample, it is found that the steric constraints imposed on the tetramethylammonium ion by the bounding clay layers contribute an additional 28 meV to the rotational barrier of the methyl groups. This additional barrier is shown to be strongly related to the volume that the tetramethylammonium ion occupies. For the trimethylammonium vermiculite sample normal mode analysis of the internal modes of the intercalated ion shows that the N-H bond is parallel to the c-axis of the host.

INTRODUCTION

Clays are a naturally occurring class of layered silicates in which the two-dimensional oxyanions are separated by layers of intercalated cations. These systems differ from the intercalation compounds of graphite in two important ways.[1] First, graphite is amphoteric, that is there is no fixed charge on the host layers. Therefore graphite intercalation compounds can be formed with guest species which either donate electrons to or accept electrons from the graphite pi orbitals. Clays on the other hand, have a fixed negative charge on the silicate layers which must be balanced by positively charged guest species. Thus one would characterize the process of forming a given clay intercalation compound as "ion exchange" whereas the formation of a graphite intercalation compound is due to a chemical reaction. Since different clays have different areal charge densities on the layers, the in-plane intercalate density is typically changed by changing the host clay. The more important difference is the rigidity of the host layers. Graphite layers consist of only a single atomic plane. Therefore the layers are rather floppy and collapse around the intercalated guest species and a microporous structure cannot be maintained. In contrast, clays are a multilayered host and as a consequence the layers are rather rigid. Thus permanent porosity can be induced in these minerals by exchanging large polyatomic cations for the naturally occurring ones. The resulting material is known as a "pillared clay" and the large cations which prop the host layers apart are referred to as "pillars".[2] Despite the utility of such structures for catalysis and molecular sieving, [3-5] relatively little information is available concerning the details of the pillar-host interaction. Here we review recent incoherent, inelastic neutron scattering results in the energy range of 20-140 meV for montmorillonite pillared with tetramethylammonium ions and vermiculite pillared with trimethylammonium ions.

Both of these clays are 2:1 layered silicates which have the basic structure shown in figure 1. There are essentially four layers in clays of this type: 1) the gallery in which the intercalated species reside; 2) a tetrahedral layer which consists of SiO_4 tetrahedra joined at the corners; 3) an octahedral layer composed of edge-joined $\text{AlO}_4(\text{OH})_2$ octahedra; and 4) another tetrahedral layer. Different clays are then formed by various substitutions on the octahedral and tetrahedral sites. For example, two major classes of clays are distinguished by the occupancy of the octahedral sites. If all of these sites are occupied, the clay is referred to as trioctahedral, while it is dioctahedral if 2/3 of the sites are occupied. The vermiculite used in this study is a trioctahedral clay where the charge on the host layer comes principally from substitutions of Al for Si in the tetrahedral sites. In addition, most of the trivalent Al on the octahedral sites is replaced by divalent Mg. The combination of the tetrahedral substitutions and the rather large areal charge density on the vermiculite host layers results in the presence of rather large crystallites in the starting material. This made it possible to sediment the pillared clay to obtain reasonably well oriented samples.

Montmorillonite on the other hand is a dioctahedral clay which has a much lower areal charge density residing principally on the octahedral layers. In other words, there is virtually no substitution of Al for Si in the tetrahedral sites. This causes the crystallites to be much smaller and therefore the sample could not be well-oriented by sedimentation. In fact the areal charge density and therefore the in-plane density of intercalated ions is less than 1/2 that of the vermiculite samples.

EXPERIMENTAL PROCEDURE

The inelastic neutron scattering results were obtained using the Be-graphite-Be filter analyzer on the BT4 spectrometer at the Neutron Beam Split-core Reactor (NBSR) at the National Institute of Standards and Technology. A pyrolytic graphite monochromator with collimations of 40'-20' before and after it respectively was employed for the energy range of 20-40 meV, while a Cu monochromator with collimations of 60'-40' was used in the energy range of 35-140 meV. The overlap of 5 meV in the two data sets was sufficient to allow the data to be scaled. Under these conditions, the energy resolution of the instrument varied from <2 meV in the low energy portion of the spectra to about 5.5 meV at 100 meV and finally to 9 meV at 140 meV. The fast neutron background was measured and subtracted. For vermiculite two sample orientations were used, one with the scattering vector perpendicular and the other with it parallel to the planes. All measurements were performed with the sample at liquid nitrogen temperatures. Both samples were prepared from naturally occurring clays using standard ion-exchange techniques. The vermiculite host material was from Llano, Texas, while the montmorillonite was from Crook County, Wyoming. Further details of the sample preparation will be given elsewhere. [6,7]

RESULTS & DISCUSSION

Tetramethylammonium montmorillonite

The incoherent, inelastic neutron scattering spectrum for tetramethylammonium montmorillonite is shown in figure 2. The four sharp peaks seen in the lower energy portion of the spectra have been assigned to the singly degenerate, symmetric torsional mode of the CH_3 groups (27.4 meV, A_2 symmetry group); the triply degenerate, antisymmetric CH_3 torsional excitation (38.0 meV, T_1 symmetry); the doubly degenerate C-N-C bending mode (45.8 meV, E symmetry); and the triply degenerate C-N-C bending vibration (57.1 meV, T_2 symmetry). It is important to note that both of

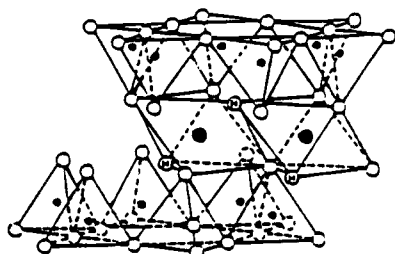


Figure 1. Schematic diagram showing the four layers of a 2:1 layered silicate. The open circles indicate the oxygen sites, the open symbols containing an "H" show the hydroxyl sites, the small closed circles indicate the tetrahedral sites, and the large closed circles represent the octahedral sites. The guest species reside in the open region between the clay layers which is termed the "gallery".

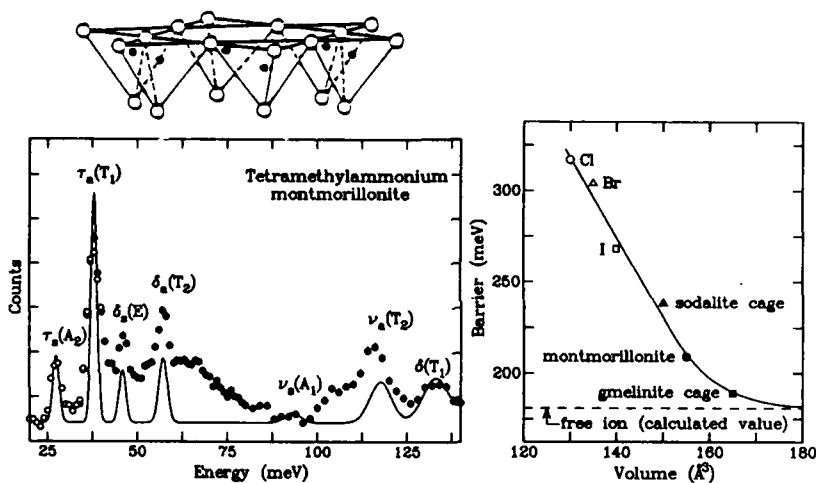


Figure 2. (left) Inelastic neutron scattering spectra of tetramethylammonium montmorillonite. The open and closed circles represent data taken with the pyrolytic graphite and Cu monochromators respectively. The solid line is a spectrum calculated for tetramethylammonium ions convoluted the result with the instrumental resolution. The label τ refers to symmetric and antisymmetric torsional modes of the methyl groups, δ refers to bond-bending vibrations, and ν refers to the stretching vibrations of the C-N bonds. The labels in parenthesis indicate the symmetry groups of the various modes. The singly degenerate A_2 mode and the triply degenerate T_1 mode are both Raman and infrared inactive.

Figure 3. (right) The barrier to rotation of the methyl groups in tetramethylammonium ions as a function of the volume available in different systems. The barrier was calculated using the simple harmonic approximation [11]. The data for the tetramethylammonium halides were taken from Ratcliffe and Waddington [12] while the data for the ions occluded in the different zeolite cages and the free ion calculation were taken from the work of Brun et al. [13].

the torsional modes are both Raman and infrared inactive. Since the intensity of a feature in an inelastic neutron scattering experiment is proportional to the square of the displacement vector, one needs only to solve for the eigenvalues and eigenvectors of the dynamical matrix in order to obtain the positions and intensities of the peaks.[8] The solid line in figure 2 is the result of such a normal mode calculation for the internal vibrations of the tetramethylammonium ions which were assumed to have no intrinsic width, convoluted with the calculated experimental resolution. While more details of this calculation will be given elsewhere [7], a couple of points are worth mentioning here. First only the eigenvectors of the H atoms were used since scattering from them dominates the spectrum due to their 80 barn cross-section. Second the positions of the higher energy peaks (the C-N stretches and one N-C-H bend) were not determined from the neutron scattering data. Instead they were taken from the Raman work of Dutta, Del Barco, and Shieh [9] and Kabisch [10].

Using the simple harmonic approximation and the fact that the barrier B is much larger than the coupling between the methyl groups, one can closely approximate B from the energies of the torsional modes using the equation [11]

$$B = \frac{1}{36F}(\tau_s^2 + 3\tau_a^2) \quad (1)$$

where the τ 's refer to the energies of the symmetric and antisymmetric torsional modes and F (= 0.677 meV for tetramethylammonium ions) is a parameter which is inversely proportional to the effective moment of inertia of the CH_3 groups. Using the above values for the torsional energies, one obtains $B = 209$ meV. Similarly the coupling between the methyl group torsions Γ can be obtained with the equation [11]

$$\Gamma = -\frac{1}{36F}(\tau_a^2 - \tau_s^2) \quad (2)$$

which gives $\Gamma = -28$ meV. Comparison of these values with those obtained from previous neutron scattering results for tetramethylammonium halides by Ratcliffe and Waddington [12] and for tetramethylammonium ions occluded in zeolites by Brun et al. [13] show that the value of Γ does not appreciably change for these vastly different systems. The value of B, on the other hand, proves to be extremely sensitive to the environment of the tetramethylammonium ion, changing from a value of 317 meV in tetramethylammonium chloride [12] to 189 meV for tetramethylammonium ions occluded within gmelinite cages of zeolites [13]. The dependence of the torsional barrier on the volume available to the ion is shown in figure 3. Here the symbols represent the values of the barriers for different systems, the dashed line indicates the value of $B = 181$ meV obtained from the torsional energies calculated for the "free" ion by Brun et al. [13], and the solid line is a guide to the eye. The striking dependence of B on the available volume is seen despite the fact that these are very dissimilar systems. The most plausible explanation for such a correlation is that steric constraints imposed by the environment dominate the additional barrier to rotation in these systems. However the observed dependence cannot be adequately reproduced by either an exponential function or a simple power law relation.

An important consequence of the sensitivity of the torsional modes to their environment is that it makes it possible to identify the presence of different tetramethylammonium sites within a given system. For instance, the existence of non-gallery sites was recently used to explain the variation from Vegard's law of the c-axis lattice constant in the system $[(\text{CH}_3)_3\text{N}][(\text{CH}_3)_3\text{NH}]$ -vermiculite [14]. Our results indicate that if non-gallery sites are present in the sample of montmorillonite used here, they must be either present in a much smaller concentration than in the samples used in reference 14 or the volume available in the non-gallery sites must be very similar to that of the gallery sites. It should be

noted that while the torsional peaks shown in figure 2 are not resolution limited they do have essentially the same intrinsic widths as those found by Brun et al. [13] for tetramethylammonium ions in gmelinite. Since there is only one size of cage occupied in the sample with the gmelinite cages, we feel that this is a good measure of the natural peak width and therefore the peak broadening observed here is not an indication for multiple sites.

Trimethylammonium vermiculite

The inelastic neutron scattering spectra for both orientations of the trimethylammonium vermiculite samples are shown in figure 4. The peaks seen at 28.8 and 36.8 meV are assigned to the symmetric and antisymmetric torsional modes of the methyl groups belonging to the A_2 and E symmetry groups respectively. Note that modes having A_2 symmetry are both Raman and infrared inactive. The two skeletal bending modes belonging to the E and A_1 symmetry groups are then identified as the peaks seen at 51.1 and 58.0 meV respectively. In addition, one sees a clear dependence of the intensities of the bending modes, particularly the E mode, on the direction of the scattering vector. This can be ascribed to the orientational ordering of the trimethylammonium ions in the galleries. In order to determine this orientation, normal mode calculations have been performed for the trimethylammonium ion for several different orientations. The best representation of the experimental data was obtained for the N-H bond parallel to the c-axis and this result is shown as the solid line in figure 4. While at first glance it seems that the asymmetry in the intensity of the 51.1 meV mode is larger in the calculation than in the data, measurements on a sample with deuterated trimethylammonium show that for $Q||c$ there is an additional background around 50 meV presumably due to excitations of the hydroxyl groups in the vermiculite whose contribution is roughly that of the calculated peak intensity. When this is taken into account, the asymmetry in the calculated intensities is approximately equal to that found experimentally. Additional support for this orientational assignment has been recently obtained using infrared techniques. Further

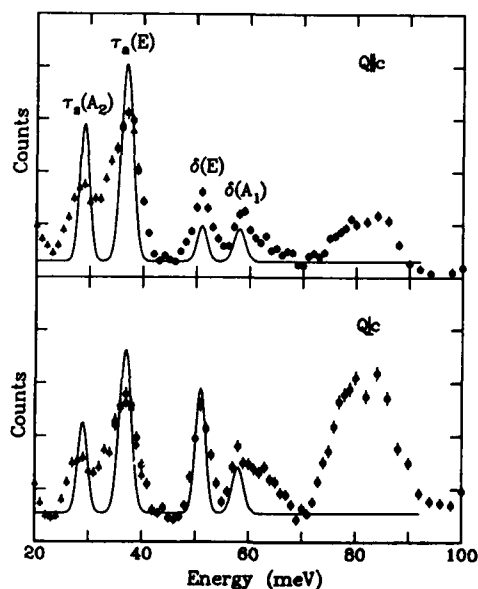


Figure 4. Inelastic neutron scattering spectra of trimethylammonium vermiculite. The top panel shows data taken with $Q||c$ and the bottom panel is data taken with $Q\perp c$. The open triangles and the closed circles are data taken with the pyrolytic graphite and Cu monochromators respectively. The solid line is a calculated spectrum for trimethylammonium ions with the N-H bond parallel to the c-axis. The label τ refers to the symmetric and antisymmetric torsional modes of the methyl groups and δ refers to the skeletal bond bending vibrations. The symmetry groups of the modes are indicated by the labels in parenthesis.

details of the normal mode calculations and the results of the experiments on the deuterated samples will be given elsewhere. [6]

This orientation of the trimethylammonium ions (N-H||c) is certainly favored by the elastic forces since it results in a smaller gallery height. However the electrostatic forces arising from the clay layers would favor the electrostatic dipole, which is along the N-H bond, to lie in the plane *i.e.* N-H|c. In addition, elastic scattering results indicate that the ion exchange is uniform, but incomplete in the vermiculite samples. [6] Thus there are point charges in the galleries that would give rise to charge-dipole interactions that also favor N-H|c. Therefore it is not obvious *a priori* that the N-H bond would be parallel to the c-axis.

The experimental data shown in figure 4 also show a large feature at about 80 meV which is not reproduced by the normal mode calculations. In addition this feature is observed in the deuterated sample. Therefore it is assigned to librations of the hydroxyl groups in the octahedral layer.

SUMMARY

We have reviewed our recent inelastic neutron scattering results on the vibrational dynamics of alkylammonium pillared clays. It has been observed that the torsional modes of the methyl groups are quite sensitive to their environment and that the bounding clay layers add roughly 28 meV to the torsional barrier in tetramethylammonium montmorillonite. We have also shown that normal mode calculations give important insights into the structural details of the pillaring process. Additional inelastic and quasielastic neutron scattering studies of the overall dynamics of the alkylammonium ions promise to yield further information on the pillar-host interactions in these potentially important materials.

ACKNOWLEDGEMENTS

The work at Michigan State University is supported by the National Science Foundation under the Materials Research Center Grant No. DMR 85-14154 and in part by the Center for Fundamental Materials Research of Michigan State University.

REFERENCES

1. S. A. Solin, *J. Mol. Catalysis* **27**, 293 (1984).
2. T. J. Pinnavaia, in Chemical Reactions in Organic and Inorganic Constrained Systems, ed. by R. Setton (D. Reidel, 1986), pg. 151.
3. T. J. Pinnavaia, *Science* **220**, 365 (1983).
4. P. Laszlo, *Science* **235**, 1473 (1987).
5. R. M. Barrer, *Clays & Clay Minerals* **37**, 385 (1989).
6. Y. B. Fan, S. Solin, H. Kim, T. Pinnavaia, D. Neumann, to be published.
7. D. A. Neumann, J. M. Nicol, N. Wada, J. J. Rush, and S. F. Trevino, to be published.
8. G. L. Squires, Introduction to the Theory of Thermal Neutron Scattering, (Cambridge University Press, Cambridge, 1978), chapter 3.
9. P. Dutta, B. del Barco, D. Shieh, *Chem. Phys. Lett.* **127**, 200 (1986).
10. G. Kabisch, *J. Raman Spect.* **9**, 279 (1980).
11. S. Weiss and G. E. Leroi, *Spectrochimica Acta* **25A**, 1759 (1969).
12. C. I. Ratcliffe and T. C. Waddington, *J. Chem. Soc. Faraday Transactions 2*, **72**, 1935 (1976).
13. T. O. Brun, L. A. Curtiss, L. E. Iton, R. Kleb, J. M. Newsam, R. A. Beyerlein, and D. E. Vaughan, *J. Am. Chem. Soc.* **109**, 4118 (1987).
14. H. Kim, W. Jin, S. Lee, P. Zhou, T. J. Pinnavaia, S. D. Mahanti, and S. A. Solin, *Phys. Rev. Lett.* **60**, 2168 (1988).

OBSERVATION OF MICELLAR FORMATION IN THE CAVITY OF POROUS SILICA GLASS

K.F. Bradley^a, S-H Chen^b, P. Thiyagarajan^c

^aDepartment of Physics; Brown University; Providence, RI 02912

^bNuclear Engineering Department, Massachusetts Institute of Technology, Cambridge, MA 02138

^cIntense Pulsed Neutron Source; Argonne National Laboratory, Argonne, IL 60439

ABSTRACT

The small angle neutron scattering intensity distribution from the empty pores of the silica glass Vycor can be satisfactorily interpreted using a simplified late stage spinodal decomposition model, due to Cahn¹, if one allows for a distribution of wave numbers in the material's density function. The result confirms that the porosity of the glass is 28% and gives the mean wave number of the density wave to be $k_0 = 0.0285 \text{ \AA}^{-1}$ with a dispersion, $\Delta k / k_0$, of about 0.29. Small angle neutron scattering measurements of the anionic surfactant SDS in the Vycor pores indicate that when the surfactant is introduced into the pores at $80 \times \text{CMC}$ in bulk solution, the surfactant forms micelles with the same average micelle separation distance as in the bulk solution, but the distribution of micelle separations is much greater in the glass pores.

INTRODUCTION

In order to understand the interaction of surfactant molecules in small pores we have performed small angle neutron scattering (SANS) measurements on dry porous silica glass and on porous silica glass filled with a solution of surfactant, sodium dodecyl sulfate (SDS), in a contrast matching $\text{H}_2\text{O}/\text{D}_2\text{O}$ mixture at 80 times the critical micelle concentration (CMC). The first part of this paper concerns the interpretation of SANS data from the empty porous glass in terms of a simplified model of the late stage spinodal decomposition. The second part of the paper shows how the pore structure modifies the SDS micelle correlations in the bulk solution.

EXPERIMENT

Our porous silica samples were "Vycor brand porous glass no. 7930," a product of the Corning Glass Works. Vycor is made by heating boron oxide glass and silica glass to above their mixing temperature and then cooling the liquid to a temperature below the spinodal line where the mixture phase separates into two interconnected regions. One region is boron rich and the other is silica rich. The boron phase is then leached out with acid leaving a silica glass with a porosity of about 30%. The pores are about 40-60 Å in diameter and run throughout the material.

Previous work has questioned some neutron scattering measurements because of the possibility of contamination of the pore surfaces by water vapor.² To prepare the glass, we slowly heated the Vycor to 550° C under an oxygen flow and maintained the heat and oxygen for at least 4 hours. This served both to dry any residual water out of

the Vycor pores and to burn off any hydrocarbon impurities present on the pore surfaces. IR measurements by Metcalfe and Shanker² indicate that this method cleans most of the hydrocarbon impurities from the glass pores. After cleaning, the Vycor was either immersed in the solution to be measured or stored in a dry nitrogen atmosphere. The Vycor samples were all rectangular in shape and were 1.6 mm thick with faces about 5x20 mm.

The measurements were performed at the SAD neutron diffractometer of the Intense Pulsed Neutron Source at Argonne National Laboratory. This spectrometer measures neutrons scattered in a q-range of 0.005 to 0.35 Å⁻¹; this q-range measurement is sensitive to structure sizes from 20 to 1200 Å. All scattering measurements were standardized to absolute units of cm⁻¹. The high q portion of the signal where the low intensity isotropic background dominates, above about 0.3 Å⁻¹, was used to estimate the incoherent contribution to the signal. This contribution has been subtracted from all data shown here.

RESULTS AND DISCUSSION

A - Dry Vycor

In 1965 Cahn suggested that the early stage spinodal decomposition could be described using a linearized form of the time-dependent Ginzburg-Landau model¹ and from this work Cahn showed how the spinodally decomposed material's density function could be simulated. The single variable in Cahn's density simulation is a wave number, k_0 , describing the length scale of a density wave. The static structure factor (SSF) measured by scattering experiments is the Fourier transform of the density correlation function. This density correlation function, when properly normalized, is called the Debye correlation function, $\chi(r)$, for the porous material.⁴ Recently Hopper^{5,6} and Berk⁷ have explicitly constructed the analytical form of the Debye correlation function. In addition, their method explicitly allows for a range of porosities, Φ , and a distribution of wave numbers in formulating the density function. In this work we extend Hopper and Berk's work by allowing for dispersion of the wave number according to the Schultz distribution. The Schultz distribution is given by

$$f(k) = \left(\frac{z+1}{k_0}\right)^{z+1} \frac{1}{\Gamma(z+1)} k^z e^{-\left(\frac{z+1}{k_0}\right)k}$$

where k_0 is the average value of k and z is a measure of the dispersion of k , $\Delta k / k_0 = 1 / \sqrt{z+1}$. Δk is the distribution's full width at half maximum.

In figure 1, we compare the SANS data of dry Vycor with 2 different static structure factors calculated using our implementation of the Cahn phenomenology. The experimental data are shown as error bars and they generally agree with the results of other workers.^{8,9} The incoherent background subtraction brings the high q portion of the dry Vycor intensity towards the q^{-4} dependence expected in the Porod region for smooth surfaces. We stress, however, that in Vycor, the Porod region, where surface structure effects dominate, should occur above 0.3 Å⁻¹ in the scattering signal considering the fact that the pore sizes are around 50 Å. The calculated static structure factors shown in figure 1 are expressed in absolute units on the same scale as the experimental data. The solid line is the SSF calculated with a density wave

having a Schultz distribution of wave numbers. The mean wave number is 0.0285 \AA^{-1} , the dispersion is 0.29, and the porosity is 28%. All three of these parameters are independent and the variation of any one of them from these values lessens the agreement between the calculated and measured structure factor. The high q region of the calculated SSF may be low because the Schultz distribution cuts off at twice its mean value and so the contribution to the scattering intensity from any wave numbers in the density distribution above 0.057 \AA^{-1} are absent from the calculation. The Schultz distribution has the advantage that it goes to zero at $q = 0$, but a distribution with a longer tail may fit the observed data better. The dotted line in figure 1 represents the SSF from a simulated structure with an almost delta function distribution of the wave numbers centered at $k_0 = 0.0285 \text{ \AA}^{-1}$. The wave number distribution is actually a narrow Gaussian in order to avoid the delta function in intensity which would otherwise arise at $q = k_0$. This comparison supports our belief that the Vycor structure can be described using Cahn's random wave simulation of the late stage spinodally decomposed structure having a 29% wave number dispersion.

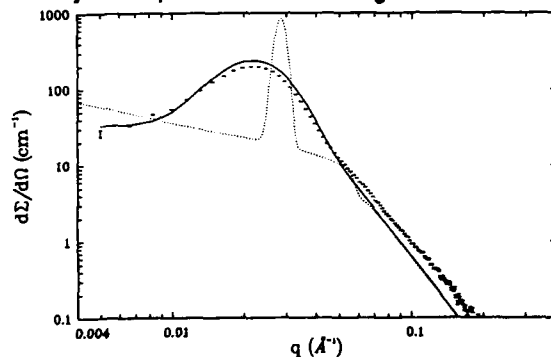


Figure 1: SANS signal from dry Vycor. The solid line is the theoretical curve, in absolute units, based on Cahn's theory of spinodal decomposition. The average wave number is 0.0285 \AA^{-1} , the porosity is 28% and the dispersion is 0.29. The dotted line is the same calculation with a dispersion of almost 0.

Figure 2 compares simulated structures with and without the wave number dispersion. Figure 2a and 2b are planar cuts of an $80 \times 80 \times 80$ cell simulation. These structures have a porosity of 34% and an average wave number of 0.785 inverse cell lengths which corresponds to a wavelength of 8 cell lengths. The structure shown in 2a has a Schultz distribution of wave numbers with $\Delta k / k_0 = 1/4$ while in the 2b it has a dispersion $\Delta k / k_0 = 0$. The difference in these two structures is responsible for the q -space variations in the calculated SSF's shown in figure 1. A comparison of figure 2a and 2b indicates that the Schultz distribution of wave numbers increases the chance of small pores occurring and also increases the interpore connectivity. The Debye correlation functions of these two structures are shown in figure 2c. The curves are the analytical forms of the Debye correlation functions and the solid points mark values calculated directly from the simulated structures shown in figures 2a and b. In addition to illustrating that the analytical integration of the simulated density distributions yield the correct results in these cases, the curves also show that the added disorder introduced when the density function contains a Schultz distribution of wave numbers causes the Debye correlation function to decay far more rapidly than

when only a single wave number is present.

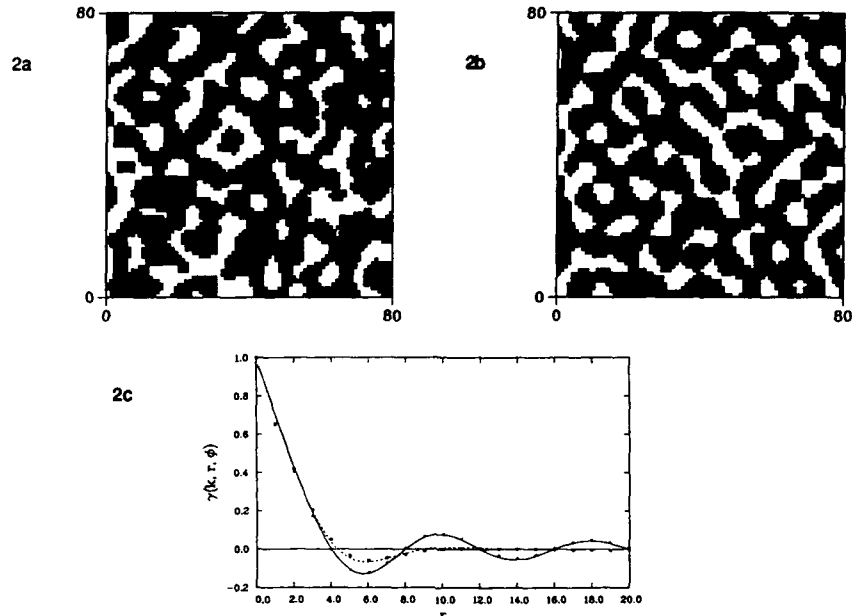


Figure 2: Simulation of spinodally decomposed structures showing the extended interconnected phase domains. 2a and b are planar cuts from 80 x 80 x 80 cell structures with $k_0 = 0.785$ inverse cell lengths and a porosity of 34%. 2a has a dispersion of 0.25 while 2b has a dispersion of zero; the different characters of these two structures arises from their different dispersions. 2c is the Debye correlation function of the two simulated structures of 2a and b. The dashed line is the analytical correlation function of the dispersion = 0.25 case and the solid line is the analytical correlation function of the zero dispersion case. The squares and circles mark correlation function points calculated by directly integrating the density functions of the structures shown in 2a and b respectively.

B - SDS In Vycor

In order to measure micellar formation in Vycor, we eliminated the strong scattering signal from the glass-pore contrast by filling the pores with a contrast matching fluid of H_2O/D_2O mixture having the same scattering length density as the glass. The open circles in figure 3 are the measured scattering signal from Vycor filled with a [40/60] proportion of H_2O/D_2O . There is some remaining signal at low q which is probably due to small pores filled with residual air bubbles. The maximum in the contrast matched signal is about 1% of the peak value of the dry Vycor signal.

In this work, we used SDS because it is an anionic surfactant with a negatively charged head group in solution. This charge creates a repulsive force between the surfactant and the OH^- groups on the glass pore surfaces and eliminates the need to consider the competition between micelle formation and surface coating actions by the surfactant molecules.

SANS signal of Vycor which has been first submerged for 2 months in a solution of

80 x CMC SDS in the H₂O/D₂O contrast matching fluid and then withdrawn and sealed in a quartz cell immediately before the measurement is shown by the solid circles in figure 3. The primary scattering peak has roughly the same shape as the dry Vycor peak but it is centered at a slightly lower q . In addition, a secondary peak is present at about 0.085 \AA^{-1} . With the contrast matched fluid in the Vycor pores the observed signal should be entirely due to scattering from the micelles.

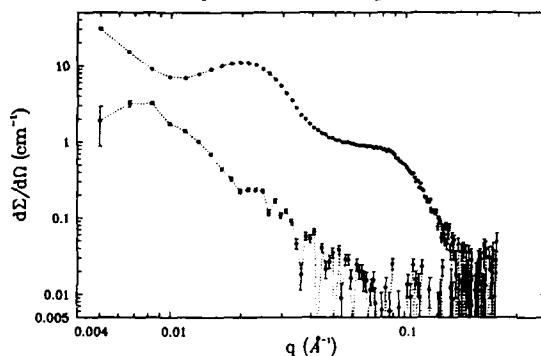


Figure 3: The open circles are the measured SANS signal from contrast matched Vycor. The filled circles are the SANS signal from Vycor imbided with a solution of SDS at 80 x CMC in the same contrast matching water.

In general SANS cross section from a bulk micelle solution can be written as¹⁰

$$\frac{d\Sigma(q)}{d\Omega} = S(q) P(q)$$

where $P(q)$ is the average form factor of the individual micelles and $S(q)$ is the SSF due to the intermicelle correlations. In addition to the factors given above, micelle formation in the glass pores leads to a third level of organization in the surfactant system. Within a pore the micelles can form a cluster with a local micelle-micelle correlation function, but there will also be an inter-cluster correlation function amongst these clusters of micelles. If the cluster-cluster correlation function is independent of the micelle-micelle correlation function in the individual cluster, we can write the scattering law for the system of micelles in glass pores as

$$\frac{d\Sigma(q)}{d\Omega} = T(q) S(q) P(q)$$

where $T(q)$ is the cluster-cluster SSF. In general $T(q)$ will be different from the pore-pore SSF because the collection of micelles in a pore will not occupy the entire pore space and so the micelle cluster center may not be located at the pore center. Nonetheless, at this time, the best estimate we have for $T(q)$ is the pore-pore SSF measured in the dry Vycor. Dividing the SANS signal shown in figure 3 by this estimate of $T(q)$ from the dry Vycor signal gives $P(q) \times S(q)$, the SSF for the collection of micelles in an average Vycor pore. This result is shown as the filled circles in figure 4. The open circles show $S(q) \times P(q)$ for the same concentration of SDS measured in a bulk solution. The coincidence of the peak positions of both curves indicates that the

average micelle-micelle separation is similar in both cases. The much broader SSF of micelles in the glass pores suggests that the distribution of micelle separations is more disordered for micelles in the glass pores than for micelles in the bulk. This result is expected because the SDS molecule is about 20 Å long and the minimum micelle diameter is about 40 Å. In the 50 Å diameter pores, only a chain-like micellar cluster can form. As a micelle moves in the glass pores, only the linearly adjacent micelles are imposing restoring forces to maintain the intermicelle distances. In the bulk, on the other hand, each micelle is surrounded on the average by more micelles and the local order is nearly face-centered cubic. In addition, inside the pore, the repulsive interaction between the micelles and the glass walls will disturb the micelle-micelle correlations.

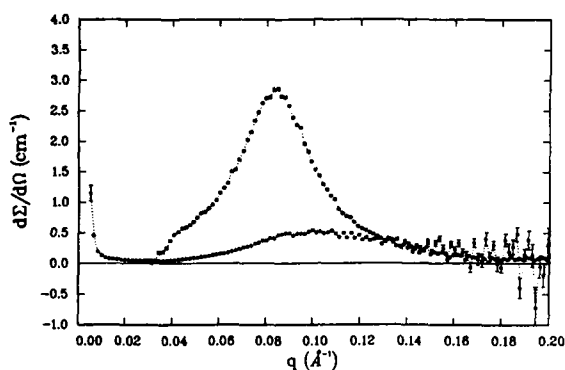


Figure 4: The open circles are the measured SANS signal from SDS in water at 80 x CMC. The filled circles are the normalized static structure factor due to the correlations of micelles within a single Vycor pore.

ACKNOWLEDGEMENTS

We would like to thank the entire staff of IPNS for many fruitful discussions and generous technical help. The work of KFB and PT was supported by the U.S. Department of Energy, Basic Energy Sciences-Materials Sciences, under Contract W-31-109-Eng-38. The work of SHC was supported by the National Science Foundation.

- ¹ J.W. Cahn, *J. Chem. Phys.*, **42**, 93 (1965)
- ² M.J. Benham, et al, *Phys. Rev.*, **B39**, 633 (1989)
- ³ A. Metcalfe, S.U. Shanker, *J. Chem. Soc. Faraday Trans.*, **74**, 1945 (1978)
- ⁴ P. Debye, et al, *J. Appl. Phys.*, **28**, 679, (1957)
- ⁵ R.W. Hopper, *J. Non-Cryst. Solids*, **49**, 263 (1982)
- ⁶ R.W. Hopper, *J. Non-Cryst. Solids*, **70**, 111 (1985)
- ⁷ N.R. Berk, *Phys. Rev. Lett.*, **58**, 2718 (1987)
- ⁸ D.W. Schaefer, et al, *Phys. Rev. Lett.*, **58**, 284 (1987)
- ⁹ P. Wiltzius, et al, *Phys. Rev.* **A36**, 2991 (1987)
- ¹⁰ S-H Chen, *Ann. Rev. Phys. Chem.*, **37**, 351 (1986)

ANALYSIS OF SANS FROM CONTROLLED PORE GLASSES

N. F. BERK*, C. J. GLINKA*, W. HALLER* AND L. C. SANDER†

* Materials Science and Engineering Laboratory,

† Center for Analytical Chemistry,

National Institute of Standards and Technology, Gaithersburg, Md 20899

Abstract

Small angle neutron scattering measurements have been performed on several samples of silica controlled pore glasses with pore sizes ranging from roughly 7 to 30 nm. The scattering intensity is strongly peaked at small Q and shows approximate Porod law behavior at large Q . Contrast variation measurements have shown that the pore space in these samples is entirely interconnected and thus forms a bicontinuous microstructure. The scattering data have been analyzed using the leveled wave method based on an early scheme for representing two-phase microstructures resulting from spinodal decomposition. In this approach interfaces are modeled by the contours of a stochastic standing wave composed of plane wave components propagating in random directions with random phases and having wave numbers distributed according to a given probability density, $P(k)$. We have determined model $P(k)$ functions by fitting the SANS data with the leveled wave scattering function and then used these to construct leveled wave images of the corresponding porous structures. The average pore sizes obtained by measuring chord lengths in the computer models turn out to agree with the values determined for these glasses by mercury porosimetry.

Introduction

Microporous materials with narrow pore size distributions, such as silica controlled pore glass (CPG), are model systems for studying the many physical and chemical processes that take place in porous environments. Small angle x-ray and neutron scattering measurements performed on CPG, primarily commercial porous Vycor[†], have thus far been analyzed either qualitatively[1] or in terms of models[2,3] that were not compared with the known microstructure of CPG. Here we report an analysis of small angle neutron scattering (SANS) measurements performed on samples of CPG with pore sizes from 7 to 30 nm in terms of a mathematical model for a bicontinuous structure[4,5] that derives from an early scheme due to Cahn[6] for representing two-phase microstructures resulting from spinodal decomposition. This so-called leveled wave model[5] yields analytic expressions that account for the main features of the observed scattering and, in addition, can be used to generate images of the physical microstructure that are remarkably similar to replica electron micrographs of CPG[7]. Physical characteristics of the model microstructure can be calculated using parameter values obtained by fitting to the scattering data. We illustrate this approach by calculating the pore chord length distributions for our samples and find that the peaks in these distributions closely coincide with pore sizes determined by mercury porosimetry.

Materials and Methods

The process used to produce the CPG samples for this study is described in detail in [7]. The composition of the borosilicate base material was the same for all samples and the pore size was controlled by adjusting both the temperature and duration of annealing. The samples have been characterized by gas adsorption (BET) and mercury porosimetry (see Table 1). Sample

porosities ranged from 50 to 75% in contrast to porous Vycor which has a porosity of 28%.

The SANS measurements were made on the 8-meter long SANS instrument at the NIST 20 MW research reactor using a pinhole collimated beam with a wavelength of 10 Å. The measurement range was 0.006 to 0.09 Å⁻¹ in terms of the scattering vector $Q = (4\pi/\lambda)\sin(\theta/2)$ where θ is the scattering angle. In addition to the measurements on dry CPG samples discussed here, data were taken on samples soaked in H₂O/D₂O mixtures to vary the scattering contrast between the pores and the silica framework. At the calculated null contrast condition, all small angle scattering was eliminated which demonstrated both that the pore space is entirely interconnected (bicontinuous) and that the silica framework is homogeneous to a high degree.

	D	S	v_p	ϕ	(β)	K	σ
CPG70	70 Å	207 m ² /g	0.48 cc/g	51%	(0)	0.036 Å ⁻¹	0.29
CPG116	116	155	0.78	63	(-0.23)	0.024	0.30
CPG156	156	166	0.90	66	(-0.29)	0.022	0.30
CPG255	255	96	0.96	68	(-0.33)	0.014	0.30

TABLE 1. Summary of data and parameters for Controlled Pore Glasses. D is pore size from mercury porosimetry, S is specific surface area from nitrogen absorption (BET), v_p is specific pore volume from mercury porosimetry, and ϕ is the corresponding porosity. β , K, and σ are the parameters used in the leveled wave model for these glasses (see text).

Results

The scattering data are shown in Figs. 1 and 2 using linear and log scales to draw out both the small-Q and large-Q behavior. At small Q the scattering shows a strong peak that moves to higher Q as nominal pore size decreases. Except for CPG116, the scattering peak positions K, nominal pore sizes D, and porosities ϕ , are approximately related by the condition $KD/\phi=5.1$ over the whole range of pore sizes (the CPG116 data give $KD/\phi=4.4$). Within the range and precision of these data we observe the Porod law at large Q, indicating more or less smooth pore surfaces. Recent scattering measurements by Schmidt, et al. [8] on commercial porous silicas find small but systematic departures from the Porod law, indicative of surface fractal roughness.

Theory

These data were analyzed using the leveled wave method in [5]. It is assumed that the physical, bicontinuous pore morphology can be mathematically modeled as the binary leveled image of a continuous, stochastic standing wave, $S(\mathbf{r})$, generated by adding plane waves over suitable distributions of wavevectors and phase constants. In particular, the individual wave directions are taken to be randomly distributed over solid angle 4π , while the wavenumbers, k , are chosen from a given $P(k)$ which, presumably, is peaked more or less sharply about a value, K, which is related to the overall scale of the structure. The density function of the porous glass is then defined pointwise by $\rho(\mathbf{r})=\rho$ or $\rho(\mathbf{r})=0$, according to

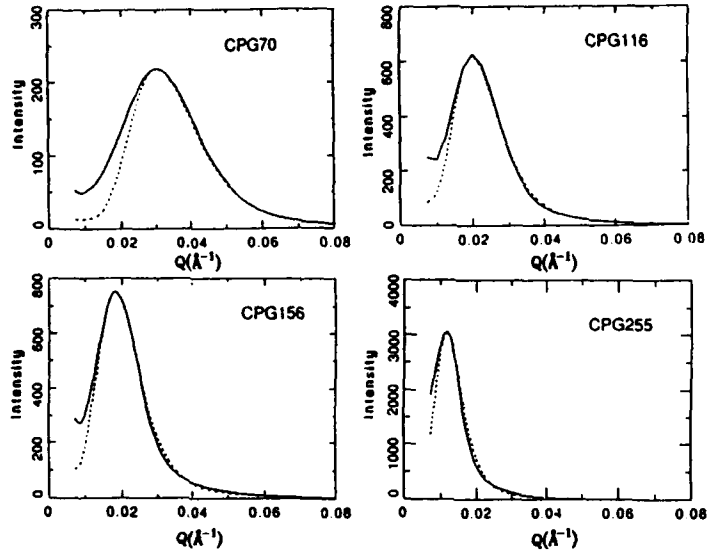


FIG. 1. Neutron scattering (I vs Q) from Controlled Pore Glasses (solid lines) and theoretical fits using the leveled wave model (dotted lines).

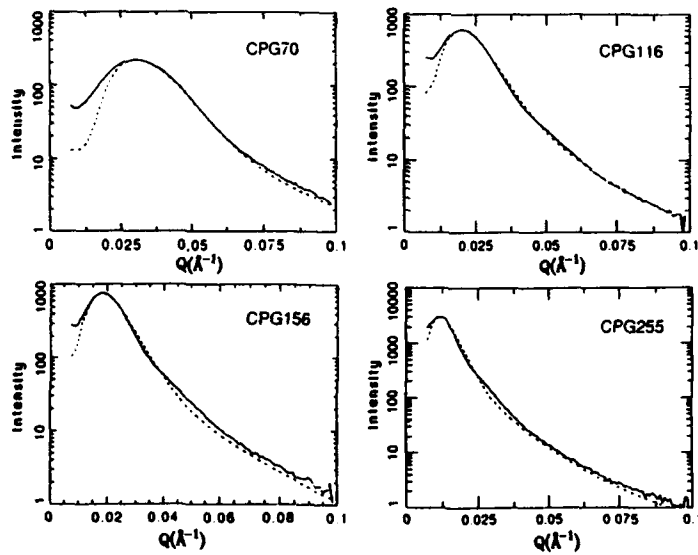


FIG. 2. Same as Fig. 1. on a logarithmic ordinate.

whether $S(\vec{r}) > \beta$ or $S(\vec{r}) < \beta$, where the level parameter β is determined by the porosity $\phi = (1 + \text{erf}(\beta))/2$, and where $\text{erf}(x)$ is the error function. As derived in [5], the scattering from a leveled wave morphology depends only on the level parameters (here β) and on the autocorrelation of the unleveled wave, $\tau(r) = 2\langle S(\vec{r})S(\vec{0}) \rangle = \int P(k)j_0(kr)dr$. In particular, the scattering intensity for this model of the pore structure can be represented exactly as the infinite series [9]

$$I(Q) = 4\pi V \rho^2 \phi (1-\phi) \sum_{n=1}^{\infty} C_n(\beta) \int r^2 \tau(r)^n j_0(Qr) dr, \quad (1)$$

where V is the sample volume,

$$C_n(\beta) = \exp(-2\beta^2) H_{n-1}^2(\beta) / (\pi n! 2^n), \quad (2)$$

and $H_n(x)$ is the Hermite polynomial. Writing (1) as $I(Q) = I_1(Q) + I_2(Q) + \dots$, then

$$I_1(Q) = \pi V \rho^2 \exp(-2\beta^2) P(Q) / Q^2, \quad (3)$$

$$I_2(Q) = \pi V \rho^2 \beta^2 \exp(-2\beta^2) / (2Q) \iint \Lambda(Q; k_1, k_2) P(k_1) P(k_2) dk_1 dk_2 / k_1 k_2, \quad (4)$$

for the first two terms, and so on, where in (4) $\Lambda(z; x, y) = 1$ for $|z-x| \leq y < z+x$, zero otherwise. The contribution I_1 can be viewed as the scattering from the underlying unleveled wave, $S(r)$, while I_2 represents the first "correction" due to the leveling operation that in the construction produces a sharply defined interface. In general the scattering at small Q is dominated by the first few terms of the series in (1), while the large- Q scattering (Porod law) requires summing the infinite series. In practice we accurately compute I_1 and I_2 and then numerically sum a large number of the remaining terms of (1) using asymptotic representations of the Hermite polynomials [10] in (2) to obtain well-behaved results for $n \gg 1$. This procedure gives a good Porod law behavior ($I \sim 1/Q^4$) at large Q .

Analysis

Theoretical curves obtained from the leveled wave scheme are shown in Figs. 1 and 2, along with the data. Lacking a first principles model for $P(k)$, we assumed a lognormal probability function with mode $k=K$: $P(k) = N(\log(k) - \xi, \sigma^2) / k$, where $\xi = \sigma^2 + \log(K)$ and $N(x, \sigma^2)$ is the normal distribution with variance σ^2 and mode $x=0$. The corresponding mean and rms k -values are then $k_{av} = K \exp(3\sigma^2/2)$ and $k_{rms} = K \exp(2\sigma^2)$. The computed curves are "good trials" rather than best fits, since the complexity of the theoretical scattering function made automatic curve fitting impractical. The level parameter β was fixed for each case by the known porosities and only K and σ were varied. The fit parameters are shown as the final entries in Table 1. The predicted scattering does not incorporate instrumental resolution, but we determined that the computed curves are relatively insensitive to these effects under the conditions of the measurement, and we found no significant resolution dependence on the reported parameters. Note that σ essentially does not vary over the range of pore sizes. In fact most of the apparent broadening of the scattering with increasing K can be attributed to the kinematical relationship of k_{rms} and K for the lognormal distribution. In particular, if $\Delta k^2 = \langle k^2 \rangle - \langle k \rangle^2$, then $\Delta k / K \approx \sigma / \sqrt{2}$ for small σ , so that the relative width of $P(k)$ is approximately constant. As the curves show, the model does not do well at small Q , leading to persistent underestimates of the scattering. One sees from the forms of I_1 and I_2 , however, that the theoretical scattering near $Q=0$ is very sensitive to the behavior of $P(k)$ near $k=0$. It is also worth mentioning that the predicted scattering at large Q is the result of the "infinite" sum in (1); I_1 and I_2

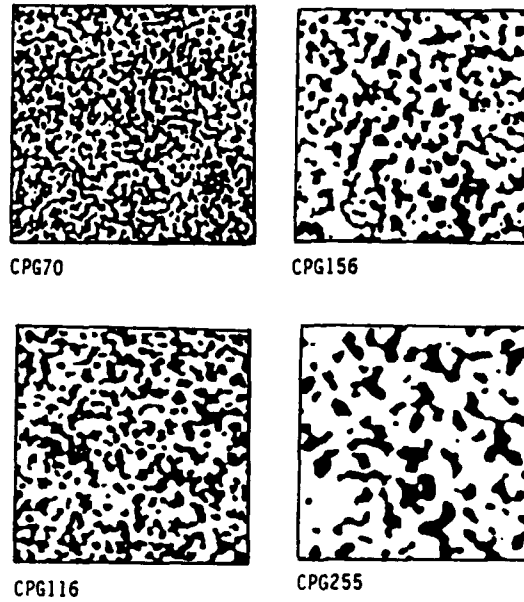


FIG. 3. Simulated "TEM" views, on a fixed length scale, of leveled wave CPG morphologies using empirically determined lognormal forms of $P(k)$ to generate 500 random k -values. The pore space is white (slightly exaggerated by effects of photocopying.)

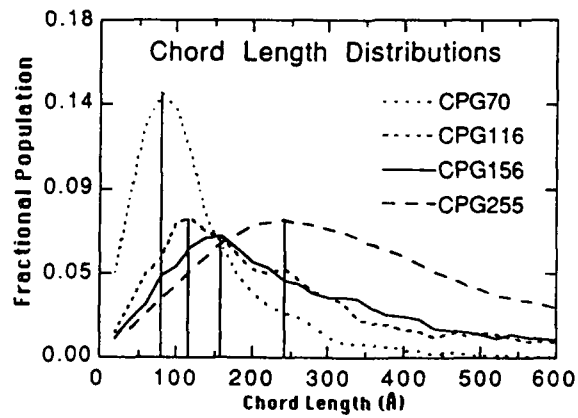


FIG. 4. Chord distributions derived from simulations in Fig. 3. (For CPG255, a larger window was used to obtain good statistics.)

are essentially zero in the Porod regime. Thus while the pointwise quality of fit is low, once σ has been determined, the predictions require only the scattering peak position and given porosity to account fairly well for the observed overall behavior.

Discussion

A central motivation of the leveled wave analysis of scattering is its basis in a constructive--i.e., realizable geometry. In particular, using the empirically determined $P(k)$ we have generated the corresponding morphologies, as shown in Fig 3, as simulated "TEM" views, and used these to obtain chord length statistics. A chord is defined here in the following way: starting at a point on the glass-pore interface and traversing pore space in a given direction, a chord is the join to the next encounter with the interface. Because the model is isotropic, chord statistics can be obtained by measuring along a fixed direction; in fact we devised a simple single-pass computer algorithm to count chords as the pixel-by-pixel leveled wave images are being generated. The resulting chord-length distributions are shown in Fig 4. In each case the mode occurs to within 10% of the nominal pore size as determined by mercury porosimetry. The porosimetry measurements indicate, on the other hand, that pore size distributions narrow with increasing pore size, while the leveled wave chord distributions broaden as the modes moves to larger sizes, although the width-to-mode ratios do not increase by much. In the absence of a detailed prescription to relate porosimetry measurements to pore-space chordal distributions, we believe the good agreement between the pore size and most probable chord length suggests the pertinence of the leveled wave model to describing the morphology of controlled pore glasses.

References

- † Identification of a commercial product in no way implies its endorsement or recommendation by the National Institute of Standards and Technology.
1. P. Wiltzius, F. S. Bates, S. B. Dierker and G. D. Wignall, *Phys. Rev. A* **36**, 2991 (1987).
 2. A. Hohn, H.-B. Neumann, P. W. Schmidt and P. Pfeifer, *Phys. Rev. B* **38**, 1462 (1988).
 3. S. K. Sinha, J. M. Drake, P. Levitz and H. B. Stanley in Fractal Aspects of Materials: Disordered Systems, edited by A. J. Hurd, D. A. Weitz and B. B. Mandelbrot (Mater. Res. Soc. Proc. S, Boston, MA 1987) pp. 118-120.
 4. R. W. Hopper, *J. Non-Cryst. Solids* **49**, 263 (1982).
 5. N. F. Berk, *Phys. Rev. Lett.* **58**, 2718 (1987).
 6. J. W. Cahn, *J. Chem. Phys.* **42**, 93 (1965).
 7. W. Haller, in Solid Phase Biochemistry - Analytical and Chemical Aspects, edited by W. H. Scouten (Wiley, New York, 1983), Chap. 11.
 8. P. W. Schmidt, A. Hohn, H.-B. Neumann, H. Kaiser, D. Avnir, and J. S. Lin, *J. Chem. Phys.* **90**, 5016 (1989).
 9. See Eqns. (8)-(9) and text ahead of (11) in Ref. [5]. The case here corresponds to $\alpha \rightarrow \infty$ in [5].
 10. I. S. Gradshteyn and I. M. Ryzhik, Table of Integrals, Series, and Products (Corrected and Enlarged Edition), edited by A. Jeffrey, Orlando: Academic Press (1980). See Sec. 8.955. In fact, these asymptotic formulas are adequate for $n \geq 3$ in this application, since β is not too large.

CHARACTERIZATION OF CHEMICALLY MODIFIED PORE SURFACES
BY SMALL ANGLE NEUTRON SCATTERING

C. J. GLINKA*, L. C. SANDER†, S. A. WISE†, AND N. F. BERK*

* Materials Science and Engineering Laboratory,

† Center for Analytical Chemistry,

National Institute of Standards and Technology, Gaithersburg, MD 20899

ABSTRACT

Small angle neutron scattering has been used to characterize the structure of linear hydrocarbon chains chemically grafted to the internal pore surfaces of microporous silica particles. The aim of this work has been to relate the structure of the bonded adsorbate layers in these particles to their performance in, for example, reverse-phase liquid chromatography. By filling the pore space in the modified silica with a solution that matches the scattering density of the silica framework, the scattering from the adsorbate layers is enhanced and provides a sensitive probe of the effective thickness, uniformity and degree of solvent penetration in the layers. Results are presented for both monomeric and polymeric phases of alkyl chains ranging from C8 to C30 bonded to silica particles with a mean pore size of 100 nm.

Introduction

Microporous particles with chemical adsorbates bound to their internal pore surfaces are being used with increasing sophistication in chemical processing, separation and quantitative analysis. Data on the submicron structure of these bonded phases that might aid in understanding or enhancing their performance in such applications is, however, still rather limited. To this end we have used small angle neutron scattering (SANS) to characterize the mean thickness, uniformity and density of linear hydrocarbon chains grafted to the pore surfaces of micron-sized silica particles with pore sizes of roughly 100 nm. Both monomeric and polymeric phases consisting of alkyl chains ranging from C8 to C30 (number of carbon atoms per chain) were studied. Silica particles with such phases are typical of so-called reverse-phase packing materials that are now widely used in high performance liquid chromatography. For the SANS measurements the pores and interparticle spaces were filled with a mixture of deuterated and protonated methanol with a neutron scattering density equal to that of the silica framework in order to suppress the scattering from the pores and thus enhance the signal from the bonded phases. A potentially important advantage of this technique is that the SANS measurements are made under conditions, i.e. in the presence of a mobile solvent phase, that closely approximate actual chromatographic conditions.

Materials and Methods

The SANS measurements were made on a commercial porous silica, (LiChrospher Si-1000, E. Merck, Darmstadt, FRG) with a mean pore size of about 100 nm. The use of a material with a pore size some 50 to 100 times larger than the thickness of the bonded adsorbate phases simplifies the analysis of the SANS measurements because the dominant features of the scattering from the pore structure and those from the bonded phases occur in widely separated regions of scattering angle.

Monomeric C8, C18 and C30 bonded phases were prepared by first vacuum drying the silica at 150 C to remove adsorbed water followed by exhaustive silanization with the corresponding monofunctional n-alkyldimethylchlorosilane in carbon tetrachloride. A polymeric C18 phase was prepared using a trifunctional reagent, octadecyltrichlorosilane in the presence of water. After refluxing in each case for about four hours, the modified silica was filtered, washed several times to remove both polar and nonpolar residues, and dried under vacuum. Further details of the synthesis are given in [1].

For the SANS measurements the modified silica was soaked in a mixture of 64% (by volume) deuterated and 36% protonated methanol to form a slurry that was transferred and allowed to settle in 2 cm diameter x 1 mm path length cylindrical quartz sample cells. Dry and methanol soaked samples of unbonded LiChrospher particles were prepared as well. The soaked unbonded sample gave a constant level of scattering for scattering vectors $Q > 0.02 \text{ \AA}^{-1}$ which confirmed that the scattering length density of the methanol mixture ($3.6 \times 10^{10} \text{ cm}^{-2}$) closely matched that of the silica matrix thus effectively masking the scattering from the pores.

The SANS measurements were made on the 8 meter long, pinhole collimation, SANS instrument [2] at the NIST research reactor. Most of the data were taken with an incident wavelength of 6 Å ($\Delta\lambda/\lambda = .25$) with the beam impinging near one edge of the instrument's 65 x 65 cm² position-sensitive detector. The resulting range of scattering vectors was $0.013 < Q < 0.16 \text{ \AA}^{-1}$ where $Q = 4\pi/\lambda \sin\theta$ and θ is half the scattering angle. The raw data were corrected for background and scattering from the quartz cell and placed on an absolute scale of cross section per unit volume by comparison with the scattering from a standard silica gel sample whose forward scattering cross section ($32 \pm 1 \text{ cm}^{-1}$) had been determined by several independent methods.

Following the SANS measurements, the mass of silica and solvent was determined and a weight percent carbon analysis was performed for each sample. For the monomeric phases, the carbon analysis provided values for the coverage area per bonded chain that could be directly compared with the SANS results.

Results and Analysis

The scattering from the dry, unbonded LiChrospher sample exhibited the characteristic $1/Q^4$ dependence known as Porod's law (Fig. 1)

$$\frac{d\Sigma}{d\Omega} = \frac{2\pi S}{V} (\rho_m - \rho_p)^2 / Q^4 \quad (1)$$

over the entire Q -range of the measurements, where S is the total surface area of the pores in the volume V exposed to the neutron beam, and $(\rho_m - \rho_p)^2$ is the scattering contrast between the silica matrix ($\rho_m = 3.6 \times 10^{10} \text{ cm}^{-2}$) and the pores ($\rho_p = 0$). From the absolute intensity of the Porod law scattering, and the measured sample mass, the specific surface area of the LiChrospher particles was determined to be $25 \pm 5 \text{ m}^2/\text{g}$ (whereas nitrogen adsorption gave $32 \text{ m}^2/\text{g}$). More importantly, the observation of Porod behavior implies that for the Q -ranged probed, $Q\xi \gg 1$ where ξ is any characteristic dimension of the pore structure such as the mean curvature or pore size. Thus details of the pore structure do not affect the scattering in the region of our measurements and need not be considered further.

Prior to filling with the $\text{CD}_3\text{OD}/\text{CH}_3\text{OH}$ pore maskant, the scattering from the bonded phase particles is dominated by the strong Porod tail from the pore scattering. Once imbibed with the maskant, however, the character of the scattering changes entirely and exhibits, as shown in Fig. 1, a $1/Q^2$ -dependence at low Q with a gradual leveling off at larger Q due to the

underlying flat incoherent scattering from the hydrogen in the methanol and bonded phase. A $1/Q^2$ dependence is characteristic of scattering from thin layers whose lateral extent is much greater than their thickness. Consequently we attempted to fit the data for the bonded phase samples to the scattering function for an ensemble of randomly oriented thin disks [3],

$$\frac{d\Sigma}{d\Omega} = \frac{2\pi S}{V} (\rho_m - \rho_{bp})^2 \frac{D^2}{Q^2} \left[\frac{\sin(QD/2)}{(QD/2)} \right]^2 + \frac{d\Sigma_i}{d\Omega} \quad (2)$$

where D is the disk thickness, ρ_{bp} is the scattering length density of the bonded phase, and $d\Sigma_i/d\Omega$ represents the structureless incoherent scattering. According to (2), the coherent scattering, which initially falls as $1/Q^2$ with increasing Q , should fall off more sharply when $1/Q \approx D$. This expected downturn is completely obscured, however, in the data shown in Fig. 1 by the incoherent scattering. Estimating the thickness D using (2) is, therefore, dependent on an accurate determination of the level of incoherent scattering. In the absence of data extending to larger angles, an estimate for the incoherent level was calculated from the results of SANS measurements on separate samples of pure CD_3OD and CH_3OH , taking into account the volume displaced by the silica in the samples of interest. This estimate of the incoherent scattering, which is shown as the dashed line in Fig. 1, is considered to be a lower limit, since it does not include any contribution from the bonded phase itself, while the large Q limit of the data provides an upper limit.

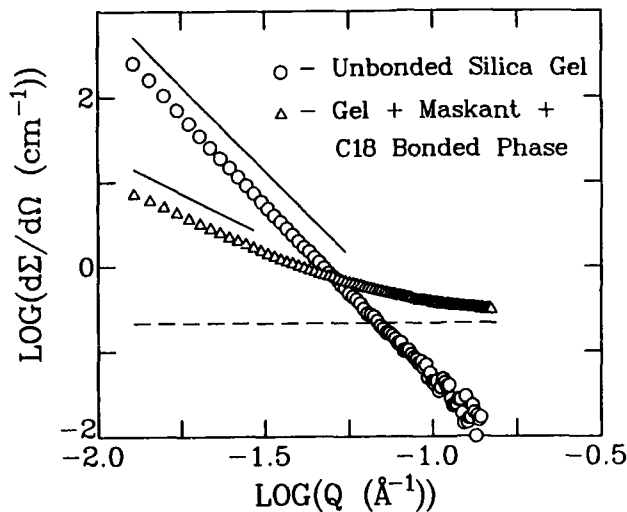


Fig. 1. Log-log plot of the scattering from a dry, unbonded sample of LiChrospher Si-1000 and from a LiChrospher sample with a monomeric bonded phase imbibed with pore maskant. The long and short solid lines have slopes of -4 and -2, respectively. The dashed line is an estimate of the incoherent scattering for the bonded phase sample as discussed in the text.

With the level of incoherent scattering constrained between narrow limits as described above, reasonably good least-squares fits (χ^2 values from 1.5 to 3) to the data for the C18 and C30 monomeric phases and the C18 polymeric phase could be obtained with (2). The results for the net

coherent scattering and fitted lineshape for the C18 monomeric phase data are shown in Fig. 2. With the incoherent background subtracted, the remaining coherent component shows the expected downward curvature that is a direct measure of the thickness of the bonded phase in both a log-log plot, Fig. 2a), and even more clearly in Fig. 2b) where the net coherent scattering has been multiplied by Q^2 to bring out the $(\sin x/x)^2$ behavior in (2). Values for the thickness of the C18 and C30 phases obtained in this

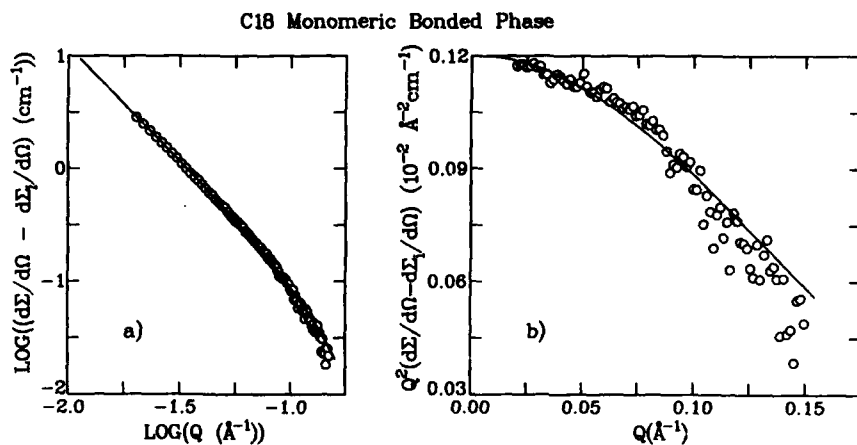


Fig. 2. The net coherent scattering for the C18 monomeric bonded phase sample a) in a log-log plot, and b) multiplied by Q^2 to emphasize the downward curvature at larger Q values.

way are listed in Table I. For the C8 sample, which gave the weakest scattering signal, the uncertainty in D obtained by this procedure was comparable to D itself. It was possible, however, to estimate D for this sample by an indirect method described below.

All of the scattering data, along with what are considered to be the best fits obtainable with (2), are shown in Fig. 3 where the total cross section (which includes the incoherent scattering) has been multiplied by Q^2 and plotted versus Q^2 . Plotted in this way the data appear nearly linear (with the exception of the low- Q region of the C30 data which may indicate that the coverage is not uniform in this case) with a limiting slope at large Q that is determined by the incoherent scattering term in (2). The reason for plotting $Q^2 d\Sigma/d\Omega$ versus Q^2 is to emphasize that although a direct determination of D is strongly affected by the incoherent background, the quantity that is well determined, and little affected by this background, is the extrapolated value of $Q^2 d\Sigma/d\Omega$ at $Q = 0$, the y-intercepts in Fig. 3. These intercepts provide a precise measure of the product, $(\rho_m - \rho_{bp})D$ in (2) (since the other factors are known independently from measurements on the unbonded silica). In this product the bonded phase scattering density, ρ_{bp} , is not known a priori because it depends on the degree of solvent penetration in the bonded phase. If we let x represent the volume fraction of the bonded phase occupied by the alkyl chains, then we can write $(\rho_m - \rho_{bp})D = (\rho_m - \rho_{ch})xD$ where ρ_{ch} is the scattering density for the particular alkyl chain which can be calculated from its chemical structure and molecular volume. Hence without any recourse to model

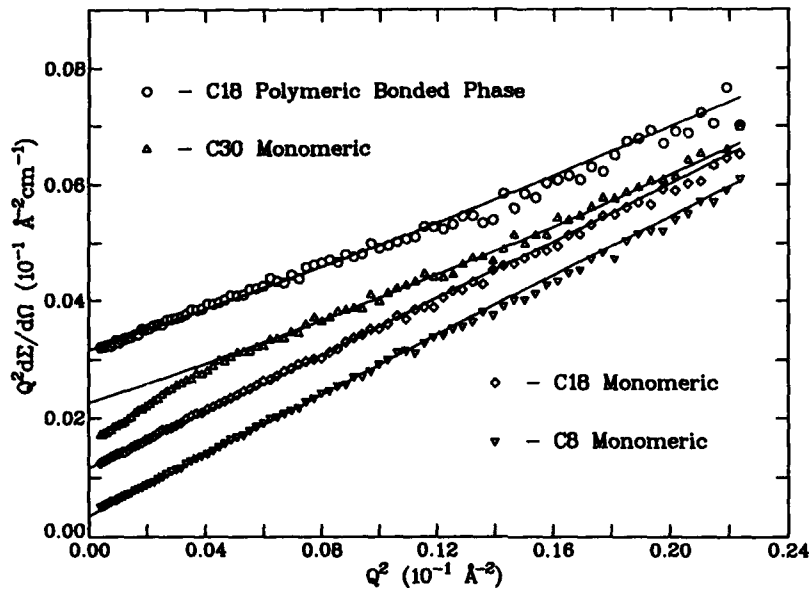


Fig. 3. SANS data and fitted lineshapes from (2) in a $Q^2 \frac{d\Sigma}{d\Omega}$ versus Q^2 plot.

Table I. SANS results for the thickness, D , and alkyl chain volume fraction, x , for the monomeric (M) and polymeric (P) bonded phase samples along with the values for the alkyl chain scattering density, ρ_c , and molecular volume, v_c , used to derive the coverage area per chain, A_C . Also listed is the weight percent carbon, P_C , for each sample and the coverage per chain, A_C , derived from the carbon analysis.

Bonded Phase	$\Delta\rho D^1$ 10^{-3}Å^{-1}	D Å	x	ρ_c^2 10^{10}cm^{-2}	v_c Å^3	P_C %	α^3 $\mu\text{mol}/\text{m}^2$	A_S^4 Å^2	A_C^5 Å^2
C8,M	2.5 ± 2	10 ± 2	$.65 \pm .15^*$	$-.38$	405	1.38	3.7	62 ± 25	45
C18,M	4.6 ± 4	17 ± 3	$.66 \pm .15$	$-.41$	544	2.70	3.7	48 ± 20	45
C30,M	6.2 ± 5	25 ± 4	$.63 \pm .15$	$-.34$	982	3.32	2.8	62 ± 20	59
C18,P	7.0 ± 5	21 ± 3	$.88 \pm .1$	$-.41$	-	4.83	-	-	-

1. $\Delta\rho D = (\rho_m - \rho_{bp})D = (\rho_m - \rho_c)x D$

2. $\rho_c = \sum b_i / v_c$, b_i is the scattering length of the i th atom in the chain.

3. $\alpha = \frac{1}{S_p} 10^4 P_C / (1200 n_c - P_C(M-1))$, n_c is the number of carbon atoms in a chain of molecular weight M .

4. $A_S = v_c / (xD)$ 5. $A_C = 1/N_A \alpha$, N_A = Avogadro's number

* assumed value based on results for other monomeric phases.

fitting, we can conclude from the plots in Fig. 3 that the quantity xD increases with alkyl chain length for the monomeric phases and increases further for the C18 polymeric phase. If x were nearly constant for the various phases, this trend in the intercepts would imply a corresponding trend in the thickness D . If, however, we make use of the values for D that were reasonably well determined for all but the C8 sample by the fitting procedure described previously, we would conclude, as listed in Table I, that $x \approx 0.65$ for the monomeric phases, but is ≈ 0.85 for the C18 polymeric phase. Thus by combining the information contained in the shape and magnitude of the scattering, we infer, for example, that the C30 monomeric and C18 polymeric phases differ not so much in thickness as in density with the polymeric phase being more dense and thus excluding more solvent.

Our SANS results are summarized in Table I along with the results of the carbon analysis. For the monomeric phases, the SANS and carbon analysis results provide independent means for calculating the coverage area per alkyl chain. Because of the number of factors involved, the SANS values for the coverage areas have rather large uncertainties and furthermore are based on the SANS determination of S_p (25 ± 5 m²/g) whereas the value 32 m²/g measured by nitrogen adsorption was used to derive the coverage area from the carbon loading.

Conclusions

The SANS technique with pore masking is a sensitive method for detecting and characterizing certain features (in particular, the product of the thickness and scattering density) of thin adsorbate layers in actual commercially used microporous materials. Furthermore, the measurements can be made under solvent conditions that closely approximate conditions of actual use. For low molecular weight adsorbates such as those in this study, an accurate determination of the incoherent scattering from all sources is required in order to extract the coherent component that is related to the structure of the bonded phase. For high molecular weight adsorbates such as polymers, SANS could provide not only average thickness and adsorbate density but also the density profile through the thickness of the adsorbed layer.

References

* Commercial materials are identified in this report solely to specify adequately the experimental procedure. Such identification does not imply recommendation or endorsement by the National Institute of Standards and Technology.

1. L. C. Sander and S. A. Wise, *Analytical Chem.*, **54**, 504 (1984).
2. C. J. Glinka, J. M. Rowe and J. G. LaRock, *J. Appl. Cryst.*, **19**, 427 (1986).
3. G. Porod, in Small Angle X-Ray Scattering, edited by O. Glatter and O. Kratky (Academic Press, New York, 1982), p.32-38.

SMALL ANGLE NEUTRON SCATTERING AND SMALL ANGLE X-RAY SCATTERING FROM BULK MICROPOROUS SILICA.

G. G. Long, S. Krueger, D. R. Black and J. P. Cline, National Institute of Standards and Technology, Gaithersburg, MD 20899, P. R. Jemian, Northwestern University, Evanston, IL 60208, and R. A. Gerhardt, Rutgers University, Piscataway, NJ 08855.

ABSTRACT

The microstructure of low-density porous silica precursor (unsintered) bodies was studied as a function of starting chemistry. The ratio of colloidal silica sol to potassium silicate is known to have a marked effect on the size distribution of pores in this material, which in turn have a major impact on the resultant physical properties of the sintered product. In the present research, the sizes and the size distributions of particles underlying the pore microstructure was investigated, and it was found that the lower the amount of colloidal silica, the greater the size distribution of particle aggregates.

INTRODUCTION

There are numerous advantages of the sol gel process, the most interesting of which may be the possibility of preparing novel materials which cannot be fabricated by conventional methods. The microstructure of the as-dried body, to a large extent, dominates other processing parameters in determining the physical character of the product (sintered) ceramic. In porous silica, the porosity influences the dielectric, optical and other properties of the material, and an important issue is the control of the number and size distribution of pores. It had earlier been demonstrated(1) that the pore size distribution is very sensitive to the chemistry of the starting materials. The present work was begun in an attempt to understand the particle microstructure underlying the successful pore distributions.

Due to the wide size range (10 nm to 0.3 μm) for the colloidal particles and the agglomerates, their scattering was measured by both small angle x-ray (SAXS) and small angle neutron scattering (SANS). In applying these techniques to the porous silica precursor bodies, several important factors were considered. In particular, the particle density is $\sim 15\%$, and thus the samples may not be dilute enough to avoid multiple scattering or interparticle interference. In order to avoid the former, the x-ray experiments were performed using 10 and 11 keV photons. Copious multiple scattering had been observed at 6 and 7 keV, but none was observed at 10 keV. Multiple scattering was not a problem in the neutron case. Interparticle interference was avoided by the nature of the scattering system, in that it is very polydisperse. It was shown(2) that because every major portion of the particle size distribution in the present system is dilute one can proceed with the analysis and derive particle volume fractions as a function of particle diameter without the added complication of assuming an interparticle interaction potential.

The porous silica samples were prepared from 10 to 30% colloidal silica and 90 to 70% potassium silicate. Prior to further processing, the dried gels must be leached to obtain nominally alkali-free precursors because upon firing the alkali ions cause the formation of cristobalite, which in turn causes the formation of cracks. A particle distribution which facilitates the removal of alkali in the leaching process is thus very desirable. It had been determined(1) that the precursor with the least colloidal silica was the one from which the alkali ions were most effectively and completely removed. The present study is concerned with the microstructure underlying this behavior.

SAMPLES

Porous silica precursor gels were prepared by the Shoup(3) technique. A colloidal silica sol with 40 wt.% SiO₂ and 0.41 wt.% Na₂O, the balance being water, was mixed in various ratios with a potassium silicate component consisting of 20.8 wt.% SiO₂ and 8.3 wt.% K₂O, the balance being water. The colloidal sol solution was at pH 9.7 while that of the silicate was pH 11.3. The two components were mixed in ratios varying from 10 to 30 wt.% colloidal silica sol and 90 to 70 wt.% potassium silicate. A 25 wt.% formamide solution was added in each case to induce gelation. The details of the sample preparation are given elsewhere(1). The gels were dried at 70° to 80° C and then, with no other intermediate steps, sliced into discs. The samples ranged in thickness from 0.066 to 0.094 cm. The final particle densities of the precursor samples were 14 to 18% of theoretical, with the 10% colloidal silica and 90% potassium silicate (10:90) being the most dense and the 30% colloidal silica and 70% potassium silicate (30:70) the least dense.

EXPERIMENT

The SAXS measurements were carried out on a modified Bonse-Hart-type double crystal diffractometer temporarily installed on the X23A3 beamline at the National Synchrotron Light Source, Brookhaven National Laboratory. The resolution of the instrument enables the measurement of scatterers as large as 0.8 μm. Measurements were performed using 10 keV incident photons and repeated with 11 keV photons to check for the presence of multiple scattering. Since the desmeared scattering curves were independent of x-ray wavelength, it was concluded that multiple scattering was negligible. Scattering curves were measured for five samples: 10:90, 15:85, 20:80, 25:75, and 30:70. These curves were first put on an absolute intensity scale by a primary calibration technique(4) and then desmeared using the technique of Lake(5). Details of the instrument function, harmonic rejection, desmearing and absolute calibration are given in reference 6.

SANS measurements were carried out on the 10:90, 15:85, 20:80, and 25:75 samples. The SANS camera was the 8 m SANS instrument installed at the 20 MW research reactor at the National Institute of Standards and Technology. This facility makes use of a helical channel velocity selector to choose the incident neutron wavelength where the wavelength spread is 0.25. The mean wavelength for these measurements was 0.6 nm. A detailed description of the SANS facility is given in reference 7.

DATA ANALYSIS AND RESULTS

The SAXS intensities are shown on a $\ln(I)$ vs. h^2 scale in Fig. 1, where $h = (4\pi/\lambda)\sin\theta$, λ is the x-ray wavelength and θ is one-half of the scattering angle. The 10:90 data has the most curvature and the 30:70 the least, with the data from the other samples falling systematically in between. Such curvature is characteristic of samples which contain a distribution of sizes of scatterers. As the amount of colloidal silica is increased, the data show a systematic narrowing of the aggregate size distribution. Estimates were made of the lower limit on the maximum particle size for each sample using data in the range $0.007 < h < 0.015 \text{ nm}^{-1}$. The results of this Guinier analysis(8) are given in Table I.

To obtain a quantitative description of particle sizes, the SAXS intensities were analyzed. Size distributions were derived using the maximum entropy technique(10) for spheres implemented in the program MAXE from the UKAEA Harwell Laboratory. The results are shown in Fig. 2. Sharp features in the distribution curves are taken as representative of actual

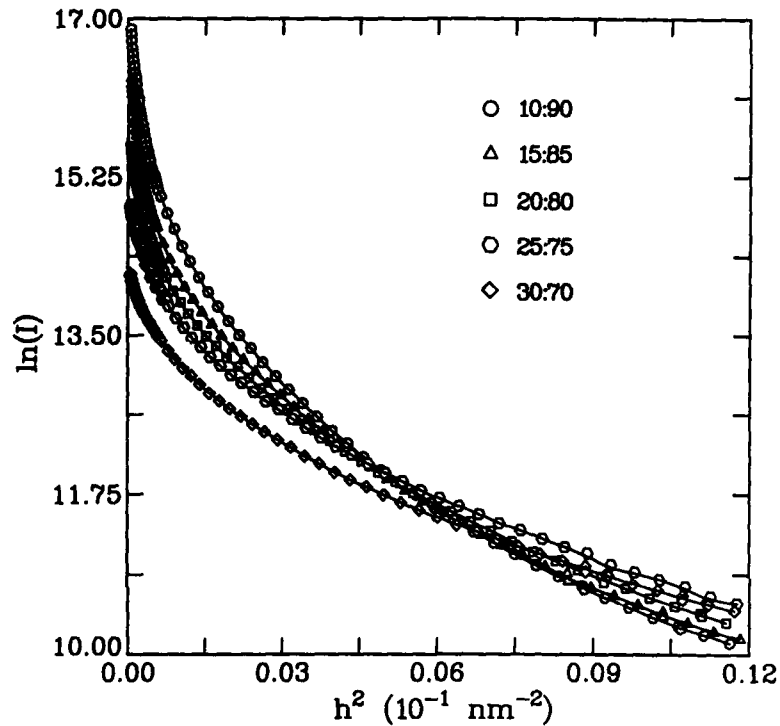


Fig. 1. $\ln(I)$ vs. h^2 for the SAXS from the porous silica precursor samples.

particle diameters, while ripples in the distribution are most likely due to the Bessel function representation of spheres. Since spheres are a reasonable approximation for these scatterers (particles and agglomerates), number distribution curves could be calculated, and these are shown on a log scale in figure 3. Figures 2 and 3 show peaks in approximate multiples (1, 2, 3, ...) of $D = 14$ nm, which is the diameter of the colloidal particle, and much larger aggregates.

The range of h values available with 0.6 nm neutrons is 0.15 to 1.1 nm^{-1} . Thus the largest measurable particle is much smaller than in the x-ray case. In the h range from 0.2 to 0.3 nm^{-1} , the data exhibit Porod behavior with $I(h)$ falling off as h^{-4} . Therefore the standard Porod analysis(9) was carried out to obtain the total surface scattering area per unit volume for each sample. The SANS Porod results are shown along with the SAXS Guinier results in Table I.

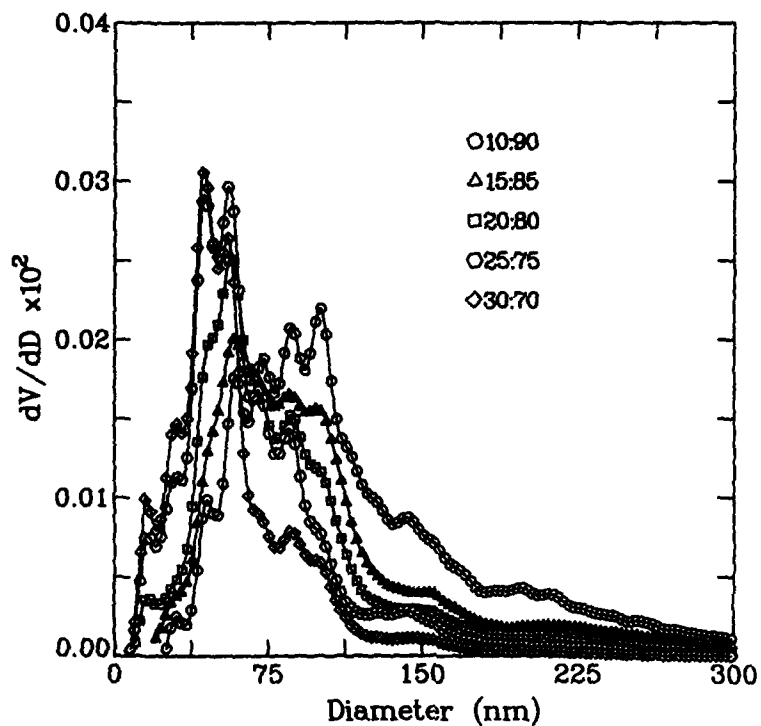


Fig. 2. Volume distribution maximum entropy results from an analysis of the SAXS from the porous silica precursor samples.

TABLE I

Effective Maximum Particle Sizes from a Guinier Analysis of the SAXS data and surface scattering area from a Porod analysis of the SANS data.

Sample	Thickness, cm	Effective Maximum R_g , nm	Total Surface Scattering Area, cm^2
10:90	0.089	126	1.16×10^5
15:85	0.089	122	1.39×10^5
20:80	0.066	104	1.79×10^5
25:75	0.091	93	1.87×10^5
30:70	0.094	75	—

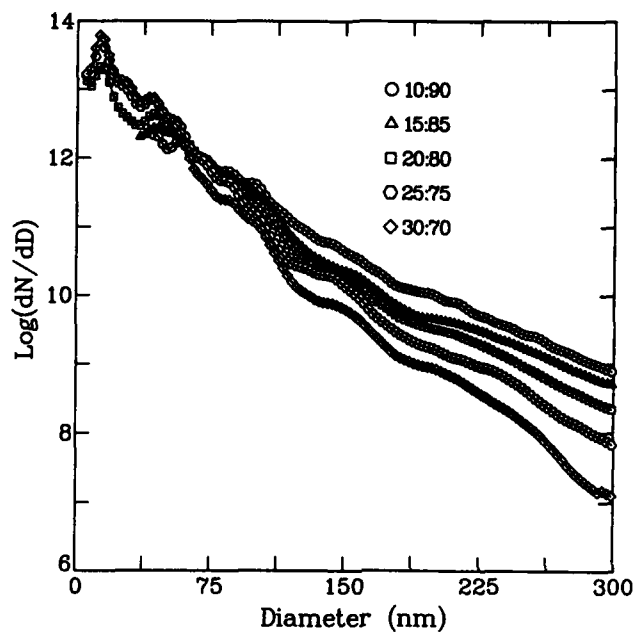


Figure 3. Logarithm of the number distribution as a function of particle diameter.

DISCUSSION AND CONCLUSIONS

For porous silica bodies, the size distributions that are determined from a maximum entropy analysis are consistent with what can be inferred from conventional Guinier and Porod analysis. In all of the samples, the results indicate the presence of single particles as well as clusters of 2, 3, 4, . . . particles and much larger aggregates. The proportion of single particles to large aggregates is a strong function of starting chemistry. The sample with the most colloidal silica (30:70) had the largest proportion of single particles and the least large aggregates. The sample with the least colloidal silica (10:90) contains the greatest fraction of large aggregates. Results for the remaining samples fall systematically between the two extremes. A larger volume fraction of spheres evidently inhibits clustering whereas a lower volume fraction favors a wide distribution of clustering. From the present study, the greatest polydispersity in pore sizes is predicted for the porous silica precursor prepared from the least colloid.

ACKNOWLEDGEMENT

The authors thank Dr. Andrew Allen for many useful discussions, and UKAEA Harwell for the MAXE software. Two of the authors (GGL and JPC) acknowledge with appreciation support for this work by a NIST Materials Science and Engineering Laboratory Director's Innovation Award.

REFERENCES

1. W. Cao, R. Gerhardt, and J. B. Wachtman, Jr., J. Am. Ceram. Soc. 71 (1988) 1108-1113.
2. G. G. Long, S. Krueger, P. R. Jemian, D. R. Black, H. E. Burdette, J. P. Cline and R. A. Gerhardt, to be published.
3. R. D. Shoup, Colloid and Interface Science. Vol. 3, New York:Academic Press (1976).
4. R. W. Hendricks, J. Appl. Cryst. 5 (1972) 315-324.
5. J. A. Lake, J. Appl. Cryst. 23 (1967) 191-194.
6. G. G. Long, P. R. Jemian, J. R. Weertman, D. R. Black, H. E. Burdette and R. Spal, to be published.
7. C. J. Glinka, J. M. Rowe and J. G. LaRock, J. Appl. Cryst. 19 (1986) 427-439.
8. A. Guinier and G. Fournet, Small Angle Scattering of X-Rays. New York:John Wiley (1952).
9. G. Kostorz, Treatise on Materials Science and Technology. Vol. 15, New York:Academic Press.
10. J. A. Potton, G. J. Daniell and D. Melville, J. Phys D: Appl Phys Vol. 17 (1984) 1567-1581

SMALL ANGLE NEUTRON SCATTERING STUDY OF CRITICAL BINARY FLUIDS IN POROUS GLASSES

S. B. DIERKER AND P. WILTZIUS
AT&T Bell Laboratories, Murray Hill, N.J. 07974

ABSTRACT

We present small angle neutron scattering measurements of the static structure factor $S(q)$ of the binary fluid mixture water-lutidine imbibed into the porous glass Vycor as a function of temperature and composition. $S(q)$ changes from a Lorentzian in the one phase region to a Lorentzian squared at the random field transition. The correlation length increases from $\sim 20 \text{ \AA}$ in the one phase region to $\sim 52 \text{ \AA}$ (\approx pore diameter) in the frozen domain state.

INTRODUCTION

Confining a critical binary fluid mixture within a porous random medium, such as porous glass, leads to dramatic changes in the mixture's physical behavior. The differences between the interaction energies of the two fluids both with the internal surface of the glass and with themselves become very important in the vicinity of the critical temperature, where the interfacial tension between the coexisting fluid phases vanishes. The wall-fluid interaction exerts an external field on the liquid mixture. When the correlation length ξ in the fluid is comparable to or larger than the pore size, this external field will be effectively random from one correlation volume to another if the host porous material is random on those length scales. We thus have a good model system for studies of finite size effects in the presence of a surface field, wetting, and the effect of random fields on phase transitions.

We have been studying the behavior of the critical binary fluid mixture water and 2,6-lutidine imbibed in porous Vycor glass.^{[1] [2] [3]} The bulk mixture is in the one phase region at room temperature and enters the two-phase region upon heating above $\sim 33^\circ \text{ C}$.

The random porous host we chose to confine the binary liquid in was commercially available Vycor glass (Vycor 7930, Dow Corning). Vycor is manufactured from a borosilicate glass-forming melt with a high concentration of B_2O_3 . This melt is cooled below its demixing temperature, forcing it to phase separate. The alkali-oxide-rich phase can subsequently be leached out, leaving a fully interconnected porous network. We previously characterized the structure of this network using small-angle neutron scattering.^[4] The two main features we want to point out here are the pronounced maximum at $Q_m \sim 0.023 \text{ \AA}^{-1}$ and the power law $S(Q) \sim Q^{-4}$ at large Q . The dominant length scale, $2\pi/Q_m \sim 270 \text{ \AA}$, can be interpreted as the mean spacing between pores (average pore radius $\sim 30 \text{ \AA}$). The Porod slope of -4 at large Q indicates that the internal surface of the glass is sharp and not fractally rough. Furthermore, it is important to note that the glass structure is rigid and does not exhibit any dynamics of its own when imbibed with a critical

binary fluid, unlike, for example, gels or polymers.^[5]

Upon warming a piece of Vycor with a critical fluid mixture imbibed into it, a first striking observation is that the fluid does not phase-separate macroscopically as it does in bulk. The sample develops a uniform cloudiness, which might be due to micro- or mesoscopic phase-separated domains. These domains must be very small because they are not observable even under a 40x microscope at 80° C.

QUASIELASTIC LIGHT SCATTERING

We previously used quasielastic light scattering (QELS) to probe temporal fluctuations in the composition of this system.^[1] In a bulk-fluid mixture, the time-autocorrelation function of these fluctuations is a single exponential, as expected for diffusive hydrodynamic processes in thermodynamic equilibrium. As T_c is approached, the time scale - inversely proportional to the decay rate of the exponential - diverges with the same critical exponent as the correlation length. This picture is dramatically altered when the fluid mixture is imbibed into Vycor. The decay time does not grow very large, even as the temperature is raised almost 30 degrees above the bulk T_c . Furthermore, the qualitative character of the autocorrelation function changes from single exponential to very strongly nonexponential at a temperature of 60° C. This is a strong signature for the occurrence of a random field transition. The fluid system has dispersed into micro- or meso- phase-separated domains that might extend over several pores inside the glass. Each small domain experiences a locally varying surface energy that must be overcome for domains to grow to larger sizes. In contrast to the bulk-liquid system where only one energy scale (set by the temperature) is present, the imbibed fluid experiences a broad distribution of energy barriers. This concept is central to our understanding of the transition from regular, non-activated dynamics in bulk-critical phenomena to activated dynamics at a random field transition.

SMALL ANGLE NEUTRONS SCATTERING

Small angle neutron scattering (SANS) is uniquely suited for studying the structure of this system. In addition to allowing access to the interesting length scales, neutrons provide the crucial ability to use contrast-variation techniques effectively to mask out the scattering from the glass-fluid interface, which at $\sim 160 \text{ m}^2/\text{cm}^3$ of Vycor is quite large. By imbibing various mixtures of H_2O and D_2O into Vycor, we measured the scattering density of Vycor to be $\rho_{Vycor} = 3.6 \times 10^{10} \text{ cm}^2$. This is in close agreement with the value calculated for amorphous silica $\rho_{SiO_2} = 3.5 \times 10^{10} \text{ cm}^2$. A quick calculation reveals that a mixture of 40% by volume of H_2O and 60% D_2O should have the same scattering-length density, or index, as Vycor. Indeed, $S(Q)$ measured on a piece of Vycor imbibed with such a mixture shows a drastically reduced signal, which is basically down to the incoherent background scattering attributable to the hydrogen of the water. Thus, in an index-matched sample, any scattering will arise from concentration variation in the imbibed binary liquid and not from the porous host.

In experiments conducted at LANSCE (Los Alamos Neutrons Scattering Center), we studied critical binary fluid mixtures composed of lutidine, water, and heavy water in the right proportions to have a scattering-length density $\rho_{mixture}$ equal to ρ_{Vycor} . In fig. 1, $S(Q)$ is depicted as a function of temperature between 10° C and 80° C for a

40% lutidine mixture. At low temperature $S(Q)$ has a Lorentzian line shape (limiting slope of -2 at large Q), which is very similar to what is observed in the one-phase region in a bulk mixture. The width of the Lorentzian in the case of a bulk homogeneous fluid mixture is inversely proportional to the correlation length ξ and collapses to zero at T_c as ξ diverges. The measured correlation length for the imbibed fluid is shown in Fig. 2. At 10°C , ξ is 26 \AA , or somewhat less than half the average pore diameter. It increases slightly as the temperature is raised, but not nearly as strongly as it would in a bulk mixture where a phase transition would have occurred by the time 40°C is reached. This is in agreement with what is observed in QELS experiments,^[6] where the autocorrelation function of the composition fluctuations had only a weak temperature dependence in the range below 40°C . An important difference between the QELS and the SANS measurements is the following: with QELS it is impossible to infer a length scale from the decay time without a hydrodynamic model; whereas, SANS yields a length scale from $S(Q)$ directly. At this point, very little is known about the relationship between the hydrodynamics of composition fluctuations in fluids confined to random, porous media and the length scale of the fluid mixture. The combination of light scattering and neutron scattering proves to be a potent tool in furthering our understanding in this field.

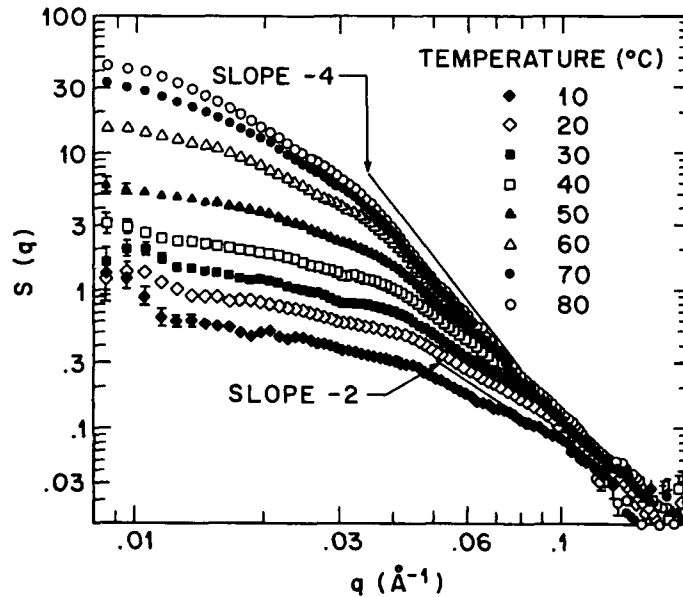


Figure 1. The structure factor $S(q)$ measured with SANS of a mixture of 40% lutidine + 60% ($\text{H}_2\text{O} + \text{D}_2\text{O}$) imbibed into Vycor as a function of temperature. The limiting slopes of -2 and -4 clearly illustrate the evolution from Lorentzian in the one phase region to Lorentzian squared in the frozen domain state.

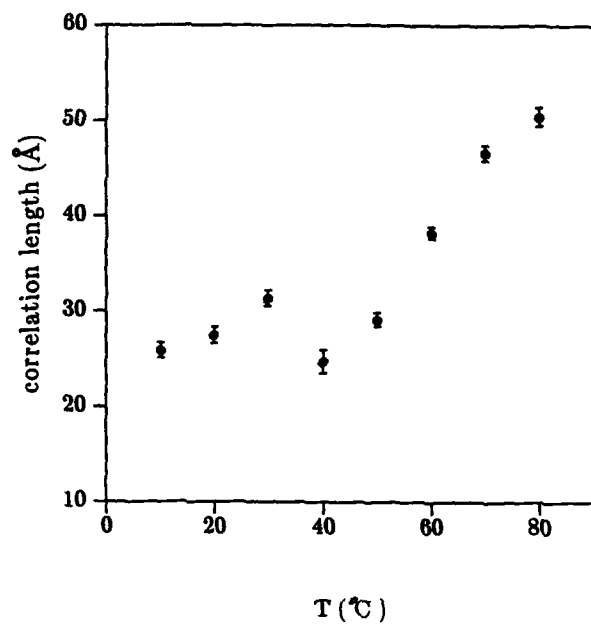


Figure 2 . The correlation length as a function of temperature for the data shown in Fig. 1.

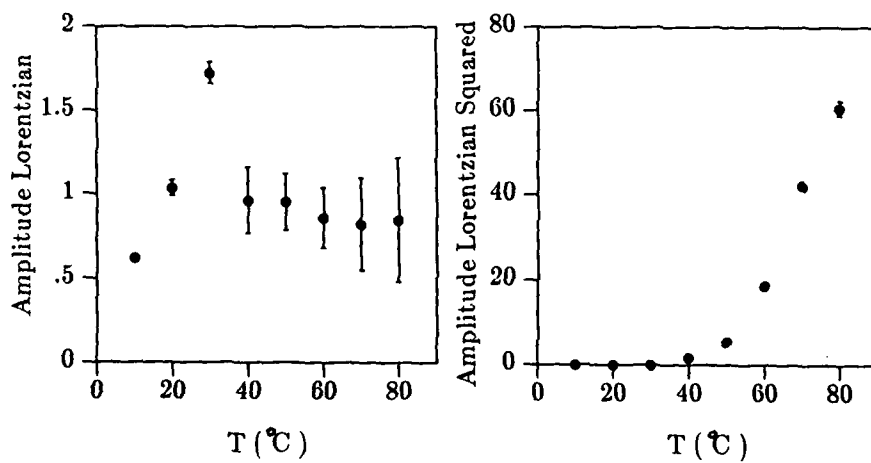


Figure 3 . The relative amplitudes of the Lorentzian and Lorentzian squared components for the data shown in Fig. 1.

Another important characteristic of the data in Fig. 1 is the change of the line shape of $S(Q)$ from a single Lorentzian, which is omnipresent in equilibrium phases, to a Lorentzian squared at high temperatures (limiting slope of -4 at large Q). The relative amplitude of the two components are shown in Fig. 3. This evolution in line shape is theoretically predicted to happen at a random field transition and has also been observed to occur in randomly diluted antiferromagnets.^[7] That systems as seemingly different as random fluids and random magnets exhibit similar behavior suggests that the effects of disorder may indeed be universal.

All of the features in the data, large and small, provide important information about the structure of the critical mixture inside the porous glass, such as fluid composition fluctuations, micro- or meso- phase separated domain formation, and wetting layers, or composition gradients, next to the glass wall. However, an analytic formalism for interpreting the measurements in terms of such types of physical structure in the mixture is nonexistent. One major difficulty is that because the Fourier transform of the pair correlation function of the fluid fluctuations is restricted to the random void space of the porous glass, the structure of the latter influences the shape of the measured structure factor, even in index-matched samples. Attempts to treat these difficulties analytically have had limited success.^[8] We are currently exploring an alternative approach to understanding our data; that is, comparison with the structure factor calculated from numerically simulated models of fluids in porous media. We are currently developing the simulations to calculate how $S(Q)$ is affected by fluid composition fluctuations, domains of phase-separated fluid in the void space, and wetting gradients next to the glass interface.

Work in progress is aimed at further understanding to what extent our findings are universal. We hope to accomplish this by analyzing experiments performed at LANSCE on mixtures both imbibed into a number of porous glasses with different pore sizes, and into porous materials with different pore geometries.

This work has benefitted from the use of facilities at the Los Alamos Neutron Scattering Center, a national user facility funded as such by the DOE/Office of Basic Energy Sciences.

REFERENCES

1. S. B. Dierker and P. Wiltzius, *Phys. Rev. Lett.* **58**, 1865 (1987).
2. P. W. Wiltzius, S. B. Dierker, and B. S. Dennis, *Phys. Rev. Lett.* **62**, 804 (1989).
3. S. B. Dierker, B. S. Dennis, and P. Wiltzius, to be published in *J. Chem. Phys.*
4. P. Wiltzius, F. Bates, S. B. Dierker, and G. D. Wignall, *Phys. Rev. A* **36**, 2991 (1987).
5. J. V. Maher, W. I. Goldburg, D. W. Pohl, and M. Lanz, *Phys. Rev. Lett.* **53**, 60 (1984).
7. R. J. Birgeneau, Y. Shapiro, G. Shirane, R. A. Cowley, and H. Yoshizawa, *Physica* **137B**, 83 (1986) and references therein. A. R. King, V. Jaccarino, D. P. Belanger, and S. M. Rezende, *Phys. Rev.* **32**, 503 (1985).
8. N. F. Berk, *Phys. Rev. Lett.* **58**, 2718 (1987).

SMALL ANGLE NEUTRON SCATTERING STUDY OF SOL-GEL GLASSES

P. WILTZIUS AND S. B. DIERKER
 AT&T Bell Laboratories, Murray Hill, N.J. 07974

ABSTRACT

We present small angle neutron scattering data of porous glasses. Analysis of the structure factor shows that the morphology on length scales between 30 Å and 800 Å depends on fabrication procedures. Fast gelation leads to a clumpy glass, whereas slow gelation produces a random smooth internal interface.

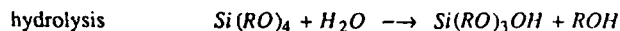
INTRODUCTION

Small Angle Neutron Scattering (SANS) has enjoyed increased application in recent years as a diagnostic tool to characterize microstructures in porous media [1..4]. The availability of high flux neutron sources, steady state as well as pulsed, in combination with two dimensional detectors has brought SANS closer to being a user friendly technique. The experiments reported in this paper were performed during the first user cycle on the low q spectrometer at the new pulsed source LANSCE (Los Alamos Neutron Scattering Center). The usable wave vector range was $0.008 \leq q \leq .23 \text{ \AA}^{-1}$ corresponding to real space dimensions between 30 Å and 800 Å.

Sol-gel glass forming techniques are very promising for the production of high quality glasses. This method has a number of advantages: the glass purity is comparable to that observed in vapor phase processes, processing temperatures are low and the glass composition is highly homogeneous. A possible area of application is the production of low cost light guides. The basic steps in sol-gel processing involve forming a solution of material that undergoes gelation and subsequent drying of the gel to form a glass. This glass is porous and can be densified by sintering at relatively low temperatures.

MATERIALS

The preparation of the two alcoxide glasses studied involves mainly two steps



In the present study R was an ethyl group. Important processing parameters are e.g. the molar ratio of $\text{Si}(\text{RO})_4 / \text{H}_2\text{O}$, temperature, pH, pressure. After completion of the reaction the gels are normally dried, which in our case was achieved with a supercritical drying procedure. All of the above parameters influence the density and the microscopic structure of the final porous glass. Glass A was produced from a sol with 4 moles $\text{H}_2\text{O}/\text{TEOS}$ (TEOS : tetraethylorthosilicate) under slow gelation conditions which took about 2 weeks. The density

of the dry glass was 0.4 gr/cm^3 . Glass *B* was started with a sol of 3 moles $H_2O/TEOS$. The pH was acidic for the first 15 minutes of the reaction and then was changed to basic which led to a fast gelation taking only three minutes. The final density of the glass was 0.2 gr/cm^3 . As will be shown below the two different procedures used for glass *A* and glass *B* resulted in different microscopic morphologies.

ALCOXIDE GEL - FAST GELATION

In Figure 1 SANS data are shown for glass *B*. The two main features are a flat $S(q)$ at low q and a rapid down turn around $q \approx .04 \text{ \AA}^{-1}$ to a final slope of -4 at large q . The solid line through the data is a fit to the function

$$S(q) = S(0)/(1 + q^4 \xi^4) \quad (1)$$

with $S(0) = 21$ and $\xi = 23 \text{ \AA}$. This function is a good approximant for the envelope of the particle form factor of a sphere with radius $R \approx 1.8\xi$. Using the envelope instead of the full form factor for spheres with its resonances mimics the effect of polydispersity in the distribution of spheres on the structure factor. Glass *B* thus exhibits a structure factor which is in agreement with $S(q)$ of a polydisperse arrangement of spheres with an average diameter of 82 \AA . The surface to volume for compact spherical aggregates is $3/R$, which yields $730 \text{ m}^2/\text{cm}^3$. This is in agreement with $1000 \text{ m}^2/\text{cm}^3$ obtained using the BET method. Note also that the final slope of -4 , known as the Porod limit, indicates sharp internal surfaces.

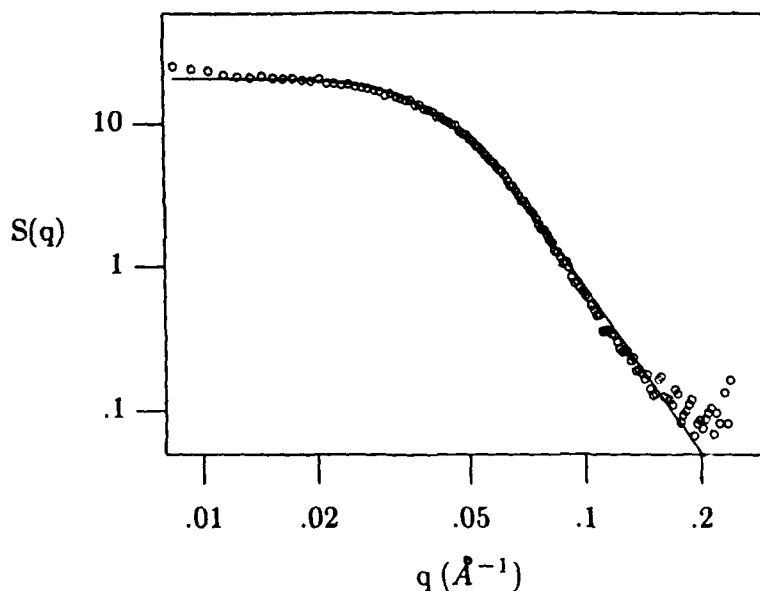


Figure 1 . The structure factor $S(q)$ measured with SANS of an alcoxide gel manufactured under fast gelation conditions. The solid line is a fit to eq. (1).

ALCOXIDE GEL - SLOW GELATION

Data for glass *A* are shown in Figure 2. The attempt to fit the above functional form for $S(q)$ to the data gives a very poor result (dotted line), indicating fundamental differences in the microscopic structure between glass *A* and glass *B*. Debye and coworkers developed a so-called two-phase model composed of a homogeneous material in which holes of varying and undetermined shape are randomly distributed. Such a system has a structure factor given by

$$S(q) = S(0)/(1 + q^2 a^2)^2 \quad (2)$$

with $a = V/S \ 4 \phi(1 - \phi)$

where S/V is the internal surface to volume and ϕ the void fraction or porosity. A fit of the data for $q \geq .03 \text{ \AA}^{-1}$ to this function shown as a solid line in Figure 2 gives a much better result with $S(0) = 11.7$ and $a = 18.5 \text{ \AA}$. A density of 0.4 gr/cm^3 yields a porosity $\phi = 0.84$ and a surface to volume ratio of $290 \text{ m}^2/\text{cm}^3$. This is also in good agreement with BET results. At long length scales ($q \leq .03 \text{ \AA}^{-1}$) $S(q)$ is systematically bigger than the fit indicating more disorder or inhomogeneities. This is somewhat surprising since glass *A* was gelled very slowly allowing a lot of time for equilibration.

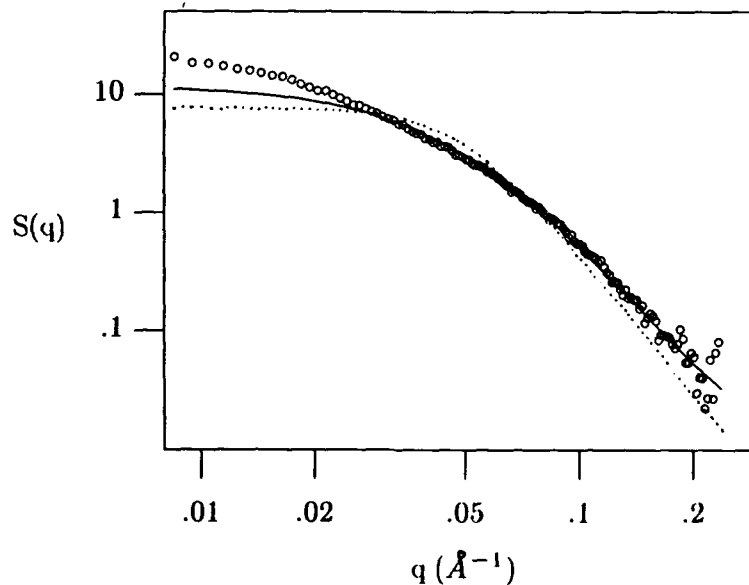


Figure 2 . The structure factor $S(q)$ measured with SANS of an alcoxide gel manufactured under slow gelation conditions. The solid line is a fit to eq. (2) and the dotted line is a fit to eq. (1).

DISCUSSION AND CONCLUSIONS

Sol-gel alcoxide glasses manufactured under slow and fast reaction conditions, respectively, exhibit qualitatively different structure factors as measured using SANS. Fast gelation leads to a clumpy glass with an average aggregate size of 82 Å. Slow gelation, however, produces a random smooth internal surface. A possible scenario explaining these differences could stem from a two step model. The first step would be rapid formation of colloidal SiO_2 (diameter 80 Å). These colloidal particles could grow together rapidly (glass *B*) under basic conditions without change in microscopic morphology, or slowly (glass *A*) leaving time for local rearrangement and sintering. The latter process would smoothen the internal surface.

SANS is a powerful technique to characterize the structure of porous glasses on length scales between 30 Å and 1000 Å. Spallation sources with time of flight analysis cover almost two decades in q -space in a single experiment allowing rapid throughput.

This work has benefitted from the use of facilities at the Los Alamos Neutron Scattering Center, a national user facility funded as such by the DOE/Office of Basic Energy Sciences.

REFERENCES

1. D. W. Schaefer, B. C. Bunker, and J. P. Wilcoxon, Proc. R. Soc. Lond. A 423, 35 (1989).
2. N. F. Berk and K. A. Hardman-Rhyne, J. Appl. Cryst. 18, 467 (1985).
3. A. Hohl, H. B. Neumann, P. W. Schmidt, P. Pfeifer, and D. Avnir, Phys. Rev B 38, 1462 (1988).
4. P. Wiltzius, F. S. Bates, S. B. Dierker, and G. D. Wignall, Phys. Rev. A 36, 2991 (1987).

NEUTRON IRRADIATED URANIUM SILICIDES STUDIED BY NEUTRON DIFFRACTION AND RIETVELD ANALYSIS*

R. C. Birtcher**, M. H. Mueller**, J. W. Richardson, Jr.** and J. Faber, Jr.***

Argonne National Laboratory, Argonne, IL 60439, *AMOCO Research Center,
P.O. Box 3011, Naperville, IL 60566

INTRODUCTION

Uranium silicides have been considered for use as reactor fuels in both high power and low enrichment applications. However, U_3Si was found to become amorphous under irradiation [1] and to become mechanically unstable to rapid growth by plastic flow [2,3]. U_3Si_2 appears to be stable against amorphization at low displacement rates, but the extent of this stability is uncertain. Although the mechanisms responsible for plastic flow in U_3Si and other amorphous systems are unknown, as is the importance of crystal structure for amorphization, it may not be surprising that these materials amorphize, in light of the fact that many radioactive nuclide - containing minerals are known to metamictize (lose crystallinity) under irradiation [4]. The present experiment follows the detailed changes in the crystal structures of U_3Si and U_3Si_2 introduced by neutron bombardment and subsequent uranium fission at room temperature. U-Si seems the ideal system for a neutron diffraction investigation since the crystallographic and amorphous forms can be studied simultaneously by combining conventional Rietveld refinement of the crystallographic phases with Fourier-filtering analysis [5] of the non-crystalline scattering component.

EXPERIMENTAL

Powdered U_3Si and U_3Si_2 specimens were fabricated from high purity Si and highly depleted Uranium, 0.022 at % ^{235}U . The high dose irradiation behaviors of these powders, roll bounded between aluminum plates, have been previously studied [2]. For this study, each powder was doubly encapsulated in thin wall Vanadium cans that had been evacuated and filled with He gas. The U_3Si specimen also contained precipitates of U_3Si_2 (<15 volume %) and the uranium oxides UO and UO_2 (< 5 volume %) introduced by vacuum annealing.

Neutron irradiations were performed at IPNS in a room temperature facility located adjacent to the neutron source [6]. Neutrons are produced as the result of 500 MeV protons striking a ^{235}U target. The neutron spectrum for this facility is characteristic of a reactor neutron spectrum with the addition of neutrons having energies up to 500 MeV. In these specimens, damage was produced primarily by uranium fission in a manner identical to damage production in operating nuclear reactor fuel. The nuclear-reaction cross sections for fast and thermal fission were determined by standard activation techniques to give a burn up rate of 5.4×10^{-27} /proton [7]. The irradiations were performed in small steps, ^{235}U burn-up $< 3 \times 10^{-6}$, in order to closely follow changes in the crystal structure. The number of defects per fission has been calculated to be 7.8×10^4 [8].

After each irradiation and appropriate cool-down, a powder pattern was measured on the General Purpose Powder Diffractometer (GPPD) at the Intense Pulsed Neutron Source (IPNS) and the data were analyzed using the Rietveld profile refinement technique [9]. Details of data collection and analysis are given in a recent paper [10].

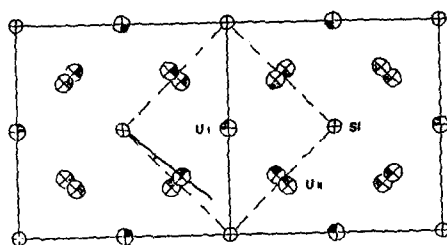


Fig. 1 [001] projection of U₃Si structure showing relationship between tetragonal and cubic Cu₃Au-like cells.

RESULTS

The crystal structure refinements of unirradiated U₃Si and U₃Si₂, including the U₃Si₂ precipitates in U₃Si, agree with those previously obtained from X-ray diffraction [11,12]. The repeated irradiation doses produced structural changes in both alloys which resulted in a broadening and shifting of the Bragg peaks. The behaviors of U₃Si, U₃Si₂ and the U₃Si₂ precipitates in U₃Si will be discussed separately.

U₃Si Unirradiated U₃Si (projection shown in Fig. 1) is tetragonal, space group I4/mcm, with $a_0 = 6.0358(1)$, $c_0 = 8.6925(1)$ Å, $c/a = 1.440$ and 16 atoms per unit cell. There are: 4 U₁ at $0, 1/2, 1/4$; 8 U₁₁ at $x, x+1/2, 0$ with $x=0.2251(1)$ and 4 Si at $0, 0, 1/4$. The base layer ($z=0$) contains U atoms only, the next layer ($z=1/4$) is $1/2$ U and $1/2$ Si, and the sequence repeats. The layer at $z = 1/2$ (U only) is rotated slightly

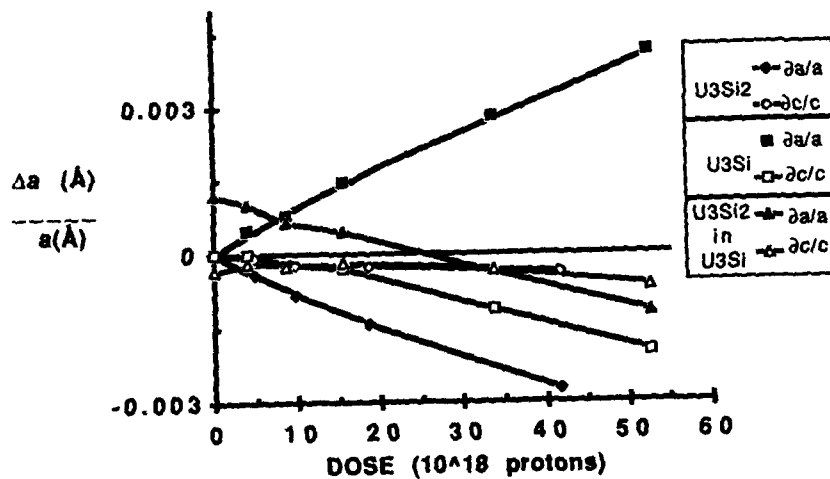


Fig. 2. Fractional lattice parameter changes for U₃Si and U₃Si₂.

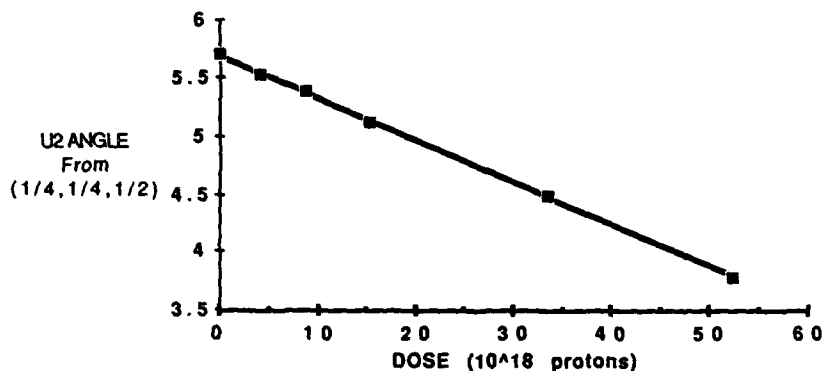


Fig 3. Variation of angle defined in Fig. 1 with irradiation dose.

relative to the base layer. This structure can be viewed as pseudo-cubic, in that if the U_{11} are shifted such that $x = 1/4$ and simultaneously the axial ratio (c/a) is reduced to $\sqrt{2}$, U_3Si would have the cubic Cu_3Au type structure ($a_c = a_T/\sqrt{2} = c_T/2$) shown by the dashed lines in Fig. 1. This transformation is known to occur upon heating to 1038K [13].

Changes produced by neutron irradiation are shown in Figs 2 and 3. After 5 irradiation cycles (52.4×10^{18} protons or 0.02 displacements per atom), the a -axis increased by 0.5% and the c -axis decreased by 0.1% (Fig. 2), resulting in a net unit cell volume increase of 0.1%. A number of other important changes occur during the irradiation. U_{11} is approaching its idealized Cu_3Au position $1/4, 3/4, 0$ (the deviation from this can be expressed as the angle of rotation (shown in Fig. 3) about the c -axis away from this position). Fig. 4 illustrates some additional features: the the $(220)_T$ and $(004)_T$ reflections are gradually converging to become the cubic $(200)_C$, all diffraction peaks broaden, and the diffuse background is significantly increased (possible evidence for amorphous phase formation). Finally, the Debye-Waller factors for all atoms increase with each irradiation and the rms values for the Si atom are somewhat less than for the U atoms. This may be indicative of deviations - static or dynamic - of the uraniums from their ideal locations. Thus, it would appear that irradiation is producing, on a defect cascade scale, a thermal spike event which is driving the tetragonal crystal structure to the reported high temperature cubic form and/or to an amorphous form.

U_3Si_2 Unirradiated U_3Si_2 is tetragonal, space group $P4/mbm$, with $a_0 = 7.3299 \text{ \AA}$, $c_0 = 3.9004 \text{ \AA}$, $c/a = 0.532$ and 10 atoms per unit cell. As shown in Fig. 5, there are: 2 U_1 at $0,0,0$; 4 U_{11} at $x, x+1/2, 1/2$ with $x=0.1820(1)$ and 4 Si at $x', x'+1/2, 0$ with $x'=0.3841(2)$. Lattice parameter changes as a function of dose are shown in Fig. 2. The unit cell volume decreases for U_3Si_2 , in contrast to the increase observed in U_3Si . The most striking feature resulting from the Rietveld refinements is the large out-of-plane displacement parameter for U_1 in all forms of the U_3Si_2 : both unirradiated and irradiated, pure phase and second phase in U_3Si (Fig. 5). This could be an indication that the space group is not correct, and that the correct structure includes ordered displacements of the U_1 atoms from the origin, either within the plane or between planes. It is conceivable, on the other hand, that the huge thermal displacement parameter represents a random distribution of static

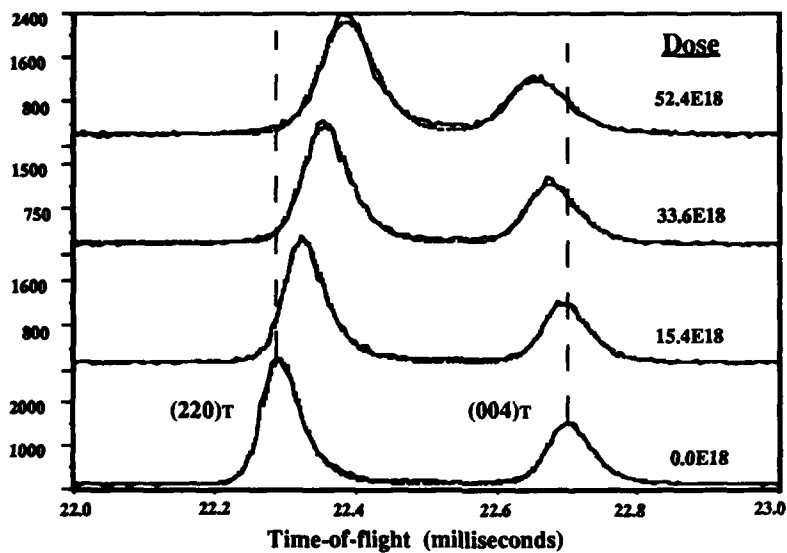


Fig 4. Multiplet peak fitting for the $(220)_T$ and $(004)_T$ reflections of U_3Si_2 . Note the gradual evolution toward cubic, broadening of both peaks, and increasing background between peaks with increasing dose.

displacements along the $[001]$ direction. With increased irradiation, U_{II} moves away from $1/4, 1/4, 1/2$ toward $1/4, 0, 1/2$. Completion of this process would require removal of a similar U_{II} site from the adjacent unit cell.

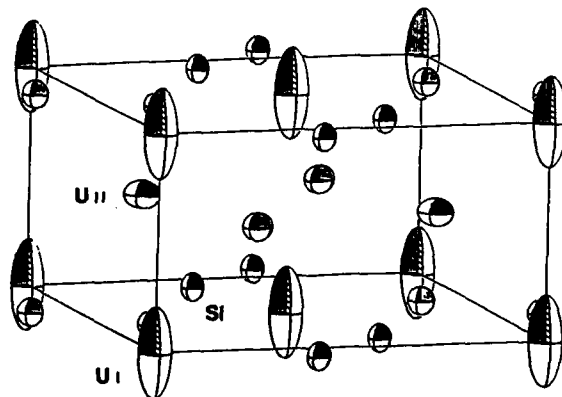


Fig 5. ORTEP drawing of U_3Si_2 structure showing dramatic out-of-plane displacements on U_I .

U₃Si₂ in U₃Si The initial structure of the U₃Si₂ precipitates in U₃Si was the same as the pure U₃Si₂ specimen, however the unirradiated precipitates were expanded 0.012% in the a-direction and contracted 0.04% in the c-direction producing an increase of 2.3×10^{-4} % in the unirradiated unit cell volume. Changes produced by neutron irradiation are also shown in Fig. 2. Both the a-axis and the c-axis contract leading to a decrease in the unit cell volume as in the pure U₃Si₂ specimen. The decrease occurs at about the same rate as for pure U₃Si₂.

SUMMARY

Since this is merely a progress report, we expect further developments with additional irradiations. **U₃Si** - we expect the complete transformation from tetragonal → cubic (Cu₃Au-type) → cubic (disordered) → amorphous as seen with electron diffraction (the use of Fourier-filtering should assist in sorting out the amorphous component). **U₃Si₂** - we will consider in more detail the implications of the large out-of-plane displacements; is there a space group change or are these simply uncorrelated static displacements. **U₃Si₂ in U₃Si** - further investigations will be concerned with the role of strain in promoting crystallographic changes and indeed whether U₃Si₂ becomes amorphous under either or both of the above conditions.

ACKNOWLEDGEMENTS

The submitted manuscript has been authored by contractors of the U. S. Department of Energy (BES-Materials Sciences) under contract No. W-31-109-ENG-38. Accordingly, the U. S. Government retains a nonexclusive royalty-free license to publish or reproduce the published form of this contribution, or allow others to do so, for U. S. Government purposes.

REFERENCES

- [1] D. G. Walker, J. Nucl. Mat. 37, 48 (1970).
- [2] G. L. Hofman, J. Nucl. Mat. 140, 256 (1986).
- [3] R. C. Birtcher, C. W. Allen, L. E. Rehn and G. L. Hofman, J. Nucl. Mater. 152, 73 (1988).
- [4] P. Bayless, F. Mazzi, R. Munno and T. J. White, Mineral. Mag. 53, 565 (1989).
- [5] J. W. Richardson, Jr. and J. Faber, Jr., Adv. X-ray anal. 29, 143 (1985).
- [6] R. C. Birtcher, T. H. Blewitt, M. A. Kirk, T. L. Scott, B. S. Brown and L. R. Greenwood, J. Nucl. Mater. 108 & 109, 3 (1982).
- [7] L. R. Greenwood, private communication.
- [8] D. M. Parkin and R. O. Elliott, Nucl. Inst. Meth. B16, 193 (1986).
- [9] H. M. Rietveld, J. Appl. Cryst. 2, 65 (1969).
- [10] J. D. Jorgensen, J. Faber, Jr., J. M. Carpenter, R. K. Crawford, J. R. Hauman, R. L. Hitterman, R. Kleb, G. E. Ostrowski, F. J. Rotella and T. G. Worton, J. Appl. Cryst. 21, 321 (1989).
- [11] W. H. Zachariasen, Acta Cryst. 2, 94 (1949).
- [12] G. Kimmel and S. Nativ, Acta Cryst. B31, 1351 (1975).
- [13] P. L. Blum, G. Silvestro and H. Vangoyan, C. R. Acad. Sci. 260, 5538 (1964).

GAS DENSITY IN HELIUM BUBBLES IN NICKEL AND IRON
DETERMINED BY SMALL ANGLE NEUTRON SCATTERING

D. SCHWAHN

Institut für Festkörperforschung der Kernforschungsanlage Jülich GmbH
Postfach 1913, D-5170 Jülich, Federal Republic of Germany

ABSTRACT

A general discussion of the gas density determination of He bubbles in Ni and Fe with neutron scattering using the contrast variation method is given. One finds, that best results are obtained using isotope combinations for Ni, and magnetic and nuclear scattering for Fe. An experiment to determine the density of He in Ni demonstrates the applicability of this method.

INTRODUCTION

A few at-ppm of helium introduced into metals can already cause severe material degradation and embrittlement. The reason is the low solubility of helium in metals and the strong tendency to form bubbles in the bulk and the grain boundaries. It is therefore of great practical interest to understand bubble nucleation and growth. (An overview about this subject is given in [1].) In recent years we have studied this process with small angle neutron scattering (SANS), whose results are published in Ref. [2-5]. In a SANS experiment we determine the size, the number density of the bubbles and the helium gas density inside. It was the purpose of these experiments to determine this quantity because the gas density strongly influences the microstructure of the bubbles [1,7], and because the scattering technique is one of the very few methods by which this quantity can be measured directly. To obtain the gas density from SANS one has to use the contrast variation method in order to eliminate all other parameters in the scattering function.

In this publication we mainly discuss the method of contrast variation for nickel and iron, and then give an example of an experimental application.

CONTRAST VARIATION IN NICKEL AND IRON TO DETERMINE THE HELIUM GAS DENSITY IN BUBBLES

The contrast variation method is based on the requirement that an identical He bubble microstructure can be measured with two different scattering contrasts [2]. For neutron scattering this can be achieved in different ways by: (1) *two specimens* with identical bubble structure but implanted with different gas isotopes or of different isotope composition, (2) *one ferromagnetic specimen* using the nuclear and magnetic contrast, and (3) different orientations of polarized neutrons with respect to the applied magnetic saturation field of the specimen. The ratio α of the neutron scattering intensities from two specimens of the same microstructure is then given by the ratio of their scattering contrast [2]

$$\alpha = \left| \frac{\frac{m_1}{\Omega_m} - \frac{g_1}{\Omega_{He}}}{\frac{m_2}{\Omega_m} - \frac{g_2}{\Omega_{He}}} \right|^2 \quad (1)$$

All the other unknown parameters in the macroscopic cross-section such as volume, number density and form factor of the bubbles cancel out. α is determined by the coherent scattering lengths of the metals, m_1 and m_2 , of the gases, g_1 and g_2 , and their respective atomic volumes, Ω_m and Ω_{He} . The only unknown number in eq. (1) which is to be determined is Ω_{He} . With $\omega \equiv \Omega_m/\Omega_{He}$ we find

$$\alpha = \left(\frac{m_1}{m_2}\right)^2 \left| \frac{1 - g_1/m_1 \omega}{1 - g_2/m_2 \omega} \right|^2 \quad (2)$$

For further discussion we assume that $m_1 < m_2$ and $g_1 > g_2$. For $\omega = 0$ (void), α is given by $(m_1/m_2)^2$ and for $\omega \rightarrow \infty$ by $(g_1/g_2)^2$. α is equal to zero at $\omega_0 = m_1/g_1$ and infinite at $\omega_\infty = m_2/g_2$ with $\omega_0 < \omega_\infty$. ω can only have values between zero and 2.6. The lower value is that of a void and the upper one of the maximum possible He density. For larger He densities dislocation loops would be punched out [1]. Therefore, a contrast combination with α between 0.1 and 10 in the possible ω range would be an optimal choice. In Fig. 1 and 2 calculated α 's are plotted for various contrast combinations of nickel and iron and He³ and He⁴, respectively. Now we discuss the results presented in both figures.

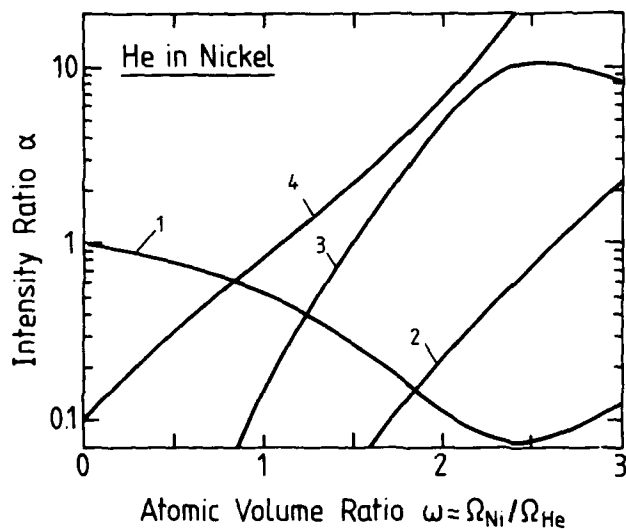


Fig. 1: Calculated α values of He in Ni for various isotope combinations: 1.) He³/He⁴ in Ni⁵⁸, 2.) He⁴ in Ni⁶⁰/Ni⁵⁸, 3.) He³ in Ni⁶⁰/Ni⁵⁸, 4.) He⁴ in Ni/(Ni⁶², Ni).

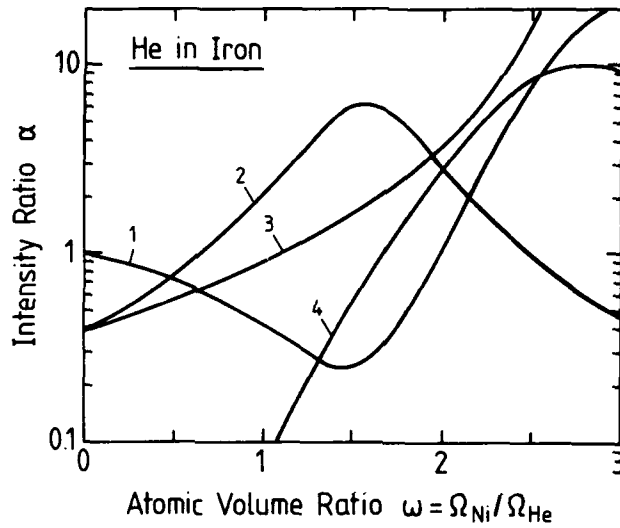


Fig. 2 Calculated α values of He in Fe for various contrast combinations: 1.) He^3/He^4 in Fe, 2.) magnetic and nuclear contrast of He^3 in Fe, and 3.) of He^4 in Fe, 4.) He^3 in Fe and polarized neutrons.

He^3 and He^4 in Nickel and Iron

The combination of different gas isotopes (He^3 and He^4 ; $g_1 \neq g_2$) implanted into the same metal ($m_1 = m_2$) leads to

$$\alpha = \left| \frac{1 - \frac{g_1}{m} \omega}{1 - \frac{g_2}{m} \omega} \right|^2 \quad (3)$$

Because $\alpha = 1$ for $\omega = 0$, $\omega_0 = m/g_1$ should be larger than 2 to avoid zero contrast in the ω range where we want to measure the gas density. The Ni^{58} isotope fulfills this condition because of its large coherent scattering length as shown in Fig. 1. In iron (Fig. 2) one finds with the He^3/He^4 combination an ambiguity for ω values below and above 1.5.

Helium in Nickel Isotopes

He in different Ni isotopes ($m_1 \neq m_2$ and $g_1 = g_2$) leads to

$$\alpha = \left(\frac{m_1}{m_2} \right)^2 \left| \frac{1 - \frac{g}{m_1} \omega}{1 - \frac{g}{m_2} \omega} \right|^2 \quad (4)$$

with $\alpha(\omega = 0) = \left(\frac{m_1}{m_2} \right)^2$ and $\alpha(\omega \rightarrow \infty) = 1$. In Fig. 1 the α 's are plotted for a combination of Ni^{60} and Ni^{58} implanted with He^4 and He^3 , respectively. He^4 in $\text{Ni}^{60}/\text{Ni}^{58}$ gives quantitatively useful results only above $\omega \approx 1.6$. This behaviour was experimentally confirmed in [2]. A better choice is the implantation of He^3 in $\text{Ni}^{60}/\text{Ni}^{58}$ where the He density can be measured in the range of $0.8 < \omega < 2.6$. Up to now we have discussed combinations of pure isotopes. However, we can also use mixtures of isotopes A and B in order to adjust the mean coherent scattering length as defined in by

$$\langle b \rangle = \phi b_A + (1-\phi) b_B \quad (5)$$

via the concentration ϕ between b_A and b_B , which are the coherent scattering lengths of the isotopes A and B. Ni is one of best candidates for this application because Ni^{62} has a large negative and Ni^{58} a large positive coherent scattering length. (A table of scattering lengths can be found in [8].) Therefore, any desired coherent scattering length between $-0.87 \cdot 10^{-12}$ cm and $1.44 \cdot 10^{-12}$ cm can be adjusted for Ni. In Fig. 1 we have plotted the α values of an optimal combination, namely Ni (natural) with ($\text{Ni}^{62}(0.72)$ Ni(0.28)) and He^4 . Because m_1 in eq. (4) has a negative value, α cannot be zero in the accessible ω range, and α changes continuously from 0.1 to 20 in the ω -range of interest (Fig. 1). Therefore, this isotope combination would be an optimal choice to determine the helium gas density with SANS.

Magnetic and Nuclear Scattering Contrast in Iron

Magnetic and nuclear scattering contrast variation can be applied in all ferromagnetic systems. The main advantage of this method is that one needs only one sample! Ni, however, is not a good candidate for this method, because its ratio of magnetic and nuclear coherent scattering length is only 0.15 and therefore α is less than 0.1 in the whole ω range. Iron is a much better candidate with a ratio of the magnetic and nuclear scattering length of 0.6 [8]. For this type of contrast variation α reads

$$\alpha = \left(\frac{m}{M} \right)^2 \frac{\omega^2}{\left(1 - \frac{g}{M} \omega \right)^2} \quad (6)$$

with the magnetic coherent scattering length M . In the magnetic part of scattering the He is of course not visible. α is plotted in Fig. 2 for He^3 and He^4 in iron. The He^3 sample shows an ambiguity for ω values above and below 1.5, but He^4 in Fe fulfills optimal experimental conditions.

Polarized Neutrons in Iron

If one employs polarized neutrons, the coherent scattering length depends on the direction of the neutron polarization and of the magnetic field applied to the sample. If the neutrons are polarized in the direction of the magnetic field one finds $m_1 = (b_{\text{nuc}} + b_{\text{mag}})$ [constructive interference] and in the direction perpendicular to the field $m_2 = (b_{\text{nuc}} - b_{\text{mag}})$ [destructive interference]. Calculated α values for He^3 (eq. 4) are plotted in Fig. 2 and lead to measurable He densities only above $\omega \approx 1$.

Experimental Results on He^3 and He^4 in Ni^{58}

Experiments of this kind are presented in Ref. [2-5]. Here only a brief description of recent results for He^3 and He^4 in Ni^{58} is given. (For a detailed presentation see Ref. [5]). The experiments have been performed at the KWS I small angle scattering instrument at the FRJ-2 reactor in Jülich. Because of the small sample thickness of $100 \mu\text{m}$ and the low He concentration of 1200 appm, long measurement times between 4 and 20 h were necessary to obtain sufficiently small statistical errors of about 2%. In Fig. 3 the experimentally obtained α is plotted as a function of the scattering vector Q after a 2 hours anneal at 923 K. For Q values larger than 0.06 \AA^{-1} an α of about 0.6 is found. The slight decrease of α with Q is due to a size distribution of the bubbles and the higher helium density in the smaller bubbles. The strong increase of α below 0.05 \AA^{-1} is caused by irradiation induced defects which were not yet annealed at this heat treatment. Using the corresponding plot in Fig. 1, the experimentally determined α values lead, for different annealing temperatures, to ω between 0.8 and 1.3. In Fig. 4 all determined ω values are plotted as a function of the mean bubble radii. The size of the bubbles has been obtained from a fit of the scattering curves with a lognormal size distribution. The dashed line in Fig. 4 represents the densities expected for bubbles in thermal equilibrium [6]. For all sizes the experimental values show a density and pressure which is higher than the equilibrium value. This is the main result of this work which was quite unexpected. Recent theoretical considerations on this subject can be found in [7].

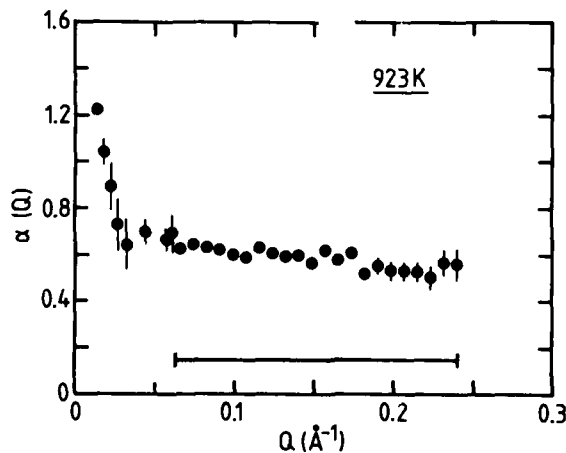


Fig. 3 Experiment α versus Q of He^3/He^4 in Ni^{58} .

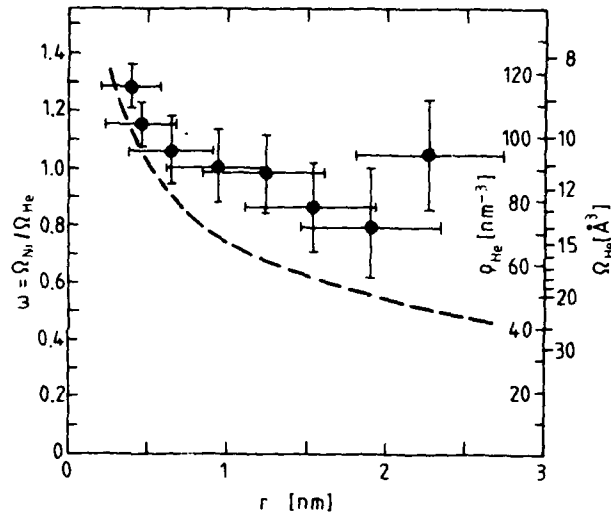


Fig. 4
Atomic volume ratio ω , helium density ρ_{He} , and helium atomic volume Ω_{He} as functions of the mean bubble radius r . The filled dots are the values obtained from the measured intensity ratios α via Fig. 1. The dashed curve shows the density in the bubbles for thermodynamic equilibrium, assuming a surface energy $\gamma = 1.8 \text{ Nm}^{-1}$.

CONCLUSIONS

The application of the contrast variation method to determine the helium density in bubbles in nickel and iron has been discussed. It was found that, for nickel, the use of different isotopes (Fig. 1), and for iron the nuclear and magnetic contrast is the best choice to determine the gas density. Especially, the possible adjustment of the coherent scattering length of nickel from negative to positive values leads to optimized experimental conditions (Fig. 1). First experiments on He^3 and He^4 in Ni^{58} demonstrate a successful application of this method.

ACKNOWLEDGEMENT

I would like to thank Prof. H. Ullmaier and Prof. T. Springer for critical reading the manuscript.

REFERENCES

- [1] H. Ullmaier, *Nuclear Fusion* **24**, 1039 (1984).
- [2] D. Schwahn, H. Ullmaier, J. Schelten, and W. Kesternich, *Acta Metall.* **31**, 2003 (1983).
- [3] W. Kesternich, D. Schwahn, and H. Ullmaier, *Scripta Metall.* **18**, 1011 (1984).
- [4] D. Schwahn, W. Kesternich, S. Spooner, H. Schober, H. Ullmaier and J. Schelten in *Atomic Transport and Defects in Metals by Neutron Scattering*, edited by C. Janot, W. Petry, D. Richter, and T. Springer (Springer Proceedings in Physics 10, 1986) pp. 197-203.
- [5] Qiang Li, W. Kesternich, K. Schroeder, D. Schwahn, and H. Ullmaier, Submitted to publication.
- [6] H. Trinkaus, *Rad. Effects* **78**, 189 (1983).
- [7] H. Trinkaus, *Scripta Metall.* **23**, 1773 (1989).
- [8] G.E. Bacon, *Neutron Diffraction*, 3rd ed (Clarendon Press, Oxford, 1975), pp. 39-41 and 211.

A SANS STUDY OF CAPILLARY CONDENSATION IN POROUS MEDIA

M.Y. LIN,^{a,b} S.K. SINHA,^{c,d} J.S. HUANG,^c B. ABELES^c, J.W. JOHNSON,^c J.M. DRAKE^c, AND C.J. GLINKA^a

a. *National Institute of Standards and Technology, Gaithersburg, MD 20889*

b. *Department of Physics, Princeton University, Princeton, NJ 08544*

c. *Ezzon Research and Engineering Co., Rt. 22 E, Annandale, NJ 08801*

d. *Brookhaven National Laboratory, Upton, NY 11973*

ABSTRACT

We use small angle neutron scattering (SANS) to study the microstructure of porous Vycor glass and the capillary condensation of fluids in the medium. Using a chord distribution model, we can predict the structure factor measured by SANS. Excellent agreement with the data is obtained. The fitted parameters characterize quantitatively the porous structure before and during the process of condensation, and are in good agreement with isotherm measurements. However, at the latest stages of the process, when all the pores are nearly filled, the model can no longer describe the system.

1. INTRODUCTION

Microporous materials such as Vycor glass are model systems for studying the many physical and chemical processes that take place in geometrically restricted environments.¹⁻³ These processes include phase transitions in fluids, critical fluctuations, transport phenomena, wetting, and localization. Therefore, it is of fundamental interest to understand and characterize the microstructure of these materials, as well as the interaction between them and the imbibed fluids. One such example of these interactions is the phenomenon of capillary condensation in porous media. Generally, bulk condensation takes place at a pressure p_0 , the saturated vapor pressure of the condensing molecules. However, when a restricted geometry is imposed on the fluids as in a porous medium, the gas molecules will experience a different physical process, and will condense at a pressure $p < p_0$. In this paper, we use small angle neutron scattering (SANS) to study the structure of Vycor glass, and the related capillary condensation process. Using a chord distribution model to characterize the structure, we show that we can obtain good agreement with the SANS data and other structural parameters measured independently. In addition, we show that the chord distribution can also describe the wetting-condensation process taking place initially, thus providing an important probe of this complex physical phenomenon.

2. MATERIALS AND ISOTHERM MEASUREMENTS

Vycor glass is commercially available from Corning Glass. It is produced at high temperature and consists of both silica and boron oxide. Upon annealing, the two phases separate by spinodal decomposition. Later, the boron containing phase is leached out by acid, and the glass is thus left with a highly interconnected porous structure. A TEM picture of a cross section cut from our sample is shown in Fig. 1.⁴ It has a porosity of 0.31, and an average pore size (neck diameter) of 67Å, both measured by nitrogen desorption. For condensation liquid we used hexane, whose saturated vapor pressure at 23°C is $p_0 = 139$ torr.

One experimental probe of the condensation process in the porous media is an isotherm measurement. It measures the quantity (weight) of the liquid condensed in the media as the molecular gas pressure increases from 0 to p_0 (adsorption), or decreases from p_0 (desorption). Figure 2 shows a plot of both processes as functions of the reduced pressure p/p_0 (activity). The process is reversible up to $p' \approx 0.4p_0$ as shown in the figure, after that it exhibits a hysteresis until p/p_0 reaches ~ 0.7 .

Following the adsorption branch of the isotherm, at very low pressure, the molecules first form a thin film on the pore surfaces due to van der Waals interaction between the molecules and the solid surface. Then, as the pressure increases, the capillary effect causes the molecules to condense at a $p < p_0$. The value of p is determined by the local radius of curvature R , molecular weight M , thermal energy kT , liquid density ρ , the surface tension σ , and the contact angle δ , as expressed in the Kelvin equation:⁵

$$\ln(p/p_0) = -(2M\sigma/R\rho kT)\cos\delta \quad (1)$$

Thus, the smaller the radius of curvature is (the more restricted geometry), the lower p will be at which condensation takes place.

The hysteresis observed arises from the fact that the values of R are different during adsorption and desorption for the same pore size as shown schematically in Fig. 3. During the process of filling, before condensation, the molecular layer covers the surface as shown in Fig. 3(a). Here, the local radius of curvature is $R = 2/(1/a_1 + 1/a_2)$, where a_1 and a_2 are the two radii of curvature in two independent directions. In one direction, $a_1 = a$ as shown, while in the other direction, $a_2 \gg a$. This results in $R = 2a$. In the case of emptying, the pores are originally filled with liquid, therefore, as shown in Fig. 3(b), $R = a_1 = a_2 = a$. Thus, for the same pore, condensation during filling and evaporation during emptying do not take place at the same p . Rather, the pressure at which the liquid evaporates is smaller. This is in agreement at least qualitatively with the isotherm measurements.



Fig. 1 Transmission electron micrograph (TEM) of a thin section of Vycor. The micrograph shows that Vycor consists of a homogeneous and isotropic distribution of pores (dark areas) and glass (light areas).

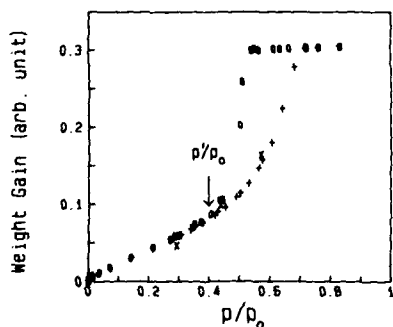


Fig. 2 Isotherm measurements of hexane in Vycor as functions of p/p_0 . Symbols (+) represent the adsorption process, (O) represent the desorption process, and (*) represent the result of the chord distribution analysis (see Section 4).

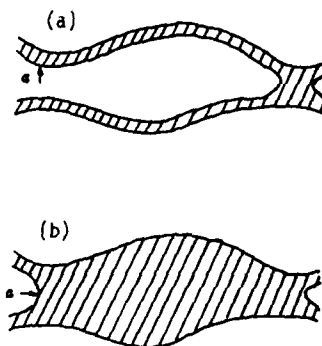


Fig. 3 A schematic drawing of a micropore during adsorption (a) and desorption (b) processes. Shaded areas represent liquid.

Another difference in the two branches of the isotherm is the steep drop in the desorption compared to the more gradual rise in the adsorption. The steep drop in the desorption isotherm results from the fact that there is a distribution in pore size, and that the liquid in many pores cannot evaporate even if the local R is very large, because it is blocked by the liquid in the neck regions which have smaller R , thus requiring a lower p for evaporation. However, as soon as this lower pressure is reached, the liquid in the whole pore as shown in Fig. 3(b) evaporates. This then produces the abrupt drop in the desorption part of the isotherm. Thus, the steepness of the desorption curve is a measure of the neck size distribution. The almost vertical drop in our desorption curve (Fig. 2) shows that the Vycor glass has a quite narrow distribution of the pore neck size. On the other hand, the more gradual increase in the counterpart of the adsorption branch indicates that there is a wider distribution of pore size other than the neck regions.

3. SANS MEASUREMENTS

While the isotherm measurements can probe certain parameters of the porous media and the condensation process, a more microscopic characterization of the microstructure can be achieved by scattering experiments. Small angle neutron scattering (SANS) has the unique advantage by which the condensing liquid can be index-matched with the porous material, largely simplifying the interpretation of the data.

The SANS measurements were made at the NIST 8-meter SANS instrument with a wavelength of 5 Å. The range of the scattering wavevector $Q = (4\pi/\lambda)\sin(\theta/2)$ is $0.006 < Q < 0.2/\text{Å}$. We chose a mixture of hexane (C_6H_{14}) and deuterated hexane (C_6D_{14}) (38:62 volume ratio) to match the neutron scattering length density of silica, $b = 3.6 \times 10^{10}/\text{cm}^2$. Figure 4 shows the scattering intensity taken at various activities p/p_0 . As can be seen, the shape and the magnitude do not change much for p/p_0 less than about 0.6. After that the shape changes from a peaked one to one somewhat flat and then monotonically decreasing, and the intensity drops substantially as the activity increases. At $p/p_0 = 1$, the peak height of the intensity is only ~ 0.01 of that at $p/p_0 = 0$, indicating a reasonable match of the scattering length density of the liquid with that of the glass.

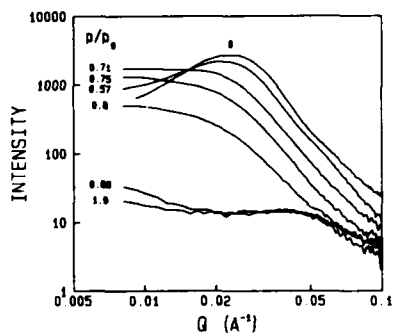


Fig. 4 SANS intensity from Vycor as condensation takes place in it. Data were taken at several activities as marked. The scales are logarithmic.

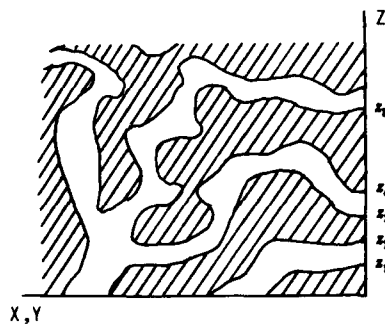


Fig. 5 A schematic drawing of a porous medium cross section. Since the medium is homogeneous and isotropic, the z -axis is arbitrary.

4. CHORD DISTRIBUTION AND ANALYSIS

In order to interpret the SANS data, we will characterize the structure using a chord distribution model.⁶ We start with the dry Vycor ($p = 0$). We assume that both the solid part and the pores in the Vycor are bicontinuous, so that they are entirely interconnected.

However, their shape can be arbitrary. This is drawn schematically in Fig. 5. We impose an arbitrary x -direction, and measure the distance on the x -axis (chord) between any two neighboring interfaces. The chord length in pores ($z_1-z_1, z_4-z_3, \dots, z_{2n}-z_{2n-1}$) are called pore chord length l_p ; and the chord length in solid ($z_2-z_2, z_3-z_4, \dots, z_{2n-1}-z_{2n-2}$) are called l_s . We define $F_p(l)$ as the pore chord distribution, where $F_p(l)dl$ is the probability of a pore chord having a value between l and $l+dl$, and $F_s(l)dl$ is the corresponding probability for a solid chord.

With the two-chord distribution model, we can derive the structure factor measured in the SANS experiments from first principles, and show that it can be expressed as⁷

$$S(Q) = \frac{N^2 \Delta \rho^2}{(1+Q^2 \xi^2)^\epsilon} \left(1 - \frac{f_p(Q) + f_s(Q) - f_p(Q)f_s(Q)}{1-f_p(Q)f_s(Q)} - \text{C.C.} \right) \quad (2)$$

where N is the average number of the interfaces per unit volume, $\Delta \rho$ is the scattering length density, C.C. is the complex conjugate of the previous term, and $f_{p,s}(Q)$ are the Fourier transforms of the chord distribution $F_{p,s}(l)$. When the surface is fractal, the exponent $\epsilon = (6-D_s)/2$, D_s is the surface fractal dimension and $\xi/2\pi$ is the relevant length scale.

We assume a form for both chord distributions given by

$$F(l) = l^\nu (Ae^{-\alpha l} + Be^{-\beta l}), \quad (3)$$

choosing ν , α , β and $l = \int lF(l)dl / \int F(l)dl$ as the fitting parameters, and obtain a least squares fit using the above forms with the SANS data taken at $p = 0$. The result is shown in Fig. 6 with the solid line representing the fitting. It agrees with the data quite well.

The fitting parameters give an average pore chord length $l_p = 76 \text{ \AA}$, an average solid chord length $l_s = 161 \text{ \AA}$, and an effective porosity $\phi_{\text{eff}} = l_p / (l_p + l_s) = 0.32$. They are in excellent agreement with the values of average pore diameter at necks $d = 67 \text{ \AA}$ and porosity $\phi_0 = 0.31$ measured independently. The fitted values indicate a fairly narrow distribution for the chords in the pores and a broader distribution for chords in the solid.

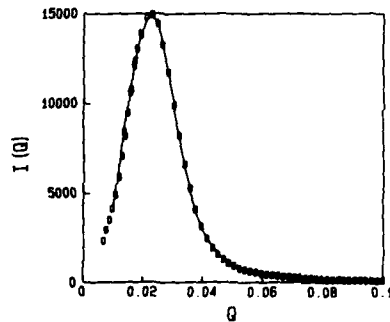


Fig. 6 SANS intensity data (squares) taken at $p = 0$ (dry Vycor) and the fit (solid line) calculated using the chord distribution model.

Interpretation of the isotherm measurements (Section 2) indicates that when $p > 0$, the gas molecules first form a thin film of about one to two molecular layers and that condensation starts where the process is no longer reversible, or at a pressure $p' \approx 0.4p_0$. Thus for $p < p'$ the film coating the pore wall is not expected to change significantly the original chord distributions, but only to change the average chord lengths, since the scattering length densities of the solid and liquid are the same. To test this idea, we try to fit the SANS data with the same chord distribution model we obtained in fitting the $p = 0$ data (namely, use the same values of $\alpha_{p,s}$, $\beta_{p,s}$ and $\nu_{p,s}$ which determine the shape of the

Table 1. Fitted Parameters

p/p_0	N	l_p	l_s	D_s	$l_p/(l_p+l_s)$	ϕ_i^7
0	376	76	161	2.29	0.32	0.31
0.29	295	69	186	2.3	0.27	0.29
0.44	224	72	265	2.0	0.21	0.19
0.57	192	72	429	1.72	0.14	0.15
0.71	155	77	$5 \cdot 10^7$	1.33	0.00	0.07

distributions). The values of l_p , l_s and N are kept floating as fitting parameters in the least squares fitting. The results are shown in Fig. 7, for $p/p_0 = 0.29, 0.44, 0.57$ and 0.71 . As can be seen, the calculations (solid lines) fit the SANS data (squares) for the samples with hexane equally well as for the dry Vycor ($p = 0$) until $p/p_0 = 0.71$, where the shape of the data at small Q changes from a peak to a plateau, and the calculated curve no longer agrees with the data.

The fitted parameters are shown in Table 1. At $p/p_0 = 0.29 < p'/p_0$, l_p decreases by 7 \AA from its value at $p = 0$, and l_s increases by 25 \AA , indicating that a thin layer of about $4 \sim 13 \text{ \AA}$ is formed on the surface. At that same time the surface is still rough, as shown by a value of the surface fractal dimension of $D_s = 2.3$ obtained by fitting with the data of large Q only. The effective porosity $\phi_{\text{eff}} = 0.27$, is in good agreement with the value of $\phi_i = 0.29$ obtained using other analysis of the same data.⁷

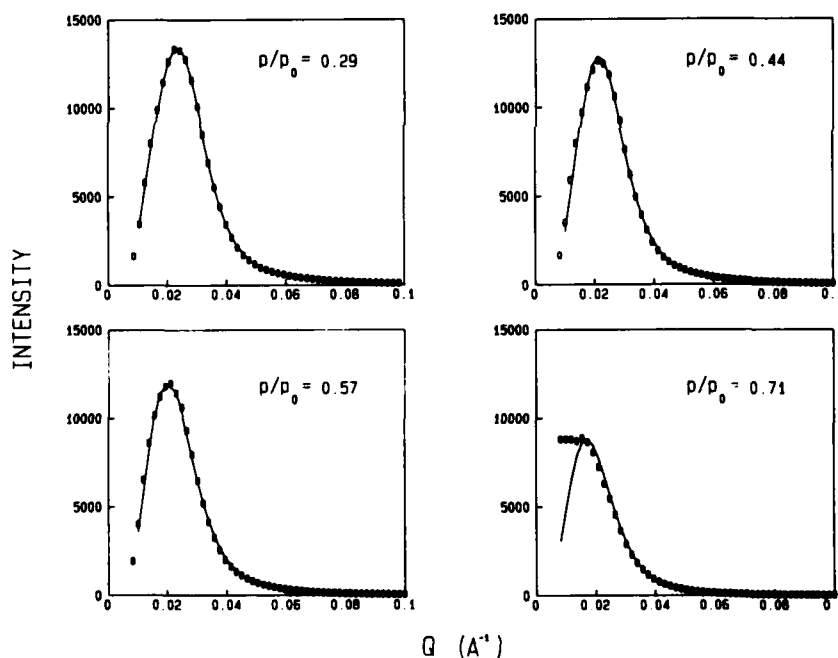


Fig. 7 SANS intensity data (squares) taken at several activities ($p/p_0 > 0$) shown with the fits (solid lines) calculated using the chord distribution model.

When $p/p_0 = 0.44 > p'/p_0$, condensation starts to occur, and we see a small increase in l_p and a large increase in l_s in the fitted parameters. We believe this indicates that as condensation takes place, some small pores are filled by the liquid, pushing the average chord l_p to a larger value. This also results in an abrupt increase in l_s , since the elimination of one pore increases the solid chord by at least a factor of two on average. At the same time, we see a decrease in N , the average number of interfaces per unit volume, which is consistent with our interpretation. In addition, the surface becomes smooth ($D_s = 2$), suggesting that the pore surface is completely covered by the liquid molecules. Later on the exponent ϵ is even larger than 4, implying a diffusive liquid surface. The volume taken by the liquid, $\phi_{\text{eff}} - \phi_0$, is also shown in Fig. 2 by the "x" symbols, compared with the isotherm measurements. One interesting fact we note here is that while the average periodicity ($l_s + l_p$) increases by a factor of 2 as p/p_0 varies from 0 to 0.57, the peak position of the scattering stays relatively constant (it changes only from $Q \approx 0.23/\text{\AA}$ to $0.21/\text{\AA}$). This behavior remains an intriguing question to be resolved.

As the activity reaches a value of 0.71, the fitted parameters indicate a complete failure of the chord distribution model, even though the calculation still agrees with the data at large Q . This is probably an indication that the remaining pores are no longer bicontinuous, but rather form many isolated voids surrounded by the condensed liquid.

5. CONCLUSION

In this paper, we show that the microstructure of a porous medium Vycor can be characterized by a two-chord distribution model. The chords in pores have a fairly narrow distribution, while the chords in the solid have a broader distribution. With the same model, the capillary condensation taking place inside the medium can also be described and understood. The liquid molecules first form a thin film of about 1–2 monolayers on the pore surface, which, combined with the solid structure, does not change the essential chord distribution. When the pressure is increased above a value $p' \approx 0.4p_0$, condensation starts taking place in the smallest pores, and the process is no longer reversible. However, the large unfilled pores are still highly interconnected since the entire structure of both solid and condensed liquid can still be described by the chord distribution, although with different average chord lengths. Finally, when $p/p_0 > 0.7$, so many pores are filled that the unfilled pores are no longer interconnected, resulting in a failure of the chord model. It is therefore worth pursuing a new model containing isolated spaces to describe the data at this stage.

In addition, the desorption part of the condensation/evaporation process would also be interesting to study. Due to limited user time at the SANS spectrometer, such data was not obtained. We are planning new experiments to investigate this problem further.

We thank the National Institute of Standards and Technology for supporting the small angle neutron scattering experiments.

REFERENCES

1. J. Klafter and J. M. Drake, eds., *Molecular Dynamics in Restricted Geometry* (Wiley, New York, 1989).
2. M. W. Cole and W. F. Saam, *Phys. Rev. Lett.* **32**, 985 (1974); W. F. Saam and M. W. Cole, *Phys. Rev. B* **11**, 1086 (1975).
3. D. D. Awschalom, J. Warnock and M. W. Shafer, *Phys. Rev. Lett.* **57**, 1607 (1986).
4. P. E. Levitz, G. Ehret and J. M. Drake, *J. Chem. Phys.*, submitted.
5. S. J. Gregg and K. S. W. Sing, *Adsorption, Surface Area, and Porosity* (Academic Press, New York, 1967), Chaps. 3 and 4.
6. S. K. Sinha, J. M. Drake, E. Levitz and H. B. Stanley, in *Fractal Aspects of Materials: Disordered Systems*, A. J. Hurd, D. A. Weitz and B. B. Mandelbrot, eds., (MRS, Pittsburgh, 1987), p.118.
7. S. K. Sinha, M. Y. Lin, B. Abeles and J. S. Huang, to be published.

PART VIII

Polymers

DYNAMICS OF STAR-BRANCHED POLYMERS IN SOLUTION

J. S. HUANG¹, L. J. FETTERS¹, D. RICHTER^{2,3}, B. FARAGO³ and B. EWEN⁴
1. Exxon Research and Engineering Co. Rt. 22 E. Annandale, NJ 08801
2. Institut Laue-Langevin, 156X, 38042 Grenoble Cedex, France
3. Institut Fur Festkorperforschung, Julich GmbH, FRG
4. Max Plank Institut Fur Polymerforschung, 6500 Mainz, FRG

ABSTRACT

We have studied star-branched polymers in solution under various labelling and contrast matching conditions by small angle neutron scattering and neutron spin echo spectroscopy. We have investigated the relation between the static and dynamic partial structure factors of the variously labeled star polymers. The system of interest is a set of solutions containing 12-arm star branched polyisoprene of arm-molecular weight of 8000, and two polystyrene 12-arm stars, one fully labelled, the other with one arm labelled. The polyisoprene star polymer arms consisted of diblock copolymers, half-deuterated, and half-protonated. Measurements were performed on a center-deuterated star in a contrasted matching deuterated solvent (shell contrast), and on a reverse labelled star with core contrast. We have also studied a solution with the solvent matched the average star scattering length density and solutions containing identical stars with protonated homopolymers. It is found that in the frame-work of the random phase approximations, the initial relaxation rate of the partial dynamic structure factors can be quantitatively accounted for by a function of the eigenmodes of the mobility matrix weighted by an appropriate combinations of the various partial static structure factors.

Introduction

A star-branched polymer is a macromolecule consisted of f -monodisperse polymer arms linked together at a small center linker-molecule. Modern anionic polymerization techniques allows a variety of these near perfect star-branched molecules to be made [1,2]. Both the static and dynamic properties of this type of regular branched polymers have been under intense study recently [3-9]. Here we report a neutron spin echo study of a system of variously labelled star polymers in order to understand the dynamics of the various parts of the molecule. Due to the fact that many polymeric arms are covalently linked together, the arms generally find themselves in a more concentrated environment, even in a very dilute solution. It is clear that for a multi-arm star, near the center of the molecule, the monomer density is high, and can approach that of the melt. As one gradually

progresses outward from the center towards the edge, the monomer density is lowered as more space is available for each of the arms to occupy. Finally, as one approaches the edge of the star, the monomer density will decrease fairly abruptly [10]. Figure 1 illustrates how a 20-arm star polymer may look like according to molecular dynamic simulation by Grest et al. [11]



Figure 1 Projection of a configuration of a simulated star polymer of 20 arms, each with 50 units of monomers

20/50

Static small angle scattering from a dilute star solution revealed a sharp drop-off [5] of the intensity at around $QR = 1$, before it crossed over into the $Q^{-\nu}$ regime (Figure 2.) In the case of a good solvent, $\nu \approx 1.6$.

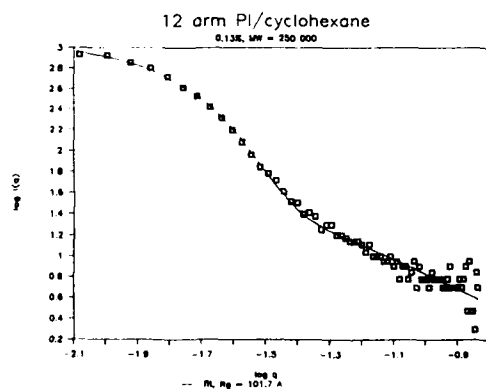


Figure 2 SANS measurement of a 12 arm polyisoprene in deuterated cyclohexane. The concentration is 0.13 %. The solid line represents a theoretical fit given in Ref.[5].

Neutron Spin Echo Spectroscopy

The dynamics of the star polymer in the Q-range of 0.01 to 0.2 Å⁻¹ was first studied by Richter, et al. [9] by neutron spin echo spectroscopy. It is a well known fact that small angle neutron scattering [12] is particularly suited for the study of hydrocarbon systems. The deuterium-hydrogen substitution allows simple labeling of the molecule further enhanced the versatility of SANS. The dynamics of a polymer in the Q range of the order of 0.1 Å⁻¹ is generally characterized by a time constant of the order of 10⁻⁸ seconds, or alternatively, this corresponds to 100 MHz. The energy transfer in a scattering process in this frequency range is of the order of 50 neV. The average energy of cold neutrons is in the range of 1meV, so to study the dynamics of polymers in solution with neutron scattering requires an energy (or wavelength) resolution of the order of 1/10⁻⁵. Fortunately, this requirement is satisfied with the neutron spin echo (NSE) technique [13].

The NSE spectroscopy takes the advantage of Lamor precession of the neutron spin in a magnetic field (the guide field). The configuration of the fields are arranged in such a way that when the scattering process is elastic, i.e. the scattering neutrons have the exact same energy as that of the incident neutrons, the net phase angle change of the spin is zero. If the scattering process is quasi-elastic, (small energy change), then the scattered neutron will have a slightly different velocity depending on the angle of scattering and the energy gain or loss in the scattering process. When this happens, the scattered neutron will have a slightly different polarization compared with elastic scattering process. The probability of this quasi-elastic scattering is given by the dynamic scattering structure factor $S(Q, \omega)$, where $h/(2\pi\omega)$ is the energy exchange in the scattering. Since the NSE measures the the scattering cross-section at Q for all ω , it can be readily shown that the quantity measured is the Fourier transform of $S(Q, \omega)$, called the intermediate structure factor $S(Q, t)$:

$$S(Q, t) = \int S(Q, \omega) \cos(\omega t) d\omega \quad [1]$$

The factor of $\cos(\omega t)$ is due to the projection of the final spin in the direction of the initial spin. For typical values of the guide fields, on the average the spins precess for several thousand turns, thus an angular resolution of 10⁻⁵ can be achieved without having to define the wavelength of the incoming flux and the scattered flux to the same exacting precision. In fact, since in an effect that each neutron carried its own internal clocking device, a spread of wavelength $\Delta\lambda/\lambda \approx 20\%$ could be admitted without compromising the instrumental resolution too much. Because of the fact that

a broad band of neutron energy can be used, the incident flux of neutron are made high enough for achieving a reasonable experimental time. The wavelength chosen for the experiments was typically around 8 Å. NSE measurements were carried out on the IN-II machine in the Institut of Laue-Langevin in Grenoble, France.

Dynamic Scattering

The intermediate structure factor $S(Q,t)$ as measured by NSE is coupled to the dynamics of the (monomer scattering length) density fluctuation, and it is expected to decay exponentially for simple relaxation processes. This is because by definition,

$$S(Q,t) = \int g(r,t) \exp(iQr) dr \quad [2]$$

Here $g(r,t)$ is the density correlation function. The characteristic frequency, Ω , is defined as the inverse of the decay time τ of the density fluctuations. A typical neutron spin echo spectrum obtained from a THF solution containing stars with a 1-labelled arm is shown in Figure 3. The solid lines are theoretical fits due to Dubois-Violette and de Gennes [14].

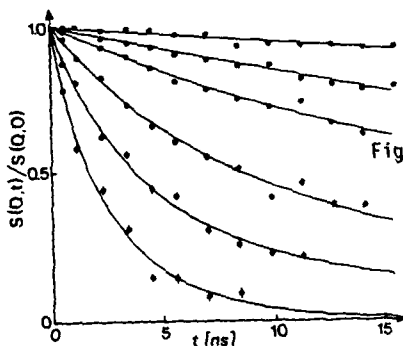


Figure 3 Neutron spin echo spectra obtained for a 1-arm labelled polystyrene star in deuterated THF. Solid lines represent theoretical fits using Ref. [14].

It is found that for a star-branched polymer, the scaled characteristic frequency Ω/Q^3 exhibited a pronounced minimum near $QR_g = 1.2$. This is in strong contrast to the smooth cross over from $1/Q$ to constant at high Q values commonly observed in the dilute linear polymer solutions. This effect was thought to be due to a de Gennes narrowing-like process owing to the enhanced correlation of the monomers in a star polymer [15]. The dynamics of the arms are never quite free on some intermediate length scale, namely, that of the characteristic size of the whole star. The collective motion of the arms apparently slowed down the relaxation rate of the (scattering length) density fluctuations. The enhancement of the monomer correlation can be best seen in the heightened peak in the Kratky plots

(where the $I(Q) \cdot Q^2$ is plotted against Q) of the star polymer as compared with an linear polymer in solution. The fact that the minimum in Ω/Q^3 was due to the collective motions of the arms was later confirmed by measurements in a similar polymer with a single (on average) labelled arm in the star structure [6]. It was found that the dynamics of a single labelled arm is very similar to that of a linear polymer in solution [16,17], and that there is no minimum observed in the scaled characteristic frequency. A comparison of the dynamics measured in the fully labelled polystyrene star and a single arm labelled star is shown in Figure 4. We also observed that the static structure factor of the single-arm labelled star is similar to that of a linear polymer.

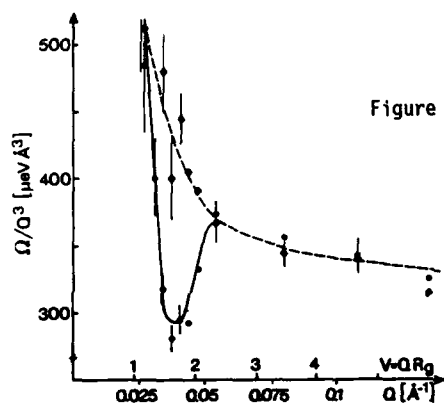


Figure 4 The scaled relaxation rate Ω/Q^3 for the one arm labelled star () and the fully labelled star (•) are plotted as a function of Q .

It turned out that there is a deeper connection between the static structure factor and the initial decay of the dynamic structure factor [7]. By appealing to the linear response theory, the rate of change of the intermediate partial structure factor $S_{\alpha\beta}(Q,t)$ for a diblock polymer can be written as follows [18]:

$$\frac{\partial S_{\alpha\beta}}{\partial t} = -\sum_{\alpha\gamma} \Omega_{\alpha\gamma} S_{\gamma\beta} \quad [3]$$

where $S_{\alpha\beta}(Q,t) = \sum_{ij} \langle \exp(iQr_{i\alpha}(0)) \exp(iQr_{j\beta}(t)) \rangle$ [4]

and α, β denote the monomers of the two blocks A and B, i and j are running index that sum over all the monomer whose spatial coordinate are given by the r_i and r_j , respectively. The first cumulant matrix Ω is given by

$$\Omega = \lim_{t \rightarrow 0} \frac{\partial}{\partial t} \underline{S}(Q,t) \underline{S}^{-1}(Q) \quad [5]$$

Furthermore, it was shown that the first cumulant is related to a generalized mobility matrix $\underline{M}(Q)$ [18]:

$$\Omega = k_B T Q^2 \underline{M}(Q) \underline{S}^{-1}(Q) \quad [6]$$

The general result stated in Equation (6) gives a simple expression for the scaled frequency in the Zimm regime, where the mobility $M(Q) \sim 1/Q$ for a Gaussian star polymer. This immediately leads to the observed relation

$$\Omega/Q^3 \sim \text{const}/[Q^2 S(Q)] \quad [7]$$

near the minimum of the scaled frequency. For $QR \gg 1$, the scattering from a Gaussian star leads to scaling relation $S(Q) \sim Q^{-2}$, which gives the expected scaling for $\Omega \sim Q^3$. As a matter of fact, the argument for the Q^3 scaling does not depend on gaussian statics, it can be shown that $M(Q) \sim 1/Q^\nu$, where ν is the Flory exponent. The ratio $M(Q)/S(Q) \sim Q^\nu/Q^{\nu-1} = Q$, which leads to the Q^3 scaling for Ω as seen in Equation (6), independent of the values of ν .

Equation (3) can be solved by the use of Laplace transformation. This allowed the derivation of a set of specific relations relating the various partial dynamic structure factors with the two normal relaxation modes corresponding to the two eigenvalues of equation 2, weighted by the appropriate combinations of the partial static structure factors.

Recently Benoit and Hadziioannou [19] have published a general scheme to calculate the the various partial static structure factors, so S_{ij} 's are known. These are quantities one can either directly measure (S_{ij} 's) or derive from measurements (S_{ij} 's). Ω_{ij} 's can be obtained by evaluating the initial slope of the corresponding dynamic structure factors. To interpret the results one needs to know $\underline{M}(Q)$, the mobility matrix. Richter et al [7] have derived an expression for $M_{\alpha\beta}$ by a pre-average scheme that allows the decoupling of the motion and the position of the monomers in the Oseen diffusion tensor. The generalized mobility is expressed as an integral function of the static structure factors:

$$M_{\alpha\beta}(Q) = 1/(3\pi^2\eta_0) \int_0^\infty S_{\alpha\beta}[(Q^2 + s^2)^{1/2}] ds \quad [8]$$

When $QR_g \ll 1$, there is an additional correction term which also depends on a second integration of the (partial) structure factor. By the use of the measured structure factors and equation (8), we can compare with the measured decay times.

Samples

To test the validity of the relations between the structure factors and dynamics of monomer concentration relaxation described by the initial decay of $S(Q,t)$, we have synthesized a series of variously labelled 12-arm polyisoprene star with molecular weight of 8000/arm. The sample 12P was a fully protonated star, sample 12PD and 12DP stars consisting of diblock copolymers, half

deuterated, and half protonated, each block having a molecular weight of 4000. The protonated portion was linked at the center of the 12PD star. Sample 12DP had a reverse labelling, i.e. a deuterated star core. The synthesis procedures were described elsewhere [1,2].

The various contrast conditions were achieved in the following way: For the core contrast, samples 12P and 12PD were dissolved in deuterated octane; for the shell contrast, sample 12DP was dissolved in a deuterated octane. From these solutions we could obtain the partial structure factors S_{22} , S_{11} , and S_{12} , respectively. For the average contrast, the solution was obtained by dissolving sample 12PD in a mixture of partially deuterated toluene, which had a lower total incoherent scattering cross-section than that of a octane-deuterated octane mixture with the same average scattering length density as that of the 12PD stars. For SANS measurements, solutions of weight concentration of 4, 2, and 1% were used. For neutron spin echo experiments only 4% solutions were used. SANS measurements were carried out on the D-17 small angle spectrometer at the ILL in Grenoble, France.

Results and Discussions

The results for small angle scattering for the core, shell and average contrast are shown in Figure 5. Here we employ a modified Kratky plot showing

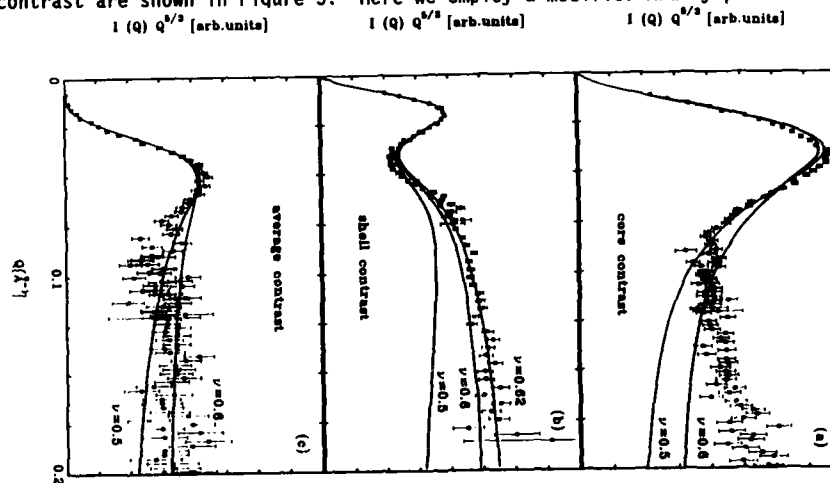


Figure 5 The Kratky plots for three different contrast conditions: (a) core contrast; (b) shell contrast; and (c) average contrast.

$Q^{1/\nu}I(Q)$ versus Q due to the good solvent conditions. The solid lines are fits for a gaussian star model ($\nu = 0.5$), and a swollen star model with Flory exponent ν set at various values as indicated. It should be noted that none of the fits are perfect. As discussed earlier in equation (6), we expected the scaled frequency $\Omega(Q)/Q^3$ to display a Q -dependence mimicking the function $1/[Q^{1/\nu}I(Q)]$. Specifically, in the modified Kratky plot for the shell contrast, a minimum was observed near $QR_g = 1.2$ where a maximum was previously observed for the core contrast. indeed we see that the extrema in the Kratky plots corresponded exactly with (inverse) extrema in the scaled frequency as shown in Figures 6, and 7. The height of the peak (or the depth of the valley) as scaled to the asymptotic values at high Q are also comparable between the static and dynamic measurements.

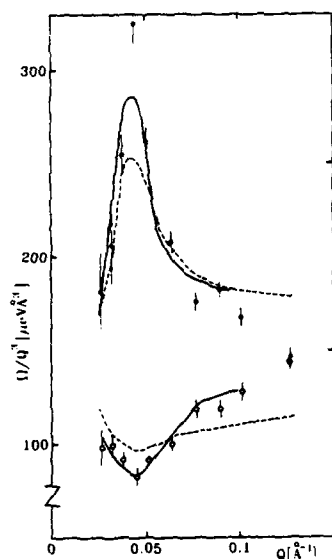
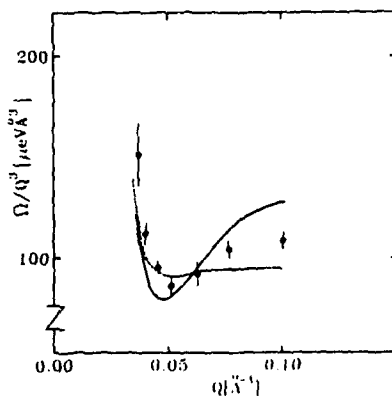


Figure 6 The scaled relaxation rate Ω/Q^3 measured for the shell contrast (\bullet) and the core contrast (\circ). The solid lines represent the fits using the structure model; the dotted line represents the fit using the Gaussian model.

Figure 7 The scaled relaxation rate Ω/Q^3 measured for the average contrast (\bullet). The solid line represent the fit using the structure model; the dotted line represents the fit using the Gaussian model.



Quantitative fits to the initial decay of the dynamic structure factor as described above in the Theory section were also obtained for the variously labelled star solutions. The solid lines in Figures 6, and 7 represented the fits using the structure model. The dotted lines represents the fits obtained from using the gaussian star model. It is clear that the structure model can account for the dynamics reasonably well, while the gaussian model even though qualitatively correct, clearly quantitatively failed.

We have also compare the dynamics of the core of the star with that of the full star. One would expect the dynamics be similar from scaling arguments. However, it is clear that from Figure 8, for the core contrast, the dynamics of the inner star measured at two Q values are retarded at longer times when compared with that of a full star. The solid lines through the data points obtained for the full star are fitted using the normalized Zimm model due to Dubois-Violette and de Gennes [14]. The fits are satisfactory. At delay time beyond 4ns or so, the inner star dynamics is seen to decay much slower. We believe this could be due to the entanglement of the arms in star polymer, as it is suggested by a recent scaling theory [20].

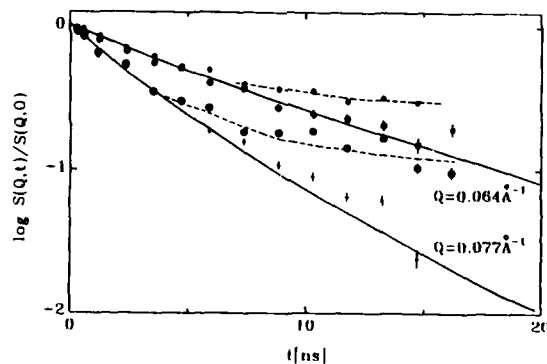


Figure 8 The relaxation spectra of a fully labeled star ($\bullet, +$) and a core contrast star ($\ast, 0$) at two different Q values. The solid lines are fits using the theory given in Ref. [14], the dotted lines are drawn to illustrate the difference in relaxation rate for the two systems.

Summary

We have studied star-branched polymers in solution under various labelling and contrast matching conditions by small angle neutron scattering and neutron spin echo spectroscopy. We have investigated the relation between the static and dynamic partial structure factors of the variously

labeled star polymers. The system of interest is a set of solutions containing 12-arm star branched polyisoprene of arm-molecular weight of 8000, and two polystyrene 12-arm stars, one fully labelled, the other with one arm labelled. The polyisoprene star polymer arms consisted of diblock copolymers, half-deuterated, and half-protonated. Measurements were performed on a center-deuterated star in a contrasted matching deuterated solvent (shell contrast), and on a reverse labelled star with core contrast. We have also studied a solution with the solvent matched the average star scattering length density and solutions containing identical stars with protonated homopolymers. It is found that in the frame-work of the random phase approximations, the initial relaxation rate of the partial dynamic structure factors can be quantitatively accounted for by a function of the eigenmodes of the mobility matrix weighted by an appropriate combinations of the various partial static structure factors.

References

1. N. Hadjichristidis, A. Guyot, and L. J. Fetters, *Macromolecules*, **11** 668 (1978).
2. N. Hadjichristidis and L. J. Fetters, *Macromolecules*, **13** 191 (1980).
3. K. Huber, S. Bantle, W. Burchard, L. J. Fetters, *Macromolecules* **19**, 1404 (1986).
4. K. Huber, W. Burchard, L. J. Fetters, *Macromolecules* **17**, 541 (1984).
5. D. Dozier, J. S. Huang, L. J. Fetters, *Macromolecules*, to be published.
6. D. Richter, B. Farago, J. S. Huang, L. J. Fetters, and B. Ewen, *Macromolecules* **22**, 468 (1989).
7. D. Richter, B. Farago, L. J. Fetters, J. S. Huang, and B. Ewen, *Macromolecules* (1989), in press.
8. B. A. Khorramion and S. S. Stivala, *Polymer comm.* **27**, 184 (1986)
9. D. Richter, B. Stühn, B. Ewen, D. Neger, *Phys. Rev. Lett.* **58**, 2462 (1987).
10. M. Daoud, J. P. Cotton, *J. Phys. (Français)* **43**, 531 (1982).
11. G. Grest, K. Kremer, T. A. Witten, *Macromolecules* **20** 1376 (1987).
12. *sans in polymers*
13. F. Mezei, in *Lecture Notes in Physics*; F. Mezei, Ed.; Springer Verlag, Berlin Heidelberg, NY, 1980, Vol. 128.
14. E. Dubois-Violette, P. G. de Gennes, *Physics (Long Island City, NY)* **3**, 181 (1967).
15. P. G. de Gennes, *Physica (Utrecht)* **25**, 825 (1959).
16. A. Z. Akcasu, M. Benmouna, and C. C. Han, *Polymer*, **21**, 866 (1980).
17. L. K. Nicholson, J. S. Higgins, and J. B. Hayter, *Macromolecules*, **14**, 836 (1980).

18. A. Z. Akcasu, M. Benmouna, and B. Hammouda, *J. Chem. Phys.* **80**, 2762 (1984).
19. H. Benoit, G. Hadziioannou, *Macromolecules* **21**, 1449 (1988).
20. G. S. Grest, K. Kremer, S. T. Milner, and T. A. Witten, *Macromolecules* **22**, 1904 (1989).

MICROSTRUCTURE AND ISOTOPIC LABELING EFFECTS ON THE MISCIBILITY OF
POLYBUTADIENE BLENDS STUDIED BY THE SMALL-ANGLE NEUTRON SCATTERING TECHNIQUE

CHARLES C. HAN*, HIROKAZU HASEGAWA AND TAKEJI HASHIMOTO**, I. GLEN HARGIS AND
S. L. AGGARWAL***

*Firstauthor Polymers Division, National Institute of Standards and
Technology, Gaithersburg, MD. 20899

**Nextauthor Department of Polymer Chemistry, Faculty of Engineering, Kyoto
University, Kyoto 606, Japan

***Nextauthor Research Division, Gen Corp, Akron, Ohio 44305

ABSTRACT

Deuterated polybutadiene and protonated polybutadiene (PBD/PBH) blends with various microstructures have been studied by the small-angle neutron scattering experiments. Correlation length, ξ , zero-wavenumber structure factor, $S(q=0)$, and interaction parameter, χ_{blend} have been obtained. All PBD/PBH blends exhibit UCST behavior. With the use of random copolymer theory, the interaction parameter, χ_{blend} , has been successfully separated into χ_1 , χ_2 and χ_3 which are interaction parameters between the same isotope labeled 1,2-unit and 1,4-unit, opposite isotope labeled 1,2-unit and 1,4-unit, and opposite isotope labeled 1,2-unit with 1,2-unit or 1,4-unit with 1,4-unit, respectively.

INTRODUCTION

Polybutadiene blends of various microstructures are widely used in the rubber industry to tailor the properties to applications⁽¹⁾. Such blends offer an ideal system to study the fundamentals of binary interaction parameters of butadiene monomers with different microstructures.

Small angle neutron scattering (SANS) should be the tool to use to study this microstructure effect.⁽²⁾ Unfortunately, the deuterium labelling of one of the components which is needed for SANS introduces a repulsive interaction⁽³⁾ between the two components. This has prevented a straightforward measurement of the binary interaction parameter, χ , between a 1,2-unit and a 1,4-unit.

In this paper, an attempt has been made to separate the isotope effect from the microstructure effect through a systematic SANS study of blends of deuterated polybutadiene (PBD) and protonated polybutadiene (PBH) with various vinyl content. Random copolymer theory⁽⁴⁻⁶⁾ was used to carry out this separation. Reasonable results have been obtained using this analysis scheme indicating that the ten Brinke, Karasz and MacKnight⁽⁴⁾ calculation works well for the PBD/PBH blends.

EXPERIMENTAL

A deuterated polybutadiene, VBRD6 (with 63% 1,2-content, $M_n=134 \times 10^3$ and $M_w/M_n=2.0$) and a protonated butadiene, VBRN6 (with 68% 1,2-content, $M_n=135 \times 10^3$, and $M_w/M_n=1.8$), were synthesized by one of the authors (I.G. Hargis from Gen Corp) for this study. Other samples, CisBR7k (7% 1,2-content, $M_n=6.9 \times 10^3$ and $M_w/M_n=1.5$), CisBR150k (8% 1,2-content, $M_n=145 \times 10^3$ and $M_w/M_n=1.8$), H-19 (PBD 28% 1,2-content, $M_n=71 \times 10^3$, $M_w/M_n=1.0$) and H-16 (40% 1,2-content, $M_n=281 \times 10^3$, $M_w/M_n=1.01$) were prepared by anionic polymerization.

Blends specimens were prepared by dissolving polymers in toluene and then cast (from approximately 5% concentration solution) into films. These polymer films were thoroughly dried in vacuum at room temperature for at least one day. Small angle neutron scattering experiments were carried out at the

SANS facility of the NIST-reactor. The instrument has been described elsewhere⁽⁷⁾. In this study, the focusing geometry with 6Å neutron wavelength was used. Absolute scattering intensity for each specimen was obtained through use of a secondary standard of dry silica gel. A copper heating block was used to control the specimen temperature to within 0.3°C of desired temperature during measurement. Most specimens were measured between room temperature and 180°C at either 20°C or 30°C intervals.

RESULTS AND DISCUSSIONS

A. Data Analysis:

All SANS data are analyzed with non-linear regression fitting routine⁽²⁾ according to the Random Phase Approximation calculation of deGennes⁽⁸⁾, polydispersity has been incorporated.⁽⁹⁾

In all non-linear regression fitting for SANS data, three adjustable parameters, a single statistical segment length, b , an interaction parameter, χ/v_0 , and a baseline value, were used. The interaction parameter, χ/v_0 has thus been obtained for various compositions and temperatures for the series of specimens.

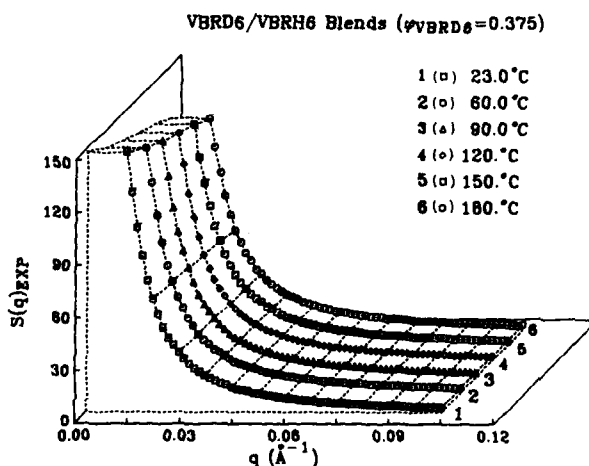


Figure 1

The static structure factors from SANS experiments for VBRD6/VBRH6 with $\phi_{VBRD6}=0.375$ at various temperatures are shown in Figure 1 together with the best fitted lines according to the RPA calculation. In Figure 2, fitted results of χ , $S(q=0)^{-1}$ and ξ^{-2} for the VBRD6/CisBR7k blend at $\phi_{VBRD6}=0.477$ are plotted vs. $1/T$. A long extrapolation is required in order to obtain the spinodal temperature, T_s , therefore, the value obtained may not be very accurate. Nevertheless, with the help of simultaneous extrapolations of 3 sets of data, reasonable results can be obtained.

CisBR7k and CisBR150K are quite different in molecular weight but very similar in microstructure. The χ_s value of the VBRD6/CisBR150K blend at $\phi_{\text{VBRD6}}=0.477$ was also calculated and is indicated in Figure 2 by broken line B. If we neglect the molecular weight difference and the small microstructure difference, we can assume the VBRD6/CisBR150K blend has the same χ value as the VBRD6/CisBR7k blend. In this case, all the χ values are above the χ_s at all temperatures below ca 600°C. Then phase separation is certainly expected for VBRD6/CisBR150k series at room temperature, which is consistent with our observation.

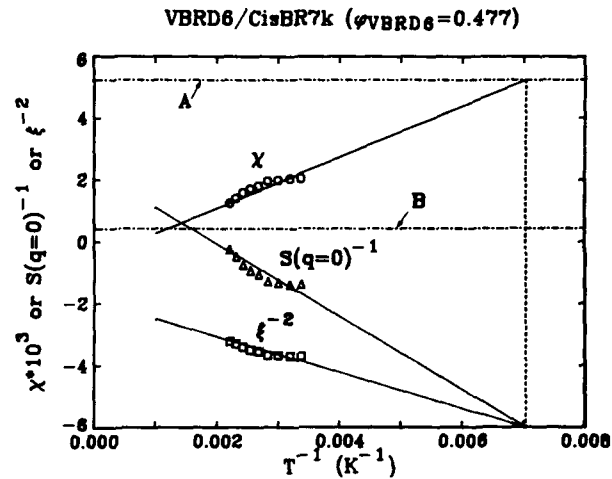


Figure 2

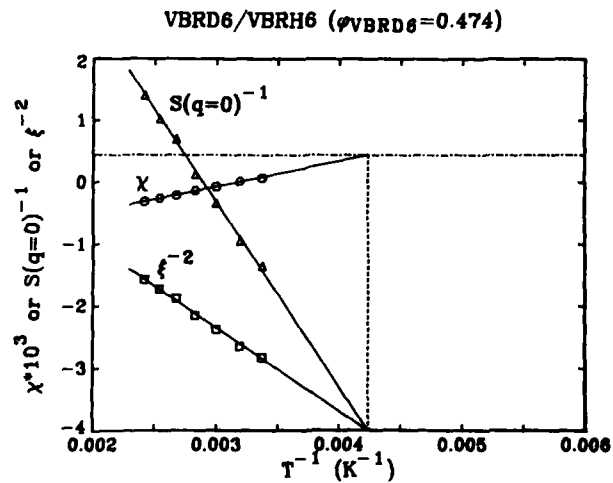


Figure 3

In Figure 3, a similar plot for the VBRD6/VBRH6 is displayed. It should be noted that all the χ values obtained for VBRD6/CisBR7k are positive as indicated in Figure 2. On the other hand, some χ values obtained for VBRD6/VBRH6 and indicated in Figure 3 are negative which would suggest the existence of a "copolymer effect" as will be discussed as follows.

In order to understand the phase behavior studied by SANS experiment, both isotope-effect⁽³⁾ and microstructure-effect have to be properly accounted for. If we define deuterated 1,2-butadiene, deuterated 1,4-butadiene, protonated 1,2-butadiene and protonated 1,4-butadiene monomers as A, B, C and D respectively, then, for a blend of A-B copolymer with C-D copolymer, the free energy of mixing can be written as:

$$\frac{\Delta F}{RT} = (\phi_1/N_1)\ln \phi_1 + (\phi_2/N_2)\ln \phi_2 + \phi_1\phi_2 \chi_{blend} \quad (1)$$

with $\chi_{blend} = xy \chi_{AC} + (1-x)y \chi_{BC} + x(1-y) \chi_{AD}$

$$+ (1-x)(1-y) \chi_{BD} - x(1-x) \chi_{AB} - y(1-y) \chi_{CD} \quad (2)$$

where x is the number fraction of A in A-B copolymer and y is the number fraction of C in C-D copolymer. x and y refer to the number fraction of repeat units in the lattice theory of blends. We equated number fractions to volume fraction for this work.

By neglecting the difference between trans and cis-1,4 polybutadiene and assuming polybutadiene is a simple random copolymer, we should be able to obtain all six χ -parameters if we have six sets of data for blends with different microstructure variations. Since we only have 3 sets of data at this time together with a set of literature value by Bates et al⁽³⁾, we have decided to make a few assumptions and compare with theoretical predictions at least semi-quantitatively. I should point out that the following assumptions can be removed when more experimental data becomes available.

First, let us assume $\chi_{AC} = \chi_{BD} \equiv \chi_3$. This assumption implies the isotope-effect is identical between 1,2 pairs and between 1,4 pairs of two different isotopes. This may be the most severe assumption, but still this may not be too bad without actually knowing what is the exact intermolecular potential energy function between two isotopically labeled microstructure pairs. Once we have made the above assumption, we can then assume $\chi_{AB} = \chi_{CD} \equiv \chi_1$ and $\chi_{AD} = \chi_{BC} \equiv \chi_2$. These two assumptions implies that pure microstructure effect (interaction between either protonated or deuterated 1,2 & 1,4 butadiene pairs) is independent of isotope used and then the cross (isotope labeled) microstructure effect is independent of which one of the two monomers is labeled. Actually, these two assumptions are implied from the previous assumption that isotope effects are identical between 1,2 pairs and 1,4 pairs.

Since χ has a $1/T$ dependence, the measured value of χ for VBRD6/VBRH6, VBRD6/CisBR7k and Bates et al. blends can be expressed as follows with molar volume of 61.1 cm³/mol for VBRD6 and VBRH6 and 60.4 cm³/mol for CisBR7k:

$$\chi(\text{VBRD6/VBRH6}) = -7.46 \times 10^{-4} + 0.248/T \quad (\phi=0.278) \quad (3a)$$

$$\chi(\text{VBRD6/CisBR7k}) = -2.57 \times 10^{-4} + 0.758/T \quad (\phi=0.24) \quad (3b)$$

$$\chi(\text{Bates et al.}) = 2.3 \times 10^{-4} + 0.326/T \quad (\phi=0.31) \quad (3c)$$

If we neglect the small composition dependence used in the above three sets of blends, then χ_1 , χ_2 and χ_3 can be obtained from eq.3 together with eq.2. Values of χ_1 , χ_2 and χ_3 thus obtained are displayed in Figure 4.

Finally, in Figure 5, χ values obtained from SANS measurements of H-19/H-16 blend are displayed as a function of $1/T$, together with the predicted values in solid line which is calculated according to χ_1 , χ_2 and χ_3 values obtained before. Although the predicted numbers are slightly lower than the

experimental values, considering the assumptions and errors involved in the calculation, in this analysis, in sample preparation, in compositions used (H-19/H-16 blend has $\phi_{PBD}=0.757$) and in SANS experiments, this agreement may be considered to be excellent.

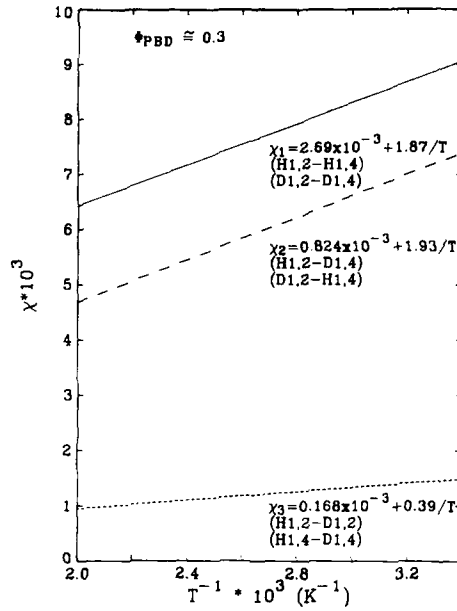


Figure 4

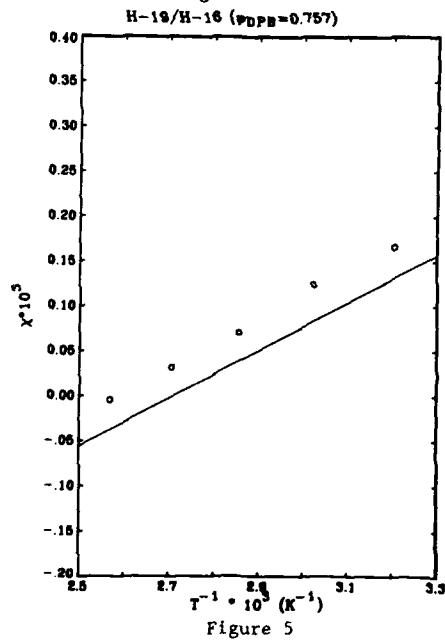


Figure 5

CONCLUSION

In this work, we have presented results for deuterated polybutadiene/protonated polybutadiene blends with various microstructures and compositions. We found that the static structure factor $S(q)$ from the SANS experiments for miscible (at room temperature) blends can be well represented by the RPA calculation. From that analysis the interaction parameter, χ/v_0 , correlation length, ξ , and zero wave number structure factor, $S(q=0)$, can be extracted. The spinodal temperature can be obtained through extrapolation. Phase diagrams for these polymer blends can be constructed, and they all show UCST behavior.

Interaction parameter, χ_{blend} , of a blend at any given composition can be represented by a simple $A + B/T$ functional form. If we neglect the molecular weight dependence of χ , then the χ_{blend} can be separated into three interaction terms. These three interaction parameters χ_1 , χ_2 and χ_3 represent binary interaction between the same isotopic labeled (with deuterated or protonated), 1,2-unit and 1,4-unit, opposite isotopic labeled 1,2-unit and 1,4-unit, and opposite isotopic labeled 1,2-unit and 1,2-unit or 1,4-unit and 1,4-unit, respectively. Reasonable success has been demonstrated by comparing the measured χ_{blend} with predicted χ_{blend} for an independent set of PBD/PBH blend.

REFERENCES

- [1] Handbook of elastomers, edited by A. K. Bhowmick and H. L. Stephens, Marcel Dekker, Inc., N.Y., N.Y. (1988).
- [2] For example: Shibayama, M.; Yang, H.; Stein, R. S.; and Han, C. C., *Macromolecules*, 1985, 18, 2179.
- [3] Bates, F. S.; Dierker, S. B.; and Wignall, G. D., *Macromolecules*, 1986, 19, 1938.
- [4] ten Brinke, G.; Karasz, F. E.; and MacKnight, W. J., *Macromolecules*, 1983, 16, 1827.
- [5] Kambour, R. P.; Bendler, J. T.; and Bopp, R. C. *Macromolecules*, 1983, 16, 753.
- [6] Paul, D. R.; and Barlow, J. W. *Polymer*, 1984, 25, 487.
- [7] Glinka, C. J.; Rowe, J. M.; and LaRock, J. G.; *J. Appl. Cryst.*, 1986, 19, 427.
- [8] de Gennes, P.-G. "Scaling Concepts in Polymer Physics", Cornell University Press, N.Y. (1979).
- [9] Sakurai, S., Hasegawa, H., Hashimoto, T.; Hargis, I. G., Aggarwal, S. L. and Han, C. C., *Macromolecules* (in press).

CHARACTERIZATION OF MOLECULAR NETWORK OF THERMOSETS
USING NEUTRON SCATTERING

WEN-LI WU

Polymers Division, Materials Science and Engineering Laboratory, National
Institute of Standards and Technology, Gaithersburg, Md 20899

ABSTRACT

Neutron scattering measurements were conducted to investigate the conformation of the molecular networks in epoxies. Emphasis was placed on the changes in the scattering intensity resulting from curing. Experimental results on homopolymerized epoxy as well as a theoretical interpretation of the results are presented.

INTRODUCTION

Neutron scattering has been used extensively to study the chain conformation of thermoplastics in bulk and in solution. The scheme used is to blend deuterium labeled chains with protonated chains. For thermosets, on the other hand, the application of this neutron technique to characterize the conformation of an average network is not straightforward since it is difficult to implant a few deuterium labeled networks amidst protonated ones without encountering the problems well known in the field of interpenetrated networks. The term network conformation refers to the spatial correlation among all the topological or directly connected neighbors in an average network. One can blend some deuterium labeled monomers into unlabeled monomers and perform neutron scattering measurements on the cured specimen. However, the scattering results of such samples contain no information regarding the average conformation of the network. This is because the distribution of all the labeled monomers stays random regardless of the curing process, i.e., the labeled monomers will not selectively crosslink among themselves. Therefore, within an average network the disposition of labeled and unlabeled monomers must be random, and no network information can be extracted from a scattering measurement.

The first successful attempt to use neutron scattering to investigate the network structure in thermosets was made by Wu and Bauer¹. The basic approach of their work is to have all of the monomer partially deuterated. The material after cure or crosslinking resembles, by a linear chain analogue, a multiple block copolymer with alternating deuterated and protonated blocks. The early neutron scattering results of partially deuterated diglycidyl ether of bisphenol A (DGEBA) cured with Jeffamines* can be fitted quantitatively using a random phase approximation (RPA) scheme¹. However, the presence of a flexible chain with an amine group on each end as the curing agent tends to complicate the experimental results; in the uncured mixtures the correlation hole peak from the partially deuterated DGEBA almost disappears due to the dilution effect of the amine chains. After cure these amine chains are connected with the deuterated DGEBA molecules. However, the interpretation

*Certain commercial materials and equipment are identified in this paper in order to specify adequately the experimental procedure. In no case does such identification imply recommendation or endorsement by the National Institute of Standards and Technology, nor does it imply necessarily the best available for the purpose.

of the scattering results is also complicated due to the presence of the amine chains, e.g. the protonated portion in the network now denotes a combination of the amine and the protonated portion of the DGEBA. Although the fit between the calculation and the neutron scattering results on Jeffamine/DGEBA is quite satisfactory¹, some uncertainty concerning the viability of neutron scattering for elucidating the network structure still remains. In other words, if the starting monomers give rise to a clear correlation hole peak in scattering intensity, will crosslinking result in a significant change in this peak?

EXPERIMENTAL

To answer this question, the following experiment was conducted. The partially deuterated DGEBA (*d*-DGEBA) was cured without any amines incorporated into the network. It is well known that homopolymerization of DGEBA will occur at elevated temperature especially in the presence of catalysts². Piperidine (5 pph) was added to *d*-DGEBA at room temperature and served as a catalyst. The material was cured at 160°C for 20 hrs. Infrared results on the amplitude of the epoxide band at 915 cm^{-1} indicated that the cure was almost complete.

Neutron scattering measurements were conducted with a 3-axis diffractometer and the small angle neutron scattering (SANS) instrument at the NIST** reactor facilities. The results for the monomer and the cured sample are given in Figures 1a and 1b for the diffractometer and the SANS measurements respectively. The thicknesses for both samples were identical (2 mm), and the apertures for these two measurements were also kept the same. Consequently, a direct comparison can be made between these two scattering curves.

RESULTS AND DISCUSSION

The diffractometer results (figure 1a) reveal that the cure of the DGEBA monomer results in (a) an enhancement in the peak intensity, (b) a downshift of the peak position, and (c) a sharpening of the peak.

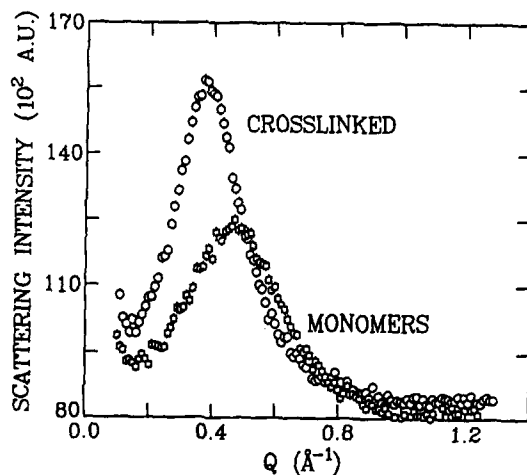


Figure 1a: Neutron diffractometer results of the monomers and the cured material of partially deuterated diglycidyl ether of bisphenol A.

The SANS results (figure 1b) indicate that the scattering intensity for both the uncured and the cured samples is virtually zero except in the region of q less than $.015 \text{ \AA}^{-1}$. Impurities are the likely causes for the scattering intensity in this low q region. The flat background level of 0.4 cm^{-1} in figure 1b is from the incoherent scattering.

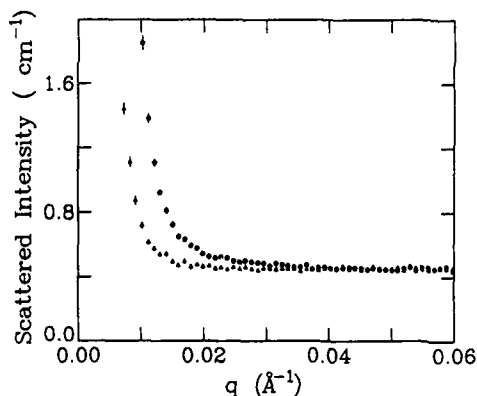


Figure 1b: Small angle neutron scattering result of the monomer (Δ) and the cured material (\bullet).

The downshift of the peak position upon cure can be understood within the context of RPA theory (RPA)³, and this point will be addressed as follows. The legitimacy of applying RPA theory to polymer networks has been established recently⁴; the fact that the number of spatial neighbors of an average network is finite in thermosets has no consequence on the use of the RPA result. Figure 2 shows the results of a RPA calculation of the DGEBA monomer, a dimer, a tetramer of four-arm star type and a virtual monomer defined below. For the DGEBA monomer the central portion is deuterated; it can be considered as a H-D-H triblock polymer. Accordingly the dimer can be represented as H-D-H-H-D-H and so on. Due to the formation of the H-H block upon cure as shown in the dimer structure, a virtual monomer is constructed as H-H-D which has the same size or molecular weight as the DGEBA monomer. The formation of the H-H block

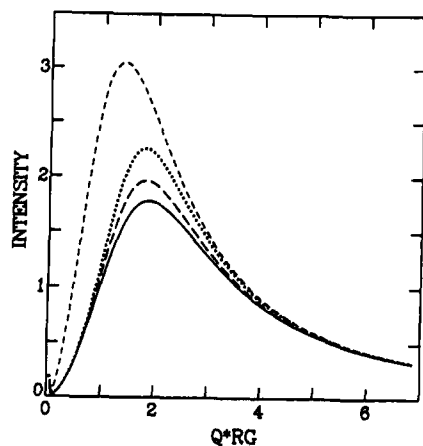


Figure 2: Theoretical results of the scattering intensities of a d-DGEBA monomer (solid line); a dimer (long dashed line); a tetramer (dotted line); and a virtual monomer (short dashed line). All the intensities were normalized to one molar volume.

apparently causes a downshift of the peak. As the molecular weight of the cluster increases during curing the population of an isolated H block dwindles, and toward the end of cure one expects that the peak position will shift to that of the virtual monomer. The results in figure 2 were based on a Gaussian chain model and all the intensities were normalized to one monomer unit. Based on this calculation it is clear that the downshift of the peak position and the increase in the scattering intensity can be understood, at least qualitatively, by a simple network formation process. As to the sharpening of the peak a more detailed model will be needed. The absence of the peak sharpening in the RPA results is apparent by comparing figure 1a to figure 2; no cross-over of the scattering intensities occurs in the RPA results while such a cross-over is present in the neutron data.

For epoxies, RPA calculations based on a simplified network model have been carried out¹. The results indicated that the peak widths depend strongly on the rigidity as well as on the molecular weight of the network. As shown in Figure 1a, the half widths of the peaks are 0.25\AA^{-1} and 0.36\AA^{-1} for the cured sample and monomer, respectively. In addition, the ratios of the half-widths to the peak positions are 0.69 and 0.76 for the cured and the uncured materials, respectively. Sharpening of the scattering peak has been explained by the formation of a network with certain spatial regularities such as the localization of the junctions.

CONCLUSIONS

In summary, the crosslinking process in thermosets results in pronounced changes in the scattering behaviors. These changes can be explained in terms of a simple network formation and an enhancement of the inter-monomer correlation among the topological neighbors.

REFERENCES

- (1) W. Wu and B. J. Bauer, *Polym. Commun.* **26**: 39 (1985), *Polymer*, **27**: 169 (1986).
- (2) C. K. Riew, E. H. Rowe and A. R. Siebert, *Advances in Chemistry Series (ACS)*, No. 154, 326 (1976).
- (3) L. Leibler, *Macromolecules* **13**: 1602 (1980).
- (4) W. Wu, submitted to *Macromolecules*.

SHEAR INDUCED PHASE BEHAVIOR OF POLYMER BLENDS
BY SMALL ANGLE NEUTRON SCATTERING

ALAN I. NAKATANI, HONGDOO KIM, and CHARLES C. HAN
National Institute of Standards and Technology, Polymers Division,
Gaithersburg, MD 20899

ABSTRACT

The phase behavior of polymer blends and solutions can be changed dramatically by a flow field using a variety of flow geometries. Unlike simple binary fluids which require extremely high shear rates to produce only small shifts in the phase boundary, polymer phase behavior may be influenced by as much as 10 degrees with the application of much lower shear rates. However, there is a large body of conflicting data concerning the nature of these shear effects in polymers.

Here we report on the effects of shear on the phase behavior of polymer blends by small angle neutron scattering (SANS). Experiments were conducted using a specially constructed, concentric cylinder apparatus for in situ studies of concentrated polymer solutions and melts. Two separate systems will be discussed: 1) a blend of polystyrene and polybutadiene. 2) a blend of polystyrene and poly(vinylmethylether). Both systems exhibit shifts in the phase behavior which indicate shear induced mixing in agreement with previous results obtained by other techniques. These results will be interpreted within the context of existing theories of shear induced phase behavior.

INTRODUCTION

In this study, we report on the shear behavior of two different homopolymer blends utilizing small angle neutron scattering (SANS). One of the blends consists of a high molecular weight deuterated polystyrene (PSD) ($M_w = 4.4 \times 10^5$) blended with a high molecular weight poly(vinylmethylether) (PVME) ($M_w = 1.8 \times 10^6$) and exhibits lower critical solution temperature (LCST) behavior. The second blend is composed of a low molecular weight deuterated polystyrene ($M_w = 1.0 \times 10^3$) blended with a low molecular weight polybutadiene (PB) ($M_w = 4.5 \times 10^3$) and displays upper critical solution temperature (UCST) behavior. The SANS data will be analyzed using treatments which have been successful for the analysis of quiescent polymer blends. An attempt will also be made to analyze the data based on the simple rotatory diffusion of the concentration fluctuations under the influence of shear as well as the mode-mode coupling treatment of Ferrell [1] and Kawasaki [2-4] for the relaxation of concentration fluctuations.

Investigations of shear effects on the critical behavior of polymer blends and solutions have grown steadily in recent years [5,6]. The data is divided between reports of shear induced mixing and shear induced phase separation. Most studies report only shifts in the cloud point obtained from turbidity changes. A few quantitative light scattering studies have also been reported but due to wavelength limitations, these studies probe concentration fluctuations on the order of 1000 Å and examine the two phase region and the so-called weak shear limit. Examination of the fluctuations on a much smaller size scale in the one phase region and strong shear limits is desirable for a microscopic understanding of the problem. The much smaller wavelength (10Å) of incident neutron radiation allows one to probe the desired size scales. However, SANS experiments are complicated by the fact that no theories exist for the structure factor of a blend of two homopolymers under the influence of a shear field.

DeGennes has shown [7] that by using a random phase approximation and assuming polymers can be modelled as a mean-field system, the scattering structure factor for a binary polymer system is as follows:

$$1/S(q) = [\phi_A N_A S_A(q)]^{-1} + [\phi_B N_B S_B(q)]^{-1} - 2\chi \quad (1)$$

where $S_i(q)$ is the single chain structure factor, $q = (4\pi/\lambda)\sin(\theta/2)$ is the magnitude of the scattering vector, χ = monomer/monomer interaction parameter, ϕ_i = volume fraction of component i , and N_i = degree of polymerization of component i . The concentration correlation length, ξ , is defined as:

$$\xi^2 = [v_o/36(\chi_s - \chi)] [(b_A^2/v_A \phi_A) + (b_B^2/v_B \phi_B)]^{-1} \quad (2)$$

where b_i = statistical segment length of monomer i , v_o = molar volume of a reference cell, v_i = molar volume of component i and χ_s is the value of the interaction parameter at the spinodal. In the vicinity of the phase separation temperature, T_c , the correlation length has the following scaling form often observed in critical phenomena:

$$\xi(\phi) \propto |T - T_c|^{-\nu} \quad (3)$$

where $\nu = 1/2$ for a system which follows mean-field behavior. Attempts to develop expressions for the scattering structure factor of polymer systems under the influence of shear have been made, however none are applicable to the polymer blends we have studied.

MATERIALS

Polystyrene- d_8 (PSD) for this experiment was prepared by anionic polymerization of styrene- d_8 in benzene with butyllithium as an initiator using standard techniques [8]. The PSD was characterized by gel permeation chromatography showing $M_w = 4.4 \times 10^5$ and $M_w/M_n = 1.28$. Poly(vinyl methyl ether) (PVME) was polymerized by cationic polymerization in toluene with BF_3 -ethyl ether complex as an initiator [9]. The polymer was fractionated in heptane/toluene and the fraction utilized in these experiments had a $M_w = 1.8 \times 10^5$ and $M_w/M_n = 1.76$ as determined by GPC. The PSD/PVME blend composition was 20:80 by weight. This composition represents the critical composition for a PSD/PVME blend based on the data of Han et al. [10]. All samples were prepared by dissolving the polymers in toluene and then pouring the solution into the bottom of the rotor and removing the toluene by vacuum in a vacuum oven at 80°C for 48 hours.

Polystyrene- d_8 (PSD) for the PSD/PB blend was also prepared by anionic polymerization techniques described above. The PSD was characterized by gel permeation chromatography showing $M_w = 1.0 \times 10^5$ and $M_w/M_n = 1.04$. Polybutadiene (PB) was purchased from Scientific Polymer Products, Inc. [11] with a nominal molecular weight of 4.5×10^5 . The sample composition was 77:23 PSD/PB by weight.

RESULTS

The shear apparatus used in this experiment has been described in detail elsewhere [12]. SANS results were obtained using an incident wavelength of 9 Å at the NIST reactor. Data was collected over a two-dimensional detector and corrected for dark current intensity due to electronic and background neutron noise. Sector averages of the scattered intensity parallel and perpendicular to the flow (horizontal and vertical) were obtained in $\pm 10^\circ$ sectors. Absolute intensity calibration was done with a dry silica gel as a secondary standard, calibrated in terms of a primary vanadium standard.

For the analysis of the data we first fit the zero shear scattering intensities with a non-linear regression routine to the deGennes scattering function for binary polymer blends. From Equation 3, plots of ξ^{-2} versus $1/T$ were made for the parallel and perpendicular directions. Extrapolation

to infinite correlation length at the different shear rates yields the spinodal temperature.

The PSD/PVME blend was studied between 100°C and 142.5°C at shear rates between 0.02 s⁻¹ and 1.30 s⁻¹. The optical cloud point at zero shear was 140°C. The estimated spinodal temperatures at zero shear parallel and perpendicular to flow are 140.5°C and 140.7°C respectively. At constant temperature, the shear rate dependence of the scattering profiles show significant differences. In the one phase region (below 140°C), parallel to flow, the scattering intensity at low q decreases with increasing shear rate. Perpendicular to the flow direction, the scattering profiles are virtually independent of shear rate. An example of the shear rate dependence is shown in Figure 1 for 137.5°C.

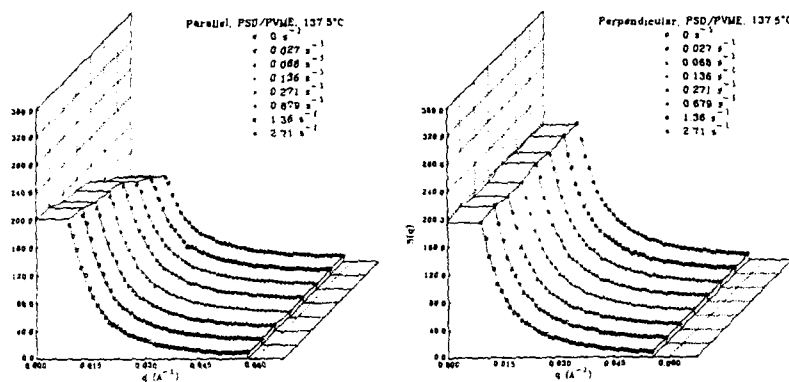


Figure 1a

Figure 1b

The solid lines in the figures represent the RPA fits to the data. However, the interpretation of the parameters obtained by RPA fits for the sheared data is subject to debate. Instead values of ξ were extracted from the low q portion of $S(q)^{-1}$ versus q^2 plots according to the Ornstein-Zernike relation. From the values of ξ , the estimated spinodal temperatures increase with increasing shear rate in the direction parallel to flow, corresponding to a shear induced mixing. At the highest shear rate examined (1.30 s⁻¹), the increase in the spinodal temperature is approximately 8°C. Perpendicular to flow no systematic change in the apparent spinodal temperature is observed. These results indicate that with the application of shear, there is a shear induced mixing effect consistent with mixing behavior observed previously by other investigators on PS/PVME [13-15] and is also consistent with the shear induced mixing behavior observed by SANS for a polymer/polymer/solvent system [16].

The scattering profiles for the PSD/PB blend were obtained between 50°C and 80°C and at shear rates ranging between 50 and 200 s⁻¹. The zero shear cloud point was determined to be approximately 40°C by optical methods. In the one phase region, from 80°C down to 45°C, there is virtually no change in the scattering profiles as a function of shear rate in either the parallel or perpendicular directions. Below 45°C, the scattering intensity at low q decreases with increasing shear rate parallel to the flow direction.

The plots of ξ^{-2} versus $1/T$ yield apparent spinodal temperatures of 38.5°C and 38.8°C in the parallel and perpendicular directions respectively at zero shear rate. The apparent spinodal temperatures as a function of shear rate can not be obtained quantitatively, due to curvature in the ξ^{-2} versus $1/T$ plots. This is an indication of the inconsistency in using the Ornstein-Zernike analysis for extracting ξ and using a mean field exponent

of 1/2 to extrapolate the spinodal temperature. The apparent good fits to the RPA function or the Ornstein-Zernike function alone are insufficient for testing this procedure. However, the decrease in scattering intensity as a function of shear rate implies that a shear stabilization of this blend is also occurring.

DISCUSSION

For each system at constant temperature, a decrease of scattering intensity at low q was observed which implies the suppression of large fluctuations. A cutoff value, q_s , is taken to be the value of q where the zero shear and sheared structure factors begin to diverge. As the shear rate increases, q_s also increases. Perpendicular to flow, no changes in the scattering behavior were observed. We will analyze this phenomena by (1) a rotatory relaxation picture and (2) the dynamic mode-mode coupling theory.

For rotatory diffusion of a sphere in solution the following relation holds [17]:

$$\tau = \theta^{-1} = 8\pi\eta R^3/k_B T \quad (4)$$

where τ is a rotational relaxation time, θ is the rotational diffusion coefficient, η is the solution viscosity, R is the radius of the sphere, k_B is Boltzmann's constant and T is the temperature. For the case of concentration fluctuations under the influence of shear, at a given shear rate $\dot{\gamma}$, concentration fluctuations with $\tau > 1/\dot{\gamma}$ (large R), will be suppressed. The suppression of these large fluctuations below q_s is related to $\dot{\gamma}$ as follows:

$$\tau = \dot{\gamma}^{-1} = (8\pi\eta/k_B T q_s^3) \quad (5)$$

The viscosity and temperature dependence of the experimental q_s values were analyzed by plotting $\log q_s - (1/3)\log \eta + (1/3)\log T$ versus $\log \dot{\gamma}$ and $\log q_s$ versus $\log(\eta\dot{\gamma}/T)$. From Equation 5, plots of this form should give a slope of 1/3 and an intercept value of $(1/3)\log(8\pi/k_B) = 5.753$. Since the viscosity of the PSD/PVME blend is non-Newtonian, the experimentally determined values of the blend viscosity were used, while for the PSD/PB blend the zero shear values of the viscosity were utilized. Data for both the PSD/PVME blend and the PSD/PB blend were combined in the $\log q_s - (1/3)\log \eta + (1/3)\log T$ versus $\log \dot{\gamma}$ plot and shown in Figure 2. A single slope value was determined by linear regression analysis to be 0.332 with a standard deviation of 0.006 using all data points. The intercept value was determined to be 5.71 with a standard deviation of 0.01. The plot of $\log q_s$ versus $\log(\eta\dot{\gamma}/T)$ is shown in Figure 3. Linear regression analysis of the plot, using all data points gives a slope of 0.333 with a standard deviation of 0.015 and an intercept value of 5.71 with a standard deviation of 0.03. The good quantitative agreement between the shear rate dependence of the experimentally measured q_s values and the predicted shear rate dependence based on the rotatory diffusion model is taken as evidence in support of this treatment.

From the mode-mode coupling analysis of Ferrell [1] and Kawasaki [2-4], the decay rate, Γ , of fluctuations with wavenumber q may be written as a sum of hydrodynamic and molecular contributions:

$$\Gamma_q = \Gamma_{q, mol} + \Gamma_{q, hyd} \quad (6)$$

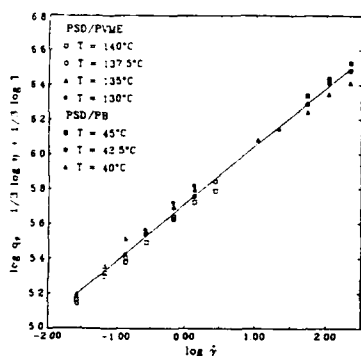


Figure 2

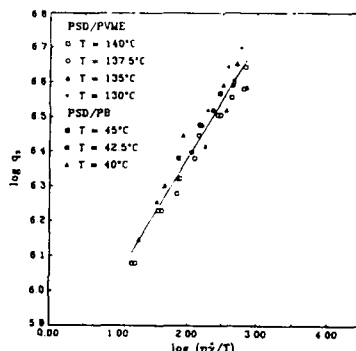


Figure 3

If we first neglect the molecular contribution to the relaxation process the hydrodynamic term is defined as $(k_B T q^2 / 6\pi\eta\xi)$ for $q\xi < 1$ and $(k_B T q^3 / 16\eta)$ for $q\xi > 1$. The shear rate dependence of the longest wavelength, q_c^{-1} , not affected by shear rate is therefore given as:

$$q_c = (6\pi\eta\xi/k_B T)^{1/2} \dot{\gamma}^{1/2} \quad \text{for } q_c \xi < 1 \quad (7a)$$

$$= (16\eta/k_B T)^{1/3} \dot{\gamma}^{1/3} \quad \text{for } q_c \xi > 1$$

(7b)

Equating the experimentally determined q_s to q_c , we would expect in the strong shear limit, a slope of 1/3 and an intercept of $(1/3)\log(16/k_B) = 5.688$ for the plots shown in Figures 3 and 4. These values are entirely consistent with those determined from the experimental data, supporting the mode-mode coupling analysis with the hydrodynamic term dominating the molecular term. Hashimoto [18,19] and Onuki [20] have argued that the molecular contribution to the relaxation should be the dominant process and predict that in the strong shear limit, q_c should vary with a $\dot{\gamma}^{1/4}$ power dependence. Our data does not support this prediction, however Hashimoto and Onuki have argued from the standpoint of a blend in the two phase region while our data is taken in the one phase region of the phase diagram.

CONCLUSIONS

The small angle neutron scattering behavior of two different bulk homopolymer blends, PSD/PVME and PSD/PB, were examined. The data was analyzed in two different fashions. The first analysis method presumes the validity of the Ornstein-Zernike relation for binary polymer mixtures under shear to obtain values for the concentration correlation length, ξ . By plotting ξ^{-2} versus $1/T$ values for the spinodal temperature as a function of shear rate were obtained. The PSD/PVME blend exhibited a substantial increase in the spinodal temperature as a function of shear rate, while quantitative determination of the shift in the spinodal temperature of the PSD/PB blend was not possible by this analysis. In both cases, the data indicates a shear induced mixing effect.

The second method of analysis does not rely on any form for the structure factor, and attempts to present a physical picture for the effect of shear on a blend of two homopolymers. Analyses following two different models were presented. The first based on the rotatory diffusion of fluctuations and the second based on the mode-mode coupling analysis of

Ferrell and Kawasaki. At a given shear rate, a critical cutoff q value, q_c , can be determined from the scattering profiles. Fluctuations with sizes larger than $1/q_c$ are presumed to be suppressed by the imposed shear field. The relation between the experimentally determined q_c values as function of shear rate is in good agreement with both the rotatory diffusion and mode-mode coupling analyses. Both analyses also lead to the conclusion that shear induced mixing behavior is observed in both the blend systems examined.

REFERENCES

- 1) Ferrell, R., Phys. Rev. Lett., 1970, 24, 1122.
- 2) Kawasaki, K.; "Phase Transitions and Critical Phenomena", ed. by Domb, C. and Green, M.S., Vol. 5a, Academic Press, New York, 1976.
- 3) Onuki, A.; Yamazaki, K.; Kawasaki, K. Ann. Phys. 1981, 131, 217.
- 4) Imaeda, T.; Onuki, A.; Kawasaki, K. Prog. Theor. Phys. 1984, 71, 16.
- 5) Rangel-Nafaile, C.; Metzner, A. B.; Wissbrun, K. F. Macromolecules 1984, 17, 1187.
- 6) Tirrell, M.; Fluid Phase Equil. 1986, 30, 367.
- 7) deGennes, P. G. "Scaling Concepts in Polymer Physics" Cornell University Press, Ithaca, New York, 1979.
- 8) Matsushita, Y.; Furuhashi, H.; Choshi, H.; Noda, I.; Nagasawa, M., Fujimoto, T.; Han, C. C. Polymer J. 1982, 14, 489.
- 9) Bauer, B. J.; Hanly, B.; Muroga, Y. Polymer Commun. 1989, 30, 19.
- 10) Han, C.C.; Bauer, B. J.; Clark, J. C.; Muroga, Y.; Matsushita, Y.; Okada, M.; Tran-cong, Q.; Chang, T.; Sanchez, I. C. Polymer, 1988, 29, 2002.
- 11) Certain equipment, instruments or materials are identified in this paper in order to adequately specify the experimental details. Such identification does not imply recommendation by the National Institute of Standards and Technology nor does it imply the materials are necessarily the best available for the purpose.
- 12) Nakatani, A. I.; Kim, H.; Han, C. C. submitted to J. of Res. of NIST
- 13) Mazich, K. A.; Carr, S. H. J. Appl. Phys. 1983, 54, 5511.
- 14) Ajji, A.; Choplin, L.; Prud'homme, R. E. J. Polym. Sci. Polym. Phys. Ed. 1988, 26, 2279.
- 15) Cheikh Larbi, F. B.; Malone, M. F.; Winter, H. H.; Halary, J. L.; Leviet, M. H.; Monnerie, L. Macromolecules 1988, 21, 3532.
- 16) Nakatani, A. I.; Kim, H.; Takahashi, Y.; Han, C. C. Polym. Comm. 1989, 30, 143.
- 17) See for example: Tanford, C. "Physical Chemistry of Macromolecules". John Wiley and Sons, New York, 1961, pp 432-451.
- 18) Hashimoto, T.; Takebe, T.; Suehiro, S. Polymer J. 1986, 2, 123.
- 19) Hashimoto, T.; Takebe, T.; Suehiro, S. J. Chem. Phys. 1988, 88, 5874.
- 20) Onuki, A. J. Chem. Phys. 1986, 85, 1122.
- 21) Full manuscript is in preparation.

SURFACE ENRICHMENT AND EVAPORATION IN A POLYMER MIXTURE OF LONG AND SHORT CHAINS

RUSSELL J. COMPOSTO*, RICHARD S. STEIN*, GIAN P. FELCHER**, ABDELKADER MANSOUR** AND ALAMGIR KARIM**

*Polymer Research Institute, University of Massachusetts, Amherst, MA 01003
**Argonne National Laboratory, Argonne, IL 60439

ABSTRACT

Neutron reflectivity has been used to determine the concentration profile at the vacuum-polymer interface for a two polymer blend. To quantify surface enrichment and evaporation due to differences in chain length, we have measured the reflectivity of a mixture of short deuterated and long protonated polystyrene chains (DPS & PS), with a weight fraction of 0.5. When a mixture of DPS and PS chains of molecular weight 720 and 910k respectively were annealed, a small but measurable increase in asymptotic reflectivity occurred, coupled with a decrease of film thickness and scattering length density. This is indicative of surface enrichment and evaporation of the light chains (DPS). Ellipsometry studies confirmed that the short chains evaporated and its rate was established as a function of the temperature. Upon increasing the DPS molecular weight to 9600, the enrichment becomes considerably greater whilst the evaporation becomes negligible.

INTRODUCTION

Recent theories dealing with surface segregation in compatible polymer blends have focused on high molecular weight (polymeric) systems in which the entropy of mixing is quite small^[1]. Experiments^[2] with such systems involving binary mixtures of protonated and deuterated polymers have shown that at equilibrium there is a surface excess of deuterated molecules. This effect is predicted to be strongly driven by reduction of surface energy of the deuterated component-- purely entropic effects are calculated to produce surface enhancements only on the order of ca. 1%^[3,4]. However, the entropic reduction could be large and dominant over energetic effects such as deuteration, in blends of short chains (oligomer) and a polymer. This could result in surface enhancement of 10% or greater of the oligomer. By using neutron reflectivity, we have tried to observe such a segregation of deuterated oligomers to the vacuum-polymer interface in a mixture of deuterated oligomer and protonated polymer. The study has been conducted for two different molecular weights of the oligomer.

EXPERIMENTAL

To measure the thickness and reflectivity in blends of oligomeric deuterated polystyrene (DPS) and polymeric protonated polystyrene (PS) chains, films were made which consisted of a thick (~1000Å) layer on top of a silicon wafer. The film was prepared from a toluene solution of a DPS:PS blend by spin casting on a

silicon wafer. The molecular weight of the monodisperse polymers were: DPS (720), DPS(9600) and PS(910k).

The neutron reflectivity measurements were performed at the reflectometer POSY II at the Intense Pulsed Neutron Source at Argonne National Laboratory. In this technique^[5], a neutron beam of wavelength λ is reflected at a grazing angle θ from the sample's surface. The reflectivity is then measured as a function of the neutron momentum perpendicular to the surface; in vacuum, $k_z = 2\pi\sin\theta/\lambda$. The reflectivity R , is the optical transform of the average nuclear scattering amplitude (b) per unit volume (V), b/V as a function of the depth z from the surfaces. Thus R as a function of k_z determines the scattering amplitude profile from which the volume fraction profile is obtained.

SURFACE EVAPORATION

The first neutron reflection measurements were taken on a thin layer of a polymer blend deposited on a silicon substrate. The blend consisted of oligomeric DPS(720) and polymeric PS(910k); the weight fraction of the oligomer being 0.20. Upon annealing this mixture above the glass transition temperature at 187°C for times ranging from 70minutes to 48hours, it was deduced from the variation of the reflectivity profile, that the sample gradually lost the oligomeric(deuterated) component. To attain a better understanding of the devolatilization of the oligomers, a Rudolph AutoEL II® ellipsometer was used to measure systematically the time dependence of the thickness of polymer films during annealing. Using samples identical to that previously used for neutron reflection, the variation of the film thickness was observed as presented in Fig.1 for annealing temperatures of 130, 150 and 170°C. The glass transition temperature is estimated to be 69°C^[6]. At all temperatures, the film thickness decreases rapidly at first and then decreases much more slowly at longer times. Note that total evaporation of the short chains would result in a thickness ratio equal to 0.80. In order to see if total evaporation is possible, a sample was heated to 150°C for 12 days in a vacuum oven. The final film thickness ratio of 0.84 suggests that some residual oligomer may still be in the blend.

In order to model the evaporation of the oligomeric polystyrene, one needs to describe the diffusion of the short chains from below the surface (source) to the air-polymer surface (sink). One complication of this diffusion process is that upon evaporation of the oligomer, the glass transition temperature (T_g) of the blend changes from its initial value of -69°C towards that of the 910k PS chains-100°C. The resulting decrease in the reduced temperature $T-T_g$ will act to slow down the diffusion. However, diffusion within the bulk is not the only rate limiting process. Once the short chains reach the surface, an energy barrier must be overcome which is associated with the adhesion energy of the chain to other chains. The two competing processes - evaporation and enrichment determine if there is a net excess or depletion of oligomers at the surface. For the evaporation process, the vapor pressure of the oligomer must be considered; while for enrichment, the molecular weight is important.

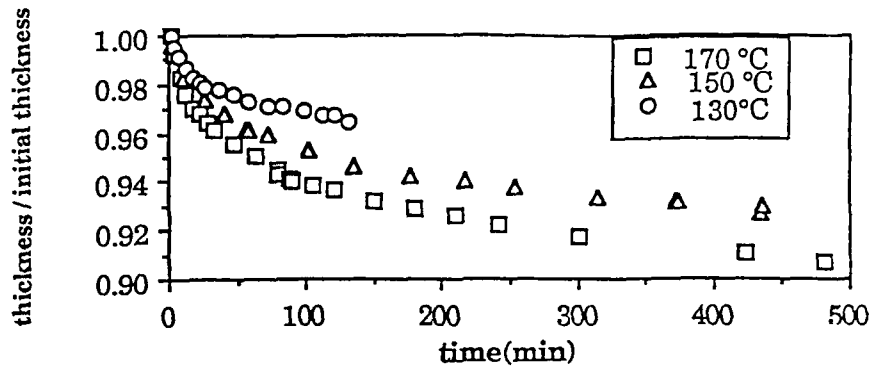


Figure 1. Ratio of film thickness to the initial film thickness for a DP(720,20%):PS(910000) blend at 130°C, 150°C and 170°C.

NEUTRON REFLECTIVITY

New neutron reflectivity measurements were performed on two blends: In the first experiment, the Mw of the deuterated oligomer was 720 while in the second the Mw was 9600. In both cases the Mw of the protonated polymer was 910k. In order to maximize the surface excess of oligomers^[1,3], its weight fraction in both blends was 0.50. Since the initial Tg is lower for the Mw=720 blend, the annealing temperature (T) was adjusted to keep T-Tg roughly the same for the two cases. Fig. 2a presents the experimental values of Rk_z^4 for the DPS(720):PS(910k) sample before and after annealing at 103°C for 410 minutes. Similarly, figure 3a corresponds to a DPS(9k):PS(910k) sample before and after annealing at 145°C for 12 hours.

The function Rk_z^4 , presented in Fig. 2, is quite informative because at large k_z

$$\frac{1}{\pi^2} R k_z^4 = D + 2 \sum_{i,j; b_j} \left[\left(\frac{b}{V} \right)_i - \left(\frac{b}{V} \right)_{i-1} \right] \left[\left(\frac{b}{V} \right)_j - \left(\frac{b}{V} \right)_{j-1} \right] \cos \left[2 \sum_{i=1}^j k_i z_i \right] \quad [1]$$

where

$$D = \sum_i \left[\left(\frac{b}{V} \right)_i - \left(\frac{b}{V} \right)_{i-1} \right]^2 \quad [2]$$

The depth profile is approximated by a histogram formed by a series of slabs with thickness z_i and scattering amplitude per unit volume $(b/V)_i$. For a homogeneous melt, Rk_z^4 oscillates around a constant value of D which is characteristic of the scattering length densities at the front and back interface of the film.

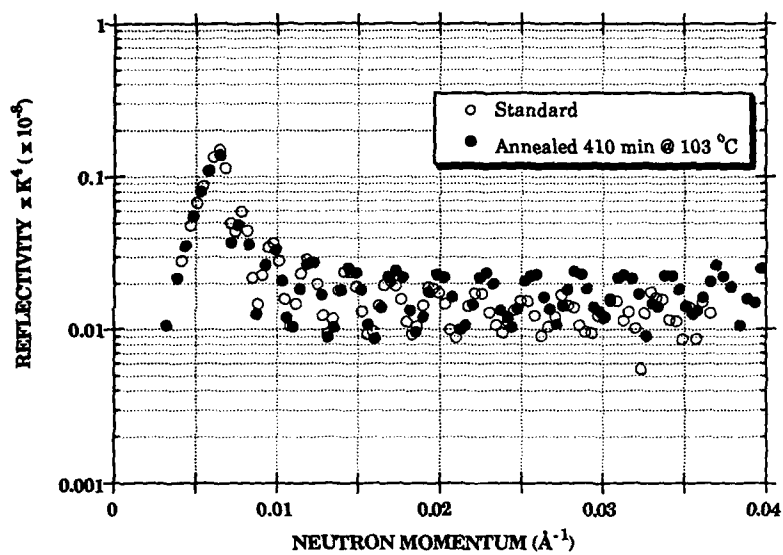


Figure 2a. Rk_z^4 for a DPS(720)PS(910k) blend before and after annealing.

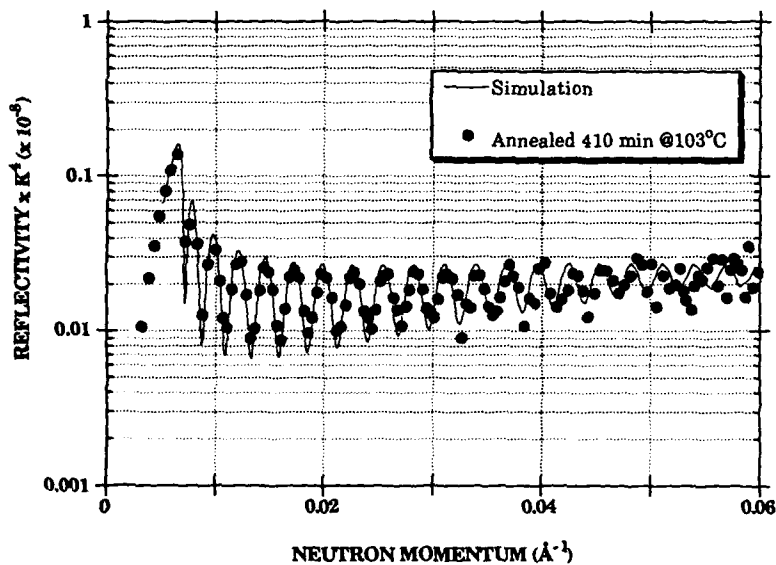


Figure 2b. Rk_z^4 for the annealed DPS(720)PS(910k) blend. Model profile: 12% enhancement of the oligomer at the surface, for a thickness of 25Å. Total polymer thickness 1085Å.

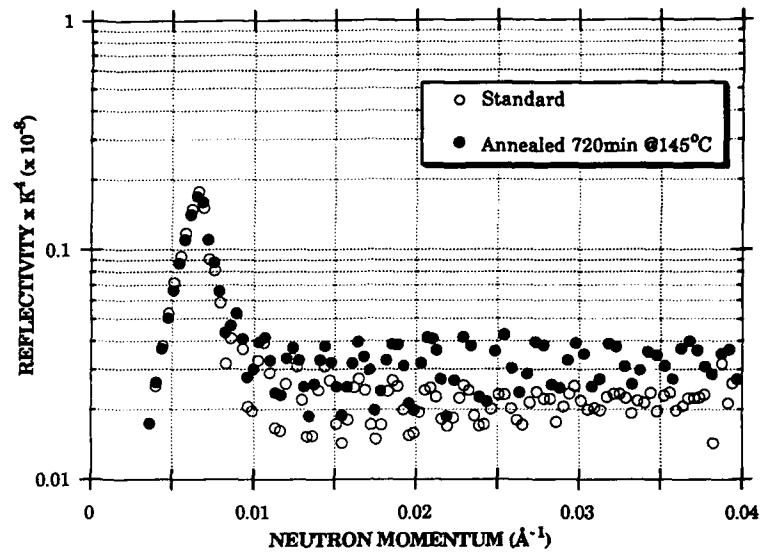


Figure 3a. Rk_z^4 for a DPS(9600)PS(910k) blend before and after annealing.

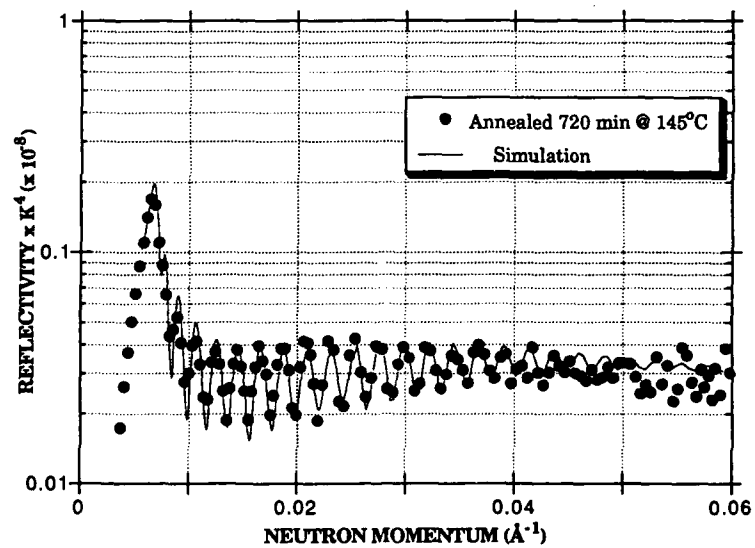


Figure 3b. Rk_z^4 for the annealed DPS(9600)PS(910k) blend. Model profile: 24% enhancement of oligomers at the surface, for a thickness of 30Å. Total polymer thickness 1350Å.

Returning to Figs. 2a and 3a, Rk_z^4 for the annealed samples is greater than that of the unannealed ones, the increase being larger for the higher molecular weight oligomer mixture DPS(9k):PS(910k) -- this gives direct evidence for segregation, since the process increases the number of components present in Eq. (1). One also observes that for the DPS(720) sample, the period of the oscillations in k increases upon annealing. This means that (cfr. the cos term in eq.(1)) the overall thickness decreases of some 2%. In contrast, oscillations of the DPS(9.6k) samples maintain the same period upon annealing.

The experimental results were compared with model scattering length density profiles corresponding to an air/polymer/silicon sandwich. In all simulations the scattering length density of silicon was taken as $2.08 \times 10^{-6} \text{Å}^{-2}$, that of PS as $1.4 \times 10^{-6} \text{Å}^{-2}$ and that of DPS as $6.5 \times 10^{-6} \text{Å}^{-2}$. For these relatively small enrichments, the quantity that can be more reliably obtained from the data is the surface excess of the volume fraction ϕ of the oligomer

$$Z^* = \int [\phi(z) - \phi(\infty)] dz \quad [3]$$

For the DPS (720):PS samples, the best value is $Z^* = 3 \text{Å}$; for the larger oligomer $Z^* = 7 \text{Å}$. The simulation for the annealed samples, presented in Fig. 2b and 3b, was done basically with a two layer model. The agreement with the present data is such that there is no hope to resolve a more detailed profile. Could the neutron reflectivity data be explained by an entirely different profile such as one in which the oligomer precipitates on the silicon substrate? While the latter model gives a poorer fit to the data, the most convincing test will be an additional experiment, where silicon is substituted with quartz. With this and other experiments in which the instrumental resolution is better controlled and the range of k further extended, we should soon be able to provide a more detailed profile. It is our hope that a parallel development of the theory would enable to adequately test such results.

ACKNOWLEDGEMENTS

The work at Argonne was performed under the auspices of the U.S. Department of Energy, Division of Materials Sciences, Office of Basic Energy Sciences, under Contract W-31-109-ENG-38; the work at University of Massachusetts was supported by NSF-DMR polymer program.

REFERENCES

1. I. Schmidt and K. Binder *J. Phys.* 79, 1631 (1985).
2. R. A. L. Jones, E. J. Kramer, M. H. Rafailovich, J. Sokolov and S. A. Schwarz, *Phys. Rev. Lett.* 62, 280 (1989)
3. A. Hariharan, S. K. Kumar and T. P. Russell, submitted *Macromolecules*.
4. R. D. Goldblatt, G. J. Scilla, J. M. Park, J. F. Johnson and S. J. Huang, *J. App. Polym. Sci.* 35, 2075 (1988).
5. G. P. Felcher, R. O. Hilleke, R. K. Crawford, J. Haumann, R. Kleb and G. Ostowski, *Rev. Sci. Inst.* 58, 609 (1987).
6. T. G. Fox and S. Loshaek, *J. Polym. Sci.* 15, 371 (1955).

Author Index

- Abeles, B., 449
 Aggarwal, S.L., 469
 Anastasiadis, S.H., 139, 145
 Ankner, J.F., 109
 Ashley, C.S., 355
 Axe, John D., 3

 Beech, F., 187
 Berk, N.F., 409, 415
 Birtcher, R.C., 437
 Biswas, R., 361
 Black, D.R., 421
 Borchers, J., 133
 Bouchard, A.M., 361
 Bowman, Jr., Robert C., 331
 Bradley, K.F., 403
 Bradshaw, J., 127
 Brinker, C.J., 355, 379
 Brown, K., 373
 Buehrer, W., 219
 Buyers, William J.L., 379

 Calderon, Hector, 255
 Caudron, Rene, 243
 Cava, R.J., 187
 Cerri, Alberto, 267
 Chen, S-H., 403
 Chen, Sow-Hsin, 103
 Choi, C.S., 293
 Chou, Henry, 237
 Cline, J.P., 421
 Composto, Russell J., 485
 Cox, Sherman D., 367
 Crow, M.L., 193

 David, W.I.F., 41, 203
 Dierker, S.B., 427, 433
 DiNardo, R., 127
 Dmowski, W., 75
 Dosch, Helmut, 211
 Downing, R. Gregory, 323, 331
 Drake, J.M., 449
 Du, R., 133
 Dudley, M., 55
 Dura, J.A., 109

 Eastman, J.A., 87
 Edge, Ronald, 175
 Egami, T., 75
 Epperson, J.E., 87, 273
 Erwin, R.W., 133
 Ewen, B., 457

 Faber, Jr., J., 195, 437

 Fan, Y.B., 397
 Farago, B., 355, 457
 Farnoux, B., 95
 Felcher, Gian P., 103, 485
 Fetters, L.J., 457
 Finel, Alphonse, 243
 Fluss, M.J., 231
 Flynn, C.P., 109, 133
 Fu, Bo, 193
 Furdyna, J.K., 115

 Gerhardt, R A., 421
 Giebultowicz, T.M., 115
 Glinka, C.J., 409, 415, 449
 Godfrin, H., 373
 Goff, J.P., 373
 Gompf, F., 361
 Gray III, G.T., 261
 Györfy, B.L., 121

 Haile, Sossina M., 81
 Haller, W., 409
 Han, Charles C., 469, 479
 Hargis, I. Glen, 469
 Hasegawa, Hirokazu, 469
 Hashimoto, Takeji, 469
 Hayes, W., 373
 Hayter, John B., 27
 Heiming, A., 161
 Heuser, Brent J., 273
 Hilleke, Russ O., 103
 Hippsley, C.A., 317
 Hitterman, R.L., 195
 Holden, T.M., 305
 Homer, Vicki, 175
 Hossain, T.Z., 323
 Howell, R.H., 231
 Huang, J.S., 449, 457
 Hutchings, M.T., 317, 373

 Janot, Chr., 75
 Jemian, P.R., 421
 Johnson, C., 127
 Johnson, D.D., 121, 225, 231
 Johnson, J.W., 449
 Jorgensen, J.D., 75

 Kamitakahara, W.A., 361
 Karim, Alamgir, 485
 Kim, H., 397
 Kim, Hongdoo, 479
 King, J.S., 273
 Kirchner, Stefan, 211
 Klosowski, P., 115
 Knudsen, John F., 331

- Kostorz, Gernot, 219, 255, 267
 Krawitz, Aaron D., 281
 Krueger, S., 61, 421
 Kupperman, D.S., 195

 Larson, Allen C., 337
 Lashmore, D., 127
 Lavine, J.P., 323
 Lawson, A.C., 261
 Liao, Y.X., 87
 Lin, M.Y., 449
 Long, G.G., 61, 421
 Low, K.S., 311
 Ludtka, G.M., 305
 Luo, H., 115

 MacEwen, S.R., 305
 Majkrzak, C.F., 109, 127, 139, 145
 Majumdar, S., 195
 Mansour, Abdelkader, 485
 Matheny, A., 109
 McGuire, T.R., 193
 Melamud, Mordechai, 385
 Meuffels, P., 181
 Mills, G., 311
 Moini, Ahmad, 391
 Moss, S.C., 237
 Mostoller, Mark, 237
 Mueller, M.H., 437

 Nakatani, Alan I., 479
 Narayanasamy, A., 87
 Neumann, D.A., 109, 127, 397
 Nicholson, D.M., 225, 231
 Nicol, Jacqueline M., 367, 397
 Nunes, A.C., 193

 Olivier, B.J., 355

 Page, John H., 379
 Page, R.A., 61
 Passell, L., 127
 Peisl, Johann, 211
 Penfold, J., 151
 Petry, W., 161
 Pickart, S.J., 193
 Pinnavaia, Thomas J., 391, 397
 Pinski, F.J., 121, 225, 231
 Pinto, Haim, 385
 Pörschke, E., 181
 Prask, H.J., 293
 Price, David L., 345
 Priesmeyer, H.G., 299
 Prince, E., 81
 Pynn, Roger, 15

 Rabolt, John F., 103
 Radler, Michael J., 67
 Rainey, V., 317
 Reinhard, L., 219
 Rhyne, J.J., 115, 133
 Richardson, Jr., J.W., 437
 Richter, D., 355, 457
 Root, John H., 305, 379
 Rupp, B., 181
 Rush, J.J., 127, 367, 397
 Russell, J.B., 323
 Russell, T.P., 139, 145

 Salamon, M.B., 133
 Salinas-Rodriguez, A., 305
 Samarth, N., 115
 Sander, L.C., 409, 415
 Santoro, A., 187
 Sarfati, Maurice, 243
 Satija, S.K., 127, 139, 145
 Schaefer, Dale W., 355, 379
 Schoenfeld, Bernd, 219, 267
 Schröder, J., 299
 Schwahn, D., 443
 Schweika, Werner, 231, 249
 Seeger, P., 355
 Shaked, Hagai, 385
 Shapiro, S.M., 237
 Shinde, S., 193
 Shivashankar, S.A., 193
 Siegel, R.W., 87
 Singh, J.P., 195
 Sinha, S.K., 449
 Sluiter, M., 225
 Solal, Francine, 243
 Solin, S.A., 397
 Staunton, J.B., 121
 Stein, Richard S., 485
 Stocks, G.M., 121, 225, 231
 Stroeve, Pieter, 103
 Stucky, Galen D., 367
 Suck, J.B., 361
 Summerfield, G.C., 273

 Thiyagarajan, P., 391, 403
 Toby, B.H., 75
 Trampenau, J., 161
 Trevino, S.F., 397
 Turchi, P.E.A., 225, 231

 Udovic, Terrence J., 367

 Vergamini, Phillip J., 337

 Wachs, A.L., 231
 Wada, N., 397
 Webster, G.A., 311
 Webster, P.J., 311
 Wenk, Hans-Rudolf, 337
 White, J.W., 87

Wiltzius, P., 427, 433
Wise, S.A., 415
Wright, Albert F., 267
Wu, Wen-Li, 475
Wuensch, B.J., 81

Zabel, H., 109
Zenner, G.P., 323

Subject Index

- ab-initio method, 121
- adsorption of surfactants, 151
- Advanced Neutron Source, 27
- aerogels, 355
- aging kinetics, 267
- air-water interface, 151
- alloys, 237
 - disordered, 121
 - magnetic, 121
 - substitutional, 121
 - transition metal, 243
- amorphization, 437
 - semiconductor, 361
- analytic expressions, 409
- anion displacements, 81
- atomic pair distribution, 75

- backscattering, 35
- beam tubes, 29
- bicontinuous structure, 409
- binary
 - fluids, 427
 - interaction parameter, 469
- bonded phases, 415
- bonding lengths, 181
- boron (10B) distribution, 331
- bubbles, 443

- capillary condensation, 449
- catalysts, 7
- central peaks, 171
- ceramic, 421
- chemical adsorbates, 415
- chord lengths, 409
- cluster, 373
- Cluster Variation Method, 225
- cold neutrons, 3, 28
- computer models, 361, 409
- concentration fluctuations, 121
- condensed matter physics, 3
- conformation, 475
- contrast variation, 10, 443
- cracked test specimen, 317
- critical fields, 133

- defective anions, 373
- deuterium labeled, 475
- diffractometers, 32
- diffuse neutron scattering, 32, 219, 225, 249, 373
- dislocations, 273
- dynamic scattering, 479

- effective cluster interactions, 231
- elastic neutron scattering, 181
- electron-phonon interaction, 237
- electronic structure, 121, 225, 231
- energy-dispersive neutron diffraction, 294
- engineering materials, 281
- environmental dependence of the moments, 121
- epitaxial, 133
- epoxies, 475
- evaporation, 485
- experimental facilities, 28

- fast-ion conducting, 81
- fatigue cycling, 317
- Fermi chopper, 301
- fermiology, 231
- ferroelastic transition, 203
- Fourier spectroscopy, 301
- fractons, 355

- glasses, 345
 - porous, 427, 433
- grain boundaries, 8, 443

- heat-treatment condition, 261
- helium gas density, 443
- high
 - resolution studies, 41
 - temperature superconductors, 7
- hot neutrons, 4, 28

- inelastic
 - neutron scattering, 345, 367, 397
 - spectrometers, 32
- interface, 22, 139, 151
- interfacial magnetism, 109
- ionic ordering, 81
- isotope separation, 35
- isotopic labeling, 3, 469

- kinetics, 257
- KKR-CPA, 121, 231
- Kohn anomaly, 237

- Langmuir-Blodgett films, 103

- lattice
 - mismatch, 255
 - parameter, 261
- leveled wave method, 409
- liquid chromatography, 415
- liquids, 345
- local chemical environment, 121
- magnetic
 - alloys and multilayers, 121
 - order, 8
 - scattering, 8
- magnetoelasticity, 133
- material degradation, 443
- materials analysis, 32
- mathematical model, 409
- metal films, 127
- microporous particles, 415
- microstructure, 421, 449, 469
- molecular
 - beam epitaxy (MBE), 109, 115
 - networks, 475
- Monte Carlo simulation, 331
- multilayers, 127
- multiple small angle neutron scattering (MSANS), 61
- neutron
 - activation analysis, 25
 - bombardment, 437
 - depolarization, 193
 - depth profiling (NDP), 25, 34, 323, 331
 - diffraction, 83, 115, 195, 286, 293, 299, 305, 311, 317, 345, 443
 - guide hall, 28
 - radiography, 24
 - reaction, 323
 - reflection, 8, 95, 103, 127, 139, 145, 485
 - scattering, 15, 27, 175, 361, 379, 475
 - spin echo, 35, 355, 457
 - strain scanner, 311
 - topography, 55
- nonlinear optical materials, 367
- normal mode analysis, 397
- nuclear fuel, 373
- nucleation, 255
- order-disorder transition, 145
- oxygen
 - and aluminum ordering, 261
 - content, 181
- pair
 - correlation functions, 121
 - interaction energies, 219
- parallel electron microscopy, 261
- phase
 - diagrams, 243
 - separation, 267
 - transitions, 41
- phonon dispersion, 163, 237
- polarization
 - analysis, 32
 - relaxation, 175
- polarized-neutron
 - reflectometry, 109
- polyisoprene star, 457
- pore sizes, 409
- porous media, 449
- powder diffraction, 6, 19, 32, 41, 67, 261
 - high resolution, 203
- precursors, 171
- preferred orientation, 337
- pulsed neutron sources, 4, 151, 287, 337
- quasi-elastic neutron scattering, 459
- railway rail, 311
- random phase approximation (RPA), 457, 475
- reactor, 4
- real-time crystallography, 41
- reflectometer, 151
- residual stress, 7, 20, 196, 281, 300, 305, 311
- Rietveld profile refinement, 67, 81, 181, 437
- rod-like scattering structures, 273
- rotational barrier, 397
- shear induced phase behavior, 479
- short range order (SRO), 219, 225, 231, 243
- SIMS, 323
- sintering, 61
- small angle
 - neutron scattering (SANS), 7, 17, 32, 61, 255, 267, 273, 391, 401, 409, 415, 421, 427, 433, 443, 449, 469
 - x-ray scattering, 421
- sol gel, 421
 - glasses, 433

solid state reactivity of
 x-ray sensitive single
 crystals, 55
spectral dimension, 355, 358
specular reflection, 151
spinodal decomposition, 403
star-branched polymers, 457
static response function, 121
steady state, 287
strain radiography, 21
structural studies, 187
structure, 181
superconducting copper
 oxides, 187
superconductivity, 184
SUPREM computer codes, 331
surface enrichment, 485
surfaces, 22, 95, 151

texture, 21, 337
thermal
 diffuse scattering (TDS),
 67
 expansion, 385
thin films, 145
time-of-flight (TOF), 299,
 337
transmutation and activation,
 neutron, 9
TRIM computer code, 331
two-phase microstructures,
 409

ultracold neutron facility,
 35

vibrational spectroscopy,
 361, 367

x-ray topography, 55

Formula and Compound Index

- a-Ge:H, 361
 a-SiC:H, 361
 AEROGEL, 379
 Al_2O_3 , 61
 ALPO-5, 367

 B, 323
 $Bi_{2.2}Sr_{1.7}CaCu_2O_{8+\delta}$, 193

 CAB-O-SIL, 379
 $CaCO_3$, 339
 cadmium Arachidate (CdA), 103
 catalysts, 391
 $Cd_{1-x}Mn_xSe$, 115, 117
 clay, 391
 Cu_3Zn , 219
 Cu-Zn, 225

 D_2 , 273
 diblock copolymers, 139
 Dy, 133

 Er, 133
 $ErBa_2Cu_3O_x$, 181
 $Fe_{0.8}Al_{10.2}$, 249
 fluorapatite, $Ca_5F(PO_4)_3$, 340
 fossil bone, 340
 fused quartz, 379

 glass pore, 409
 graphite, 385
 H_2 , 127
 HF , 161
 $Hg_{0.7}Cd_{0.3}Te$, 331
 HNO_3 -graphite intercalates,
 385
 hyperstoichiometric uranium
 dioxide - UO_2 , 373

 KD_2PO_4 , 175

 $La_{1.9}Ca_{1.1}Cu_2O_6$, 187
 $La_{1.9}Sr_{1.1}Cu_2O_{6+\delta}$, 187
 $LaNbO_4$, 203
 layered silicates, 397

 micelle, 403
 muscovite, 339
 NbO_x , 212, 213
 Ni-Al-Mo alloys, 255
 Ni-Cr, 231
 Ni-Ti, 267

 para-nitroaniline, 267
 Pd, 273

 pillared clays, 391
 poly(vinylmethylether), 479
 polybutadiene, 479
 blends, 469
 polymer blends, 479, 485
 polymethylmethacrylate, 139
 polystyrene, 139, 479
 PTS, 55
 pyrochlore, 81
 pyrene, 55

 Si, 323, 331
 SiC/Al composite, 288
 silica
 aerogels, 355
 controlled pore glasses, 409
 ion implant, 331
 porous, 421
 sol, 391
 SiO_2 (quartz), 339
 films, 332
 sodium dodecyl, sulfate (SDS),
 403
 sol, 391

 tetramethylammonium
 montmorillonite, 397
 Ti, 161
 Ti-8.6 wt.% Al, 261
 $Tl_2Ba_2CaCu_2O_8$, 78
 trimethylammonium vermiculite,
 397

 U-0.75 wt% Ti ("U-3/4Ti"), 295
 U-alloys, 305
 U_3Si , 437
 U_3Si_2 , 437
 UO_2 , 373

 Vycor, 401, 449

 ω -phase, 161, 214
 WC/Ni cemented carbide
 composites, 290

 Y/Gd interface, 109
 $Y_2(Zr_{0.6}Ti_{0.4})_2O_7$, 81
 $YBa_2Cu_3O_{7-\delta}$, 193, 195

 zeolites, 7, 41
 ZnSe/MnSe multilayer, 118
 ZnSe/MnSe superlattices, 116
 Zr, 116

MATERIALS RESEARCH SOCIETY SYMPOSIUM PROCEEDINGS

ISSN 0272 - 9172

- Volume 1—Laser and Electron-Beam Solid Interactions and Materials Processing, J. F. Gibbons, L. D. Hess, T. W. Sigmon, 1981, ISBN 0-444-00595-1
- Volume 2—Defects in Semiconductors, J. Narayan, T. Y. Tan, 1981, ISBN 0-444-00596-X
- Volume 3—Nuclear and Electron Resonance Spectroscopies Applied to Materials Science, E. N. Kaufmann, G. K. Shenoy, 1981, ISBN 0-444-00597-8
- Volume 4—Laser and Electron-Beam Interactions with Solids, B. R. Appleton, G. K. Celler, 1982, ISBN 0-444-00693-1
- Volume 5—Grain Boundaries in Semiconductors, H. J. Leamy, G. E. Pike, C. H. Seager, 1982, ISBN 0-444-00697-4
- Volume 6—Scientific Basis for Nuclear Waste Management IV, S. V. Topp, 1982, ISBN 0-444-00699-0
- Volume 7—Metastable Materials Formation by Ion Implantation, S. T. Picraux, W. J. Choyke, 1982, ISBN 0-444-00692-3
- Volume 8—Rapidly Solidified Amorphous and Crystalline Alloys, B. H. Kear, B. C. Giessen, M. Cohen, 1982, ISBN 0-444-00698-2
- Volume 9—Materials Processing in the Reduced Gravity Environment of Space, G. E. Rindone, 1982, ISBN 0-444-00691-5
- Volume 10—Thin Films and Interfaces, P. S. Ho, K.-N. Tu, 1982, ISBN 0-444-00774-1
- Volume 11—Scientific Basis for Nuclear Waste Management V, W. Lutze, 1982, ISBN 0-444-00725-3
- Volume 12—In Situ Composites IV, F. D. Lemkey, H. E. Cline, M. McLean, 1982, ISBN 0-444-00726-1
- Volume 13—Laser-Solid Interactions and Transient Thermal Processing of Materials, J. Narayan, W. L. Brown, R. A. Lemons, 1983, ISBN 0-444-00788-1
- Volume 14—Defects in Semiconductors II, S. Mahajan, J. W. Corbett, 1983, ISBN 0-444-00812-8
- Volume 15—Scientific Basis for Nuclear Waste Management VI, D. G. Brookins, 1983, ISBN 0-444-00780-6
- Volume 16—Nuclear Radiation Detector Materials, E. E. Haller, H. W. Kraner, W. A. Higinbotham, 1983, ISBN 0-444-00787-3
- Volume 17—Laser Diagnostics and Photochemical Processing for Semiconductor Devices, R. M. Osgood, S. R. J. Brueck, H. R. Schlossberg, 1983, ISBN 0-444-00782-2
- Volume 18—Interfaces and Contacts, R. Ludeke, K. Rose, 1983, ISBN 0-444-00820-9
- Volume 19—Alloy Phase Diagrams, L. H. Bennett, T. B. Massalski, B. C. Giessen, 1983, ISBN 0-444-00809-8
- Volume 20—Intercalated Graphite, M. S. Dresselhaus, G. Dresselhaus, J. E. Fischer, M. J. Moran, 1983, ISBN 0-444-00781-4
- Volume 21—Phase Transformations in Solids, T. Tsakalakos, 1984, ISBN 0-444-00901-9
- Volume 22—High Pressure in Science and Technology, C. Homan, R. K. MacCrone, E. Whalley, 1984, ISBN 0-444-00932-9 (3 part set)
- Volume 23—Energy Beam-Solid Interactions and Transient Thermal Processing, J. C. C. Fan, N. M. Johnson, 1984, ISBN 0-444-00903-5
- Volume 24—Defect Properties and Processing of High-Technology Nonmetallic Materials, J. H. Crawford, Jr., Y. Chen, W. A. Sibley, 1984, ISBN 0-444-00904-3
- Volume 25—Thin Films and Interfaces II, J. E. E. Baglin, D. R. Campbell, W. K. Chu, 1984, ISBN 0-444-00905-1

MATERIALS RESEARCH SOCIETY SYMPOSIUM PROCEEDINGS

- Volume 26—Scientific Basis for Nuclear Waste Management VII, G. L. McVay, 1984, ISBN 0-444-00906-X
- Volume 27—Ion Implantation and Ion Beam Processing of Materials, G. K. Hubler, O. W. Holland, C. R. Clayton, C. W. White, 1984, ISBN 0-444-00869-1
- Volume 28—Rapidly Solidified Metastable Materials, B. H. Kear, B. C. Giessen, 1984, ISBN 0-444-00935-3
- Volume 29—Laser-Controlled Chemical Processing of Surfaces, A. W. Johnson, D. J. Ehrlich, H. R. Schlossberg, 1984, ISBN 0-444-00894-2
- Volume 30—Plasma Processing and Synthesis of Materials, J. Szekely, D. Apelian, 1984, ISBN 0-444-00895-0
- Volume 31—Electron Microscopy of Materials, W. Krakow, D. A. Smith, L. W. Hobbs, 1984, ISBN 0-444-00898-7
- Volume 32—Better Ceramics Through Chemistry, C. J. Brinker, D. E. Clark, D. R. Ulrich, 1984, ISBN 0-444-00898-5
- Volume 33—Comparison of Thin Film Transistor and SOI Technologies, H. W. Lam, M. J. Thompson, 1984, ISBN 0-444-00899-3
- Volume 34—Physical Metallurgy of Cast Iron, H. Fredriksson, M. Hillerts, 1985, ISBN 0-444-00938-8
- Volume 35—Energy Beam-Solid Interactions and Transient Thermal Processing/1984, D. K. Biegelsen, G. A. Rozgonyi, C. V. Shank, 1985, ISBN 0-931837-00-6
- Volume 36—Impurity Diffusion and Gettering in Silicon, R. B. Fair, C. W. Pearce, J. Washburn, 1985, ISBN 0-931837-01-4
- Volume 37—Layered Structures, Epitaxy, and Interfaces, J. M. Gibson, L. R. Dawson, 1985, ISBN 0-931837-02-2
- Volume 38—Plasma Synthesis and Etching of Electronic Materials, R. P. H. Chang, B. Abeles, 1985, ISBN 0-931837-03-0
- Volume 39—High-Temperature Ordered Intermetallic Alloys, C. C. Koch, C. T. Liu, N. S. Stoloff, 1985, ISBN 0-931837-04-9
- Volume 40—Electronic Packaging Materials Science, E. A. Giess, K.-N. Tu, D. R. Uhlmann, 1985, ISBN 0-931837-05-7
- Volume 41—Advanced Photon and Particle Techniques for the Characterization of Defects in Solids, J. B. Roberto, R. W. Carpenter, M. C. Wittels, 1985, ISBN 0-931837-06-5
- Volume 42—Very High Strength Cement-Based Materials, J. F. Young, 1985, ISBN 0-931837-07-3
- Volume 43—Fly Ash and Coal Conversion By-Products: Characterization, Utilization, and Disposal I, G. J. McCarthy, R. J. Lauf, 1985, ISBN 0-931837-08-1
- Volume 44—Scientific Basis for Nuclear Waste Management VIII, C. M. Jantzen, J. A. Stone, R. C. Ewing, 1985, ISBN 0-931837-09-X
- Volume 45—Ion Beam Processes in Advanced Electronic Materials and Device Technology, B. R. Appleton, F. H. Eisen, T. W. Sigmon, 1985, ISBN 0-931837-10-3
- Volume 46—Microscopic Identification of Electronic Defects in Semiconductors, N. M. Johnson, S. G. Bishop, G. D. Watkins, 1985, ISBN 0-931837-11-1
- Volume 47—Thin Films: The Relationship of Structure to Properties, C. R. Aita, K. S. SreeHarsha, 1985, ISBN 0-931837-12-X
- Volume 48—Applied Materials Characterization, W. Katz, P. Williams, 1985, ISBN 0-931837-13-8
- Volume 49—Materials Issues in Applications of Amorphous Silicon Technology, D. Adler, A. Madan, M. J. Thompson, 1985, ISBN 0-931837-14-6

MATERIALS RESEARCH SOCIETY SYMPOSIUM PROCEEDINGS

- Volume 50—Scientific Basis for Nuclear Waste Management IX, L. O. Werme, 1986, ISBN 0-931837-15-4
- Volume 51—Beam-Solid Interactions and Phase Transformations, H. Kurz, G. L. Olson, J. M. Poate, 1986, ISBN 0-931837-16-2
- Volume 52—Rapid Thermal Processing, T. O. Sedgwick, T. E. Seidel, B.-Y. Tsaur, 1986, ISBN 0-931837-17-0
- Volume 53—Semiconductor-on-Insulator and Thin Film Transistor Technology, A. Chiang, M. W. Geis, L. Pfeiffer, 1986, ISBN 0-931837-18-9
- Volume 54—Thin Films—Interfaces and Phenomena, R. J. Nemanich, P. S. Ho, S. S. Lau, 1986, ISBN 0-931837-19-7
- Volume 55—Biomedical Materials, J. M. Williams, M. F. Nichols, W. Zingg, 1986, ISBN 0-931837-20-0
- Volume 56—Layered Structures and Epitaxy, J. M. Gibson, G. C. Osbourn, R. M. Tromp, 1986, ISBN 0-931837-21-9
- Volume 57—Phase Transitions in Condensed Systems—Experiments and Theory, G. S. Cargill III, F. Spaepen, K.-N. Tu, 1987, ISBN 0-931837-22-7
- Volume 58—Rapidly Solidified Alloys and Their Mechanical and Magnetic Properties, B. C. Giessen, D. E. Polk, A. I. Taub, 1986, ISBN 0-931837-23-5
- Volume 59—Oxygen, Carbon, Hydrogen, and Nitrogen in Crystalline Silicon, J. C. Mikkelsen, Jr., S. J. Pearton, J. W. Corbett, S. J. Pennycook, 1986, ISBN 0-931837-24-3
- Volume 60—Defect Properties and Processing of High-Technology Nonmetallic Materials, Y. Chen, W. D. Kingery, R. J. Stokes, 1986, ISBN 0-931837-25-1
- Volume 61—Defects in Glasses, F. L. Galeener, D. L. Griscom, M. J. Weber, 1986, ISBN 0-931837-26-X
- Volume 62—Materials Problem Solving with the Transmission Electron Microscope, L. W. Hobbs, K. H. Westmacott, D. B. Williams, 1986, ISBN 0-931837-27-8
- Volume 63—Computer-Based Microscopic Description of the Structure and Properties of Materials, J. Broughton, W. Krakow, S. T. Pantelides, 1986, ISBN 0-931837-28-6
- Volume 64—Cement-Based Composites: Strain Rate Effects on Fracture, S. Mindess, S. P. Shah, 1986, ISBN 0-931837-29-4
- Volume 65—Fly Ash and Coal Conversion By-Products: Characterization, Utilization and Disposal II, G. J. McCarthy, F. P. Glasser, D. M. Roy, 1986, ISBN 0-931837-30-8
- Volume 66—Frontiers in Materials Education, L. W. Hobbs, G. L. Liedl, 1986, ISBN 0-931837-31-6
- Volume 67—Heteroepitaxy on Silicon, J. C. C. Fan, J. M. Poate, 1986, ISBN 0-931837-33-2
- Volume 68—Plasma Processing, J. W. Coburn, R. A. Gottscho, D. W. Hess, 1986, ISBN 0-931837-34-0
- Volume 69—Materials Characterization, N. W. Cheung, M.-A. Nicolet, 1986, ISBN 0-931837-35-9
- Volume 70—Materials Issues in Amorphous-Semiconductor Technology, D. Adler, Y. Hamakawa, A. Madan, 1986, ISBN 0-931837-36-7
- Volume 71—Materials Issues in Silicon Integrated Circuit Processing, M. Wittmer, J. Stimmell, M. Strathman, 1986, ISBN 0-931837-37-5
- Volume 72—Electronic Packaging Materials Science II, K. A. Jackson, R. C. Pohanka, D. R. Uhlmann, D. R. Ulrich, 1986, ISBN 0-931837-38-3
- Volume 73—Better Ceramics Through Chemistry II, C. J. Brinker, D. E. Clark, D. R. Ulrich, 1986, ISBN 0-931837-39-1
- Volume 74—Beam-Solid Interactions and Transient Processes, M. O. Thompson, S. T. Picraux, J. S. Williams, 1987, ISBN 0-931837-40-5

MATERIALS RESEARCH SOCIETY SYMPOSIUM PROCEEDINGS

- Volume 75—Photon, Beam and Plasma Stimulated Chemical Processes at Surfaces, V. M. Donnelly, I. P. Herman, M. Hirose, 1987, ISBN 0-931837-41-3
- Volume 76—Science and Technology of Microfabrication, R. E. Howard, E. L. Hu, S. Namba, S. Pang, 1987, ISBN 0-931837-42-1
- Volume 77—Interfaces, Superlattices, and Thin Films, J. D. Dow, I. K. Schuller, 1987, ISBN 0-931837-56-1
- Volume 78—Advances in Structural Ceramics, P. F. Becher, M. V. Swain, S. Sōmiya, 1987, ISBN 0-931837-43-X
- Volume 79—Scattering, Deformation and Fracture in Polymers, G. D. Wignall, B. Crist, T. P. Russell, E. L. Thomas, 1987, ISBN 0-931837-44-8
- Volume 80—Science and Technology of Rapidly Quenched Alloys, M. Tenhover, W. L. Johnson, L. E. Tanner, 1987, ISBN 0-931837-45-6
- Volume 81—High-Temperature Ordered Intermetallic Alloys, II, N. S. Stoloff, C. C. Koch, C. T. Liu, O. Izumi, 1987, ISBN 0-931837-46-4
- Volume 82—Characterization of Defects in Materials, R. W. Siegel, J. R. Weertman, R. Sinclair, 1987, ISBN 0-931837-47-2
- Volume 83—Physical and Chemical Properties of Thin Metal Overlayers and Alloy Surfaces, D. M. Zehner, D. W. Goodman, 1987, ISBN 0-931837-48-0
- Volume 84—Scientific Basis for Nuclear Waste Management X, J. K. Bates, W. B. Seefeldt, 1987, ISBN 0-931837-49-9
- Volume 85—Microstructural Development During the Hydration of Cement, L. Struble, P. Brown, 1987, ISBN 0-931837-50-2
- Volume 86—Fly Ash and Coal Conversion By-Products Characterization, Utilization and Disposal III, G. J. McCarthy, F. P. Glasser, D. M. Roy, S. Diamond, 1987, ISBN 0-931837-51-0
- Volume 87—Materials Processing in the Reduced Gravity Environment of Space, R. H. Doremus, P. C. Nordine, 1987, ISBN 0-931837-52-9
- Volume 88—Optical Fiber Materials and Properties, S. R. Nagel, J. W. Fleming, G. Sigel, D. A. Thompson, 1987, ISBN 0-931837-53-7
- Volume 89—Diluted Magnetic (Semimagnetic) Semiconductors, R. L. Aggarwal, J. K. Furdyna, S. von Molnar, 1987, ISBN 0-931837-54-5
- Volume 90—Materials for Infrared Detectors and Sources, R. F. C. Farrow, J. F. Schetzina, J. T. Cheung, 1987, ISBN 0-931837-55-3
- Volume 91—Heteroepitaxy on Silicon II, J. C. C. Fan, J. M. Phillips, B.-Y. Tsaur, 1987, ISBN 0-931837-58-8
- Volume 92—Rapid Thermal Processing of Electronic Materials, S. R. Wilson, R. A. Powell, D. E. Davies, 1987, ISBN 0-931837-59-6
- Volume 93—Materials Modification and Growth Using Ion Beams, U. Gibson, A. E. White, P. P. Pronko, 1987, ISBN 0-931837-60-X
- Volume 94—Initial Stages of Epitaxial Growth, R. Hull, J. M. Gibson, David A. Smith, 1987, ISBN 0-931837-61-8
- Volume 95—Amorphous Silicon Semiconductors—Pure and Hydrogenated, A. Madan, M. Thompson, D. Adler, Y. Hamakawa, 1987, ISBN 0-931837-62-6
- Volume 96—Permanent Magnet Materials, S. G. Sankar, J. F. Herbst, N. C. Koon, 1987, ISBN 0-931837-63-4
- Volume 97—Novel Refractory Semiconductors, D. Emin, T. Aselage, C. Wood, 1987, ISBN 0-931837-64-2
- Volume 98—Plasma Processing and Synthesis of Materials, D. Apelian, J. Szekely, 1987, ISBN 0-931837-65-0

MATERIALS RESEARCH SOCIETY SYMPOSIUM PROCEEDINGS

- Volume 99—High-Temperature Superconductors, M. B. Brodsky, R. C. Dynes, K. Kitazawa, H. L. Tuller, 1988, ISBN 0-931837-67-7
- Volume 100—Fundamentals of Beam-Solid Interactions and Transient Thermal Processing, M. J. Aziz, L. E. Rehn, B. Stritzker, 1988, ISBN 0-931837-68-5
- Volume 101—Laser and Particle-Beam Chemical Processing for Microelectronics, D.J. Ehrlich, G.S. Higashi, M.M. Oprysko, 1988, ISBN 0-931837-69-3
- Volume 102—Epitaxy of Semiconductor Layered Structures, R. T. Tung, L. R. Dawson, R. L. Gunshor, 1988, ISBN 0-931837-70-7
- Volume 103—Multilayers: Synthesis, Properties, and Nonelectronic Applications, T. W. Barbee Jr., F. Spaepen, L. Greer, 1988, ISBN 0-931837-71-5
- Volume 104—Defects in Electronic Materials, M. Stavola, S. J. Pearton, G. Davies, 1988, ISBN 0-931837-72-3
- Volume 105—SiO₂ and Its Interfaces, G. Lucovsky, S. T. Pantelides, 1988, ISBN 0-931837-73-1
- Volume 106—Polysilicon Films and Interfaces, C.Y. Wong, C.V. Thompson, K-N. Tu, 1988, ISBN 0-931837-74-X
- Volume 107—Silicon-on-Insulator and Buried Metals in Semiconductors, J. C. Sturm, C. K. Chen, L. Pfeiffer, P. L. F. Hemment, 1988, ISBN 0-931837-75-8
- Volume 108—Electronic Packaging Materials Science II, R. C. Sundahl, R. Jaccodine, K. A. Jackson, 1988, ISBN 0-931837-76-6
- Volume 109—Nonlinear Optical Properties of Polymers, A. J. Heeger, J. Orenstein, D. R. Ulrich, 1988, ISBN 0-931837-77-4
- Volume 110—Biomedical Materials and Devices, J. S. Hanker, B. L. Giammara, 1988, ISBN 0-931837-78-2
- Volume 111—Microstructure and Properties of Catalysts, M. M. J. Treacy, J. M. Thomas, J. M. White, 1988, ISBN 0-931837-79-0
- Volume 112—Scientific Basis for Nuclear Waste Management XI, M. J. Apter, R. E. Westerman, 1988, ISBN 0-931837-80-4
- Volume 113—Fly Ash and Coal Conversion By-Products: Characterization, Utilization, and Disposal IV, G. J. McCarthy, D. M. Roy, F. P. Glasser, R. T. Hemmings, 1988, ISBN 0-931837-81-2
- Volume 114—Bonding in Cementitious Composites, S. Mindess, S. P. Shah, 1988, ISBN 0-931837-82-0
- Volume 115—Specimen Preparation for Transmission Electron Microscopy of Materials, J. C. Bravman, R. Anderson, M. L. McDonald, 1988, ISBN 0-931837-83-9
- Volume 116—Heteroepitaxy on Silicon: Fundamentals, Structures, and Devices, H.K. Choi, H. Ishiwara, R. Hull, R.J. Nemanich, 1988, ISBN: 0-931837-86-3
- Volume 117—Process Diagnostics: Materials, Combustion, Fusion, K. Hays, A.C. Eckbreth, G.A. Campbell, 1988, ISBN: 0-931837-87-1
- Volume 118—Amorphous Silicon Technology, A. Madan, M.J. Thompson, P.C. Taylor, P.G. LeComber, Y. Hamakawa, 1988, ISBN: 0-931837-88-X
- Volume 119—Adhesion in Solids, D.M. Mattox, C. Batich, J.E.E. Baglin, R.J. Gottschall, 1988, ISBN: 0-931837-89-8
- Volume 120—High-Temperature/High-Performance Composites, F.D. Lemkey, A.G. Evans, S.G. Fishman, J.R. Strife, 1988, ISBN: 0-931837-90-1
- Volume 121—Better Ceramics Through Chemistry III, C.J. Brinker, D.E. Clark, D.R. Ulrich, 1988, ISBN: 0-931837-91-X

MATERIALS RESEARCH SOCIETY SYMPOSIUM PROCEEDINGS

- Volume 122—Interfacial Structure, Properties, and Design, M.H. Yoo, W.A.T. Clark, C.L. Briant, 1988, ISBN: 0-931837-92-8
- Volume 123—Materials Issues in Art and Archaeology, E.V. Sayre, P. Vandiver, J. Druzik, C. Stevenson, 1988, ISBN: 0-931837-93-6
- Volume 124—Microwave-Processing of Materials, M.H. Brooks, I.J. Chabinsky, W.H. Sutton, 1988, ISBN: 0-931837-94-4
- Volume 125—Materials Stability and Environmental Degradation, A. Barkatt, L.R. Smith, E. Verink, 1988, ISBN: 0-931837-95-2
- Volume 126—Advanced Surface Processes for Optoelectronics, S. Bernasek, T. Venkatesan, H. Temkin, 1988, ISBN: 0-931837-96-0
- Volume 127—Scientific Basis for Nuclear Waste Management XII, W. Lutze, R.C. Ewing, 1989, ISBN: 0-931837-97-9
- Volume 128—Processing and Characterization of Materials Using Ion Beams, L.E. Rehn, J. Greene, F.A. Smidt, 1989, ISBN: 1-55899-001-1
- Volume 129—Laser and Particle-Beam Modification of Chemical Processes on Surfaces, A.W. Johnson, G.L. Loper, T.W. Sigmon, 1989, ISBN: 1-55899-002-X
- Volume 130—Thin Films: Stresses and Mechanical Properties, J.C. Bravman, W.D. Nix, D.M. Barnett, D.A. Smith, 1989, ISBN: 1-55899-003-8
- Volume 131—Chemical Perspectives of Microelectronic Materials, M.E. Gross, J. Jasinski, J.T. Yates, Jr., 1989, ISBN: 1-55899-004-6
- Volume 132—Multicomponent Ultrafine Microstructures, L.E. McCandlish, B.H. Kear, D.E. Polk, and R.W. Siegel, 1989, ISBN: 1-55899-005-4
- Volume 133—High Temperature Ordered Intermetallic Alloys III, C.T. Liu, A.J. Taub, N.S. Stoloff, C.C. Koch, 1989, ISBN: 1-55899-006-2
- Volume 134—The Materials Science and Engineering of Rigid-Rod Polymers, W.W. Adams, R.K. Eby, D.E. McLemore, 1989, ISBN: 1-55899-007-0
- Volume 135—Solid State Ionics, G. Nazri, R.A. Huggins, D.F. Shriver, 1989, ISBN: 1-55899-008-9
- Volume 136—Fly Ash and Coal Conversion By-Products: Characterization, Utilization and Disposal V, R.T. Hemmings, E.E. Berry, G.J. McCarthy, F.P. Glasser, 1989, ISBN: 1-55899-009-7
- Volume 137—Pore Structure and Permeability of Cementitious Materials, L.R. Roberts, J.P. Skalny, 1989, ISBN: 1-55899-010-0
- Volume 138—Characterization of the Structure and Chemistry of Defects in Materials, B.C. Larson, M. Ruhle, D.N. Seidman, 1989, ISBN: 1-55899-011-9
- Volume 139—High Resolution Microscopy of Materials, W. Krakow, F.A. Ponce, D.J. Smith, 1989, ISBN: 1-55899-012-7
- Volume 140—New Materials Approaches to Tribology: Theory and Applications, L.E. Pope, L. Fehrenbacher, W.O. Winer, 1989, ISBN: 1-55899-013-5
- Volume 141—Atomic Scale Calculations in Materials Science, J. Tersoff, D. Vanderbilt, V. Vitek, 1989, ISBN: 1-55899-014-3
- Volume 142—Nondestructive Monitoring of Materials Properties, J. Holbrook, J. Bussiere, 1989, ISBN: 1-55899-015-1
- Volume 143—Synchrotron Radiation in Materials Research, R. Clarke, J. Gland, J.H. Weaver, 1989, ISBN: 1-55899-016-X
- Volume 144—Advances in Materials, Processing and Devices in III-V Compound Semiconductors, D.K. Sadana, L. Eastman, R. Dupuis, 1989, ISBN: 1-55899-017-8

Recent Materials Research Society Proceedings listed in the front.

MATERIALS RESEARCH SOCIETY CONFERENCE PROCEEDINGS

Tungsten and Other Refractory Metals for VLSI Applications, Robert S. Blewer, 1986; ISSN 0886-7860; ISBN 0-931837-32-4

Tungsten and Other Refractory Metals for VLSI Applications II, Eliot K. Broadbent, 1987; ISSN 0886-7860; ISBN 0-931837-66-9

Ternary and Multinary Compounds, Satyen K. Deb, Alex Zunger, 1987; ISBN 0-931837-57-X

Tungsten and Other Refractory Metals for VLSI Applications III, Victor A. Wells, 1988; ISSN 0886-7860; ISBN 0-931837-84-7

Atomic and Molecular Processing of Electronic and Ceramic Materials: Preparation, Characterization and Properties, Ilhan A. Aksay, Gary L. McVay, Thomas G. Stoebe, J.F. Wager, 1988; ISBN 0-931837-85-5

Materials Futures: Strategies and Opportunities, R. Byron Pipes, U.S. Organizing Committee, Rune Lagneborg, Swedish Organizing Committee, 1988; ISBN 1-55899-000-3

Tungsten and Other Refractory Metals for VLSI Applications IV, Robert S. Blewer, Carol M. McConica, 1989; ISSN 0886-7860; ISBN 0-931837-98-7

Tungsten and Other Advanced Metals for VLSI/ULSI Applications V, S. Simon Wong, Seiji Furukawa, 1990; ISSN 1048-0854; ISBN 1-55899-086-2

High Energy and Heavy Ion Beams in Materials Analysis, Joseph R. Tesmer, Carl J. Maggiore, Michael Nastasi, J. Charles Barbour, James W. Mayer, 1990; ISBN 1-55899-091-7

Physical Metallurgy of Cast Iron IV, Goro Ohira, Takaji Kusakawa, Eisuke Niyama, 1990; ISBN 1-55899-090-9